EDITED and PUBLISHED quarterly at the *offices of The American Society of* Mechanical Engineers, United Engineering Center, 345 E. 47th St., New York, N. Y. 10017. Cable address, "Mechaneer," New York. Second-class postage paid at New York, N. Y., and at additional mailing offices.
CHANGES OF ADDRESS must be received at Society headquarters seven weeks before they are to be effective. Please send old label and new address.
PRICES: To members, $25.00, annually; to nonmembers, $50.00. Single copies, $15.00 each. Add $1.50 for postage to countries outside the United States and Canada.
STATEMENT from By-Laws. The Society shall not be responsible for statements or opinions advanced in papers or . . . printed in its publications (B 13, Par. 4).

INDEXED by the Engineering Index, Inc.

transactions of the ASME

Published Quarterly by
The American Society of
Mechanical Engineers
Volume 99 • Series C • Number 2
MAY 1977

journal of heat transfer

(Contents continued on page 162)

CONTENTS (CONTINUED)

TECHNICAL NOTES

DISCUSSION

J. W. Ramsey
Department of Mechanical Engineering,
University of Minnesota,
Minneapolis, Minn.

B. P. Gupta
G. R. Knowles
Energy Resources Center,
Honeywell, Inc.,
Minneapolis, Minn.

Experimental Evaluation of a Cylindrical Parabolic Solar Collector

Results are presented for a series of solar collector experiments in which the incident solar flux was concentrated by a single-axis tracking parabolic trough mirror. The concentrated solar flux was directed onto an absorber tube whose axis coincided with the focal axis of the concentrator. The performance of the collector was evaluated using three different absorbers; a black painted tube designed to operate near ambient temperature, a heat pipe which had a selective solar absorber coating applied to its surface, and a heat pipe which had its surface coated with a nonselective black paint. The peak efficiency for the collector in the absence of heat losses is approximately 62 percent when the incoming solar energy is normal to the collector aperture. The heat losses which occurred at elevated temperatures (300°C) decreased the peak efficiencies to 50 and 30 percent, respectively, for the selectively coated and black painted tubes. The experimental results establish the technical feasibility of using parabolic trough collectors for applications requiring thermal energy at temperatures up to 300°C.

Introduction

A number of solar thermal power systems are currently being extensively studied. The function of these systems is to utilize solar energy as a fuel for generating electricity. A parabolic trough solar collector is one device capable of collecting solar energy and delivering it in the form of heated fluid at a temperature high enough for the operation of a steam turbine [1].[1] In this type of collector, the incident solar flux is concentrated by a cylindrical parabolic mirror and is directed onto an absorber tube where the energy is removed in the form of heat. The efficiency of this type of collector is limited by two factors; (*a*) the ability of the system to concentrate and absorb the incident flux (i.e., the optical performance) and (*b*) the heat losses from the absorber tube. The purpose of this study was to evaluate experimentally these factors and to establish the overall performance of a typical cylindrical parabolic solar collector.

The approach used was first to establish the optical performance of the collector by measuring its ability to concentrate and absorb the incident flux in the absence of heat losses. This was accomplished by conducting experiments with the absorber tube operating at near ambient temperature. The next step was to investigate the heat losses from the system as a function of the temperature and radiation surface properties of the absorber. For this part of the investigation the performance of the collector was measured at a series of absorber temperatures between 210 and 300°C. These elevated-temperature experiments were performed for both selectively coated (solar absorptance = 0.91 and infrared emittance = 0.2) and nonselectively coated (solar absorptance and infrared emittance = 0.96) absorber tubes. The tests were conducted at a desert test site at a latitude of 34°N near Phoenix, Arizona. This paper describes the experimental apparatus, the test procedures, and the experimental results.

Experimental Apparatus

The solar collector concept studied in the project is shown schematically in Fig. 1. The actual collector module that was tested is shown in operation in Fig. 2. The incident solar flux is concentrated by the parabolic trough concentrator. The concentrator rotates as shown in Fig. 1 to accomplish single axis tracking of the sun. The cylindrical parabolic trough concentrator of the test module is 1.2 m wide and 4.2 m long. The parabolic contour has a focal length of 19.4 cm or an *f*-number of 0.16. Alzak, anodized aluminum reflector sheeting, is used for the concentrator surface. The solar reflectance of the Alzak was measured and determined to be 0.81. The concentrators are mounted on special trunnions which have their center of rotation at the focal axis of the concentrator. The trunnions are supported by pedestals. The concentrator is rotated about the focal axis by a servomotor acting through a chain drive. The motor is controlled by a sun sensor.

The collected sunlight is concentrated on a 2.54 cm OD absorber tube whose axis coincides with the focal axis of the concentrator. A 10 cm ID glass envelope surrounds the absorber tube. The annular

[1] Numbers in brackets designate References at end of paper.

Contributed by the Heat Transfer Division and presented at the Winter Annual Meeting, New York, N.Y., December 5–10, 1976 of THE AMERICAN SOCIETY OF MECHANICAL ENGINEERS. Revised manuscript received by the Heat Transfer Division December 3, 1976. Paper No. 76-WA/HT-13.

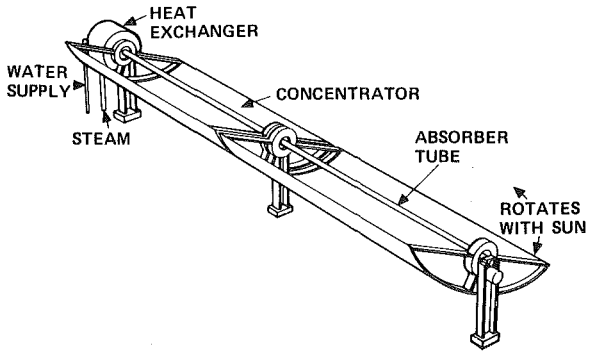

Fig. 1. Solar collector concept

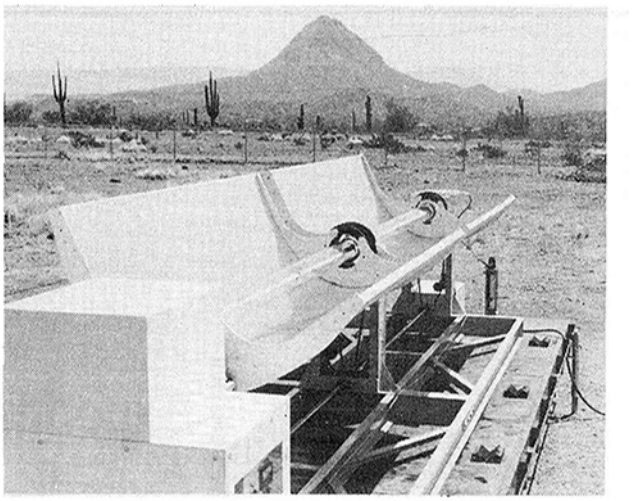

Fig. 2 View of collector operating at the test site

space between the absorber tube and envelope is evacuated to a pressure of approximately 10^{-6} torr to reduce the heat losses from the absorber tube. The absorber tube does not rotate and is supported by the surrounding glass envelope which is rigidly attached to the support pedestals.

Three absorber tubes have been used. The first of these was used only for the optical performance tests and, therefore, was designed to operate near ambient temperature. It consisted of a stainless steel tube sealed at one end. Within the tube, a second tube of smaller diameter was positioned so as to form a concentric annulus. Cooling water was introduced into the central tube and traversed its entire length. At the downstream end of the tube, passages were provided to enable the water to enter the annulus, from which point it flowed back to the end of the tube where it was first introduced. Thus, the central tube and the annulus constituted a counterflow heat exchanger. This arrangement gave rise to a relatively uniform temperature on the surface of the absorber tube.

The water, upon leaving the annulus, passed through mixing baffles. A five-junction differential thermopile was used to measure the difference in water temperature between the inlet and outlet. This temperature difference along with measurements of the water flow rate and water properties was used to evaluate the rate at which heat was absorbed by the system. The flow rate was set to produce a nominal 10°C temperature rise in the water. Three thermocouples were welded to the exposed surface of the absorber to measure its temperature. These indicated that the surface was 13–16°C above the inlet water temperature. Typically, the water inlet temperature was 2–5°C below the ambient temperature. The external surface of the absorber tube was painted with 3M Black Velvet. The absorptance of the paint has been estimated to be 0.95 over the entire solar wavelength range.

The second absorber tube was a stainless steel heat pipe with water as the working fluid.[2] A selective solar absorber surface was applied by Honeywell to the evaporator section of the heat pipe by first electroplating it with bright nickel and then depositing an Al_2O_3-MoO_x-Al_2O_3 (AMA) coating over the nickel. The resulting surface had a solar absorptance of 0.91 and an emittance at 300°C of 0.2. This absorber tube was used to evaluate operational performance up to 300°C.

The third absorber tube was also a heat pipe. However, its surface was coated with a nonselective black paint with a solar absorptance and an infrared emittance of 0.96. This absorber was also used to obtain data at temperatures up to 300°C.

The energy absorbed by the heat pipe absorber tubes was removed and measured using a gas-gap calorimeter. The calorimeter consists of a water-cooled brass collar which fits around the condenser end of the heat pipe. A gap was maintained between the inner surface of the calorimeter and the outer surface of the heat pipe condenser. The heat pipe and calorimeter temperatures are maintained constant for varying heat transfer rates by adjusting the thermal resistance across the gap. This was achieved by supplying an adjustable mixture of helium and argon to the gap. The net heat collected and delivered to the calorimeter was calculated using measured values of the mass flow rate and temperature rise of the calorimeter cooling water and the properties of water. As in the case of the low temperature absorber,

[2] The heat pipe was designed and built by Dynatherm, Inc. of Cockeysville, Md.

Nomenclature

A = geometric factor defined by equation (3)
A_a = aperture area of collector
A_c = area of concentrator end
A_s = obstructed area at the concentrator end
A_1 = composite cross-sectional area of the conducting elements
A_2 = surface area of the absorber tube
C_{op} = system optical constant
e_s = focusing accuracy due to slope errors of concentrators
f = focal length of the concentrator
$F(\alpha)$ = function combining the effects of the incidence angle
$F(\phi)$ = tracking error factor
h = depth of the parabola
k = thermal conductivity
L = length of the conducting elements
Q_{abs} = heat absorbed per unit aperture area per unit time
Q_{dnf} = direct normal solar flux
Q_{loss} = heat loss per unit aperture area per unit time
Q_{out} = net heat delivered per unit aperture area per unit time
r_a = fraction of area of concentrator free from shadowing by glass tube
T_{abs} = temperature of the absorber surface
T_g = temperature of the glass envelope
W_c = width of the concentrator
α = incidence angle
α_s = mean solar absorptance of absorber tube coating
ϵ = emittance of the absorber tube coating
η_{op} = optical efficiency
η_{sys} = total system efficiency
ϕ = tracking angle error
ρ_c = reflectance of concentrator surface
σ = Stefan-Boltzmann constant
τ_g = transmission of glass envelope

a five-junction thermopile was used to measure the temperature rise of the water and mixing chambers were used to insure that bulk temperatures were being measured.

Several thermocouples were welded to the absorber tubes to measure their temperatures. In the case of the heat pipe absorber tubes measurements were made on the evaporator, adiabatic, and condenser zones. The thermocouples on the evaporator were illuminated by the concentrated solar flux which appears to have had some effect on the readings. The thermocouples on the adiabatic zone of the heat pipe measure the vapor temperature in the heat pipe. Although it is slightly below the average absorber surface temperature (approximately 10°C), it is considered to be the most reliable and representative measure of the operating temperature. Therefore this is the value quoted in this paper as the absorber operating temperature.

The experimental collector module was located during the entire test sequence at the facility of Desert Sunshine Exposure Tests, Inc., approximately 30 miles north of Phoenix, Arizona. This site was selected for its long record of clear days, its insolation measuring facilities, and the test site security. Tests were conducted with the collector axis oriented both east-west and north-south. Data recording instruments were housed in a camper located just to the northwest of the collector module.

The direct solar flux was measured using an Eppley Model Normal Incidence Pyrheliometer (NIP). This instrument has a solid angle of acceptance of 5.7 deg. For the purposes of comparison, the total solar flux (diffuse plus direct) was measured with a pyranometer which was directed toward the sun. During the collector tests the ratio of direct to total flux was in the range of 0.75–0.9.

Experimental Results

Data for the directly incident solar flux and the net heat delivered by the collector was obtained to determine the collector efficiency. The efficiency was evaluated as the net heat delivered (measured calorimetrically) divided by the product of the aperture area and the direct normal solar flux (i.e., the solar flux measured normal to the sun). It is important to note that by using this definition for efficiency, the maximum obtainable efficiency is equal to the cosine of the incidence angle, α. This angle is the angle between the normal to the aperture and a ray coming from the center of the solar disk. This definition of the efficiency imposes a penalty owing to nonalignment of the solar rays with the normal to the aperture opening. All collectors which do not track the sun along two axes experience some degree of nonalignment.

The efficiency of the collector operating with each of the three previously described absorber tubes was measured for both east-west and north-south orientations. Data was also obtained on the effects on performance that would be introduced by inaccuracies of tracking.

Performance With Low Temperature Absorber. The tests performed with the first absorber tube configuration were conducted at an operating temperature of approximately 40°C. The complete test results for this operating temperature are presented in reference [2]. Since at the low operating temperature the thermal losses are negligible, these data describe the optical performance of the collector. Fig. 3 presents the collector efficiency as a function of apparent solar time. (Apparent solar time is the time system based on the sun being at its zenith at 1200.) The peak efficiency is seen to be about 62 percent. This measured value is consistent with the product of the efficiencies of the various processes which contribute to the overall efficiency. The component efficiencies were either measured or computed to have the following values: (*a*) reflectance of concentrator surface, 0.81; (*b*) contour focusing accuracy of the concentrator, 0.95; (*c*) transmission of glass envelope, 0.91; (*d*) absorptance of black paint, 0.95; and (*e*) effective fraction of aperture resulting from the glass envelope shadowing the concentrator, 0.94. The product of these component efficiencies is 63 percent. Therefore it is convenient to define a system optical constant, C_{op}, as

$$C_{op} = \rho_c \cdot e_s \cdot \tau_g \cdot \alpha_s \cdot r_a \tag{1}$$

In the east-west orientation the drop-off of the efficiency curve with departure from solar noon is primarily due to the variation of the incidence angle. However, secondary effects also exist which reduce the optical efficiency as the incidence angle increases. The secondary effects which contribute to the lesser efficiency are (*a*) shadows due to obstructions of incoming radiation by supporting structure at the end of the collector; (*b*) losses associated with solar radiation that is reflected from the concentrator but does not reach the absorber tube owing to blockage by structural elements or to its being directed beyond the end of tube; and (*c*) variations in optical properties due to angular effects.

The north-south data presented in Fig. 3 are seen to be relatively flat. This is because for the time of year the data were obtained, the cosine of the incidence angle during the day was always greater than 0.97.

The effects of the incidence angle, α, including secondary effects, can be combined into a function, $F(\alpha)$:

$$F(\alpha) = (1 - A \tan\alpha) \cos\alpha \tag{2}$$

where the term $A \tan\alpha$ expresses the apparent reduction in aperture area due to end losses, blockages, and shadows. The coefficient, A, is a geometric factor determined by the specific collector design and is given by

$$A = \frac{W_c(f + h) + A_s - A_c}{A_a} \tag{3}$$

The parameters in equation (3) are defined in Fig. 4. Equation (2) does not include variations in optical properties due to angular effects. For the collector under consideration, A is estimated to be 0.23.

For the case of perfect one-axis tracking, the heat absorbed per unit aperture area and unit time will be given by the product $Q_{dnf} \times C_{op} \times F(\alpha)$. Where Q_{dnf} is the direct normal solar flux. If sun tracking errors exist, these can be accounted for by the introduction of an empirical tracking error factor $F(\phi)$. The pointing angle error or tracking angle error, ϕ, is defined in the inset of Fig. 6.

Therefore the heat absorbed per unit aperture area per unit time, Q_{abs}, is

$$Q_{abs} = Q_{dnf} \times C_{op} \times F(\alpha) \times F(\phi) \tag{4}$$

The optical efficiency, η_{op} (no heat losses), is then given by

$$\eta_{op} = \frac{Q_{abs}}{Q_{dnf}} \tag{5}$$

Note that in defining the efficiency the direct normal solar flux has been used. This selection has been made since only the direct flux can be concentrated and, therefore, it represents the upper limit of the energy which can be absorbed by the collector. Equation (5) can be rewritten in terms of the various performance parameters as

$$\eta_{op} = C_{op} \times F(\alpha) \times F(\phi) \tag{6}$$

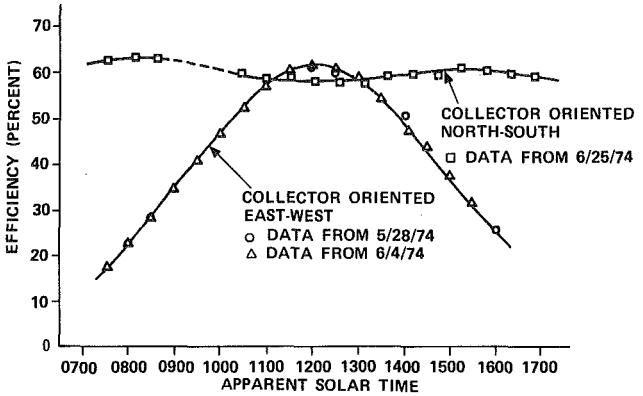

Fig. 3 Optical efficiency versus time of day (40°C operating temperature)

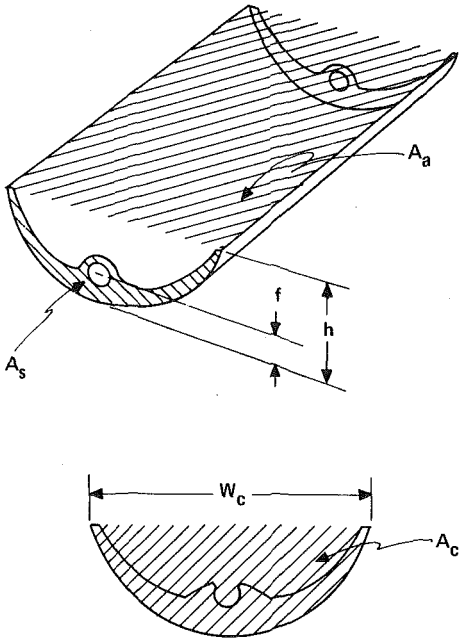

Fig. 4 Concentrator areas and dimensions used in equation (3)

The experimental evaluation of optical efficiency was conducted in two steps. Tests were first performed to establish the efficiency as a function of incidence angle with the tracking carefully aligned (i.e., $F(\phi) = 1$). Next the effects of tracking errors were evaluated by purposely introducing known errors in the tracking. Fig. 5 presents the measured optical efficiency of the collector as a function of the cosine of the incidence angle. Also presented in Fig. 5 is equation (6). It is seen that the efficiency data correlate well as a function of the cosine α, and equation (6) provides a reasonable representation of the results.

Solar collectors with any significant concentration ratio must be able to track the sun in one or more axes of rotation. The better the tracking accuracy that is demanded, the more expensive the tracking and drive mechanism will be. Therefore an experiment was conducted to determine the effect on performance that a small error in the pointing angle will cause. Pointing angle errors were deliberately introduced and the tracking mechanism was set to track the sun with a given amount of error. Fig. 6 shows the correction factor, $F(\phi)$, as a function of pointing angle error. It is seen from the data that there

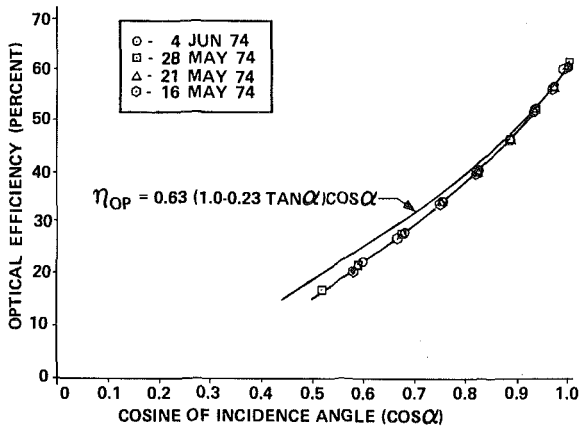

Fig. 5 Optical efficiency versus cosine of the incidence angle for east-west collector orientation (40°C operating temperature)

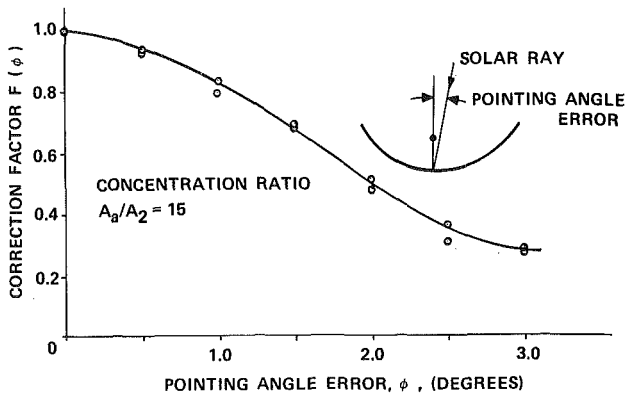

Fig. 6 Tracking accuracy correction factor versus pointing angle error

is only a small penalty for pointing errors of ±0.5 deg, but beyond that the degradation in performance with increasing pointing angle: becomes much more severe.

Performance Results at High Temperature. A typical operating temperature of the absorber tube in a solar-thermal power system of the type studied in this project would be 300°C. Therefore the objective of the high-temperature tests was to obtain performance data with the absorber at the design temperature. Data were also obtained at somewhat lower temperatures. (The overall range was from 210 to 300°C.) The tests were performed using both a selective and nonselective coated absorber tube. Recall that the tubes used for these high temperature tests were heat pipes. Therefore the absorber temperature was constant (within a range of approximately 10°C) over the entire length. The complete test results for the selective and nonselective absorber tubes are presented in references [3, 4], respectively.

At the elevated temperatures a heat loss exists from the absorber tube and the net heat delivered by the collector is given by

$$Q_{out} = Q_{abs} - Q_{loss} \tag{7}$$

The total system efficiency, η_{sys}, is obtained from the measured quantities by the relation

$$\eta_{sys} = Q_{out}/Q_{dnf} \tag{8}$$

(Recall that Q_{out} is directly measured with the calorimeter.) The heat loss in the system due to the high-temperature operation can be evaluated by comparing the high-temperature performance with the low-temperature, or optical, performance previously described. That is, the heat loss is calculated from

$$Q_{out} = Q_{dnf} \times C_{op}(1 - 0.23 \tan\alpha) \cos\alpha \times F(\phi) - Q_{loss} \tag{9}$$

The high-temperature data were taken with accurate tracking (i.e., $F(\phi) = 1$).

High-temperature data for the collector with the selectively coated absorber tube are presented in Fig. 7. The properties of the selectively coated absorber result in a C_{op} equal to 0.60. Fig. 7 presents the system efficiency, Q_{out}, Q_{dnf}, and Q_{loss} as a function of apparent solar time for the east-west orientation. Data taken during portions of three different days are presented. Due to dense cloud cover for an extended period, data could not be obtained over an entire single day. The maximum efficiency obtained around solar noon is approximately 50 percent. The dropoff of the efficiency curve with departure from solar noon is due to the effect of non normal incidence of the solar radiation on the plane of the aperture. The heat loss is seen to remain at a constant value of approximately 100 W/m^2 throughout the day.

The black painted absorber tube in the third test configuration has an absorptance of 0.96 which results in the optical constant, C_{op}, equal to 0.63. Fig. 8 presents the system efficiency, Q_{dnf}, Q_{out}, and Q_{loss} obtained with the collector oriented in the east-west direction and

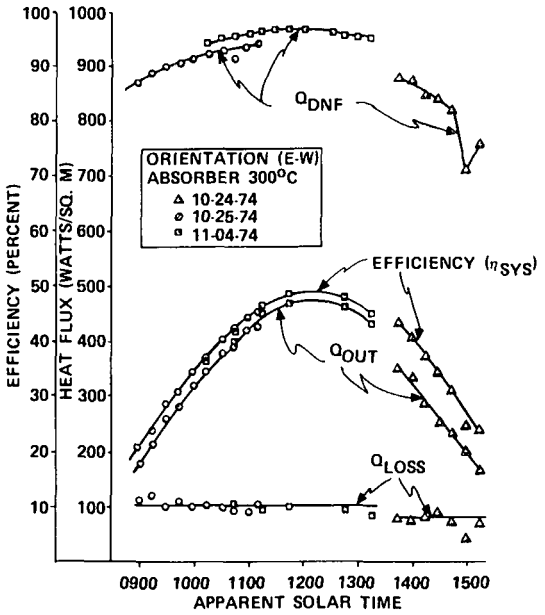

Fig. 7 Performance data: east-west orientation, 300°C absorber temperature, selective coated absorber tube

the nonselectively coated absorber tube operating at 300°C. These values are again plotted as a function of the apparent solar time. The maximum efficiency obtained around solar noon is approximately 22 percent. No data before 1030 hours could be obtained due to the long time required for the absorber to reach the operating temperature of 300°C. Note that for the black painted configuration the heat loss, Q_{loss}, is relatively constant at 340 W/m^2. This is higher than the heat delivered, Q_{out}.

Data were also obtained when the absorber was maintained at temperatures other than 300°C, namely, at 210, 230, 250, and 275°C. For each temperature case, the heat loss was found to be constant over

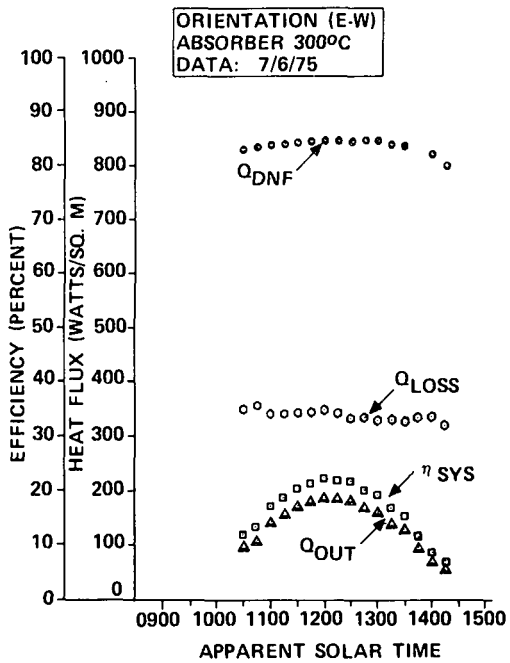

Fig. 8 Performance data: east-west orientation, 300°C absorber temperature, nonselective coated absorber tube

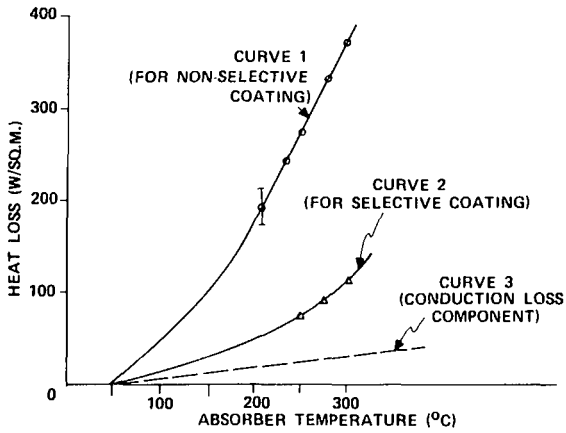

Fig. 9 Heat loss as a function of absorber temperature

the test period. Fig. 9 shows how the heat loss varies as a function of the absorber temperature. Curve 1 is for the black painted absorber, whereas curve 2 is for the selectively coated absorber tube. It is seen that for the selective coated absorber operating at 300°C, the thermal loss is substantially lower than that for the nonselective case and therefore results in the higher operating efficiency of the collector module.

The total heat losses measured for the experiment are specific to the apparatus employed. The absorber tube is enclosed in a vacuum jacket. Therefore the only heat losses from the tube are by radiation exchange between the absorber and the surrounding glass enclosure and by conduction through the mechanical supports which fix the absorber tube inside the enclosure. While the radiative heat transfer is universal for collectors of the type considered (for a given emittance of the absorber tube), the conduction losses are specific to the way in which the absorber tube is supported. An estimate of the relative importance of the two heat loss mechanisms for the current experiments can be obtained by expressing the total heat loss as

$$A_a Q_{loss} = A_2 \epsilon \sigma (T_{abs}^4 - T_g^4) + \frac{kA_1}{L}(T_{abs} - T_g) \qquad (10)$$

The first (radiation) term of equation (10) will be present for any design where the absorber tube is surrounded by a uniform temperature enclosure. (It has been assumed that the glass enclosure is a black body for the wavelengths at which the radiative exchange occurs.) Therefore this term represents the minimum heat loss. A number of collector analyses have been performed considering only this term, thus predicting the upper limit for performance.

The conduction losses are represented by the second term of equation (10). This loss has been expressed as a conductance factor, (kA_1/L), multiplied by the temperature difference between the absorber tube and glass tube. The conduction heat loss can be considered as a departure from the ideal performance. The magnitude of this heat loss component can be estimated from equation (10) by using the measured value of the total heat loss and the calculated value of the radiation heat loss. (Note that all the necessary quantities for calculating the radiation term are known.) Curve 3 of Fig. 9 shows the estimated loss of heat due to the conduction through the mechanical supports. At an operating temperature of 300°C, the conduction losses were 29 percent and 8 percent of the total heat losses for the selectively coated and nonselectively coated absorbers, respectively. If the conduction loss were not present, the maximum efficiency would increase from 50 to 53 percent for the selectively coated absorber and from 22 to 25 percent for the nonselectively coated absorber.

Comparison of Test Results. The data with the three different absorber configurations were obtained at different times of the year when the insolation was different. To directly compare the heat delivered for each of the three configurations, a comparison for similar

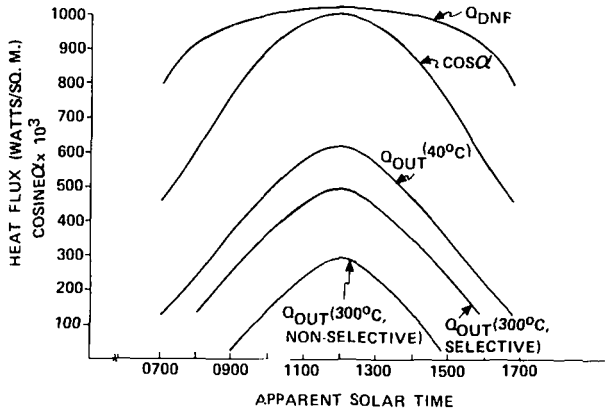

Fig. 10 Comparison of results obtained with three different absorber configurations: east-west orientation

flux conditions was made based on the test results. The flux values used for the comparison are for a clear air model for 15 June at +33°N latitude. The results are shown in Fig. 10 where Q_{dnf} and Q_{out} are presented for the three absorber configurations and with the collector in the east-west orientation. The value of the cosine of the incidence angle ($\cos\alpha$) was also computed for 15 June and is plotted to show its effect on the horizontally mounted single-axis tracking collector.

Note that the maximum heat delivered by the collector system is about 63 percent of the direct normal flux entering the aperture at solar noon. The reduction of 37 percent is due to the optical constant, C_{op}, for this system. The effects of non-normal incidence reduced the heat delivered on either side of solar noon. The maximum heat delivered is reduced to 50 percent of the direct flux when the absorber is operating at 300°C with a selective coating. This is primarily due to the radiation losses with an emittance of 0.2. When the absorber is coated with the black paint ($\epsilon = 0.96$), the heat delivered is reduced to 30 percent of the direct normal flux entering the aperture at solar noon. This performance reduction is due to the substantial increase in the radiation losses.

Acknowledgments

This research was performed under the auspices of Grant No. GI-34871, initially sponsored by NSF (RANN) and subsequently by ERDA.

References

1 Duffie, J. A., and Beckman, W. A., *Solar Energy Thermal Processes*, Wiley-Interscience, New York, 1974.

2 "Research Applied to Solar-Thermal Power Systems," Report No. 4 (1 Jan. 1974 to 31 June 1974). Report: NSF/RANN/SE/GI-34871/PR/74/2.

3 "Research Applied to Solar-Thermal Power Systems," Report No. 5 (1 July 1974 to 31 Dec. 1974). Report: NSF/RANN/SE/GI-34871/PR/74/4.

4 "Research Applied to Solar-Thermal Power Systems," Report No. 6 (1 Jan. 1975 to 31 Aug. 1975). Report: NSF/RANN/SE/GI-34871/PR/75/2.

J. C. McMurrin
Research Assistant.

N. A. Djordjevic
Research Assistant.

H. Buchberg
Professor. Mem. ASME

Energy and Kinetics Department,
School of Engineering and Applied Science,
University of California,
Los Angeles, Calif.

Performance Measurements of a Cylindrical Glass Honeycomb Solar Collector Compared With Predictions

A glass tube honeycomb solar collector, composed of a conventional single-glazed flat-plate water cooled nonselective black absorber with a cylindrical glass honeycomb mounted between the plate and cover glass, was designed, fabricated, and tested. The test procedure followed the National Bureau of Standards Method of Testing for Rating Solar Collectors. The honeycomb consists of individual cylindrical thin-wall glass tubes standing on end on the absorber plate in a hexagonal close-packed pattern. The tubes are 9.5-mm ID, 0.2-mm wall thickness, 5.3 length to diameter ratio made of glass with mean solar absorptive index ($\bar{k}$), 2.6 × 10^{-6} μ^{-1}, evaluated from spectral transmittance-reflectance measurements on a tubing specimen. The collector performance equalled or surpassed theoretical predictions for measurements made over a broad range of collector inlet temperatures and environmental conditions. Performance comparisons are made with a baseline double-glazed solar collector tested alongside the honeycomb collector. For applications requiring a working fluid temperature of 65°C above the ambient air temperature, honeycomb collector efficiencies of 35–55 percent may be expected for approximately a six hour period on clear days; for fluid temperature 40°C above ambient air temperature, efficiencies of 50–65 percent may be expected.

Introduction

Designers of solar collectors are interested in reducing heat losses to minimize the collector area required for a particular application. It is known [1–7][1] that the placement of a properly designed honeycomb structure between the solar absorber plate and cover glass is an effective means of suppressing the most damaging form of natural convection and minimizing reradiation losses from the hot absorber. It has been shown [8] that cylindrical glass honeycombs used for heat loss control in flat plate solar collectors exhibit superior performance at temperatures greater than about 35°C above ambient air temperature.

The purpose of this paper is to present the results of performance tests conducted with an experimental (0.61- × 0.61-m) thin-walled cylindrical glass honeycomb collector and to compare these results with predicted behavior.

Experimental Glass Honeycomb Collector

The test solar collector, Fig. 1, is a single-glazed, nonselective black flat plate type with a glass honeycomb mounted between the plate and cover glass. A cross-sectional view of the 0.61- × 0.61-m test solar collector is shown in Fig. 2. The glass honeycomb comprises individual 9.5-mm ID, 0.20-mm wall, 51-mm long cylindrical glass tubes, in a close-packed hexagonal pattern with axes perpendicular to the absorber plate, with approximately 1.6-mm clearance (δ_c) between the cover glass and honeycomb.

The absorber plate is 3.2-mm thick copper sheet painted with 3M Company Velvet Coating, Nextel Brand No. 101-C10, a nonselective black coating. To minimize outgassing during tests, the painted plate was baked at 175°C for 72 hr. Solar absorptance and total hemispherical emittance of the plate are both assumed to be 0.95.

One 5-m length of copper tubing, 6.4-mm OD, 0.8-mm wall, con-

[1] Numbers in brackets designate References at end of paper.

Contributed by the Heat Transfer Division and presented at the Winter Annual Meeting, New York, N.Y., December 5–10, 1976, of THE AMERICAN SOCIETY OF MECHANICAL ENGINEERS. Revised manuscript received by the Heat Transfer Division October 26, 1976. Paper No. 76-WA/Sol-3.

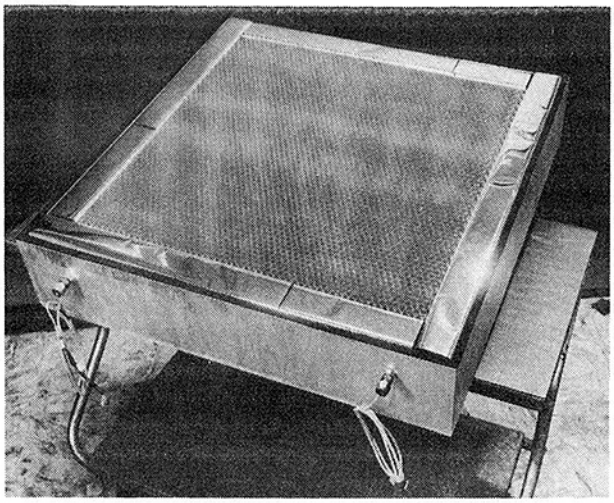

Fig. 1 Experimental 0.61 × 0.61 m-cylindrical glass honeycomb solar collector, shown with cover removed

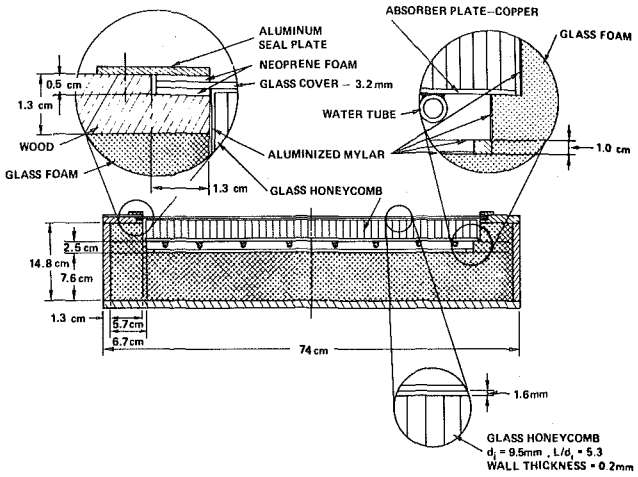

Fig. 2 Glass honeycomb solar collector, cross-sectional view

tinuously soldered to the underside of the absorber plate in a serpentine pattern, carries the working fluid through the collector. Glass foam insulation supports the edges of the plate, and a 2.5-cm air gap below the plate, with two aluminized mylar films stretched laterally across the space, provides thermal insulation in addition to about 7.5 cm of bottom foam insulation. Aluminized mylar film which lines the edge insulation serves, in part, to reflect solar radiation, which passes through the cover glass and outer portions of the honeycomb, back into the honeycomb and on to the absorber. Thus, edge shadow effects at large incidence angles are minimized. Such edge effects are much more significant for the 0.61- × 0.61-m test collector than would be the case for a full-scale model.

The collector housing is a box made of 1.3-cm plywood, painted silver, and mounted on a tiltable table which can be manipulated to position the absorber plate normal to any point above the horizon.

Performance Tests of Experimental Collector

Test Loop. Fig. 3 is a schematic drawing of the test loop. Tap water stored in a small steel tank is used as the working fluid. The water is drawn from the top of the tank and pumped through the test loop by an Oberdorfer 3000 gear pump. Downstream of the pump the test loop divides into two branches with the flow in each controlled by a needle valve and measured independently with rotometers. Additional flow and pressure control is obtained with a valved pump return circuit. The two branches permit the testing of two collectors simultaneously under identical environmental conditions, with independent control of flow rates and collector inlet temperatures.

The electric resistance preheaters are simply high-resistance flat wire wrapped around electrically insulated tubing, and heavily insulated with asbestos cloth and a fiberglass blanket. The preheaters are independently controlled by 240-V variable transformers and provide a means for raising the inlet temperature so that the effect of this variable can be ascertained during performance tests.

The working fluid flows from the heaters through the collectors, and then the separate branches rejoin. A small expansion chamber, vent valve and pressure gauge are installed at the most elevated point in the loop. A heat exchanger and by-pass are provided in the return line to simulate a load when required. The working fluid then returns to the bottom of the storage tank. This routing, which provides a delayed mixing in the storage tank, as well as a complete wrapping of insulation around the test loop, is important for minimizing short-period fluid temperature fluctuations.

Instrumentation. Copper-constantan thermocouples measure the water temperature at the entrance and exit of the collector, at five points on the absorber plate, at two points on the glass foam insulation

Nomenclature

a = defined by equation (2)
A_c = collector aperture area
A_{LM} = log-mean area of resistance across gap δ_c
b = defined by equation (3)
c_p = specific heat of working fluid
d_i = inside diameter of honeycomb cell
f_w = glass fraction of cross-sectional area
G_s = solar irradiation
$\bar{h}_f$ = mean fluid heat transfer coefficient
k = absorptive index
$\bar{k}$ = mean value of k/λ (which yields correct integrated solar absorptance)
k_a = thermal conductivity of air
k_w = thermal conductivity of cell wall
ℓ = length of flow channel
L = cell length
$\dot{m}$ = mass flow rate of working fluid per unit collector area
n = refractive index
P = perimeter of flow channel
R_A = resistance to radiative and convective heat transfer between cover glass and environment
R_C = resistance to heat conduction, convection and radiation in the honeycomb structure
R_D = resistance to heat conduction through insulation and heat exchange with surroundings
R_E = resistance to heat transfer between absorber plate and working fluid
T_e = ambient air temperature
$T_{f,i}$ = fluid temperature at collector inlet
$T_{f,o}$ = fluid temperature at collector outlet
$\bar{T}_f$ = mean fluid temperature $(T_{f,i} + T_{f,o})/2$
T_g = cover glass temperature
T_p = absorber plate temperature
t_w = cell wall thickness
u_e = wind speed
$(\alpha_s)_g$ = solar absorptance of cover glass
$(\alpha_s)_p$ = solar absorptance of absorber plate
β_d = fraction of diffuse solar radiation
δ_c = air gap between honeycomb and cover glass
ϵ_g = hemispherical emittance of cover glass
ϵ_{EB} = effective bottom emittance of honeycomb (further defined in text)
η = solar collector efficiency
θ_s = vertical angle of incidence of solar rays
λ = wavelength
σ = Stefan-Boltzmann constant
τ = collector angle of tilt with horizontal plane
τ_s = combined transmittance of cover glass and honeycomb

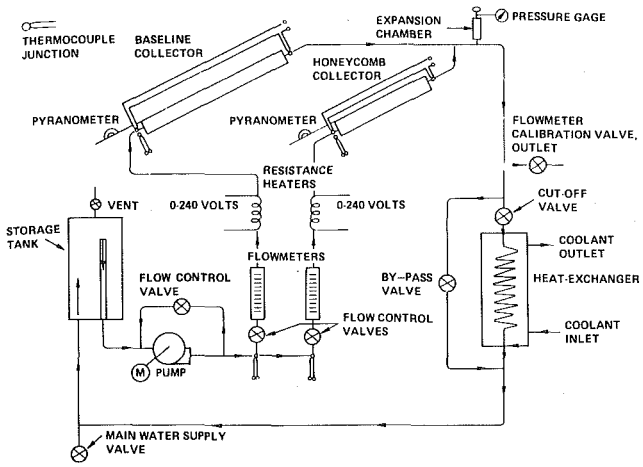

Fig. 3 Test flow loop

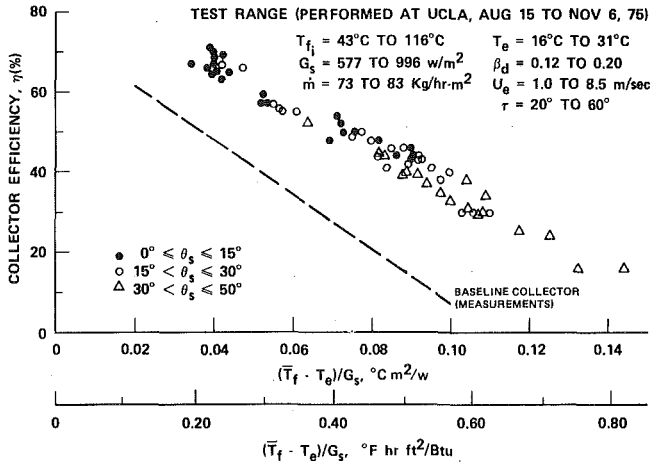

Fig. 4 Solar collector efficiency, cylindrical glass honeycomb, d_i = 9.5 mm, t_w = 0.2 mm, L/d_i = 5.3, $\bar{k}$ = 2.6 × 10^{-6} μm^{-1}

below the plate and mylar sheets, on the outer surface of the cover glass, and at the flowmeter inlets. A 12-channel Honeywell chart recorder with compensated reference junction prints out the temperature in degrees F. The fluid temperature increase in each collector is measured by thermocouple differencing and is continuously read on a Honeywell Electronik 196 potentiometer recorder within 0.05°C.

Solar irradiation and total hemispherical irradiation are continuously measured with an Eppley Model 10 pyrheliometer and a Beckman and Whitley Model TCH188-01 total thermal radiometer (based upon the Gier and Dunkle design) both mounted coplanar with the honeycomb collector, and are individually recorded on two Leeds and Northrup Speedomax H single channel millivolt chart recorders. The recording instruments are regularly calibrated with a Leeds and Northrup 8690 potentiometer. The flow meters gravimetrically calibrated at temperature are expected to be correct within ±1 percent.

Wet and dry bulb environmental temperatures and wind speed are continuously measured with a Beckman and Whitley micrometeorological recording station located at the collector site. The foregoing data are periodically corroborated with wet and dry bulb temperatures measured with a Cenco sling psychrometer, and wind speed measured with an Alnor Model 6000 air velocity meter.

The vertical solar angle of incidence θ_s is determined by measuring the length of the shadow, in the plane of the collector, of a rod mounted normal to the collector, with an accuracy of ±1 deg.

Test Procedure. In general the test procedure followed is similar to that recommended by the U.S. National Bureau of Standards [9]. A simple technique is used to approach system equilibrium in the least amount of time for any particular inlet fluid temperature. With the storage tank full of water, the pump is turned on and flow rate and heater are set at maximum output. By circulating water, temporarily heated to about 20°C above the designated value of inlet fluid temperature, system equilibrium is typically reached within 30 min.

The input line from the water main is left open throughout the test, maintaining a minimum system pressure of 3.2 atm, which allows water temperatures up to 130°C without boiling or cavitation. Air or vapor in the lines collects in the expansion chamber and is periodically vented. No test is conducted with any sign of bubbles in the fluid, which may be observed passing through the glass flowmeter.

A constant collector inlet temperature is generally used for an entire day's tests to minimize effects due to thermal capacity and to reduce the time necessary to change to new equilibrium conditions. Data taken in the morning during increasing G_s or in the afternoon during decreasing G_s show no measurable difference attributable to capacitive effects.

Test Results. Instantaneous collector efficiency is shown in Fig. 4, plotted against average fluid temperature above ambient air temperature divided by solar irradiation, $(\bar{T}_f - T_e)/G_s$. The collector efficiency is calculated as the product of the heat capacity rate per unit collector area and water temperature rise in the collector divided by the solar irradiation, $\dot{m}c_p(T_{f,o} - T_{f,i})/G_s$.

Sixty nine data points are shown, obtained during clear weather days at the University of California, Los Angeles, intermittently from August 15, 1975, to November 6, 1975. The sky was very clear to somewhat hazy during test periods. Diffuse irradiation remained fairly constant during the day, becoming a larger fraction of the total solar irradiation for higher angles of incidence.

Collector performance was tested over the following range:
Collector inlet temperature ($T_{f,i}$) = 43–116°C
Mass flow rate per unit collector area ($\dot{m}$) = 73–83 kg/hr − m^2
Environmental temperature (T_e) = 16–31°C
Wind speed (u_e) = 1–9 m/s
Solar incidence angle (θ_s) = 0–50 deg
Tilt angle (τ) = 20–60 deg
Total solar irradiation (G_s) = 577–996 W/m^2
Percent diffuse solar irradiation (β_d) = 12–20 percent

Each data point represents measurements averaged over 15-min intervals when quasi-steady state was known to exist. A best fit straight line was not drawn through the data so as not to incorrectly imply a particular value for the intercept.

Predictions of Solar Collector Performance

The predicted performance of the experimental cylindrical glass honeycomb collector is compared with actual test results. A brief description of the prediction model is given.

Calculation Model. A steady-state, nonlinear thermal resistance network representing the heat transfer modes that occur in the solar-thermal conversion processes was described by Buchberg and Roulet [10] and further elucidated by Buchberg and Edwards [8]. It was shown that the instantaneous conversion efficiency (η) for a single glazed collector may be given as

$$\eta = a - b[(T_{f,i} - T_e)/G_s] \quad (1)$$

where

$$a = R_D[R_A(\alpha_s)_g + (R_A + R_C)(\alpha_s)_p\tau_s]/[R_E(R_A + R_C + R_D) + R_D(R_A + R_C)] \quad (2)$$

$$b = (R_A + R_C + R_D)/[R_E(R_A + R_C + R_D) + R_D(R_A + R_C)]A_c \quad (3)$$

The thermal resistances (R_A, R_C, R_D, and R_E) represent, respectively, resistance to radiative and convective exchange at the cover glass-environment interface, at the cover glass-environment interface,

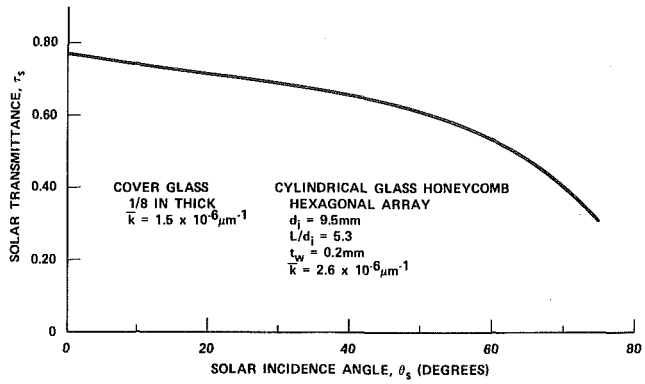

Fig. 5 Solar transmittance of honeycomb and cover glass

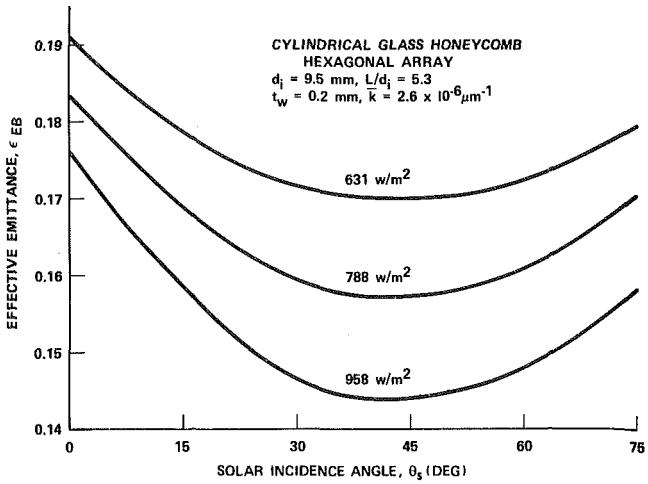

Fig. 6 Effective emittance of honeycomb structure

conduction, convection and radiation in the honeycomb structure, conduction through the insulation and heat exchange with the surroundings, and heat transfer from the hot solar absorber to the working fluid entering at a temperature ($T_{f,i}$). The resistances are temperature dependent and in addition R_A is a function of wind speed and direction and net infrared radiation exchange at the environment-cover glass interface. The solar absorptance properties $(\alpha_s)_g$ and $(\alpha_s)_p$ are considered to be constant but the solar transmittance (τ_s, a composite property including the cover glass and honeycomb) varies with the vertical angle of incidence of the sun's rays (θ_s) for a particular glass system. Morris, et al. [11] present calculations for the directional solar transmittance of cylindrical cell glass honeycomb as a function of L/d_i, using a Monte Carlo algorithm with account taken of transmission with polarization, absorption within the glass, and scattering. The value of $\bar{k} = 2.6 \times 10^{-6}\ \mu m^{-1}$, which was inferred from transmittance + reflectance measurements on a glass cell wall specimen, and $n = 1.5$ were used in the calculations. As shown in [11] calculations of τ_s versus θ_s compared well with test data on glass honeycomb specimens. The product of the honeycomb solar transmittance from [11] and the cover glass solar transmittance from [5] is plotted as a function of θ_s in Fig. 5.

The thermal resistance (R_C) provided by the honeycomb accounts for cell wall conduction, radiation exchange and conduction across an air gap (δ_c) between the honeycomb and cover glass, conduction across air cells of length ($L + \delta_c$) and the net infrared radiation exchange between the hot solar absorber and cover glass. Since the honeycomb cells were designed to prevent the initiation of the significant natural convection component, in accordance with Fig. 2 of reference [8], natural convection across the air cells was assumed to be effectively zero. Thus, R_C may be given by the expression,

$$\frac{1}{R_C} = 1/[1/(f_w A_c k_w/L) + 1/(A_{LM} k_a/\delta_c + f_w A_c \epsilon_g 4\sigma T_g^3)] + (1 - f_w)A_c[k_a/(L + \delta_c) + \epsilon_{EB}\sigma(T_p^2 + T_g^2)(T_p + T_g)] \quad (4)$$

The terms in equation (4) represent thermal conductances as follows:

$f_w A_c k_w/L$	= conductance due to wall conduction
$A_{LM} k_a/\delta_c$	= conductance due to conduction across air gap (δ_c) of mean area, $A_{LM} = A_c(1 - f_w)/\ln(1/f_w)$
$f_w A_c \epsilon_g 4\sigma T_g^3$	= effective conductance due to radiation exchange between tube edge and cover glass
$(1 - f_w)A_c k_a/(L + \delta_c)$	= conductance due to air cell conduction
$(1 - f_w)$ $A_c \epsilon_{EB}\sigma(T_p^2 + T_g^2)(T_p + T_g)$	= conductance due to radiation exchange between absorber plate and cover glass.

The effective bottom emittance (ϵ_{EB}) of the honeycomb is defined [11] as the ratio of the net radiant flux at the bottom, just above the absorber plate, to the net radiation exchange between black surfaces at the absorber plate and cover glass temperatures. Following the calculation procedure [11] for ϵ_{EB} which accounts for the wall absorption of incident solar radiation and the reststrahlen resonance reflection bands in the infrared spectrum of glass, values were obtained as a function of θ_s and G_s. The characteristic curves of ϵ_{EB} computed for the cylindrical glass honeycomb used in the experimental collector are shown in Fig. 6 for several constant values of G_s. For a specified value of θ_s, the bottom effective emittance decreases as the solar irradiation increases. However, for a constant solar input, ϵ_{EB} reaches a minimum at a value of θ_s of approximately 45 deg. As expected [8], solar radiation absorbed by the cell walls acts as a "guard heater" to limit the net radiant flux leaving the absorber plate.

Based on a linear fluid temperature rise, negligible "fin effect" between flow tubes and negligible bond resistance between absorber plate and flow tube, the thermal resistance R_E is simply $1/\bar{h}_f P\ell + 1/2\dot{m}c_p$.

Performance Calculation and Results. Using a reiterative calculation procedure, the nonlinear thermal resistance network equations are solved for successive sections of the test collector establishing the temperature rise of the working fluid traversing the section. The exit fluid temperature of any section becomes the inlet fluid temperature of the succeeding section. The calculation proceeds until the total temperature rise is obtained, establishing the amount of useful energy converted and the instantaneous solar collector efficiency. Values of η were computed for the same environmental and operating conditions that pertained for each experimental data point. The experimental and computed performance results are compared in Fig. 7.

Calculations of collector efficiency showed some dependency on θ_s, which is consistent with the variation of τ_s with θ_s indicated in Fig. 5. For the range of θ_s measured during the tests (0–50 deg.) a variation in η between 9 and 14 percentage points was predicted over a spread of 0.03–0.13°C m^2/W for $(\overline{T}_f - T_e)/G_s$. A variation in η of about 2 percentage points was calculated due to changes in wind speed between 1 and 9 m/s, observed during the test period.

Discussion and Conclusions

Measured values of instantaneous collector efficiency plotted in Fig. 4 exhibit a scatter of 10 percentage points for fixed values of the abscissa. This scatter in the data is not unexpected since computed predictions indicated some dependency of η on θ_s and wind speed as reported in the previous section on Performance Calculations and Results. The experimental data do not seem to display a systematic effect due to θ_s; however, a best fit straight line through the data for 0 deg $\leq \theta_s \leq$ 15 deg appears to have a flatter slope than the best fit for the larger angles of incidence. It is notable that a relatively large incidence angle does not significantly impair collector performance.

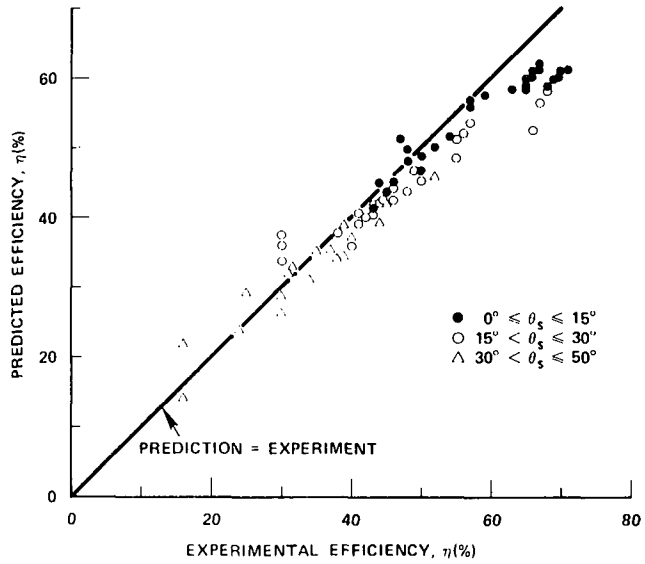

Fig. 7 Comparison of experimental and calculated efficiency

Some scatter in the data may also be expected because of a continuously changing environment and small random errors in measurements and in reading recorder charts.

As shown in Fig. 7, the predicted values of η compare very well with the measured values over most of the efficiency range. The predictions may be interpreted as somewhat conservative, particularly for data points at the high efficiency end of the scale for average fluid temperatures of about 35°C or less above the ambient air temperature. Since the predictions are on the conservative side it may be that the predicted directional solar transmittances are somewhat low. Values of τ_s for the actual cover glass used are not known. As mentioned previously, the data used were taken from [5]; the values 0.86–0.82 (for θ_s = 0 and 50 deg) may be low. Also, the value of $\bar{k}$ inferred from measurements may be somewhat high. Another contribution to some uncertainty in the calculated result is the lack of precise knowledge of the thermal conductivity of the honeycomb glass and the contact resistance at both ends of the honeycomb. Using the same value (0.95) for α_s and ϵ for the absorber plate surface is somewhat conservative. The hemispherical emittance may be expected to be somewhat less than α_s again introducing some conservatism in the predicted results.

Some performance data were obtained for a double glazed nonselective black flat-plate "baseline" solar collector mounted adjacent to the honeycomb collector. The characteristic performance curve for the baseline collector, shown in Fig. 4, represents the best straight line drawn through the experimental data. It can be seen that the average honeycomb collector efficiency is about 15–30 percentage points above the average baseline collector efficiency over the full range of values of $(\overline{T}_f - T_a)/G_s$ shown. This represents a very substantial improvement over the baseline collector which can be approximately interpreted as a 20–40 percent improvement in daily collection depending upon the ratio of collector temperature above ambient to the integrated incident solar power. The higher the ratio, the greater is the advantage of the honeycomb collector. In making this estimate it is assumed that the double glazed baseline collector and single glazed honeycomb collector respond similarly to diffuse solar irradiation, an assumption which has not yet been systematically tested.

It is apparent from the solar transmittance data in [8] for improved glass ($\bar{k} = 1.5 \times 10^{-6}\ \mu m^{-1}$) and the optimization studies, that further improvements in the performance of glass honeycomb collectors may be expected in the future.

The glass tubes were cleaned prior to mounting in the collector by soaking in warm distilled water containing 5 percent trisodium phosphate in solution, then rinsing in a 5 percent antistatic solution in cool distilled water, and finally rinsing in pure cool distilled water. However, after mounting the tubes, it appeared that a whitish residue remained on most of the tubes. Presumably, the transmittance of the glass honeycomb could be measurably improved in the future by use of a more effective cleaning process.

The performance of the cylindrical glass honeycomb collector may be interpreted from the point of view of applications. For a 6-hr period of collection on clear weather days, the following approximate performance ranges can be derived from Fig. 4: For space air conditioning requiring working fluid temperatures of about 100°C when the outdoor temperature is about 35°C, efficiencies between 35 and 55 percent may be expected. If the collector is used for a space heating appication with sensible heat storage requiring working fluid temperatures of about 65°C when the outdoor air temperature is about −10°C, expected efficiencies would be between 20 and 45 percent. For applications where the required fluid temperature is about 30°C above ambient air temperature, efficiencies of 50–65 percent may be expected.

The particular tube size used for the honeycomb array was mainly dictated by procurement constraints. In Fig. 2 of ref. [8], it can be seen that free convection is adequately suppressed for a cell diameter of 9.5 mm. Experimental and analytical studies of glass honeycomb systems for energy loss control in solar collectors and fenestrations are continuing at UCLA. Studies include various cell shapes in addition to the cylindrical tube.

Acknowledgments

The authors wish to gratefully acknowledge the financial support of NSF/RANN and the U.S. Energy Research and Development Administration (ERDA). We also wish to thank Dr. D. K. Edwards and his students for providing us with essential solar transmittance and effective emittance calculations for the cylindrical glass honeycomb used in our experimental solar collector.

References

1 Veinberg, V. B., "Optics in Equipment for the Utilization of Solar Energy," State Publishing House of Defense Industry, Moscow, 1959 (English Translation), p. 144.

2 Francia, G., "A New Collector of Solar Radiant Energy—Theory and Experimental Verification," United Nations Conference on New Sources of Energy, Rome 4, 1971, pp. 554–558.

3 Hollands, K. G. T., "Honeycomb Devices in Flat-Plate Solar Collectors," *Solar Energy*, Vol. 9, 1965, pp. 159–164.

4 Buchberg, H., Edwards, D. K., and Lalude, O. A., "Design Considerations for Cellular Solar Collectors," ASME Paper No. 68-WA/SOL-3, 1968.

5 Buchberg, H., Lalude, O. A., and Edwards, D. K., "Performance Characteristics of Rectangular Honeycomb Solar Thermal Converters," *Solar Energy*, Vol. 13, 1971, pp. 193–211.

6 Lalude, O. A., and Buchberg, H., "Design of Honeycomb Porous Bed Solar Air Heaters," *Solar Energy*, Vol. 13, 1971, pp. 223–242.

7 Buchberg, H., Catton, I., and Edwards, D. K., "Natural Convection in Enclosed Spaces: A Review of Application to Solar Energy Collection," ASME *Paper No. 74-WA/HT-12, 1974; (revised version in* JOURNAL OF HEAT TRANSFER, TRANS. ASME, Series C, Vol. 98, 1976, pp. 182–188.

8 Buchberg, H., and Edwards, D. K., "Design Considerations for Solar Collectors With Cylindrical Glass Honeycombs," *Solar Energy*, Vol. 18, 1976, pp. 193–203.

9 Hill, J. E., and Kusuda, T., "Method of Testing for Rating Solar Collectors Based on Thermal Performance," National Bureau of Standards Report No. NBSIR 74-635, Dec. 1974.

10 Buchberg, H., and Roulet, J. R., "Simulation and Optimization of Solar Collection and Storage for House Heating," *Solar Energy*, Vol. 12, 1968, pp. 31–50.

11 Morris, P. A., et al., "Radiative Transfer Through Thin-Walled Glass Honeycomb," ASME Paper No. 76-HT-68, 1976.

F. W. Schmidt
R. R. Somers, II
J. Szego
D. H. Laananen

Mechanical Engineering Department,
The Pennsylvania State University,
University Park, Pa.

Design Optimization of a Single Fluid, Solid Sensible Heat Storage Unit

The optimization of the design of a solid sensible heat storage unit initially at a uniform temperature is presented. The storage unit is composed of a number of rectangular cross-sectional channels for the flowing fluid, connected in parallel and separated by the heat storage material. The complex method for constrained nonlinear optimization as presented by M. J. Box is utilized, with some modifications. The design optimization is based upon achieving maximum utilization of the heat storage or removal capabilities of the material for a given set of operating conditions. This is achieved by varying the storage unit's geometry while placing constraints on the maximum and minimum length of the unit, fluid channel size, storage material thickness, maximum and minimum outlet fluid temperature, and the minimum amount of heat to be stored.

Introduction

The large increase in the cost of energy during the past several years has encouraged industrial and commercial groups to carefully review their energy consuming requirements. These reviews or reassessments of energy utilization have resulted in the redesign and modifications of energy consuming units to improve their efficiency, and in the reduction of the energy loss through initiation of energy conservation measures. In many instances energy management systems have been developed. Analysis of the results of these studies have indicated ways in which substantial savings in energy can be obtained. Often it is discovered that many different sources and demands for energy exist and that it is possible to utilize the heat rejected by one process as the energy source for another. The flexibility of the energy management system is greatly increased if an economical and efficient method for storing thermal energy can be found.

There are a number of ways in which energy can be stored. This paper deals with the storage of energy in solid sensible heat storage units. It is assumed that a source of high temperature gas is available and the gas can be passed through straight rectangular cross-sectional channels in the storage material.

The amount of heat stored will be dependent on the mass rate of flow and the inlet temperature of the hot gas, the storage material and fluid used and the length and thickness of the storage material. Since the quantity of energy stored is time dependent, it is necessary to know the transient response characteristics of the units.

A typical solid sensible heat storage unit is shown in Fig. 1(*a*). The transient response of this unit has been presented by Schmidt and Szego [1].[1] For the purposes of this analysis lines of symmetry were considered to exist at the midpoints of the storage material and flow channel. The section to be analyzed is shown in Fig. 1(*b*). The following assumptions have been made:

(*a*) constant fluid and material properties;
(*b*) uniform heat transfer coefficient;
(*c*) step change in fluid inlet temperature;
(*d*) initial temperature distribution in the material is uniform;
(*e*) two dimensional heat transfer in the storage material;
(*f*) constant fluid mean velocity;
(*g*) side effects are negligible.

The equations which govern the transient response of the storage unit are the one-dimensional conservation of energy equation for the moving fluid and the transient two-dimensional heat conduction equation for the storage material.

The following nondimensional groups are introduced:

$$Z \equiv \frac{z}{w} \qquad Y \equiv \frac{y}{w}$$

$$V^+ \equiv \frac{w}{L} \qquad \mathrm{Fo} \equiv \frac{\alpha\theta}{w^2}$$

Contributed by the Heat Transfer Division and presented at the Winter Annual Meeting, Houston, Texas, November 30–December 5, 1976 of THE AMERICAN SOCIETY OF MECHANICAL ENGINEERS. Revised manuscript received by the Heat Transfer Division March 1, 1977. Paper No. 76-WA/HT-64.

[1] Numbers in brackets designate References at end of paper.

$$\text{Bi} \equiv \frac{hw}{k_m} \qquad T \equiv \frac{t - t_o}{t_{fi} - t_o}$$

$$G^+ \equiv \frac{P_h k_m}{\dot{m} C_f}.$$

The complete set of nondimensional equations neglecting the heat capacity of the fluid becomes:

moving fluid: $$\frac{dT_f}{dZ} + (G^+)(\text{Bi})(T_f - T_w) = 0$$

storage material: $$\frac{\partial^2 T_m}{\partial Z^2} + \frac{\partial^2 T_m}{\partial Y^2} = \frac{\partial T_m}{\partial \text{Fo}}$$

with the initial condition:

$$\text{Fo} = 0 \qquad T_m = T_f = T_o = 0$$

and the boundary conditions:

$$Z = 0 \qquad T_f = 1 \qquad \frac{\partial T_m}{\partial Z} = 0 \qquad \text{for } 0 < Y < 1$$

$$Z = \frac{1}{V^+} \qquad \frac{\partial T_m}{\partial Z} = 0 \qquad \text{for } 0 < Y < 1$$

$$Y = 1 \qquad \frac{\partial T_m}{\partial Y} = \text{Bi}(T_f - T_m) \qquad \text{for } 0 \le Z \le \frac{1}{V^+}$$

$$Y = 0 \qquad \frac{\partial T_m}{\partial Y} = 0 \qquad \text{for } 0 \le Z \le \frac{1}{V^+}$$

The results for the transient nondimensional fluid outlet temperature, T^+, and the fraction of the maximum possible heat stored, Q^+, were presented in a series of curves. In order to simplify the use of these results in the design of storage units, they were retained in the computer and a program written to perform the necessary interpolations. The program has been named HSSF. For a given set of fluid flow conditions and storage unit configuration the value of Fo, Bi, and G^+/V^+ can be computed and the program used to determine the nondimensional outlet fluid temperature and the fraction of the maximum possible heat that is stored.

The selection of the thickness of the storage material and its length, and flow channel thickness for a given set of flow conditions is difficult since a great number of different combinations of these parameters may yield similar operating characteristics. The objective of this paper is to present the designer with a technique for the optimization of the design parameters to obtain the maximum utilization of the storage material during a given time for a specific fluid flow rate and inlet temperature.

Although this paper is written with reference to heat storage the results are also applicable to systems where heat is transferred from the storage unit to the fluid. The only limitation is that the unit is initially in temperature equilibrium, at a uniform temperature. All heat quantities will be negative since heat is rejected by the storage material.

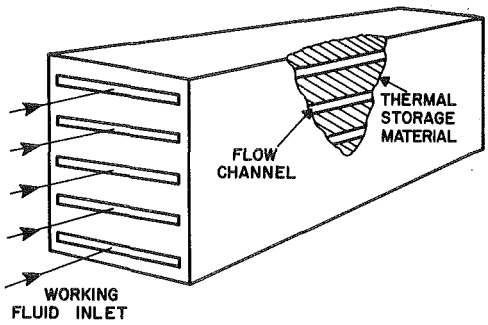

Fig. 1(*a*) Thermal storage unit

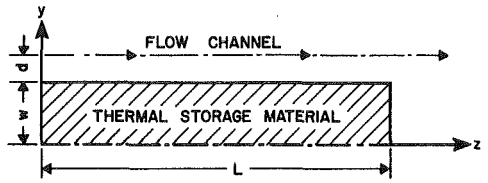

Fig. 1(*b*) Cross section of storage unit

Fig. 1 Storage unit

Complex Optimization Method

The selection of a method for optimizing the design of the thermal energy storage unit was limited by the mathematical model describing the system. Seven variables are involved in the process. Since these are limited by either explicit or implicit constraints, applicable optimization methods were restricted, by practical considerations, to those involving direct search techniques developed for nonlinear constrained optimization. Of the several such methods available, the complex optimization method of Box [2] was chosen. This selection was based upon the ability of the method to:

i handle both explicit and implicit constraints;

ii avoid time consuming gradient calculations;

iii increase the probability that a global; rather than a local, optimum would be obtained;

Nomenclature

A = flow cross-sectional area

A^+ = fraction of available energy stored, $Q/\dot{m}C_f(t_{fi} - t_o)\theta$

C = specific heat at constant pressure

D = hydraulic diameter, $\frac{4A}{P_w}$

d = flow channel semithickness

f = friction factor

h = convective film coefficient

k = thermal conductivity

L = length of heat storage unit

$\dot{m}$ = mass rate of flow per unit width for one half the channel

p = pressure

P_h = heated perimeter of flow channel

P_w = wetted perimeter of flow channel

Q = total heat storage

$Q_{\max}$ = maximum heat storage, $\rho_m V C_m(t_{fi} - t_o)$

Q^+ = fraction of maximum possible heat stored, $Q/Q_{\max}$

t = temperature

T = nondimensional temperature, $\frac{t - t_o}{t_{fi} - t_o}$

T^+ = nondimensional fluid outlet temperature $\frac{t_{fo} - t_o}{t_{fi} - t_o}$

V = volume of the storage material

v = fluid velocity

w = semithickness of the storage material

x = independent variable

y = transverse coordinate

Y = nondimensional transverse coordinate, y/w

z = axial coordinate

Z = nondimensional axial coordinate, z/w

α = thermal diffusivity of storage material

θ = duration of active storage

μ = absolute viscosity

ρ = density

Subscripts

f = moving fluid

fo = fluid outlet

fi = fluid inlet

o = initial condition

m = thermal storage material

iv require only straightforward computer coding.

The complex method is particularly suited for convex search regions and has been used with considerable success in the optimization of the solutions to many practical problems. Examples of these have been presented by Adelman and Stevens [3] and Kobayashi, et al. [4].

The complex method of nonlinear constrained optimization is an adaptation of the simplex method originally proposed by Spendley, et. al [5]. The objective is to maximize functions of the form $f[x_1, x_2, x_3 \ldots x_n]$ where x's are the independent variables. This maximization may be limited by explicit constraints of the form $a_i \leq x_i \leq b_i$ where $i = 1, 2, 3 \ldots n$ and implicit constraints of the form

$$c_p \leq g_p [x_1, x_2 \ldots x_n] \leq d_p$$

In the optimization of the design of the thermal storage system the optimized function f is Q^+. The functional relationship is given by the HSSF computer program and may be represented as Q^+ [Bi, Fo, G^+/V^+] or in dimensional form as Q^+ [$h, w, k_m, \dot{m}, L, \alpha, \theta, P_h, \rho_f, C_f, \upsilon, A$]. Once the storage material and the fluid are selected, the number of variables is reduced, giving Q^+ [$h, w, L, \theta, P_h, \upsilon, A$]. Several of these variables are interrelated. The convective film coefficient, h, is a function of the mass rate of flow of the fluid, the dimensions of the channel, the length of the storage unit and the physical properties of the fluid. This can be expressed as h [$D, L, \upsilon, k_f, \mu_f, \rho_f, C_f$]. The selection of the flow passage dimensions is to a large extent determined by the permissible pressure drop in the flow passages. This pressure drop is functionally related to the other variables by Δp [$L, D, \upsilon, \rho_f, f$] where f is the friction factor. The friction factor is a function of the Reynolds number and the channel's surface roughness.

The design of the storage unit can be optimized with respect to the nondimensional heat storage ratio, Q^+, or with respect to the ratio of the amount of heat actually stored to the amount of available heat, A^+. When a heat storage unit of a given material is optimized with respect to Q^+ the capital costs involved in initially constructing the unit are minimized. If the heat storage unit is optimized using A^+, the total amount of energy stored for a specified operating period is maximized and, as a result, the value of the energy saved is maximized. The values of A^+ and Q^+ are functionally related by

$$\frac{A^+}{Q^+} = \frac{(G^+/V^+)}{\mathrm{Fo}} = \left[\frac{\rho_m C_m P_h{}^w}{\dot{m} C_f \theta}\right] L$$

All of the terms in the brackets are initially specified. Optimization runs, using A^+ as the maximized parameter, yielded designs with the maximum length. The optimization runs made using Q^+ as the maximized parameter arrived at a final design in which the outlet temperature of the fluid reached its upper constraint. The results obtained by maximizing A^+ and Q^+ define a bounded region and all optimized units satisfying the constraints must fall within these bounds. The designs within this region were obtained by maximizing the value of Q^+ for a specific total heat storage, Q.

The details of the optimization procedure are given in the Appendix. When optimizing with respect to Q^+, the program initializes itself and proceeds to determine the value of d and L which will give a maximum Q^+ within the constraints listed. The program prints out the value of Q^+, T^+, d, L, Δp, Q, as well as the fraction of the available energy stored, A^+, and the air horsepower per cm of heat storage unit width. Typical computational time on the IBM 360/168 for an optimization run was 10 s.

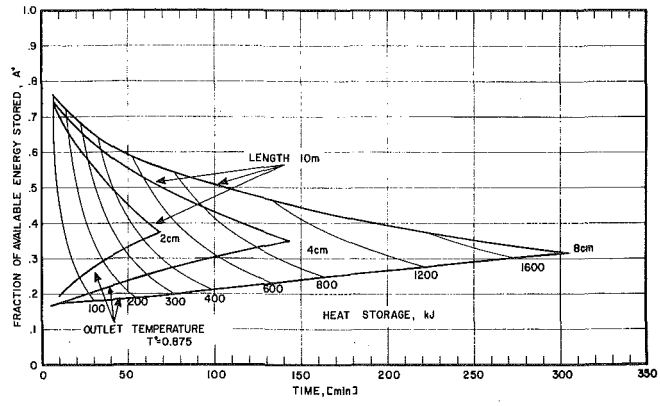

Fig. 2 Fraction of available energy stored

The new functional relationships for the calculation of the convective film coefficient and the friction factor are given in Table 1.

Table 1 Friction factor and film coefficient relationship

Fanning friction factor [9]

for $5 \times 10^3 < \mathrm{Re}_D < 3 \times 10^4$:

$$f = 0.079\,\mathrm{Re}_D{}^{-0.25}$$

for $3 \times 10^4 < \mathrm{Re}_D < 10^6$:

$$f = 0.046\,\mathrm{Re}_D{}^{-0.2}$$

Convective film coefficient [10]

for $\mathrm{Re}_L < 25 \times 10^3$; $\dfrac{L}{D} < 60$

$$h = 0.22 \frac{k_f}{L} \mathrm{Re}_L{}^{0.6} \left(\frac{L}{D}\right)^{0.08}$$

for $\mathrm{Re}_L > 25 \times 10^3$; $\dfrac{L}{D} < 60$

$$h = 0.029 \frac{k_f}{L} \mathrm{Re}_L{}^{0.8} \left(\frac{L}{D}\right)^{0.08}$$

for $\mathrm{Re}_D > 10^4$; $\dfrac{L}{D} > 60$

$$h = 0.018 \frac{k_f}{D} \mathrm{Re}_D{}^{0.8}$$

Since the problem was assumed to be two-dimensional, and side effects were neglected, the optimization results are given for a horizontal unit width of 1.0 cm, thus the value of P_h was 1 cm. The total heat storage for a particular storage unit may be obtained by multiplying the results presented by the number of channels connected in parallel and by the width of the storage unit. When working with Feolite as the storage material and air as the fluid the following quantities were specified before starting the optimization process:

(*a*) mass rate of flow of the fluid, $\dot{m}$;
(*b*) semithickness of the storage material, w;
(*c*) duration of the storage process, θ.

The explicit constraints for this case were:

(*a*) length $0.2 \leq L \leq 10$ m;
(*b*) flow channel semithickness $0.5 \leq d \leq 2$ cm;

while the implicit constraints associated with conditions at the end of the active storage period were:

(*a*) fluid outlet temperature $0.2 \leq T^+ \leq 0.875$;
(*b*) minimum heat storage $Q \geq Q_{\min}$;
(*c*) pressure drop $0 \leq \Delta p \leq 12.7$ cm H_2O (5 in. H_2O).

It should be noted that the values for these constraints were chosen such as to insure a practical final design. The upper limit for the length was changed when working with concrete or cast-iron and air storage units.

Results and Conclusions

In the design of a heat storage unit it was felt that the most frequently encountered independent variables would be the thermal storage material, the energy transporting fluid, the mass rate of flow of the fluid, the maximum allowable pressure drop, the thickness of the storage material, the time duration during which storage is to occur and the maximum fluid outlet temperature. A nondimensional temperature is used which takes into consideration the temperature of the the fluid entering the unit and the initial temperature of the storage material. In all the results to be presented air is used as the energy transporting fluid.

The influence of variations in the mass flow rate, the maximum allowable pressure drop, and the outlet fluid temperature were evaluated for three different storage materials, Feolite, concrete, and cast iron, and are tabulated in Tables 2–4. The time, $\theta = 60$ minutes, and

Table 2

Optimum Heat Storage Units - Feolite

Duration of active storage - 60 minutes
Inlet temperature - 100°C
Initial storage unit temperature - 20°C
Semi-thickness of storage material - 4 cm

Fluid: Air
density: 0.106×10^{-2} g/cm^3
specific heat: 1.01 J/g°C
thermal conductivity: 2.88×10^{-4} W/cm °C
kinematic viscosity: 0.188 cm^2/sec

Storage Material: Feolite
density: 3.9 g/cm^3
specific heat: 0.92 J/g°C
thermal conductivity: 0.021 W/cm °C
thermal diffusivity: 0.58×10^{-2} cm^2/sec

Constraints: length: $.2 \leq L \leq 10$ m
semi-thickness of channel: $.5 \leq d \leq 2$ cm

	RUN NUMBER						
	F-1	F-2	F-3	F-4	F-5	F-6	F-7
mass flow rate, g/sec/cm width	4	2	6	4	4	4	4
semi-thickness of channel, cm	1.01	.53	1.47	1.72	.807	1.26	1.63
length, m	3.55	1.78	5.30	3.49	3.61	6.87	14.94
outlet temperature, T^+	.875	.875	.875	.875	.875	.75	.50
heat storage, kJ/cm width	292	150	432	247	311	478	768
Q^+	.718	.732	.709	.616	.750	.606	.448
A^+	.252	.258	.248	.213	.268	.412	.662
ΔP, cm water	12.7	12.7	12.7	2.54	25.4	12.7	12.7
air horsepower/cm width	.0063	.0031	.0094	.00126	.0126	.0063	.0063

Table 4

Optimized Heat Storage Unit - Cast Iron

Duration of active storage - 60 minutes
Inlet temperature - 100°C
Initial storage unit temperature - 20°C
Semi-thickness of storage material - 4 cm

Fluid: Air
density: 0.106×10^{-2} g/cm^3
specific heat: 1.01 J/g°C
thermal conductivity: 2.88×10^{-4} W/cm °C
kinematic viscosity: 0.188 cm^2/sec

Storage Material: Cast Iron
density: 7.26 g/cm^3
specific heat: 0.42 J/g °C
thermal conductivity: 0.518 W/cm °C
thermal diffusivity: .1708 cm^2/sec

Constraints: length: $.2 \leq L \leq 20$ m
semi-thickness of channel: $.5 \leq d \leq 2$ cm

	RUN NUMBER						
	CI-1	CI-2	CI-3	CI-4	CI-5	CI-6	CI-7
mass flow rate, g/sec/cm width	4	2	6	4	4	4	4
semi-thickness of channel, cm	1.108	.586	1.609	1.816	.900	1.326	1.652
length, m	4.66	2.40	6.89	4.11	5.00	7.99	15.46
outlet temperature, T^+	.875	.875	.875	.875	.875	.75	.50
heat storage kJ/cm width	379	198	554	295	420	558	782
Q^+	.836	.848	.828	.739	.865	.718	.520
A^+	.326	.340	.318	.254	.362	.480	.674
ΔP, cm water	12.7	12.7	12.7	2.54	25.4	12.7	12.7
air horsepower/cm width	.0063	.0031	.0094	.0013	0.0126	.0063	.0063

the semithickness, $w = 4$ cm, were held constant. The constraints placed upon the other variables are given in the tables.

The effect of changes in the flow rates on the optimum designed heat storage unit using Feolite as the storage material is shown in Table 2. An optimum unit with a mass flow rate of 4.g/s/cm of unit width, a nondimensional outlet fluid temperature of $T^+ = 0.875$ and a pressure drop of 12.7 cm of water was selected. The influence of variations in the flow rate can be obtained by comparing Runs F-1, F-2, and F-3. Increasing the flow rate will cause a slight decrease per unit length in Q, Q^+, and A^+ while the total volume of material for the optimum design will be increased. The effects are not dramatic and one can conclude that connecting three units in parallel, each having a flow rate of 2.0 g/s/cm of width, will store approximately four percent more heat than a single channel, 2.98 times longer, having a flow rate of 6.0 g/s/cm of width.

Table 3

Optimized Heat Storage Unit - Concrete

Duration of active storage - 60 minutes
Inlet temperature - 100°C
Initial storage unit temperature - 20°C
Semi-thickness of storage material - 4 cm

Fluid: Air
density: 0.106×10^{-2} g/cm^3
specific heat: 1.01 J/g°C
thermal conductivity: 2.88×10^{-4} W/cm °C
kinematic viscosity: 0.188 cm^2/sec

Storage Material: Concrete
density: 2.1 gm/cm^3
specific heat: 0.878 J/g°C
thermal conductivity: 0.011 W/cm °C
thermal diffusivity: $.6 \times 10^{-2}$ cm^2/sec

Constraints: length: $.2 \leq L \leq 30$ m
semi-thickness of channel: $.5 \leq d \leq 2.5$ cm

	RUN NUMBER						
	C-1	C-2	C-3	C-4	C-5	C-6	C-7
mass flow rate, g/sec/cm width	4	2	6	4	4	4	4
semi-thickness of channel, cm	1.279	.671	1.864	2.154	1.021	1.566	1.982
length, m	7.17	3.61	10.70	6.86	7.31	13.16	26.70
outlet temperature, T^+	.875	.875	.875	.875	.875	.75	.50
heat storage, kJ/cm width	329	168	488	286	345	525	813
Q^+	.778	.788	.773	.706	.800	.675	.515
A^+	.284	.289	.280	.246	.297	.452	.700
ΔP, cm water	12.7	12.7	12.7	2.54	25.4	12.7	12.7
air horsepower/cm width	.0063	.0031	.0094	.0013	.0126	.0063	.0063

The energy storage process is a combined convection-conduction process. Increasing the fluid velocity in the channels by allowing a larger maximum pressure drop will result in a reduction in the fluid channel semithickness and a greater convective film coefficient in the optimized unit design. The total length of the optimized unit and the total heat storage will increase slightly but not in a direct proportion to the change in the pressure drop. As an example a ten fold increase in the pressure drop, from 2.54 to 25.4 cm of water, will increase the total heat storage by 26 percent, the Q^+ by 21.7 percent and A^+ by 25.8 percent. These comparisons are obtained using Runs F-1, F-4, and F-5.

A decrease in the maximum permissible fluid outlet temperature will increase the length of the heat storage unit, the total amount of heat stored and the fraction of the total available energy stored. The value of Q^+ and thus the average temperature of the storage unit will, however, be decreased as shown by Runs F-1, F-6 and F-7.

The most unexpected results of this study are those associated with a comparison of the different storage materials. In the past all comparisons of storage materials were made with geometrically identical units. The results usually indicated that those units constructed of cast iron and Feolite had similar storage characteristics while those with concrete had much less desirable storage properties. The relative merits of the different materials were found to be dependent to a certain extent on the length of time during which storage took place. Quite different trends were found when using the optimum design. A comparison of the results for the 60-min storage duration presented in Tables 2, 3, and 4 indicates that for the standard conditions (F-1, C-1, and CI-1) the concrete storage unit is about twice as long as the Feolite unit but is able to store more heat, has better utilization of the storage material since Q^+ is greater and stores more of the available energy. When one considers installation cost it is obvious that the use of concrete as a storage material must be given serious consideration. It must, however, be again emphasized that the trends are dependent on the duration of heat storage or removal and longer or shorter storage duration can be expected to alter the relative merits of the different storage materials. The effect of changes in mass flow rates, maximum pressure drop and maximum outlet temperature for concrete and cast iron are essentially the same as those previously noted for Feolite.

The effect of changes in the semithickness of the storage material and the duration of the heat input to the storage unit on the value of A^+ for a given flow rate and storage material can be seen in Fig. 2. A

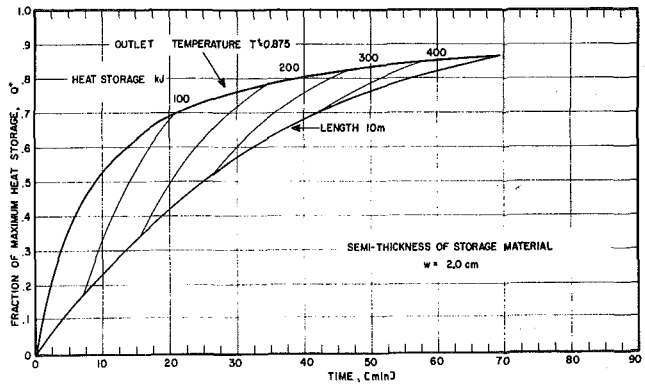

Fig. 3 Fraction of maximum heat stored; 2.0 cm semithickness

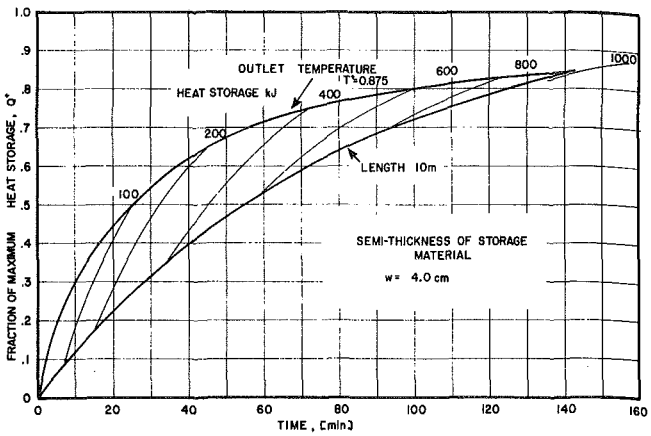

Fig. 4 Fraction of maximum heat stored; 4.0 cm semithickness

series of runs were made using the optimization program to generate this figure. For each thickness three distinct regions exist. The line at the bottom indicates a constant outlet fluid temperature of $T^+ = 0.875$ with points falling in the region below this line being units which have greater outlet temperature. The top line represents a constant unit length of ten meters thus all points in the region above this line represent longer units. The area bounded by these two lines represents the operating region for units satisfying the constraints. The mass flow rate used was 4.g/s/cm of width and the pressure drop was 12.7 cm of water.

As the thickness of the unit increases the bounded region increases as indicated in the figure. To assist in the evaluation of these results, curved lines of constant heat storage were drawn. These lines are only valid in the bounded region associated with the storage thickness selected. If the designer selects a given storage duration, θ, he can immediately determine, through the use of Fig. 2, the operating ranges of A^+ and Q which are possible while still satisfying constraints. As an example, for a storage duration of 80 min it is impossible to design a unit with 2-cm semithickness and still satisfy the constraints. A unit of 4-cm semithickness will have the following limits on A^+ and Q:

$$0.275 \leq A^+ \leq 0.475$$

and

$$430 \leq Q \leq 735 \text{ kJ/cm of width}$$

If the semithickness is 8 cm the limits are:

$$0.21 \leq A^+ \leq 0.54$$

and

$$330 \leq Q \leq 840 \text{ kJ/cm of width}$$

The fraction of the maximum possible heat storage may be determined using Figs. 3–5. Once again lines of constant outlet temperature, length and heat storage are plotted. It should be noted that the lines reverse their position indicating that the maximum value of Q^+ is determined by the outlet temperature constraint. The range over which Q^+ may vary can be determined by viewing the appropriate figure, thus, for the 4-cm semithickness:

$$0.64 \leq Q^+ \leq 0.77$$

and for the 8-cm semithickness

$$0.365 \leq Q^+ \leq 0.515.$$

These curves or similar curves can be used to size a heat storage unit for a given operating condition. The first step is to specify the storage material, the mass rate of flow per cm of width, the maximum allowable pressure drop and the duration of the storage period. Physical constraints are placed on the semi-width of the flow channel and the length of the storage unit. The inlet temperature of the fluid, the initial temperature of the storage unit and the maximum fluid outlet

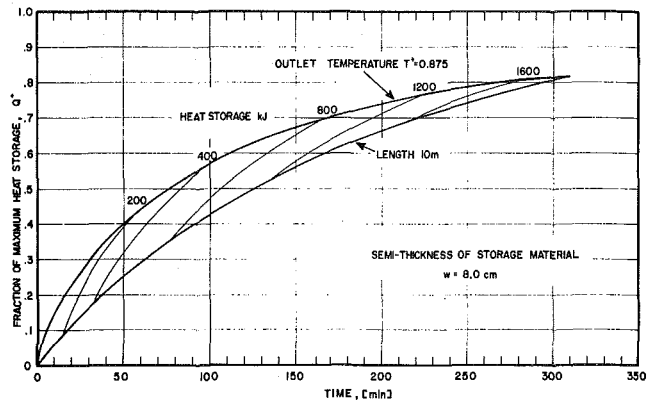

Fig. 5 Fraction of maximum heat stored; 8.0 cm semithickness

temperature are specified. A series of runs are made at various values of $Q_{\min}$ and semithicknesses and the results tabulated. The information obtained will fall on a vertical line in Figs. 2–5. The limits of Q^+, A^+, and Q for each thickness can then be determined. Economic considerations which take into account the cost of the storage material or the capital investment involved and the value of the energy stored will be used, in conjunction with the amount of heat to be stored, to select the operating point for the unit. This procedure can be illustrated using the results presented in Figs. 2 and 5. For a storage duration of 90 min a unit with a semi-thickness of 8 cm, a mass flow rate of 4 g/s cm width and the capability of storing 800 kJ/cm of width has been selected. From Figs. 2 and 5 it is found that the unit has a $Q^+ = 0.426$ and $A^+ = 0.459$. The length can be determined by noting that

$$\frac{Q^+}{A^+} = \frac{\dot{m}C_f\theta}{\rho_m C_m P_h L w}$$

which yields:

$$L = \frac{\dot{m}C_f\,\theta}{\rho_m C_m P_h}\,\frac{A^+}{w\,Q^+} \tag{1}$$

For the stated conditions the length of the optimum unit is 8.19 m. The semithickness of the channel can be obtained using the pressure drop

$$\Delta p = 48.\, f\frac{\dot{m}^2 L}{d^3} \quad \text{cm } H_2O$$

$$d = \left[\frac{48.\, f\dot{m}^2 L}{\Delta p}\right]^{1/3} \tag{2}$$

where L is in meters while all other quantities have units of length in cm. For the stated flow conditions and assuming a smooth channel the expression for the friction factor is obtained from Table 1. The Reynolds number for the stated conditions, $\mathrm{Re} = 4\,\dot{m}/\mu_f$, has the value of 8×10^4, thus,

$$f = 0.046\,(\mathrm{Re})^{-0.2} = 0.046\left(\frac{4\,\dot{m}}{\mu_f}\right)^{-0.2}$$

which for the specific conditions of this illustration gives a value of 0.0048. The value of the semithickness of the channel obtained using equation (2) is 1.34 cm. The sizing of the unit has been completed and yielded the following heat storage unit dimensions for the optimum design:

length	8.19 m
thickness	8 cm
semithickness of channel	1.34 cm

Summary

A technique suitable for the optimization of the design of a solid sensible heat storage unit has been presented. The program optimizes the design to obtain the maximum utilization of the heat storage material. The optimization program can be used to establish possible operating ranges for the fraction of the maximum possible heat stored and the fraction of the available energy stored at a given set of conditions and system constraints. Economic considerations can then be used to select the most feasible operating conditions and the unit can be sized.

Acknowledgments

The authors wish to acknowledge that this work was performed under NSF-RANN Grant AER 75-16216.

References

1 Schmidt, F. W., and Szego, J., Transient Response of Solid Sensible Heat Thermal Storage Units—Single Fluid," JOURNAL OF HEAT TRANSFER, TRANS. ASME, Series C, Vol. 98, 1976, p. 471–477.

2 Box, M. J., "A New Method of Constrained Optimization and a Comparison With Other Methods," *Computer Journal*, Vol. 8, 1965, pp. 42–52.

3 Adelman, A., Stevens, W. F., "Process Optimization by the Complex Method," *AIChE Journal*, Vol. 18, 1972, pp. 20–24.

4 Kobayashi, S., Umeda, T., and Ichikawa, A., "Synthesis of Optimal Heat Exchanger Systems—An Approach by the Optimal Assignment Problem in Linear Programming," *Chemical Engineering Science*, Vol. 26, 1971, pp. 1367–1380.

5 Spendley, W., Hext, G. R., and Himsworth, F. R., "Sequential Applications of Simplex Designs in Optimization and Evolutionary Optimization," *Technometrics*, Vol. 4, 1962, pp. 441–461.

6 Box, M. J., Davies, D., and Swann, W. H., "Nonlinear Optimization Techniques," Monograph No.5, *Mathematical and Statistical Techniques for Industry*, Imperial Chemical Industries, Ltd., Edinburgh, 1969.

7 Ghani, S. N., "An Improved 'Complex' Method of Function Optimization," *Computer Aided Design*, Vol. 4, 1972, pp. 71–78.

8 Guin, J. A., "Modification of the Complex Method of Constrained Optimization," *Computer Journal*, Vol. 10, 1968, pp. 416–417.

9 Kays, W. M., *Convective Heat and Mass Transfer*, McGraw-Hill, New York, 1966, p. 73.

10 Legkiy, V. M., and Makarov, A. S., "Heat Transfer in the Thermal Entry Region of Circular Pipes and Rectangular Ducts With Stabilized Turbulent Flow of Air," *Heat Transfer—Soviet Research*, Vol. 3, No. 6, 1971, pp. 1–9.

APPENDIX

Optimization Procedure

Basically, the complex method constructs a polygon of m vertices within the n dimensional space to be searched, $m \geq n + 1$. Box [2] refers to the polygon as a complex, hence the name of this method. Each vertex of the polygon consists of a set of independent variables which satisfy all the explicit and implicit constraints when the function $f\,[x_1, x_2, x_3, x_4 \ldots x_n]$ is evaluated. The vertex with the smallest value of f is removed from the complex and replaced by a new vertex with a larger value of f. This process is repeated until the values of f at all vertices converge to a maximum, thus determing the values of the independent variables. Evaluations of Box's complex method have been presented by Box, et al. [5], Ghani [6], and Swann [7].

The complex method used forms the following algorithm in which it is assumed that the desired optimum occurs at a maximum value of the function:

1 An initial set of independent variable values, satisfying all implicit and explicit constraints, is generated. This self-generation of the initial vertex is based upon a pattern search. Eleven equally spaced values are selected from the permissible region of each independent variable: the lower and upper bounds and nine intermediate points. The search for the independent variables starts at their lowest constraints. The value of one variable is increased and the value of the function f determined. If all the implicit constraints are met, the vertex is retained as the initial starting point. If the vertex does not satisy all the constraints, the independent variable is increased and the calculations repeated until a suitable vertex has been found or the upper bound on the variable reached. Once the upper bound is reached the variable is reset to its lowest value and another variable is increased one step. The first variable is again increased in a stepwise fashion. This process is repeated until a feasible initial vertex is reached.

2 The additional m-1 vertices, also satisfying the constraints, are randomly generated thereby completing the initial complex.

3 The function $f_i\,[x_{i1}, x_{i2}, x_{i3} \ldots x_{in}]$ is evaluated at each ith vertex of the complex. The vertex at which the function has its lowest value is found, and the geometric centroid $(x_{1c}, x_{2c}, \ldots x_{n-1c})$ of the remaining vertices is calculated using

$$x_{ic} = \frac{1}{m-1}\sum_{j=1}^{m-1} x_{ij} \text{ where } i = 1,2 \ldots, n$$

4 A new point is found to replace the vertex dropped in step 3. It is located on the line through the vertex to be removed and the centroid on the side of the centroid away from the vertex. The new point and the centroid are separated by a distance equal to the distance between the centroid and the vertex to be removed times a constant, β. If the new point selected violates an explicit constraint, the offending independent variable(s) is reset to a value within 10^{-6} of the constraint. If an implicit constraint is violated, the new point is moved halfway toward the centroid in a repeated fashion until the constraint is satisfied.

5 The value of f is calculated at the new point. If it is greater than the the value for the vertex which is being replaced, the point becomes the new vertex of the complex. If f is less than the vertex to be replaced, the new point is moved half the distance toward the centroid and re-evaluated. This process continues until a new vertex is found whose value of f is greater than the replaced vertex. If the replacement vertex is within 10^{-5} times the distance between the centroid and the original lowest valued vertex, the lowest valued vertex is retained and the next lowest value vertex replaced by reverting back to step 4. This modification of the original algorithm was proposed by Guin [8] to help prevent the vertices from collapsing onto the centroid. If this occurred too often, the number of vertices remaining would be less than n and the remaining complex could not successfully search an n dimensional space.

6 Convergence has been reached when the minimum value of f is within 10^{-7} for five consecutive iterations.

The number of complex vertices is set at $2n$ in the program. The reflection parameter, β, was assigned the value of 1.3.

S. V. Patankar
C. H. Liu
E. M. Sparrow

Department of Mechanical Engineering,
University of Minnesota,
Minneapolis, Minn.

Fully Developed Flow and Heat Transfer in Ducts Having Streamwise-Periodic Variations of Cross-Sectional Area

The concepts of fully developed flow and heat transfer have been generalized to accommodate ducts whose cross-sectional area varies periodically in the streamwise direction. The identification of the periodicity characteristics of the velocity components and of a reduced pressure function enables the flow field analysis to be confined to a single isolated module, without involvement with the entrance region problem. A similar modular analysis can be made for the temperature field, but the periodicity conditions are of a different nature depending on the thermal boundary conditions. For uniform wall temperature, profiles of similar shape recur periodically. On the other hand, for prescribed wall heat flux which is the same for all modules, the temperature field itself is periodic provided that a linear term related to the bulk temperature change is subtracted. The concepts and solution procedure for the periodic fully developed regime were applied to a heat exchanger configuration consisting of successive ranks of isothermal plate segments placed transverse to the mainflow direction. The computed laminar flow field was found to be characterized by strong blockage effects and massive recirculation zones. The fully developed Nusselt numbers are much higher than those for conventional laminar duct flows and show a marked dependence on the Reynolds number.

Introduction

For constant property flow in a duct of constant cross section, the velocity distribution becomes independent of the streamwise coordinate at sufficiently large distances from the inlet. Such an unchanging velocity distribution is said to be fully developed. For the temperature field, the fully developed regime is not as easily characterized as that for the velocity. In fact, aside from certain special cases, the temperature distribution does not become independent of the streamwise coordinate. The usual definition of the thermally developed regime is that the *shapes* of the temperature distributions at successive streamwise locations are the same, so that the successive distributions can be brought together by a suitable scaling [1].[1] In such a thermally developed flow, the heat transfer coefficient is independent of the streamwise coordinate.

By employing the aforementioned properties of the fully developed velocity and temperature distributions, the fluid flow and energy conservation equations can be significantly simplified. The main feature of the simplification is that fully developed friction factors and Nusselt numbers can be determined without having to deal with the relatively difficult task of solving the entrance region problem. The fully developed forms of the conservation equations have been solved for a broad range of duct cross-sectional shapes (for example, [1–3]).

A significant number of technically important duct configurations do not admit fully developed solutions of the type discussed in the preceding paragraphs. Among such ducts are those in which the flow cross section is not constant but, instead, varies in a periodic manner along the direction of flow. There are numerous instances of ducts with periodically varying flow cross sections. One example is a circular tube with a succession of annular ring inserts uniformly spaced along the length of the tube wall (such ring inserts are used for heat transfer

[1] Numbers in brackets designate References at end of paper.

Contributed by the Heat Transfer Division for publication in the JOURNAL OF HEAT TRANSFER. Manuscript received by the Heat Transfer Division October 28, 1976.

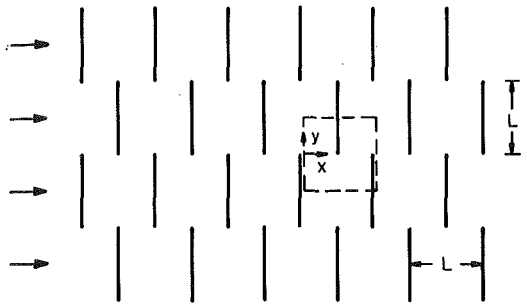

Fig. 1 Schematic diagram of a transverse plate array

augmentation). A second is a channel whose bounding walls are periodically interrupted by gaps, as in an offset plate-fin heat exchanger. Another configuration belonging to this class of duct flows is illustrated in Fig. 1, which is a schematic diagram of a staggered array of plates positioned transversely to the streamwise direction. In addition to the periodic character of its flow geometry, this configuration is unusual because, unlike conventional ducts, there are no bounding walls parallel to the direction of the mainflow.

The objective of this paper is to formulate a generalization of the concepts of fully developed flow and heat transfer in order to accommodate ducts of periodically varying cross section. The motivation for such a generalization is to provide an analytical framework which enables fully developed solutions to be obtained for these duct flows without having to deal with the entrance region problem.

The first task is to describe and analyze the fully developed velocity regime. Then, for the heat transfer problem, consideration is given to the two standard cases of uniform wall temperature and prescribed heat flux. The former is much more difficult to deal with and is, therefore, given primary attention. The procedure for dealing with the latter closely parallels that for the velocity problem.

In formulating the momentum and energy equations which govern the generalized fully developed regime, the streamwise second derivatives (i.e., streamwise diffusion) will be retained. This is in contrast to the treatment of the conventional fully developed regime, where these terms are discarded. The motivation for retaining these terms is that they are of first order importance in flow configurations of the type illustrated in Fig. 1.

A numerical scheme for solving the generalized fully developed regime is described. It employs the cyclic tridiagonal matrix algorithm. To illustrate the formulation and the solution method, as well as to provide results of practical interest, application is made to the flow configuration of Fig. 1. Solutions are obtained for a range of laminar Reynolds numbers. From these solutions, streamline maps have been prepared and are presented to illustrate the path of the flow. Results are also given for pressure drop, Nusselt number, and bulk temperature change, and the procedure for employing these results is described. The heat transfer results correspond to Pr = 0.7.

The Generalized Fully Developed Regime

The Velocity Field. For the description and analysis of the generalized fully developed regime, consideration is given to two-dimensional or axisymmetric duct flows with x as the streamwise coordinate and y or r as the transverse coordinate. Although certain three-dimensional duct flows exhibit a generalized fully developed regime, they will not be treated here. Furthermore, even though all conceptual aspects of the generalized regime apply equally well to both laminar and turbulent duct flows, only the laminar conservation equations will be dealt with in this paper.

For a two-dimensional duct flow, let the flow cross section normal to the x-direction be characterized by $Y_1(x) \leq y \leq Y_2(x)$. The quantities Y_1 and Y_2 represent the coordinates of the duct wall or of a symmetry line across which fluid does not pass. Then, for a duct of periodically varying cross section

$$Y_1(x) = Y_1(x + L) = Y_1(x + 2L) = \ldots$$
$$Y_2(x) = Y_2(x + L) = Y_2(x + 2L) = \ldots \quad (1)$$

where L is the period of the variation. The flow configuration of Fig. 1 well illustrates the periodicity condition expressed by equation (1). Y_1 and Y_2 correspond, respectively, to the symmetry lines $y = -\frac{1}{2}L$ and $y = \frac{1}{2}L$ for all x values except those where the plates jut out into the flow cross section. The periodicity condition for an axisymmetric flow is similar to equation (1), except that Y is replaced by the local duct radius $R(x)$.

Consideration may now be given to the velocity field in a duct of periodically varying cross section as defined by equation (1) and, for concreteness, reference may be made to Fig. 1. It is clear that for such a flow configuration, the conditions $\partial u/\partial x = 0$ and $v = 0$ that characterize a conventional fully developed velocity distribution cannot be fulfilled. Rather, u varies continuously with x, and v is not zero (except on the plate surfaces). On the other hand, at sufficiently large downstream distances, the velocity field repeats itself in a succession of cross sections that are separated from each other by the period length L. Consequently, the velocity components exhibit a periodic behavior

$$u(x, y) = u(x + L, y) = u(x + 2L, y) = \ldots$$
$$v(x, y) = v(x + L, y) = v(x + 2L, y) = \ldots \quad (2)$$

Equation (2) characterizes the periodic fully developed regime for the velocity field, replacing the conventional conditions $\partial u/\partial x = 0$, $v = 0$. The essential message conveyed by equation (2) is that whereas u and v vary throughout the entire flow field, it is only necessary to study their variations in a typical module which encompasses the period length L. Furthermore, the periodicity condition expressed by equation (2) enables the fully developed solution to be obtained without involvement with the entrance region problem.

Nomenclature

A = heat transfer surface area
c_p = specific heat
h = heat transfer coefficient, $(Q/A)/(T_w - T_x^*)$
k = thermal conductivity
L = period length of cross-sectional variations
$\dot{m}$ = mass flow rate
Nu = Nusselt number, hL/k
P = reduced pressure, equation (5)
Pr = Prandtl number
p = pressure
Q = surface heat transfer rate
Re = Reynolds number, $\bar{u}L/\nu$
T = temperature
T_{bx} = local bulk temperature
T_w = wall temperature
$\hat{T}$ = reduced temperature, equation (17)
T_x^* = absolute-velocity-weighted mean temperature, equation (25)
u = streamwise velocity
$\bar{u}$ = mean velocity, see text after equation (39)
v = transverse velocity
x = streamwise coordinate
Y = coordinate of duct walls
y = transverse coordinate
α = thermal diffusivity
β = pressure gradient, equation (4)
γ = temperature gradient, equation (15)
Δp = pressure drop between successive ranks of plates
θ = dimensionless temperature variable, equation (24)
λ = dimensionless T^* gradient, equation (29)
μ = viscosity
ν = kinematic viscosity
ρ = density
ϕ = function representing u, v, or p

Another essential ingredient for the analysis of the flow field is an understanding of the behavior of the pressure. It is apparent that in order for there to be a net mass flow in the positive x-direction, the pressure level must decrease with x. Therefore, the pressure does not obey the same type of periodicity condition as is expressed by equation (2) for the velocity components. There is, however, another type of periodicity condition for the pressure, as will now be described.

Consider a graph in which transverse pressure distributions (p versus y) are plotted for two axial stations x and $(x + L)$ situated well downstream of the inlet. The two curves will have identical shapes and will differ only in that the curve corresponding to $(x + L)$ is displaced downward from that for x by a uniform distance. Then, if the p versus y curve at $(x + 2L)$ is plotted in the same graph, it will have the same shape as the others and will be situated below that for $(x + L)$ such that the separation distance is identical to that between the two initial curves. It then follows that

$$p(x, y) - p(x + L, y) = p(x + L, y) - p(x + 2L, y) = \ldots \quad (3)$$

This relationship applies at any x that is situated sufficiently far from the inlet.

It can readily be understood from the prior paragraph that the pressure drop expressed by equation (3) is responsible for the global mass flow in the positive x-direction. If we define

$$\frac{p(x, y) - p(x + L, y)}{L} = \beta \quad (4)$$

where β is a constant, then it is reasonable to subdivide the pressure field into two components

$$p(x, y) = -\beta x + P(x, y) \quad (5)$$

The βx term is related to the global mass flow and $P(x, y)$ is related to the detailed local motions. Furthermore, by reconsidering the pressure graph discussed in the prior paragraph, it is evident that P is periodic, that is

$$P(x, y) = P(x + L, y) = P(x + 2L, y) = \ldots \quad (6)$$

This completes the description of the periodically fully developed flow, and attention can now be turned to the governing equations and their solution. In view of the periodicity, the solution domain can be limited to the streamwise length $x^+ \leq x \leq (x^+ + L)$, where x^+ is any convenient location. The conservation equations for mass and momentum for a constant property flow can then be written as

$$\partial u/\partial x + \partial v/\partial y = 0 \quad (7)$$

$$\rho[u(\partial u/\partial x) + v(\partial u/\partial y)] = \beta - \partial P/\partial x + \mu(\partial^2 u/\partial x^2 + \partial^2 u/\partial y^2) \quad (8)$$

$$\rho[u(\partial v/\partial x) + v(\partial v/\partial y)] = -\partial P/\partial y + \mu(\partial^2 v/\partial x^2 + \partial^2 v/\partial y^2) \quad (9)$$

where equation (5) has been employed in the evaluation of the pressure terms. It is worth noting that the terms involving $\partial^2/\partial x^2$ have been retained in recognition of the fact that large local streamwise gradients may occur in periodically fully developed flows.

Equations (7)–(9) constitute a coupled system of partial differential equations for the three unknown functions $u(x, y)$, $v(x, y)$, and $P(x, y)$. The quantity β may be regarded as an assignable parameter, the given values of which will generate corresponding mass flows (or Reynolds numbers).

On the solid bounding walls

$$u = v = 0 \quad (10)$$

whereas on bounding symmetry lines

$$\partial u/\partial y = 0, \qquad v = 0 \quad (11)$$

At the upstream and downstream ends of the solution domain, the periodicity conditions give

$$\phi(x^+, y) = \phi(x^+ + L, y), \qquad \phi = u, v, P \quad (12)$$

It is the periodicity condition (12) which decouples the solution domain from the remainder of the flow field and, in particular, from the entrance region problem.

The differential equations (7)–(9) and the boundary and periodicity conditions (10)–(12) constitute a complete mathematical description of the periodic fully developed flow. For duct configurations of practical interest, it is almost a certainty that a numerical solution will be required, with the differential equations being replaced by difference equations. We may, therefore, envision the solution domain as being partitioned by a finite difference grid in which the nodal points i, j are numbered from $i = 1$ to N and $j = 1$ to M, respectively, in the x- and y-directions.

It is interesting to examine the manner in which the periodicity condition is incorporated into the difference equations. For this purpose, let $i = 1$ and $i = N$, respectively, denote the upstream and downstream boundaries of the solution domain. In view of the periodicity, it follows that

$$\phi_{0,j} = \phi_{N-1,j}, \qquad \phi_{1,j} = \phi_{N,j}, \qquad \phi_{2,j} = \phi_{N+1,j} \quad (13)$$

for $\phi = u, v, P$. It may also be noted that the difference equation at any point i, j will contain, among others, terms involving $\phi_{i-1,j}$ and $\phi_{i+1,j}$. Then, with the aid of equation (13), it is readily seen that the difference equations along the line $i = 1$ are identical to those along the line $i = N$. Therefore, the calculation domain can be confined to the range $i = 1$ to $i = N - 1$. Furthermore, in accordance with equation (13), the difference equations at the $i = 1$ grid points will contain $\phi_{N-1,j}$ terms and, similarly, the equations at the $i = N - 1$ points will contain $\phi_{1,j}$ terms. It thus follows that the difference equations do not contain unknowns from points outside the solution domain. This insures that the number of unknowns will not exceed, but will equal, the number of difference equations.

There are many finite-difference schemes that can be employed to solve the governing equations for the periodic fully developed regime. It is the preference of the present authors to solve these problems in terms of the basic dependent variables u, v, and P rather than to transform to the stream function and vorticity. For the solutions to be discussed later, a differencing procedure and a grid layout (i.e., a staggered grid) similar to that of [4] were employed. The derivatives in the inertia terms were discretized according to the hybrid model and the pressure field was dealt with via a guess and correct procedure, all described in [4]. For the solution of the difference equations, the cyclic tridiagonal matrix algorithm was applied. Compared with other methods, this procedure is especially well suited for solving the periodic fully developed regime and is, therefore, described in the Appendix.

Although most of the prior discussion was concerned with two-dimensional duct flows, only slight modifications need to be made to accommodate axisymmetric flows.

The Temperature Field. The analysis of the periodic fully developed temperature field follows a different pattern depending on the thermal boundary condition. The first case to be considered is that in which the wall heat flux is prescribed and is the same from module to module. This case can be analyzed by extending concepts that were already discussed in connection with the velocity field. Subsequently, the uniform wall temperature case and its special features will be treated. Besides these standard thermal boundary conditions, there are other possible boundary conditions, for example, those which involve conjugate heat transfer between the fluid and its bounding solid walls. These cases will not be considered here.

For conventional duct flows with prescribed and uniform wall heat flux, the thermally developed regime is characterized by $\partial T/\partial x =$ constant. There are two factors which cause this condition to be invalid for ducts of periodically varying cross section. First, the heat transfer surface area is not uniform with x, which effectively precludes uniform heat addition to the fluid. For instance, in Fig. 1, significant portions of the boundaries $y = \pm\frac{1}{2}L$ are not heat transfer surfaces. The second factor is the presence of net axial conduction (i.e., $\partial^2 T/\partial x^2 \neq 0$).

The periodic thermally developed regime for prescribed, modularly repeating wall heat transfer can be visualized by considering temperature profiles (T versus y) at a succession of axial stations x, $(x +$

$L)$, $(x + 2L)$, ... These profiles will have identical shapes and, for the case of heating, will be displaced one above the other by the same distance so that

$$T(x + L, y) - T(x, y) = T(x + 2L, y) - T(x + L, y) = \ldots \quad (14)$$

In view of this, we define

$$\frac{T(x + L, y) - T(x, y)}{L} = \gamma \quad (15)$$

where it can be easily shown that

$$\gamma = Q/\dot{m}c_pL \quad (16)$$

in which Q is the rate of heat addition (per unit span) to the fluid in the period length L. Then, the temperature field can be subdivided into two components

$$T(x, y) = \gamma x + \hat{T}(x, y) \quad (17)$$

Furthermore, $\hat{T}$ is periodic, so that

$$\hat{T}(x, y) = \hat{T}(x + L, y) = \hat{T}(x + 2L, y) = \ldots \quad (18)$$

As was the case for the velocity problem, the periodicity condition (18) enables the solution domain for the temperature problem to be limited to the streamwise length $x^+ \leq x \leq (x^+ + L)$. By making use of equation (17), the energy equation can be written as

$$u(\partial\hat{T}/\partial x) + v(\partial\hat{T}/\partial y) + u\gamma = \alpha(\partial^2\hat{T}/\partial x^2 + \partial^2\hat{T}/\partial y^2) \quad (19)$$

To facilitate the statement of the boundary conditions, let q denote the prescribed local heat flux at the heat transfer surfaces

$$\partial T/\partial n = \gamma(\partial x/\partial n) + \partial\hat{T}/\partial n = -q/k \quad (20)$$

where n is the surface normal, whereas on symmetry boundaries

$$\partial T/\partial n = \gamma(\partial x/\partial n) + \partial\hat{T}/\partial n = 0 \quad (21)$$

In addition, at the upstream and downstream ends of the solution domain, the periodicity condition gives

$$\hat{T}(x^+, y) = \hat{T}(x^+ + L, y) \quad (22)$$

The energy equation (19) and the boundary and periodicity conditions (20)–(22) constitute a complete mathematical description of the problem to be solved for the temperature field. The numerical considerations that were discussed in connection with the solution of the velocity field also pertain here, and the advantages afforded by the cyclic tridiagonal matrix algorithm (Appendix) continue to apply.

Attention will now be turned to the uniform wall temperature boundary condition. For this case, as the fluid flows through the duct, its temperature approaches more and more closely to the wall temperature. In conventional duct flows at a sufficient distance from the inlet, the fluid-to-wall temperature differences decay exponentially to zero along the length of the duct, so that [1]

$$\frac{T(x, y) - T_w}{T_{bx} - T_w} = f(y), \qquad \frac{d(T_{bx} - T_w)/dx}{T_{bx} - T_w} = \text{constant} \quad (23)$$

where T_{bx} is the local bulk temperature and T_w is the wall temperature. Equation (23) defines the thermally developed regime for a conventional duct flow with uniform wall temperature. The first of these equations expresses the fact that the shapes of the temperature profiles at successive streamwise locations are the same. It is also relevant to note that although it is customary to use T_{bx} as a local reference quantity in equation (23), any other temperature in the cross section could be used instead (e.g., center-line temperature, area-weighted mean temperature).

Equation (23) ceases to be an appropriate definition of the thermally developed regime for a duct of periodically varying cross section. This is because the isothermal bounding surfaces are not uniformly distributed along the length of the duct (see, for example, Fig. 1). In addition, in the event that the flow contains separated regions and recirculation zones, the definition of the bulk temperature is no longer unique, so that any other convenient reference quantity may be used in its stead.

To formulate the concept of the thermally developed regime for a duct of periodically varying cross section, we first introduce a dimensionless temperature

$$\theta(x, y) = \frac{T(x, y) - T_w}{T_x^* - T_w} \quad (24)$$

where the local reference temperature T_x^*, defined to take account of possible recirculation zones where u is negative, is

$$T_x^* - T_w = \left[\int_{Y_1}^{Y_2} (T - T_w)|u|dy\right] \Big/ \left[\int_{Y_1}^{Y_2} |u|dy\right] \quad (25)$$

For a flow where u is always positive (no recirculation), $T_x^* \equiv T_{bx}$.

The periodic thermally developed regime is a logical generalization of the conventional thermally developed regime. In the periodic case, the shapes of the temperature profiles at successive streamwise locations separated by the period length L are the same. In terms of the temperature variable θ, this similarity condition is expressed as

$$\theta(x, y) = \theta(x + L, y) = \theta(x + 2L, y) = \ldots \quad (26)$$

Equation (26) is the periodic generalization of the first of equations (23).

When θ is introduced into the energy equation, there results

$$u(\partial\theta/\partial x) + v(\partial\theta/\partial y) - \alpha(\partial^2\theta/\partial x^2 + \partial^2\theta/\partial y^2) = \sigma \quad (27)$$

where

$$\sigma = [2\alpha(\partial\theta/\partial x) - u\theta]\frac{(dT_x^*/dx)}{T_x^* - T_w} + \alpha\theta\frac{(d^2T_x^*/dx^2)}{T_x^* - T_w} \quad (28)$$

Inasmuch as the left-hand side of equation (27) is periodic, it is necessary that σ also be periodic. To facilitate the examination of this condition, let

$$\lambda(x) = \frac{dT_x^*/dx}{T_x^* - T_w} = \frac{d(T_x^* - T_w)/dx}{T_x^* - T_w} \quad (29)$$

so that σ can be rewritten as

$$\sigma = [2\alpha(\partial\theta/\partial x) - u\theta]\lambda + \alpha\theta[\lambda^2 + (d\lambda/dx)] \quad (30)$$

It can be seen from equation (30) that σ will be periodic provided that λ is periodic, so that

$$\lambda(x) = \lambda(x + L) = \lambda(x + 2L) = \ldots \quad (31)$$

Equation (31) is the periodic generalization of the second of equations (23). Thus, equations (26) and (31), taken together with the definitions (24) and (29), characterize the periodic thermally developed regime and serve as a generalization of equations (23).

To determine the temperature field in the periodic module between x^+ and $(x^+ + L)$, it is necessary to solve the energy equation (27) (supplemented by (30)), together with periodicity conditions on θ and λ that follow from (26) and (31) and with the boundary conditions

$$\theta = 0 \text{ on heat transfer surfaces} \quad (32)$$

$$\partial\theta/\partial n = 0 \text{ on symmetry boundaries} \quad (33)$$

The task of obtaining solutions is made complicated by the presence of the unknown function $\lambda(x)$. The $\lambda(x)$ distribution must be such that the resulting θ solution satisfies

$$\int_{Y_1}^{Y_2} \theta|u|dy = \int_{Y_1}^{Y_2} |u|dy \quad (34)$$

at all x in the solution domain. Equation (34) follows directly from equations (24) and (25).

To describe how solutions for θ and λ can actually be obtained, it is expedient to deal directly with the finite difference form of the problem. Suppose that the difference equations corresponding to equations (27) and (30) have been derived, taking account of the boundary and periodicity conditions. At a typical interior point i, j, the difference equation can be written as

$$a_{i,j}\theta_{i,j} = b_{i,j}\theta_{i-1,j} + c_{i,j}\theta_{i+1,j} + d_{i,j}\theta_{i,j-1} + e_{i,j}\theta_{i,j+1} + P_{i,j}\lambda_{i-1} + Q_{i,j}\lambda_i + R_{i,j}\lambda_{i+1} + S_{i,j} \quad (35)$$

The last four terms, which represent the σ function of equation (30), will play the role of source terms during the iterative solution of equation (35). In particular, the θ and λ which appear in the coefficients P, Q, R, and S will be evaluated from the results of the iteration just prior to that which is in progress.[2] Thus, for the current iteration, P, Q, R, and S may be regarded as known.

To start the solution, values of θ and λ are assigned at all of the grid points, and the expression $(P_{i,j}\lambda_{i-1} + Q_{i,j}\lambda_i + R_{i,j}\lambda_{i+1} + S_{i,j})$ is evaluated at all points. The finite difference equations are then solved for θ, and the thus-determined θ distribution is denoted by θ^{I}. In general, θ^{I} will not satisfy equation (34), so that we evaluate

$$\Omega(x) = \left[\int_{Y_1}^{Y_2} |u|dy\right] \Big/ \left[\int_{Y_1}^{Y_2} \theta^{\mathrm{I}}|u|dy\right] \quad (36)$$

at each x station in the finite difference grid. Then, with these $\Omega(x)$, a new θ distribution is obtained as

$$\theta^{\mathrm{II}}(x, y) = \Omega(x)\theta^{\mathrm{I}}(x, y) \quad (37)$$

The change of θ from θ^{I} to θ^{II} implies a change in the associated λ values. To determine the new λ's (say, λ^{II}), we require that θ^{II} and λ^{II} satisfy an overall finite difference equation at each x, obtained by summing equation (35) over all points j in the cross section

$$\left(\sum_j P_{i,j}\right)\lambda_{i-1}{}^{\mathrm{II}} + \left(\sum_j Q_{i,j}\right)\lambda_i{}^{\mathrm{II}} + \left(\sum_j R_{i,j}\right)\lambda_{i+1}{}^{\mathrm{II}} + \left(\sum_j S_{i,j}\right) = \sum_j a_{i,j}\theta_{i,j}{}^{\mathrm{II}} - \sum_j (b_{i,j}\theta_{i-1,j}{}^{\mathrm{II}} + \ldots + e_{i,j}\theta_{i,j+1}{}^{\mathrm{II}}) \quad (38)$$

where, as noted earlier, P, Q, R, and S are held fixed at their initial values. The solution of equation (38) yields $\lambda^{\mathrm{II}}(x)$.

With θ^{II} and λ^{II} as input, the next round of the iteration is initiated and the successive steps are carried out as described in the foregoing paragraphs. This procedure is continued until convergence is attained to within a preassigned tolerance, and it has been the authors' experience that convergence is achieved rapidly and monotonically.

Once the solution for θ and λ has been obtained, various quantities relevant to the heat transfer characteristics of the duct flow can be evaluated. These quantities and their application will be discussed within the context of the heat exchanger analysis of the next section.

Transverse Plate Heat Exchanger

The concepts and solution procedure that have been described in the foregoing sections of the paper will now be applied to the transverse plate array that is illustrated in Fig. 1. This configuration was selected because it represents a severe test of the aforementioned solution methodology. It also may be regarded as an idealized model of certain types of heat exchangers. For the heat transfer problem, the uniform wall temperature boundary condition was chosen because it, too, provides a very demanding test of the methodology and numerical procedures.

For a typical flow channel bounded by the symmetry lines $y = \pm\frac{1}{2}L$, the cross-sectional area normal to the x-direction varies periodically, with a period length L. The solution domain selected for the analysis of the periodic fully developed flow and heat transfer is depicted by the dashed lines in the figure. The solution domain is positioned downstream of the entrance region.

If the governing equations (7)–(9) for the velocity problem are nondimensionalized, a dimensionless pressure gradient involving β emerges as the only parameter. For each prescribed value of this parameter, the solution yields a value of the Reynolds number, so that there is a one-to-one correspondence between the two quantities. Therefore, for all practical purposes, the Reynolds number may be regarded as the independent parameter of the problem. It is defined as

$$\mathrm{Re} = \bar{u}L/\nu \quad (39)$$

where $\bar{u}$ is the mean velocity of the net flow passing through the gap height L between adjacent plates in a given rank (for instance, the flow passing through the gap $0 \le y \le L$ at $x = 0$). The Reynolds number range extended from 140 to 1040.[3] For the temperature solutions, the Prandtl number is an additional parameter whose value was fixed at 0.7, which pertains to air and other gases.

The solutions were obtained numerically using a finite difference grid having 60×30 nodal points, respectively, in the x- and y-directions, with a finer spacing of points adjacent to the plate surfaces. For each case characterized by a specific value of the Reynolds number, about 250 iterations were required to obtain a converged solution (to three significant figures) for the velocity field. This corresponds to about 550 s on the CDC 6600. The converged velocity field was used as input to the temperature field calculation, which converged within 20 iterations in a computer time of 25 s.

The presentation of results will begin with a portrayal of the flow field via streamline maps as shown in Figs. 2 and 3, respectively, for Re = 140 and 1040, the smallest and largest of the Reynolds numbers investigated. The streamlines were constructed from values of the stream function obtained from $\psi = \int u dy$. The flow patterns for the two cases are quite similar. There are two features that dominate the flow field. The first is the very rapid turning of the flow in response to the blockage imposed by the front faces of the plates. The second is the massive recirculation zone situated downstream of each plate. The size of the recirculation zone is somewhat larger at higher Reynolds numbers because the more rapidly moving fluid particles require a larger turning radius in their sweep around the end of the plate. Approximately half the flow space is occupied by recirculating fluid.

A heavier line has been employed in the figures to emphasize the separation streamlines which partition the flow space into recirculation zones and throughflow zones. The cross sections through which the throughflow passes, measured normal to the streamlines, are considerably smaller than that associated with the mean velocity $\bar{u}$ that appears in the Reynolds number. Therefore, there are throughflow velocities substantially larger than $\bar{u}$, the largest being about four times $\bar{u}$. These large velocities have a decisive influence on both the heat transfer coefficients and on the pressure drop.

It may also be noted in either of Figs. 2 and 3 that the streamline pattern is repeated (but reversed from top to bottom) in the upstream and downstream portions of the solution domain. This characteristic is specific to the transverse plate array and, in order to maintain the generality of the solution procedure, it was not incorporated into the present computations.

The solutions of the energy equation enable heat transfer coefficients to be evaluated. Here, we present the respective average coefficients for the front and rear faces of a plate as well as the average coefficient for the plate as a whole (i.e., for both faces). These quantities and their dimensionless counterpart, the Nusselt number, are defined as

$$h = \frac{Q/A}{T_w - T_x{}^*}, \qquad \mathrm{Nu} = \frac{hL}{k} \quad (40)$$

where $T_x{}^*$ corresponds to the x coordinate of the plate at which Q/A is evaluated (i.e., $x = 0, \frac{1}{2}L, L, \ldots$). Q is the rate of heat transfer on the front, the rear, or both faces, and A is the corresponding surface

[2] For rapid convergence, λ^2 has been linearized as $\Lambda^2 + 2\Lambda(\lambda - \Lambda)$ in the spirit of the Newton-Raphson procedure. Here, Λ is the value of λ from the prior iteration; the terms $S_{i,j}$ in equation (35) results from $-\alpha\theta\Lambda^2$.

[3] These seemingly irregular values of Reynolds number are the result of the pressure gradient being the prescribed input quantity for the numerical solutions.

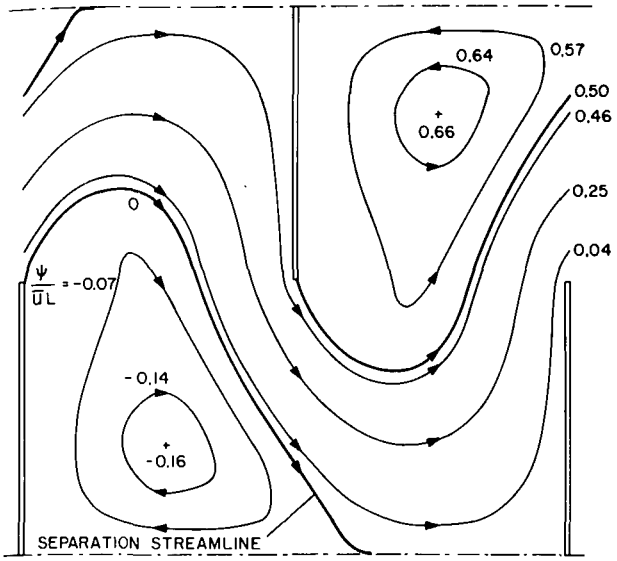

Fig. 2 Streamline maps, Re = 140

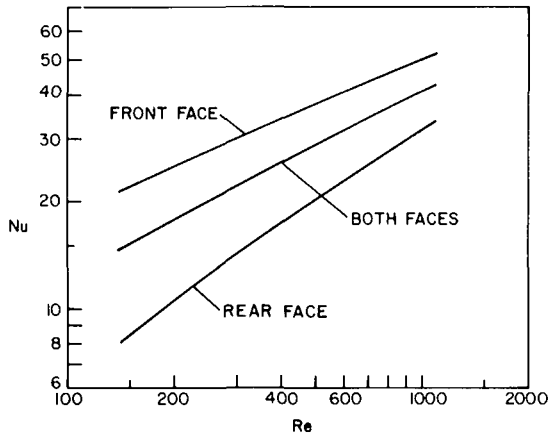

Fig. 4 Nusselt number results

area. It is readily verified that the Nusselt number for the plate as a whole is the average of those on the front and rear faces.

The Nusselt number results are presented in Fig. 4 as a function of the Reynolds number. These results are for a Prandtl number of 0.7. The figure shows that the Nusselt numbers on both faces increase significantly with the Reynolds number, with a more rapid rate of increase for the rear face. As a consequence, the large spread between the curves at low Reynolds numbers diminishes as the Reynolds number increases. The presence of a Reynolds number dependence is, in itself, worthy of note. For conventional thermally developed laminar duct flows, the Nusselt number is generally independent of Reynolds number (and also of Prandtl number), except when the Peclet number is relatively small (on the order of ten or less). The important influence of the Reynolds number on the present results is related to two factors: (*a*) large transverse velocities, (*b*) the primacy of axial conduction relative to transverse conduction. Neither of these factors are present in conventional duct flows.

It is also interesting to compare the magnitudes of the present Nusselt numbers with those of other cases. It can be shown that an array of parallel-plate channels with a plate-to-plate spacing of L has the same heat transfer surface area as the transverse plate array of Fig. 1. The Nusselt number hL/k for a parallel plate channel is 3.77, which is significantly lower than those of Fig. 4.

The involvement of the temperature difference $(T_w - T_x^*)$ in the definition of the heat transfer coefficient, equation (40), arises naturally from the dimensionless variables that were used in the analysis. In employing the Nusselt number results to compute Q at plates situated in the successive ranks $x = 0, \frac{1}{2}L, L, \ldots$, it is necessary that the T_x^* values at these streamwise stations be known. In this connection, it follows from equation (29) that

$$\frac{(T_x^* - T_w)_{x=L/2}}{(T_x^* - T_w)_{x=0}} = \exp\left[\int_0^{L/2} \lambda dx\right] \equiv G \tag{41}$$

Furthermore, at any rank of plates $x = K(L/2)$

$$\frac{(T_x^* - T_w)_{x=KL/2}}{(T_x^* - T_w)_{x=0}} = G^K \tag{42}$$

Therefore, if G is known, the value of T_x^* at any rank of plates is easily evaluated in terms of T_x^* at $x = 0$. Values of G are plotted in Fig. 5 (right-hand ordinate) as a function of the Reynolds number. The fact that higher values of G are encountered at larger Reynolds numbers confirms the expectation that the fluid will experience a smaller streamwise temperature change at higher rates of mass flow.

The need to know T_x^* at $x = 0$ is similar to the need to know the bulk temperature at a downstream location when applying conventional fully developed Nusselt numbers. Whatever means are used for estimating the latter should be applicable to the former. In fact, since the recirculation region occupies only a small part of the cross section at $x = 0, \frac{1}{2}L, L, \ldots$ (see Figs. 2 and 3), T_x^* at $x = 0$ can be taken to be equal to the bulk temperature at the $x = 0$ cross section. One common approach is to ignore the entrance region altogether, and in that case T_x^* at $x = 0$ would equal the inlet fluid temperature. This approach has considerable merit in flow configurations such as the transverse plate heat exchanger where the entrance region is expected to be short.

To supplement the heat transfer results, pressure drop information will now be presented. In Fig. 5 (left-hand ordinate), the dimensionless pressure drop Δp between any two successive ranks of plates, respectively, at $x = K(L/2)$ and $(K + 1)(L/2)$, is plotted as a function of the Reynolds number. In assessing these results, it should be noted that the velocities of the throughflow are substantially larger than $\bar{u}$, so that it is not surprising that pressure drops measured in terms of $\frac{1}{2}\rho\bar{u}^2$ are large. The pressure drops of eight to ten velocity heads that are in evidence in the figure are comparable to the losses caused by various types of valves.

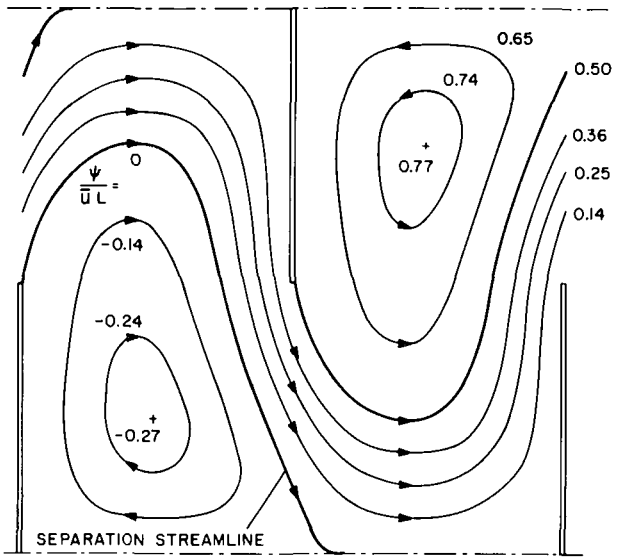

Fig. 3 Streamline maps, Re = 1040

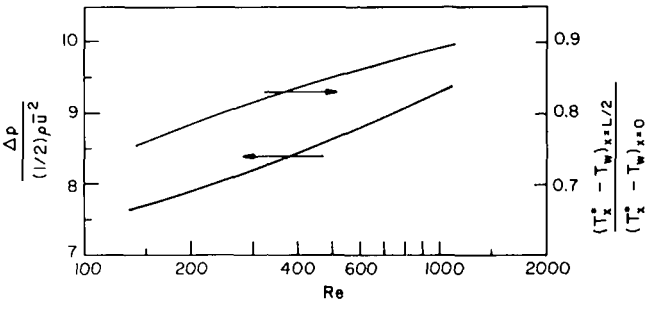

Fig. 5 Pressure drop and change in T_x^* between successive ranks of plates

Concluding Remarks

Generalized concepts of fully developed flow and heat transfer have been formulated for ducts of periodically varying cross section. Under fully developed conditions, the velocity components are periodic and the pressure can be reduced to a periodic function after subtraction of a linear term which is related to the global throughflow. The thermally developed regime is of a different character depending on the thermal boundary conditions. For the case of prescribed, modularly repeating wall heat flux, the temperature field is periodic after a linear term related to the bulk temperature change is subtracted. For uniform wall temperature, profiles of similar shape recur periodically but the temperature field is not periodic.

On the basis of the aforementioned properties, it is sufficient to confine attention to a single isolated module in analyzing the periodic fully developed regime. The mathematical formulation for the various cases was carried out in the paper and salient features of the numerical solution of the governing equations have been discussed.

The concepts and solution procedures were applied to study the laminar flow and heat transfer in a heat exchanger configuration consisting of successive ranks of isothermal plate segments placed transverse to the mainflow direction. The flow field was found to be characterized by strong blockage effects and massive recirculation zones. The Nusselt number exhibited a marked dependence on the Reynolds number, in contrast to the Reynolds number independence that characterizes conventional fully developed laminar Nusselt numbers. Both the Nusselt number and the dimensionless pressure drop for the transverse plate array are substantially higher than those of conventional laminar duct flows.

As a final perspective, it may be noted that periodic fully developed flow and temperature regimes may result from causes other than periodic variations in the duct cross sectional area. For instance, one such cause is the presence of streamwise-periodic roughness patches in an otherwise smooth constant-area duct. A second example is a succession of bends interconnected by identical segments of straight duct.

Acknowledgment

This research was performed under the auspices of NSF Grant ENG-7518141.

References

1 Shah, R. K., and London, A. L., "Thermal Boundary Conditions and Some Solutions for Laminar Duct Flow Forced Convection," JOURNAL OF HEAT TRANSFER, TRANS. ASME, Series C, Vol. 96, 1974, pp. 159–165.

2 Shah, R. K., and London, A. L., "Laminar Flow Forced Convection Heat Transfer and Flow Friction in Straight and Curved Ducts—A Summary of Analytical Solutions," TR No. 75, Department of Mechanical Engineering, Stanford University, Stanford, Calif., Nov., 1971.

3 Kays, W. M., *Convective Heat and Mass Transfer*, McGraw-Hill, New York, 1966.

4 Patankar, S. V., and Spalding, D. B., "A Calculation Procedure for Heat, Mass, and Momentum Transfer in Three-Dimensional Parabolic Flows," *International Journal of Heat and Mass Transfer*, Vol. 15, 1972, pp. 1787–1806.

5 Ahlberg, J. H., Nilson, E. N., and Walsh, J. L., *The Theory of Splines and Their Applications*, Academic Press, New York, 1967.

APPENDIX

The Cyclic Tridiagonal Matrix Algorithm

The following algorithm is a special case of Gaussian elimination. The algorithm can be found, among other places, in [5].

Our task is to solve the set of equations

$$A_i\phi_i = B_i\phi_{i+1} + C_i\phi_{i-1} + D_i \tag{A1}$$

for $i = 1, 2, \ldots, N-1$. Here, it is to be understood that

$$\text{for } i = 1: \qquad \phi_{i-1} = \phi_{N-1}$$

$$\text{for } i = N-1: \qquad \phi_{i+1} = \phi_1$$

At first we seek the following transformation

$$\phi_i = E_i\phi_{i+1} + F_i\phi_{N-1} + G_i \tag{A2}$$

where $E_1 = B_1/A_1$, $F_1 = C_1/A_1$, $G_1 = D_1/A_1$, and, for $i = 2, 3, \ldots, N-2$,

$$E_i = \frac{B_i}{A_i - C_iE_{i-1}}, \qquad F_i = \frac{C_iF_{i-1}}{A_i - C_iE_{i-1}},$$

$$G_i = \frac{D_i + C_iG_{i-1}}{A_i - C_iE_{i-1}} \tag{A3}$$

The next step is to find the value of ϕ_{N-1}. This is accomplished by writing equation (A1) for $i = N-1$ and substituting for ϕ_1 in terms of ϕ_2 and ϕ_{N-1} (from equation (A2)), then for ϕ_2 in terms of ϕ_3 and ϕ_{N-1}, and so on until ϕ_{N-1} is the only unknown left in the equation. This sequence of calculations can be expressed as follows

$$p_1 = A_{N-1}, \qquad q_1 = B_{N-1}, \qquad r_1 = D_{N-1}$$

and, for $i = 2, 3, \ldots N-2$,

$$p_i = p_{i-1} - q_{i-1}F_{i-1}, \qquad q_i = q_{i-1}E_{i-1},$$

$$r_i = r_{i-1} + q_{i-1}G_{i-1} \tag{A4}$$

$$\phi_{N-1} = \frac{(q_{N-2} + C_{N-1})G_{N-2} + r_{N-2}}{p_{N-2} - (q_{N-2} + C_{N-1})(E_{N-2} + F_{N-2})} \tag{A5}$$

Finally, equation (A2) is used to find the values of ϕ_i for $i = N-2, N-3, \ldots, 3, 2, 1$ by back substitution.

Summary. (i) Using equations (A3) and (A4), obtain E_i, F_i, G_i, p_i, q_i, r_i for $i = 1, 2, \ldots N-2$. (ii) Evaluate ϕ_{N-1} from equation (A5). (iii) Back-substitute into equation (A2) and obtain ϕ_i for $i = N-2$, $N-3, \ldots, 3, 2, 1$.

Leonardo Goldstein, Jr.
E. M. Sparrow

Department of Mechanical Engineering,
University of Minnesota,
Minneapolis, Minn.

Heat/Mass Transfer Characteristics for Flow in a Corrugated Wall Channel

Experiments based on the naphthalene sublimation technique were carried out to determine the local and average transfer characteristics for flow in a corrugated wall channel. The range of the experiments encompassed the laminar, transition, and low-Reynolds-number turbulent regimes. Local mass transfer measurements were made both in the spanwise (i.e., cross stream) and streamwise directions, and overall transfer rates were also determined. The experiments demonstrated the existence of a variety of complex transfer processes and related fluid flow phenomena. These included secondary flows and associated spanwise mass transfer variations, suppression of the secondary flow by counteracting centrifugal forces, and destruction of the secondary flow by the onset of turbulence. Flow separation on the leeward facets of the corrugated wall caused a sharp decrease in the local transfer rates, but relatively high transfer rates were in evidence in the reattachment region. In the laminar range, the average transfer coefficients for the corrugated wall channel were only moderately larger than those for a parallel-plate channel. On the other hand, in the low-Reynolds-number turbulent regime, the wall corrugations were responsible for an increase of nearly a factor of three in the average coefficient compared with the smooth wall channel.

Introduction

This paper is concerned with the local and average heat/mass transfer characteristics for laminar, transitional, and low-Reynolds-number turbulent flow in a corrugated wall channel. The wall corrugations are arranged perpendicular to the streamwise direction, and their presence induces complex flow phenomena which may have a profound influence on the heat/mass transfer results. Owing to streamline curvature which is a consequence of the waviness of the wall, centrifugal forces are set up that may induce a secondary flow superposed on the mainflow. Furthermore, in the course of its passage through the channel, the flow encounters the successive windward and leeward facets of the corrugated walls, and separation may occur on the leeward facets. The distribution of the local transfer coefficients on the channel walls is expected to reflect the complexity of the fluid flow pattern.

Measurements of local heat fluxes and temperatures needed to determine the distribution of the local heat transfer coefficient on the corrugated walls are very difficult to perform and are subject to accuracy limitations. Mass transfer techniques also present certain difficulties, but offer advantages in minimizing extraneous losses, permitting highly localized measurements, and affording the possibility of high accuracy. Among the mass transfer techniques, the naphthalene sublimation technique is especially attractive because the Schmidt number for naphthalene-air diffusion is not too different from the Prandtl numbers for heat transfer to air flow and to water flow, thereby permitting extrapolation of results via a Sc^n or Pr^n relation. The utilization of mass transfer results for heat tansfer problems is based on the heat-mass transfer analogy whereby, for a given Reynolds number, the Sherwood and Nusselt numbers are equal for equal values of the Schmidt and Prandtl numbers.

Refinements in the use of the naphthalene sublimation technique have been under development in recent years at the Heat Transfer Laboratory of the University of Minnesota [1, 2].[1] In order to utilize the technique in the present research, there were two novel problem areas that had to be resolved. The first was the fabrication of corrugated-surfaced naphthalene plates whose surface facets possessed a high degree of smoothness and flatness in their own planes. The

Contributed by the Heat Transfer Division for publication in the JOURNAL OF HEAT TRANSFER. Manuscript received by the Heat Transfer Division August 26, 1976.

[1] Numbers in brackets designate References at end of paper.

second was the highly accurate measurement of the surface contours of the facets, which are sloped relative to the horizontal. The procedures employed to deal with these problems are discussed briefly in this paper and in depth in [2].

Surface contour measurements performed before and after a data run enabled the determination of local mass transfer coefficients. Particular attention was given to the spanwise (i.e., cross stream) distributions of the transfer coefficients, inasmuch as they revealed the presence or absence of a periodic variation indicative of a spanwise array of longitudinal vortices superposed on the mainflow. Average transfer coefficients for each corrugated wall were determined by direct weighings with a precision balance, both before and after a data run.

A search of the literature revealed very little published information of direct relevance to the present research. A paper by Beloborodov and Volgin [3] presents some average Nusselt number results for corrugated wall channels for the turbulent flow range from Re = 4000 to 40,000. The description of the channel configurations is overly brief and no diagrams are given, so that there is uncertainty as to differences among various channels and as to which of several correlations one should employ. Local coefficients were not obtained, and it appears that the average coefficients were determined without direct measurement of the wall temperature. Comparisons between the turbulent results of the present investigation and those of [3] will be attempted later in the paper. Corrugated wall channels were also studied in [4] and [5], but with the positioning of the walls arranged so that the corrugations formed a succession of converging and diverging sections.

The literature has also been examined for investigations of other channel configurations which might provide background information for the present research. Cheng and Akiyama [6] analyzed laminar flow and heat transfer in curved-wall ducts of rectangular cross section, with the largest aspect ratio being 1:5. The solutions indicate a secondary flow pattern with a pair of vortices, which differs from the array of vortices encountered in the present experiments. Kreith [7] employed a simple turbulence model for analyzing the flow and heat transfer in a curved channel bounded by a pair of circular arcs. The analysis showed that the heat transfer coefficient at the concave surface of the channel was appreciably larger than that at the convex surface, and this finding was supported by sparse experimental data. Tubes and ducts with a variety of surface configurations are employed where augmented heat transfer characteristics are desired. A survey of such flow passages and their characteristics is available in [8, 9].

The sublimation of naphthalene (or para-dichlorobenzene) has been used previously as a qualitative visualization tool to identify the presence of secondary flow vortices [10, 11], but not for quantitative determinations of the associated transfer coefficients. In addition, [10] reports some fragmentary information about the effect of wall curvature on the spanwise distributions of velocity and heat transfer for a boundary layer flow along a curved flat plate.

Experimental Apparatus and Procedure

The experiments were performed with a test section that is shown in schematic side view in Fig. 1. As seen there, the flow channel is bounded by a pair of corrugated-surfaced naphthalene plates, each

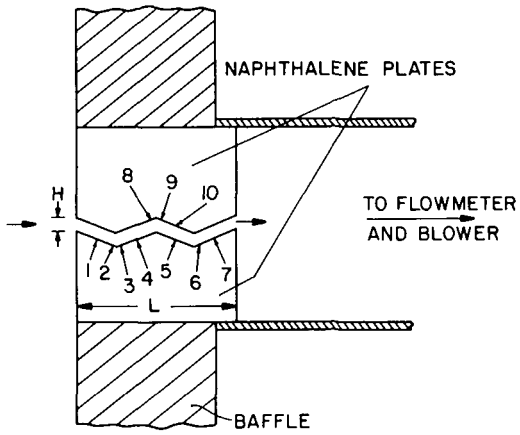

Fig. 1 Schematic side view of the test section

of which has four facets. The slope of the facets relative to the horizontal is about 21 deg. The upper and lower bounding walls are arranged so that the axial location of a crest on one of the walls coincides with the axial location of a trough on the other wall. A plan view of the channel showing nomenclature and coordinates is presented in Fig. 2. The channel dimensions H, W, and L are 1.65, 70.1, and 18.5 mm, respectively. The relatively large cross-sectional aspect ratio, $W/H = 42.5$, was chosen to minimize edge effects. The lateral walls of the channel, which served to establish the spacing between the naphthalene plates, do not participate in the mass transfer process.

The naphthalene plates were cast in specially designed and carefully fabricated molds. Inasmuch as the two walls of the channel have different corrugation patterns, it was necessary to employ a different mold for each wall. Corrugations were cut into one of the surfaces of each mold by means of a special form cutter used in conjunction with a horizontal end milling machine. All of the active surfaces of the molds were of aluminum and were hand polished and lapped to a high degree of smoothness. The molds were fitted with auxiliary parts to insure correct alignment.

When fully assembled, the walls of each mold enclosed a rectangular cavity that was open at the top to facilitate pouring the molten naphthalene. Subsequent to the initial filling of the mold, additional molten naphthalene was added to compensate for the contraction associated with solidification. The solidification was allowed to take place under air cooling conditions.

The removal of a cast plate from its mold was accomplished without the use of lubricants. Rather, unmolding was achieved by the artful application of hammer blows at strategic points on the surface of the mold. The quality of the naphthalene surfaces produced by the casting procedure was such that no subsequent machining was necessary. All naphthalene plates used in the data runs were cast from fresh (i.e., not previously used) reagent grade naphthalene.

As portrayed in Fig. 1, the experiments were performed in the

Nomenclature

A = surface area of one corrugated wall
C = constant in the correlation (11)
D_h = hydraulic diameter, $2H$
$\mathcal{D}$ = mass diffusion coefficient
H = channel height, Fig. 1
$\overline{K}$ = average mass transfer coefficient, equation (6)
L = projected streamwise length, Figs. 1 and 2
ℓ = width of measurement zone, Fig. 2
$\dot{M}$ = overall mass transfer rate for one corrugated wall
$\dot{m}$ = local mass transfer rate per unit area
$\overline{\dot{m}}$ = spanwise average mass transfer rate
$\dot{m}_{av}$ = average mass transfer rate for one corrugated wall, equation (5)
Re = Reynolds number, equation (10)
Sc = Schmidt number
$\overline{Sh}$ = average Sherwood number, equation (6)
W = channel width, Fig. 2
x = streamwise coordinate
z = spanwise coordinate
ν = kinematic viscosity
ρ_n = concentration of naphthalene vapor

Subscript

i = at streamwise station i

suction mode, with air from the laboratory room being drawn through the test section by a blower situated at a downstream location. The suction mode was selected rather than the blowing mode to avoid possible preheating of air which might have occurred had the blower been upstream of the test section. In addition to the use of the suction mode, another measure that was employed to insure thermal equilibrium between the air stream and the naphthalene plates was to leave the plates (sealed in an impervious plastic wrapper) in the temperature-controlled laboratory room for 12–24 hr prior to a data run. The concern about the attainment of thermal equilibrium is based on the fact that the vapor pressure of naphthalene is very sensitive to temperature (about 10 percent variation per deg C) at the temperature level of the experiments (about 20°C).

Upon emerging from the channel, the flow passed through a plenum chamber and was successively ducted to a flow meter, a blower, and an exhaust system which vented to the atmosphere at the roof of the building. The use of an outside exhaust insured that the room air was free of naphthalene vapor.

A well defined hydrodynamic inlet condition was obtained by the arrangement indicated in Fig. 1. The upstream end of the channel was placed in a slot that had been machined in a baffle plate. The upstream edges of the naphthalene plates were carefully aligned so as to be flush with the face of the baffle. To guard against extraneous mass transfer, all surfaces and edges of each naphthalene plate were covered with pressure-sensitive tape, except for the corrugated surface which bounded the flow channel.

The initial phase of each data run was the measurement of surface contours on the corrugated facets of the naphthalene plates, which was followed by the determination of the mass of each plate by direct weighing. The test section was then assembled and the experiment initiated. The duration time of an experiment ranged from 1200 to 5600 s, depending on the Reynolds number. The duration time was selected to limit the extent of the sublimation so as to avoid excessive changes in the channel height. For this purpose, the average sublimation from each plate was limited to about 0.03 mm (0.001 in.). Immediately after the completion of the experiment, the plates were weighed and the surface contours were again measured.

Further details of the apparatus and the experimental technique are available in [2].

Measurements

The surface contour measurements were performed with the aid of a sensitive dial gage which had a smallest scale division of 0.00005 in. (~ 0.001 mm). It was mounted on a fixed strut that overhung a horizontal coordinate table that could be independently traversed in two coordinate directions. The gage was able to accommodate an overall variation in vertical height of 0.008 in. Inasmuch as the height variation along a sloping facet is substantially greater than 0.008 in. (see Fig. 1), it was necessary to devise a fixture that would cradle the naphthalene plate so as to position the surface of a facet in the horizontal plane. Such a fixture was designed and fabricated [2]. It was fitted with stops and a clamping device to insure reproducible positioning of the naphthalene plate. Accurate positioning was aided by the high degree of flatness of the naphthalene surfaces which contact the fixture. With the aid of the fixture, two of the four facets (the first and third, or the second and fourth) were simultaneously positioned in the horizontal plane.

The surface contour measurements were made within the portion of the channel indicated by the dashed lines in Fig. 2. The spanwise length ℓ of the section is 19 mm. At a fixed streamwise position, the contour measurements were accomplished by traversing the stylus of the dial gage in the spanwise direction. Readings were taken at every 0.2 mm, so that each spanwise traverse contained 96 points. This dense spacing of data points was selected to insure accurate definition of the pattern of the spanwise variations. The traversing was controlled by micrometer heads that could be read to 0.002 mm.

The spanwise traverses were performed at each of the 10 streamwise positions indicated in Fig. 1. These positions were selected on the basis of preliminary data runs and were chosen to include both cases in which spanwise variations were either present or absent. For those facets where traverses are not indicated in Fig. 1, it had been established earlier that the spanwise variations were negligible.

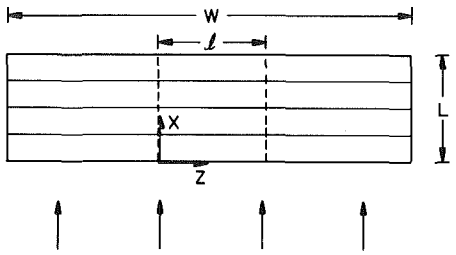

Fig. 2 Schematic plan view of the corrugated wall channel

To examine the possible effects of flow separation, streamwise traverses were made along a leeward facet—the second facet of the upper bounding wall. These measurements were carried out along the centerspan of the facet, that is, along the line $z = \ell/2$.

The precision balance employed to determine the overall mass transfer rates was capable of detecting 0.05 mg for specimens having a mass up to 200 g. The typical change in the mass of a naphthalene plate during a data run was about 45 mg.

The rate of air flow through the test section was measured with the aid of either of two rotameters, depending on the Reynolds number. The rotameter used for Reynolds numbers up to 1800 had been especially calibrated by means of a volume displacement apparatus [2] and is believed to be accurate to well within 1 percent over its entire range. The flow rates for the larger rotameter exceeded the capacity of the calibration apparatus and, as a consequence, it was necessary to accept the calibration provided by the manufacturer.

Data Reduction

By differencing the surface contour measurements before and after a data run and applying certain corrections, the local mass transfer rates can be calculated. Two corrections were applied to account for extraneous mass transfer by natural convection. The first of these was for natural convection which occurred during the period when surface contour measurements were being made with the naphthalene plate in place on the coordinate table. The second was for transfers during the set-up time of the test section. Both of these corrections were determined from auxiliary in situ experiments.

A third correction was made to account for any changes in elevation that might have occurred as a result of the removal and subsequent reinstallation of the naphthalene plate in the positioning fixture on the coordinate table. This correction was determined from before and after measurements of the surface elevation at positions under the spacer blocks that formed the lateral walls of the channel. Since these surface locations are covered during an experiment, any measured change in their elevations can be attributed to natural convection or to positioning. When the natural convection correction is applied, the remainder can be identified as the positioning correction.

The accuracy of these correction procedures has been examined in other experiments [1, 2] where it was possible to close an overall mass balance. For the mass balance, the overall mass transfer obtained by integrating the locally measured values was compared with that from direct weighing. The closure was usually within a few percent, with an extreme deviation of about 8 percent. For the present experiments, the complexity of the mass transfer distributions along the surface precluded an attempt to close an overall mass balance.

If δ denotes the corrected local change in elevation, then the local rate of mass transfer per unit area can be evaluated from

$$\dot{m} = \rho_s \delta / t_0 \tag{1}$$

where ρ_s is the density of solid naphthalene and t_0 is the duration time of a data run. At each of the streamwise locations 1, 2, . . . , 10 indicated

in Fig. 1, the spanwise distributions of $\dot{m}$ were integrated to yield the spanwise-average mass transfer rate $\overline{\dot{m}}$

$$\overline{\dot{m}_i} = \frac{1}{\ell}\int_0^{\ell} \dot{m}_i dz \tag{2}$$

in which a subscript i has been appended to identify the streamwise location.

The spanwise mass transfer distributions will be presented in terms of the dimensionless ratio

$$\dot{m}_i(z)/\overline{\dot{m}_i} \tag{3}$$

The amplitudes of these distribution curves indicate the extent of the spanwise variations relative to the local average at streamwise location i. To gain another perspective on the amplitude of the variations, a second set of distribution curves will be plotted in the form

$$\dot{m}_i(z)/\dot{m}_{\text{av}} \tag{4}$$

The denominator of this ratio is the overall average mass transfer rate for one of the corrugated walls, whichever is relevant to the streamwise location i. It was evaluated from the relation

$$\dot{m}_{\text{av}} = \dot{M}/A \tag{5}$$

where $\dot{M}$ is the overall rate of mass transfer, obtained from before and after weighings of a naphthalene plate, and A is the surface area of the corrugated wall. Values of $\dot{m}_{\text{av}}$ were separately determined for the upper and lower bounding walls.

The average mass transfer characteristics of each wall can be expressed in terms of the average mass transfer coefficient $\overline{K}$ and the average Sherwood number $\overline{\text{Sh}}$ defined as

$$\overline{K} = \frac{\dot{M}/A}{\text{log mean } \Delta\rho_n}, \qquad \overline{\text{Sh}} = \frac{\overline{K}D_h}{\mathcal{D}} \tag{6}$$

Inasmuch as the mass transfer is driven by the difference between the concentrations of the naphthalene vapor in the bulk and at the wall, $\rho_{n,b}$ and $\rho_{n,w}$ respectively, the log mean concentration difference is appropriately evaluated as

$$\text{log mean } \Delta\rho_n = \frac{(\rho_{n,w} - \rho_{n,bi}) - (\rho_{n,w} - \rho_{n,be})}{\ln\left((\rho_{n,w} - \rho_{n,bi})/(\rho_{n,w} - \rho_{n,be})\right)} \tag{7}$$

The subscripts bi and be, respectively, denote the inlet and exit bulk conditions. For the present experiments, $\rho_{n,bi} \approx 0$. The hydraulic diameter D_h was evaluated as if the channel were of infinite aspect ratio, so that

$$D_h = 2H \tag{8}$$

The concentration of the vapor at the wall, $\rho_{n,w}$, can be determined from a vapor pressure—temperature relation [12]. The wall temperature is uniform and is equal to the air temperature. The exit bulk concentration $\rho_{n,be}$ was evaluated from an overall mass balance

$$\rho_{n,be} = \rho_{n,bi} + (\Sigma\dot{M})/\dot{Q} \tag{9}$$

where $\Sigma\dot{M}$ is the sum of the mass transfer rates at the two walls, and $\dot{Q}$ is the volume flow.

The mass diffusion coefficient $\mathcal{D}$ appearing in equation (6) is related to the Schmidt number via the definition $\text{Sc} = \nu/\mathcal{D}$. For naphthalene-air mixtures, Sc = 2.5 [12]. In addition, the concentrations of naphthalene vapor are so small that ν is equal to the kinematic viscosity of air. The results will be parameterized by the Reynolds number Re evaluated as

$$\text{Re} = 2H\bar{u}/\nu \tag{10}$$

in which $\bar{u}$ is the mean velocity.

Attention should also be called to the fact that the wall boundary condition for the mass transfer process is uniform concentration of the naphthalene vapor. For the analogous heat transfer problem, the corresponding boundary condition is uniform wall temperature.

Results and Discussion

The subsequent presentation will deal successively with three types of results: (*a*) spanwise variations and effects of secondary flow, (*b*) streamwise variations along a leeward facet and effects of flow separation, (*c*) average transfer coefficients.

Spanwise Mass Transfer Distributions. Measurements of the spanwise mass transfer distribution were carried out at the ten streamwise locations indicated in Fig. 1 for each of six Reynolds numbers ranging from 500 to 3100. Spanwise traverses at other streamwise locations had been made in preliminary runs and showed variations that were in the range of the resolving power of the instrumentation. The onset of spanwise variations was observed to occur at a Reynolds number of about 370 [2], but significant amplitudes did not appear until the Reynolds number reached the 500 level.

The spanwise mass transfer distributions are presented in Figs. 3–8, with each figure corresponding to a specific Reynolds number beginning with 510 and ending at 3080. In each figure, there are two graphs. The left-hand graph gives results for the dimensionless distribution $\dot{m}_i(z)/\overline{\dot{m}_i}$, where $\overline{\dot{m}_i}$ is the spanwise average mass transfer rate at the streamwise location i. The right-hand graph contains results for the dimensionless distribution in the form $\dot{m}_i(z)/\dot{m}_{\text{av}}$, in which $\dot{m}_{\text{av}}$ denotes the average value for the corrugated wall as a whole.

Each of the distribution curves is identified by its streamwise location. Furthermore, each distribution curve has its own ordinate origin. To identify the origin for each of the $\dot{m}_i(z)/\overline{\dot{m}_i}$ curves, its 1.0

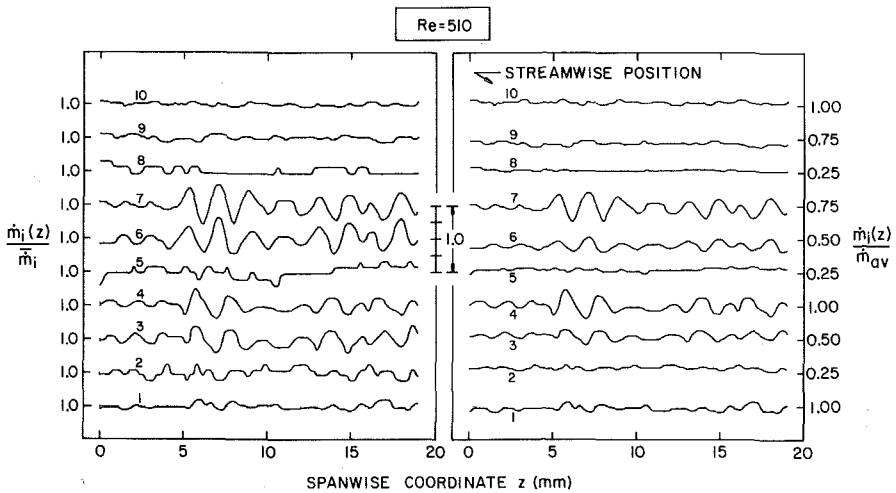

Fig. 3 Spanwise mass transfer distributions, Re = 510

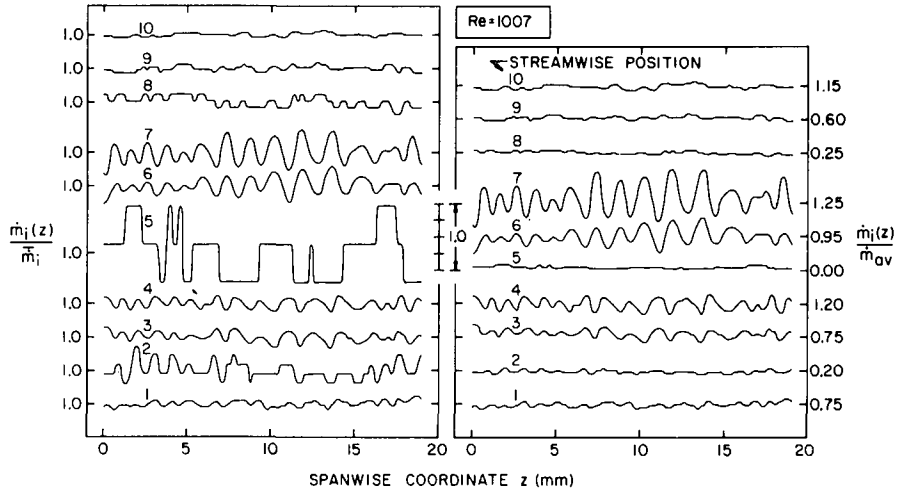

Fig. 4 Spanwise mass transfer distributions, Re = 1007

ordinate is indicated in the left-hand graphs of Figs. 3–8. The size of the ordinate scale for $\dot{m}_i(z)/\overline{\dot{m}_i}$ is common to all of the curves on a given graph and is indicated along the boundary which separates the right- and left-hand portions of each figure. Each of the $\dot{m}_i(z)/\dot{m}_{av}$ curves (right-hand graphs) also has its own ordinate origin, which is identified by the ordinate values listed along the right margin of the figure. The identified ordinate for each curve is approximately equal to $\overline{\dot{m}_i}/\dot{m}_{av}$. The size of the ordinate scale is the same for all the $\dot{m}_i(z)/\dot{m}_{av}$ curves and is identical to that for the $\dot{m}_i(z)/\overline{\dot{m}_i}$ curves. As noted earlier, each of the distribution curves represents 96 discrete data points.

A brief discussion of the motivation for using a dual presentation, respectively in terms of $\dot{m}_i(z)/\overline{\dot{m}_i}$ and $\dot{m}_i(z)/\dot{m}_{av}$, will also aid in interpreting the results. The $\dot{m}_i(z)/\overline{\dot{m}_i}$ distribution curves enable assessment of the extent of the spanwise variations at a given streamwise location relative to the average mass transfer rate at that location. However, such a presentation does not permit a comparison of the absolute extent of the spanwise variations at different streamwise locations. This is because $\overline{\dot{m}_i}$ varies appreciably as a function of streamwise location. At a location where $\overline{\dot{m}_i}$ is small, the amplitude of the $\dot{m}_i(z)$ variation may appear large when viewed in terms of $\dot{m}_i(z)/\overline{\dot{m}_i}$ but, in absolute terms, it may actually be small compared with the amplitude at some other location where $\overline{\dot{m}_i}$ is large. It is for this reason that the $\dot{m}_i(z)/\dot{m}_{av}$ distributions are also presented. Since they are based on a reference quantity that is the same[2] for all streamwise locations, comparisons among these distributions are truly indicative of where the absolute extent of the spanwise variations is large and where it is small.

Attention will first be turned to distribution curves for stations 3 and 4 and stations 6 and 7, which are respectively situated on the second and fourth facets, the windward facets, of the lower wall. These stations are characterized by spanwise variations that are the most regular and most prominent among all of the others, both when viewed in the $\dot{m}_i(z)/\overline{\dot{m}_i}$ and $\dot{m}_i(z)/\dot{m}_{av}$ formats. The regular and nearly periodic spanwise variations in evidence at these stations is a clear indication of the presence of secondary-flow vortices that are superposed on the mainflow. It is not surprising that the effects of the secondary flow are most strongly felt on windward facets where the impingement-like character of the flow presses the vortices against the surface.

[2] At a given Reynolds number, the respective $\dot{m}_{av}$ values for the two bounding walls differ only slightly, as indicated later.

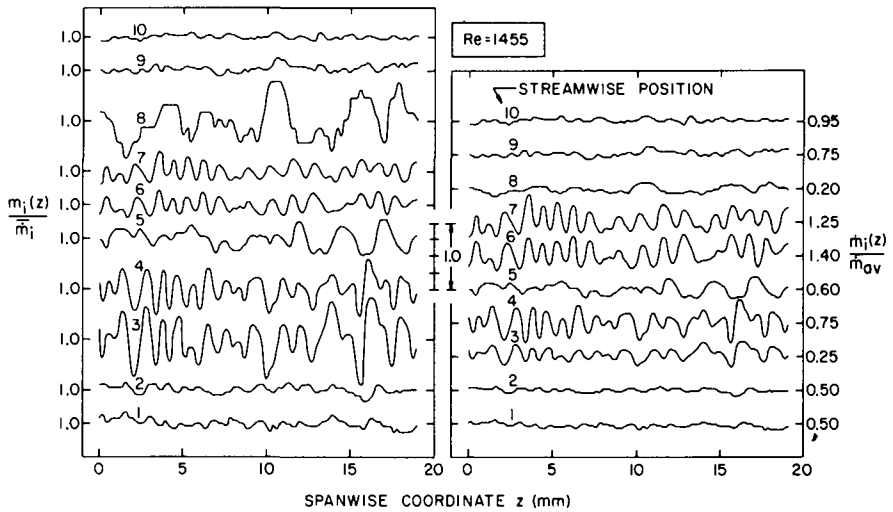

Fig. 5 Spanwise mass transfer distributions, Re = 1455

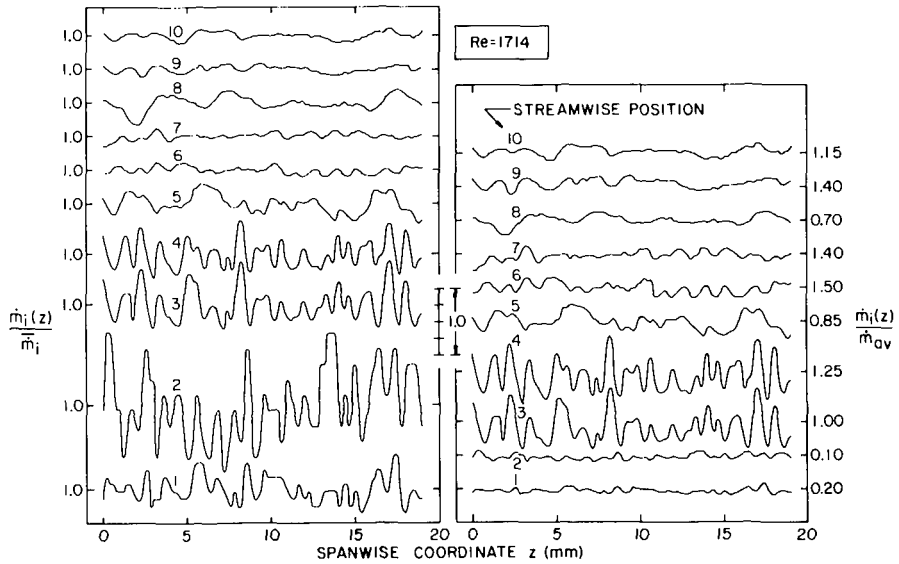

Fig. 6 Spanwise mass transfer distributions, Re = 1714

These longitudinal vortices are similar to the Görtler vortices that are formed in the boundary layer on a concave wall. They are shown pictorially in Fig. 17.32(*b*) of Schlichting [15].

It is interesting to trace the evolution of the spanwise variations on these facets as a function of the Reynolds number. At Re = 510 and especially at Re = 1007, the amplitudes on the fourth facet (stations 6 and 7) are somewhat greater than those on the second facet (stations 3 and 4). Then, with increasing Reynolds number, the variations on the fourth facet tend to diminish, so that at Re = 3080 they are hardly evident. This disappearance of the spanwise variations can be attributed to the destruction of the secondary-flow vortices by the onset of turbulent flow. On the other hand, the spanwise variations continue to be in evidence on the second facet, although they are somewhat muted at Re = 3080. It appears, therefore, that the flow in the initial portion of the channel is not fully turbulent at this Reynolds number, whereas turbulence has taken over in the downstream portion.

In considering the magnitude of the amplitudes, care must be taken to designate whether $\overline{\dot{m}_i}$ or $\dot{m}_{av}$ is being used as a reference. In either case, there is no difficulty in perceiving the fact that large amplitude variations do occur at various Reynolds numbers. For example, at Re = 1714, $\dot{m}_i(z)/\dot{m}_{av}$ varies in the range from 0.6 to 1.5 at station 3.

A careful examination of the pattern of the spanwise variations for Reynolds numbers up to 1455 reveals a 180-deg phase shift between the second and the fourth lower-wall facets. For large Reynolds numbers, the regular pattern of the variations persists on the second facet but not on the fourth. Wavelengths λ characterizing the regular pattern of variations have been determined by averaging along the spanwise distributions and are reported in Table 1. Owing to the evident departures of the distribution curves from perfect periodicity, the tabulated values are probably uncertain in the second decimal place. Notwithstanding this, it appears that the wavelength is virtually independent of the Reynolds number over most of the range.

Consideration will now be given to the results at the other streamwise locations (i.e., other than 3, 4, 6, and 7). If attention is focused on stations 9 and 10 which are situated on the third upperwall facet, a windward facet, a somewhat surprising outcome may be noted by inspection of Figs. 3–8. The surprise is the absence of clearly patterned and strong spanwise variations as might be expected on a windward facet. Although these streamwise stations are not altogether devoid of spanwise variations, the nature of their variations is different from those discussed earlier.

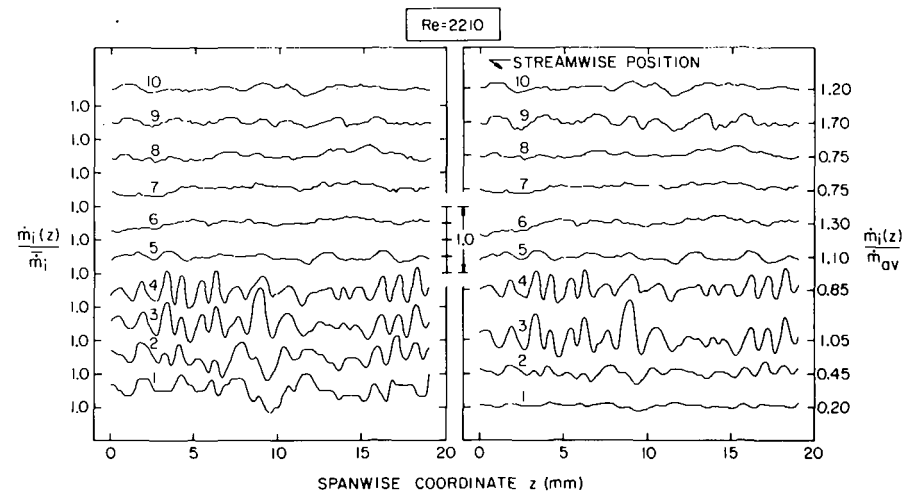

Fig. 7 Spanwise mass transfer distributions, Re = 2210

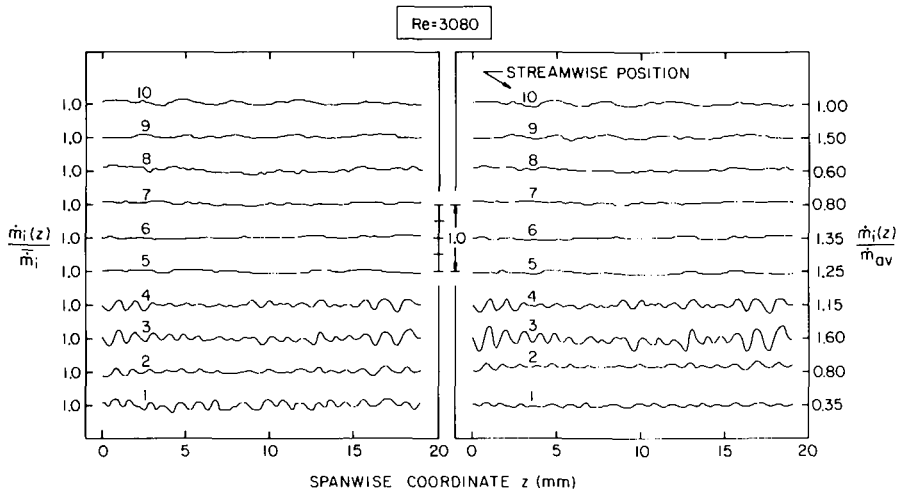

Fig. 8 Spanwise mass transfer distributions, Re = 3080

A tentative explanation of this behavior may be offered with the aid of Fig. 1. If one first imagines the streamline pattern of the mainflow, then it is easily understood that the centrifugal force induced by streamline curvature changes direction as the flow passes from the first valley of the channel to the first peak, etc. The centrifugal force induced in the first valley creates the secondary flow pattern evidenced by the distribution curves for stations 3 and 4. With respect to the centrifugal force at the first peak, it is believed that its main effect is to neutralize the aforementioned secondary flow that was created upstream. It is for this reason that a strong secondary flow pattern is not in evidence at stations 9 and 10. Subsequent to the neutralization which takes place at the first peak, the flow approaching the second valley is once again susceptible to having a new secondary flow induced by the action of the centrifugal forces there.

The distribution curves at stations 5 and 8 are intended to typify the results for a leeward facet. At the lower Reynolds numbers 510 and 1007, separation plays a significant role. This is evidenced in the figures in two ways. First, the distribution has a somewhat odd shape. Second, the identifying ordinate in the $\dot{m}_i(z)/\dot{m}_{av}$ graph, which is approximately equal to $\overline{\dot{m}_i}/\dot{m}_{av}$, is very small. In particular, at station 5 for Re = 1007, $\overline{\dot{m}_i}$ is on the order of the resolving power of the instrumentation, so that the corresponding distribution is probably strongly affected by noise. On the other hand, the spanwise variations that appear in the curves for stations 5 and 8 at Re = 510 and in the curve for station 8 at Re = 1007 may be accepted as valid results. Their pattern is somewhat related to those on the lower windward facets.

At larger Reynolds numbers, the reattachment of the separated region tends to augment the transfer rates. Spanwise distributions exhibiting patterns with various degrees of regularity are in evidence at stations 5 and 8 up to Re = 2210, whereas the distributions for Re = 3080 are essentially flat.

Stations 1 and 2 are somewhat special in that they may be influenced by entrance region phenomena as well as by separation and/or reattachment. It is evident from the figures that the distribution curves for these stations are affected by the secondary flow that is induced in the first valley of the channel. The evidences of the secondary flow persist up to the highest Reynolds number investigated, Re = 3080. As noted earlier in connection with the discussion of stations 3 and 4, the persistence of secondary flow at that Reynolds number is suggestive that turbulence is not yet dominant in the initial portion of the channel.

Separation and Reattachment on a Leeward Facet. The spanwise mass transfer distributions that were discussed in the preceding section suggested that flow separation and reattachment significantly affected the mass transfer results on the leeward facets. A more systematic examination of these effects will now be made. To this end, streamwise mass transfer distributions, measured along the spanwise centerline $z = \ell/2$ of the second upper-wall facet, are presented in Fig. 9. The figure contains seven graphs, each of which corresponds to a specific Reynolds number. In each graph, $\dot{m}(x)/\dot{m}_{av}$ is plotted as a function of the streamwise distance along the facet (the facet length is 4.95 mm).

As shown in the figure, for Reynolds numbers up to 1455, the rate of mass transfer at all points on the facet is very much lower than the overall average for the corrugated wall. This is indicative of a relatively quiescent separated region. Then, with increasing Reynolds number, a distinct maximum appears near the downstream end of the facet. This maximum can be identified as the point at which the flow reattaches to the wall. The drop-off downstream of the reattachment point is due to redevelopment of the velocity profile.

The height of the reattachment peak increases with increasing Reynolds number and the point of reattachment moves upstream. At the higher Reynolds numbers, the mass transfer rates at the reattachment peak actually exceed the overall average for the cor-

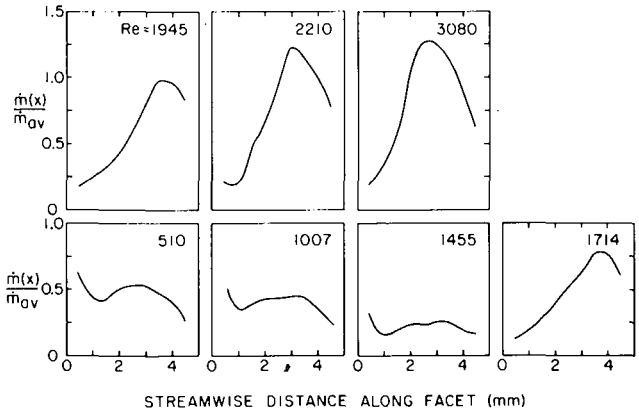

Fig. 9 Streamwise mass transfer distributions along a leeward facet (second upper-wall facet)

Table 1 Wavelength of the spanwise distributions

Re	510	1007	1455	1714	2210	3080
λ/H	1.13	0.78	0.63	0.61	0.68	0.58

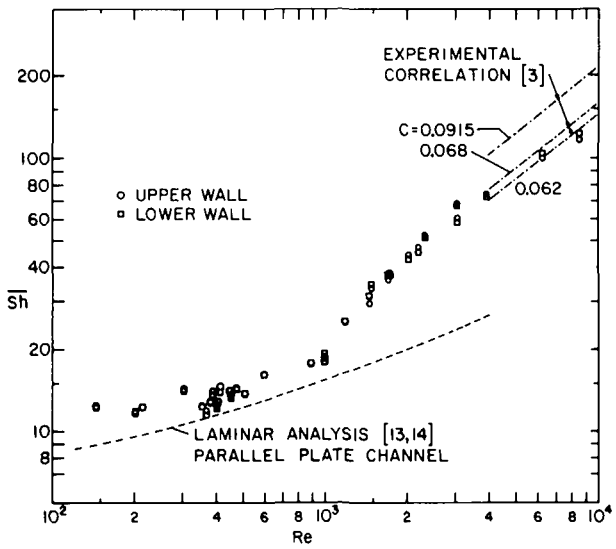

Fig. 10 Average mass transfer coefficients

rugated wall. On the other hand, locations near the upstream end of the facet continue to be dominated by separation and are characterized by mass transfer rates that are well below the overall average.

Average Transfer Coefficients. Owing to the significantly simpler data acquisition requirements, a substantially larger number of runs were able to be made to obtain average mass transfer coefficients than were performed for the local coefficient study. The Reynolds number range for the average coefficients extended from about 150 to 8550. The results thus obtained are presented in Fig. 10 in terms of the average Sherwood number $\overline{Sh}$. At each Reynolds number, the Sherwood numbers for the upper and lower walls are plotted as distinct data points. In all cases, the two points are nearly coincident.

Inspection of the figure indicates that in the range of Reynolds numbers up to about 1000, the Sherwood number gradually increases with Reynolds number. Then, somewhere between Re = 1000 and 1200, there is a change of slope so that, thereafter, the Sherwood number increases more rapidly.

The onset of this more rapid rise in the Sherwood number could be indicative of post-separation reattachment and/or of the beginning of turbulence in the downstream portion of the channel. However, on the basis of the local results presented earlier in the paper, the onset of the rise would be expected in the Reynolds number range from 1400 to 1700 rather than in the range from 1000 to 1200. Evidently, the phenomena which initiated the rise evidenced in Fig. 10 were not detected during the local coefficient study.

The scatter of the data in the Reynolds number range between 350 and 420 may be related to the instability phenomena associated with the onset of the secondary-flow vortices.

In addition to the present data, Fig. 10 contains several curves depicting information from the literature. The dashed line represents the analytical prediction for simultaneously developing laminar concentration and velocity profiles in the entrance region of a parallel-plate channel with uniform wall concentration [13, 14]. In the Reynolds number range up to 1000, the deviation of the data from this line is only 10–25 percent. This is a surprising outcome, inasmuch as larger differences would have been expected on the basis of geometrical and flow field differences between the two types of channels.

The several dot-dashed lines at the upper right of the figure represent correlations of data by Beloborodov and Volgin [3] for corrugated wall channels. The fact that several lines have been included in the figure is indicative of the present authors' difficulty in understanding the overly brief test section descriptions given in [3]. One aspect of the difficulty is a tabulation which lists values of channel width, minimum channel width, and maximum channel width, none of which are defined in a sketch or by discussion. In three cases listed in the table, there was no evident inter-relationship between the values of the width, the minimum width, and the maximum width. In two cases, the width and the minimum width were the same.

The correlation of [3] is of the form

$$\overline{Nu} = CRe^{0.8}Pr^{n}(Pr/Pr_w)^{0.25} \tag{11}$$

with $n = 0.43$ for heating and 0.3 for cooling. The values of the constant C are specific to the various configurations tested. The range of C was from 0.062 to 0.0915, and these values are portrayed by the upper and lower dot-dashed lines. The correlation for the cases where the width and the minimum width were the same has a C value of 0.068, and the corresponding line is also shown in the figure. It is the intuitive feeling of the present authors that the latter line is the one to which most attention should be paid. In evaluating equation (11), $\overline{Nu}$ was replaced by $\overline{Sh}$ and Pr was replaced by Sc; furthermore, Sc = 2.5, $n = 0.43$, and $Sc/Sc_w = 1$. According to [3], the correlation (11) is for Re > 4000.

The figure indicates very good agreement between the present data and the correlations of [3] based on C values of 0.062 and 0.068. The agreement is especially remarkable in view of the significant differences between the experimental apparatus and instrumentation of the two investigations.

Concluding Remarks

The present experiments have demonstrated an interesting variety of complex transfer processes and related fluid flow phenomena. These include: (*a*) secondary flows with associated spanwise variations in the mass transfer rate, (*b*) suppression of secondary flow effects by a counteracting centrifugal force, (*c*) destruction of the secondary flow by the onset of turbulence, (*d*) the coexistence of turbulent and nonturbulent flows in different parts of the channel, and (*e*) the respective suppression and augmentation of the mass transfer rates by separation and by reattachment.

From the standpoint of the average transfer coefficients, it appears that the flow can be regarded as laminar up to a Reynolds number of 1000–1200. In this range, the experimentally determined transfer coefficients for the corrugated wall channel are only moderately larger than those for a parallel-plate channel. The situation is quite different at higher Reynolds numbers, for example, Re = 6000–8000. If average turbulent Sherwood numbers for a smooth wall channel are evaluated from the Dittus-Boelter equation and compared with the present measurements, it is found that the corrugated wall results exceed those for the smooth channel by nearly a factor of three. This indicates that wall corrugations can serve as effective augmentation devices for low-Reynolds-number turbulent flows.

Acknowledgment

Scholarship support from the Brazilian National Council of Research (CNPq) extended to Leonardo Goldstein, Jr. is gratefully appreciated. The research was supported by the National Science Foundation under Grant ENG-7503221.

References

1 Saboya, F. E. M., "Local and Average Transfer Coefficients in Plate Fin and Tube Heat Exchanger Configurations," PhD thesis, University of Minnesota, Minneapolis, Minn., 1974.

2 Goldstein, L., Jr., "Local Mass Transfer in Corrugated-Walled Ducts and Heat Exchanger Configurations," PhD thesis, University of Minnesota, 1975.

3 Beloborodov, V. G., and Volgin, B. P., "Heat Transfer and Pressure Drop in Heat Transfer Equipment With Slot Channels of Varying Cross Section," *International Chemical Engineering*, Vol. 11, 1971, pp. 229–233.

4 Kirpikov, V. A., Gutarev, V. V., and Tsirel'man, N. M., "A Study of the Heat Transfer and Frictional Resistance in a Diverging-Converging Duct," *Heat Transfer Soviet Research*, Vol. 2, No. 2, 1970, pp. 48–53.

5 Kirpikov, V. A., and Tsirel'man, N. M., "Heat Transfer and Frictional Resistance in Turbulent Gas Flow in the Field of an Alternating Pressure Gradient," *Heat Transfer Soviet Research*, Vol. 3, No. 2, 1971, pp. 116–121.

6 Cheng, K. C., and Akiyama, A., "Laminar Forced Convection Heat Transfer in Curved Rectangular Channels," *International Journal of Heat and Mass Transfer*, Vol. 13, 1970, pp. 471–490.

7 Kreith, F., "The Influence of Curvature on Heat Transfer to Incompressible Fluids," TRANS. ASME, Vol. 77, 1955, pp. 1247–1256.

8 Bergles, A. E., Survey and Evaluation of Techniques to Augment Convective Heat and Mass Transfer, in *Progress in Heat and Mass Transfer*, Vol. 1, Pergamon Press, 1969, pp. 331–424.

9 Bergles, A. E., "Recent Developments in Convective Heat Transfer Augmentation," *Applied Mechanics Reviews*, Vol. 26, 1973, pp. 675–682.

10 McCormack, P. D., Welker, H., and Kelleher, M., "Taylor-Goertler Vortices and Their Effect on Heat Transfer," JOURNAL OF HEAT TRANSFER, TRANS. ASME, Series C, Vol. 92, 1970, pp. 101–112.

11 Kestin, J., Discussion of a paper in the JOURNAL OF HEAT TRANSFER, TRANS. ASME, Series C, Vol. 89, 1967, pp. 175–176.

12 Sogin, H. H., "Sublimation From Disks to Air Streams Flowing Normal to Their Surfaces," TRANS. ASME, Vol. 80, 1958, pp. 61–71.

13 Sparrow, E. M., "Analysis of Laminar Forced Convection Heat Transfer in the Entrance Region of Flat Rectangular Ducts," NACA TN 3331, 1955.

14 Stephan, K., "Wärmeübergang und Druckfall beinicht ausgebildeter Laminarströmung in Rohren und in eben Spalten," *Chemie-Ingr.-Tech.*, Vol. 31, 1959, pp. 773–778.

15 Schlichting, H., Boundary Layer Theory, Sixth ed., McGraw-Hill, New York, 1968.

R. B. Holmberg

AB Svenska Flaktfabriken,
Jönköping, Sweden

Heat and Mass Transfer in Rotary Heat Exchangers With Nonhygroscopic Rotor Materials

Heat and mass transfer in rotary heat exchangers with nonhygroscopic rotor materials have been investigated. A numerical method of the finite-difference type is applied to the steady-state performance under conditions of finite rotational speed and finite longitudinal heat conduction. Temperature and absolute humidity distributions are calculated for a set of rotary heat exchanger parameters typical in air conditioning, and temperature and humidity efficiencies are evaluated for different inlet air conditions.

Introduction

This study of rotary heat exchangers with nonhygroscopic rotor materials is concerned with the heat and moisture recovery for air conditioning. However, the results may be applicable to rotary heat exchangers in other fields. The exchanger consists essentially of a rotor matrix, comprising a set of passages, through which hot and cold fluids flow in separate parts of the rotor. The heat given up to the rotor surfaces from the hot fluid is stored in the rotor material during the rotation of the rotor, and is subsequently transferred to the cold fluid. The heat transfer in rotary heat exchangers has been analyzed by several authors [1–4][1] in connection with gas turbine-regenerator applications. In particular, the steady-state behavior has been treated [3] in respect to both finite rotational speed and finite longitudinal heat conduction in the solid.

In this paper simultaneous heat and mass transfer are analyzed for nonhygroscopic rotor materials and the problem is described for the air-conditioning case. Thus, the moisture of the exhaust air is transferred by condensing on the rotor surface, when the surface temperature falls below the inlet dew-point temperature of the exhaust air. The condensed water vapor then follows the rotor to the supply air side, where it is evaporated into the supply air. If the surface temperature falls below the ice-point temperature also, the moisture is deposited on the surface as frost and is sublimated on the supply-air side. The used method, based on the heat and mass transfer analogy, gives satisfactory results for the air-conditioning case, since the mass transfer rate is low. The heat and mass transfer rate equations result in two first-order ordinary differential equations, and the energy balance results in a parabolic second order partial differential equation. The parabolic equation, represented by the Crank-Nicholson finite-difference scheme, is solved by the Gauss-Seidel iterative method. The calculation method is applied to the steady-state behavior including finite rotational speed and finite longitudinal heat conduction.

Governing Equations

The governing differential equations for the simultaneous heat and mass transfer in a rotary heat exchanger with a nonhygroscopic rotor material will be given with the following idealizations:

1 The thermal resistance of the rotor material is infinite in the tangential direction, finite in the fluid-flow (axial) direction and zero in the radial direction.

2 The thermal properties of the two fluids and of the rotor material are constant with temperature and time.

3 No mixing of the fluids occurs either as a result of direct leakage or carry-over.

4 The heat and mass transfer coefficients between the fluids and the rotor matrix are constant with flow length.

5 The fluids pass in counterflow directions.

6 The inlet temperature and humidity distributions of the fluids are uniform over the flow-inlet cross sections and constant with time.

7 The transferred water vapor is condensed and evaporated at the same cross section, viewed in the fluid-flow direction.

8 The heat capacity of the two fluids and of the condensed water vapor or frost is negligible in comparison with the heat capacity of the rotor material.

9 The energy change of the water vapor during its transport through the boundary layer is neglected.

[1] Numbers in brackets designate references at end of paper.

Contributed by the Heat Transfer Division for publication in the JOURNAL OF HEAT TRANSFER. Manuscript received by the Heat Transfer Division September 7, 1976.

10 Regular periodic conditions are established for all matrix elements; i.e., steady-state operation.

On the basis of these idealizations a set of differential equations can be expressed for the hot-fluid side (similar equations can be expressed for the cold-fluid side).

The heat-transfer rate equation is

$$C_h \frac{\partial t_h}{\partial y} = -\frac{(hA)_h}{L}(t_h - t_r) \tag{1}$$

The mass-transfer rate equation is

$$W_h \frac{\partial x_h}{\partial y} = -\frac{(\beta_x A)_h}{L}(x_h - x_s) \tag{2}$$

The energy balance is

$$W_h \frac{\partial i_h}{\partial y} + M_h = -\left(\frac{m_r c_r}{L}\frac{\partial t_r}{\partial \tau} - kA_{k,h}\frac{\partial^2 t_r}{\partial y^2}\right) \tag{3}$$

where the melting heat of the frost is represented by

$$M_h = r_i W_h \frac{\partial x_h}{\partial y} \qquad \text{for } t_{rh} < 0°\text{C},$$

$$M_h = -r_i \int_0^\tau W_h \frac{\partial x_h}{\partial y}\, d\tau \qquad \text{for } t_{rh} = 0°\text{C},$$

$$M_h = 0 \qquad \text{for } t_{rh} > 0°\text{C}$$

The enthalpy derivative for moist air is expressed by

$$\frac{\partial i_h}{\partial y} = c_{ph}\frac{\partial t_h}{\partial y} + r_0 \frac{\partial x_h}{\partial y} \tag{4}$$

where $c_{ph} = c_{pa} + x_h c_{pv}$ is assumed to be constant with $x_h = (x_{h1} + x_{h2})/2$. The results are given for $c_{pa} = 1.005$ kJ/kg-°C for dry air, $c_{pv} = 1.86$ kJ/kg-°C for water vapor, $r_0 = 2.500$ kJ/kg and $r_i = 333$ kJ/kg.

The absolute humidity of the air at the rotor surface is related to the surface temperature. When this temperature is below the dew-point temperature of the air, condensation will occur and when it is below the ice-point temperature too, frosting will occur. In both cases the air at the surface will become saturated. The saturation absolute humidity is obtained from

$$x_s = 0.62198 \frac{p_{vs}}{p_{\text{atm}} - p_{vs}}$$

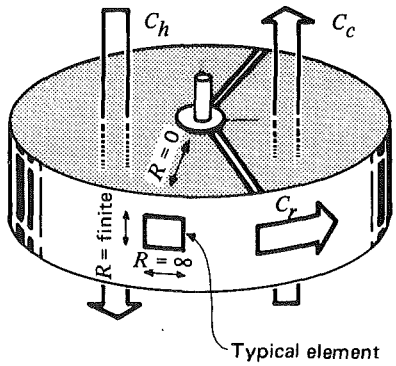

Fig. 1 Illustrative rotor arrangement

where the saturation pressure p_{vs} over liquid water for the temperature range of 0 to 100°C and over ice for the range of −100 to 0°C is determined according to Goff formulas [5].

Calculation Method

The governing differential equations are solved by a finite-difference method. The rotor matrix shown in Fig. 1 can be subdivided into a finite number of elements, as indicated schematically in Fig. 2. A typical element (i, j) on the hot-fluid side is shown in Fig. 3. Although Fig. 1 is an axial-flow type exchanger, typical elements can be selected in the same way for a radial-flow type exchanger. It is apparent from Fig. 3 that each of these elements can be regarded as a cross-flow exchanger with an air stream and a "rotor stream."

For the element (i, j) on the hot-fluid side, the heat transfer rate equation (1) is represented by an ordinary central difference scheme

$$t_h(i, j) - t_h(i + 1, j) = \frac{(hA)_h}{C_h N_r}\Delta t_{h,\text{av}}(i, j) \tag{5}$$

where the mean temperature difference between the air and the rotor matrix is assumed as the arithmetic mean value according to

$$\Delta t_{h,\text{av}}(i, j) = \frac{1}{2}[t_h(i, j) + t_h(i + 1, j)] - \frac{1}{2}[t_{rh}(i, j) + t_{rh}(i, j + 1)]$$

Nomenclature

A = heat-transfer area on one side, m²
A_k = cross-sectional area for longitudinal heat conduction on one side, m²
$A_{k,t}$ = total cross-sectional area for longitudinal heat conduction, $A_{k,c} + A_{k,h}$, m²
c_p = specific heat of fluid (at constant pressure), J/kg dry gas-°C
c_r = specific heat of rotor matrix, J/kg-°C
C = heat capacity rate of fluid, Wc_p, W/°C
C_r = heat capacity rate of rotor matrix, $m_r c_r n$, W/°C
h = heat transfer coefficient, W/m²-°C
i = enthalpy of fluid, J/kg dry gas
k = thermal conductivity, W/m-°C
L = flow length, m
m_r = mass of rotor matrix, kg
n = rotational speed of rotor, r/s
N = number of subdivisions
p = pressure, Pa
p_{atm} = atmospheric pressure, Pa
r_0 = latent heat of vaporization, J/kg
r_i = melting heat, J/kg
R = thermal resistance, °C/W
t = temperature of fluid, °C
Δt = temperature change in passing through exchanger, °C
t_r = temperature of rotor matrix, °C
U = overall heat transfer coefficient, $1/(A/(hA)_c + A/(hA)_h)$, W/m²-°C
W = mass flow rate of fluid, kg dry gas/s
W_w = mass flow rate of drainage liquid, kg/s
x = absolute humidity of fluid, kg vapor/kg dry gas
y = flow length coordinate measured from hot-fluid inlet
β_x = mass transfer coefficient, kg vapor/m²-s-Δx
φ = relative humidity of fluid, p_v/p_{vs}
τ = time, s
(i, j) = typical element on hot-fluid side
(f, g) = typical element on cold-fluid side

Nondimensional Parameters

η_t = temperature efficiency, $\Delta t/(t_{h1} - t_{c1})$
η_x = humidity efficiency, $\Delta x/(x_{h1} - x_{c1})$
C_c/C_h = capacity rate ratio of fluid streams
$C_r/C_{\min}$ = capacity rate ratio of rotor matrix to minimum fluid capacity rate
$N_{tu,0}$ = overall number of transfer units, $UA/C_{\min}$
$(hA)^+$ = thermal resistance ratio, $(hA)_c/(hA)_h$
$A_k{}^+$ = conduction area ratio, $A_{k,c}/A_{k,h}$
Λ = total conduction parameter, $kA_{k,t}/(LC_{\min})$
ϕ = mixing parameter, $h/(\beta_x c_p)$

Subscripts

1 = inlet
2 = outlet
a = air
av = average
c = cold fluid or cold-fluid side
h = hot fluid or hot-fluid side
min = minimum
r = rotor matrix
s = saturation
v = water vapor

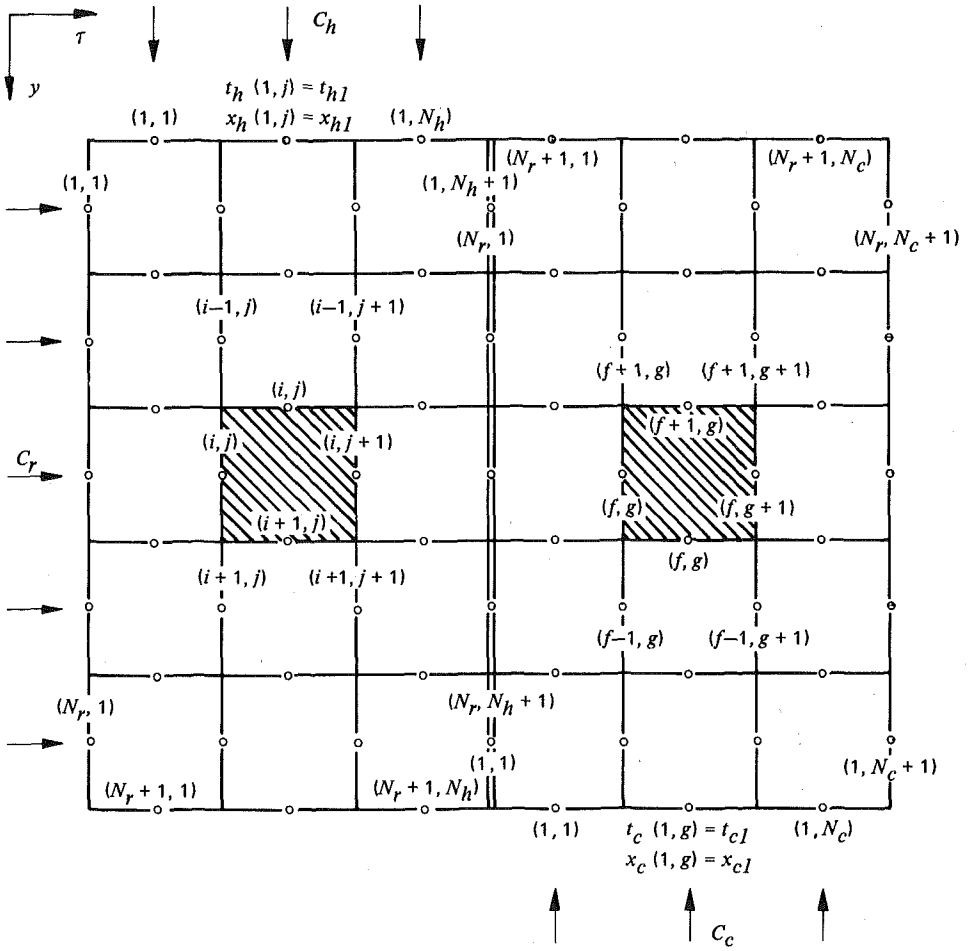

Fig. 2 Schematic representation of a rotary heat exchanger

Similarly, the mass transfer rate equation (2) is represented by

$$x_h(i, j) - x_h(i + 1, j) = \frac{(hA)_h}{C_h N_r} \frac{1}{\phi} \Delta x_{h,\mathrm{av}}(i, j) \tag{6}$$

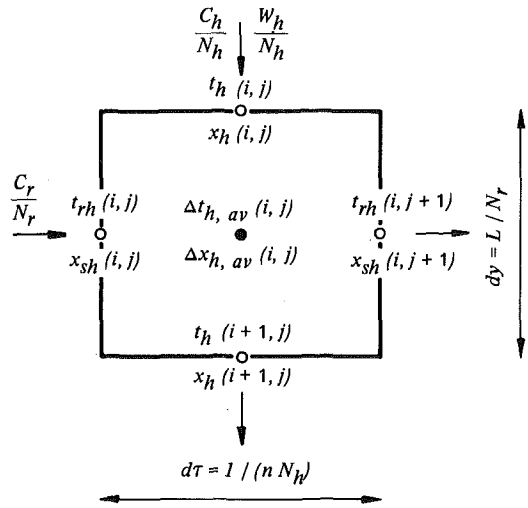

Fig. 3 Typical element (*I*, *j*) on the hot-fluid side

where the mean difference between the absolute humidity in the air and at the rotor surface is assumed to be

$$\Delta x_{h,\mathrm{av}}(i, j) = \frac{1}{2}[x_h(i, j) + x_h(i + 1, j)] - \frac{1}{2}[x_{sh}(i, j) + x_{sh}(i, j + 1)]$$

and $\phi = h/(\beta_x c_p)$ is the mixing parameter. The Lewis relation $\phi = 1$ is assumed to be valid for the water-air mixture. Reference [6] gives more details about the mixing parameter for different mixtures.

The energy balance (3) together with the enthalpy expression (4) is represented by the implicit Crank-Nicholson scheme

$$\begin{aligned} t_h(i, j) - t_h(i + 1, j) + \frac{r_0}{c_{ph}}[x_h(i, j) - x_h(i + 1, j)] + \overline{M}_h \\ = \frac{C_r N_h}{C_h N_r}[t_{rh}(i, j + 1) - t_{rh}(i, j)] \\ - \frac{kA_{k,h}N_r}{LC_h 2}[t_{rh}(i + 1, j) + t_{rh}(i - 1, j) - 2t_{rh}(i, j) \\ + t_{rh}(i + 1, j + 1) + t_{rh}(i - 1, j + 1) - 2t_{rh}(i, j + 1)] \end{aligned} \tag{7}$$

where the melting heat of the frost is represented by

$$\overline{M}_h = 0 \qquad \text{for } 0 \leq t_{rh}(i, j) < t_{rh}(i, j + 1),$$

$$\overline{M}_h = -\frac{r_i}{c_{ph}} \sum_{k=1}^{j-1} [x_h(i, k) - x_h(i + 1, k)]$$

$$\text{for } t_{rh}(i, j) < 0 \leq t_{rh}(i, j + 1),$$

$$\overline{M}_h = \frac{r_i}{c_{ph}} [x_h(i, j) - x_h(i + 1, j)] \text{ for } t_{rh}(i, j) < t_{rh}(i, j + 1) < 0$$

Similarly, equations for the heat transfer rate, the mass transfer rate and the energy balance can be expressed for the element (f, g) on the cold-fluid side.

The boundary conditions are as follows:

For the inlet on the hot-fluid side

$$t_h(1, j) = t_{h1}, \qquad j = 1, 2, N_h$$

$$x_h(1, j) = x_{h1}, \qquad j = 1, 2, N_h$$

For the inlet on the cold-fluid side

$$t_c(1, g) = t_{c1}, \qquad g = 1, 2, N_c$$

$$x_c(1, g) = x_{c1}, \qquad g = 1, 2, N_c$$

On the cold-rotor seal

$$t_{rh}(i, 1) = t_{rc}(f, N_c + 1), \qquad i = 1, 2, N_r, \quad f = N_r + 1 - i$$

which means that the left edge in Fig. 2 is physically the same as the right edge. This will later be referred to as the reversal condition.

On the hot-rotor seal

$$t_{rc}(f, 1) = t_{rh}(i, N_h + 1), \qquad f = 1, 2, N_r, \quad i = N_r + 1 - f$$

The longitudinal heat conduction is zero at the ends of the rotor in fluid-flow direction, i.e.,

$$t_{rh}(0, j) = t_{rh}(1, j), \qquad j = 1, 2, N_h$$

$$t_{rh}(N_r + 1, j) = t_{rh}(N_r, j), \qquad j = 1, 2, N_h$$

$$t_{rc}(0, g) = t_{rc}(1, g), \qquad g = 1, 2, N_c$$

$$t_{rc}(N_r + 1, g) = t_{rc}(N_r, g), \qquad g = 1, 2, N_c$$

The moisture transfer during one rotor revolution proceeds as follows. The water vapor in the hot exhaust air condenses on the rotor surfaces, when the matrix temperature $t_{rh}(i, 1)$ is lower than the inlet dew-point temperature t_{hd} of the exhaust air. Since the matrix temperature $t_{rh}(i, j)$ at a certain cross section of the matrix (row i) increases during the rotation on the hot-fluid side (increasing j), the condensed water vapor begins to evaporate already on the hot-fluid side as soon as $t_{rh}(i, j)$ exceeds t_{hd}. On the other hand, if $t_{rh}(i, j)$ is lower than t_{hd} during the whole hot-fluid period, the condensed water vapor will begin to evaporate at first on the cold-fluid side. Thus, the moisture transfer is determined by the condensation on the hot-fluid side, as long as the supply air is able to absorb all the condensed water vapor. Assuming that the condensed water vapor evaporates at the same cross section (viewed in the fluid-flow direction) as it condensed, the following conditions for the moisture transfer can be expressed.

The evaporation on the hot-fluid side is limited by the condensation

$$\frac{1}{j} \sum_{k=1}^{j} x_h(i + 1, k) \leq x_{h1} \qquad \text{for } j = 1, 2, N_h \text{ and } i = 1, 2, N_r.$$

The evaporation on the cold-fluid side is limited by the net condensation on the hot-fluid side

$$\frac{W_c}{N_c} \sum_{k=1}^{g} [x_c(f + 1, k) - x_c(f, k)] \leq \frac{W_h}{N_h} \sum_{j=1}^{N_h} [x_h(i, j) - x_h(i + 1, j)]$$

for $g = 1, 2, N_c$, $i = 1, 2, N_r$ and $f = N_r + 1 - i$

If the matrix temperature is lower than the ice-point temperature, the moisture in the exhaust air is deposited on the rotor surface as frost instead of liquid water. If the matrix temperature exceeds the ice-point temperature during the rotation on the hot-fluid side, the frost will melt and the liquid water will begin to evaporate on the cold-fluid side. However, if the matrix temperature is cooled below the ice-point temperature during the rotation on the cold-fluid side, the liquid water will freeze and the frost will sublimate instead of evaporate.

When the humidity of the exhaust air is very high and/or the temperature of the supply air is very low, the supply air will become saturated and will not be able to absorb all the moisture deposited on the rotor surface in the hot-fluid period. A water surplus will thus result in the rotor, and this water will be drained away, unless it is frozen during the whole revolution. The energy of this drainage has been neglected in the theory discussed previously, which is evident from expression (4). The water surplus for the whole rotary heat exchanger can be expressed as

$$W_w = W_h(x_{h1} - x_{h2,av}) - W_c(x_{c2,av} - x_{c1})$$

The water surplus will remain frozen during the whole revolution at the cross section of the matrix (row i), where the matrix temperature is lower than the ice-point temperature during the whole revolution, i.e., $t_{rh}(i, N_h + 1) \leq 0°C$. This limit, at which frost will begin to be built up, is referred to as the frosting limit. The theory given in this paper does not cover the transfer process at which frost is built up.

The ordinary nondimensional parameters in this field defined on the minimum and maximum heat capacity rates cannot be used, since we have to distinguish between the hot and cold fluids. The mass transfer rate depends on the rotor surface temperature, and the absolute humidity of the air at the surface is not linear with the surface temperature. Thus, the nondimensional parameters are chosen as follows

$$C_c/C_h,\ C_r/C_{\min},\ N_{tu,0},\ \Lambda,\ (hA)^+,\ A_k{}^+,\ \phi$$

The temperature and humidity efficiencies of the heat exchanger are defined as

$$\eta_{zh} = \frac{z_{h1} - z_{h2,av}}{z_{h1} - z_{c1}}, \qquad \eta_{zc} = \frac{z_{c2,av} - z_{c1}}{z_{h1} - z_{c1}}$$

where z stands for t and x, and the average values for z_{h2} and z_{c2} are

$$z_{2,av} = \frac{1}{N} \sum_{k=1}^{N} z(N_r + 1, k)$$

The finite-difference equations are solved for $t(i + 1, j)$, $x(i + 1, j)$ and $t_r(i, j + 1)$ and are given in the Appendix. The calculation method becomes iterative and the Gauss-Seidel method is used. After each iteration, an energy balance is made and before a solution is accepted for a particular set of parameters, the energy balance error together with the reversal condition must be satisfied to a specified accuracy. The energy balance error is determined from the difference between the hot-fluid and the cold-fluid enthalpy changes compared to the hot-fluid enthalpy change.

The accuracy of the calculated efficiencies by this method depends on the error criterion as well as on the number of subdivisions. The error of 0.005 percent for both convergence conditions, together with the number of subdivisions $N_r = N_h = N_c = 16$, gives the calculated efficiencies good to four significant figures. As an example, the temperature efficiency for the parameter values without mass transfer

$$C_c/C_h = 1,\ N_{tu,0} = 5,\ C_r/C_{\min} = 5,\ \Lambda = 0,\ (hA)^+ = A_k{}^+ = 1$$

becomes $\eta_t = 0.8289$, which agrees completely with the data given in [3].

Calculated Results

In order to study how mass transfer influences heat transfer, the temperature distribution has been calculated with and without mass transfer for these parameter values and the following inlet air conditions:

Inlet air temperatures $t_{h1} = 20°C$, $t_{c1} = -10°C$ and inlet absolute

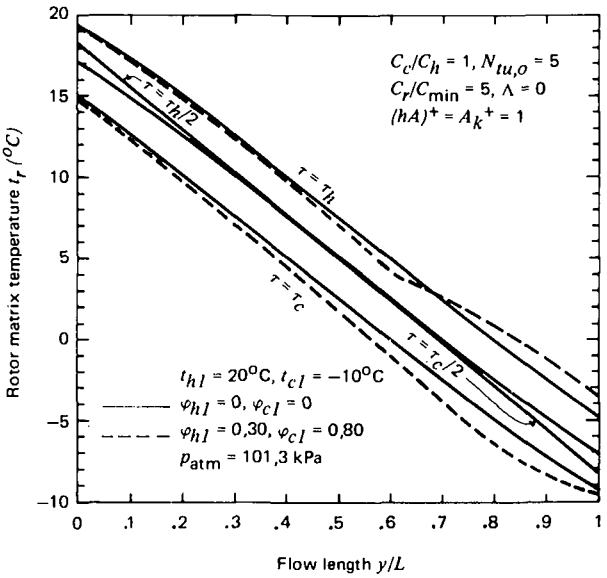

Fig. 4 Effect of moisture transfer on matrix temperature distribution

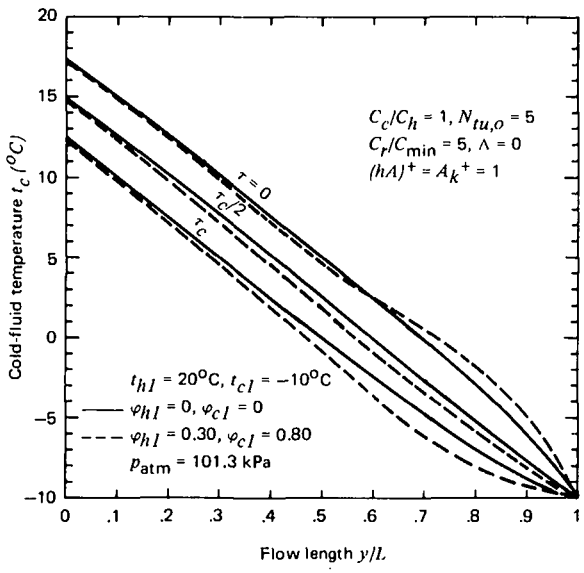

Fig. 6 Effect of moisture transfer on cold-air temperature distribution

humidities in the case of mass transfer $x_{h1} = 0.00427$ kg/kg ($\varphi_{h1} = 0.30$), $x_{c1} = 0.00127$ kg/kg ($\varphi_{c1} = 0.80$) for atmospheric pressure $p_{atm} = 101.3$ kPa.

The temperature efficiencies in the case of no mass transfer become $\eta_{th} = \eta_{tc} = 0.8289$, while in the case of mass transfer the efficiencies are somewhat decreased to 0.8222. From Fig. 4, it is clear that the maximum temperature change of the rotor matrix over one rotational period increases in that part of the rotor matrix, where moisture is transferred. This is understood by the fact that the latent heat, which is released on condensation on the hot-fluid side, is picked up by the rotor and is transferred to the cold-fluid side, where it is expended in evaporating the condensate. Thus, the rotor must not only transfer the sensible heat but also the latent heat. If the moisture is transported as frost on the rotor surface, the rotor must transfer the melting heat too. The hot-air and cold-air temperatures for these cases are shown in Figs. 5 and 6 as a function of the flow length and the rotational periods as parameters. The cyclic temperature fluctuations are shown in Fig. 7.

The humidity efficiencies in the case of mass transfer become $\eta_{xh} = 0.5631$ and $\eta_{xc} = 0.5617$ with the mass-flow rate ratio $W_c/W_h = (C_c/C_h)\cdot(c_{ph}/c_{pc}) = 1.0025$. Fig. 8 illustrates that the hot air begins to give up its moisture at about $y/L = 0.5$ where, according to Fig. 4, the matrix temperature is 1.75°C which correspond to the inlet dew-point temperature of the hot air. Since the matrix temperature increases during the hot-fluid period, some of the condensed water vapor evaporates already during that period. Fig. 8 also shows that the cold air absorbs most of the moisture deposited on the rotor surface as water or frost in the beginning of the cold period, as the matrix temperature in that part is high. In this case, all the moisture is absorbed by the cold air before the cold-fluid period is finished, which is clearly shown by Fig. 9.

In Fig. 10 the temperature and humidity efficiencies are given for

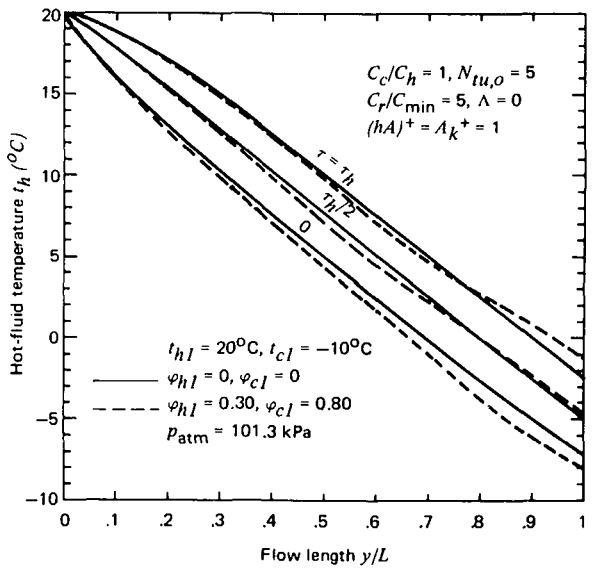

Fig. 5 Effect of moisture transfer on hot-air temperature distribution

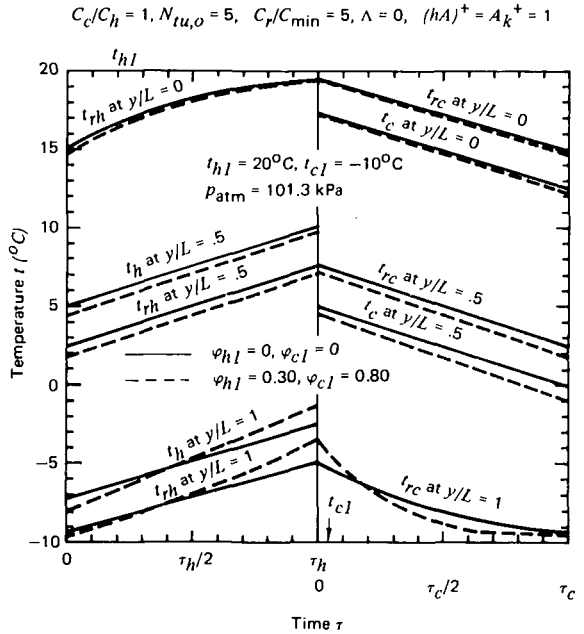

Fig. 7 Effect of moisture transfer on cyclic temperature fluctuations

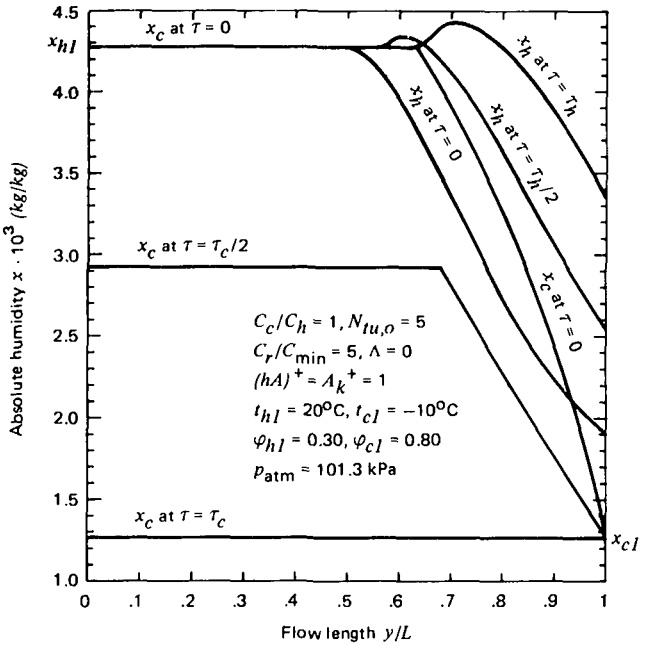

Fig. 8 Absolute humidity distributions in fluid-flow direction for hot and cold air

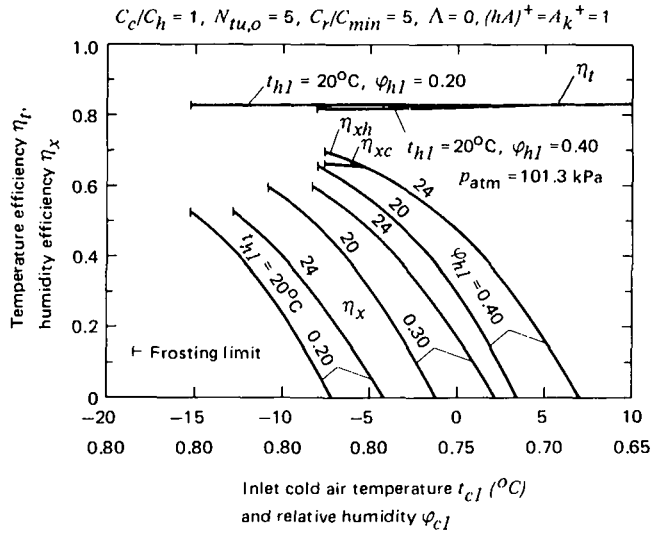

Fig. 10 Temperature and humidity efficiency for different inlet conditions

typical different inlet values in air conditioning. It is seen that the humidity efficiencies increases with decreasing inlet temperature of the cold air and with increasing temperature and humidity of the hot air. It also appears that no water surplus ($\eta_{xc} < \eta_{xh}$) is obtained without building up frost for the given inlet hot-air conditions except for $t_{h1} = 24°C$ and $\varphi_{h1} \approx 0.40$. The frosting limits, which are marked in the figure, indicate that frost is built up for lower inlet cold-air temperatures. Furthermore, we note that the temperature efficiency here is very little influenced by the moisture transfer, as the rotor heat capacity is high. For lower rotor heat capacities the temperature efficiency is more influenced by the moisture transfer, which is shown in Fig. 11. However, the humidity efficiency decreases faster than the temperature efficiency for decreasing rotor heat capacity, which may be useful in cases where low moisture transfer is desired. The frosting limit is at the same time moved to lower inlet cold-air temperatures.

Conclusions

The numerical method used to calculate heat and mass transfer in rotary heat exchangers with nonhygroscopic rotor materials is completely general for the problem of steady-state performance in respect to fluid and matrix capacity rates, heat and mass transfer coefficients, transfer areas, longitudinal heat conduction, and inlet air conditions.

The moisture transfer influences the heat transfer due to the fact that the maximum temperature change of the rotor matrix over a rotational period increases when moisture is transferred, since not only the sensible but also the latent heat and melting heat, if any, must be transferred by the rotor.

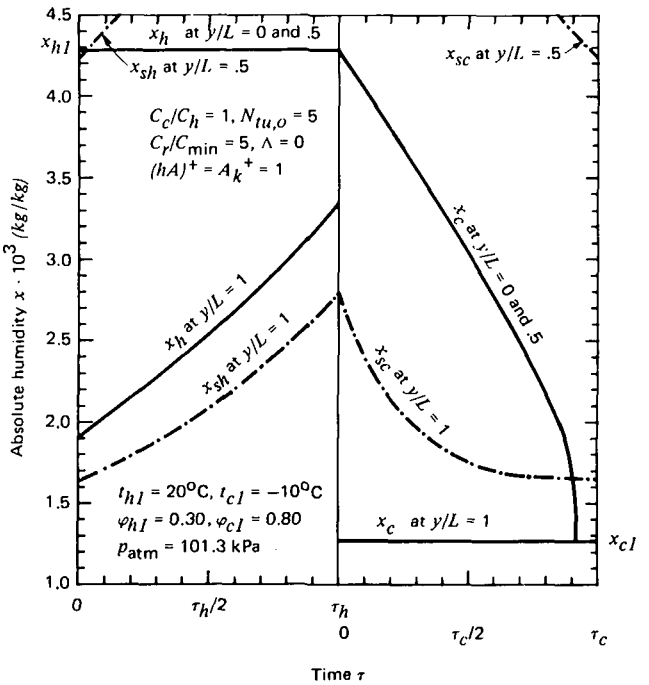

Fig. 9 Cyclic absolute humidity fluctuations

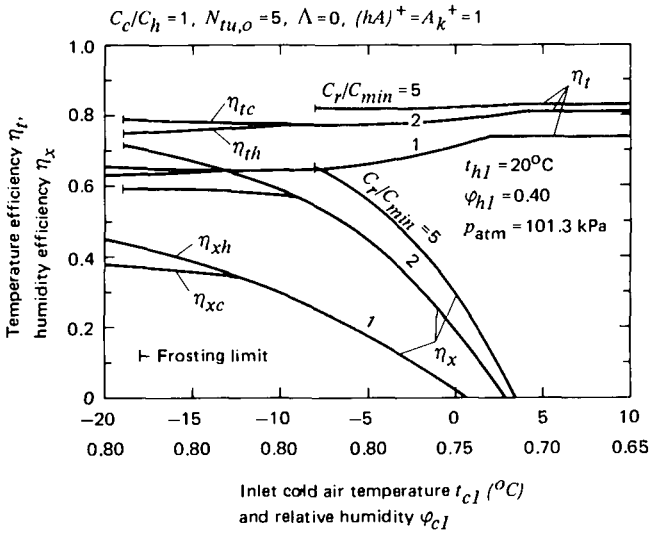

Fig. 11 Temperature and humidity efficiency for different rotor heat capacities and different inlet conditions

The humidity efficiency increases with decreasing inlet cold-air temperature and with increasing inlet hot-air temperature and humidity. However, it is limited by the risk of frost formation.

Acknowledgment

The author wishes to express his thanks to AB Svenska Fläktfabriken for permission to publish this paper.

References

1 Coppage, J. E., and London, A. L., "The Periodic-Flow Regenerator—A Summary of Design Theory," TRANS. ASME, Vol. 75, 1953, pp. 779–787.

2 Lambertson, T. J., "Performance Factors of a Periodic-Flow Heat Exchanger," TRANS. ASME, Vol. 80, 1958, pp. 586–592.

3 Bahnke, G. D., and Howard, C. P., "The Effect of Longitudinal Heat Conduction on Periodic-Flow Heat Exchanger Performance," JOURNAL OF ENGINEERING POWER, TRANS. ASME, Series A, Vol. 86, 1964, pp. 105–120.

4 Mondt, J. R., "Vehicular Gas Turbine Periodic-Flow Heat Exchanger Solid and Fluid Temperature Distributions," JOURNAL OF ENGINEERING POWER, TRANS. ASME, Series A, Vol. 86, 1964, pp. 121–126.

5 ASHRAE Handbook of Fundamentals, ASHRAE Inc., New York, 1972.

6 Schlünder, E. U., "Einfluss molekularer Transportvorgänge auf die Zustandsänderung von Gas/Dampf-Gemischen," *Chemie-Ing.-Techn.*, Vol. 35, 1963, pp. 169–174.

Appendix

The equations (5), (6), and (7) for the hot-fluid side can be expressed in the following equation system:

$$t_h(i+1,j) = B_1 t_h(i,j) + B_2\,[t_{rh}(i,j) + t_{rh}(i,j+1)],$$

$$x_h(i+1,j) = B_3 x_h(i,j) + B_4[x_{sh}(i,j) + x_{sh}(i,j+1)],$$

$$t_{rh}(i,j+1) = B_5 t_h(i,j) + B_6[x_h(i,j) - x_h(i+1,j)]r_0/c_{ph} + B_6\overline{M}_h - B_7 t_{rh}(i,j) + B_8[t_{rh}(i-1,j) + t_{rh}(i-1,j+1) + t_{rh}(i+1,j) + t_{rh}(i+1,j+1)]$$

where

$$B_1 = (1 - C_1)/(1 + C_1), \qquad B_2 = C_1/(1 + C_1),$$

$$B_3 = (1 - C_2)/(1 + C_2), \qquad B_4 = C_2/(1 + C_2),$$

$$B_5 = 2C_1/C_5, \qquad B_6 = (1 + C_1)/C_5,$$

$$B_7 = [C_1 + (1 + C_1)(2C_4 - C_3)]/C_5, \qquad B_8 = (1 + C_1)C_4/C_5,$$

and

$$C_1 = \frac{(hA)_h}{2N_r C_h} = \frac{1}{2N_r}\frac{C_{\min}}{C_h} N_{tu,0}\left[1 + \frac{1}{(hA)^+}\right],$$

$$C_2 = \frac{(\beta_x A)_h}{2N_r C_h} = \frac{C_1}{\phi},$$

$$C_3 = \frac{N_h}{N_r}\frac{C_r}{C_h} = \frac{N_h}{N_r}\frac{C_{\min}}{C_h}\frac{C_r}{C_{\min}},$$

$$C_4 = \frac{kA_{k,h}}{LC_h}\frac{N_r}{2} = \frac{N_r}{2}\frac{C_{\min}}{C_h}\Lambda\frac{1}{1 + A_k{}^+},$$

$$C_5 = C_1 + (1 + C_1)(2C_4 + C_3)$$

Similarly, the corresponding equations can be expressed for the cold-fluid side.

H. B. Becker
Engineer,
Herman Research Laboratory,
State Electricity Commission of Victoria,
Australia

A Mathematical Solution for Gas-to-Surface Radiative Exchange Area for a Rectangular Parallelepiped Enclosure Containing a Gray Medium

The transfer of heat in a gas filled enclosure can be calculated by the zone method put forward by Hottel and Cohen [1, 2].[1] *For a shape which can be divided into cylindrical or cubic zones, tabulated and graphical data on exchange areas are available, however, insufficient data exist for subdivision into rectangular zones. The present contribution provides a mathematical solution for the gas-to-surface exchange area between a rectangular parallelepiped gas volume and an adjacent face. The rules for manipulating and scaling of exchange areas are reviewed, and their application to the zoning of a rectangular furnace chamber into concentric rectangular volume elements is demonstrated.*

Introduction

Radiative transfer between emitting and absorbing gas volumes, and bounding surfaces, of various geometrical shapes occurs in many instances of practical importance in industry, notably where the gas contains significant quantities of water vapor and carbon dioxide at elevated temperatures. This applies particularly to combustion chambers where heat transfer is dominated either by radiation from nonluminous gas, or gas with soot, char or ash particles in suspension. A suitable method for the calculation of radiative heat transfer in these situations is the zone method of Hottel and Cohen [1, 2].

In the basic zone method the gas-containing enclosure is divided into a number of gas and surface zones, each of which is assumed to be at constant temperature and to have uniform radiating properties. An energy balance calculation is carried out on all gas and wall zones simultaneously, to solve for unknown radiative fluxes and temperatures. For the full details of this method the reader is referred to [1, 2]. Of fundamental importance in this calculation are the direct exchange areas which specify the energy transfer by direct radiation between zones. Hottel and Cohen provide graphical data on exchange areas, for enclosures which can be divided into cuboid zones, while for cylindrical enclosures Hottel and Sarofim provide numerically derived tables, from the work of Erkku [7]. For cartesian zoning other than cubic there are no data available for direct use with the zone method, although Oppenheim and Bevans [3] have presented a scheme whereby the quadruple integral representing exchange between rectangular surfaces, either at right angles or parallel, through an absorbing medium, is reduced to the sum of single integrals. For a linear absorption law the integration was carried out by Dunkle [4] who obtained a completely analytical result. Dunkle's surface-to-surface exchange areas may be manipulated to produce gas-to-surface, or gas-to-gas exchange areas for the optically thin limit. However, an exponential rather than a linear absorption law is required in Hottel's method of simulating real gas absorption by means of a hypothetical gray gas mixture [2, 6, 8].

The current contribution gives a solution for the "gray gas-to-surface exchange area" for a rectangular parallelepiped gas volume and an adjacent face, in terms of elementary functions and single integrals, which can be readily evaluated by computer. This solution is compared to Hottel and Cohen's [1, 2] data for cubes and its limiting behavior checked against results of Port [2] and Dunkle [4], in the optically thin limit, and against a solution for an infinitely long rectangular prism by Mikk [5]. The present paper also reviews the rules

[1] Numbers in brackets designate References at end of paper.

Contributed by the Heat Transfer Division for publication in the JOURNAL OF HEAT TRANSFER. Manuscript received by the Heat Transfer Division March 22, 1976.

for manipulating exchange areas and demonstrates the usefulness of the new solution in the zoning of a rectangular furnace in terms of a series of concentric rectangular slices.

Basic Equations

The exchange area representing gray gas to black surface exchange is defined by the following multiple integral [2]:

$$\overline{gs} = \int_A \int_V Ke^{-Kr} \cos\theta/(\pi r^2)\, dVdA \tag{1}$$

where V is the gas volume and A the receiving face. The surface-to-surface exchange area $\overline{ss}$, and gas-to-gas exchange area $\overline{gg}$, have similar integral definitions. However, it is generally not necessary to solve all three types, because energy conservation laws for enclosures comprising surfaces and gas volumes in radiative equilibrium, namely

$$\Sigma\overline{ss} + \Sigma\overline{gs} = A \tag{2}$$

and

$$\Sigma\overline{gs} + \Sigma\overline{gg} = 4KV \tag{3}$$

may be used for calculating $\overline{gs}$ from $\overline{ss}$, and $\overline{gg}$ from $\overline{gs}$, respectively [2].

To integrate equation (1), the integration over the rectangular parallelepiped volume V was done by hemispherical shells. The order of integration was chosen such that shell surface elements were first combined with the $\cos\theta$ to produce projections onto the base plane, followed by double integration over A, and the integration with respect to r was left till last. The full solution is given in the Appendix at the end of this paper and further details on the method of integration are contained in a report by the Author [9].

Results and Discussion

The solution given in the Appendix was used for computing the dimensionless gas-to-surface exchange area parameter $\psi = \overline{gs}/KV$ for rectangular parallelepiped gas volumes and adjacent surfaces over a wide range of side length ratios and for various K. These results are presented in Fig. 1(a)-1(d). When $c \neq 1$, the scaling law, given by equation (9) in the following, may be used for calculating $\overline{gs}$ from these figures.

Fig. 1(a) shows a comparison of the present results for $K = 0$, with those from two other sources. The first one is an exact solution derived from results by Dunkle [4] for surfaces placed parallel and at right angles in a medium with a linear absorption law. By substituting the first few terms of the exponential series for $\exp(-kr)$ in the multiple integral for surface-to-surface exchange through a gray medium and by standard analysis, with the aid of equation (2), it may be shown that the optically thin limit is given by,

$$\psi_0 = Z_p + 2(Z_{r_1} + Z_{r_2}) \tag{4}$$

where Z_p and Z_r are the exact solutions given by Dunkle [4], for surfaces placed parallel and at right angles in a linearly absorbing medium. The other data is by Port [2], who used a Gaussian double integration. All three results are in excellent agreement, except below $b = 0.2$ where Port's results deviate slightly from the other two. By using large values of side length ratio, Port's results for $a \to \infty$ were reproduced accurately by the other two methods.

The results given in Fig. 1(b), 1(c), and 1(d), for $K \neq 0$ also include curves for $a \to \infty$, derived in the same way, from the current solution. These were compared to an approximate solution by Mikk [5] for an infinitely long rectangular enclosure, containing a gray medium with $K = 1$. For other K the scaling law, equation (9), was used. For $K = 1$ and 2, the maximum discrepancy between Mikk's and the present curves is below 1 percent, and for $K = 0.5$, it is around 2 percent in the range $b = 1$–5, and less elsewhere. Thus the agreement is well within the 3 percent accuracy claimed by Mikk.

Fig. 2 shows the variation of $(\overline{gs})_b$ with KB for a gas cube radiating to all its faces, comparing the present solution with that determined graphically by Hottel and Cohen [2]. In the technically important regime below $K = 1$, the discrepancy does not exceed 3 percent, however, for larger K it increases to above 10 percent. The optically thick approximation, equation (A14) was used to investigate this discrepancy. In terms of the optically thick approximation, the plotted parameter is given by

$$(gs)_b/4KB^3 \simeq 3/2KB - (4 - 3/2KB)/(KB)^2\pi \tag{5}$$

Fig. 2 shows that there is good agreement between the computed curve and this approximation from $KB \simeq 2$ onwards. A lower order approximation is given by the first term of equation (5), i.e., by $3/2KB$. This approximation is also plotted in Fig. 2 and it appears to coincide with Hottel and Cohen's curve from $K \simeq 7$ onwards.

Figs. 3 and 4 show further comparisons between data by Hottel and Cohen [1, 2] and present data on exchange areas between cubes and squares and cubes and cubes. This data was generated by manipulating the results from the basic solution in accordance with the exchange area algebra given later. The present data is based on the computed $(\overline{gs})_b$, whereas Hottel and Cohen's data would have been based on their values of $(\overline{gs})_b$ as shown in Fig. 2. Hence, one would also expect that there would be discrepancies in the comparisons shown in Figs. 3 and 4. The largest discrepancy can be seen to exist in Fig. 3, for the 2,2,1 case, where a cube radiates to a square in its base plane, diagonally opposite its base. Here Hottel and Cohen's curve is approximately 10 percent low at $K = 0.4$ and 20 percent low at $K = 1$. As this curve is calculated by difference between the result for a $2 \times 2 \times 2$ cube radiating to its base and four unit cubes radiating to their own base and two adjacent squares, any error in the basic method would have been aggravated.

Exchange Area Algebra

The method of deriving $\overline{gg}$ from $\overline{gs}$ is to apply equation (3) to a

Nomenclature

A = receiving face area
a, b = side lengths of receiving face
B = cube edge length
c = scale factor, volume height
E = emissive power
$E_n(r)$ = exponential integral of nth order
$g(r)$ = geometrical function
$\overline{gg}$ = gas-to-gas direct exchange area
$\overline{gs}$ = gas-to-surface direct exchange area
$(\overline{gs})_b$ = ditto, with respect to all faces of a cube
K = gray gas absorption coefficient
n = total number of zone levels in furnace
Q = rate of radiative heat transfer
r = radial coordinate
r_{ab}, r_{ac}, r_{bc} = constant radial coordinates, $r_{ab} = (a^2 + b^2)^{1/2}$, etc.
r_{max} = maximum radial coordinate, $= (a^2 + b^2 + c^2)^{1/2}$
$\overline{ss}$ = surface-to-surface exchange area
S_b, S_w = base and wall surface zones
t = zone height
V = rectangular parallelepiped gas volume
V_c, V_0 = central and outer furnace volume zones
$\mathbf{x}$ = vector specifying geometry of a radiating volume (a, b, c)
z = dimensionless mean beam length parameter
ρ = radius, $(r^2 - c^2)^{1/2}$
ϕ = generalized direct exchange area between zones in a system
ψ = dimensionless direct gas-to-surface exchange area, $\overline{gs}/(KV)$
ψ_0 = optically thin limit of ψ

Subscripts

1, 2, . . . , 6 = volume or zone number
i, j = level number
k = type of exchange area
Z = separation index
x, y, z = faces normal to x, y, and z axes
p = parallel rectangles
r = perpendicular rectangles

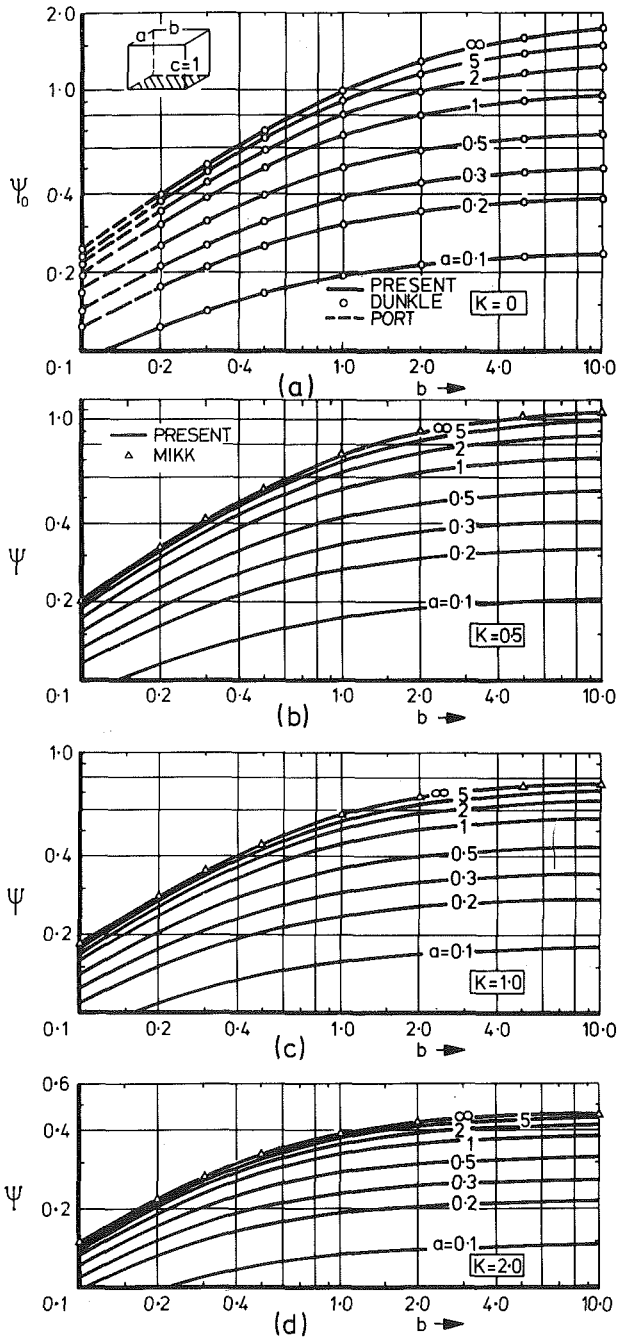

Fig. 1 Dimensionless exchange area between rectangular parallelepiped volume $a \times b \times 1$ and face $a \times b$

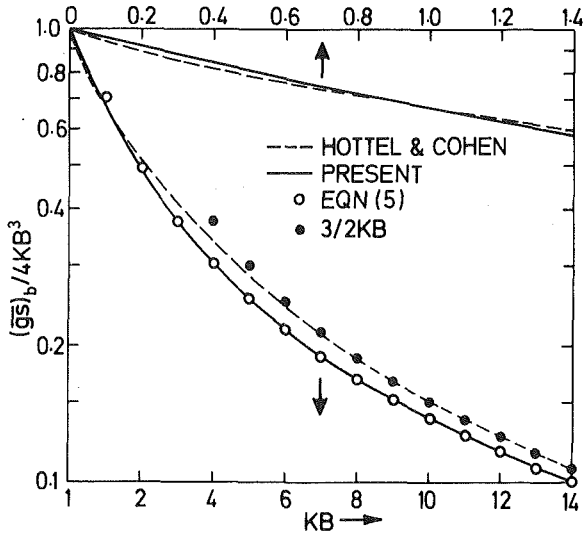

Fig. 2 Dimensionless exchange area between a cube and all its faces

single rectangular parallelepiped gas volume, and compute a "self exchange area" as follows

$$\overline{gg}_{1,1} = 4KV - 2(\overline{gs}_{1,1} + \overline{gs}_{1,2} + \overline{gs}_{1,3}) \tag{6}$$

The rules for combining exchange areas of either type are based on the distributive properties of the defining integrals, and on the laws of reciprocity $\phi_{12} = \phi_{21}$, and the Yamauti principle [2], which is a consequence of the conservation laws, equations (2) and (3). For two volumes the combined self exchange area is given by

$$\overline{gg}_{1+2,1+2} = \overline{gg}_{1,1} + \overline{gg}_{2,2} + 2\overline{gg}_{1,2} \tag{7}$$

which provides a means of computing the "cross exchange area" $\overline{gg}_{1,2}$. Similar equations hold for combining two sets of $\overline{gs}$ or $\overline{ss}$, providing reciprocity or the Yamauti principle applies.

For exchange between each of two volumes and a common third volume, the combination follows a straight application of the distributive law, viz.,

$$\overline{gg}_{1+2,3} = \overline{gg}_{1,3} + \overline{gg}_{2,3} \tag{8}$$

The same law applies to exchange between two volumes and a common surface, or two surfaces and a common third surface.

The scaling law which applies to all geometrically similar volume-surface combinations follows from the integral definition of $\overline{gs}$, equation (1):

$$\overline{gs}(K, \mathbf{x}) = c^2\overline{gs}(cK, \mathbf{x}/c) \tag{9}$$

where c is a scale factor and $\mathbf{x}$ specifies the geometry of the system, i.e., for a rectangular parallelepiped volume it is convenient to specify

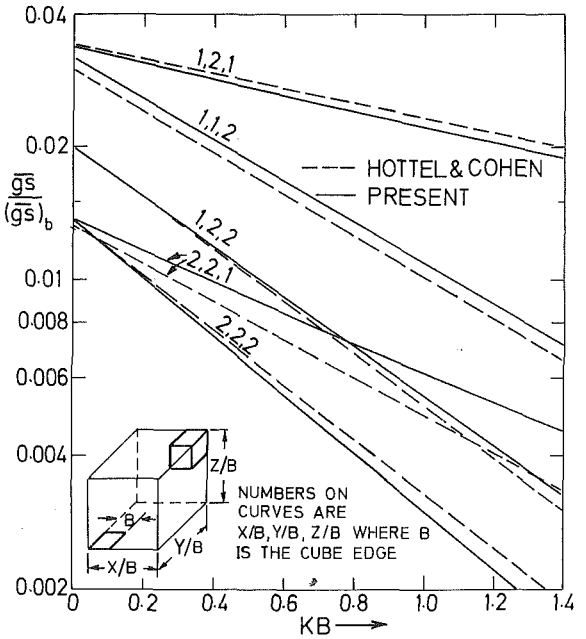

Fig. 3 Exchange area between cubes and squares

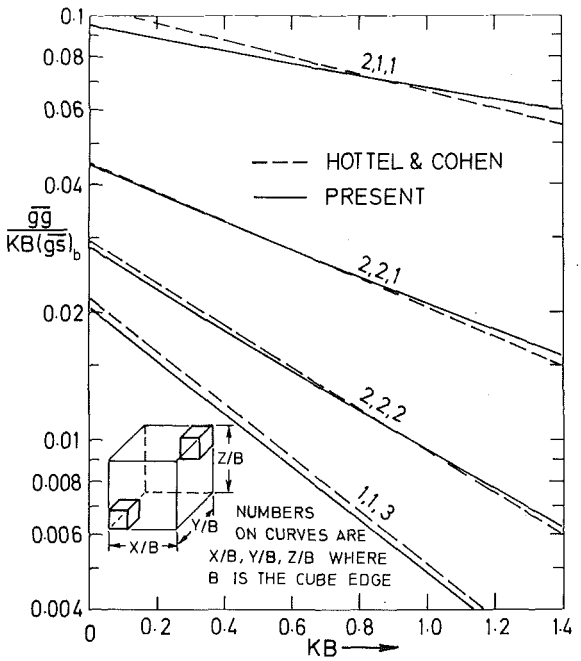

Fig. 4 Exchange area between cubes and cubes

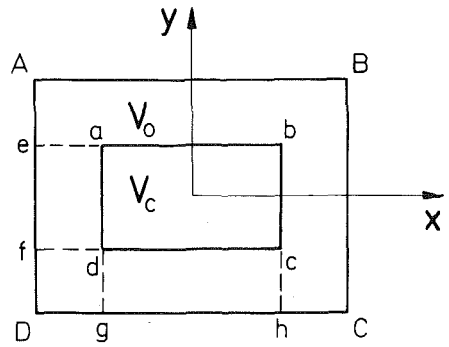

Fig. 5 Furnace cross-sectional zoned as two concentric rectangles

the sides of the receiving face by the first two components of **x**, and its height by the third. The scaling law also applies to $\overline{gg}$ or $\overline{ss}$.

The application of these rules for manipulating exchange areas is best illustrated by an example. Fig. 5 shows a section through a rectangular furnace divided into n slices each containing a concentric pair of volume zones. The exchange areas for this type of configuration can be derived from eighteen basic gas-to-surface exchange areas, corresponding to six volumes defined by the rectangular areas *ABCD, ebhD, abcd, eagD, fchD* and *fdgD*, each of height t, denoted by subscripts 1–6, with receiving faces denoted by subscripts x, y, and z, according to the direction of their normals.

They are:

$$\overline{gs}(V_c, S_w) = 2(\overline{gs}_{2x} - \overline{gs}_{4x} - \overline{gs}_{5x} + \overline{gs}_{6x} + \overline{gs}_{2y} - \overline{gs}_{4y} - \overline{gs}_{5y} + \overline{gs}_{6y}) \quad (10)$$

$$\overline{gs}(V_0, S_w) = 2(\overline{gs}_{1x} + \overline{gs}_{1y}) - \overline{gs}(V_c, S_w) \quad (11)$$

$$\overline{gs}(V_c, S_b) = \overline{gs}_{2z} - \overline{gs}_{4z} - \overline{gs}_{5z} + \overline{gs}_{6z} \quad (12)$$

$$\overline{gs}(V_0, S_b) = \overline{gs}_{1z} - \overline{gs}(V_c, S_b) \quad (13)$$

$$\overline{gg}(V_c, V_0) = \overline{gg}_2 - \overline{gg}_3 - \overline{gg}_4 - \overline{gg}_5 + \overline{gg}_6 \quad (14)$$

$$\overline{gg}(V_0, V_0) = \overline{gg}_1 - \overline{gg}_3 - 2\overline{gg}(V_c, V_0) \quad (15)$$

$$\overline{gg}(V_c, V_c) = \overline{gg}_3 \quad (16)$$

Exchange areas between zones at different levels in the furnace are obtained by computing these seven factors for all heights $t, 2t, \ldots nt$, and by application of equation (7) to compute cross exchange areas between the first level and the combined zones above the first, up to $(i-1)$ and also up to the ith. The direct exchange areas between the first and the ith level zones are then obtained by subtraction of these two results from one another in accordance with equation (8). For uniform spacing of levels, the direct exchange areas between the first and the ith level, apply to any pair of levels, $(i-1)$ levels apart, and may be designated $\phi_{k,Z}$ where k denotes the type and Z the separation. So that in an energy balance on a zone at the jth level, the direct transfer from all other zones in the system, of type k, is given by

$$Q_{k,j} = \sum_{i=1}^{n} \phi_{k,(|i-j|+1)} \cdot E_i \quad (17)$$

Conclusions

A new mathematical solution for calculation of direct radiative exchange areas for rectangular parallelepiped enclosures containing gray gas, for use in zonal radiative analyses has been presented. This new method offers the following advantages:

(*a*) subdivision into zones other than cubes;
(*b*) greater accuracy and versatility;
(*c*) use of computer subroutines rather than graphical data;
(*d*) reduced computing time and core storage space.

Inter-zonal direct gas-to-gas, and gas-to-surface exchange areas for a subdivided enclosure, such as a furnace, can easily be derived from the basic solution using exchange area algebra.

Acknowledgment

This study is published with the permission of the State Electricity Commission of Victoria, Australia. The work was carried out at the Herman Research Laboratory.

References

1 Hottel, H. C., and Cohen, E. S., "Radiant Heat Exchange in a Gas-Filled Enclosure: Allowance for Non-Uniformity of Gas Temperature," *Amer. Inst. of Chem. Eng. Journal*, Vol. 4, No. 1, 1958, pp. 3–14.

2 Hottel, H. C., and Sarofim, A. F., *Radiative Transfer*, McGraw-Hill, New York, 1967.

3 Oppenheim, A. K., and Bevans, J. T., "Geometric Factors for Radiative Heat Transfer Through an Absorbing Medium in Cartesian Co-ordinates," JOURNAL OF HEAT TRANSFER, TRANS. ASME, Series C, Vol. 82, 1960, pp. 360–368.

4 Dunkle, R. V., "Geometric Mean Beam Lengths for Radiant Heat-Transfer Calculations," JOURNAL OF HEAT TRANSFER, TRANS. ASME, Series C, Vol. 86, 1964, pp. 75–80.

5 Mikk, I. R., "View Factors for an Absorbing Medium," *Engineering Science Journal*, Vol. 5, No. 11, Mar. 1962, pp. 25–31 (in Russian).

6 Johnson, T. R., Lowes, T. M., and Beer, J. M., "Comparison of Calculated Temperatures and Heat Flux Distributions With Measurements in the IJmuiden Furnace," *Journal of the Institute of Fuel*, Vol. 47, Mar. 1974, pp. 39–51.

7 Erkku, H., ScD., Thesis in Chemical Engineering, M.I.T. 1959.

8 Taylor, P. B., and Foster, P. J., "The Total Emissivities of Luminous and Non-Luminous Flames," *International Journal of Heat and Mass Transfer*, Vol. 17, 1974, pp. 1591–1603.

9 Becker, H. B., "A Mathematical Solution for Gas-to-Surface Radiative Exchange Area for a Rectangular Parallelepiped Enclosure Containing a Gray Medium," *Report 329, Herman Research Laboratory, Research and Development Department, State Electricity Commission of Victoria, Australia*, Dec. 1976.

APPENDIX

Integration of Equation (1)

It has been shown by Hottel and Sarofim [2] that the integration of equation (1) by hemispherical shells allows the multiplicity of the integral to be reduced effectively from quintuplet to triple order,

$$\overline{gs} = \int_A \int_{r=0}^{r_{max}} g(r) K e^{-Kr} dr dA \quad (A1)$$

where $g(r)$ is a geometrical function representing the projections of the hemispherical shells within the emitting volume, onto the receiving plane, all divided by πr^2. From here on Hottel proceeded by graphical integration, whereas in the present work $g(r)$ was expressed in terms of equations of circular segments which were double integrated analytically over A. The final integration with respect to r was complicated by the introduction of the exponential factor, and did not yield an entirely analytical result. However, the parts which had to be evaluated numerically were limited to three types of exponential integrals, i.e., the standard one,

$$E_n(r) = -\int_r^\infty r^n e^{-Kr} dr \tag{A2}$$

and two others, viz.

$$E_{n,p,a}(r_1, r_2) = \int_{r_1}^{r_2} r^n [1 - (a/r)^2]^p e^{-Kr} dr \tag{A3}$$

and

$$E_a(r_1, r_2) = \int_{r_1}^{r_2} (\rho/r)^2 \arccos(a/\rho) e^{-Kr} dr \tag{A4}$$

The complete solution is given by

$$\overline{gs} = K[G_0 - H_0 - (2/\pi)(G_x + G_y - H_x - H_y) + (4/\pi)(G_{xy} - H_{xy})] \tag{A5}$$

where

$$G_0 = ab[E_0(r_{ab}) - E_0(0)] + (a^2b^2/\pi)[E_{-2}(r_{max}) - E_{-2}(r_{ab})] \tag{A6}$$

$$G_x = (2b/3)[E_1(r_{ab}) - E_1(0)] + [ab \arccos(a/r_{ab}) - b^2 + b^4/(3r_{ab}^2)]E_0(r_{ab}) - (2b/3K)E_{0,3/2,a}(a, r_{ab}) \tag{A7}$$

$$G_y = \text{same as } G_x \text{ with } a \text{ and } b \text{ interchanged} \tag{A8}$$

$$G_{xy} = [a^2E_0(a) + b^2E_0(b) - (a^2 + b^2)E_0(r_{ab})]/4 - [aE_1(a) + bE_1(b) - (a + b)E_1(r_{ab})]/3 + [E_2(a) + E_2(b) - E_2(0) - E_2(r_{ab})]/8 - [a^4E_{-2}(a) + b^4E_{-2}(b) - (a^4 + b^4)E_{-2}(r_{ab})]/24 \tag{A9}$$

$$H_0 = ab[E_0(r_{max}) - E_0(c)] - abc^2[E_{-2}(r_{max}) - E_{-2}(c)] \tag{A10}$$

$$H_x = (2b/3)E_{1,3/2,c}(c, r_{max}) - bE_{1,1/2,r_{ac}}(r_{ac}, r_{max}) + bc^2E_{-1,1/2,r_{ac}}(r_{ac}, r_{max}) + (b/3)E_{1,3/2,r_{ac}}(r_{ac}, r_{max}) + abE_a(r_{ac}, r_{max}) \tag{A11}$$

$$H_y = \text{the same as } H_x \text{ with } a \text{ and } b \text{ interchanged} \tag{A12}$$

and

$$H_{xy} = [c^2E_0(c) + (a^2 - c^2)E_0(r_{ac}) + (b^2 - c^2)E_0(r_{bc}) + (c^2 - a^2 - b^2)E_0(r_{max})]/4 + [E_2(r_{ac}) + E_2(r_{bc}) - E_2(c) - E_2(r_{max}) + (c^4 - 2a^2c^2 - a^4/3)E_{-2}(r_{ac}) - c^4E_{-2}(c) + (c^4 - 2b^2c^2 - b^4/3)E_{-2}(r_{bc}) + [2(a^2 + b^2)c^2 + (a^4 + b^4)/3 - c^4]E_{-2}(r_{max})]/8 + (a/3)E_{1,3/2,c}(r_{ac}, r_{max}) + (b/3)E_{1,3/2,c}(r_{bc}, r_{max}) \tag{A13}$$

When $K = 0$ the foregoing solution is singular in its present form, however an optically thin limit of $\overline{gs}/K$ can be computed from these equations, by omitting the factor K in equation (A5), and by replacing $\exp(-Kr)$ by 1.0 in all exponential integrals. Note that equation (A2) must be redefined as a positive proper integral with limits $(0, r)$ and that the last term in equation (A7) becomes $+(26/3)E_{1,3/2,a}(a, r_{ab})$.

An optically thick limit can be derived by inclusion of only those terms which arise from the integration limit $r = 0$, i.e., contributions come from equations (A6) to (A9) only, giving

$$\overline{gs}_{\text{thick}} = ab - [4(a + b)/3 - 1/K]/(K\pi) \tag{A14}$$

B. F. Armaly
Professor,
Thermal Radiative Transfer Group.

H. S. El-Baz
Graduate Student,

Department of Mechanical and Aerospace Engineering,
University of Missouri—Rolla,
Rolla, Missouri

Influence of Substrate Properties on the Apparent Emittance of an Isothermal Isotropically Scattering Medium[1]

The apparent directional and hemispherical emittances of an isothermal, isotropically scattering, emitting, and absorbing medium that is bounded by a diffusely emitting and reflecting substrate has been investigated. The exponential kernel approximation is used to develop a closed-form algebraic expression which describes the apparent directional and hemispherical emittances as a function of the optical thickness, substrate reflectance and emittance, and scattering albedo of the medium. The approximation also provides a closed-form solution for the intensity and flux distribution within the medium. Comparison, when possible, with exact solutions indicates very good agreement.

Introduction

Edwards and Bobco [1][2] examined the directional and hemispherical emittances of a finite isothermal medium having a unity refractive index that absorbs, emits, and isotropically scatters thermal radiation. Crosbie [2] presented expressions that describe the asymptotic behavior of these properties in the limits of optically thin and thick media. The influence of substrate emittance and reflectance either on these properties or on the intensity and flux distribution within such a medium has not been reported. The objective of the present study is to examine the influence that the properties of the substrate have on the properties of the medium and to present an approximate but simple, closed-form, algebraic expression which describes the apparent emittance as a function of optical thickness, substrate emittance and reflectance, and scattering albedo. It should be possible to use the results in the interpretation of experimentally measured emittance and in the calculation of either heat transfer or remote sensing.

The emittance of a nonisothermal layer has been examined by Chupp and Viskanta [3] and by Anderson [4]. The influence of refractive index has been reported by Francis and Love [5] and by Abrams [6]. These studies, however, consider only the case of a nonscattering medium.

Formulation

A finite, isothermal, isotropically scattering planar medium of unity refractive index that is bounded by a diffusely emitting and reflecting substrate is the subject of our interest. This medium is not subjected to external radiation from above. A schematic diagram of the system is shown in Fig. 1.

The following analysis can be applied on a monochromatic basis or for a gray medium. The intensity distribution within the medium is given by [7]

$$I^+(\tau, \mu, \phi) = I^+(0, \mu, \phi) \exp(-\tau/\mu) + \int_0^\tau S(t, \tau_0) \exp[-(\tau - t)/\mu] dt/\mu \quad (1)$$

and

$$I^-(\tau, \mu, \phi) = I^-(\tau_0, \mu, \phi) \exp[-(\tau_0 - \tau)/\mu] + \int_\tau^{\tau_0} S(t, \tau_0) \exp[-(t - \tau)/\mu] dt/\mu \quad (2)$$

in which

$$S(\tau, \tau_0) = (1 - \omega) I_b(T)$$

[1] Supported in part by the National Science Foundation, ENG 75-06237.
[2] Numbers in brackets designate References at end of paper.
Contributed by the Heat Transfer Division for publication in the JOURNAL OF HEAT TRANSFER. Manuscript received by the Heat Transfer Division October 4, 1976.

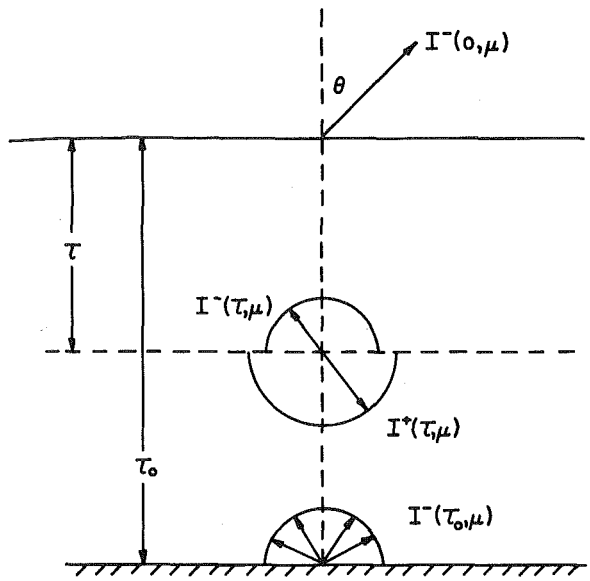

Fig. 1 Schematic diagram

$$+\frac{\omega}{2}\left[\int_0^1 I^+(\tau,\mu,\phi)d\mu+\int_0^1 I^-(\tau,\mu,\phi)d\mu\right]. \quad (3)$$

The boundary conditions are given by

$$I^+(0,\mu,\phi)=0 \quad (4)$$

and

$$I^-(\tau_0,\mu,\phi)=R(\tau_0)/\pi \quad (5)$$

The radiosity, $R(\tau_0)$, for the diffuse substrate is given by

$$R(\tau_0)=\epsilon_b\pi I_b(T)+\rho_b\int_0^{2\pi}\int_0^1 I^+(\tau_0,\mu,\phi)\mu d\mu d\phi \quad (6)$$

The hemispherical emittance, ϵ_b, and the reflectance, ρ_b, of an opaque substrate are related by

$$\epsilon_b=1-\rho_b \quad (7)$$

For a transparent nonemitting substrate, the reflectance and the transmittance, τ_b, are related by

$$\rho_b=1-\tau_b \quad (8)$$

By making appropriate substitutions in equation (3), the source function can be expressed as

$$S(\tau,\tau_0)/I_b(T)=(1-\omega)\Phi(\tau,\tau_0)+\omega[R(\tau_0)/\pi I_b(T)]F(\tau_0-\tau,\tau_0) \quad (9)$$

in which

$$\Phi(\tau,\tau_0)=1+\frac{\omega}{2}\int_0^{\tau_0}\Phi(t,\tau_0)E_1(|\tau-t|)dt \quad (10)$$

$$F(\tau,\tau_0)=E_2(\tau)/2+\frac{\omega}{2}\int_0^{\tau_0}F(t,\tau_0)E_1(|\tau-t|)dt \quad (11)$$

and

$$\overline{R}(\tau_0)=R(\tau_0)/\pi I_b(T)=\left[\epsilon_b+2\rho_b(1-\omega)\int_0^{\tau_0}\Phi(t,\tau_0)E_2(\tau_0-t)dt\right]\Big/\left[1-2\omega\rho_b\int_0^{\tau_0}F(\tau_0-t,\tau_0)E_2(\tau_0-t)dt\right] \quad (12)$$

The solution to the source function, equation (9), and its use in equations (1) and (2) provide the intensity distribution within the medium. The apparent directional emittance can be evaluated by using

$$\epsilon(\mu)=I^-(0,\mu,\phi)/I_b(T) \quad (13)$$

and the hemispherical emittance can be evaluated by using

$$\epsilon_H=2\int_0^1\epsilon(\mu)\mu d\mu \quad (14)$$

The exact solution for the foregoing equations, specifically equations (10–12), is lengthy and complicated. The values of both $\Phi(\tau,\tau_0)$ and $F(\tau,\tau_0)$ at the two boundaries can be expressed simply in terms of the zero moments of the Chandrasekhar X and Y functions [8]. The distribution of these functions within the medium, which is needed to evaluate the intensity, the flux distribution, and the radiosity of the substrate, is more difficult to determine. For this purpose, the closed-form approximate solution, which was obtained by using an exponential kernel approximation, is used to examine the influence of the substrate on the apparent emittance of the system.

Approximate Solution

The application of the exponential approximation to the exponential integral given by $E_1(t)=q\exp(-qt)$ provides a closed-form approximate solution for the two dimensionless source functions that appear in equations (10) and (11). The solutions are given by [9]

$$\Phi(\tau,\tau_0)=C_1\exp(-b\tau)+C_2\exp(b\tau)+1/(1-\omega) \quad (15)$$

and

$$F(\tau,\tau_0)=C_3\exp(-b\tau)+C_4\exp(b\tau) \quad (16)$$

in which the constants are as follows

$$b^2=q^2(1-\omega) \quad (17)$$

$$C_1=C_2\exp(b\tau_0) \quad (18)$$

$$C_2=q(b^2-q^2)\exp(-b\tau_0)/\{b^2[(b+q)-(b-q)\exp(-b\tau_0)]\} \quad (19)$$

$$C_3=C_4(b+q)\exp(2b\tau_0)/(b-q) \quad (20)$$

and

$$C_4=q(b-q)\exp(-2b\tau_0)/[(b+q)^2-(b-q)^2\exp(-2b\tau_0)] \quad (21)$$

For the conservative case, $\omega=1$, the solution for these equations takes the following simple form:

Nomenclature

F = dimensionless source function, equation (11)
I^+, I^- = radiation intensity in positive and negative directions
$I_b(T)$ = blackbody radiation intensity at temperature T
R = radiosity of the substrate
$\overline{R}$ = nondimensional radiosity, $R/\pi I_b(T)$
S = total source function
β = extinction coefficient
θ = angular direction as measured from the normal, Fig. 1
ϕ = azimuthal angle
Φ = dimensionless source function, equation (10)
μ = $\cos\theta$
ρ_b = substrate hemispherical reflectance
ϵ_b = substrate hemispherical emittance
$\epsilon(\mu)$ = apparent directional emittance
ϵ_H = apparent hemispherical emittance
τ = optical depth, $\tau=\int_0^x\beta dx$
τ_0 = optical thickness $\tau_0=\int_0^L\beta dx$
τ_b = substrate transmittance
ω = scattering albedo

$$\Phi(\tau, \tau_0) = -(q^2\tau^2/2) + (q^2\tau_0\tau/2) + (q\tau_0/2) + 1 \quad (22)$$

$$F(\tau, \tau_0) = [1 + q(\tau_0 - \tau)]/(2 + q\tau_0) \quad (23)$$

A comparison [9] of the approximate and exact solutions for the dimensionless source functions shows an error of less than 10 percent over a wide range of optical parameters; $0.1 \le \tau_0 \le 10$ and $0 \le \omega \le 1$.

The use of these equations provides the following expression for the radiosity:

$$R(\tau_0)/\pi I_b(T) = [\epsilon_b + 2\rho_b(1-\omega)\{C_1[\exp(-q\tau_0) - \exp(-b\tau_0)]/(b-q) + C_2[\exp(b\tau_0) - \exp(-q\tau_0)]/(b+q) + [1 - \exp(-q\tau_0)]/q(1-\omega)\}]/[1 - 2\omega\rho_b\{C_3(1 - \exp[-(b+q)\tau_0])/(b+q) + C_4(\exp[(b-q)\tau_0] - 1)/(b-q)\}] \quad (24)$$

Similarly, the apparent directional and hemispherical emittances are given by

$$\epsilon(\mu) = [R(\tau_0)/\pi I_b(T)]\{\exp(-\tau_0/\mu) + \omega C_3[\exp(-\tau_0/\mu) - \exp(-b\tau_0)]/(\mu b - 1) + \omega C_4[\exp(b\tau_0) - \exp(-\tau_0/\mu)]/(\mu b + 1)\} + C_1(1-\omega)[1 - \exp(-(b + 1/\mu)\tau_0)]/(\mu b + 1) + C_2(1-\omega)[\exp[(b - 1/\mu)\tau_0] - 1]/(\mu b - 1) + [1 - \exp(-\tau_0/\mu)] \quad (25)$$

and

$$\epsilon_H = [R(\tau_0)/\pi I_b(T)]\{\exp(-q\tau_0)/q + C_3\omega[\exp(-q\tau_0) - \exp(-b\tau_0)]/(b-q) + C_4\omega[\exp(b\tau_0) - \exp(-q\tau_0)]/(b+q)\} + 2C_1(1-\omega)[1 - \exp(-(b+q)\tau_0)]/(b+q) + 2C_2(1-\omega)[\exp((b-q)\tau_0) - 1]/(b-q) + 2[1 - \exp(-q\tau_0)]/q \quad (26)$$

For the conservative case of $\omega = 1$, the source function, equation (9), depends only on $F(\tau, \tau_0)$, and the results take the following simple forms:

$$R(\tau_0)/\pi I_b(T) = \epsilon_b/\{1 - 2\rho_b[\tau_0/(2 + q\tau_0)]\} \quad (27)$$

$$\epsilon(\mu) = [R(\tau_0)/\pi I_b(T)] \times \{[1 + q\mu + (1 - \mu q)\exp(-\tau_0/\mu)]/(2 + q\tau_0)\} \quad (28)$$

and

$$\epsilon_H = [R(\tau_0)/\pi I_b(T)]\{4/[q(2 + q\tau_0)]\} \quad (29)$$

Results and Discussion

The apparent properties and the radiosity of the substrate have been evaluated over a wide range of optical parameters. The constant, q, which is used in the exponential approximation for the exponential integral, has been chosen as $q = 2$. The use of this value has been discussed by Viskanta [7]. Two types of diffuse substrate have been examined: an opaque emitting and reflecting substrate (OERS) and a transparent nonemitting but reflecting substrate (TNERS). The radiosity of the substrate, equation (24), is equal to the substrate emittance when the optical thickness is zero and increases as the optical thickness increases to an asymptotic level, which is given by

$$\overline{R} = [\epsilon_b + \rho_b\{[\sqrt{1-\omega} - 1)/(\sqrt{1-\omega} + 1)] + 1\}]/\{1 - \omega\rho_b[1/(1 + \sqrt{1-\omega})^2]\} \quad (30)$$

This asymptotic level is higher for the (OERS) substrate case. The results indicate that this asymptotic level is approached at a smaller optical thickness when the scattering albedo is small. This and other results [10] suggests that for a scattering medium the parameter $b\tau_0$ should be used as a measure of opacity rather than the optical thickness alone. The radiosity decreases as the scattering albedo increases. An increase in the substrate reflectance increases the radiosity for the (TNERS) substrate case and decreases it for the (OERS) substrate case. The latter behavior is due to the corresponding decrease in the substrate emittance. The apparent directional and hemispherical emittances are affected by the substrate reflectance in a manner similar to the radiosity.

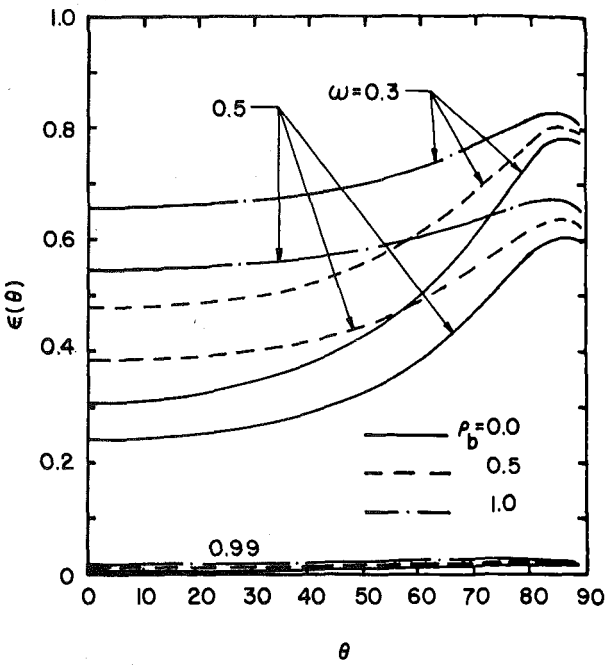

Fig. 2 Directional emittance with a transparent nonemitting substrate, $\tau_0 = 0.5$

The directional emittance is presented in Figs. 2 and 3. As expected, the influence of the substrate reflectance is significant when the optical thickness is small and diminishes as the optical thickness becomes large. As the angular direction increases, the influence of the substrate reflectance decreases as a result of the longer optical path in that direction. The emittance decreases with an increase in the

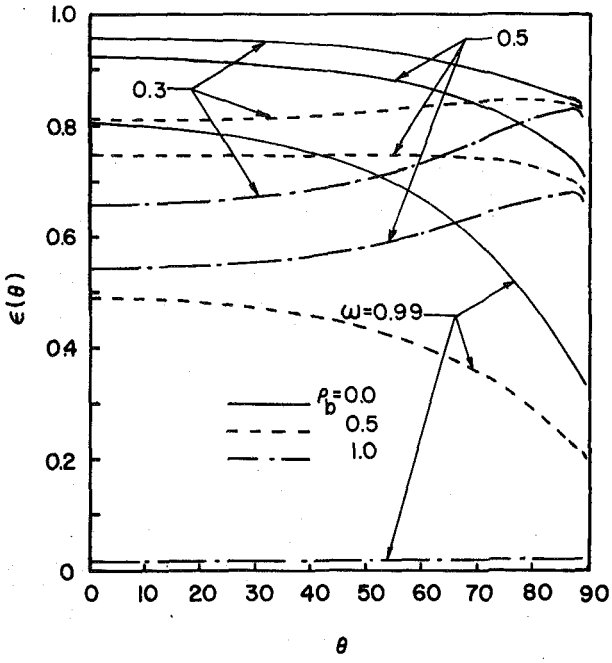

Fig. 3 Directional emittance with an opaque emitting substrate, $\tau_0 = 0.5$

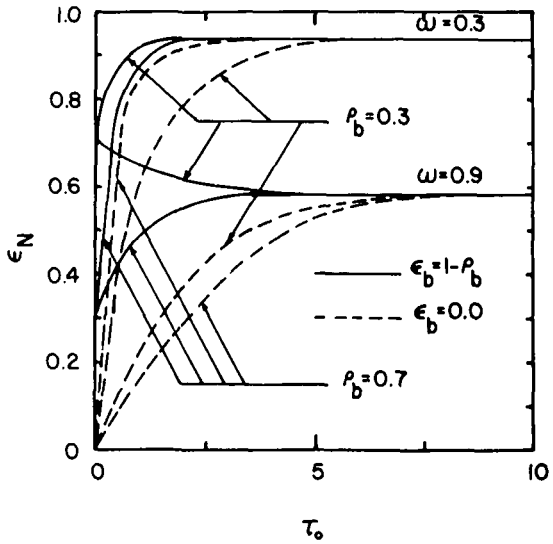

Fig. 4 Normal emittance with (OERS) and (TNERS) substrates

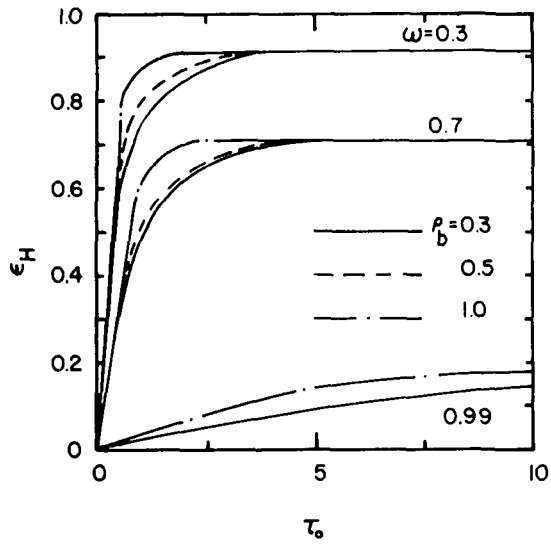

Fig. 6 Hemispherical emittance with an opaque emitting substrate

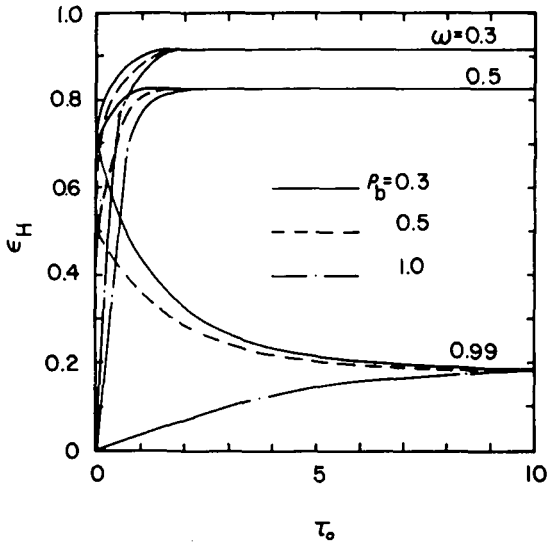

Fig. 5 Hemispherical emittance with a transparent nonemitting substrate

scattering albedo, and its magnitude is greater for the (OERS) substrate case. The behavior for a case in which $\rho_b = 0$ and $\epsilon_b = 0$ has been examined by Crosbie [2], and the present results compare very favorably with the exact solution.

The normal, ϵ_N, and the hemispherical, ϵ_H, emittances are presented in Figs. 4–6. These emittances are equivalent to the substrate emittance when the optical thickness is zero and approach the asymptotic level as the optical thickness increases. These conditions are given by

$$\epsilon_N = 3\sqrt{1-\omega}/(2\sqrt{1-\omega}+1) \tag{31}$$

and

$$\epsilon_H = 2\sqrt{1-\omega}/(\sqrt{1-\omega}+1) \tag{32}$$

These asymptotic values, which are independent of the substrate properties, agree with the results presented by Armaly, et al. [11] for a semi-infinite, isotropically scattering medium. The normal emittance is always larger than the hemispherical emittance. The approximate hemispherical emittance compares very well with the exact values [2] that are available only for the case in which $\rho_b = 0$ and $\epsilon_b = 0$.

Conclusion

The closed-form approximate solution appears to predict the apparent properties with an error of less than 10 percent. The approximate solution provides a closed-form algebraic expression for these properties and for both the intensity and flux distribution within the medium. The radiosity and the apparent emittance decrease with an increase of the scattering albedo. An increase in the substrate reflectance increases the radiosity and the apparent properties when the substrate is transparent and nonemitting. This trend is reversed when the substrate is opaque and emitting. Optically thick behavior is approached when the parameter $b\tau_0$ is larger than four. At this point, the apparent properties become independent of the substrate properties.

References

1 Edwards, R. H., and Bobco, R. P., "Radiant Heat Transfer From Isothermal Dispersion with Isotropic Scattering," JOURNAL OF HEAT TRANSFER, TRANS. ASME, Series C, Vol. 89, Nov., 1967, p. 300.

2 Crosbie, A. L., "Emittance of an Isothermal Isotropic Scattering Medium," *AIAA Journal*, Vol. 11, No. 8, 1973, p. 1203.

3 Chupp, R. E., and Viskanta, R., "Thermal Emission Characteristics of a Nonisothermal Dielectric Coating on a Conductor Surface," *AIAA Journal*, Vol. 8, 1970, p. 551.

4 Anderson, E. E., "Estimating the Effective Emissivity of Nonisothermal, Diathermanous Coating," JOURNAL OF HEAT TRANSFER, TRANS. ASME, Series C, Vol. 97, Aug. 1975, p. 480.

5 Francis, J. E., and Love, T. J., "Effect of Optical Thickness on the Directional Transmittance and Emittance of a Dielectric," *Journal of the Optical Society of America*, Vol. 56, No. 6, 1966, p. 779.

6 Abrams, M., "The Effective Absorptance of a Semi-Transparent Layer on a Diffuse Opaque Substrate," ASME Paper No. 76-HT-4, 1976.

7 Viskanta, R., "Radiation Transfer and Interaction of Convection With Radiation Heat Transfer," *Advances in Heat Transfer*, Vol. 3, 1966, p. 175.

8 Chandrasekhar, S., *Radiative Transfer*, Dover Publications, New York, 1960.

9 El-Baz, H. S., MS thesis, University of Missouri—Rolla, 1976.

10 Hottel, H. C., Sarofim, A. F., and Sze, D. K., "Radiative Transfer in an Absorbing-Scattering Medium," *Proceedings of the Third International Heat Transfer Conference*, Vol. 5, 1966, p. 112.

11 Armaly, B. F., Lam, T. T., and Crosbie, A. L., "Emittance of Semi-Infinite Absorbing and Isotropically Scattering Medium With Refractive Index Greater than Unity," *AIAA Journal*, Vol. 11, 1973, p. 1498.

D. E. Negrelli[1]
J. R. Lloyd
J. L. Novotny[2]

Department of Aerospace and Mechanical Engineering,
University of Notre Dame,
Notre Dame, Ind.

A Theoretical and Experimental Study of Radiation–Convection Interaction in a Diffusion Flame

An experimental and theoretical investigation of the interaction of gaseous thermal radiation with natural convection was made for a laminar methane-air diffusion flame in the lower stagnation region of a horizontal porous cylinder. The exponential wide-band gas radiation model was employed in this nonhomogeneous (nonuniform in temperature and composition) problem through the use of scaling techniques. Using a numerical scheme, the compressible energy, flow, and species-diffusion equations were solved simultaneously with and without the radiative component. In the experiment, methane was blown uniformly from the surface of the porous cylinder, setting up (upon ignition) a diffusion flame within the free-convection boundary layer. Using a Mach-Zehnder interferometer and a gas chromatograph, temperature and composition measurements were obtained along the stagnation line. Excellent agreement was found between the results based on the nongray wide-band model and the experimental data. Furthermore, it was found that the wide-band model yielded results that were superior to those results that excluded radiation-interaction effects. Thus, this study demonstrates that the exponential wide-band model can be accurately applied to nonhomogeneous combustion situations in order to account for the radiation-convection interactions.

Introduction

Recently there have been numerous investigations of the interaction of thermal radiation in heat transfer processes at moderate temperatures [e.g., 1–3].[3] There have also been several papers dealing with higher temperature situations such as found in a diffusion flame which have excluded the effects of radiation [e.g., 4–7]. In these situations dealing with a fire environment, radiation from the hot gases can significantly alter temperatures both in the flame itself and in the surrounding areas.

In the studies of the less complex, nonfire situations, the ability of the exponential wide band gas radiation model [8] to account for real gas behavior has been clearly demonstrated [2, 9, 10]. At the same time the shortcomings and limitations of the gray gas radiation model have been revealed [11, 12]. In the past the extension of this band absorptance model to the nonisothermal nonuniform gas composition situations has been treated by parameter scaling [13–16]; applications of this technique have generally been limited to comparisons between the various scaling approximations.

The present study looks at a diffusion flame located in the lower stagnation region of a porous horizontal cylinder. Tsuji and Yamaoka [17–19] and Abdel-Khalik, Tamaru, and El-Wakil [20] have studied similar problems on a horizontal porous cylinder but Tsuji and Yamaoka ignored the radiation. While Abdel-Khalik, Tamaru, and El-Wakil did include some radiation effects, they treated it from a nonpredictive point of view and did not make use of the latest advances in radiative heat transfer techniques.

In light of this the present study is presented. It is both an analytical and experimental study of the diffusion flame located in the lower stagnation region of a porous cylinder. Methane is the fuel used in the experiments and the temperature and species concentration fields are measured using the interferometer and gas chromatograph, respectively. The analysis makes use of the exponential wide band model of Edwards and Menard [8] and includes nonhomogeneous gas effects. Comparisons are made to a gray-gas analysis. Without this combined analytical experimental approach, the ability of the analytical models cannot be adequately assessed.

In the first part of this paper, the analysis is discussed in detail, and

[1] Present address: Bettis Atomic Power Laboratory, Westinghouse, West Mifflin, Pa.

[2] Deceased.

[3] Numbers in brackets designate References at end of paper.

Contributed by the Heat Transfer Division for publication in the JOURNAL OF HEAT TRANSFER. Manuscript received by the Heat Transfer Division August 2, 1976.

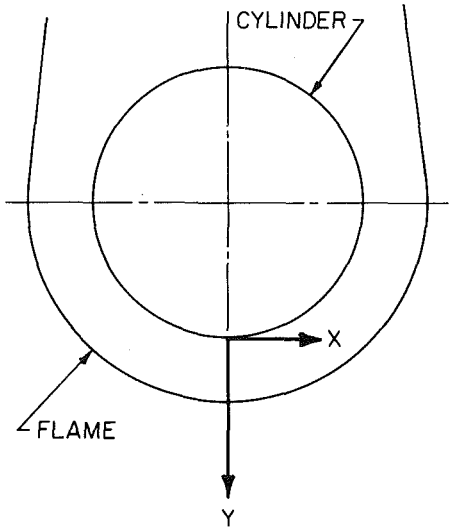

Fig. 1 Sketch of coordinate system

in the second part, the experiments are presented. The results of these two parts are discussed in the final section.

Theoretical Analysis

Governing Equations. A schematic diagram of the physical problem showing the coordinate system employed is given in Fig. 1. Methane, blown uniformly from the surface of the cylinder, combines, upon ignition, with the oxygen in the air to form a diffusion flame at the location within the boundary layer where the fuel/air ratio exhibits a stoichiometric condition. A five-component mixture of gases is considered to exist. These gases are methane (the fuel), oxygen (the oxidizer), carbon dioxide and water vapor (the products of combustion), and nitrogen (the nonreacting gas). The presence of any intermediate species of combustion is excluded, and the combustion is considered to be complete and clean, with no carbon monoxide produced. The composition measurements of Tsuji and Yamaoka [17–19] provided the basis for these assumptions, and the present experiments, as will be shown later, confirm their validity. The chemical equation for complete combustion of methane is given by

$$\nu_F' CH_4 + \nu_0' O_2 \rightarrow \nu_H'' H_2O + \nu_c'' CO_2 + Q \tag{1}$$

where the molar coefficients are:

$$\nu_F' = 1, \qquad \nu_0' = 2, \qquad \nu_c'' = 1, \qquad \nu_H'' = 2$$

The superscript ′ denotes reactants and the superscript ″ denotes products. The combustion flame-sheet model of Kim, DeRis, and Kroesser [6] is employed in this analysis. The combustion is considered to be instantaneous and the reaction zone is considered to be infinitesimal. Therefore, as is the case for diffusion flames, it is the interdiffusion of the fuel and oxygen rather than the rate at which the reactants chemically combine that governs the burning rate of the fuel. Additionally, it is necessary to impose two physical conditions—first, that there exists no oxygen between the flame sheet and the surface; and second, that there exists no fuel in the region beyond the flame sheet.

The governing equations for steady, laminar, two-dimensional flow in the forward stagnation region of a horizontal cylinder with combuston are to be formulated. All of the physical properties of the fluid are assumed to be constant except density and viscosity. The conservation of mass for a compressible fluid in steady, laminar flow is given by

$$\frac{\partial(\rho u)}{\partial x} + \frac{\partial(\rho v)}{\partial y} = 0 \tag{2}$$

Since the region of the stagnation point is being considered, the convective terms in the x-direction are negligible, and the species equations including the species generation term become

$$\rho v \frac{\partial \omega_F}{\partial y} = \frac{\partial}{\partial y}\left(\rho D \frac{\partial \omega_F}{\partial y}\right) + \dot{\omega}_F \tag{3}$$

Nomenclature

$\overline{A}_{kj}$ = dimensionless total band absorptance of species k of the jth band region
$c = g/R$, 1/s
c_p = specific heat at constant pressure, cal/K-g
D = diffusion coefficient, cm²/s
e_b = emissive power of a black body, cal/cm²-s
e_ν = Planck's function, cal/cm²-s
$E_n(t)$ = nth exponential integral
f = nondimensional stream function
g = acceleration of gravity, cm/s²
$\overline{K}_p$ = mean Planck absorption coefficient, 1/cm
L = cylinder length, cm; or distance in y-direction from surface to free-stream, cm
Le = Lewis number, $\frac{\alpha}{D}$
M_i = molecular weight of component, i, g/g-mole
Pr = Prandtl number $\frac{\nu}{\alpha}$, dimensionless
Q = heat of combustion, cal/g-mole
$\dot{Q}$ = volumetric heat generation, cal/cm³-s
Q_F = fuel flow rate, cc/min
q_r = radiative heat flux, cal/s-cm²
R = cylinder radius, cm
Sc = Schmidt number, ν/D, dimensionless
$\hat{T} = c_pT/Q$, g-mole/g
T = absolute temperature, K
u = velocity component in the x-direction, cm/s
v = velocity component in the v-direction, cm/s
$W_i = (\hat{\omega}_i + \hat{\omega}_{0,\infty} - \hat{\omega}_0)\frac{Q}{c_pT_\infty}$, dimensionless
$\overline{W}_i = W_i/W_{iw}$, dimensionless
x = coordinate which is tangent to the cylinder surface at the lower stagnation point, cm
X_i = mole fraction of component i, dimensionless
y = coordinate measured in the direction away from the cylinder surface, cm
y_f = location of flame sheet, cm
α = integrated band intensity, 1/cm²-atm
$\overline{\alpha}$ = scaled band intensity, 1/cm²-atm
η = dimensionless y coordinate
$\theta_i = [\hat{T} - \hat{\omega}_i]\frac{Q}{c_pT_\infty} + \frac{Q\hat{\omega}_{i,\infty}}{c_pT_\infty} - 1$, dimensionless
$\overline{\theta}_i = \theta_i/\theta_{iw}$
μ = dynamic viscosity, g/s-cm
ν = kinematic viscosity, cm²/s, or frequency, 1/s
ν_i' = molar coefficient of reactant i, dimensionless
ν_i'' = molar coefficient of product i, dimensionless
ρ = density, g/cm³
τ = optical coordinate, dimensionless
τ_H = optical thickness at the band head, dimensionless
τ_ν^* = exponential factor, $\exp(-(\nu - \nu_0)/\overline{\omega}))$
ψ = stream function, cm²/s
ω_i = mass fraction of species i, dimensionless
ω = band width parameter, cm⁻¹
$\overline{\omega}_i$ = scaled band width parameter of band i, cm⁻¹
$\dot{\omega}$ = volumetric fuel consumption rate, g-mole/s-cm³
$\dot{\omega}_i$ = generation of species i, g/s-cm³
$\hat{\omega}_i = \omega_i/M_i(\nu_i'' - \nu_i')$, g-mole/g

$$\rho v \frac{\partial \omega_0}{\partial y} = \frac{\partial}{\partial y}\left(\rho D \frac{\partial \omega_0}{\partial y}\right) + \dot{\omega}_0 \tag{4}$$

$$\rho v \frac{\partial \omega_P}{\partial y} = \frac{\partial}{\partial y}\left(\rho D \frac{\partial \omega_P}{\partial y}\right) + \dot{\omega}_P \tag{5}$$

and

$$\dot{\omega}_N = 1 - \dot{\omega}_F - \dot{\omega}_0 - \dot{\omega}_P \tag{6}$$

where

$$\dot{\omega}_P = \dot{\omega}_H + \dot{\omega}_C \tag{7}$$

It is also assumed that the ratio of the local molar concentrations of carbon dioxide and water vapor is a constant throughout the boundary layer, and that this X_H/X_C ratio is equal to that formed from the combustion of a stoichiometric mixture of methane and oxygen.

The momentum equation for compressible fluid flow by natural convection in the stagnation region of a horizontal cylinder of radius R is given by

$$\rho\left(u\frac{\partial u}{\partial x} + v\frac{\partial u}{\partial y}\right) = g(\rho_\infty - \rho)\frac{x}{R} + \frac{\partial}{\partial y}\left(\mu\frac{\partial u}{\partial y}\right) \tag{8}$$

Finally, the energy equation with heat generation and a radiative flux is

$$\rho c_p v \frac{\partial T}{\partial y} = \frac{\partial}{\partial y}\left(k\frac{\partial T}{\partial y}\right) - \frac{\partial q_R}{\partial y} + \dot{Q} \tag{9}$$

The fluid is assumed to be in local thermal equilibrium, and viscous dissipation effects are considered to be negligible. Note that for stagnation flow, the convective term in the x-direction vanishes from the energy equation.

The mass generation rates $\dot{\omega}_i$ can be eliminated from equations (3)–(5) by defining the dimensionless parameter

$$W_i \equiv (\hat{\omega}_i + \hat{\omega}_{0,\infty} - \hat{\omega}_0)\frac{Q}{c_p T_\infty} \quad i = 0, F, P \tag{10}$$

where

$$\hat{\omega}_i = \frac{\omega_i}{M_i(\nu_i'' - \nu_i')}$$

Note that

$$\frac{\dot{Q}}{Q} = \frac{-\dot{\omega}_F}{M_F\nu_F'} = \frac{\dot{\omega}_P}{M_P\nu_P''} = \frac{-\dot{\omega}_0}{M_0\nu_0'}$$

The oxygen species equation is thus eliminated and the remaining species equations become

$$\rho v \frac{\partial W_F}{\partial y} - \frac{\partial}{\partial y}\left(\rho D \frac{\partial W_F}{\partial y}\right) = 0 \tag{11}$$

$$\rho v \frac{\partial W_P}{\partial y} - \frac{\partial}{\partial y}\left(\rho D \frac{\partial W_P}{\partial y}\right) = 0 \tag{12}$$

If one defines the following temperature parameter

$$\theta = \frac{T - T_\infty}{T_\infty} - (\hat{\omega}_0 - \hat{\omega}_{0,\infty})\frac{Q}{c_p T_\infty} \tag{13}$$

and assumes that Sc = Pr, the energy equation becomes

$$\rho v \frac{\partial \theta}{\partial y} - \frac{\partial}{\partial y}\left(\frac{k}{c_p}\frac{\partial \theta}{\partial y}\right) = -\frac{1}{c_p T_\infty}\frac{\partial q_R}{\partial y} \tag{14}$$

The system of partial differential equations can be reduced to a set of ordinary differential equations by making the similarity transformation

$$\eta = \sqrt{\frac{c}{\nu_\infty}}\int_0^y \frac{\mu_\infty}{\mu}\,dy \tag{15}$$

where $c = \sqrt{g/R}$ and by letting the stream function be defined by

$$\psi = \sqrt{c\nu_\infty}\, x f(\eta) \tag{16}$$

It is also necessary to assume an equation of state ρT = constant and to relate the viscosity to the density variation by $\rho\mu = \rho_w\mu_w$ = constant.

Due to the assumption that

$$\hat{\omega}_0 = 0 : 0 \le \eta \le \eta_f$$

$$\hat{\omega}_F = 0 : \eta \ge \eta_f$$

the momentum equation takes on a different form on each side of the flame sheet discontinuity

$$\left.\begin{aligned} 0 \le \eta \le \eta_f \quad & f''' + ff'' - (f')^2 + \theta - \frac{\hat{\omega}_{0,\infty}Q}{c_p T_\infty} = 0 \\ \eta \ge \eta_f \quad & f''' + ff'' - (f')^2 + \theta - W_F = 0 \end{aligned}\right\} \tag{17}$$

The transformed species and energy equations thus, become

$$\left.\begin{aligned} \frac{1}{\mathrm{Sc}}W_F'' + fW_F' = 0 \\ \frac{1}{\mathrm{Sc}}W_P'' + fW_P' = 0 \end{aligned}\right\} \tag{18}$$

$$\frac{1}{\mathrm{Pr}}\theta'' + f\theta' = \frac{1}{\rho c_p T_\infty}\frac{\partial q_R}{\partial y} \tag{19}$$

with the following boundary conditions:

$$\eta = 0: f = f_w = \frac{-\rho_w v_w}{\rho_\infty\sqrt{\nu_\infty c}}$$

$$f' = 0$$

$$W_F = W_{Fw}$$

$$W_P = W_{Pw}$$

$$\theta = \theta_w = \frac{T_w}{T_\infty} - 1 + \frac{\hat{\omega}_{0,\infty}Q}{c_p T_\infty}$$

$$\eta \to \infty: \theta = W_P = W_F = 0$$

The subscript w denotes the value of the variable at the wall ($\eta = 0$). The values of W_{Fw} and W_{Pw} are found as functions of the blowing parameter f_w:

$$W_{Fw} = W_F(0) = \frac{-W_F'(0)}{\mathrm{Sc}f_w} + \frac{Q}{c_p T_\infty M_F(\nu_F'' - \nu_F')} + \frac{Q}{c_p T_\infty} \tag{20}$$

$$W_{Pw} = W_P(0) = \frac{W_P'(0)}{\mathrm{Sc}f_w} + \frac{\hat{\omega}_{0,\infty}Q}{c_p T_\infty} \tag{21}$$

By defining the following set of normalized variables

$$W_F = \frac{W_F}{W_{Fw}}, \qquad W_P = \frac{W_P}{W_{Pw}}, \qquad \bar{\theta} = \frac{\theta}{\theta_w}$$

the system of equations and related boundary conditions become

$$0 \le \eta \le \eta_f:$$

$$f''' + ff'' - (f')^2 + \bar{\theta}\theta_w - \frac{\hat{\omega}_{0,\infty}Q}{c_p T_\infty} = 0 \tag{22}$$

$$\eta \ge \eta_f$$

$$f''' + ff'' - (f')^2 + \bar{\theta}\theta_w - \overline{W}_F W_{Fw} = 0$$

$$\eta = 0: f = f_w, f' = 0$$

$$\eta \to \infty: f' = 0$$

$$\bar{\theta}'' + \mathrm{Pr}f\bar{\theta}' = \frac{\mathrm{Pr}}{\theta_w \rho c_p T_\infty c}\frac{\partial q_R}{\partial y} \tag{23}$$

$$\eta = 0: \bar{\theta} = 1.0,$$

$$\eta \to \infty: \bar{\theta} = 0$$

$$\overline{W}_F'' + \mathrm{Sc}f\overline{W}_F' = 0 \tag{24}$$

$$\overline{W}_P'' + \mathrm{Sc} f \overline{W}_P' = 0$$

$$\eta = 0: \overline{W}_F = \overline{W}_P = 1.0, \overline{W}_P = \overline{W}_{Fw}, \overline{W}_P - \overline{W}_{P_\omega}$$

$$\eta \to \infty: \overline{W}_F = \overline{W}_P = 0$$

With the assumption that Le = 1 (Pr = Sc), the species equation, the mathematically homogeneous energy equation and their respective boundary conditions become identical; therefore, their solutions become identical. This greatly reduces the computer time required to solve the set of equations.

Gaseous Radiation Model

This investigation takes into consideration the presence of five gases. Two of the gases, oxygen and nitrogen, are transparent to thermal radiation when at the temperatures encountered in the combustion process. The other three gases, methane, carbon dioxide, and water vapor, being composed of unsymmetrical, polyatomic molecules, radiate and absorb thermal energy when at elevated temperatures.

The absorption and emission by participating gases is a function of the frequency of the radiation as well as a function of the temperature and pressure of the gas. Because the gases in a flame are nonuniform in temperature and composition, it is necessary to compensate for these nonuniformities by using a scaling technique such as the one proposed in [13], whereby the absorption coefficient is cast in terms of the scaled parameters $\overline{\omega}$ and $\overline{\alpha}$, the band width and integrated intensity, respectively. With the assumption that the absorption bands are fully broadened (a valid assumption for a flame at atmospheric pressure), the expression for the total band absorptance can be cast into a closed form function of $\overline{\omega}$ and $\overline{\alpha}$.

In order to solve the system of governing equations (22)–(24), an expression for the radiative heat flux is required. In formulating this expression, the surface of the cylinder is considered to be black and diffuse, and the surrounding medium is considered nonhomogeneous, nonscattering, and fully broadened, exhibiting at infinity the characteristics of a black surface. Radiation due to soot is excluded, since it has been shown in reference [3] that the existence of soot particles in the lower stagnation region is negligible. The limitation to one-dimensional radiative transfer is shown in reference [21] to be a good approximation for boundary layer flows.

From Sparrow and Cess [22], the equation of one-dimensional radiative transfer at y in an absorbing-emitting gas can be written as

$$q_R(y) = e_b(0) - e_b(L) + \int_0^y \int_0^\infty \frac{de_\nu}{dx}\left[1 - 2E_3(\tau_\nu - \tau_\nu')\right] d\nu\, dx + \int_y^L \int_0^\infty \frac{de_\nu}{dx}\left[1 - 2E_3(\tau_\nu' - \tau_\nu)\right] d\nu\, dx \quad (25)$$

where

$$\tau_\nu = \int_0^y K_\nu \rho\, dy' \qquad \tau_\nu' = \int_0^x K_\nu \rho\, dy'$$

As suggested by Edwards and Balakrishman [23], with the incorporation of the wide-band exponential model into the absorption coefficient, the expression for optical thickness, gives

$$\tau_\nu = \int_0^y \frac{\alpha}{\omega}\rho \exp\left[-\left(\frac{\nu - \nu_0}{\overline{\omega}}\right)\right] dy', \qquad \nu_0 < \nu \quad (26)$$

where α and ω are properties of the gas which can be expressed in terms of temperature. The scaled value of ω, as proposed by Felske and Tien [31], is obtained from $\overline{\omega} = \omega(\overline{T})$, where $\overline{T}$ is the integrated average temperature. This technique is not expected to cause any significant inaccuracies [31] as compared to the techniques outlined in references [13, 14].

The optical thickness can be expressed as the product of the optical thickness at the band head or center (where the most intense absorption occurs) and the exponential factor:

$$\tau_\nu = \tau_H \exp\left[-\left(\frac{\nu - \nu_0}{\overline{\omega}}\right)\right] \text{ and } \tau_\nu' = \tau_H' \exp\left[-\left(\frac{\nu - \nu_0}{\overline{\omega}}\right)\right] \quad (27)$$

Note

$$\tau_H = \int_0^y K_\nu dy'$$

and

$$\tau_H' = \int_0^x K_\nu dy'$$

Using the exponential kernel approximation, the transfer equation can be expressed as

$$q_R(y) = e_b(0) - e_b(L) + \int_0^y \frac{dT}{dx} \sum_{k,j} \overline{\omega}_{k,j} \frac{de_{\nu k}}{dT} \overline{A}_{k,j}\left[\frac{3}{2}(\tau_H - \tau_H')\right] dx + \int_y^L \frac{dT}{dx} \sum_{k,j} \overline{\omega}_{k,j} \frac{de_{\nu k}}{dT} \overline{A}_{k,j}\left[\frac{3}{2}(\tau_H' - \tau_H)\right] dx \quad (28)$$

where $\overline{A}_{k,j}$, the total band absorption ratio of species j in the kth band region. To solve the energy equation, equation (23), the derivative of q_R is required. Upon differentiation and some manipulation, equation (28) becomes

$$\frac{dq_R(y)}{dy} = \int_0^y \frac{dT}{dx} K_1(x, y)\, dx - \int_y^L \frac{dT}{dx} K_2(x, y)\, dx \quad (29)$$

where

$$K_1(x, y) = \frac{3}{2}\left\{\sum_{k,j} \overline{\omega}_{k,j} e_{b\nu k}' \left(\frac{d\tau_H}{dy}\right)_{k,j} \overline{A}_{k,j}'\left[\frac{3}{2}(\tau_H - \tau_H')\right]\right\} \quad (30)$$

$$K_2(x, y) = \frac{3}{2}\left\{\sum_{k,j} \overline{\omega}_{k,j} e_{b\nu k}' \left(\frac{d\tau_H}{dy}\right)_{k,j} \overline{A}_{k,j}' \times \left[\frac{3}{2}(\tau_H' - \tau_H)\right]\right\} \quad (31)$$

For the gray-gas model, the derivative of the radiative flux is

$$\frac{dq_R(y)}{dy} = 4K_P\sigma T^4 - 2\overline{K}_P\sigma\left[T_w^4 \exp(-2\overline{K}_P y) + T_\infty^4 \times \exp(-2\overline{K}_P(L - y)) + 2\int_0^L \overline{K}_P T^4(x) \times \exp(-2\overline{K}_P|y - x|)\, dx\right] \quad (32)$$

where τ, τ_0, and τ' are optical path lengths defined by

$$\tau = \overline{K}_P y, \qquad \tau_0 = \overline{K}_P L \qquad \text{and } \tau' = \overline{K}_P x$$

and where $\overline{K}_p$, the mean Planck absorption coefficient, is defined by

$$\overline{K}_P = \frac{\int_0^\infty K_\lambda e_{b\lambda} d\lambda}{e_b}$$

Due to the nonhomogeneous nature of the problem, the value of the Planck mean absorption coefficient to be used in equation (32) was obtained from the relation

$$\overline{K}_p = p_{wH}\overline{K}_{pH} + p_{wC}\overline{K}_{pC}$$

where K_{pH} and K_{pC} are the Planck mean absorption coefficients for pure water vapor and pure carbon dioxide evaluated at the temperature of the wall, and p_{wH} and p_{wC} are the partial pressures of the gases at the wall. The band-width and integrated band intensity correlation parameters in the present analysis are taken from reference [30].

To obtain theoretical temperature and composition profiles equations (22)–(24) are solved numerically for various fuel blowing

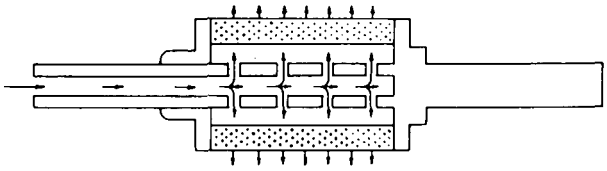

Fig. 2 Sketch of experimental test cylinder

rates. A technique of Nachtsheim and Swigert [24], is used to find the three additional boundary conditions $f''(0)$, $\bar{\theta}'(0)$, and $\bar{W}'(0)$, necessary to solve the system. First of all, the system is solved without the radiative term (i.e., $dq_R/dy = 0$). The resulting temperature profile is then used to generate a profile for the radiative derivative. Again the governing equations are solved, but this time the radiative profile is included in the energy equation. Thus, a new profile of the radiative derivative is generated for use in the next iteration. This procedure is then repeated until there is less than 0.1 K change between the peak temperature of the old and new profiles. Usually eight iterations are sufficient to insure a convergent solution.

Experiments

The experimental apparatus in the present study consisted of a test cylinder, a Mach-Zehnder interferometer, and a gas chromatograph with associated probes. The test cylinder, shown schematically in Fig. 2, was fabricated from 58 percent dense nickel Foametal. It was 5.2-cm long with an outside diameter of 3.81 cm and an inside diameter of 2.22 cm. Methane gas was injected into the cylinder through a 1.27-cm diameter tube which had a series of holes around its circumference and along its axis. This was done to insure uniform injection through the cylinder. The outside of this tube was threaded so that nuts could hold shoulders firmly in place to seal the ends of the cylinder. The surface of the cylinder was blackened with soot to approximate a surface emissivity of one. A large screened enclosure consisting of three layers of window screen surrounded the test section to prevent random air currents in the room from disturbing the flame. Methane was selected as the combustile gas since its wide-band spectroscopic correlation parameters were readily available. The surface blowing rate of the fuel was controlled by a fine metering valve and measured using a flowmeter 250 mm in length.

A 15.2 cm Mach-Zehnder interferometer with a mercury vapor light source (5461°A) was the principal measuring instrument in determining temperature profiles along the lower stagnation line. Operational theory of the interferometer is described in references [25, 26]. The interferometer is well-suited for this type of measurement, because it introduces no disturbances into flow or temperature fields; can record instantly the entire two-dimensional field that is in its view. By proper analysis of the interferograms, which in the case of gas mixtures requires knowledge of the composition, it is possible to make very accurate temperature measurements.

A gas chromatograph with a microprobe sampling system was used to determine the concentration profiles along the lower stagnation line. Detailed accounts of basic chromatographic theory can be found in references [27, 28], and specifications of the complete chromatographic system used in this study are presented in Table 1. The microprobe was designed following the recommendations of Fristom and Westenberg [29] in order to provide effectively quenched samples for chromatographic analysis. The probe was made of 3-mm dia quartz tubing tapered at the tip to a 0.2-mm OD with a 50-mm orifice. Because water vapor would be irreversibly absorbed by the column packing material, only dry samples could be analyzed; therefore, as suggested by Adbel-Khalik [3], the water vapor concentrations were approximated as being two times the carbon dioxide values.

Table 1 Chromatographic system specifications

Carrier gas:	helium, 6 ml/min
Column dimensions:	length: 10.3 ft., ID: 1/8 in
Column packing:	molecular sieve No. 5A, 36-64 mesh
Detector:	thermal conductivity cell at 150°C
Oven temperature:	20°C for 10 minutes, programmed to 350°C at 32°C/minute
Gases separated:	O_2, N_2, CH_4, CO, and CO_2

Finally, it should be reemphasized that this study constitutes a first-time attempt at predicting the total behavior of a nonhomogeneous gas radiation. To check the validity of the model, it was necessary to obtain the appropriate experimental data, without which the accuracy of the analytical model could not be adequately assessed.

Results and Discussion

Temperature and concentration profiles obtained both experimentally and theoretically for various methane blowing rates are presented. The theoretical profiles are given for the wide-band model, the gray-gas model, and for the case of no radiation-interaction at all. Also included in the results are the convective wall heat fluxes, experimental and theoretical, calculated from the temperature distributions.

All experimental measurements were made for three surface blowing rates of fuel: Q_F = 2100 cc/min, Q_F = 2300 cc/min, and Q_F = 2600 cc/min. The blowing rate Q_F = 2100 cc/min was chosen as the lower extreme, because it was the lowest flow rate that would sustain a steady flame on the porous cylinder. It was found that any flow rate less than Q_F = 2100 cc/min would cause the flame to become unstable due to thermal-quenching effects. The flow rate Q_F = 2600 cc/min was chosen as the other extreme, because for values of Q_F any higher, the flame would become luminous due to soot formation, and the fringe lines on the interferogram would become badly blurred and thus, unreadable. The effects of soot were not included in this study.

The following property values, which were assumed constant, were used in the solution of the governing equations: c_p = 0.25 cal/K-gm, and Pr = Sc = 0.7. The following values, which were measured in the experiment, were also used: T_w = 530°C for Q_F = 2100 cc/min, T_w = 529°C for Q_F = 2300 cc/min, and T_w = 524°C for Q_F = 2600 cc/min. The ambient temperature (T_∞) was 27°C for each case.

The temperature profiles predicted by a numerical solution of the governing equations using the wide-band model to formulate the radiation term are presented in Figs. 3–5 for the three blowing rates, Q_F = 2100 cc/min, Q_F = 2300 cc/min, and Q_F = 2600 cc/min. Three noteworthy effects of an increase in surface blowing are readily discernible; an increase in the temperature boundary layer thickness; movement of the flame front away from the surface; and higher temperatures in the flame. Higher flame temperatures were the result of both an increase in the rate of heat released (because of a larger fuel-consumption rate) and the fact that the flame front was at a greater distance from the relatively cool cylinder surface. It should be mentioned that in no case did the theoretical flame temperature reach the adiabatic flame temperature for methane. The experimental flame temperature also fell below the adiabatic flame temperature, an observation consistent with the measurements of Klugheim [7].

The effect of including gaseous radiation in the analysis can be seen in the figures which show the theoretical temperature profiles based on the wide-band model and the profiles for the case of no radiation interaction. It is evident that radiation-interaction lowers the predicted temperatures in the high temperature region of the boundary layer near the flame front and raises the temperature in the cooler region near the edge of the boundary layer. Furthermore, this interaction effect is seen to increase for larger blowing rates. The effect of radiation interaction can be interpreted to result from a transfer of energy by gaseous radiation heat transfer from the hotter region to

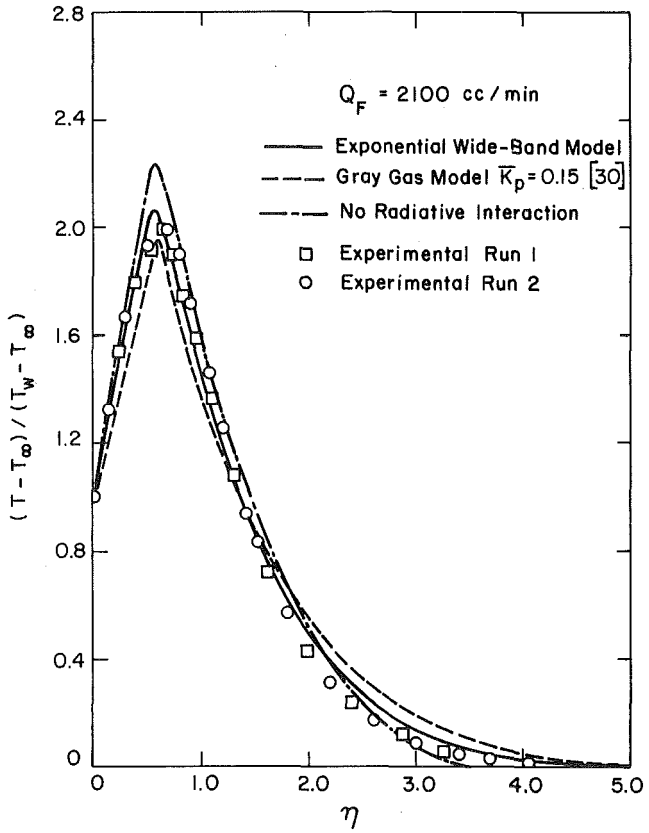

Fig. 3 Experimental and theoretical temperature profiles—Q_F = 2100 cc/min

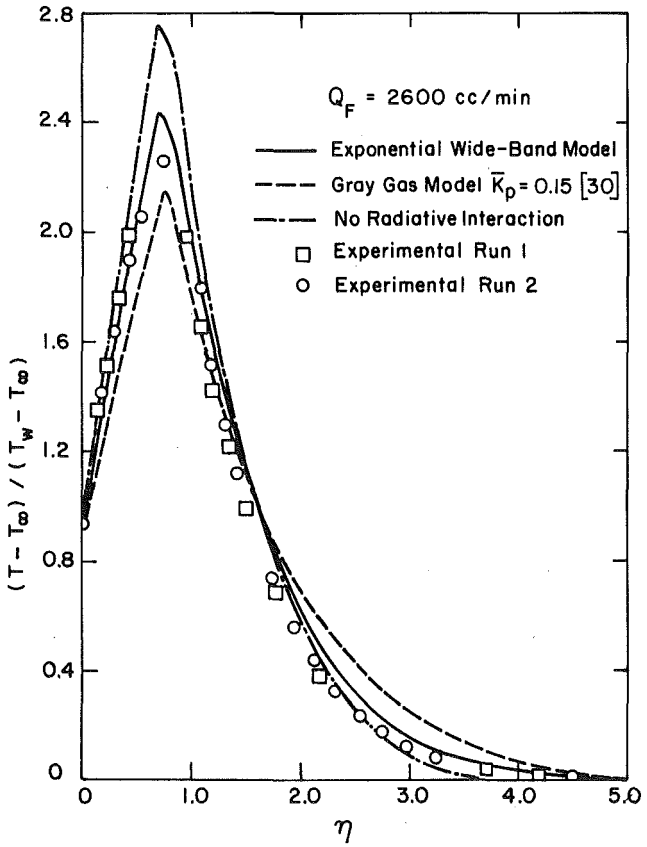

Fig. 5 Experimental and theoretical temperature profiles—Q_F = 2600 cc/min

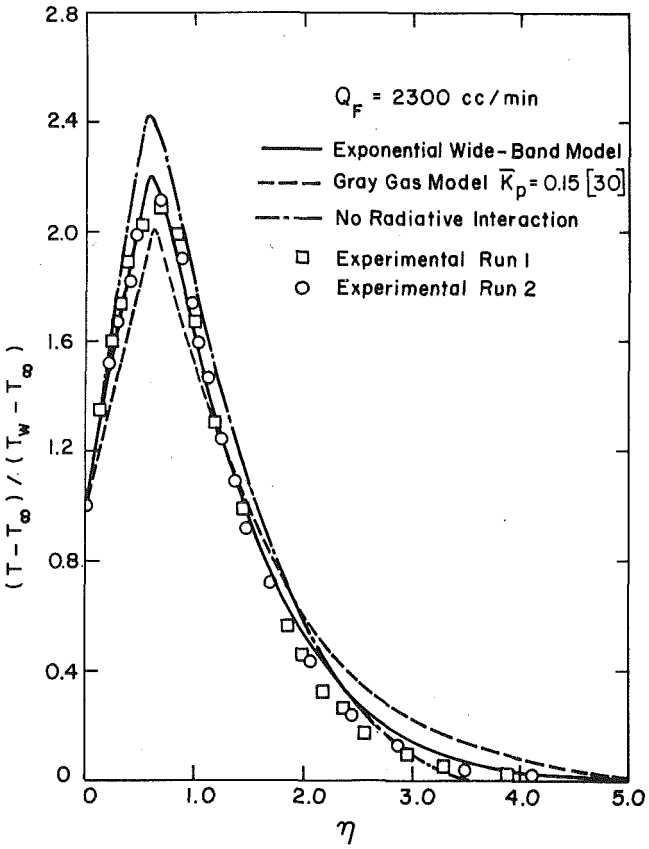

Fig. 4 Experimental and theoretical temperature profiles—Q_F = 2300 cc/min

the cooler portion of the boundary layer, thus reducing the higher temperatures and raising the lower ones. It is also important to note that radiation interaction tends to increase the thermal boundary layer thickness, and this effect becomes larger for higher blowing rates. Finally it should be noted that the radiation regime for this problem cannot be classified as either optically thick or optically thin, since it was found to involve intermediate values of the optical thickness parameter.

The temperature predictions based on the gray-gas model (dashed lines) can also be seen in Figs. 3–5. In all three cases, the gray-gas model with an absorption coefficient independent of wavelength overpredicts the influence of radiation. Note that, as has been discussed previously, the effect of radiation is to lower the high temperatures in the region of the flame front and raise the low temperatures near the edge of the boundary layer.

An attempt was made to determine an arbitrary value for $\overline{K}_p$ which when used in the gray-gas model would yield temperature profiles matching the experimental results. It was found that matching values of $\overline{K}_p$ did indeed exist. However, a different value of $\overline{K}_p$ was required for each fuel-flow condition; thus precluding the possibility of being able to define a single value for $\overline{K}_p$ that would be universally applicable to all methane-air flames.

Interferograms of the burning cylinder corresponding to the methane flowing at Q_F = 2100 cc/min are presented in Figs. 6 and 7. With the reference fringes horizontal as in Fig. 6, the symmetrical nature of the problem is clearly evident. From the relatively thin appearance of the flame flow front (seen as a bright line wrapped partially around the cylinder), the flame sheet model seems to be a suitable representation of this diffusion flame. The temperature results, as will be discussed later, also attest to the flame-sheet model's suitability. The other interferogram (Fig. 7) with vertical reference fringes is typical of the ones from which fringe shift measurements

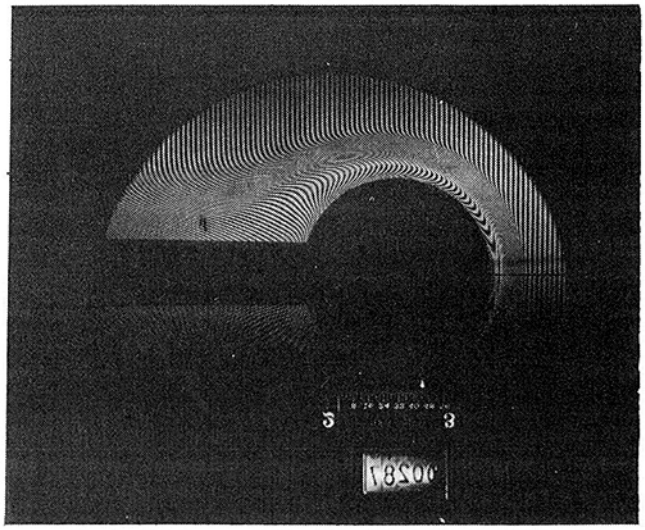

Fig. 6 Interferogram of burning cylinder—horizontal fringes

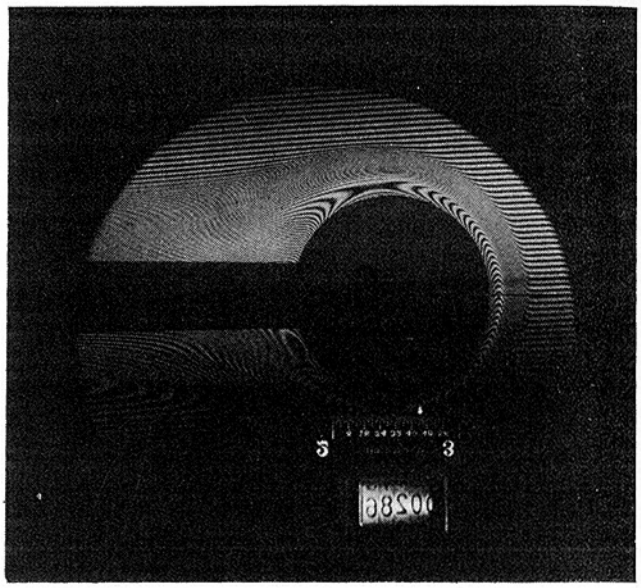

Fig. 7 Interferogram of burning cylinder—vertical fringes

were made. It should be noted that these measurements were corrected both for refraction effects and for end effects (reference [3]).

Comparisons between the experimental temperature data and the theoretical predictions are again presented in Figs. 3–5 for the three blowing rates. The theoretical profiles determined using the wide-band and gray-gas models are given as a continuous and dashed curves, respectively, while the experimentally determined temperatures (for two different runs in each blowing rate) are represented as distinct points. It is well to note the excellent repeatability between the experimental runs for all three fuel blowing rates. In many instances the data points coincide exactly.

Evident from Figs. 3–5 is the consistently good agreement between the profiles of experimental temperatures and those of the wide-band model. The agreement near the wall is of particular significance, since the convective wall heat fluxes (which will be discussed in detail later) are proportional to the wall temperature gradients. In all three cases the wide-band model predicts a peak flame temperature that is slightly higher than the measured one. This discrepancy may be a consequence of the fact that the theory in this study is based on infinitely fast combustion reactions, whereas in reality the reactions are of finite rate. Also, the measured flame regions or flame fronts appear to be only slightly wider than their predicted counterparts. Based on this, it can be concluded that the assumption of an infinite reaction rate imposes no severe limitations on the theoretical results.

The performance of the wide-band and gray-gas models can be further evaluated by considering the convective wall heat fluxes given in Table 2, which have been calculated from their respective temperaure profiles. The percent deviation of the theoretical from the experimental values are also listed, as well as the fluxes calculated from the no-interaction temperature profiles. It can be seen from this table that, for all three run conditions, the fluxes given by the wide-band model are considerably closer to the experimental values than the convective fluxes found from the no-interaction profile. It is also noted that the gray-gas model consistently underestimates the convective flux by a considerable percentage. This is obviously due to the low temperature predictions, which were caused by considerable radiative interaction.

The total radiative heat flux at the wall was calculated using the wide-band model only. Table 3 presents both the total radiative flux and the radiative flux due solely to gas radiation for the three run conditions. Note that at the higher fuel flow rates the contribution of radiation increases. The effect of the individual absorption bands was also isolated. The contribution of each is listed in Table 4 for a blowing rate of 2100 cc/min. It can be seen in Table 5 that the 4.3 μm band of CO_2 has by far the greatest effect of all bands in this study. It should be mentioned that the total radiative participation by the individual absorption bands of any gas in a nonhomogeneous situation is a function of temperature and partial pressure as well as the strength of the band as determined by its band intensity and band width.

The composition results are presented in Figs. 8–10 for the same blowing rates. The experimental data (determined in two separate runs for each blowing rate) are presented as distinct points while the theoretical profiles, determined using the wide-band model, are given as continuous curves. Fine agreement between theory and experiment is apparent for all three fuel blowing rates. However, all of the theoretical composition profiles seem to predict thinner concentration boundary layers than those which were measured. This result can be attributed to the approximation in the analysis that the Lewis number

Table 2 Convective wall heat fluxes (cal/s-cm^2)

Fuel Flow (cc/min)	Experimental	Wide-Band	% from Exp.	Gray-Gas	% from Exp.	$q_r = 0$	% from Exp.
2100	-0.697	-0.672	-3.6	-0.541	-22.4	-0.746	6.8
2300	-0.704	-0.681	-3.2	-0.521	-25.9	-0.770	9.3
2600	-0.730	-0.697	-4.6	-0.495	-32.1	-0.809	10.7

Table 3 Wide-band radiative wall heat fluxes and convective wall heat fluxes (cal/s-cm)

Fuel Flow Rate (cc/min)	q_{rw}(total)	q_{rw}(gaseous)	q_{cw}(wide-band)
2100	0.5157	-0.0365	-0.672
2300	0.5072	-0.0422	-0.681
2600	0.4802	-0.0499	-0.697

Table 4 Contributions of the individual bands to the total gaseous-radiation flux at the wall

Gas	Band	Contribution (%)
CO_2	4.3 μ	57.0
CO_2	15.0 μ	3.9
CO_2	2.7 μ	2.5
H_2O	6.3μ	21.0
H_2O	2.7 μ	12.0
H_2O	1.87 μ	0.8
H_2O	1.38 μ	0.2
CH_4	3.3 μ	1.6
CH_4	7.6 μ	1.0

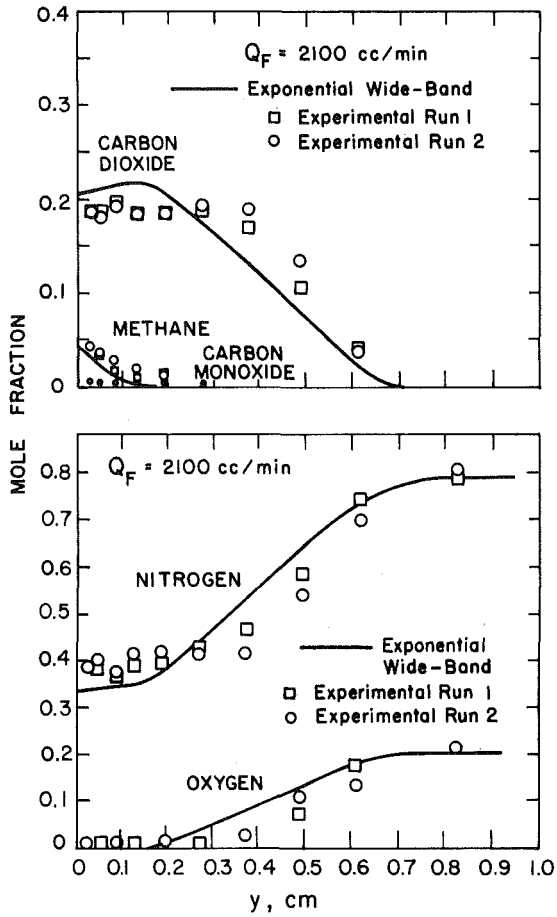

Fig. 8 Experimental and theoretical composition profiles—Q_F = 2100 cc/min

is equal to unity which leads to the prediction of equally thick thermal and species boundary layers. However, by examining the actual Lewis numbers of the constituent gases, it can be seen that the species boundary layer should be thicker than the temperature layer as, in fact, was observed in the experiments. The predicted composition profiles had little dependency on the radiation model used. Also, the repeatability of data between the two runs appears to be very good considering the difficulty in making measurements in flames. Note that only very small amounts of carbon monoxide (less than 0.5 percent mole percent) were found in the boundary layers. Therefore, the assumption in the analysis neglecting the existence of carbon monoxide appears to be valid. Finally, the general agreement found in these profiles reaffirms the validity of the flame sheet model in diffusion flame applications.

From this combined experimental and theoretical study, it can be concluded that radiation-interaction in a nonhomogeneous, combustion situation is satisfactorily predicted by the utilization of the nongray gas-radiation model of Edwards and Menard [8] with scaled wide-band parameters. In addition, the nongray model yields results that are superior to those based on the use of the gray-gas model as well as the results that ignore the effect of radiation.

Acknowledgments

The authors wish to acknowledge the support given under NSF Grant GK-43618.

References

1 Novotny, J. L., and Kelleher, M. D., "Conduction in Nongray Radiating Gases," *International Journal of Heat and Mass Transfer*, Vol. II, No. 2, Feb. 1968, pp. 365–369.

2 Schimmel, W. P., Novotny, J. L., and Olsofka, F. A., "Interferometric Study of Radiation-Conduction Interaction," *Proceedings of the Fourth International Heat Transfer Conference*, Paper R2.1, Elsevier Publishing Co., Amsterdam, 1970.

3 Abdel-Khalik, S. I., "An Investigation of the Diffusion Flame Surrounding a Simulated Fuel Droplet," PhD thesis, University of Wisconsin, 1973.

4 Spalding, D. B., "The Combustion of Liquid Fuels," *Fourth Symposium (International) on Combustion*, Williams and Wilkins, 1953, pp. 847–864.

5 Spalding, D. B., "Mass Transfer in Laminar Flow," Proceedings Royal Society, Vol. 221A, 1954, pp. 78–99.

6 Kim, J. S., DeRis, J., and Kroesser, F. W., "Laminar Free-Convective Burning of Fuel Surfaces," *Thirteenth Symposium (International) on Combustion*, the Combustion Institute, 1971, pp. 949–961.

7 Klugheim, N. G., "Transport Processes in a Combustible Turbulent Boundary Layer," *Journal of Fluid Mechanics*, TRANS. ASME, Vol. 12, 1962, pp. 417–437.

8 Edwards, D. K., and Menard, W. A., "Comparison of Models for Correlation of Total Band Absorption," *Appl. Opt.*, Vol. 3, No. 5, May 1964, pp. 621–625.

9 Novotny, J. L., and Olsofka, F. A., "The Influence of a Non-Absorbing Gas and Radiation-Convection Interaction," *AIAA Progress in Astronautics and Aeronautics*, Vol. 24, 1971.

10 Bratis, J. C., and Novotny, J. L., "Radiation-Convection Interaction in the Boundary Layer Regime of an Enclosure," *International Journal of Heat and Mass Transfer*, Vol. 17, No. 1, Jan. 1972, pp. 23–36.

11 Audunson, T., and Gebhart, B., "An Experimental and Analytical Study of Natural Convection With Appreciable Thermal Radiation Effects," *Journal of Fluid Mechanics*, Vol. 52, Part 1, Mar. 1972, pp. 57–95.

12 Novotny, J. L., "Radiation Interaction in Nongray Boundary Layers," *International Journal of Heat and Mass Transfer*, Vol. 11, No. 12, Dec. 1968, pp. 1823–1826.

13 Edwards, D. K., and Morizumi, S. J., "Scaling of Vibration-Rotation Band Parameters for Nonhomogeneous Gases," *J. Quant. Spec. Rad. Transfer*, Vol. 10, No. 3, Mar. 1970, pp. 175–188.

14 Chan, S. H., and Tien, C. L., "Total Band Absorptance of Non-Isothermal Infrared Gases," *J. Quant. Spec. Rad. Transfer*, Vol. 9, No. 9, Sept. 1969, pp. 1261–1271.

15 Cess, R. D., and Wang, L. S., "A Band Absorptance of Non-Isothermal

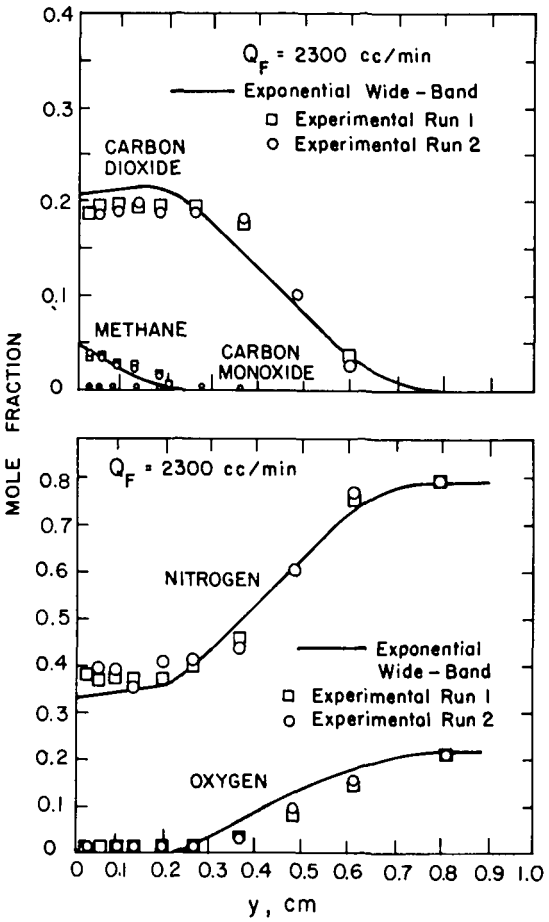

Fig. 9 Experimental and theoretical composition profiles—Q_F = 2300 cc/min

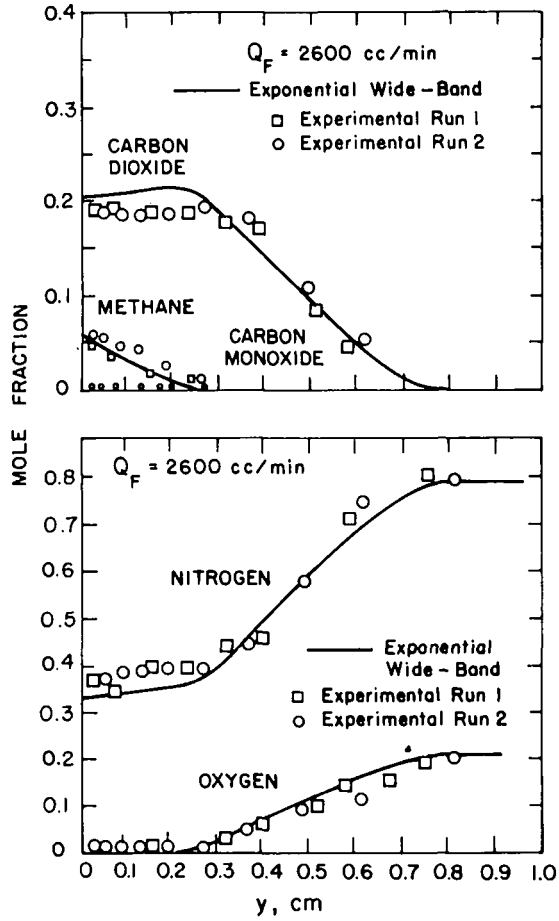

Fig. 10 Experimental and theoretical composition profiles—Q_F = 2600 cc/min

Gaseous Radiation," *International Journal of Heat and Mass Transfer*, Vol. 13, No. 3, Mar. 1970, pp. 547–555.

16 Chan, S. H., and Tien, C. L., "Infrared Radiative Heat Transfer In Non-Gray Non-Isothermal Gases," *International Journal of Heat and Mass Transfer*, Vol. 14, No. 1, Jan. 1971, pp. 19–26.

17 Tsuji, H., and Yamaoka, I., "The Counter Flow Diffusion Flame in the Forward Stagnation Region of a Porous Cylinder," *Eleventh Symposium (International) on Combustion*, The Combustion Institute, 1967, pp. 979–984.

18 Tsuji, H., and Yamaoka, I., "The Structure of Counterflow Diffusion Flames in the Stagnation Region of a Porous Cylinder," *Twelfth Symposium (International) on Combustion*, The Combustion Institute, 1969, pp. 997–1005.

19 Tsuji, H., and Yamaoka, I., "Structure Analysis of Counterflow Diffusion Flames in the Forward Stagnation Region of a Porous Cylinder," *Thirteenth Symposium (International) on Combustion*, The Combustion Institute, 1971, pp. 723–731.

20 Abdel-Khalik, S., Tamaru, T., and El-Wakil, M. M., "An Experimental and Analytical Determination of Heat and Mass Transfer in a Diffusion Flame," *Proceedings 1973 International Center for Heat and Mass Transfer Seminar—Heat Transfer from Flames*, Scripta Publishing, 1974.

21 Novotny, J. L., Bankston, J. D., and Lloyd, J. R., "Local Nonsimilarity Applied to Free Convection Boundary Layers with Radiation Interaction," *Heat Transfer with Thermal Control Applications, Progress in Astronautics and Aeronautics*, Vol. 39, 1975, pp. 309–330.

22 Sparrow, E. M., and Cess, R. D., *Radiation Heat Transfer*, Brooks/Cole Publishing, 1966.

23 Edwards, D. K., and Balakrishnan, A., "Slab Bound Absorptance for Molecular Gas Radiation," *J. Quant. Spec. Rad. Transfer*, Vol. 12, No. 10, Oct. 1972, pp. 1379–1387.

24 Nachtsheim, P. R., and Swigert, D., "Satisfaction of Asymptotic Boundary Conditions in the Numerical Solution of Boundary-Layer Equations," *Developments in Mechanics*, Vol. 3, Part 2, 1965, pp. 361–371.

25 Eckert, E. R. G., Drake, R. W., and Soehngen, E., "Manufacture of Zehnder-Mach Interferometer," Air Force Report 5721, ATI No. 34235, 1948.

26 Novotny, J. L., "Interferometric Study of Laminar Convection in a Parallel Plate Channel With Uniform Heat Sources in the Fluid," PhD thesis, Department of Mechanical Engineering, University of Minnesota, 1962.

27 Stockland, R., and Rice, C. B. F., *Chromatographic Methods*, Chapman and Hall, Ltd., 1963.

28 Jeffery, P. G., and Kipping, P. J., *Gas Analysis by Chromatography*, Pergamon Press, 1972.

29 Fristrom, R. M., and Westenberg, A. A., *Flame Structure*, McGraw-Hill, New York, 1965.

30 Tien, C. L., "Thermal Radiation Properties of Gases," *Advances in Heat Transfer*, Vol. 5, Academic Press, New York, 1968, pp. 254–324.

31 Fleske, J. D., and Tien, C. L., "Infrared Radiation From Non-Homogeneous Gas Mixtures Having Overlapping Bands," *J. Quant. Spec. Rad. Transfer*, Vol. 14, No. 1, Jan. 1974, pp. 35–48.

R. K. James
Research Asst.

D. K. Edwards
Professor and Chairman.
Mem. ASME

Energy and Kinetics Department,
School of Engineering, UCLA,
Los Angeles, Calif.

Effect of Molecular Gas Radiation on a Planar, Two-Dimensional, Turbulent-Jet-Diffusion Flame

Non-gray radiation described by the exponential model for molecular gas bands was added to the numerical solution of turbulent combustion of methane in a planar, enclosed, jet-diffusion flame. The planar jet of methane is injected with velocity u_{fuel} into a stream of air flowing with velocity u_{air} parallel to the fuel. Diffusion-controlled combustion occurs in the mixing region of the jet. Plane-parallel, isothermal, black walls symmetrically located above and below the jet form the combustion chamber. A soot-free flame is assumed to exist so that molecular gas bands determine the thermal radiative transfer to the walls.

Velocity, composition, and temperature fields and heat flux at the wall are obtained numerically. Approximately 40 percent of the requisite computation time is expended on the radiation calculation. Solutions are obtained to show the effect of channel size, air preheat, and product recirculation. Also the effect of reaction zone thickness was examined by varying an effective first Damköhler or mixing number which parameterizes the mixing-controlled reaction rate. It is found that a given reduction in maximum combustion temperature to reduce nitric oxide formation can be accomplished with a much less detrimental reduction on heat transfer by recirculating exhaust product into the combustion air than by reducing air preheat.

Introduction

Heat radiation and turbulent diffusion are the two dominant energy transport mechanisms operating in a combustion chamber. Radiation transfer is often the goal sought, as in the radiant section of a boiler or in a process furnace used for melting or heating. It is the turbulent diffusion which brings air and fuel together and sets the combustion rate and the thickness of the actual combustion zone. These factors affect importantly the radiation heat transfer, and the radiation itself affects the combustion in that it renders the combustion nonadiabatic. Small changes in peak temperature have a large influence upon nitric oxide production for a given residence time. Nitric oxide emissions are restricted by air pollution control agencies. It is of interest to know how various control strategies such as lowering combustion air preheat or recirculating exhaust products into the combustion air affect the unwanted nitric oxide emissions and the desired radiation heat transfer.

Much progress has been made in modeling turbulent transport in combustion flows [1, 2].[1] Techniques for modeling the radiation transfer realistically taking into account large spectral variations [3] in gas radiant transport have also been developed [4–6].

In this work the nongray radiation analysis previously developed is incorporated into an implicit finite difference method for the calculation of an internal boundary layer flow, a turbulent jet diffusion flame. In order to vary parametrically the reaction zone thickness, which is not well known at the present state of our knowledge, a dimensionless mixing parameter is introduced, an effective first Damköhler number. The numerical program is used to examine the effect of air preheat and exhaust recirculation on peak temperature and radiation heat transfer.

Analysis

Problem Description. Fig. 1 shows a jet of fuel with initial half thickness δ_f injected at velocity u_f into a flow of preheated combustion air at velocity u_a. The air may be premixed with recirculated combustion product so that its mole fraction of product in the mixture is x_p. The jet is enclosed by two-symmetrically-located isothermal

Contributed by the Heat Transfer Division of THE AMERICAN SOCIETY OF MECHANICAL ENGINEERS, and presented at the National Heat Transfer Conference, St. Louis, Mo., August 9–11, 1976. Revised manuscript received by the Heat Transfer Division November 3, 1976. Paper No. 76-HT-54.

[1] Numbers in brackets designate References at end of paper.

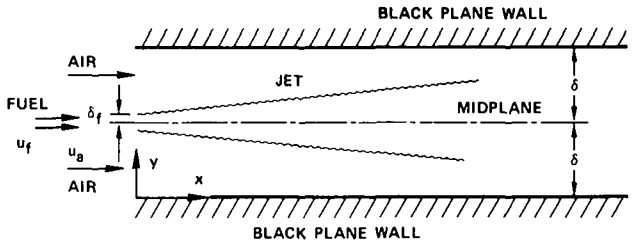

Fig. 1 Problem situation

black plane walls a distance 2δ apart. Within the channel formed by the planes the jet of fuel and stream of air mix turbulently with combustion occurring. A stream-wise coordinate x measures distance from the inlet, and y is taken to be the distance normal to the lower wall. The fuel is taken to be methane, and the air-to-fuel-flow ratio is stoichiometric. The combustion is assumed to be free of soot, and buoyancy forces are neglected in both the conservation equations and turbulence model.

The governing equations and boundary conditions are the usual.

$$\frac{\partial}{\partial x}(\rho u) + \frac{\partial}{\partial y}(\rho v) = 0 \tag{1}$$

$$\rho u \frac{\partial u}{\partial x} + \rho v \frac{\partial u}{\partial y} = -\frac{dP}{dx} + \frac{\partial}{\partial y}\left(\rho \nu \epsilon^+ \frac{\partial u}{\partial y}\right) \tag{2}$$

$$\rho u c_p \frac{\partial T}{\partial x} + \rho v c_p \frac{\partial T}{\partial y} = \frac{\partial}{\partial y}\left(\kappa \epsilon_h{}^+ \frac{\partial T}{\partial y}\right) - \frac{\partial}{\partial y}(q_r) + \sum_j \left\{\rho \mathcal{D}_{j,m} \epsilon_s{}^+ c_{p,j} \frac{\partial m_j}{\partial y}\frac{\partial T}{\partial y} - \hat{h}_j \dot{m}_j{}'''\right\} \tag{3}$$

$$\rho u \frac{\partial m_j}{\partial x} + \rho v \frac{\partial m_j}{\partial y} = \frac{\partial}{\partial y}\left(\rho \mathcal{D}_{j,m} \epsilon_s{}^+ \frac{\partial m_j}{\partial y}\right) + \dot{m}_j{}''' \tag{4}$$

$$y = 0, \quad u = v = \frac{\partial m_j}{\partial y} = 0 \quad \text{and } T = T_w \tag{5}$$

$$y = \delta, \quad \frac{\partial u}{\partial y} = v = \frac{\partial m_j}{\partial y} = \frac{\partial T}{\partial y} = 0 \tag{6}$$

$$x = 0 \quad \text{and } y < (\delta - \delta_f): u = u_a{}^0, \quad v = 0, \quad T = T_a{}^0, \quad m_f = 0 \tag{7}$$

$$x = 0 \quad \text{and } \delta - \delta_f < y < \delta: u = u_f{}^0, \quad v = 0, \quad T = T_f{}^0, \quad m_f = 1 \tag{8}$$

The stoichiometric constraint on $u_a{}^0$ is given by

$$\rho_a{}^0 u_a{}^0 (1 - m_p)(\delta - \delta_f) = r \rho_f{}^0 u_f{}^0 \delta_f \tag{9}$$

where r is the stoichiometric air-fuel ratio.

Radiation Heat Flux. In the spirit of the boundary layer assumptions already employed in the conservation equations, x-direction radiation is neglected. Absorption and emission of heat radiation in the gas occurs primarily in the wings of vibration-rotation bands which have exponential spectral variations. Accordingly the relations in the appendix of reference [5] can be taken over.

$$q_r = -\sum_{k=1}^{n} \int_0^{\delta} K_k(y, y') \frac{dB_k}{dy'} dy' \tag{10}$$

$$K_k(y, y') = A_s(\zeta_{k,\ell}(y, y') + \zeta_{k,\ell}(\delta, y)) - A_s(|\zeta_{k,\ell}(y, y')|) \tag{11}$$

$$A_s(\zeta_{k,\ell}(y, y')) = \bar{\omega}_k A_s{}^*(\bar{\tau}_{H,k}) \tag{12}$$

$$\bar{\omega}_k = \zeta_{k,2}/\zeta_{k,1}, \qquad \tau_{H,k} = \zeta_{k,1}/\bar{\omega}_k \tag{13}$$

$$\zeta_{k,1}(y, y') = \int_{y'}^{y} \alpha_k \rho_j dy'' = \zeta_{k,1}(y) - \zeta_{k,1}(y') \tag{14}$$

$$\zeta_{k,2}(y, y') = \int_{y'}^{y} \omega_k \alpha_k \rho_j dy'' = \zeta_{k,2}(y) - \zeta_{k,2}(y') \tag{15}$$

Nomenclature

A^+ = turbulence constant = 26.0
A_s = slab band absorption, equation (12)
$A_s{}^*$ = slab band absorptance, equation (16)
b = half the jet width at half depth (m)
B = turbulence constant, usually = 3.4
B_k = Planck black body radiosity function ($W/m^2 cm^{-1}$)
C = mixing rate coefficient, equation (22)
C^* = effective first Damköhler number, equation (23)
c = speed of light = 2.9969×10^8 (m/s)
c_p = mixture heat capacity (J/kg K)
$c_{p,j}$ = species heat capacity (J/kg K)
$\mathcal{D}_{j,m}$ = species diffusion constant (m^2/s)
h = Planck's constant = 6.6256×10^{-34} (J s)
$\hat{h}_j$ = species enthalpy (J/kg)
k = Boltzmann's constant = 1.38054×10^{-23} (J/mol K)
K = von Karman's constant = 0.40
K_k = radiation matrix, equation (11)
m_j = species mass fraction
$\dot{m}_j{}''$ = species production rate ($kg/m^3 s$)
n = number of radiation bands
Nu_C = convective Nusselt number = $q_{c,w}\delta/\kappa(T_{vol} - T_w)$
Nu_R = radiative Nusselt number = $q_{r,w}\delta/\kappa(T_{vol} - T_w)$
P = pressure
Pr = Prandtl number = $\nu \rho c_p/\kappa$
q_c = convective heat flux (W/m^2)
q_r = radiative heat flux (W/m^2)
r = stoichiometric air-fuel ratio
$\dot{r}$ = reaction rate ($kg/m^3 s$)
R_t = turbulent Reynolds number, equation (20)
Sc = Schmidt number = $\nu/\mathcal{D}_{j,m}$
T = temperature (K)
T_{ad} = adiabatic flame temperature (K)
u = local x-direction fluid velocity (m/s)
v = local y-direction fluid velocity (m/s)
x = streamwise coordinate (m)
x^* = dimensionless coordinate = x/δ
x_p = mole fraction of product recirculated into air
y = cross stream coordinate (m)
y^+ = dimensionless y coordinate in law of the wall
y^* = dimensionless coordinate = y/δ
α_k = integrated band intensity ($cm^{-1} m^2/kg$)
β = fraction of reaction heat removed
γ = Euler-Mascheroni constant = 0.5772156 ...
δ = channel half-width (m)
δ_f = initial fuel-jet half width (m)
ϵ = eddy diffusivity (m^2/s)
ϵ^+ = dimensionless eddy diffusivity, equation (18)
$\epsilon_{VD}{}^+$ = Van Driest law of the wall dimensionless eddy diffusivity
$\zeta_{k,1}$, $\zeta_{k,2}$ = radiation functions, equations (14) and (15)
η = bulk fraction of fuel that has burned
κ = thermal conductivity (W/m K)
ν = kinematic viscosity (m^2/s)
ν_k = wavenumber at radiation band origin (cm^{-1})
ρ = density (kg/m^3)
ρ_j = species partial density (kg/m^3)
$\bar{\tau}_{H,k}$ = band head optical depth, equation (13)
ω_k = spectral band width parameter (cm^{-1})
$\bar{\omega}_k$ = scaled band width, equation (13)

Subscripts

a = air
ad = adiabatic
f = fuel
j = individual species number
k = radiation band number
m = momentum
max = maximum
P = product
s = species
t = turbulent
vol = volume average
w = wall

Superscripts

0 = inlet or reference condition
$\cdot$ = rate

Table 1 Radiation band properties

Species	Band Location ν_k cm^{-1}	Band Intensity α_k^o $cm^{-1}/g\text{-}m^{-2}$	Band Width ω_k^o cm^{-1}
CH_4	3020	46.0	58.0
	4220	3.0	86.0
H_2O	1600	45.6	71.2
	3760	28.5	39.6
	5350	3.35	54.5
	7250	2.35	49.0
CO_2	2410	110.0	12.5

$$A_s^*(t) = \ln(t) + E_1(t) + \gamma + \frac{1}{2} - E_3(t) \tag{16}$$

$$B_k = \frac{2\pi \mathcal{H}\mathcal{C}^2 \nu_k^3}{{}_c\mathcal{H}\mathcal{C}\nu_k/\mathcal{K}T_{-1}} \tag{17}$$

Table 1 shows the bands selected and the properties used [3] in the radiation calculations. For simplicity in view of the high temperatures occurring, the long wavelength bands of H_2O and CO_2 were neglected, and the 2.7 μm CO_2 band was ignored in comparison to the 2.7 μm H_2O band. Neglect of the former leads to the radiation heat transfer being underpredicted, perhaps as much as 8 percent at temperatures as low as 1400 K. The error in neglecting the overlapping 2.7 μm CO_2 band is truly negligible in comparison.

Turbulence. Near $y = 0$ the Van Driest law of the wall [7] is used. The wall region plays a minor role in blocking some radiation by self-absorption.

$$\epsilon^+ = 0.5 + 0.5\{1 + 4Ky^{+2}[1 - \exp(-y^+/A^+)]^2\}^{1/2} \tag{18}$$

$$K = 0.40, \qquad A^+ = 26, \qquad y^+ = R_t y^*(\nu_w/\nu) \tag{19}$$

$$R_t = (\delta/\nu_w)(\tau_w/\rho_w)^{1/2}, \qquad \tau_w = \rho_w \nu_w \left.\frac{\partial u}{\partial t}\right|_{y=0} \tag{20}$$

In the important central region of the channel where turbulence is generated by the jet shear layer, the relations from Schlichting [8] are used.

$$\epsilon = 0.037 b(u_{\max} - u_{\min}) \tag{21}$$

The maximum velocity is at $y = \delta$, and the minimum was taken at $y = \delta/4$ as a matter of convenience. Following Mei and Squire [9] the two expressions were patched together using a simple term $1/(1 + By^*)$ multiplied into the Van Driest expression to make the patching smoother. The quantity B was chosen to make the Van Driest expression match the channel expression at $y = \delta - b$. If a value of B higher than the Mei and Squire value of 3.4 is indicated, the 3.4 value is used, as the wall-generated turbulence overwhelms that generated by the jet. No adjustment was made for the effect of radiation from one turbulent eddy to another, the effect being thought to be rather small [10, 11]. It was felt that this simple modeling of the turbulence was appropriate, because the object of the paper was to investigate the coupling between the radiation and turbulent transport.

Combustion. Although the combustion is assumed to be diffusion controlled, the controlling diffusion is not just that bringing the air and fuel to the edge of the jet. Such an assumption would lead to the combustion occurring only at an infinitesimally thin flame front. In actuality the combustion occurs at the edges of eddies of air and fuel. Thus, one is led to believe that the combustion zone is spread over a few eddy mean free paths, when one takes a Prandtl turbulent mixing length point of view. To simulate the finite combustion zone a turbulent-mixing-controlled reaction rate is postulated.

$$\dot{r} = C m_f m_a \tag{22}$$

The coefficient C was specified in terms of a dimensionless parameter C^*

$$C = C^* \frac{u_{\max}}{\delta} \tag{23}$$

One might argue that b should replace δ, but such arguments can be resolved only by careful experimentation, which was beyond the scope of this internally funded research. The quantity C^* is an effective first Damköhler number, effective in that turbulent mixing is taken to be the rate-controlling factor.

Another factor to be taken into consideration is the limiting of flame temperature by formation of OH, NO, O and other such species. In order to account simply for this complicating and physically important phenomenon, equilibrium calculations were performed for the composition versus temperature of stoichiometric methane-air mixtures. The ten species H, H_2, H_2O, O, O_2, OH, N_2, NO, CO, CO_2 were included. This equilibrium mixture is called "product," and the combustion reaction is taken to be

$$CH_4 + r \text{ air} \rightarrow \text{product}$$

The effects of high temperature species are thus included in a temperature-dependent heat of reaction and product heat capacity. The latter quantity accounts for the enthalpy change with shift in the product composition as temperature changes. The product composition changes throughout the flow field depending upon local temperature.

Numerical Methods. A widely used method for solving the governing equations is that of Patankar and Spalding [12]. Only one variable per equation is evaluated implicitly, and the others appearing in that equation are evaluated at the previous marching step or iterate. Where a high degree of coupling exists between the governing equations, the lagging of the other variables leads to computational difficulties. For this reason a more highly implicit method was developed as described briefly in the following. Additional details are presented in a thesis by the first author [13].

The nonlinear equations were quasilinearized with respect to all dependent variables about the last known values denoted by an asterisk. For example,

$$\rho u = \rho u^* + \rho^* u - \rho^* u^*$$

As a matter of personal preference the von-Mises transformation was not made, but it could have been with no difficulty. The x-derivatives were backward differenced; and y-derivatives were three-point centrally differenced, except for the continuity equation which was two-point centrally differenced. The y-direction convection terms were upwind differenced. The resulting set of linear algebraic equations for the variables at node point y_i are in the form

$$A_i V_{i+1} + C_i V_i + B_i V_{i-1} = D_i$$

where A, B, C, and D are matrices containing known quantities including variables at the previous x-location, and V is a column matrix or vector containing all the unknown variables at the x-location of interest. The set of equations are solved by marching in the y-direction over the nodes from one boundary, expressing solution vector V_i in terms of V_{i+1}, until the other boundary is encountered, allowing V_N to be determined, and marching back finding V_i. The reader unfamiliar with this type of numerical analysis is referred to Newman [14].

The pressure gradient dP/dx, taken to be constant in the y-direction under the boundary layer assumption, is included in vector D_i, and an additional constraint is added, namely $v = 0$ at the midplane $y = \delta$. Because of the inclusion of pressure gradient D_i the turn-around at the boundary involves the last three node points, but straightforward elimination gives the vector V_N and dP/dx.

Three to six iterations are usually required in the y-direction, and

Table 2 Base values of parameters

δ_f, Half width of fuel jet, 0.0135 m

δ, Half width of channel, 1.0 m

C*, Reaction rate parameter, 1.0

u_f^o, Initial fuel velocity, 20 m/sec

x_p, Recirculated product fraction, 0

T_a^o, Initial air preheat, 1000 K

T_f^o, Initial fuel temperature, 300 K

T_w, Wall temperature, 500 K

ν, Kinematic viscosity, $3.736 \times 10^{-5}(T/500)^{1.7}$ m^2/sec

Sc, Pr, Sc_t, Pr_t, 0.7

an x-direction step size of 0.2δ was used. Run times for 41 y-points and 110 x-points were 100 s on an IBM 360/91 computer costing 17 dollars each. The radiation calculation accounted for 40 percent of the cost.

Results and Discussion

Reaction Rate Parameter. Table 2 shows the set of nominal conditions chosen as a basis for comparison. Fig. 2 shows the resulting profiles at $x = 2$ m beyond the point of injection. Steep gradients in the velocity and composition profiles exist in the edge region of the fuel jet, say $0.7 \leq y^* \leq 0.9$. The maximum temperature occurs in this region, because the rate of combustion is high according to equation (22). Fig. 3 shows the effect on the temperature profile of varying the reaction rate parameter C^*. At a value of $C^* = 10$ the temperature profile manifests a bit of a spike, characteristic of flame front combustion. The lower value of $C^* = 0.5$ or 1.0 spreads the high temperature combustion region over a somewhat greater portion of the channel.

Heat Radiation and Channel Size. It was a goal of this work to show the effect of radiation upon combustion temperatures. Figs. 4(a) and 4(b) show the effect of varying channel size with and without radiation. The relative fuel jet size and dimensionless reaction rate parameter are fixed along with the other parameters at the standard conditions. Fig. 4(a) computed with no radiation shows that as the channel is made smaller the flame fills a greater portion, because the turbulent mixing is more effective over the shorter distances, but the peak temperature is affected little. Fig. 4(b) shows that the larger

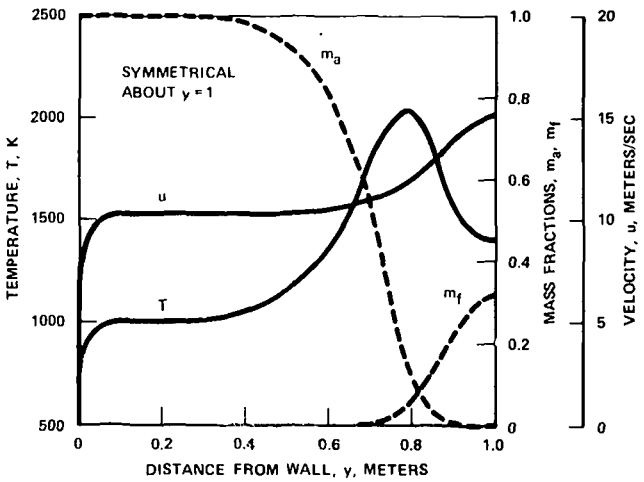

Fig. 2 Temperature, velocity, and mass fraction profiles for $x = 2$ m and the standard conditions (Table 2)

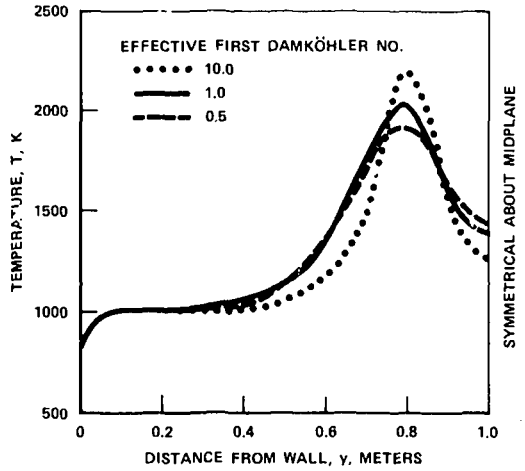

Fig. 3 Effect of C^* on temperature profile at otherwise standard conditions (Table 2) and $x = 2$m

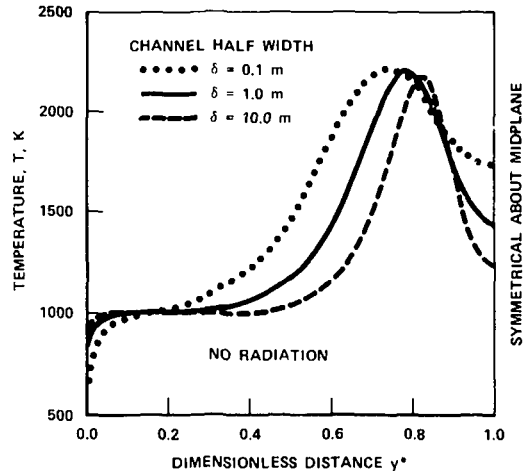

Fig. 4 (a) without radiation

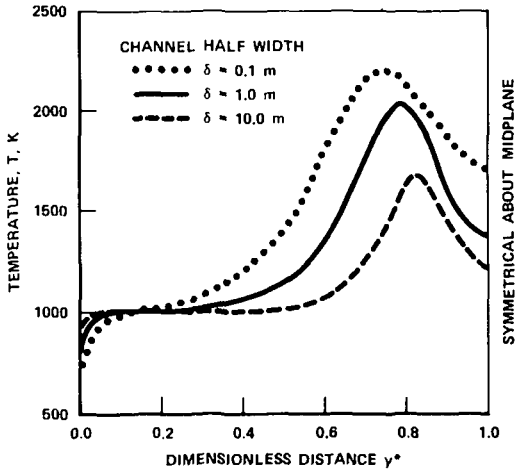

Fig. 4 (b) with radiation

Fig. 4 Effect of combustion chamber size δ on temperature profile at constant $x^* = x/\delta$

Table 3 Effect of preheat and recirculation upon axial flowfield conditions

Axial Distance x m	Max. Temp. T_{max} K	Vol. Avg. Temp. T_{vol} K	Fraction of Fuel Burned η	Fraction of Combustion Heat Removed β	Radiative Nusselt Number Nu_R	Convective Nusselt Number Nu_C
(a) No Recirculation $x_p = 0$						
(T_a^o = 500 K, T_{ad} = 2374 K)						
0.4	1666	800	0.165	0.000	4383	0
1.2	1814	929	0.235	0.026	4959	0
2.0	1799	995	0.276	0.053	4980	0
4.0	1796	1132	0.356	0.114	4741	1.1
10.0	1740	1309	0.530	0.242	3796	17
20.0	1604	1367	0.704	0.345	3028	65
(T_a^o = 1000 K, T_{ad} = 2541 K)						
0.4	1780	1155	0.194	0.012	2704	206
1.2	2045	1279	0.261	0.047	3940	129
2.0	2048	1316	0.292	0.085	4197	110
4.0	1987	1364	0.349	0.169	4336	93
10.0	1865	1425	0.481	0.345	3976	78
20.0	1693	1414	0.635	0.511	3308	82
(b) Recirculation $x_p = 0.2$						
(T_a^o = 500 K, T_{ad} = 2146 K)						
0.4	1414	734	0.137	0.000	2713	0.3
1.2	1613	861	0.203	0.004	3356	1.8
2.0	1618	720	0.239	0.036	3468	3.2
4.0	1619	1036	0.313	0.048	3472	6.8
10.0	1609	1220	0.481	0.174	3062	24.7
20.0	1531	1311	0.654	0.292	2689	68.0
(T_a^o = 1000 K, T_{ad} = 2368 K)						
0.4	1544	1098	0.174	0.019	2199	231
1.2	1823	1215	0.241	0.049	3186	146
2.0	1867	1260	0.274	0.079	3381	124
4.0	1852	1305	0.325	0.149	3518	105
10.0	1756	1354	0.453	0.303	3345	91
20.0	1630	1366	0.576	0.459	2975	92

channels (δ = 1 m and 10 m) have markedly lower peak temperatures because of the greater gaseous radiation transfer.

It should be remembered, of course, that the combustion was assumed to be soot free. A previous study [15] showed that when soot is considered the temperatures decrease at first with increasing δ, but after the soot becomes opaque, further increases destroy the effectiveness of the radiation, and the flame temperature rises. In gas radiation no such optimum in combustion chamber size is seen as long as the major bands are not overlapped. For this reason steam injection to control soot formation in large sized units appears attractive.

Preheat and Recirculation. Table 3 shows the axial variations of two temperatures, two fractions describing the extent to which combustion has occurred and how nonadiabatic it has been, and two-dimensionless wall heat fluxes. Maximum temperature T_{max} gives a qualitative indication of the production of nitric oxide. Volume average temperature likewise gives an indication of the potential for radiation transfer. The fraction η is the fuel burned divided by the initial fuel supplied and indicates the extent to which the combustion is complete. The quantity β is the heat transferred to the wall up to the axial station in question divided by the heat which has been released by combustion by that point. It indicates the degree to which the combustion has been nonadiabatic. The radiative and convective Nusselt numbers are the radiative and convective heat fluxes at the wall, respectively, made dimensionless by $(\kappa_w/\delta)(T_{vol} - T_w)$. For the stations in the table turbulent Reynolds number $R_t = \delta^+$ ranged between approximately 6000 and 10000.

The first observation that can be made is that peak temperatures pretty well track adiabatic flame temperature. However, the low-preheat, zero circulation case did have a peak temperature of 1814 K somewhat below the 1867 K value for the high-preheat case with recirculation, even though the adiabatic flame temperature of the former 2374 K was actually a little lower than that of the latter, 2368 K. Nevertheless, in the main peak temperature is lowered simply by lowering adiabatic flame temperature whether by dropping the preheat or by recirculating exhaust gas.

Recirculating exhaust gas while maintaining or raising the preheat appears advantageous for a number of other reasons. Of course, a high preheat presumably means a good recuperator with a lower stack temperature and better combustion efficiency. Beyond that factor is the higher radiation heat transfer obtained by recirculating and

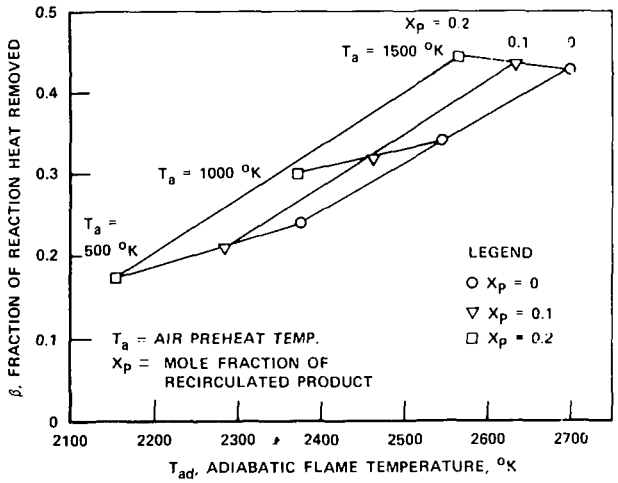

Fig. 5 Effect of preheat and recirculation upon fraction of heat removed and adiabatic flame temperature for x = 2 m

maintaining preheat. Also the combustion is more nonadiabatic with a higher fraction of the heat removed by radiation. Somewhat slower combustion is also seen to occur from comparison of the results of Table 3.

Fig. 5 summarizes and reinforces these observations. Preheat and recirculation are shown as parameters on the graph. They may be regarded as the independent variables. Depending upon these variables one gets a certain adiabatic flame temperature, and the peak temperature which goes with it, and a certain fraction of heat removed predominantly by radiation in the radiant section. For a fixed adiabatic flame temperature a much higher value of β can be obtained by using high recirculation and high preheat.

Summary and Conclusions

This paper has demonstrated that realistic nongray radiation transfer analysis can be coupled to an implicit numerical method for solution of the highly coupled nonlinear partial differential conservation equations without undue expenditure of computation time. The practical import of the results is that raising recirculation while maintaining or raising preheat appears preferable as a means of nitric oxide pollution control to merely lowering preheat. Not only is combustion efficiency presumably higher, but better radiation transfer is obtained in the radiant section.

References

1 Lockwood, F. C., and Naguib, A. S., "The Prediction of the Fluctuations in the Properties of Free, Round-Jet, Turbulent Diffusion Flames," *Combustion and Flame*, Vol. 24, 1975, pp. 109-124.

2 Spalding, D. B., "The Calculation of Convective Heat Transfer in Complex Flow Systems," *Heat Transfer 1974, Proceedings of the Fifth International Heat Transfer Conference*, Tokyo, Japan, 1974, Vol. VI, pp. 44-60.

3 Edwards, D. K., and Balakrishnan, A., "Thermal Radiation by Combustion Gases," *International Journal of Heat and Mass Transfer*, Vol. 16, 1973, pp. 25-40.

4 Edwards, D. K., and Balakrishnan, A., "Nongray Radiative Transfer in a Turbulent Gas Layer," *International Journal of Heat and Mass Transfer*, Vol. 16, 1973, pp. 1003-1015.

5 Edwards, D. K., and Balakrishnan, A., "Self Absorption of Radiation in Turbulent Molecular Gases," *Combustion and Flame*, Vol. 20, 1973, pp. 401-417.

6 Edwards, D. K., and Balakrishnan, A., "Radiative Cooling of a Turbulent Flame Front," JOURNAL OF HEAT TRANSFER., TRANS. ASME Series C, Vol. 95, 1973, pp. 433-438.

7 Van Driest, E. R., "On Turbulent Flow Near a Wall," *Journal of the Aeronautical Sciences*, Vol. 23, 1956, pp. 1007-1011.

8 Schlichting, H., *Boundary Layer Theory*, McGraw Hill, New York, Sixth ed., 1968, pp. 696-698.

9 Mei, J., and Squire, W., "A Simple Eddy Viscosity Model for Turbulent Pipe and Channel Flow," *AIAA Journal*, Vol. 10, 1972, pp. 350-352.

10 Wassel, A. T., "Nongray Radiative Transfer in a Turbulent Cylindrical Medium," PhD dissertation, UCLA School of Engineering, 1973.

11 Edwards, D. K., and Wassel, A. T., "Interpretation of a Turbulent Radiating Gas as a Low-Prandtl-Number Fluid," *Letters in Heat and Mass Transfer*, Vol. 1, 1974, pp. 19-24.

12 Patankar, S. V., and Spalding, D. B., *Heat and Mass Transfer in Boundary Layers*, Intertext, London, Second ed., 1970.

13 James, R. K., "Non-Gray Gas Radiation Heat Transfer in a Planar Combustion Chamber," MS thesis, UCLA School of Engineering, 1976.

14 Newman, J. S., *Electrochemical Systems*, Prentice Hall, Englewood Cliffs, N. J., 1973, pp. 414-425.

15 Balakrishnan, A., and Edwards, D. K., "Radiative Flame Cooling for Reduction of Nitric Oxide Emissions," JOURNAL OF HEAT TRANSFER, TRANS. ASME Series C, Vol. 76, 1974, pp. 37-42.

R. R. Gilpin
Assoc. Professor.
University of Alberta

R. B. Robertson
Canadian Forces, Maritime Command.

B. Singh
Graduate Student.
University of Alberta,
Alberta, Canada

Radiative Heating in Ice

The energy fluxes that exist in an ice sheet exposed to a collimated beam of radiant energy were examined. A theoretical model was used which includes the effects of anisotropic scattering as well as the spectral dependence of the absorption coefficient of ice and of the incident radiation beam. Laboratory measurements were also made which generally confirm the predictions of the model. The results calculated from the model are primarily intended for use in analyzing two particular problems involving radiative transfer in ice. These are: (a) the assessment of the feasibility of using radiant energy sources as a means of removing ice from structures, and (b) the prediction of temperatures and internal melting in ice covers on lakes and rivers due to the absorption of solar radiation.

Introduction

Radiative heating of ice plays an important role in the break-up of lakes and rivers. Solar energy absorbed in the ice sheet, first goes to raising the ice temperature to the freezing point. Thereafter, additional energy absorbed in the ice produces internal melting. This melting occurs primarily at grain boundaries and results in the weakening and eventual disintegration of the ice structure [1].[1] The use of thermal radiation sources has also been proposed as a means of artificially removing ice sheets from airport runways and other structures subject to atmospheric icing.

To predict the temperatures and the extent to which melting will occur in an ice sheet it is necessary to understand the behavior of the radiation in the ice. In particular it is necessary to know the distribution with depth of the energy absorbed in the ice sheet.

Williams [2] has used a grey absorption model to estimate the heating that would be produced in an ice sheet. However, the absorption coefficient of ice has a very strong spectral dependence in the visible and near infrared wavelength range which makes this model inappropriate. A normal ice sheet may also have a large scattering coefficient. This scattering may be produced by air bubbles that form in the ice during the freezing process. Also the ice covers on lakes and rivers are often formed by the freezing of wet snow. This results in a "white" ice having a very high scattering coefficient. It is therefore necessary to analyze radiative energy transfer in a scattering medium with a strong spectral variation of absorption coefficient.

A number of methods are available for analyzing the behavior of radiant energy in a scattering-absorbing medium. Dunkle and Bevans [3] did an approximate analysis of penetration of solar radiation through a snow cover. They used a two flux model introduced first by Schuster [4] and subsequently extended by Duntley [5] and Hulbert [6]. Their model ignored the spectral nature of the absorption coefficient of ice and only considered isotropic scattering. Chu, Churchill, and co-workers [7, 8] have presented approximate methods for engineering applications which take account of the effects of multiple scattering and the spectral nature of the absorption coefficient in studying the transmission of electromagnetic radiation through dense dispersions of particles. Viskanta and Toor [9] have formulated the problem to analyze radiant energy transfer in water with scattering. Their results, however, are restricted to cases in which scattering is small.

In this paper the two flux model was used with some extensions. In particular, the effects of a collimated incident beam, of anisotropic scattering and of the spectral variation of the absorption coefficient and the radiation source are included. Some measurements were also made with which the predictions of the model could be compared.

Theory

In the model used the ice medium was assumed to be a homogeneous and one-dimensional sheet. The basic integro-differential equation of radiative transfer in a one-dimensional, scattering, nonemitting medium is [10].

$$\mu \frac{dI(\nu, \vec{r}, \vec{\Omega})}{dx} = -k_t I(\nu, \vec{r}, \vec{\Omega}) + \frac{k_s}{4\pi} \int_{\Omega'} I(\nu, \vec{r}, \vec{\Omega}') p(\theta) d\Omega' \quad (1)$$

The first term on the right-hand side of equation (1) is the rate of loss from a beam travelling in the direction $\vec{\Omega}$ and the second term is the gain in intensity in the $\vec{\Omega}$ direction due to scattering from all other directions $\vec{\Omega}'$. The phase function $p(\theta)$ where θ is the angle between $\vec{\Omega}'$ and $\vec{\Omega}$ is the probability of scattering from the direction $\vec{\Omega}'$ into the direction $\vec{\Omega}$. In the model used the intensity, I, is assumed to be composed of three components. These are a diffuse flux isotropically distributed in the positive x-direction, $q^+(\nu, x)$, a diffuse flux isotropic

[1] Numbers in brackets designate References at end of paper.

Contributed by the Heat Transfer Division for publication in the JOURNAL OF HEAT TRANSFER. Manuscript received by the Heat Transfer Division October 27, 1976.

in the negative x-direction, $q^-(\nu, x)$, and a collimated flux, $q_c(\nu,x)$, confined to a small solid angle about the positive x axis. Equation (1) for the collimated beam reduces to

$$\frac{dq_c(\nu, x)}{dx} = -k_t q_c(\nu, x) \tag{2}$$

Losses occur from the collimated beam due to scattering into the diffuse directions and due to absorption by the ice. Gains in the collimated beam due to scattering from the diffuse fluxes are negligible because of the small solid angle of the collimated beam. There is a strong component of forward scattering from the collimated beam that is experimentally indistinguishable from the original beam because it stays within the cone of that beam. The scattering coefficients used throughout the paper represent the fraction of light scattered out of the cone of the incident beam. Light scattered less than this amount then would be considered part of the unscattered collimated beam.

Using a Legandre polynomial expansion of the phase function, $p(\mu) = \Sigma a_i P_i(\mu)$, and the fact that the fluxes are azimuthally independent, the integral over azimuth in the scattering term in equation (1) can be carried out [10]. Further, if equation (1) is integrated separately over the positive and negative x hemispheres the two equations for the diffuse fluxes result. These are

$$\frac{dq^+(\nu, x)}{dx} = -2(k_t - k_s f')q^+(\nu, x) + 2k_s b' q^-(\nu, x) + k_s f q_c(\nu, x) \tag{3}$$

and

$$-\frac{dq^-(\nu, x)}{dx} = -2(k_t - k_s f')q^-(\nu, x) + 2k_s b' q^+(\nu, x) + k_s b q_c(\nu, x) \tag{4}$$

where

$$f' = \frac{1}{2}\sum_i a_i \left[\int_0^1 P_i d\mu\right]^2; \qquad b' = 1 - f'$$

and

$$f = \frac{1}{2}\sum_i a_i \int_0^1 P_i d\mu; \qquad b = 1 - f$$

In equations (3) and (4) the components of forward, f, and back, b, scatter are different for the diffuse and collimated beams. Analyzing the terms in the Legandre series suggests that f' is actually $1/2(f + 1/2)$. Similarly $b' = 1/2(b + 1/2)$. The use of the Legandre series, thus provides a convenient analytic relationship between f' and f and b' and b that is independent of the experimentally measured phase function. A numerical integration over the measured phase function then need only be done to find one of these four parameters, for example f, and the others f', b and b' can be calculated from it.

It will be noted that a factor of two appears in equations (3) and (4) in front of the scattering and absorption coefficients for the diffuse fluxes. This factor which results from the integration of equation (1) over each hemisphere, represents the fact that the rays of the diffuse flux experience an average path length that is twice as long as that experienced by the collimated beam when it traverses an incremental depth layer, dx.

The boundary conditions required at the top surface of the ice are

$$q_c(\nu, 0) = (1 - r_s)q_{ic}(\nu) \tag{5}$$

and

$$q^+(\nu, 0) = r_s' q^-(\nu, 0) \tag{6}$$

where q_{ic} is the incident collimated flux. The surface reflectivities, r_s and r_s', for collimated and diffuse radiation were obtained from the Fresnel relationships [10].

Reflection at the bottom of the ice sheet would theoretically result in an upward travelling collimated flux. However, since the surface reflectivity for normally incident radiation is only 0.04, this flux is very small. As an approximation this upward travelling collimated flux was included in the upward travelling diffuse flux at the bottom surface of the ice. That is

$$q^-(\nu, d) = r_s' q^+(\nu, d) + r_s q_c(\nu, d) \tag{7}$$

Some calculations were done where a separate upward collimated flux was included; however, these calculations produced results which were indistinguishable from those of the model outline here.

At a given wavelength equations (2)–(4) along with the boundary conditions (5)–(7) can be solved explicitly for the three fluxes as a function of depth in the ice. From these results the amounts of energy transmitted, $T(\nu)$, and reflected $R(\nu)$, by the ice sheet can immediately be calculated;

$$T(\nu) = (1 - r_s')q^+(\nu, d) + (1 - r_s)q_c(\nu, d) \tag{8}$$

and

$$R(\nu) = (1 - r_s')q^-(\nu, 0) + r_s q_{ic}(\nu) \tag{9}$$

The rate of internal heating, Q, at any depth in the ice is given by the divergence of the net downward flux. That is

$$Q(\nu, x) = -\frac{d}{dx}(q^+(\nu, x) - q^-(\nu, x) + q_c(\nu, x))$$

Substituting equations (2)–(4) into this expression gives

$$Q(\nu, x) = k_a q_c(\nu, x) + 2k_a(q^+(\nu, x) + q^-(\nu, x)) \tag{10}$$

The equations derived to this point apply only at one wavelength since both the absorption coefficient, k_a, and the incident flux, q_{ic}, are functions of wavelength. Note that it will be assumed that the scattering coefficient, k_s, is not a function of wavelength. Measurements of k_s over the visible and near infrared spectrum show very little wavelength dependence [11]. The spectral dependence of the absorption coefficient of ice is shown in Fig. 1. The values used were based on the averages of the measurements made by a number of investigators [12, 13]. There was general agreement among the various

Nomenclature

b = backscattering fraction for collimated beam
b' = backscattering fraction for diffuse beam
d = thickness of ice sheet
f = forward scattering fraction for collimated beam
f' = forward scattering fraction for diffuse beam
k_a = absorption coefficient
k_s = scattering coefficient
k_t = extinction coefficient ($k_s + k_a$)
$p(\theta)$ = phase function for scattering
q_c = collimated flux
q_{ic} = incident collimated flux
q^+ = forward diffuse flux
q^- = backward diffuse flux
r_s = surface reflection coefficient
r_s' = surface reflection coefficient for diffuse beam
r = position vector
t = time
x = depth into ice sheet
C = heat capacity of ice
I = radiation intensity
P_i = Legandre polynomial
Q = Internal heating produced by radiation absorption
Q' = Normalized internal heating
R = Reflected energy
R' = Normalized reflected energy
T = Transmitted energy
T' = Normalized transmitted energy
μ = direction cosine ($\cos\theta$)
ν = radiation frequency
ρ = ice density
Ω = solid angle
$\vec{\Omega}$ = direction vector

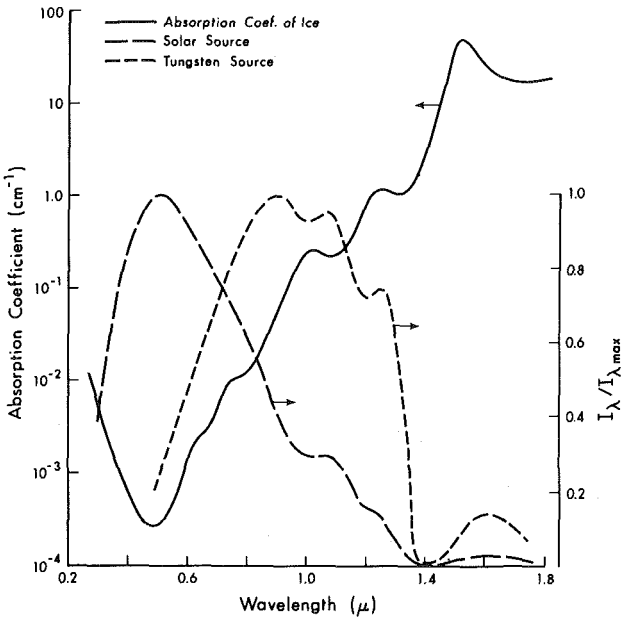

Fig. 1 Spectral dependence of the absorption coefficient of ice and of the two radiation sources used

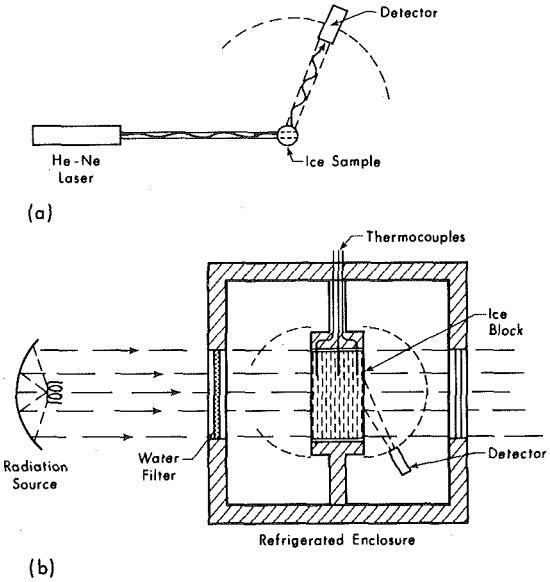

Fig. 2 Experimental apparatus: (*a*) for making monochromatic scattering measurements; and (*b*) for measuring energy absorption, transmission and reflection for an ice block exposed to a collimated beam of radiant energy

measurements, however, in some wavelength ranges discrepancies of as much as a factor of five exist. Also shown in Fig. 1 are the two incident spectra which were used with the model. The simulated solar spectrum was obtained by taking a 5870 K blackbody spectrum and subtracting off the energy absorbed in a 2-mm thick water layer. Similarly the tungsten source was a 3000 K blackbody spectrum passed through a 2-mm water filter. The purpose of introducing the 2-mm water filter was: (*a*) to make the spectra similar to those used in the laboratory tests, and (*b*) to make the simulated solar spectrum more like the real solar spectrum received at the ground surface. Some runs were made with a measured solar spectrum, however differences in the absorbed energy only occurred in the top few millimeters of the ice sheet. The fractions of these incident spectra that are transmitted and reflected are obtained by integrating over the wavelength spectrum;

$$T' = \int T(\nu)d\nu / \int q_{ic}(\nu)d\nu \tag{11}$$

and

$$R' = \int R(\nu)d\nu / \int q_{ic}(\nu)d\nu \tag{12}$$

Similarly the rate of internal heating is written

$$Q'(x) = \int Q(\nu, x)d\nu / \int q_{ic}(\nu)d\nu \tag{13}$$

The function $Q'(x)$ has the units of reciprocal distance and is the fraction of the incident flux that is absorbed per unit depth in the ice at a given depth, x.

Monochromatic Scattering Measurements

To use the model just developed knowledge of the scattering coefficients and the angular distribution of scattered energy must be obtained. Some information exists of scattering coefficients for typical ice sheets; however, no information could be found on the angular distribution of scattering for ice. Measurements were therefore made using a technique similar to that described by Duntley [11] for measuring the scattering function for water. The apparatus used in these tests is shown in Fig. 2(*a*). The He–Ne laser light at 0.63 μ has negligible absorption in the ice sample so that only scattering was important. The ice samples used were cylinders approximately 1 cm in diameter. The use of a cylindrical sample minimized the problems of calculating the detector solid angles and of refraction of the scattered light. The detector could be scanned through a complete circle except for approximately 10 deg either side of the incoming laser beam.

As a check of the accuracy of the measurement an integration of the scattered energy over all angles was compared with the energy in the incident laser beam. The typical discrepancy was in the range of 10 to 15 percent which was considered acceptable for this type of measurement.

The phase function calculated from these measurements is shown in Fig. 3. The strong component of forward scattering is apparent in the figure. Values calculated for the scattering parameters in the model were

$$f = 0.8; \qquad f' = 0.65; \qquad b = 0.2; \qquad b' = 0.35$$

Measurements Using Radiant Energy Sources

In addition to the monochromatic scattering measurements just

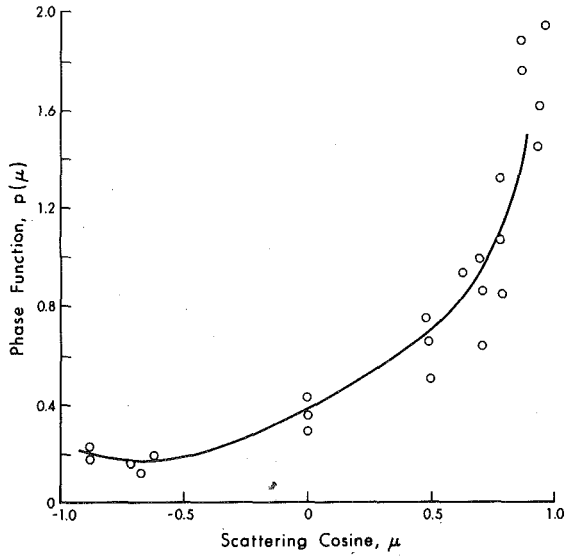

Fig. 3 The measured phase function for scattering from an ice sample

described, measurements were also made of the radiant energy fluxes that result when an ice block is exposed to a light source with a spectrum of wavelengths. Fig. 2(*b*) shows schematically the apparatus used in these studies. The two light sources used were a 600-W tungsten filament lamp and a 7.5 kW carbon arc "Solar Simulator." Measurements made with a monochromator showed that the tungsten lamp produced a 3000 K blackbody radiation and the solar simulator was close to a black body source at 5780 K at wavelengths between 0.3 and 2.0 μ. Outside this wavelength range absorption due to quartz windows and atmospheric water vapor was significant. The 2-mm thick water filter used with each source eliminated the variable and unknown nature of the spectrum at short and long wavelengths. The resulting spectra were incident on an ice block 15- × 15- × 12-cm thick. The ice block had three thermocouples frozen into it. To minimize direct absorption of radiation by the thermocouples they were enclosed in polished stainless steel tubes. The sides of the ice block were also surrounded by polished stainless steel sheets to simulate as nearly as possible an infinite ice sheet. Clear ice blocks were made by slowly freezing distilled, deaerated water. To show the effects of scattering two ice blocks were produced by rapidly freezing water that had previously been aerated at 0°C. The later freezing method produced a white ice with scattering coefficients as measured with the He–Ne Laser of 0.7–1.2 cm^{-1}.

In an experiment the ice block would be mounted in a controlled temperature cold chamber. The block would then be allowed to come to equilibrium with the chamber temperature, usually at −5 to −10°C. The radiation source was then turned on. A small, <0.1°C, rise in indicated temperature would occur immediately. This was assumed to be due to the direct absorption of energy by the thermocouples. A more gradual linear rise of temperatures was then observed. The rate of temperature rise during this period was used as a measure of the local rate of heating. That is

$$Q = \rho C dT/dt \tag{14}$$

At longer times as temperature differences developed in the ice the rates of temperature rise again change. These changes were presumably due to the conduction of heat between various layers of the ice.

An estimation can be made of the time at which heat conduction effects would be expected to become significant. That is, for a conducting slab exposed to a sudden change in conditions conduction would be expected to have a major effect on temperatures for times $t \geq L^2/\alpha$ where L is the distance over which significant temperature variations occur and α is the thermal diffusivity of ice (1.24 mm^2/s). For the temperature measurement point nearest the radiation source, significant differences in heating rate occur over distances of 10 mm; therefore, the time during which measurements of the heating rate can be taken is less than about 80 s. Fortunately, the heating rate is high in this region and results could be obtained in 10–20 s. At the center of the ice sample L is of the order of 60 mm and t is approximately 50 min. That is, a much longer time span is available in order to obtain the measurement. The time constant for heat conduction to develop to the stainless steel reflector around the ice is also of the order of 50 min.

As indicated in equation (14) the local rate of heating was obtained from the rate of change of the local temperature. Calculations made on the basis of a rate of change of a measured parameter introduce inevitable uncertainties into the results. To increase the accuracy of the results and to determine their repeatability, each data point that will be presented represents the average of at least three separate experimental runs.

Measurements of the incident energy, q_{ic}, the transmitted energy, T, and the reflected energy, R, were also made. The transmitted and reflected energies for the high scattering ice blocks were obtained by taking measurements at a number of angular positions over the front and back of the ice block and integrating the measurements over the appropriate hemispheres. The angle range over which measurements of reflected energy could be made was restricted if the detector was not to interfere with the incident beam. The general result of these measurements was, however, that the transmitted and reflected diffuse fluxes were very nearly isotropically distributed over their respective hemispheres and therefore good estimates of the total fluxes could be made with measurements made only at a limited number of angular positions. The results of these measurements will be shown along with the theoretical predictions in the next section.

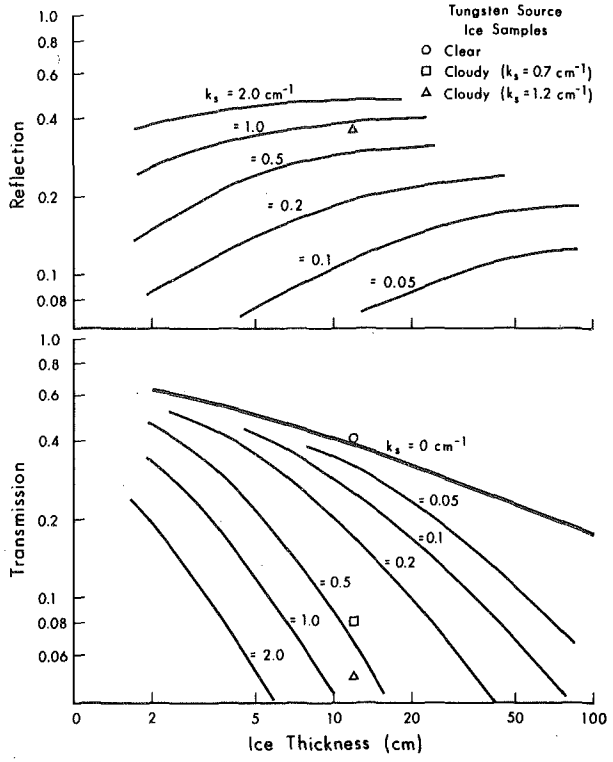

Fig. 4 Reflection and transmission for an ice sheet exposed to a tungsten source

One area of concern was the fact that surface roughness or, in the case of ice, frost on the ice surface can have a large and relatively unpredictable effect on surface reflectivities. To overcome this difficulty the ice surfaces were smoothed with a hot plate prior to the experiments. Measurements with a laser beam on the clear ice samples indicated that surface reflectivities were very close to the values given by the Fresnel relationships which were used in the theory.

Results

Theoretical and experimental results for the fractions of the incident energy that are transmitted and reflected from an ice sheet for a tungsten and a simulated solar light source are shown in Figs. 4 and 5. The fraction of energy reflected or "albedo" of the ice can be interpreted as a measure of the total energy absorbed in the ice and its substrate. The substrate could be water for a lake or river or for atmospheric icing it could be the structure on which the ice formed. Comparison of the two reflectivity figures shows that the fraction of the radiation from the tungsten source that is absorbed is greater than that for the solar source for all scattering coefficients and ice sheet thicknesses. Although the total fraction of energy delivered to the ice and substrate is greater for the tungsten source a comparison of the transmission figures shows that the fraction of the energy delivered to the substrate is greater for the solar source. These qualitative trends are due to the fact that the absorption coefficients of ice at the tungsten radiation wavelengths are much larger than those for wavelengths at which the solar simulator radiation is emitted.

Experimental results are also shown on Figs. 4 and 5 for a 12-cm thickness of clear ice and for two samples of cloudy ice $k_s = 0.7$ and 1.2 cm^{-1}. These results are in rough agreement with the theoretical predictions. In particular, they would appear to verify that the theory

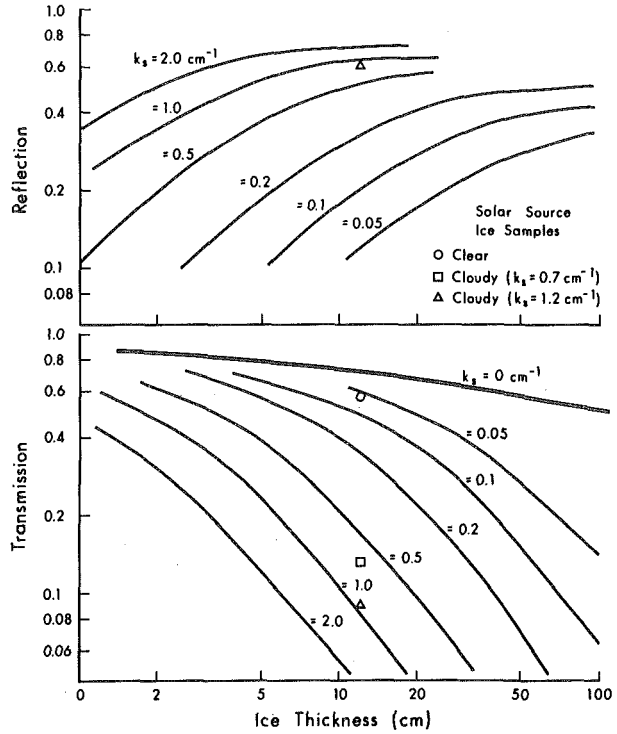

Fig. 5 Reflection and transmission for an ice sheet exposed to a solar radiation source

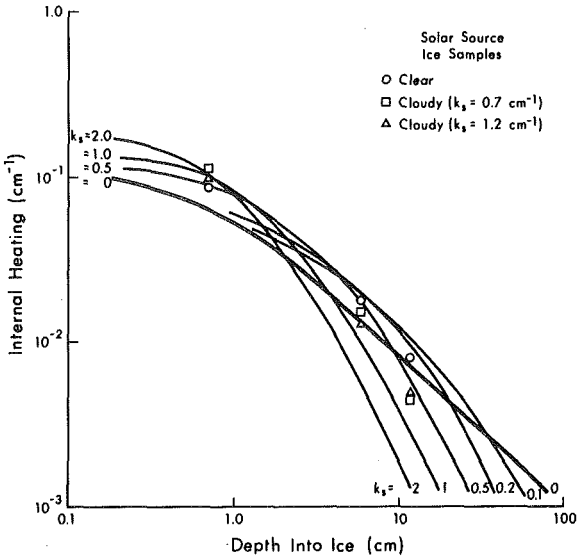

Fig. 7 The distribution with depth of the internal heating produced in an ice sheet by a solar radiation source

gives approximately the right quantitative predictions for the very high scattering coefficients that can occur in ice. The poorest agreement between theory and experiment occurs for the case of clear ice subjected to solar radiation. The measured transmission for this case is about 20 percent less than predicted. This discrepancy could have been caused by the fact that the "clear" ice blocks could not be made completely free from scattering centers. As indicated by the theoretical curves a small amount of scattering has a large effect on the transmission of the solar source.

Figs. 6 and 7 show the internal heat generation, Q', produced by the absorption of energy from the two radiation sources. The figures show Q' as a function of depth for a very thick ice sheet. Calculations were also made for thinner ice sheets, however, the only differences that occurred were within about one centimeter of the bottom of the ice sheet. This would indicate that the surface reflectivity of the interface at the bottom of the ice does not have a large effect on the distribution of heating produced in the ice.

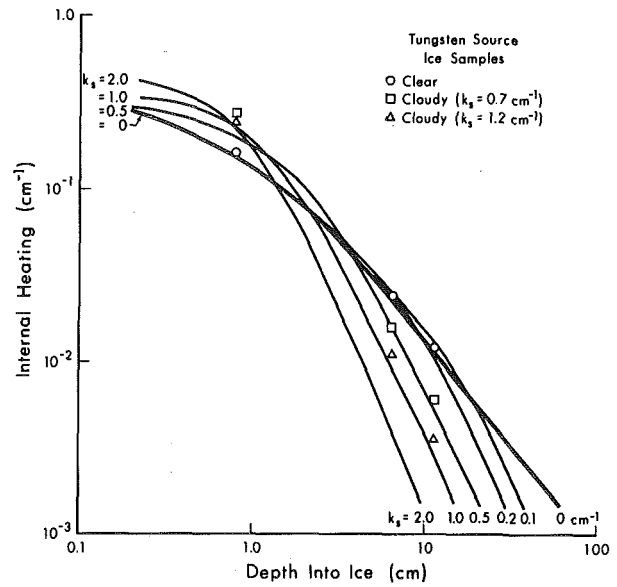

Fig. 6 The distribution with depth of the internal heating produced in an ice sheet by a tungsten source

First examining the curves for clear ice. The tungsten source produces substantially greater internal heating than the solar source at shallow ice depths. The heating produced by the two sources becomes equal only at a depth of 60 cm. It will be noted that for depths of 1 cm and more that log Q' is close to a linear function of log x implying a power law relationship, $Q' = Cx^{\alpha}$, as has previously been derived for radiant heating of water [14]. This is a substantially different functional dependence than the exponential behavior normally associated with the Bouquer-Lambert law. The difference is due to the spectral dependencies of the absorption coefficient and the incident light source.

The long and short wavelengths are absorbed mainly in the depths of ice less than 1 cm. It is therefore the depth range 0 to 1 cm that is affected most by using a simulated solar spectrum as opposed to an actual solar spectrum. It is also the depth range that is affected most by the air mass that the solar light passes through before reaching the ice.

The most interesting result is the effect of scattering on internal heat in the ice. The effect of scattering in the ice, as shown in Figs. 6 and 7, is to increase the heating that occurs near the ice surface and to decrease the heating further down in the ice. This behavior presumably results from the two opposing effects that scattering has. First the scattering tends to increase the path length of radiation that is in the ice and second the scattering tends to reflect more of the radiation back out of the ice. Because of these opposing effects of scattering its net effect on the internal heating in the ice is only important at very large ice depths. For example, ice with a scattering coefficient of 0.5 cm^{-1} subjected to solar radiation experiences an order of magnitude decrease in internal heating between the surface and a depth of 10 cm. On the other hand assuming an exponential decay one might have predicted a e^{-5} decrease in the heating rate. Also of importance in determining the effects of scattering is the predominance of forward scattering. Radiation that is forward scattered experiences a longer path length in the ice before it can escape than does the backward scattered flux. It is, therefore, not surprising that increasing the fraction of forward scattering increases the internal heating and

decreases the albedo of the ice. Calculations, not included here, verified this trend.

Measurements made of internal heating showed the same trends as the predictions. In particular by comparing the results for the clear ice with those for the cloudy ice it can be seen that the scattering in the ice does in agreement with the theory, increase internal heating near the ice surface and decrease heating at larger depths. The actual measured values, however, tend to be higher than predicted particularly for the solar radiation source. Each of the data points in these figures represents the average of three or more experimental runs. For any one data point the range between the highest and lowest value obtained was of the order of ±15 percent. The difference between the theory and experiment is somewhat greater than this range in the experimental results. The differences, however, probably do not reflect inaccuracies in the theory but again are due to uncertainties in the properties of ice and of the incident radiation spectra. It will be noted that the amount of energy absorbed is only a very small fraction of the total incident energy. Measured at the midpoint of the ice block, 6-cm depth, only one percent of the incident energy is being absorbed per centimeter of ice depth.

Conclusions

The predictions of the two flux radiation model were found to agree within 20–30 percent with the measured values for reflected and transmitted energies as well as for the internal heating in an ice sheet. By repeating all the experimental measurements at least three or more times the repeatability of the measurements was found to be of the order of ±15 percent. This level of agreement between theory and experiment and observed degree of repeatability would appear at first sight to be relatively rough. It must be noted, however, that the phenomena under study do vary by two or more orders of magnitude over the range of parameters in the experiments and thus inaccuracies of the order experienced are relatively insignificant compared to the range in the values measured. The inaccuracies in these radiation measurements can be attributed mainly to the statistical nature of the scattering phenomenon and uncertainties in the properties of ice and of the spectra of the radiation sources. Fortunately, for most practical calculations the accuracy obtained is probably adequate.

The model does successfully show the differences in the radiative heating produced by the tungsten as opposed to the solar radiation source. The tungsten source produces the larger heating near the ice surface. The solar source on the other hand has the greater penetration into the ice sheet and through to its substrate. This behavior is not surprising considering the fact, as seen in Fig. 1, that the wavelength at which the maximum solar intensity occurs coincides almost exactly with the minimum in the absorption coefficient of ice. Alternatively, the tungsten source has a much larger portion of its radiation in the near infrared where the absorption coefficient of ice is larger. The most interesting results concern the effects of scattering on the internal heating generated in the ice. It was found that scattering in the ice in spite of the fact that it causes more of the radiation to be reflected out of the ice, can actually cause an increase in radiative heating in an ice slab at least near the ice surface. This increase in heating occurs because scattering lengthens the path length that the radiation experiences in traversing the ice slab. In effect a radiation "trapping" due to scattering is occurring.

These results provide some guidance in the choice of a radiation source to use in deicing applications. A radiation source could be used to remove ice either by melting its bond to the substrate on which it formed or by producing internal melting in the ice itself. If the object is to destroy the bond between the ice and its substrate the solar source would be best because of its greater penetration. Alternatively, if the object is to weaken the ice by producing internal melting a tungsten source would probably be more efficient. One concern about using a radiation source for deicing applications is the effect that scattering in the ice would have on the transmission of the radiation. Ice resulting from atmospheric icing would normally have a fairly high scattering coefficient. The results in this paper show that even a small amount of scattering can greatly reduce the transmission of solar light and thus decrease the effectiveness of a solar source in melting the substrate bond. On the other hand scattering may actually be helpful when a tungsten source is used to produce internal melting in that the scattering enhances internal heating for shallow ice depths.

For ice covers on lakes and rivers temperature profiles have been observed to be considerably altered by the effects of solar heating [15]. The predictions in this paper show, however, that only a small fraction of the incident energy goes to produce internal heating in the ice at depths from 10 to 100 cm. The large effects of this internal heating on the temperatures presumably occur because the heat absorbed in the center of an ice sheet is only very slowly conducted out. To quantify these assumptions calculations of the temperature profiles and of the internal melting due to solar radiation could now be made using the predicted internal heating as a function of depth in the ice along with the heat conduction equation. In this regard some modification of the heat generation function is required to account for a non-normal incident flux.

Acknowledgment

This work was supported by the National Research Council of Canada.

References

1 Knight, C. A., *The Freezing of Supercooled Liquids,* Van Nostrand, Princeton, 1967, pp. 125–126.

2 Williams, G. P., "Water Temperatures During the Melting of Lake Ice," *Water Resources Research,* Vol. 5, No. 5, 1969, pp. 1134–1138.

3 Dunkle, R. V., and Bevans, J. T., "An Approximate Analysis of the Solar Reflectance and Transmittance of a Snow Cover," *Journal of Meteorology,* Vol. 13, 1956, pp. 212–216.

4 Schuster, A., *Astrophys. J.,* Vol. 21, No. 5, 1905.

5 Duntley, S. Q., "The Optical Properties of Diffusing Materials," *J. of Op. Soc. of Am.,* Vol. 32, 1942, pp. 61–70.

6 Hulburt, E. O., "Propagation of Radiation in a Scattering and Absorbing Medium," *J. of Op. Soc. of Am.,* Vol. 33, 1943, pp. 42–45.

7 Chin, J. H., and Churchill, S. W., "Anisotropic, Multiply Scattered Radiation From an Arbitrary, Cylindrical Source in an Infinite Slab," JOURNAL OF HEAT TRANSFER, TRANS. ASME, Series C, May 1965, pp. 167–172.

8 Evans, L. B., Chu, C. M., and Churchail, S. W., "The Effect of Anisotropic Scattering on Radiant Transport," JOURNAL OF HEAT TRANSFER, TRANS. ASME, Series C, Aug., 1965, pp. 381–387.

9 Viskanta, R., and Toor, J. S., "Effect of Multiple Scattering on Radiant Energy Transfer in Waters," *Journal of Geophysical Research,* Vol. 78, 1973, pp. 3538–3551.

10 Hottel, H. C., and Sarafim, A. F., *Radiative Transfer,* McGraw-Hill, New York, Chapters 4 and 13, 1967.

11 Duntley, S. Q., "Light in the Sea," *J. of Op. Soc. of Am.,* Vol. 53, 1963, pp. 214–233.

12 Goodrich, L. E., "Review of Radiation Absorption Coefficients for Clear Ice in the Spectral Region 0.3 to 3 Microns," National Research Council of Canada, NRCC 11761, 1970.

13 Irvine, W. M., and Pollack, J. B., "Infra Red Optical Properties of Water and Ice Spheres," *ICARUS 8,* 1968, pp. 324–360.

14 Gilpin, R. R., "Heat Transfer in a Horizontal Water Layer With Radiative Heating," *Trans. CSME,* Vol. 1, No. 4, 1972, pp. 213–218.

15 Lazier, S. S., and Metge, M., "Temperature Gradients in a Lake Ice Cover," IAHR Ice Symposium, Reykjovik, Paper 2.3, 1970.

M. Epstein,
A. Yim,[1]
F. B. Cheung

Argonne National Laboratory,
Reactor Analysis and Safety Division,
Argonne, Ill.

Freezing-Controlled Penetration of a Saturated Liquid Into a Cold Tube

The penetration of a saturated liquid (a liquid at its freezing temperature) into a tube that is initially empty and maintained at a temperature below the freezing temperature of the liquid is treated theoretically and experimentally. A convenient approximate method is introduced which involves postulating a reasonable functional form for the instantaneous shape of the frozen layer along the tube wall. Graphical velocity-time and penetration distance-time curves are presented displaying the principal effects of a single dimensionless parameter. In the limit of negligible liquid inertia, shown to be relevant to high Prandtl number materials, a closed-form expression for the liquid penetration length is obtained. The expression compares well with the experimental results.

1 Introduction

A number of researchers have reported experimental and analytical studies of the freezing of a flowing liquid in a cold tube. Zerkle and Sunderland [1][2] presented experimental results on liquid solidification in the thermal entrance region of a laminar tube flow under steady-state conditions. They calculated the steady-state shape of the frozen layer (or crust) and the freezing section pressure drop by recognizing that the problem can be treated as a Graetz type. Mulligan and Jones [2] and Depew and Zenter [3] also conducted experimental investigations of solidification in steady thermal entrance region flow. The determination of the conditions that will lead to a complete freeze blockage in such a flow was considered by DesRuisseaux and Zerkle [4].

Several workers have studied the transient growth of the frozen layer for the case where a fully developed tube flow is suddenly disturbed by the introduction of a uniform and steady subfreezing temperature along a certain length of the tube wall. Ozisik and Mulligan [5] and Bilenas and Jiji [6] presented solutions by assuming that the liquid mass flow rate is independent of time. Chun, et al. [7] published an analytical and experimental study of transient flow in a cylindrical freezing section. The time required for complete occlusion of the tube was measured. Martinez and Beaubouef [8] assumed the pressure drop in the freezing section to be a linear function of the liquid flow (as would occur in systems equipped with a linear pump) and obtained detailed numerical solutions which describe the conditions leading to complete blockage of the tube flow.

A closely related problem of importance to fast nuclear reactor safety analysis is the transient freezing of a liquid as it penetrates into a long, initially empty, cold channel or tube [9]. This problem differs from those mentioned in the foregoing in that the freezing length increases with time. Cheung and Baker [10] conducted a series of tests in which various liquids were allowed to flow under gravity into long copper tubes cooled by liquid nitrogen or by a dry ice-acetone bath. Different constant driving heads in the liquid reservoir were used, and the penetration distances were measured. Recently, Madejski [11] obtained a simple solution to the penetration and freezing of a liquid at its fusion temperature in a cold channel. His analysis is based on the assumption that the pressure drop over the instantaneous freezing length is the same as in channels of constant cross section.

The purpose of this work is to provide approximate predictions of the penetration of a saturated liquid (a liquid at its freezing temperature) into a cold tube before solidification is complete. The tube is initially empty and maintained at a constant subfreezing temperature below that of the liquid. A potentially useful closed-form expression for the penetration length is obtained in the extreme of negligible liquid inertia. This expression gives reasonable agreement with penetration lengths obtained experimentally.

2 Physical Model and Method of Solution

In keeping with our objectives, we consider the transient flow and freezing system shown in Fig. 1 (a schematic diagram of the apparatus used in reference [10] and in this study). The reservoir (or tank) contains a liquid at its freezing temperature T_f (saturated liquid) having density ρ and kinematic viscosity ν. At time $t = 0$, the liquid

[1] Based in part on a dissertation to be submitted to the faculty of Northwestern University by A. Yim in partial fulfillment of the degree of Master of Science.

[2] Numbers in brackets designate References at end of paper.

Contributed by the Heat Transfer Division for publication in the JOURNAL OF HEAT TRANSFER. Manuscript received by the Heat Transfer Division October 8, 1976.

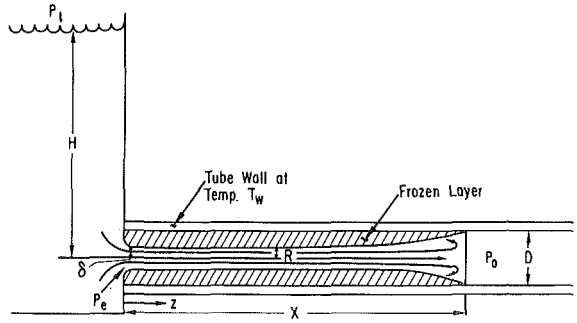

Fig. 1 Schematic of physical configuration and instantaneous frozen layer profile, indicating nomenclature

is allowed to drain out at the bottom of the tank and enter a cold tube at temperature $T_w (T_w < T_f)$. The problem is formulated by asking what the flow penetration length $X(t)$ is at the moment solidification is complete in the tube inlet region. The tank is sufficiently large so that the liquid level is maintained at a constant height H above the outlet during the penetration. In addition, the liquid flow-freezing process is subject to the following set of simplifying assumptions.

(A1) It is assumed that most of the liquid penetration occurs under turbulent flow conditions; i.e., the liquid flow is initially highly turbulent. Moreover, the growing solid-liquid interface is smooth and the turbulent friction factor is given by the Blasius formula. A discussion of the expected accuracy of this approximation is postponed to Section 6.

(A2) The temperature of the liquid-solid interface is constant and equal to the liquid freezing temperature. The wall temperature T_w is sufficiently below the liquid fusion temperature so that the effect of local supercoolings is negligible.

(A3) All physical properties are considered constant, and the densities of liquid and solid deposit are taken to be the same.

(A4) The pressure loss in the entrance region of the tube can be neglected. This implies: (i) the entrance from the reservoir to the tube is well-rounded, (ii) the loss due to the contraction in the tube cross section in the entrance region of the freezing zone is negligible.[3] Interestingly enough, the shape of the frozen crust is such that the "crust tube" has a natural well-rounded entrance [see Fig. 1 and Assumption (A7) in the following]. For well-rounded entrance geometry the entrance loss is less than 5 percent of the pressure loss associated with converting the pressure "energy" within the reservoir into velocity "energy" ($\frac{1}{2}\rho U^2$) at the tube entrance [12]. The latter pressure loss is fully accounted for in the present analysis. In general, from the results of the analysis, it is found that all such pressure losses may be neglected compared with the frictional loss when the ratio of the penetration length, X, to the tube diameter, D, satisfies the inequality $4fX/D > 1.0$, where f is the friction factor.

(A5) The complex "tumbling" flow pattern that must exist in the vicinity of the penetrating liquid flow front at $z = X$ is ignored. Departures from the Blasius friction law in the vicinity of the advancing liquid front are to be expected. Here the liquid layers in the core of the tube must advance over the slower moving layers near the tube wall so that there must be a continual "tumbling" of liquid down (or up) the flow front, which advances over the wall. No solution of this problem has been made, although one anticipates that the mathematics might be something like an inverse entrance region problem with the friction coefficient given by a quasi-steady approximation (such as (A1)) just several tube diameters behind the flow front.

(A6) The tube wall has negligible thermal resistance and is maintained at constant temperature T_w.

(A7) During the entire transient, the solidified layer is thin compared with its extension in the direction of flow so that heat conduction in this direction is negligible. In addition, the axial curvature of this layer is sufficiently small so that the pressure drop over the instantaneous freezing length depends only on the axial position z. It should be noted that the one-dimensional conduction approximation in the solid phase breaks down in the vicinity of the tube entrance. For a saturated liquid flow, however, axial conduction effects will die out within an axial distance less than the instantaneous crust thickness. Physically, this means that the crust thickness, starting from zero thickness at $z = 0$, passes through a maximum value $[R_0 - \delta(t)]$ within a very short distance of the tube entrance. This is illustrated in Fig. 1. This negligible behavior in the immediate vicinity of the tube entrance is ignored, and it is assumed that $R = \delta$ at $z = 0$.

For a saturated liquid, convective heat exchange at the solid-liquid interface is absent so that the growth of the solid layer is not influenced by the local flow. The local crust thickness [or radial interface location $R(z, t)$], however, does depend on the time of arrival of the flow front. Meanwhile, the flow front velocity $\dot{X}(t)$ is dependent on both its position, $X(t)$, and the instantaneous crust shape $R(z, t)$. This coupling between crust growth and fluid flow results in a second order nonlinear integro-differential (momentum) equation for $X(t)$. To determine $X(t)$ the crust shape $R(z, t)$ should be determined simultaneously with $X(t)$ from the one-dimensional conduction equation applied to the frozen layer. In order to avoid this formidable computational problem, we postulate a reasonable functional form for the axial dependence of the liquid-solid interface location $R(z, t)$ in terms

[3] In an actual laboratory apparatus, a short insulated tube section (not shown in Fig. 1) must separate the reservoir and freezing zone.

Nomenclature

a = crust profile exponent; equation (13)
A = dimensionless penetration parameter; equation (18)
B = solidification parameter; equation (17)
c = heat capacity
D = tube diameter; Fig. 1
f = friction factor; equation (12)
$F_m(\delta/R_0)$ = radial liquid-solid interface location function; equation (15)
g = gravitational constant
H = liquid level in reservoir; Fig. 1
L = latent heat of fusion
P_t = pressure above liquid reservoir; Fig. 1
P_e = pressure at tube inlet; Fig. 1
P_0 = initial pressure in empty tube; Fig. 1
Pr = Prandtl number
r = radial coordinate
R = radial location of liquid-solid interface; Fig. 1
$R_0 = D/2$, tube radius
Re = $(2\Delta P/\rho)^{1/2}D/\nu$, Reynolds number based on pressure drop ΔP
s = dimensionless location of advancing liquid front; equation (20)
t = time
T_f = freezing point of liquid
T_w = temperature of tube wall
u = axial component of velocity
U = fluid velocity in tube entrance region
v = radial component of velocity
X = location of advancing liquid front; Fig. 1
$\dot{X}$ = velocity of advancing liquid front
y = dimensionless radial location of liquid-solid interface; equation (21)
z = axial coordinate measured from tube inlet; Fig. 1
α = thermal diffusivity
δ = radial location of liquid-solid interface at tube inlet; Fig. 1
ΔP = total pressure drop; equation (10)
ν = kinematic viscosity
ρ = density
τ = dimensionless time; equation (19)
τ' = shear stress

Subscripts

ℓ = liquid
p = at completion of freezing
s = solid

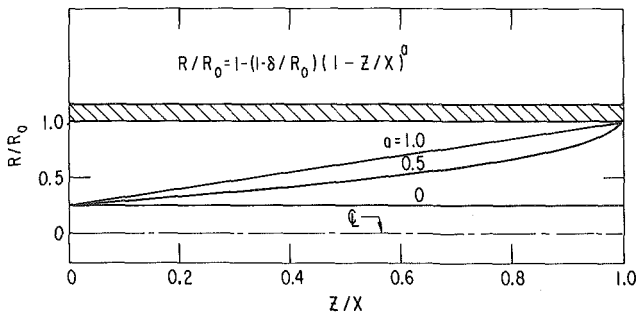

Fig. 2 Normalized instantaneous frozen layer thickness profiles; shaded area represents tube wall and ℄ refers to tube centerline

of $\delta(t)$ and $X(t)$. With this approach, we do not attempt to satisfy the conduction equation within the entire frozen crust nor accurately predict $R(z, t)$ as part of the solution to the penetration problem. Instead, the approximate nature of the crust shape is inferred from the reasoning given in the following. Clearly, at every instant, the solid-layer profile is such that its thickness is maximum in the cold tube inlet region (see (A7)) and decreases monotonically to zero at the leading edge of the penetrating fluid. Moreover, since the flow velocity $\dot{X}(t)$ must decrease with time while the crust thickness is everywhere increasing with time, the crust shape must be convex (as viewed from the liquid region) and, therefore, must fall between two bounding profiles: a linear crust profile and a uniform crust profile (see Fig. 2).[4] It is evident that substituting a linear profile into the momentum equation will yield an upper bound for the flow penetration length, X_p, since this profile provides the maximum cross-sectional area for flow. On the other hand, a uniform profile will yield a lower bound for X_p. As will be shown in Section 4, the upper and lower bounds are sufficiently close together so that the choice of a profile that lies approximately midway between the bounding uniform and linear profiles will yield results shown to be within 20 percent of an exact calculation, indicating that a rigorous solution for the crust shape is not mandatory.

Utilizing this profile technique, the governing integro-differential momentum equation is replaced by an ordinary differential equation. This is combined with an available approximate solution for the radial location of the solid-liquid interface in the inlet region of the cold tube, $\delta(t)$, and integrated numerically and in closed form for tractable limiting cases of practical importance.

3 Analysis

In this section we derive the equations governing the penetrating tube flow incorporating the assumptions of Section 2. The velocity field in the transient tube flow must satisfy the mass conservation relation

$$\frac{1}{r}\frac{\partial}{\partial r}(rv) + \frac{\partial u}{\partial z} = 0 \tag{1}$$

the momentum equation for the z-direction

$$\frac{\partial u}{\partial t} + v\frac{\partial u}{\partial r} + u\frac{\partial u}{\partial z} = -\frac{1}{\rho}\frac{\partial P}{\partial z} - \frac{1}{\rho r}\frac{\partial}{\partial r}(r\tau') \tag{2}$$

and the boundary conditions

$$u = 0, \quad v = 0 \text{ at } r = R; \quad \text{and } v = 0, \quad \frac{\partial u}{\partial r} = 0 \text{ at } r = 0 \tag{3}$$

If equations (1) and (2) are multiplied by r and integrated from $r = 0$ to $r = R(z, t)$, we derive the following integral equations

$$\frac{\partial}{\partial z}\left(\int_0^R rudr\right) = 0 \tag{4}$$

$$\frac{\partial}{\partial t}\left(\int_0^R rudr\right) + \frac{\partial}{\partial z}\left(\int_0^R ru^2dr\right) + \frac{1}{2}\frac{R^2}{\rho}\frac{\partial P}{\partial z} + R\frac{\tau'}{\rho} = 0 \tag{5}$$

In arriving at equation (5), the continuity equation was used to eliminate the term $\int_0^R v\partial u/\partial r r dr$ in favor of $\frac{1}{2}\int_0^R \partial u^2/\partial z r dr$.

Now the integrals appearing in equations (4) and (5) can be calculated from experimental velocity profiles (e.g., the $\frac{1}{7}$-power law); but in problems dealing with turbulent flow a slug-flow axial velocity profile $u = u(z, t)$ is a very good approximation. With this choice of profile the continuity equation becomes (see (A7))

$$uR^2 = U\delta^2 = \dot{X}R_0^2 \tag{6}$$

where U is the fluid velocity at the tube entrance and $\dot{X}$ is the average flow velocity at the leading edge. The momentum equation becomes

$$\left(\frac{R_0}{R}\right)^2\frac{d\dot{X}}{dt} + \left(\frac{R_0}{R}\right)^2\left[\frac{\partial}{\partial z}\left(\frac{R_0}{R}\right)^2\right]\dot{X}^2 + \frac{1}{\rho}\frac{\partial P}{\partial z} + \frac{2\tau'}{\rho R} = 0 \tag{7}$$

Integrating equation (7) with respect to z from $z = 0$ to $z = X(t)$ and making use of Torricelli's law [12], which gives approximately the velocity U in terms of the height of the liquid in the reservoir and the pressure difference $P_t - P_e$, viz.[5]

$$U = [2(P_t - P_e)/\rho + 2gH]^{1/2} \tag{8}$$

we obtain

$$\left[\int_0^X \left(\frac{R_0}{R}\right)^2 dz\right]\frac{d\dot{X}}{dt} + \frac{1}{2}\dot{X}^2 + \frac{2}{\rho}\int_0^X \frac{\tau'}{R}dz = \frac{\Delta P}{\rho} \tag{9}$$

where ΔP is defined as

$$\Delta P = P_t - P_0 + \rho gH \tag{10}$$

In view of (A1) we locally apply the shear stress definition

$$\tau' = \frac{1}{2}f\rho u^2 \tag{11}$$

where f, the friction factor, is considered to be well-described by the Blasius formula:

$$f = 0.0791\left(\frac{2uR}{\nu}\right)^{-1/4} \tag{12}$$

Evaluation of the integrals in equation (9) requires a knowledge of the variation of the interface location $R(z, t)$ along the tube. Of course, the interface location is unknown and should be calculated as part of the solution of the freezing problem. As mentioned is Section 2, while this approach is numerically tractable, it is much more convenient to postulate a reasonable functional form for the axial dependence of the interface location and transform equation (9) into an ordinary differential equation. In particular, we consider the following class of profiles for the normalized crust thickness:

$$\frac{R}{R_0} = 1 - \left(1 - \frac{\delta}{R_0}\right)\left(1 - \frac{z}{X}\right)^a \tag{13}$$

Equation (13) satisfies the conditions $R = \delta$ at $z = 0$ (see (A7)) and $R = R_0$ at $z = X$. The exponent "a" appearing in the above equation takes on values in the range $0 \le a \le 1$. As shown in Fig. 2, when $a = 0$ the solid phase is deposited uniformly[6]—a freezing process which is unlikely. We have a square-root solidification profile and linear

[4] This is readily seen, for example, in a channel geometry. For demonstration purposes, assume $X(t) \sim t^{1/n}$ where $n > 1$. Now $R_0 - R(z, t) \sim (t - t')^{1/2}$, where t' is the time for the flow front to arrive at axial location z [i.e., $X(t') = z$]. After some algebraic manipulation, we obtain the convex crust shape $R/R_0 = 1 - (1 - \delta/R_0)[1 - (z/X)^n]^{1/2}$.

[5] Equation (8) is valid when the kinetic energy of the liquid in the tank is small compared with its potential energy. This is usually the situation when the cross-sectional area of the tube is small compared with that of the tank.

[6] It should be noted that the pressure drop approximation employed in [11] is equivalent to the selection of a uniform crust profile.

profile for $a = \frac{1}{2}$ and $a = 1$, respectively. Thus, the profiles given by equation (13) span the entire range of physically possible profiles (see Section 2).

In the discussion that follows we will concern ourselves with the crust profile corresponding to $a = \frac{1}{2}$, though results will be presented in Section 4 for the $a = 0$ and $a = 1$ cases. Substituting equation (13) into the integral coefficients in equation (9), and with the help of equations (6), (11), and (12) the equation of motion for the penetrating liquid becomes

$$XF_2(\delta/R_0)\frac{d}{dt}\left(\frac{\dot{X}}{\Delta P/\rho}\right)+\frac{\dot{X}^2}{2\Delta P/\rho}+0.1582\mathrm{Re}^{-1/4}\left(\frac{\dot{X}}{\sqrt{2\Delta P/\rho}}\right)^{7/4}\cdot\frac{X}{R_0}F_{19/4}(\delta/R_0)=1 \quad (14)$$

where

$$F_m\left(\frac{\delta}{R_0}\right)=\frac{2}{(1-\delta/R_0)^2}[[(\delta/R_0)^{-m+1}-1]/(m-1) - [(\delta/R_0)^{-m+2}-1]/(m-2)] \quad (15)$$

To complete the system of equations it remains to specify the radial location of the solid-liquid interface at the inlet to the cold tube, viz $\delta(t)$. Clearly, the crust growth behavior in the inlet region is equivalent to the problem of freezing a saturated liquid inside a cylinder. The problem of the inward freezing of a circular cylinder has been treated in numerous papers (see, e.g., [13, 14]). Stefan [14] utilized an approximate collocation method which takes full account of the movement of the phase conversion front and transient heat conduction within the frozen layer. For freezing a saturated liquid inside a cylinder this technique yields the inverted solution (see equation (37) of reference [14]).

$$2(\delta/R_0)^2\ln(\delta/R_0)-(\delta/R_0)^2+1=\frac{4\alpha_s}{R_0^2}[[1+2c_s(T_f-T_w)/L]^{1/2}-1]t \quad (16)$$

A comparison of equation (16) with numerical results [13] shows that the error is less than ~20.0 percent. This solution is to be employed in the present study.

It is now convenient to introduce the following set of dimensionless parameters and variables:

$$B\equiv[1+2c_s(T_f-T_w)/L]^{1/2}-1 \quad (17)$$

$$A\equiv 0.0198\frac{\mathrm{Re}^{3/4}\mathrm{Pr}(\alpha_\ell/\alpha_s)}{B} \quad (18)$$

$$\tau\equiv\frac{16\alpha_s B}{D^2}t \quad (19)$$

$$s\equiv\frac{16B}{\mathrm{RePr}(\alpha_\ell/\alpha_s)}\cdot\frac{X}{D} \quad (20)$$

$$y\equiv\frac{\delta}{R_0} \quad (21)$$

From equations (14)–(16), the following dimensionless equation of fluid motion is obtained

$$2sF_2(y)\frac{d^2s}{d\tau^2}+\left(\frac{ds}{d\tau}\right)^2+AsF_{19/4}(y)\left(\frac{ds}{d\tau}\right)^{7/4}=1 \quad (22)$$

where

$$F_m(y)=\frac{2}{(1-y)^2}[(y^{-m+1}-1)/(m-1)-(y^{-m+2}-1)/(m-2)] \quad (23)$$

and

$$2y^2\ln(y)-y^2+1=\tau \quad (24)$$

The behavior of the dimensionless penetration distance s is seen to depend only on the dimensionless parameter A. While equations (22)–(24) are analytically tractable in two special limiting cases (see the following), in general they are more conveniently dealt with numerically by transforming equation (24) into a first-order differential equation. Equations (22) and (24) are readily treated as a system of three first-order differential equations defining the τ-evolution of the dependent variables s, $ds/d\tau$, and y subject to the initial conditions $s = 0$, $ds/d\tau = 1$ (see equation (8)), and $y = 1$ when $\tau = 0$.

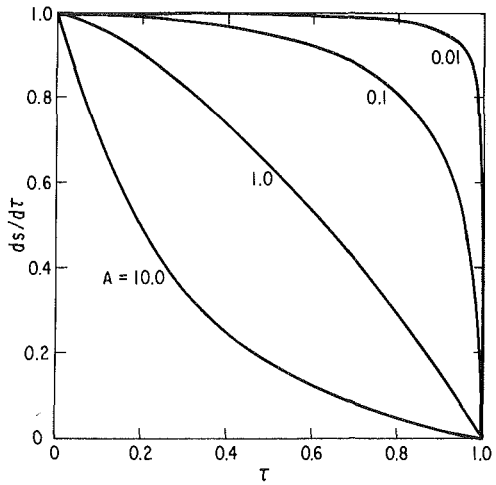

Fig. 3 Effect of penetration parameter *A* on advancing liquid front velocity—time histories

4 Results and Discussion

Typical results for a square-root solidification profile ($a = \frac{1}{2}$), showing the effects of the dimensionless parameter A on the evolution of penetation velocity and distance, are displayed in Figs. 3 and 4. It can be shown that A is the ratio of the time it takes for solidification to be complete at the tube entrance, $D^2/(16\alpha_s B)$, to the time necessary for the development of the turbulent velocity profile, $\sim D/(f\sqrt{2\Delta P/\rho})$. When A is very small [i.e., $A \to 0$], complete occlusion of the tube layer occurs before the retarding frictional effect of the growing frozen layer begins to be felt. In this case the flow velocity is practically constant and the liquid penetration is seen to increase linearly with time. Conversely, if $A \gg 1$, fluid inertia is small in comparison with the

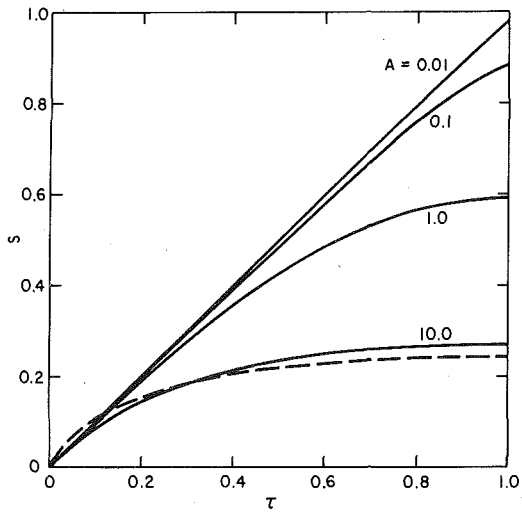

Fig. 4 Effect of pentration parameter *A* on advancing liquid front location—time histories; dashed curve obtained from equation (25)

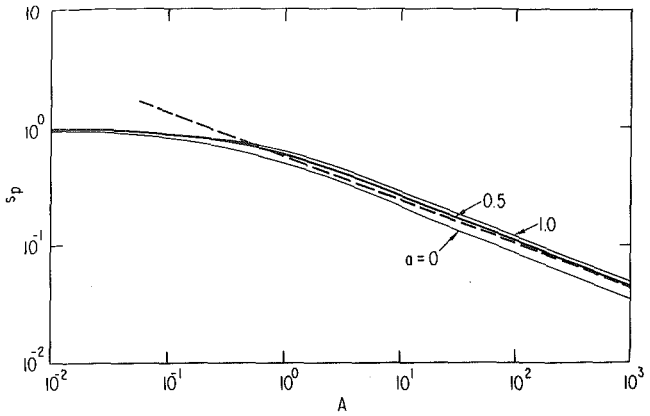

Fig. 5 Effect of frozen layer thickness profile on final liquid penetration length; dashed curve obtained from equation (25)

frictional force. In the limit $A \to \infty$, after neglecting the inertia terms in equation (22), the penetration distance can be calculated from the integral relation

$$s = \frac{1}{A^{4/11}}\left[\frac{44}{7}\int_y^1 \frac{\xi \ln(1/\xi)d\xi}{[F_{19/4}(\xi)]^{4/7}}\right]^{7/11} \qquad \text{for } A \gg 1 \qquad (25)$$

where the dimensionless crust location y is related to τ via equation (24). This expression is plotted in Fig. 4 for $A = 10.0$.

The dependence of the final penetration length s_p on parameter A is illustrated in Fig. 5 for crust shape exponents $a = 0$, ½, and 1. Had we postulated a linear crust profile (i.e., $a \approx 1.0$) for the axial variation of the interface, the predicted s_p would still be within 10 percent of that predicted using the square-root profile. Even in the nonphysical extreme of an instantaneous uniform crust thickness ($a = 0$), s_p falls below the square-root result by less than 20 percent. Since the actual crust shape lies between the uniform profile ($a = 0$) and the linear profile ($a = 1$), we conclude that the error associated with the square-root profile is less than 20 percent. It is interesting to note that the work of reference [8] suggests that more detailed numerical analysis which solves for the crust shape can involve maximum errors as high as 15 percent. The approximation used in the present analysis thus represents a useful tool in treating problems of this type.

With regard to limiting behavior, if A is so small that $ds/d\tau$ is constant during most of the fluid penetration period, then s_p will be nearly unity. In terms of the physical variables (see equation (20)), we have

$$\frac{X_p}{D} = \frac{\mathrm{RePr}(\alpha_\ell/\alpha_s)}{16B} \text{ for } A \ll 1 \qquad (26)$$

In the extreme $A \gg 1$, we integrate equation (25) between the limits $y = 0$ and 1 by, say, Simpson's rule to obtain the closed-form result $s = 0.584A^{-4/11}$ —or in terms of the physical variables

$$\frac{X_p}{D} = 0.155\,\mathrm{Re}^{8/11}\left[\frac{\mathrm{Pr}(\alpha_\ell/\alpha_s)}{B}\right]^{7/11} \qquad \text{for } A \gg 1 \qquad (27)$$

As shown in Fig. 5, equation (27) represents the penetration length for values of parameter A as low as 1.0. This leads us to expect negligible inertial limitations when $4fX_p/D > 1.0$.

5 Experimental Method

The experimental apparatus (see Fig. 1) and procedures used are essentially the same as those used in reference [10]. There are, however, a few exceptions: first, the reservoir containing the saturated liquid is pressurized up to ~1 atm so that the liquid flows into the cold tube under the influence of both gravity and a pressure gradient. Second, in correlating the data the characteristic velocity is based on measured ΔP values (as suggested by the theory given in the foregoing), rather than the measured average flow velocity used in reference [10]. The cold tube consists of a copper coil immersed in a bath of liquid coolant. When the tube is cooled to the bath temperature, a valve which separates the coil and reservoir is opened to initiate the flow of liquid. The valve is located in a short connecting tube (not shown in Fig. 1) which separates the reservoir and freezing coil. The reservoir is constructed of glass, with a convergent glass nozzle in the wall near the bottom which feeds the connecting tube. The liquid penetration before freezing is obtained by measuring the difference in weights of the copper coil before and after penetration. The principal working fluid used in this study was Freon 112A which melts at 40.5°C. The penetration data for Freon 112A compares well with equation (27), as shown in Fig. 6. Experiments were also carried out with both water and benzene flows. The predicted penetration lengths fall below the experimental data, due undoubtedly to the difficulty in maintaining a constant tube-wall temperature with these materials. The Biot number, or index of the relative resistance to heat transfer in the boiling liquid nitrogen and in the growing frozen layer, is ~0.09 for Freon 112A. This is to be compared with Biot numbers of 0.4 and 1.6 for benzene and water flows, respectively.

6 Concluding Remarks

The turbulent flow assumption (A1) and, therefore, equations (11) and (12) are not expected to be applicable when the local Reynolds number falls below ~2100. However, it is intuitively clear that if the initial Reynolds number, $\mathrm{Re} = \sqrt{2\Delta P/\rho}D/\nu$, is sufficiently large most

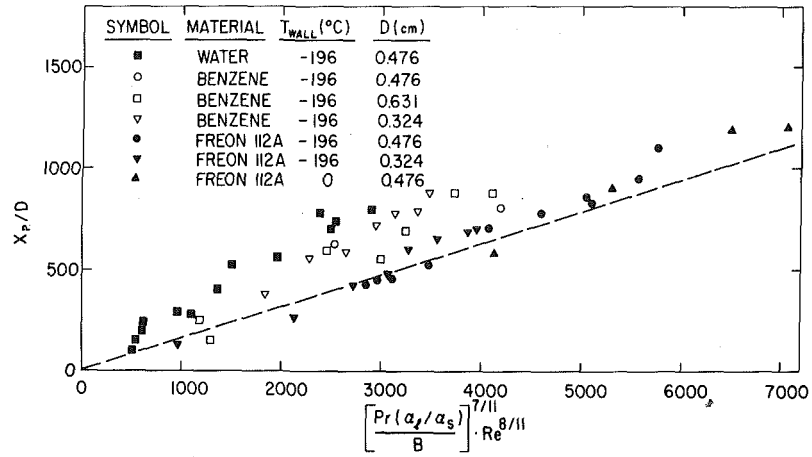

Fig. 6 Comparison of the data with equation (27) (dashed)

of the liquid penetration will occur in a turbulent manner. For example, utilizing our solutions, it can be shown that the liquid will travel 80 percent of its final penetration length, X_p, before transition from turbulent to laminar flow takes place near the tube entrance if

$$\mathrm{Re} > \begin{cases} 1200 \left(\dfrac{\mathrm{Pr}\alpha_\ell/\alpha_s}{B}\right)^{2/3} & A > 2 \\ 2100 & A < 2 \end{cases} \tag{28}$$

The experimental initial Reynolds numbers reported here are in the range 10^4–10^5.

Even when the local Reynolds number exceeds 2100, the classical Blasius formula for fully developed turbulent tube flow can, at best, only represent a reasonable approximation to the drag force during transient liquid penetration since the cases are not identical. The error incurred by using the Blasius equation could be most serious when A is small. For sufficiently short liquid penetration, a transient laminar component of the shear stress, viz. $\tau' = u/(\pi\nu t)^{1/2}$, may arise and considerably exceed the quasi-steady turbulent value used here. On the other hand, the results of experimental investigations into decelerated turbulent pipe flow suggests that the friction factor can be less than the equivalent steady value (see, e.g., reference [15]).[7] The problem of unsteady turbulent pipe flow has not yet been adequately resolved in the literature [16]. Actually, even if the quasi-steady Blausius friction law is justified, a hydrodynamic entrance length on the order of $10D$ is present over which appreciable departures from this law are to be expected. A detailed treatment of the development of a penetrating tube flow based on the full equations of motion including viscosity seems to be too complicated to be practical. In the absence of sufficient information on the details of the flow, the assumption that τ' is well-represented by equations (11) and (12) is probably best.

In particular systems of experimental interest, it may be necessary to relax the isothermal tube wall Assumption (A6) [see Section 5]. Moreover, in fast reactor safety applications, the inside surface of the tube wall may melt upon contact with the penetrating liquid [17]. Both of these extensions are readily handled using the present method. It is recognized that the crust profile method exploited here will not apply when the liquid entering the tube is at a temperature higher than the freezing point (superheated). In this case complete occlusion of the tube with frozen material ultimately occurs at some location between the inlet and the leading edge of the liquid flow. Calculation of the penetration distance in this most general situation is quite difficult but would constitute a useful next step.

[7] In reference [15] the flow transient was preceded by an initial period of steady turbulent pipe flow. Our problem is further complicated by the presence of an advancing interface (see (A5)).

Acknowledgments

It is a pleasure to acknowledge the extensive computational assistance of F. Pellett and the assistance rendered by W. E. Holloway in performing the experiment. We also wish to thank Dr. S. G. Bankoff for his helpful discussions of aspects of this work. This work was performed under the auspices of the U. S. Energy Research and Development Administration.

References

1 Zerkle, R. D., and Sunderland, J. E., "The Effect of Liquid Solidification in a Tube Upon Laminar-Flow Heat Transfer and Pressure Drop," JOURNAL OF HEAT TRANSFER, TRANS. ASME, Series C, Vol. 90, 1968, pp. 183–190.

2 Mulligan, J. C., and Jones, D. D., "Experiments on Heat Transfer and Pressure Drop in a Horizontal Tube With Internal Solidification," *International Journal of Heat and Mass Transfer*, Vol. 19, 1976, pp. 213–218.

3 Depew, C. A., and Zenter, R. C., "Laminar Flow Heat Transfer and Pressure Drop With Freezing at the Wall," *International Journal of Heat and Mass Transfer*, Vol. 12, 1969, pp. 1710–1714.

4 DesRuisseaux, and Zerkle, R. D., "Freezing of Hydraulic Systems," *Can. J. Chem. Eng.*, Vol. 47, 1969, pp. 233–237.

5 Ozisik, M. N., and Mulligan, J. C., "Transient Freezing of Liquids in Forced Flow Inside Circular Tubes," JOURNAL OF HEAT TRANSFER, TRANS. ASME, Series C, Vol. 91, 1969, pp. 385–391.

6 Bilenas, J. A., and Jiji, L. M., "Variational Solution of Axisymmetric Fluid Flow in Tubes With Surface Solidification," *Journal of Franklin Institute*, Vol. 289, 1970, pp. 265–279.

7 Chun, M. H., Gasser, R. D., Kazimi, M. S., Ginsberg, T., and Jones, Jr., O. C., "Dynamics of Solidification of Flowing Fluids With Applications to LMFBR Post-Accident Fuel Relocation," to appear in *Proceedings International Meeting on Fast Reactor Safety and Related Physics*, Oct. 5–8, Chicago, Ill., 1976.

8 Martinez, E. P., and Beaubouef, R. T., "Transient Freezing in Laminar Tube Flow," *Can. J. Chem. Eng.*, Vol. 50, 1972, pp. 445–449.

9 Epstein, M., Grolmes, M. A., Henry, R. E., and Fauske, H. K., "Transient Freezing of a Flowing Ceramic Fuel in a Steel Channel," *Nucl. Sci. Eng.*, Vol. 61, 1976, pp. 310–323.

10 Cheung, F. B., and Baker, Jr., L., "Transient Freezing of Liquids in Tube Flow," *Nucl. Sci. Eng.* Vol. 60, 1976, pp. 1–9.

11 Madejski, J., "Solidification in Flow Through Channels and Into Cavities," *International Journal of Heat and Mass Transfer*, Vol. 19, 1976, pp. 1351–1356.

12 Streeter, V. L., *Fluid Mechanics*, McGraw-Hill, New York, 1958.

13 Tao, L. C., "Generalized Numerical Solutions of Freezing a Saturated Liquid in Cylinders and Spheres," *AIChE Journal*, Vol. 13, 1967, pp. 165–169.

14 Stephan, K., "Influence of Heat Transfer on Melting and Solidification in Forced Flow," *International Journal of Heat and Mass Transfer*, Vol. 12, 1969, pp. 199–214.

15 Daily, J. W., Hankey, Jr., W. L., Olive, R. W., and Jordaan, J. M., Jr., "Resistance Coefficients for Accelerated and Decelerated Flows Through Smooth Tubes and Orifices," TRANS. ASME, Vol. 78, 1956, pp. 1071–1077.

16 Kalishevskii, L. L., and Selikhovkin, S. V., "Some Results of Investigating Unsteady Turbulent Flow," *Teploenergetika* (*High Temperature*-English Translation), Vol. 14, 1967, pp. 69–72.

17 Epstein, M., "Heat Conduction in the UO_2-Cladding Composite Body With Simultaneous Solidification and Melting," *Nucl. Sci. Eng.*, Vol. 51, 1973, pp. 84–87.

Y. Hayashi
Associate Professor

A. Aoki
Postgraduate student

S. Adachi
Postgraduate student

K. Hori
Postgraduate student

Department of Mechanical Engineering,
Kanazawa University,
Kanazawa, Japan

Study of Frost Properties Correlating With Frost Formation Types

Frost formation process was studied by photographic observation, and frost formation types were classified into several groups according to their structure in the temperature range of 0 ~ −25°C. Frost properties, density and effective thermal conductivity, were clarified in connection with the classified frost formation types, and the prediction of the thermal conductivity was performed by the presented structural model of a frost layer.

1 Introduction

Frost deposition is an important phenomenon in the cryogenic industries in connection with gas coolers, refrigerators, freeze-out purification, etc. When humid air is exposed to a cold surface, whose temperature is below 0°C, frost deposition occurs and continues to accumulate on the surface. In general, this kind of problem should be treated as a moving boundary problem to predict heat and mass flux from a gas stream to a deposit surface, but cannot be solved simply because of lack of information about frost thermal properties. Trammell, et al. [1][1] have studied the effect of velocity, humidity, and temperature on frost formation and have discussed the density profile in a frost layer. Brian, et al. [2] and Reid, et al. [3] have determined the frost density and the thermal conductivity taking account of the internal diffusion of water vapor in a frost layer. Biguria, et al. [4] have presented correlations to estimate the frost density and their thermal conductivity, concentrating on the observed behavior of the frost crystal deposit in the early stage of frost formation. In spite of these researches, the frost properties have not been clarified in detail up to now. Since the frost formation process is influenced by time and by the history of frost layer, the nature of the frost formation process is too complicated to be decided briefly for constant environmental parameters. Therefore, in order to discuss the properties of the frost layer whose nature is very complicated, there is need of a study corresponding to the phenomena.

The study reported in this paper is concentrated on the relation between the frost properties and the frost formation phenomena. In the first place, the growth of a frost layer was investigated by the photographic observation, and the type of frost formation was classified into the several groups according to their structure, taking account of the crystal growth to some extent. Next, the frost density was clarified phenomenologically in connection with the classified frost formation types, and the frost thermal conductivity was predicted using a simple theoretical model of a frost layer. The experiment of frost deposition was carried out on the fixed position of a flat plate, which was parallel to flow, under forced convection, but the local study over the whole plate was not performed. As the range of this experiment, the temperature of the cryosurface is from 0 to −25°C, the temperature of the main stream is from 15–30°C, its humidity is from 0.0045 to 0.01 Kg/Kg′, and its velocity is from 1.0 to 6.0 m/s.

2 Experimental Apparatus and Procedure

The experimental setup is described in Fig. 1. The air stream which enters the 1500-mm long test section through 250- by 250-mm opening, passes through a temperature-humidity controlling section and a blower, and is recirculated back to the test section through regulating fins, a number of screens, and a convergent section. The test section is made of 5-mm thick acryl plate and has a removal top to facilitate the photographic observation. The test plate, which is made of stainless steel plate 95-mm wide, 1000-mm long, and 21-mm thick is situated in the test section. The plate is cooled with ethylene glycol water solution and its surface temperature is maintained at constant within ±0.2°C during a run.

[1] Numbers in brackets designate References at end of paper.

Contributed by the Heat Transfer Division for publication in the JOURNAL OF HEAT TRANSFER. Manuscript received by the Heat Transfer Division July 19, 1976.

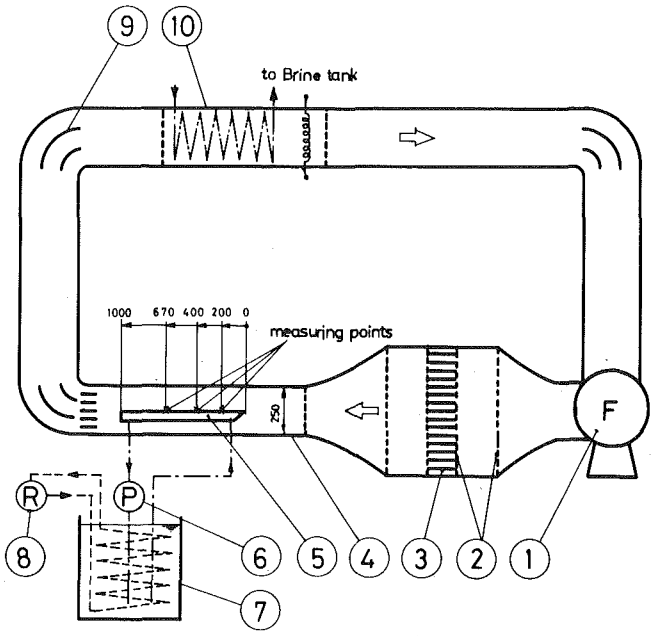

Fig. 1. Experimental setup: 1 blower 2 screen 3 honeycomb 4 test section 5 test plate 6 pump 7 brine tank 8 refrigerator 9 regulating fin 10 temperature-humidity controlling section

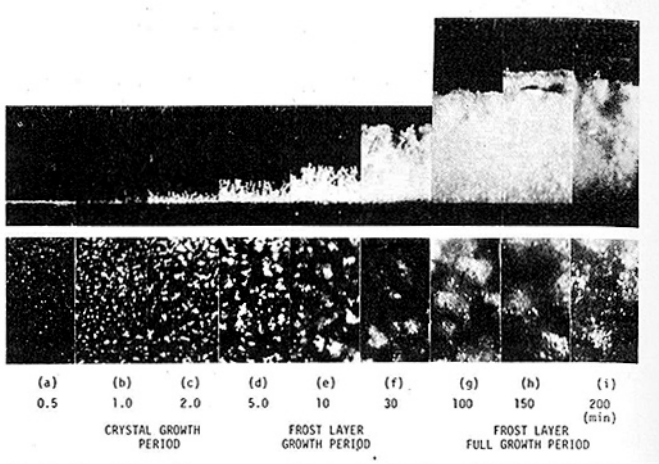

Fig. 2 Frost formation process (U_∞ = 4 m/s, C_∞ = 0.0075 Kg/Kg′, t_s = −12.4 °C, × 12)

Measurements and photographic observations are made at the three fixed positions, as shown in Fig. 1, at frequent intervals. As for the frost properties, measurements are made at the fixed position, 670 mm from the leading edge. Frost surface temperature is measured to ±0.2°C with copper-constantan thermocouple, 25$\mu\phi$, by physical contact between thermocouple and frost surface. Heat flux is obtained by a comparative method of measuring heat flux passed across the test plate. A cathetometer is used to measure frost height. Turbulence intensity and air velocity measurements are made with a hot-wire anemometer. The turbulence intensity of the main stream was about 0.5 percent for a stream at 6.0 m/s. Its distribution in the boundary layer was not measured.

3 Classification of Frost Formation Types

3.1 Frost Formation Process. Fig. 2 shows the typical results of the frost formation process obtained by the photographic observation. The mechanisms of frost formation are complicated due to the effects of many environmental parameters, but the frost formation process itself is something common and can be divided largely into three periods: "crystal growth period," "frost layer growth period," and "frost layer full growth period." Such a division of the frost formation process has not been done in the past, however, it seems to be effective in order to relatively compare the complex nature of the frost layer whose growth rate varies with the frost formation conditions. These expressions used here are named as a matter of convenience by authors, and are not popular in this field.

In the crystal growth period, a thin frost layer covers the cryosurface at first (Fig. 2(a)). Next, frost crystals, which are relatively far apart from each other, generate on the thin frost layer, and grow in a vertical direction at about the same rate. Namely, the frost formation in this period is almost characterized by the crystal growth in linear dimension, then the frost becomes like a forest of trees without the growth of a homogeneous layer (Fig. 2(b) and 2(c)).

In the frost layer growth period, the rough frost, which is a cluster of rod type crystals, changes its shape by the generation of branch around the top of a crystal or by the interaction of each crystal (Fig. 2(d) and 2(e)), and then grows gradually into a meshed and more uniform frost layer until the frost surface becomes nearly flat (Fig. 2(f)). In this period, the frost density increases with the growth of frost layer, because of three-dimensional growth, and the internal diffusion of water vapor in the frost layer.

In the frost layer full growth period, the frost layer does not change its shape especially until the frost surface temperature comes to 0°C due to an increase in frost thermal resistance. The frost surface then begins to melt. The melted water soaks into the frost layer and freezes into the ice layer. The melting and freezing cause a sudden increase in the frost layer density and a sudden decrease in its thermal resistance, and the frost deposition occurs again. Then a cycle process of melting, freezing, and deposition often continues periodically until the frost formation stops when the equilibrium condition of heat transfer is reached (Fig. 2(g), 2(h), and 2(i)). Namely, in this period, the frost layer becomes a dense and tight layer, and ripes into the aged frost.

The process of the frost layer growth is divided into the three characteristic periods as described in the foregoing, but this process

Nomenclature

A, B, C, D = frost formation types
C = concentration of water vapor
ΔC = concentration difference between a main stream and a cryosurface
D = diffusion coefficient
Kg/Kg′ = absolute humidity
L = frost height
L_H = latent heat
p = pressure
p_s = saturation vapor pressure
R = gas constant
t = temperature
T = absolute temperature
u = stream velocity
α = proportion of cross-sectional area of frost columns
α_{ice} = proportion of cross-sectional area of ice columns
θ = time
λ = thermal conductivity
λ_{eff} = effective thermal conductivity of frost layer
λ_g = thermal conductivity of air in taking account of water vapor diffusion
ρ = frost density

Subscripts

air = air
comp = ice-air composite part
ice = ice column
s = cryosurface
∞ = main stream
− = representative value at the end of "frost layer growth period"

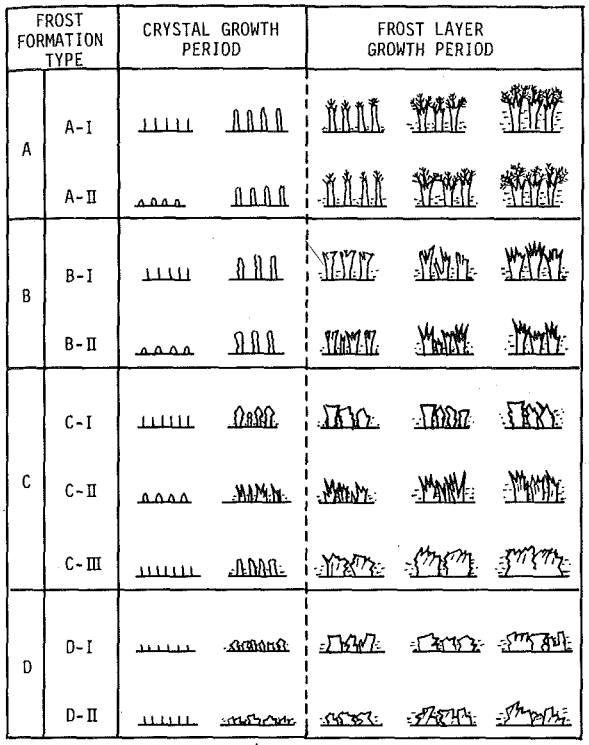

Fig. 3 Classification of frost formation type

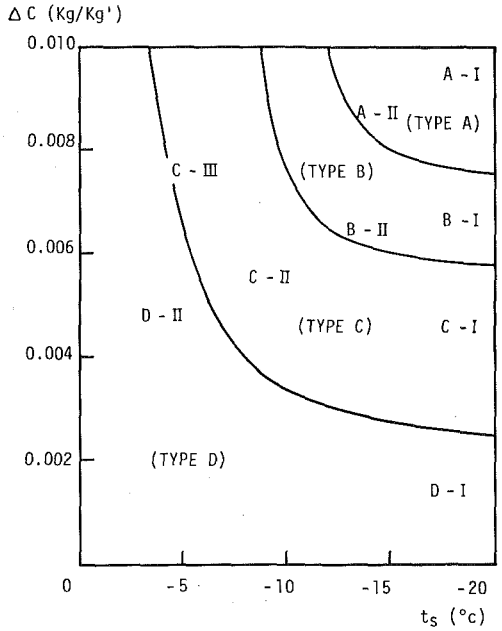

Fig. 4 ΔC-t_s plane

does not appear uniformly over the whole plate and is varied with longitudinal position. The frost layer grows faster in the upstream than in the downstream of the plate even for the same condition, and each period appears gradually from the front to the rear of the plate. This means that the time required for each period varies not only with the frost formation conditions but also with the frost deposit position. For example, the time required for the crystal growth period is about 10 s in the brief case, or about half an hour in the long case. This can be explained by the rate determining concepts of the linear growth rate of pillar-shaped crystal and the rate of mass transfer to the top of it, but the explanation is omitted here [5].

3.2 Classification of Frost Formation Types. The process of frost formation described previously was studied by a macroscopic observation. Comparatively, however, the detailed mechanism of frost formation and the shape of frost layer during each period are different in a microscopic viewpoint by the various frost formation conditions. Here, frost formation is classified into several types according to the structure in taking account of the clarified frost formation process. In classifying the frost formation types, the following are focused on: (1) The shape of crystals in the initial stage of frost formation, the presence of the transition from the rod type crystal to the feather type crystal and the state of its transition at the end of the crystal growth period. (The end of the crystal growth period means phenomenologically one of common representative time. Namely, the frost layer, whose growth rate varies by the frost formation conditions and by the deposit position, is compared relatively at this point.) (2) The regional position of frost formation conditions in a ΔC-t_s plane, where ΔC is the concentration difference between a main stream and a cryosurface, and t_s is the cryosurface temperature. (In crystallography, ΔC and t_s are generally considered to be the most significant parameters, since t_s affects the linear growth rate of crystal and ΔC affects the stability of the curved interface of crystal which is dependent on the radius of curvature. Namely ΔC seems to be a driving force which tends to increase the radius of curvature.) Generally, the ΔC-t_s plane is considered to be composed of the supersaturation degree ΔC and the temperature t_s at the crystal surface. However, the supersaturation degree at the frost crystal surface cannot be obtained briefly, and ΔC, t_s cannot be treated as constant parameters because of the dynamic nature of frost formation. Then the initial state of ΔC-t_s plane is adapted here. In order to discuss the structure of the frost layer, it seems to be proper to adapt the initial state quantities, because the frost layer grows on the basis of the frost columns generated in the crystal growth period and the historical process of frost formation is affected considerably by the initial state of conditions.

The types of frost formation were classified largely into four groups, A, B, C, and D, as shown schematically by Fig. 3. The frost formation conditions, where these types appear, can be represented on the ΔC-t_s plane as shown in Fig. 4. In order to obtain the ΔC-t_s diagram, the experiments were made under a number of combinations of the deposit conditions, which were slightly changed by steps of 2°C and of 0.001 kg/kg'. The border of each region, of course, does not clearly exist. Next, these types are explained as follows.

Type A is the most representative type whose process has been described before, for example, by Fig. 2. In the crystal growth period, crystals generate and grow in almost linear dimension after the formation of thin frost layer. The rough frost in the crystal growth period turns gradually into the close-knit meshed frost in the frost layer growth period. It is the most characteristic point for this type that the transition of the two periods takes place by the generation of feather-type crystal around the top of the crystal. The difference between A-I and A-II is distinguished by the presence of a needle-type crystals in the initial stage of the crystal growth period.

Type B is almost the same as type A, however, the transition of crystal occurs due to generation of the developed plate-type branch instead of the feather-type branch. When the frost formation conditions come near to the region C in the ΔC-t_s plane, it becomes difficult to confirm the transition from the crystal growth period to the frost layer growth period by the transition of crystals.

Type C forms the dense frost layer in comparison with type A or B. In the crystal growth period, the linear dimensional growth rate of frost crystal is small and the roughness of the frost surface is also small, because the frost is deposited not only on the top of the crystal but also on the sides and on the bottom of it. Consequently the transition of crystals to the top of the frost crystal does not take place. Due to the combination and the interference of each crystal by enlargement of it, the crystal generation period shifts to the frost layer growth period. C-I, C-II, and C-III are distinguished according to the presence of the needle-type crystals as shown in the figure.

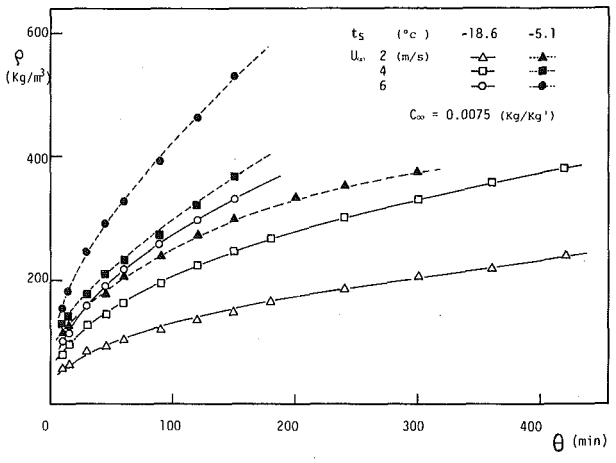

Fig. 5 Frost density variation with time

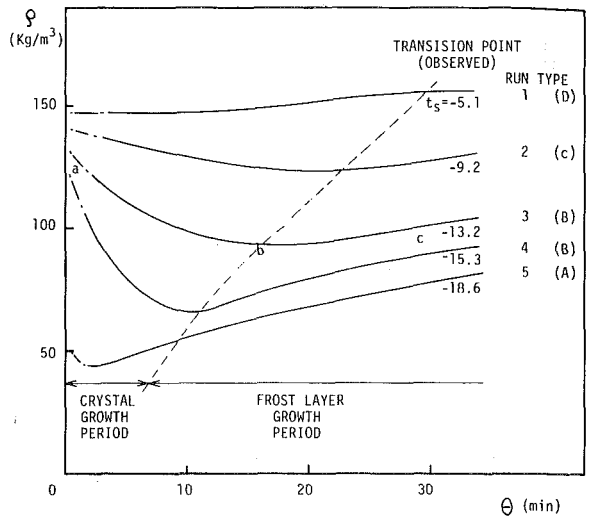

Fig. 6 Frost density variation during comparative early stage of frost formation

Type D takes almost the same frost formation pattern as type C. However, the tendency of the dense frost formation is stronger than for type C, and the frost formation for this type seems to be the accumulation of the nearly homogeneous frost layer. The distinction between D-I and D-II is due to the shape of crystals. Crystals of type D-I grow in the shape of a regular square plate, and crystals of type D-I grow with the surface of thin irregular form.

Classifying the frost formation types, only ΔC and t_s were considered as frost formation conditions. The effects of another conditions such as the main stream velocity and its temperature were recognized experimentally as follows. Higher stream velocity appears to increase the number of frost columns in the crystal growth period, and to advance the rate of the frost layer growth even for the same frost deposit rate. This can be explained by the reason that the distance of the frost columns becomes short, the interference of each frost columns occurs quickly to form the more uniform frost layer. The effect of the main stream temperature was not recognized at all within the limits of this experiment. The effect of the longitudinal deposit position, which appeared in the frost formation process, could not be confirmed for the frost formation types experimentally. In conclusion, it is considered that the shape of each crystal and the frost formation types themselves are almost not affected by the stream velocity and the deposit place, but are strongly dependent on ΔC and t_s. This means that it is sufficient to discuss the frost properties for constant main stream temperature and at the fixed position of the cryosurface in order to clarify the frost properties correlating with the frost formation types.

Henceforth, experiments and measurements are carried out at constant main stream temperature, 25°C, and at the fixed position, 670 mm from the leading edge.

4 Frost Density

Fig. 5 shows the change of frost density with time at various cryosurface temperatures and stream velocities. The increase in frost density is approximately parabolic with time. This tendency is explained, as well known, by the reason that the increase in frost height is quite rapid during the early stage and becomes slower with time comparing to the almost constant increase of frost weight. As to be expected, a larger driving force of mass transfer and a higher velocity produce a heavier frost, but the detailed frost density variation cannot be explained only by the transfer consideration. Next, Fig. 6 shows the results of the frost density variation during the comparative early stage in connection with the frost formation types.

The frost density, corresponding to the types A and B, changes very greatly with time, and the tendency of each period, the crystal growth period and the frost layer growth period, is distinguished remarkably. Namely, for the case of run No. 3, after the generation of a thin frost layer (point a), the frost density decreases in the crystal growth period due to the linear dimensional growth crystal, but increases in the frost layer growth period due to the generation of branch and the internal diffusion of water vapor in a frost layer. At the point b, which is corresponding to the transition point of these periods, the frost density takes a minimum value and this is coincident with the phenomenological observed result represented with the dotted line. On the other hand, for the case of the type D, the density does not change greatly and increases monotonously throughout two periods. this tendency is agreement with the predescribed notion that the frost formation of the type D is characterized with the nearly constant accumulation of the homogeneous frost layer. The more the developed type A, where ΔC is large and t_s is low comes near, the more the frost deposits roughly in the initial stage of frost deposition, and the more the frost layer varies in proportion to growth.

Fig. 7 shows the change of frost density as a function of the nondimensional frost height, $L/\bar{L}$. $\bar{L}$ is a frost height when its surface becomes nearly flat at the end of the frost layer growth period, and is correspondingly a phenomenologically representative common point. Using $L/\bar{L}$, the nature of frost formation, whose growth rate is different under the various frost formation conditions, can be compared relatively. From this figure, the change of the frost density can be explained more clearly in connection with the frost formation types. Up to $L/\bar{L} = 1$, the density changes less for the type D due to nearly

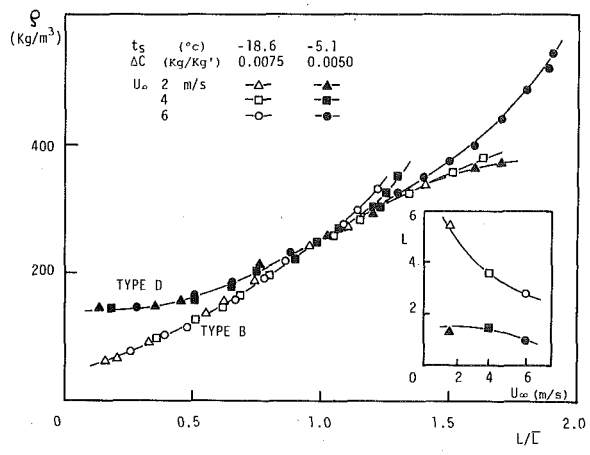

Fig. 7 Frost density variation with nondimensional frost height

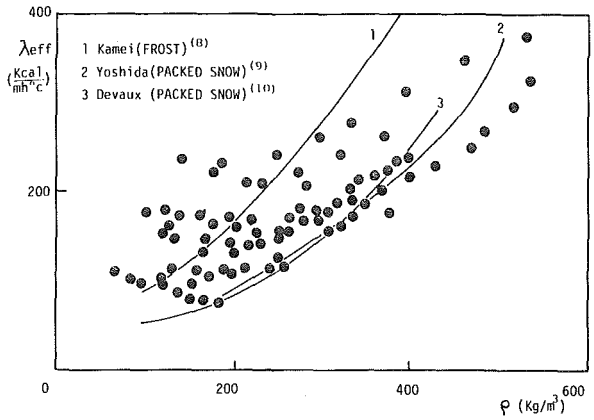

Fig. 8 Thermal conductivity variation with frost density

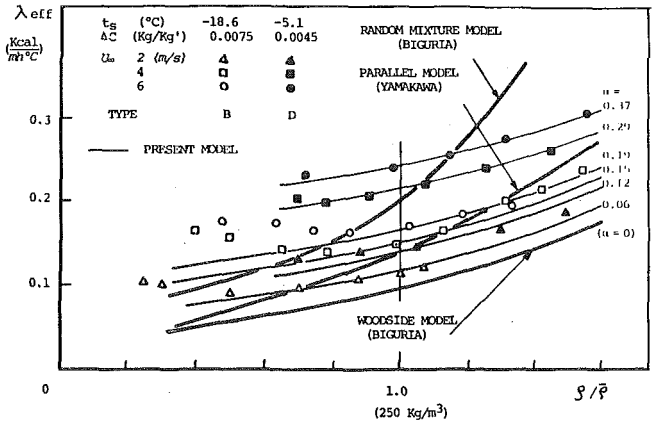

Fig. 9 Experimental and theoretical results of frost thermal conductivity as a function of nondimensional frost density

constant accumulation of the homogeneous frost layer, and changes much for the types A and B in order to fill up a roughness of the frost layer formed in the crystal growth period. The frost density variation is settled by $L/\overline{L} = 1$ and is not due to stream velocity. This coincides with the predescribed observed result that the frost formation types are almost not affected by stream velocity. In the region, $L/\overline{L} > 1$, the density variation of each frost formation type cannot be explained briefly in relation to $L/\overline{L}$, because of the complicated change of state in a frost layer in the frost layer full growth period.

5 Frost Thermal Conductivity

A frost layer is a porous substance which is composed of ice crystals and air, and its effective thermal conductivity is related to the density. The effective thermal conductivity of the frost layer, λ_{eff}, is calculated from the instantaneous measured values of frost height, heat flux, frost surface temperature, and cryosurface temperature on the assumption that the temperature profile across the frost layer is linear at any time. In Fig. 8, experimental curves for frost and packed snow are presented together with our experimental results. The Yoshida [9] and Devaux [10] curves for packed snow give low bounds of the frost thermal conductivity. The Kamei [8] curve, which has been obtained by the experiment of the frost formation in a low temperature cooler condenser, agree approximately with our results, but a close relationship between λ_{eff} and ρ cannot be found because of large scattering of the experimental values. This means that the heat transport in a frost layer is affected not only by the density but also by additional factors. Biguria [4], Parker [6], Yamakawa [7] and the other many investigators have predicted the effective thermal conductivity considering these factors. These are:

1 structure of a frost layer;

2 internal diffusion of water vapor caused by the temperature distribution in a frost layer;

3 eddy generated by the roughness of frost surface.

Factor (3) means that the eddy due to the roughness of frost surface makes the thermal conductivity apparently increase. Biguria and Wenzel have discussed precisely on the critical relation between the frost height and the turbulence induction, and reported that, in the very low density region, the convective heat transfer by eddies within the air phase is a significant contributor to the frost thermal conductivity.

In order to compare the difference of the thermal conductivity affected by the frost formation types, the data points, which belong to the types B and D, are picked out from Fig. 8 and are shown as a function of nondimensional density, $\rho/\overline{\rho}$, in Fig. 9. Where $\overline{\rho}$ is a representative density (about 250 kg/m^3 in this condition) at the point when the frost surface becomes nearly flat. From this figure, the effect of the factor (3) can be explained qualitatively as follows. In the early stage of frost formation, where the surface roughness cannot be negligible hydrodynamically, λ_{eff} is affected considerably by the secondary flow due to the surface roughness and is large in spite of a low density. Namely, in the region where $\rho/\overline{\rho}$ is nearly less than unity, λ_{eff} decreases as ρ increases. After reaching a minimum value, λ_{eff} increases again as ρ increases. In case of the type D which is characterized with the nearly constant accumulation of the homogeneous frost layer, the surface roughness is small and the effect of the factor (3) almost does not appear during the all process of frost formation. Here, λ_{eff} is predicted considering factors (1) and (2).

5.1 Structural Model of a Frost Layer. Predictions of $\overline{\lambda}_{eff}$ taking account of the factors (1) and (2) have been done on the basis of the arbitrary structural model of a frost layer. However, usual structural models, which have been developed by many investigators, are determined respectively only by the density and do not contain a delicate distinction of a frost structure which is different with the frost formation conditions. As can be seen from Fig. 9, λ_{eff} is defferent by the frost formation types and stream velocity for the same density in the region, $\rho/\overline{\rho} > 1$, where the effect of factor (3) can be considered to be negligible. These large discrepancy of λ_{eff} due to the frost formation conditions cannot be filled up even if the water vapor diffusion in a frost layer is taken into account.

Fig. 10 shows a structural model which is presented here. This model is a parallel model which is composed of two parts of materials, ice columns and ice-air composite material, and the proportion of these two parts in a frost layer is dependent on the frost formation conditions. The frost layer grows on the basis of the frost columns, which generate in the crystal growth period, and the proportion of the frost columns which occupies the frost layer is different by the frost formation conditions; numbers of the frost columns are affected by stream velocity, and their thicknesses are different by t_s, ΔC and are related to the frost formation types. By this structural model, ice columns, with which frost columns are replaced, play a basic part of the frost structure, and the ice-air composite material plays a additional part of the frost layer growth. Namely porosity of the composite part is large in the early stage of frost deposition (at the end of the crystal growth period, the frost layer is composed of only ice columns), and decreases with time.

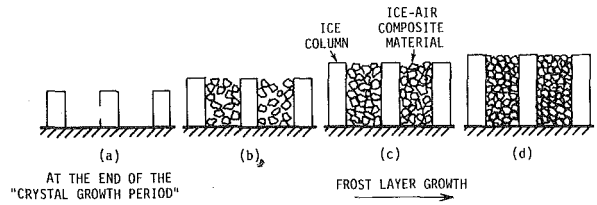

Fig. 10 Structural model of frost layer

Table 1 Values of α and α_{ice}

t_S (°C)	U_∞ (m/s)	α	α_{ice}
-18.6	2	0.06	0.013
	4	0.15	0.033
	6	0.19	0.042
-5.1	2	0.12	0.026
	4	0.29	0.064
	6	0.37	0.082

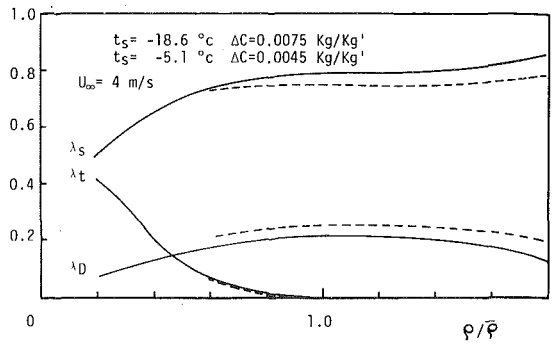

Fig. 11 Contributions of λ_s, λ_D, and λ_t to effective thermal conductivity

5.2 Prediction of Effective Thermal Conductivity. The effective thermal conductivity of a frost layer is predicted on the basis of the presented structural model. Heat is transfered in the parallel parts, ice columns, and ice-air composite material. Then the effective thermal conductivity is represented as follows, using the thermal conductivity of each part, λ_{ice} and λ_{comp}, and the cross-sectional area of the ice columns per unit area of the frost layer, α_{ice}.

$$\lambda_{eff} = \alpha_{ice} \cdot \lambda_{ice} + (1 - \alpha_{ice})\lambda_{comp} \tag{1}$$

Predicting the thermal conductivity of the ice-air composite material, λ_{comp}, the Woodside's equation is adopted here in taking account of the contribution of the water vapor diffusion to the air conductivity. The Woodside's equation [11] is

$$\frac{\lambda_g}{\lambda_{comp}} = 1 - \left(\frac{6s}{\pi}\right)^{1/3}\left[1 - \left(\frac{a^2-1}{a}\right)\ln\left(\frac{a+1}{a-1}\right)\right]$$

where

$$a = \left\{1 + \frac{4}{\pi\left(\frac{\lambda_{ice}}{\lambda_g} - 1\right)\left(\frac{6s}{\pi}\right)^{2/3}}\right\}^{1/2}, \qquad s = \frac{\rho - \rho_g}{\rho_{ice} - \rho_g} \tag{2}$$

and is valid for $0 \le s \le 0.5236$. Krisher (Woodside, 1958) gives the following expression for the effective conductivity of the air inside the pore of a material whose pore walls are wetted:

$$\lambda_g = \lambda_{air} + \frac{D}{RT}\left(\frac{P}{P - P_s}\right)\frac{dP_s}{dT} \cdot L_H \tag{3}$$

where

$$D = 0.086\,\frac{10000}{P}\left(\frac{T}{273}\right)^{2/3} \tag{4}$$

The theoretical results of the effective conductivities were calculated by using the foregoing equations, and were shown with the solid line in Fig. 9. The proportion of the cross-sectional area of the ice columns and the frost columns, α_{ice} and α, are represented, respectively, in Table 1. α_{ice} could be estimated from α, which was obtained by the photographic observation by the conversion of the frost column weight into the ice column weight. However, here, α_{ice} values were inversely deduced from the experimental data of λ_{eff} for $t_s = -18.6$°C, $u_\infty = 4$ m/s, and $\rho = 250$ kg/m^3 (shown by ⊡ in the figure), and the other values of α_{ice} were obtained using its conversion ratio.

From this figure, it is obvious that the theoretical results of λ_{eff} agree well with the experimental results in the region $\rho/\bar{\rho} > 1$. Particularly, the effects of the stream velocity and the frost formation types on λ_{eff} are represented clearly. Of course, some effects of the internal water vapor diffusion are recognized in the calculated results, but the large discrepancy of λ_{eff} at the same density cannot be filled up with its contribution. For a numerical comparisons of our results with others, some results are shown in the same figure. One of the results shows Yamakawa's numerical results [7], which has been calculated on the basis of the air-ice parallel model. In his calculation, the internal diffusion are taken into account, but its result only represents a simple correlation between λ_{eff} and ρ. The other two results, which are presented in Biguria's paper [4], are obtained on the basis of Woodside's model and the random mixture model, but these only give rough predictions as Yamakawa's does.

On the contrary, the present structural model, which is the composite parallel model composed of ice columns and ice-air composite material, fairly expresses the practical frost layer, and gives a good prediction of λ_{eff}. According to this model, the thermal conductivity decreases with increasing ice-air composite part at the same frost density, and it takes a minimum value when ice column disappears in a frost layer. At this point, the thermal conductivity coincides with the result obtained by the Woodside's model.

In the region, $\rho/\bar{\rho} < 1$, the theoretical values of λ_{eff} do not coincide with the experimental values due to neglecting the air turbulence contribution to λ_{eff}. The prediction of the thermal conductivity in this region is the subject for a future study considering the air turbulence.

In Fig. 11, the contributions of the frost structure, internal water diffusion, and the air turbulence to the effective conductivities (each of them are expressed with λ_s, λ_D, and λ_t) are represented against with $\rho/\bar{\rho}$ for the frost formation conditions, $C = 0.0075$ Kg/Kg′ and $u_\infty = 2$ m/s. λ_t was obtained on the assumption that the difference between the predicted value and the experimental value was owing to the turbulent effect on the effective conductivity. λ_s was calculated without taking account of the contribution of the water vapor diffusion to the air conductivity, and λ_D was given as a difference between λ_{eff} and λ_s. From this figure, it is obvious that the contributions of the each factor to the effective conductivity are varied with $\rho/\bar{\rho}$, and is fairly related with the frost layer growth.

6 Conclusion

Frost formation, whose nature changed dynamically and was different as a result of changes in various environmental parameters, was classified into several types according to the structure considering the regional position of the frost formation conditions in the ΔC-t_s plane.

Frost densities and effective thermal conductivities are clarified phenomenologically in connection with the classified frost formation types.

The structural model of a frost layer, which was composed of the ice columns and the ice-air composite parts, was presented and was verified to express the practical frost layer structure in comparing of the experimental results with the calculated results for the effective thermal conductivities.

References

1 Trammel, G. J., Little, D. C., and Killgore, E. M., "A Study of Frost Formed on a Flat Plate Held at Sub-Freezing Temperatures," *ASHRAE Journal*, Vol. 10, No. 7, 1968, pp. 42–47.

2 Brian, P. L. T., Reid, R. C., and Stah, Y. T., "Frost Deposition on Cold Surfaces," *Ind. Eng. Chem. Fundamentals*, Vol. 9, No. 3, 1970, pp. 375–380.

3 Reid, R. C., Brian, P. L. T., and Weber, M. E., "Heat Transfer and Frost Formation Inside a Liquid Nitrogen Cooled Tube," *AIChE Journal*, Vol. 12, Nov., 1966, pp. 1190–1195.

4 Biguria, G., and Wenzel, L. A., "Measurement and Correlation of Water Frost Conductivity and Density," *I. E. and C. Fundamentals*, Vol. 19, No. 1, Feb., 1970, pp. 129–138.

5 Hayashi, Y., Aoki, K., and Yuhara, H., "Study of Frost Formation in Forced Convection," *Trans. JSME*, Vol. 42, No. 355, 1976, pp. 885–892.

6 Jones, B. W., and Parker, J. D. "Frost Formation With Varying Environmental Parameters," JOURNAL OF HEAT TRANSFER, TRANS. ASME, Series C, Vol. 97, No. 2, 1976, pp. 255–259.

7 Yamakawa, N., and Ootani, S., "Heat and Mass Transfer in Frost Layer," *Kagaku Kōgaku*, Vol. 36, No. 2, 1972, pp. 197–203.

8 Kamei, S., Mizushina, T., Kifune, S., and Koto, T., "Research on the Frost Formation in a Low Temperature Cooler Condenser," *The Japanese Science Review*, Vol. 2, No. 3, 1952.

9 Yoshida, Z., "Heat Transfer by Water Vapor in Snow Cover," *Low Temperature Science*, Vol. 5, 1950, pp. 93–100.

10 Coles, W. D., "Experimental Determination of Thermal Conductivity of Low Density Ice," NACA Tech. Note, No. 3143, Mar., 1954.

11 Woodside, W., *Can. J. Phys.*, Vol. 36, 1958, p. 815.

A. Singh
General Electric Co.,
San Jose, Calif.

B. B. Mikic
W. M. Rohsenow
Massachusetts Institute of Technology,
Cambridge, Mass.

Effect of Superheat and Cavity Size on Frequency of Bubble Departure in Boiling

A theoretical model has been developed to predict the effect of cavity size (both radius and depth), and superheat on frequency of bubble departure by considering the effect on waiting time (time between the last bubble departure and appearance of the next one on the surface) and bubble growth time. An increase in cavity size or decrease in surface superheat results in longer waiting time and bubble growth time, thus causing a lower frequency. The model explains qualitatively the observed effect of superheat and cavity size on bubble departure frequency during pool boiling experiments with water on artificial cavities drilled by laser.

Introduction

The process of nucleate boiling from a heated surface consists of three major processes, e.g., bubble initiation, growth, and departure. A successful prediction of the nucleate boiling heat flux requires a precise evaluation of the bubble departure frequency, which directly depends upon the duration of the three forementioned processes. Bubble initiation and growth rates were extensively investigated in the last few decades. Determination of frequency of bubble departure has been divided into the following two major parts: determination of waiting time, i.e., the time between the last bubble departure and appearance of the next one on the surface, and determination of bubble growth time before it departs. Various theories have been presented in the past to predict waiting time and bubble growth time, e.g., Hsu [1],[1] Han and Griffith [2], Hatton and Hall [3], Mikic, Rohsenow, and Griffith [4], Plesset and Zwick [5], etc. Most of the existing theories are based on the assumption that there exists a hemispherical vapor bubble nucleus over the cavity in the boiling surface and at the beginning of the bubble cycle relatively cool bulk liquid which has replaced the void left by a departed bubble, surrounds this nucleus. As time goes on, the liquid is heated up through the transient conduction process, and the thermal layer grows. At the end of the waiting period t_w, when the thermal layer is of sufficient thickness, the nucleus starts growing. A one-dimensional conduction model was used without any consideration of evaporation or condensation at vapor-liquid interface of the nucleus. While it is conceivable that the time required to vaporize the quantity of liquid which penetrated the cavity may be insignificant for very small cavities such as natural cavities existing on a smooth surface, the liquid penetration may significantly delay the appearance of vapor nucleus at cavity mouth in case of large artificially made cavities drilled by laser. Theory presented in this investigation considers the effect of superheat and large cavity size on waiting time and frequency of bubble departure. A comparison between the predicted waiting time based on present theory and theory presented in reference [2] shows that liquid penetration may cause substantial increase (up to a factor of 2 to 3) in waiting time for large cavities (10^{-3}-in. mouth radius) and at small values of wall superheat. In the investigation by Singh, Mikic, and Rohsenow [6], effect of cavity depth on the nucleation from a cavity in boiling was recognized. A transient theoretical model was developed for the stability of a cylindrical cavity in boiling considering penetration of fluid, and transient inertial, viscous and heat transfer effects. Theory presented in this study is a simplified approximation of the model described in reference [6]. The present theory considers two dimensional transient conduction heat transfer and evaporation at the liquid vapor interface to estimate the waiting period as a function of surface superheat and cavity size (radius and depth). Bubble growth or contact time is evaluated using method described in reference [4].

Theory

Entrapment of Vapor in the Cavity. As the growing bubble departs from a cavity in boiling, the liquid in the vicinity of cavity moves into the cavity mouth. The vapor entrapment model described in reference [6] is shown in Fig. 1.

The penetration of liquid into the cavity depends upon contact

[1] Numbers in brackets designate References at end of paper.

Contributed by the Heat Transfer Division for publication in the JOURNAL OF HEAT TRANSFER. Manuscript received by the Heat Transfer Division October 4, 1976.

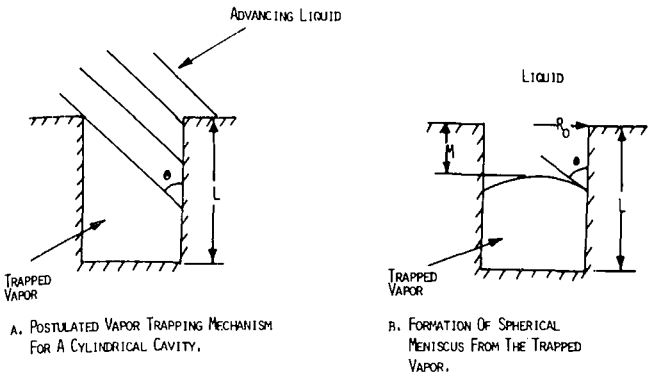

Fig. 1 Sketch of the postulated vapor trapping mechanism for a cylindrical cavity

angle ϕ, cavity radius R_0 and depth L. For $L/D \gg 1$, the meniscus penetration M (for given ϕ) is a function only of R_0 as is clear from Fig. 1. The postulated vapor trapping mechanism assumes a plane liquid vapor interface with an incidence angle ϕ on cavity walls. It is obvious that when $L > 2R \cot \phi$, volume of liquid penetrated into the cavity and hence liquid penetration M will depond only upon R_0. M was evaluated by equating the volumes of liquid inside the cavity shown in Figs. 1(a) and 1(b). At the completion of the entrapment process, the liquid vapor interface is assumed to take a spherical segment shape as shown in Fig. 1(b). If the wall superheat is high enough so that the cavity is in stable boiling, evaporation will eventually start at the meniscus which will recede toward the cavity mouth and finally come out of cavity as depicted in Fig. 2(a). The time elapsed between departure of the previous bubble and appearance of the new vapor nucleus on the surface (as shown in Fig. 2(a)) is defined as the waiting time, t_w in the present analysis (note that the time for penetration to occur is assumed to be zero). Beyond this point, the bubble grows until it finally detaches from the heated surface. The time of bubble growth is defined as the bubble contact time t_c. Thus the total bubble cycle time period τ is equal to the sum $(t_w + t_c)$.

In general the heat transfer at the liquid vapor interface may be influenced by convection effects in liquid and vapor; these effects have been neglected for simplicity in the present analysis and a two-dimensional transient conduction formulation has been used. The motion of liquid vapor interface may also cause compression or expansion of vapor trapped inside the cavity and thus may influence its thermodynamic state; this effect has also been neglected in the present analysis, however a more complete analysis of the effects of interface motion including the effects of liquid inertia and viscosity is provided in reference [8].

Fig. 2(a) shows a cavity of radius R_0 and depth L, which is assumed to be in stable boiling. The region of influence [2] of the bubble is shown extending up to $2R_0$ from the centerline of cavity. For analytical convenience, liquid layer of a finite thickness equal to $8R_0$ extending from the surface into the saturated bulk of liquid (at T_{sat}) is considered to be influenced by the transient heat transfer effects. The pressure of the vapor inside the cavity is assumed to remain constant at $P_{2\sigma}/R_0 = P_{bulk} + 2\sigma/R_0$, and the temperature of liquid-vapor interface at $T_{2\sigma}/R_0$, the saturation temperature at $P_{2\sigma}/R_0$. For simplicity

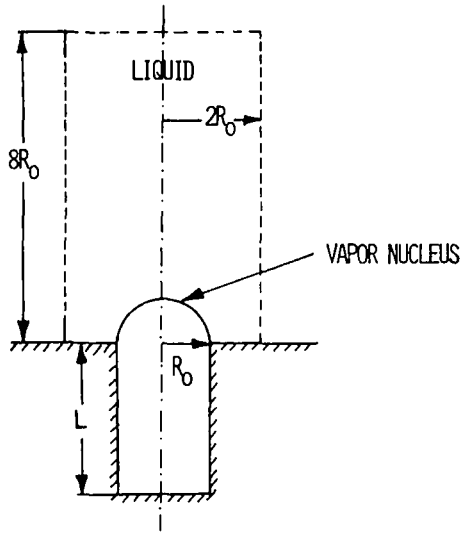

Fig. 2(a)

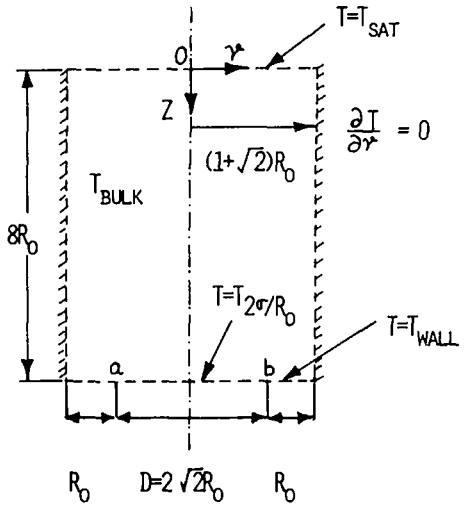

Fig. 2(b)

Fig. 2 Sketch of theoretical model for prediction of waiting time T_w

of solution the hemispherical surface of the liquid vapor meniscus is stretched into a circular plane surface ab, as shown in Fig. 2(b), such that the surface area of the circular surface ab is equal to the surface area of the hemispherical surface; thus, the new radius of circular plane meniscus is $\sqrt{2}R_0$. The region of influence of bubble is extended correspondingly to a radius $(1 + \sqrt{2})R_0$, beyond which the liquid is assumed to be isolated from the heat transfer effects of the sur-

Nomenclature

L = cavity depth, cm
f = frequency of bubble departure
g = gravitational constant
M = initial penetration of liquid into the cavity, Fig. 1(b)
P = pressure, dynes/cm^2
Q = heat, calories
R_0 = cavity radius, cm
t = time, s
t_c = bubble contact or growth time, s
t_w = waiting time, s
T = temperature, °C
ΔT = wall superheat, °C
v_{fg} = specific volume change at evaporation cm^3/gm
m_v = mass of vapor, gm
h_{fg} = latent heat of evaporation, cal/gm
v_g = specific volume of vapor, cm^3/gm
α = thermal diffusivity, cm^2/s
σ = surface tension, dynes/cm
τ = bubble time period $(t_w + t_c)$, s
ρ_ℓ, ρ_v = density of liquid and vapor, respectively, gm/cm^3

rounding liquid ($\partial T/\partial r = 0$). The boundary conditions in terms of temperature T of the liquid body are shown in Fig. 2(*b*), T_{wall} being the temperature of the surface. Just after the bubble departure, fresh liquid at T_{sat} rushes to the surface; this time is taken as $t = 0$ and $T = T_{sat}$ throughout the body of the liquid. Coordinates Z and r are selected as shown in Fig. 2(*b*).

Let $T(r, z, t)$ describe the temperature field at any r, z, and time t; then letting $\theta = T - T_{sat}$ and applying two-dimensional transient energy equation in cylindrical coordinates leads to the following equation

$$\frac{\partial\theta}{\partial t} = \alpha\left[\frac{1}{r}\frac{\partial}{\partial r}\left(r\frac{\partial\theta}{\partial r}\right) + \frac{\partial^2\theta}{\partial z^2}\right] \tag{1}$$

with initial condition,

$$\text{at } t = 0, \quad \theta = 0 \quad \text{at all } r \text{ and } z$$

and boundary conditions,

1 $\dfrac{\partial\theta}{\partial r} = 0$ at $r = R_0(1 + \sqrt{2})$

2 $\dfrac{\partial\theta}{\partial r} = 0$ at $r = 0$

3 θ = finite at $r = 0$

4 $\theta = 0$ at $Z = 0$

5 At $Z = 8R_0$

$$\theta = \frac{\theta_{2\sigma}}{R_0} = \frac{T_{2\sigma}}{R_0} - T_{sat} \quad \text{for } 0 \leq r \leq \sqrt{2}R_0$$

$$\theta = \theta_w = T_w - T_{sat} \quad \text{for } \sqrt{2}R_0 \leq r \leq (1 + \sqrt{2})R_0$$

Solution

The complete solution can be written in the following form:

$$\theta = \theta_s + \theta_t$$

or

$$\theta = bz + \sum_{n=1}^{\infty} a_n \sinh(\alpha_n z) J_0(\alpha_n r) + \sum_{m=1}^{\infty} C_{0m} e^{-\alpha\gamma_m^2 t} \sin(\gamma_m z) + \sum_{n=1}^{\infty}\sum_{m=1}^{\infty} C_{nm} e^{-\alpha(\alpha_n^2+\gamma_m^2)t} J_0(\alpha_n r)\sin(\gamma_m z) \tag{2}$$

where α_n's are the roots of equation, $J_1[\alpha_n(1 + \sqrt{2})R_0] = 0$, for $n = 1, 2, 3, \ldots, \infty$,

$$\gamma_m = \frac{m\pi}{8R_0}, \; m = 1, 2, \ldots, \infty$$

$$a_n = \frac{\dfrac{J_1(\sqrt{2}R_0\alpha_n)}{\alpha_n}\sqrt{2}R_0\left[\dfrac{\theta_{2\sigma}}{R_0} - \theta_w\right]}{\dfrac{(1+\sqrt{2})^2}{2}R_0^2[J_0^2|\alpha_n(1+\sqrt{2})R_0|]\sinh(8\alpha_n R_0)}$$

$$C_{0m} = \frac{-b/\gamma_m^2[-m\pi\cos(m\pi)]}{4R_0}$$

$$C_{nm} = \frac{a_n\gamma_m\cos(8R_0\gamma_m)\sinh(8R_0\alpha_n)}{4R_0(\alpha_n^2 + \gamma_m^2)}$$

and

$$b = \frac{\theta_w + \theta_{2\sigma}/R_0}{16R_0}$$

Heat flux to the meniscus (at $z = 8R_0$) from the liquid is given by:

$$(q/A)_{z=8R_0} = -\kappa\left(\frac{\partial\theta}{\partial z}\right)_{z=8R_0} \quad \text{for } 0 \leq r \leq \sqrt{2}R_0$$

Total amount of heat transferred to the meniscus up to time t_w could be found by integrating the foregoing.

$$Q(t_w) = \int_0^{t_w}\int_0^{\sqrt{2}R_0} -\kappa\left(\frac{\partial\theta}{\partial z}\right)_{z=8R_0} 2\pi r\, dr\, dt \tag{3}$$

Substituting equation (2) in equation (3) and carrying out the integration, one obtains:

$$Q(t_w) = 2\pi\kappa R_0^2 t_w b + 2\pi\kappa R_0^2 \sum_{m=1}^{\infty} C_{0m}\gamma_m\cos(m\pi)\left[\frac{e^{-\alpha(\gamma_m^2)t_w} - 1}{\alpha\gamma_m^2}\right] + \int_0^{t_w}\left[-\sum_{n=1}^{\infty} 2\pi\kappa a_n\sqrt{2}R_0\cosh(8R_0\alpha_n)J_1(\alpha_n\sqrt{2}R_0)\right]dt + \int_0^{t_w}\left(\frac{-2\pi\kappa}{\alpha_n}\right)\sum_{n=1}^{\infty}\sum_{m=1}^{\infty} C_{nm}\gamma_m(\sqrt{2}R_0) \times \cos(m\pi)J_1(\alpha_n\sqrt{2}R_0)e^{-\alpha(\alpha_n^2+\gamma_m^2)t}dt$$

or,

$$Q(t_w) = -2\pi\kappa b R_0^2 t_w + \frac{2\pi\kappa R_0^2}{\alpha}\sum_{m=1}^{\infty} C_{0m}\gamma_m\cos(m\pi)\frac{e^{-\alpha\gamma_m^2 t_w} - 1}{\gamma_m^2} - 2\pi\kappa\sqrt{2}R_0\left[\sum_{n=1}^{\infty} a_n\cosh(8R_0\alpha_n)J_1(\alpha_n\sqrt{2}R_0)t_w\right] + \frac{2\pi\kappa\sqrt{2}R_0}{\alpha_n}\left[\sum_{n=1}^{\infty}\sum_{m=1}^{\infty} C_{nm}\gamma_m\cos(m\pi)J_1(\alpha_n\sqrt{2}R_0) \times \frac{e^{-\alpha(\alpha_n^2+\gamma_m^2)t_w} - 1}{\alpha(\alpha_n^2 + \gamma_m^2)}\right] \tag{4}$$

Mass of vapor generated by heat $Q(t_w)$,

$$m_v = \frac{Q(t_w)}{h_{fg}} \tag{5}$$

where h_{fg} and other properties of vapor are evaluated at saturated vapor pressure $P_{2\sigma}/R_0$. Volume of this vapor, v_{vap} is equal to $m_v v_g$. If the liquid penetrates into the cavity up to a distance M from the mouth (Fig. 1(*b*)) the vapor nucleus will appear on the surface when, $m_v v_g = \pi R_0^2 M + \frac{2}{3}\pi R_0^3$, which is roughly the volume of liquid to be displaced by vapor for the vapor nucleus to appear at cavity mouth as shown in Fig. 2(*a*). Hence, the equation

$$m_v v_g = \frac{Q(t_w)v_g}{h_{fg}} = \pi R_0^2 M + \frac{2}{3}\pi R_0^3 \tag{6}$$

implicitly gives t_w in terms of M, R_0, and T_w.

Estimation of the Bubble Contact Time, t_c

For a growing bubble on a heated surface at superheat $\Delta T_w = T_w - T_{sat}$ in a liquid at temperature T_b and pressure p_∞ (T_{sat} = sat temp at P_∞), Mikic, Rohsenow, and Griffith [4] obtained the following expression:

$$R^+ = (t^+)^{1/2}\left(1 - \Delta\theta\left[\left(1 + \frac{t_w^+}{t^+}\right)^{1/2} - \left(\frac{t_w^+}{t^+}\right)^{1/2}\right]\right) \tag{7}$$

where

$$R^+ = \frac{AR}{B^2}, \qquad R = \text{radius of bubble at time } t.$$

$$A = \left(\frac{\pi}{7}\frac{h_{fg}\rho_v\Delta T_w}{\rho_\ell T_{sat}}\right)^{1/2}$$

$$B = \left(\frac{12}{\pi}\alpha_\ell\right)^{1/2} J_a, \qquad J_a = \frac{\Delta T_w\rho_\ell C_\ell}{h_{fg}\rho_v}$$

$$t^+ = \frac{A^2 t}{B^2}$$

$$t_w^+ = \frac{A^2 t_w}{B^2}$$

$$\Delta\theta = \frac{T_w - T_{bulk}}{T_w - T_{sat}}$$

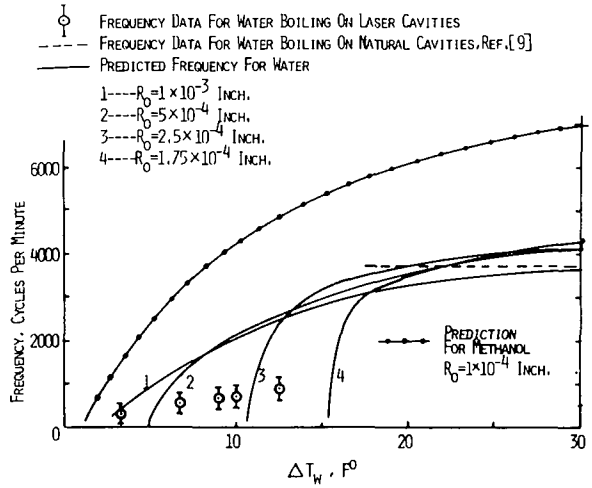

Fig. 3 Effect of wall superheat and cavity size on bubble departure frequency

when $t_w^+ \gg t^+$, equation (7) reduces to

$$R = B\sqrt{t}\,. \tag{8}$$

The condition $t_w^+ \gg t^+$ strictly holds when ΔT_w is small as happens during nucleation from deep laser cavities having large depth/diameter ratio [6]. When ΔT_w is large, the previous inequality does not hold and time t predicted by equation (8) for a given bubble radius R, is an underestimation of the real bubble growth time [4]. However, equation (8) will be used to estimate the bubble contact time and qualitative effect of wall superheat on frequency in the following analysis. It will be seen later that this approximation is fortuitously good when compared with experimental data shown in Fig. 3. Staniszowski [7] suggested the following empirical equation for the bubble departure radius, R_d, when breaking off the heating surface.

$$R_d = 12.85\phi \left(\frac{2\sigma}{g(p_l - p_v)}\right)^{1/2} (1 + 164.6\dot{R}) \tag{9}$$

where R_d is in cm, ϕ in radians and $\dot{R}$ in cm/s. Evaluating $\dot{R}$ from equation (8) and substituting in equation (9) leads to the following expression for the bubble contact time t_c,

$$B\sqrt{t_c} = 12.85\phi \left(\frac{2\sigma}{g(p_l - p_v)}\right)^{1/2} \left(1 + 82.3\frac{B}{\sqrt{t_c}}\right) \tag{10}$$

Results of Numerical Analysis

For cavities having large depth/diameter ratio, ($L/D \gg 1$), penetration M (Fig. 1(*b*)) of liquid with a given contact angle ϕ is a function of cavity mouth radius R_0 only. It was shown in reference [8] that for water the effect of cavity depth L decreases asymptotically when $L > 2R_0$. Hence, a cavity with $L > 2R_0$ very nearly behaves as a very deep cavity (i.e., $L/D \gg 1$). Hence, for such cavities waiting time t_w for a given fluid varies with cavity size R_0 and wall superheat T_w. Results of some numerical calculations for such cavities are presented in Fig. 3 which shows the effect of cavity size R_0 and wall superheat ΔT_w or predicted frequency. For large ΔT_w, t_w is small as compared to t_c, hence frequency $f = 1/(t_w + t_c)$ depends only upon t_c, which on the other hand is a weak function of wall superheat. As ΔT_w decreases, t_w increases and frequency decreases; the rate of decrease becoming faster as ΔT_w approaches $\Delta T_{2\sigma}/R_0$. The cavity with larger size R_0 has a smaller $\Delta T_{2\sigma}/R_0$ and smaller rate of decrease in frequency with superheat.

The effect of varying ΔT_w in boiling with methanol for $R_0 = 0.001$ in. is also shown in Fig. 3. Results of the numerical calculation, plotted in Fig. 3, were obtained using equation (6) for t_w and equation (10) for t_c. First two terms of the series in equation (6) were used for estimating t_w, the effect of additional terms is expected to be small.

Experimental Data

Boiling data were taken with water on artificial cavities drilled by laser on a copper surface [6]. Mouth radius of the laser cavities R_0, as observed microscopically, varied from 4.445×10^{-4} to 6.35×10^{-4} cms. (1.75×10^{-4} to 2.5×10^{-4} in.) and depth to diameter (L/D) ratio was in the range of about 2 to 4. Boiling data were taken with decreasing heat flux and frequency of bubble departure was measured using a variable frequency stroboscope. Details of experiments are given in reference [8]. Frequency data taken at low heat flux values is plotted in Fig. 3. The observed frequency decreases with a decrease in superheat, as predicted by the theoretical model. Moreover, the frequency observed on artificial laser cavities is much smaller than that measured in reference [9] for water boiling on a smooth surface, at higher heat flux values of 1.514–6.307 W/cm^2 (Fig. 3). This could be attributed to the fact that most of the natural cavities existing on an ordinary smooth surface are smaller in size. Frequency data could not be taken successfully with Methanol since the stroboscope method used was not precise enough to measure the observed large values of frequencies with methanol.

Prediction of theoretical model for sizes $R_0 = 4.445 \times 10^{-4}$–$6.35 \times 10^{-4}$ cms. (1.75×10^{-4} and 2.5×10^{-4} in.) which represent correspondingly the minimum and maximum sizes of laser cavities are plotted in Fig. 3. Comparison with observed frequency is only qualitative since the laser cavities had arbitrary shapes rather than being cylindrical, as assumed in the analysis. It should be pointed out that the more commonly accepted theories, such as presented in reference [2] lead to an underestimation of the waiting time period by a factor of 2 to 3 at lower superheat values, as compared to the present theory based on liquid penetration; this will lead to further deviation in prediction of the observed frequency values shown in Fig. 3. Effect of liquid penetration on cavity stability in boiling with more wetting fluids such as organics are even more significant as compared to water, as discussed in reference [8].

Summary and Conclusions

A theoretical model has been developed to predict the frequency of bubble departure in nucleate boiling considering the effect of surface superheat and cavity size. An increase in cavity size or decrease in superheat causes a longer waiting time and bubble growth time with a consequent decrease in frequency. The model explains qualitatively the observed effect of superheat and cavity size on bubble departure frequency in boiling with water.

Acknowledgment

The authors wish to express gratitude to the U.S. Army Research Office for the financial support of this work.

References

1 Hsu, Y. Y., "On the Size Range of Active Nucleation Cavities on a Heating Surface," JOURNAL OF HEAT TRANSFER, TRANS. ASME, Series C, Vol. 84, No. 3, Aug. 1962, pp. 207–216.

2 Han, C. Y., and Griffith, P., "The Mechanism of Heat Transfer in Nucleate Pool Boiling," *International Journal of Heat and Mass Transfer*, Vol. 8, No. 6, pp. 887–904.

3 Hatton, A. P., and Hall, I. S., "Photographic Study of Boiling on Prepared Surfaces," Paper No. 115, *3rd International Heat Transfer Conference*, Chicago, 1966.

4 Mikic, B. B., Rohsenow, W. M., and Griffith, P., "On Bubble Growth Rates," *International Journal of Heat Mass Transfer*, Vol. 13, pp. 657–666, 1970.

5 Plesset, M., and Zwick, S. A., "The Growth of Vapor Bubbles in Superheated Liquids," *Journal of Applied Physics* Vol. 25, pp. 493, 1954.

6 Singh, A., Mikic, B. B., and Rohsenow, W. M., "Active Sites in Boiling," Paper No. CSChE/CSME 75-Ht-11, Presented at 15th National Heat Transfer Conference, San Francisco, Aug. 1975.

7 Staniszowski, B. B., "Nucleate Boiling Growth and Departure," Technical Report No. 16, DSR 7673, Heat-Transfer Laboratory, M.I.T., Aug. 1959.

8 Singh, A., "Effects of Surface Conditions on Nucleation and Boiling Characteristics," ScD thesis, Department of Mechanical Engineering, M.I.T., Sept. 1974.

9 Tolubinskey, V. I., and Ostrovsky, J. N., "On the Mechanism of Boiling Heat Transfer (Vapor Bubbles Growth Rate in the Process Boiling of Liquids, Solutions, and Binary Mixtures)," *International Journal of Heat and Mass Transfer*, Vol. 9, 1966, pp. 1463–70.

V. Dhir,
Asst. Professor.

I. Catton,
Assoc. Professor.

Energy and Kinetics Department,
University of California, Los Angeles, Calif.

Dryout Heat Fluxes for Inductively Heated Particulate Beds[1]

Experimental observations of the dryout heat fluxes for inductively heated particulate beds have been made. The data were obtained when steel and lead particles in the size distribution 295–787 microns were placed in a 4.7-cm dia pyrex glass jar and inductively heated by passing radio frequency current through a 13.3-cm dia multiturn work coil encircling the jar. Distilled water, methanol and acetone were used as coolants in the experiments, while the bed height was varied from 1.9 to 8.9 cm. Different mechanisms for the dryout in deep and shallow beds have been identified. Dryout in shallow beds is believed to occur when the vapor velocity in the gas jets exceeds a certain critical velocity at which choking of the vapor, leading to obstruction in the flow of the liquid towards the bed occurs. However, deep beds dry out when gravitational force can no longer maintain a downward coolant flow rate necessary to dissipate the heat generated in the bed. Finally, the heat flux data of the present investigation and that from two previous investigations made at Argonne Laboratory and at UCLA have been correlated with semitheoretical correlations based on the proposed hydrodynamic models.

Introduction

A considerable amount of work is being done at this time to study various safety aspects of commercial liquid metal fast breeder reactors. The aim of these research activities is to provide a better design basis for the reactors so that risks to public health in case of a hypothetical core disruptive accident are minimized. The study of the removal of decay heat after a hypothetical accident in which the core looses its integrity is one of many such activities.

This paper deals with the determination of dryout heat fluxes for beds of heat generating particles. Such beds can be formed on various horizontal surfaces in the primary reactor containment after the molten fuel solidifies on interaction with sodium. If the heat generation rate in the bed exceeds a certain critical value, the bed would dry out because of an insufficient supply of coolant and the fuel particles will eventually remelt. The remelting of the fuel particles can lead to failure of the supporting steel structure, and in turn result in loss of integrity of the primary containment. The limiting value of the heat generation rate at which a bed dries out is thus an essential safety consideration.

The earliest work on heat transfer from beds of heat generating particles was done by Holman, Moore, and Wong [1][2] and Young and Holman [2]. In these studies, stainless steel particles were inductively heated and the convective and nucleate boiling heat transfer mechanisms were studied when the particulate bed was fluidized with a stream of water. The magnitude of the heat fluxes attained in their studies was much lower than needed for the bed to dry out and the flow configuration was entirely different than the present study.

The first study most pertinent to the present work was made at Argonne National Laboratory by Gabor, Sowa, Baker, and Cassulo [3]. Gabor, et al., measured the dryout heat fluxes for sodium or water cooled UO_2 particulate beds. The beds were either bottom heated or volumetricly heated. In the bottom heated beds, the base of the bed was heated by flame or by a glass blower's torch and the heat flux was measured by noting the temperature distribution in the base copper plates. The heat flux was also measured by noting the temperature rise and flow rate of the coolant in the reflux condenser. The bed was believed to have dried out when its temperature was found to increase rapidly without an increase in heat input. The volumetricly heated tests were performed by generating heat in the coolant (joule heating) rather than in the particles. This procedure was justified on the presumption that the dryout heat flux was dictated by the gross properties of the bed rather than details of the heat exchange mechanism between particles and the coolant. In these tests, the heat flux was measured by noting the power input to the electrodes.

The authors at Argonne relate that in volumetricly heated tests with sodium, no actual dryout was achieved. The reported heat flux values are the maximum, at which increased voltage applied to the electrodes

[1] This work is being supported by the Reactor Safety Research Division of the Nuclear Regulatory Commission under Agreement No. AT (04-3)-34 P.A. 223, Mod. I.

Contributed by The Heat Transfer Division and presented at the Winter Annual Meeting, Houston, Texas, November 30–December 5, 1975 of THE AMERICAN SOCIETY OF MECHANICAL ENGINEERS. Revised manuscript received by The Heat Transfer Division November 12, 1976. Paper No. 75-WA-HT-19.

[2] Numbers in brackets designate References at end of paper.

resulted in no further increase in the heat flux. Thus, their sodium data may be lower than the actual dry-out heat flux. Also, in the experiments with UO_2 and sodium, no direct measurements of the porosity of the bed could be made. The porosity was measured by radiographing the bed and any experimental and data reduction errors are absorbed in the reported values of porosity.

The Argonne study revealed that vapor escaped from the particulate bed in narrow vertical channels located discretely in the bed. In shallow beds, the vapor channels were found to extend through the full depth of the bed whereas in deep beds, the channels were developed in the top portion only. The particles were levitated in the region containing vapor channels but remained packed in the region without vapor channels. The dryout heat fluxes were found to be much higher in shallow beds than in deep beds. Some of the bottom heated and volume heated bed data of reference [3] are reproduced in Fig. 1.

More recently Keowen [4] studied dryout heat fluxes from beds of inductively heated steel and lead particles. Keowen's gross observations are similar to those of Gabor, et al. [3], but the values of the dryout heat fluxes for beds of the same height and porosity are much higher as is shown in Fig. 1.

In the present work, an effort has been made to explain the difference in the magnitude of the dryout heat flux in these two previous studies [3, 4]. To do so, we start with the development of theoretical models for deep and shallow beds. The beds are categorized as deep and shallow beds depending on whether the vapor channels extend only part way into the bed or reach the bottom of the bed. We also obtain new data for inductively heated particulate beds under carefully controlled experimental conditions. The data are obtained at atmospheric pressure and with different coolants and for a range of particle sizes and porosities. To test the suggested correlation some of the data are also obtained at pressures less than 1 atm.

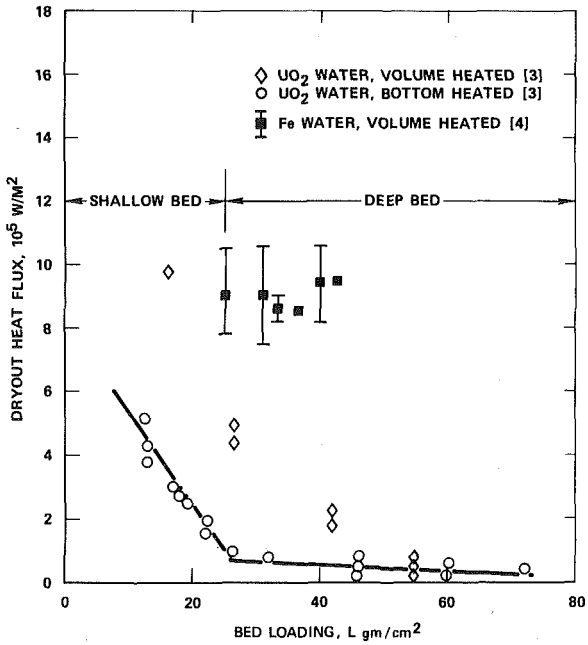

Fig. 1 Dryout heat flux for bottom heated and volume heated UO_2 water debris bed [3]

Analysis

The formation of vapor flow paths in deep and shallow beds is shown in Fig. 2. These configurations are based on many visual observations. The visual observations showed that vapor formed in the bed simply cuts its way through the bed and moves in paths which appear similar to holes drilled in a solid. The vapor channels in the lower portion of a deep bed are very thin. As the vapor moves upward the vapor channels grow in size. The vapor channels are well formed in the upper region of a deep bed and the vapor flow induces drag on the particles. The particles are levitated and conditions similar to a fluidized bed exist in this region. However, because of little or no vapor drag the particles in the lower region of the deep bed remain packed.

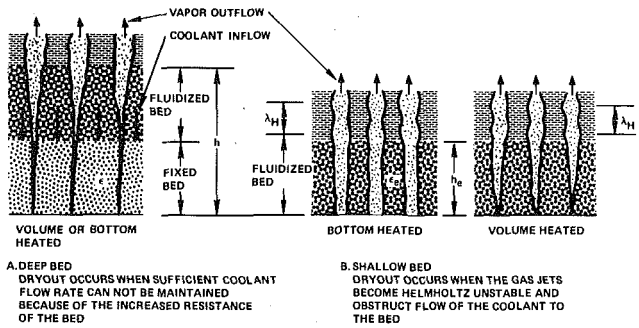

Fig. 2 Deep and shallow bed models for dryout heat flux

Nomenclature

A_b = cross-sectional area of the bed
A_c = cross-sectional area of the gas jets supported by an area A_b of the bed
C_2, C_3
C_4, C_5 = experimental constants
D = jar diameter
D_c = vapor jet or channel diameter at the top of the bed
d = particle diameter
$\bar{d}$ = mean particle diameter
$\bar{d}'$ = dimensionless mean particle diameter, $\bar{d}/\sqrt{\sigma/g(\rho_f - \rho_g)}$
f = friction factor
g = gravitational acceleration
h = initial bed height
h_e = expanded bed height
h' or h_e' = dimensionless bed height, h or $h_e/\sqrt{\sigma/g(\rho_f - \rho_g)}$
h_{fg} = latent heat of vaporization of the coolant
h_t = transitional bed height
K = permeability of the bed
K_1 = Kozeny factor, $\epsilon^3/(1-\epsilon)^2$
L = bed leading, gm/cm^2
M = dimensionless number, $\rho_f^{1/2}\rho^{3/4}/\mu_f[g(\rho_f - \rho_g)]^{1/4}$
n = number of vapor channels supported by an area A_b of the bottom heated bed
P = system pressure
Q_v = volumetric heat generation rate
q_{bd} = dryout heat flux in a bottom heated deep bed
q_{bs} = dryout heat flux in a bottom heated shallow bed
q_{vd} = dryout heat flux in a volume heated deep bed
q_Z = Zuber's predicted value for peak heat flux on flat plates
U = velocity of gas in the jet
U_c = critical velocity of gas in the jet
U_c' = dimensionless critical gas velocity in the jet, $U_c/\sqrt[4]{(\rho_f - \rho_g)g\sigma/\rho_g^2}$
u = superficial velocity of the coolant in the packed bed
y = position coordinate perpendicular to the bed cross-section
Γ = ratio of liquid and vapor densities, ρ_f/ρ_g
ϵ = initial porosity of the bed
ϵ_e = porosity of the expanded bed
λ_c = critical wavelength
λ_H = Helmholtz unstable wavelength
μ_f = liquid viscosity
ρ_f, ρ_g = saturated liquid and vapor densities, respectively
σ = surface tension between liquid and its vapor

In shallow beds, the vapor channels are fully developed throughout the depth of the bed, the particles are fluidized and the entire bed is in an expanded state.

Transition from a deep to shallow bed occurs when the channels start to develop throughout the bed. The transition height at which this occurs depends on the vapor volume flux from the bed and on the mean diameters of the particles. In this work we will fix the transition height either from visual observations or by noting a sharp increase in the dryout heat flux when the bed height is decreased slightly.

Deep Beds. The dryout heat flux in a deep bed is controlled by the maximum possible coolant flow rate through the lower packed region of the bed. The downward flow rate of the coolant at the top surface of the bed adjusts itself to balance the outflow of vapor from the bed. The difference in density between the liquid and vapor phases acts as the driving force for the downward flow of the coolant. The liquid encounters minimal resistance in the upper fluidized portion of the bed. However, in the packed bed region the liquid has to flow through the interstitial spaces between the particles and thus faces a larger resistance. The deep bed dries out at a particular section in the lower region of the bed where gravity can no longer maintain the flowrate necessary to compensate for the evaporation rate. Although, the vapor volume flux is much larger than the liquid volume flux, the resistance to vapor flow does not limit the heat flux because the vapor moves in well-defined paths which offer much less flow resistance. Now, if we assume that:

(i) The liquid flow velocity is small so that the inertia of the liquid can be neglected.

(ii) The vapor is inviscid and the relative velocity of vapor is not large so that the upward flow of vapor introduces little or no drag on the coolant.

(iii) The cross-sectional area occupied by the vapor in the packed bed region is negligibly small. (The assumptions (ii) and (iii) are true only as long as vapor volume fluxes are not excessively large. This condition is met in the lower region of the bed only.)

(iv) The particles are spherical and the mean diameter of the particles represent a weighed average for all the particles in a given size range. The integrated momentum equation for the flow of coolant through the lower packed bed can be written as[3]

$$\frac{\mu_f}{K}\frac{u}{(\bar{d})^2} = (\rho_f - \rho_g)g \tag{1}$$

where K is the permeability of the bed and $\bar{d}$ is the mean diameter of the particles. The mean diameter of the particles has been chosen as the characteristic length. The average superficial velocity, u, of the coolant at a cross section of the bed can be written from equation (1) as

$$u = \frac{K}{\mu_f}(\rho_f - \rho_g)g(\bar{d})^2 \tag{2}$$

The dependence of the permeability, K, of the bed on the porosity, ϵ, of the bed has been shown by Kozeny [5] to be

$$K \sim \frac{\epsilon^3}{(1-\epsilon)^2} \tag{3}$$

Equation (3) has also been verified experimentally by Carman [6]. Equation (2) for the superficial velocity does not contain a nonlinear term in $\bar{d}$, which has been demonstrated by Ergun [7] to represent kinetic energy losses. For very small coolant velocities expected in the present situation, the neglect of the kinetic energy term does not impose serious error and we assume that the gravitational force mainly acts to overcome the viscous drag of the particles. Thus equation (2) can be rewritten as

$$u = C_1 \frac{\epsilon^3}{(1-\epsilon)^2}\frac{g(\rho_f - \rho_g)(\bar{d})^2}{\mu} \tag{4}$$

In equation (4) C_1 will be established from the experimental data. The constant C_1 is not taken to be that established by Ergun [7] for flow through packed beds; because we do not know the magnitude of the effective resistance to downcoming coolant due to nucleation and convective processes occurring at the surface of the particles and in the pores of the bed. A deep bed will dry out when the evaporation rate is greater than what can be sustained by the superficial velocity as given by equation (4).

Bottom Heated. The energy transferred from the heater is utilized in evaporating the liquid next to the heater surface. The maximum rate at which this liquid can be replenished is given by equation (4). An energy balance at the surface of the heater results in an expression for the dryout heat flux from the bottom heated deep bed as

$$q_{bd} = \rho_f h_{fg} u \tag{5}$$

or

$$q_{bd} = C_1 \frac{\epsilon^3}{(1-\epsilon)^2}\frac{g(\rho_f - \rho_g)\rho_f h_{fg}}{\mu}(\bar{d})^2 \tag{6}$$

Next we nondimensionalize equation (6) with Zuber's [8] expression for the peak heat flux on a flat plate heater.

$$q_Z = \frac{\pi}{24}\sqrt{\rho_g} h_{fg}[\sigma g(\rho_f - \rho_g)]^{1/4} \tag{7}$$

No physical significance is attached to this nondimensionalization except that as the bed height goes to zero, we would expect the dryout heat flux for bottom heated beds to approach the flat plate value. The dimensionless form of equation (6) is

$$\frac{q_{bd}}{q_Z} = C_2 K_1 \Gamma^{1/2}(\bar{d}^*)^2 M \tag{8}$$

Equation (8) contains all the dimensionless groups (defined in the Nomenclature) formed out of the basic physical variables of the problem except the ratio of the width and depth of the bed to the particle diameter. These ratios are unimportant as long as the particle diameter is much smaller than either the depth or width of the bed. It may be noted here that the dryout heat flux is thought to be independent of the bed height as long as the bed is deep enough so that a deep bed model holds good.

Volumetrically Heated. The heat is assumed to be generated uniformly in each particle and is dissipated to form vapor at the surface of the particles. Experimentally it may not be possible to obtain uniform heat generation throughout the bed and thus the assumed uniformity should be considered as an approximation which should be verified. The demand on the coolant flow rate is maximum at the top of the bed and decreases in proportion to the bed height; being zero at the bottom of the bed. The average superficial velocity in the bed is half of what it would be if there was no heat generation in the particles but an equivalent amount of heat was dissipated at the bottom. The superficial velocity corresponding to the dryout heat flux at a cross section can be assumed to be proportional to the maximum or average superficial velocity in the bed and an expression similar to equation (8) can be written for dimensionless dryout heat flux in a volumetrically heated deep bed

$$\frac{q_{vd}}{q_Z} = \frac{Q_v h(1-\epsilon)}{q_Z} = C_3 K_1 (\bar{d}^*)^2 \Gamma^{1/2} M \tag{9}$$

In equation (13), Q_v, is the volumetric heat generation rate in the bed and C_3 is an experimental constant, which should probably be twice of C_2.

The development of equations (8) and (9) is based on assumptions listed earlier at different places in the text. In a real situation any deviations from these assumptions would limit the usefulness of these semitheoretical equations.

Shallow Beds. In shallow beds, the particles are in a fluidized state and the coolant has an easy access to the particles or to the bottom of the bed, through the region not occupied by the channels. The flow of vapor in the channels is similar to that in a pipe. A hydrostatic pressure head equal to the bed height drives the vapor

[3] Symbols not explained here are those in common use and are defined in the Nomenclature.

through these channels. The flow configuration in the channels within the bed is very stable. However, if the vapor velocity exceeds a certain critical value, the vapor jets in the overlying liquid may become unstable and lead to choking of the flow. The blockage of the vapor flow through the channels would inhibit the flow of the coolant into the bed. A deficiency in the liquid inflow to the bed will lead to the dryout of a local region in the bed which may grow in size with time. The dryout heat flux in shallow beds is, thus, limited by the maximum or critical velocity of the vapor jets. To determine the dryout heat flux, we follow an approach similar to that of Zuber [8] for the peak heat flux on flat plate heaters.

Bottom Heated. The channels are formed at the heater surface and maintain a nearly uniform diameter throughout the bed. If we assume that the density of the bed is equal to the density of the liquid minus the density of the vapor, the vapor velocity in the channels can be written as

$$U^2 = \frac{2D_c}{4f}\frac{(\rho_f - \rho_g)g}{\rho_g} \tag{10}$$

where D_c is the diameter of the channel or the jet and f is the friction coefficient. The value of the friction coefficient is not known apriori. Pipe flow values cannot be used as suggested by Gabor, et al. [3] because some particles will be entrained by the vapor, thereby causing the effective resistance to flow of vapor to increase.

The vapor velocity at which the gas jets in an inviscid liquid become Helmholtz unstable [9] can be written as

$$U_c = \sqrt{\frac{2\pi\sigma}{\rho_g \lambda_H}} \tag{11}$$

In equation (11) λ_H is the Helmholtz unstable wavelength. As the upper region of the bed is highly turbulent, it is difficult to know what wavelength will be dominant at the liquid-vapor interface. In the absence of any strong reason for choosing a particular wavelength at the jet interface, we assume that the dominant wavelength is the critical Rayleigh wavelength (equal to circumference to the jet). The critical vapor velocity through the channel can then be written as

$$U_c = \sqrt{\frac{2\sigma}{\rho_g D_c}} \tag{12}$$

Solving equations (10) and (12) simultaneously for U_c and D_c gives

$$U_c = \sqrt[4]{\frac{(\rho_f - \rho_g)g\sigma}{\rho_g{}^2 f}}; \quad D_c = 2 \cdot \sqrt{f} \cdot \sqrt{\frac{\sigma}{(\rho_f - \rho_g)g}} \tag{13}$$

From equation (13) it is seen that the surface tension and buoyant forces determine the characteristic length for the shallow beds.

If A_c is the area of cross section of a vapor channel and n is the number of vapor channels supported by an area A_b of the bottom heater, the energy balance at the surface of the heater results in an expression for the dryout heat flux to be

$$q_{bs} = \frac{nA_c}{A_b} h_{fg} \sqrt{\rho_g}\,[\sigma(\rho_f - \rho_g)g/f]^{1/4} \tag{14}$$

Nondimensionalization of equation (14) with Zuber's flat plate value results in

$$\frac{q_{bs}}{q_Z} = \frac{24n}{\pi}\frac{A_c}{A_b}\frac{1}{\sqrt[4]{f}} \tag{15}$$

The derivation of maximum heat flux on flat plates is based on Taylor and Helmholtz instabilities where as in the shallow bed model we use only Helmholtz instability to determine the maximum vapor velocity in the jets. The vapor jet spacing in the two cases is determined from different considerations and as such, the peak heat flux on flat plate should only be considered as a convenient nondimensionalizing parmeter.

Equation (15) in its present form is of little use as in reality it is very difficult to count precisely the number of vapor channels in the bed. However, an alternate and more useable form can be obtained if we make a volumetric summation for the expanded bed. The total volume of the expanded bed is the sum of the volume occupied by the vapor channels, the volume of the particles and the volume of the pores in the region of the bed not occupied by the vapor chnnels. If h and h_e are the initial and expanded bed heights, respectively, and ϵ and ϵ_e are the initial bed porosity and the expanded bed porosity in the region not occupied by the vapor channels, the total volume of the bed can be written as

$$A_b h_e = nA_c h_e + A_b h(1 - \epsilon) + \epsilon_e(A_b - nA_c)h_e \tag{16}$$

or

$$\frac{nA_c}{A_b} = \left[1 - \frac{h(1 - \epsilon)}{h_e(1 - \epsilon_e)}\right] \tag{17}$$

The second term on right-hand side of equation (17) represents the ratio of the initial potential energy of the bed to the potential energy of an expanded bed having a uniform porosity ϵ_e. It is well known that an ideally fluidized bed has the maximum potential energy. If we accept the hypothesis that the process would try to optimize itself, it follows that once a bed is fluidized, it would try to attain this maximum value irrespective of the bed height. As the bed height is reduced, the number of vapor channels would simply increase in such a way so that the bed attains this maximum potential energy. This is consistant with the minimum irreversibility principle, as any other adjustment of the bed (i.e., change in channel diameter or vapor velocity) will lead to a lower potential energy. Thus, the term $h_e(1 - \epsilon_e)$ can be assumed to be a constant, independent of bed height. However, there is one difficulty with equation (17). In the limit as $h \to 0$, the equation predicts that $nA_c/A_b \to 1$ or the whole cross section of the bed is occupied by vapor. This is physically not possible. Numerous peak heat flux observations on a variety of finite heaters (width of heater greater than vapor jet diameter) placed in a pool of liquid [10] show that the maximum area occupied by the vapor per unit area of the heater is always less than $\pi/16$ or the minimum area occupied by the downcoming liquid is $1 - \pi/16$. As the proposed dryout mechanism in shallow beds is similar to the occurrence of peak heat flux on finite heaters, the equation (17) can be corrected to read

$$\frac{nA_c}{A_b} = \frac{\pi}{16}\epsilon_e\left[1 - \frac{h(1 - \epsilon)}{h_e(1 - \epsilon_e)}\right] \tag{18}$$

In multiplying right-hand side of equation (17) by $\pi/16\epsilon_e$, we have not disturbed the volume balance made in equation (16), but have simply changed the number of vapor channels from an unknown n to another unknown $16n/\pi\epsilon_e$. Substitution of equation (18) in equation (15) gives

$$\frac{q_{bs}}{q_Z} = 1.50\frac{\epsilon_e}{\sqrt[4]{f}}\left[1 - \frac{h(1 - \epsilon)}{h_e(1 - \epsilon_e)}\right] \tag{19}$$

The initial and the expanded bed heights when nondimensionalized with the channel diameter (characteristic length of the shallow beds) result in

$$\frac{q_{bs}}{q_Z} = 1.50\frac{\epsilon_e}{\sqrt[4]{f}}\left[1 - \frac{h'(1 - \epsilon)}{h'_e(1 - \epsilon_e)}\right] \tag{20}$$

The expanded bed porosity, ϵ_e, and the friction coefficient, f, are inter-related through the vapor velocity and the particle diameter. But, the vapor velocity cannot be determined explicitly as long as f is unknown. However, if we assume that $\epsilon_e \propto U'_c$, it is clear from equation (13) that the term $\epsilon_e/\sqrt[4]{f}$ depends only on the dimensionless channel diameter and is independent of the bed height. Thus, as long as particle diameter and in turn dimensionless channel diameter is constant, equation (20) can be looked at as

$$\frac{q_{bs}}{q_Z} = C_4\left[1 - \frac{h'(1 - \epsilon)}{C_5}\right] \tag{21}$$

where C_4 and C_5 are empirical constants. At this stage of this study on the subject, we are unable to offer any stronger arguments about C_4 and C_5 than what has been said previously. The advantage of equation (21) over equation (15) is that now the dryout heat flux is presented as a function of initial dimensionless bed height and bed porosity; the quantities which can be determined quantitatively easily. If we assume, that as the bed height goes to zero, the dryout heat flux

in a bottom heated bed approaches the peak heat flux on a flat plate, the constant C_4 can be readily set equal to 1.

Volume Heated. The vapor channels in shallow volume heated beds are conical in shape because of the addition of vapor along the axis of the channel. The cone angle of the channel can be obtained by assuming that the vapor velocity along the channel axis remains constant. This assumption would be consistant with the minimum kinetic energy principle. The rest of the analysis would be similar to that for the bottom heated shallow beds. At this time, we defer the development of an expression for the dryout heat flux for shallow volume heated beds until there is more data available.

Experiment

Fig. 3 shows the experimental apparatus used to obtain dryout heat flux data for deep beds of inductively heated particles. The particulate bed was contained in a 4.70-cm dia pyrex jar and inductively heated with a 13.3-cm dia multiturn work coil. The work coil was powered by a 10 kw, 453 kHz Cycle-Dyne frequency generator. The frequency generator and work coil are the same as used by Keowen [4].

A reflux condenser was used as an efficient means of condensing the large amounts of vapor generated during dryout runs. The reflux condenser is made of a helical copper tube 0.6 cm in diameter and is housed in a 4.70-cm dia glass tube. A knurled threaded coupling joins the condenser glass tube and the jar containing the particulate bed. The condenser glass tube was open to atmosphere in most of the experiments. But, in a few of the low pressure experiments, it was closed at the top and connected to an aspirator in order to reduce the pressure in the test section. Tap water was used as coolant in the condenser.

The temperature at different locations in the bed was measured by using four copper-constantan thermocouples arranged in the form of a comb having teeth of different lengths. Thirty gage thermocouples were carried in thin glass capillary tubes of the comb and connected to a multichannel strip chart recorder. A filtering system was used with the thermocouples to eliminate radio-frequency noise picked by the thermocouples. The filtering system was built by Keowen and details of it are given in his thesis [4]. The mass of the bead of the thermocouple was kept small so as to minimize the induced heating of the thermocouple itself. This was confirmed when the thermocouples were subjected to full field intensity in the absence of particles and coolant. The thermocouples registered very little rise in temperature.

Commercially available cast steel and lead particles were used in the present study. The particles were graded according to U.S. standard mesh sizes and stored in air tight cans to avoid any oxidation during prolonged storage. A small amount of calcium sulfate was kept in each can to absorb moisture in the air. Prior to each run the particles were rinsed with acetone at least three times and were shaken vigorously during rinsing. Thereafter, the particles were dried by placing them on a hot plate. This procedure was necessary to get rid of any dirt or grease sticking to the particles. Dirty particles were found to cause wide variations in the data.

The washed and dried particles were poured into the pyrex jar to a certain height and weighed. The height and weight information was used to determine the porosity of the bed in the absence of any fluidization. Coolant was then added to the bed. The depth of the coolant was kept close to the bed height for the calibration runs but was increased to about 5 cm above the bed during actual dryout experiments. The weight of the coolant added to the bed was also noted for use in the calibration calculations. The pyrex jar containing the particles was then placed on the support stand and centered in the work coil. Thereafter, the thermocouples and the reflux condenser were put in place.

Calibration of the heat generation rate in the particles as a function of generator power setting was made before or after each dryout run. Starting with the bed at an equilibrium reference temperature and a certain power input to the workcoil, the temperature of one of the thermocouples in the bed was recorded as a function of time till the coolant started to boil. The temperature was recorded on a X-Y recorder. This recorder was used during calibration because it had a better resolution than the multichannel recorder. Knowing the rate of temperature rise of the bed and the thermal capacity of the bed (particles and coolant) the heat input rate to the bed was determined. The convective heat losses from the surfaces of the cell were found to be very small and were neglected. In a few of the early calibration runs the rate of temperature rise at different locations in the bed was recorded. The difference in any of the observations was within ±15 percent. Subsequently, calibration of each run was made by noting the temperature rise of either the upper, middle, or side thermocouples, as these thermocouples were found to give nearly mean values for the power input.

Starting with a bed of given height and material content, the power to the work coil was set at a low value and the temperature of the bed raised to the saturation temperature of the coolant. Thereafter, the power was increased in steps. At each power setting, enough time was allowed so that the dryout of the bed would occur if the heat generation rate was high enough. Dryout of the bed was observed visually as well as by noting the sharp rise in the temperature of one or more of the thermocouples. Generally, dryout was visually observed in the lower outermost portions of the bed before it was recorded by the thermocouples. This delay was probably on account of the build in thermal capacity of the bed. Power was turned off after dryout was recorded and the bed allowed to reflood. The observation was repeated at least once more under the same test conditions. The maximum probable error in the measurement of the dryout heat flux is within ±12 percent.

Results

A total of forty-six dryout heat flux observations for deep beds of inductively heated particles were made. Twenty-eight of these observations were made at 1-atm pressure and for steel and lead particles in the size range 295–787 micron and for three different coolants (water, acetone, and methanol). Eighteen observations were made at pressures varying from one atmosphere to 20 kPa for lead particles in the size range 416–848 micron and using acetone or methanol as coolant. All of these data are contained in reference [11]. The bed height in these tests varied from 1.9 to 8.9 cm and the bed porosity from 0.38 to 0.45. The dryout heat flux data for 589–789 micron steel

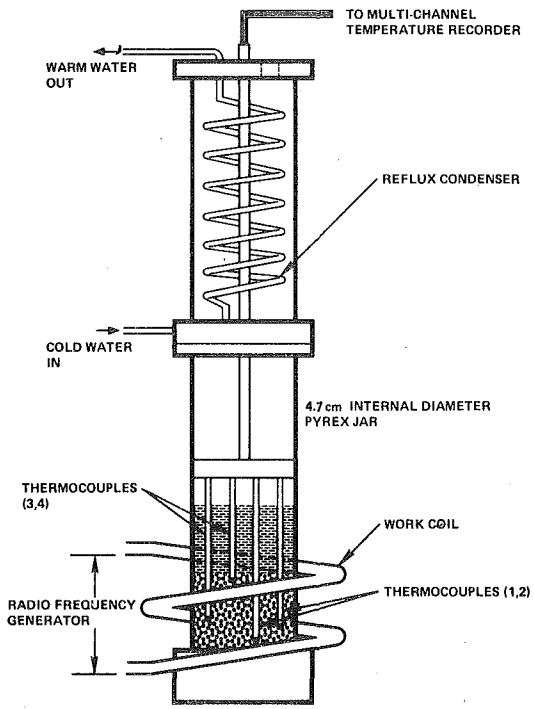

Fig. 3 Test setup for inductively heated particulate beds

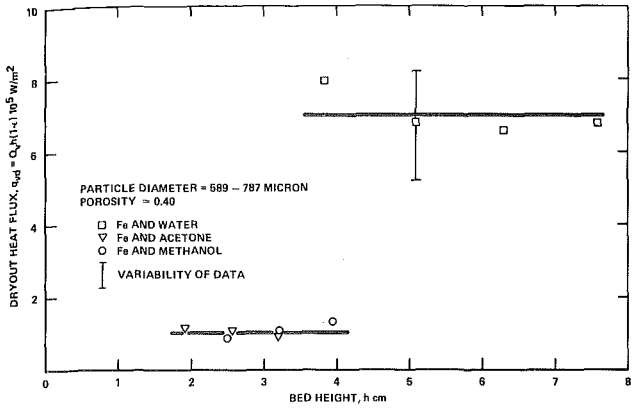

Fig. 4 Deep bed dryout heat fluxes for inductively heated particles

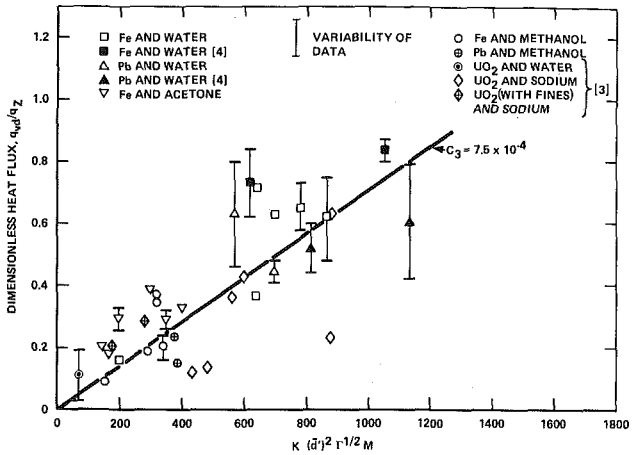

Fig. 5 Dryout heat flux correlation for volumetrically heated deep beds

particles are plotted in Fig. 4 as a function of bed height. The ordinate in Fig. 4 denotes the volumetric heat generation rate multiplied by the bed height and the volume fraction of the solids. For a deep bed of given porosity, the dryout heat flux is independent of bed height but strongly depends on the fluid properties.

The present data and the data of Gabor, et al. [3] and Keowen [4] for deep beds are plotted in Fig. 5 along with the correlation equation (13). The data of Gabor, et al., are for UO_2 particulate beds with water and sodium as coolants. As seen from Fig. 1, their volume heated bed data are significantly dependent on bed loading. We think that this change in dryout heat flux is a manifestation of change in bed porosity with bed loading. Thus, while plotting their data we have assumed that all the dryout heat flux data are for deep beds and are independent of bed height. Also, while reducing their data, we have used their lower value of the mean particle diameter; as pressure loss during downward flow of water through the bed has been reported to be correlated with this diameter. All the data (plotted in Fig. 5) representing a three-fold variation in $\bar{d}$, seven-fold variation in M and K_1 and three-fold variation in Γ are correlated well when the correlation constant C_3 is taken to be 7.5×10^{-4}.

Overall, the data show considerable variability. This variability in data is inherent in the nature of the experimental parameters. A small error in the mean particle diameter and the bed porosity would significantly affect the values of the correlation parameters $(\bar{d})^2$ and K_1. The walls of the jar, non-sphericity and segregation at a particular cross section of particles of certain size during pouring may also play a significant role in triggering an early dryout patch. The presence of vapor or gas trapped during pouring of the particles may also lead to an early dryout. If, while making the observations one is not very careful, it is also very easy to overshoot the dryout heat flux and thus record a false value.

Some of the data for coarse UO_2 particles and sodium lie very low on Fig. 5. These data points probably do not represent a true dryout. Gabor, et al., report that in some of the volumetrically heated UO_2-sodium bed experiments actual dryout was not achieved and the reported data represent the maximum power input to the electrodes. Such data are liable to be low. One of the Pb-water data points of Keowen is also quite low. A check on the mean particle diameter shows that the reported value is probably higher than the size of the particles actually used by Keowen in this run, so this data point should probably be shifted slightly to the left. Almost all of the data plotted in Fig. 5 are bounded when the correlation constant assumes a value $4 \times 10^{-4} < C_3 < 12 \times 10^{-4}$.

A test of the workability of the correlation equation (13) would be to see if it correlates the experimental data at pressures that are considerably less than 1 atm. To do so, we obtained deep bed data with a five-fold variation in the pressure. This allowed about a five fold variation in Γ and relatively small variation in M and $\sqrt{\sigma/g(\rho_f - \rho_g)}$. The data are plotted in Fig. 6 and are seen to be correlated well by equation (13).

Next, we plot in Fig. 7 the bottom heated deep bed dryout heat flux data for UO_2-water and UO_2-sodium against our correlation equation (8). As anticipated, all the data except a few data points for UO_2-sodium are correlated well when the constant C_2 is taken to be 3.5×10^{-4} or *nearly half* of C_3. While studying heat transfer processes from cylinders placed in liquid filled porous media, Schrock, et al. [12] also observed the heat flux at which the region near the cylinder dried out. The magnitude of these heat fluxes is about the same as the water data for bottom heated beds. Schrock, et al., also noted that the less porous media of finer particles dried at lower heat fluxes than a more porous media of coarser particles. This is consistent with out deep bed model and provides further support to the model.

The shallow bottom heated deep bed dryout heat flux data for water and sodium are plotted in Fig. 8. The abscissa denotes non-dimensional bed height multiplied by $(1 - \epsilon)$ and the ordinate represents the dryout heat flux nondimensionalized with Zuber's flat plate value. The dryout heat flux increases linearly with h' and approaches flat plate value in the limit $h' \to 0$. The data obtained for two fluids of differing thermophysical properties and for beds of widely varying heights and porosities but of about same size particles are correlated well when empirical constant C_4 and C_5 in equation (26) are taken to be 1 and 0.092, respectively.

Interestingly enough, the visual observation of the number of channels existing per unit cross-sectional area of the bed is consistant with our theoretical model for bottom heated shallow beds. The di-

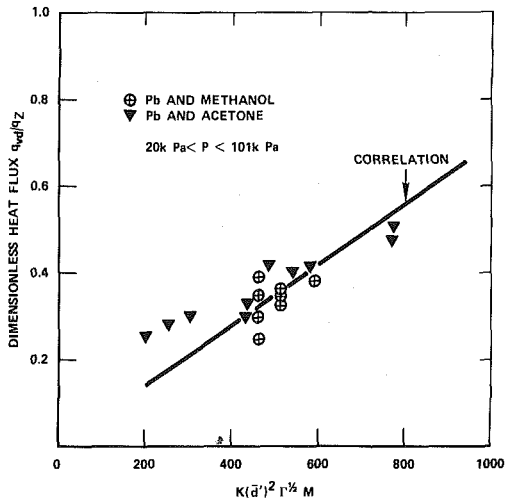

Fig. 6 Dimensionless dryout heat flux in volume heated deep beds subjected to different system pressures

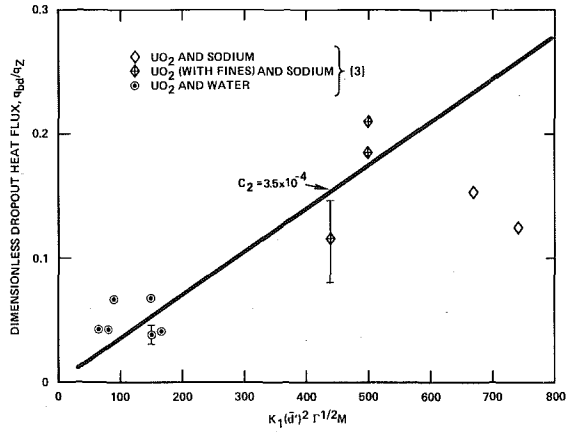

Fig. 7 Dimensionless dryout heat flux in bottom heated deep beds

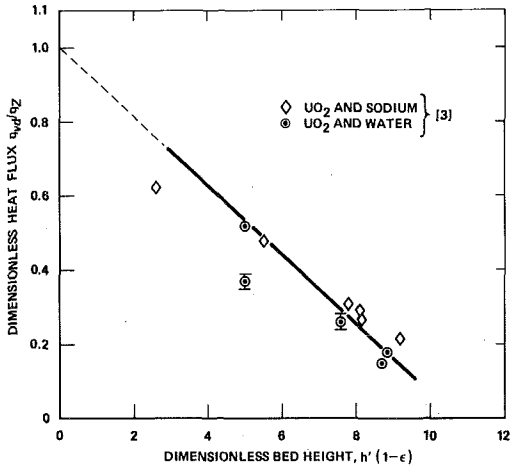

Fig. 8 Dryout heat flux in bottom heated shallow beds

ameter of vapor channels in water is observed to be approximately 0.30 cm in beds of about 5-cm height. From equation (13) this diameter corresponds to a friction fraction, f, of about 0.40. The value of the dryout heat flux for a 5-cm bed, the value for the friction factor and the value for ϵ_e obtained from equation (20), when used in equation (18) results in about 1.7 channels per 6.5-cm^2 area of the bed or roughly 1 channel per 4 cm^2. This is exactly the number reported by Gabor, et al. For a constant friction factor, our model would suggest existence of about two channels per cm^2 of bed area as $h' \to 0$.

Conclusions

1 New dryout heat flux data for inductively heated particulate beds have been obtained.

2 Different mechanisms for dryout in deep beds and shallow beds have been identified and semitheoretical correlations for the dryout heat fluxes have been suggested.

3 Dryout heat flux in deep beds is independent of bed height. A variety of data has been correlated with the suggested correlations. The data show considerable scatter which is probably due to experimental difficulties involved with the control of the important variables or due to limitation of the analysis to completely model the complicated flow situation.

4 Dryout heat flux in shallow beds is dependent on bed height and is found to increase linearly with decreasing bed height.

References

1 Holman, J. P., Moore, T. W., and Wong, V. M., "Particle to Fluid Heat Transfer in Water-Fluidized Systems," *I and E C Fundamentals*, Vol. 4, No. 1, Feb. 1965, pp. 21–31.

2 Young, F. M., and Holman, J. P., "Particle to Fluid Nucleate Boiling Heat Transfer in a Water Fluidized System," *I and E C Fundamentals*, Vol. 7, No. 4, Nov. 1968, pp. 561–567.

3 Gabor, J. D., Sowa, E. S., Baker, L., Jr., and Cassulo, J. C., "Studies and Experiments on Heat Removal from Fuel Debris in Sodium," ANS Fast Reactor Safety Meeting, Los Angeles, Apr. 1974.

4 Keowen, R. S., "Dryout of a Fluidized Particle Bed With Internal Heat Generation," MS thesis, University of California, Los Angeles, 1974.

5 Kozeny, J., *Sitzbar-Akad. Wiss. Wien*, Math.-Naturw. Klasse, Vol. 136, Abt IIa, 1927, p. 271.

6 Carman, P. C., "Fluid Flow Through Granular Beds," *Trans. Inst. Chem. Engrs.* (London) Vol. 15, 1937, pp. 150–166.

7 Ergun, S., "Fluid Flow Through Packed Columns," *Chemical Engineering Progress*, Vol. 48, No. 2, 1952, pp. 89–94.

8 Zuber, N., "Hydrodynamic Aspects of Boiling Heat Transfer," AEC Report No. AECU-4439, *Physics and Mathematics*, 1959.

9 Lamb, Sir H., *Hydrodynamics*, Sixth ed., Dover, New York, 1945.

10 Lienhard, J. H., and Dhir, V. K., "Extended Hydrodynamic Theory of the Peak and Minimum Pool Boiling Heat Fluxes," NASA CR-2270, July 1973.

11 Dhir, V., and Catton, I., "Dryout Heat Fluxes in Beds of Inductively Heated Particles," UCLA Eng. 7678, Aug. 1976.

12 Schrock, V. E., Fernandez, R. T., and Kesavan, K., "Heat Transfer From Cylinders Embedded in a Liquid Filled Porous Medium," *Proceedings of 4th International Heat Transfer Conference*, Vol. VII, Paper No. CT 3-6, Paris/Versailles, France, 1970.

Y. Mori
Professor.

K. Hijikata
Assoc. Researcher.

K. Utsunomiya
Graduate Student.

Department of Physical Engineering,
Tokyo Institute of Technology,
Meguro, Tokyo, Japan

The Effect of Noncondensable Gas on Film Condensation Along a Vertical Plate in an Enclosed Chamber

Experiments on film condensation including noncondensable gas in an enclosed chamber have been carried out to clarify the effects of molecular weights of vapor and noncondensable gas and the convective motion induced by the vapor flow. From the experimental results of R113-air and CH_3OH-mixed gas of He and Ar, it is shown that the separation of vapor and gas in the main flow is realized when the direction of gas flow in free convective boundary layer driven by concentration distribution of gas is the same as that of supplied vapor, whereas the homogeneous main flow occurs in the case of counter direction. It is also shown that in case of the separation of vapor and gas in the main flow the heat transfer coefficient is higher than that for an homogeneous main flow.

Introduction

With recent developments in the quality and performance of apparatus and equipment used in various fields of thermal power engineering and big computers using large current, there is a demand for further improvements of heat transfer performance. However, the construction of heat transfer systems is getting more complicated. In such systems as heat pipes, boiling and condensation take place simultaneously.

It is well known that the presence of small amount of noncondensable gas in such system leads to an enormous reduction in heat transfer coefficient. This has been explained by the following phenomenon. When noncondensable gas is present in the system, it moves with the vapor toward the condensing surface where the vapor is condensed; but, since the gas does not condense, it concentrates in the neighborhood of the condensing surface. This noncondensable gas layer impedes the movement of vapor to the condensing surface. Various analyses have been made by assuming the aforementioned mechanism and recently considerable progress has been made toward both the experimental and theoretical understanding of such problems. Referring and comparing their results with the Nusselt theory, Sparrow, et al. [1-3][1] carried out numerical analyses of steam-air system using a model which included the effects of noncondensable gas, superheating and temperature dependencies on physical properties. Rose [4] presented an approximate solution by using a boundary layer integral method for application to various vapor and noncondensable gas combinations.

However, these analyses were made under an assumption of constant bulk temperature and concentration of noncondensable gas. Substantially higher heat transfer coefficient found in the experimental works [5, 6] reported so far are considered to be due to significant forced convection of condensing vapor. Rose, et al. [7] measured heat transfer coefficients for the film condensation of steam on a vertical flat surface in the presence of air, argon, neon, and helium. They eliminated forced convection effects with a flow straightening section and obtained a good agreement between experimental results and the theory. They also reported that substantially smaller heat transfer coefficients are obtained when the molecular weight of noncondensing gas is smaller than that of vapor. The effects of forced convection [8, 9] and combined forced and free convection [10, 11] have been studied. The authors [12] and others [13] have also reported such effects as fog formation.

It is considered that these analyses can only be applied to limited combinations of noncondensable gas and vapor and the construction

Contributed by the Heat Transfer Division and presented at the Winter Annual Meeting, New York, N.Y., December 5-10, 1976 of THE AMERICAN SOCIETY OF MECHANICAL ENGINEERS. Revised manuscript received by the Heat Transfer Division February 15, 1977. Paper No. 76-WA/HT-66.

[1] Numbers in brackets designate References at end of paper.

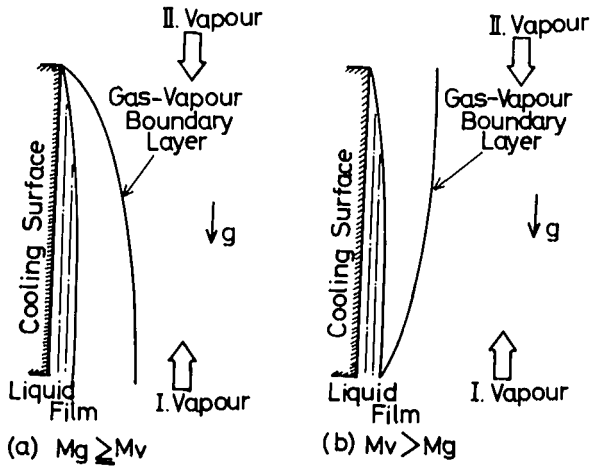

Fig. 1 Scheme of boundary layer

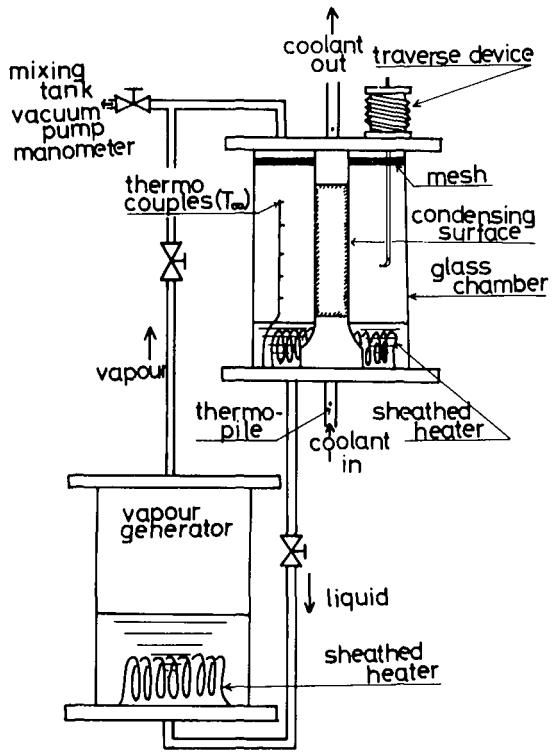

Fig. 2 Experimental apparatus

of heat transfer system is also restricted. However, little study has been done on the effect of the difference between the molecular weight of noncondensable gas and that of vapor and on the effect of the shape of the heat transfer system. For an example, when a certain amount of air is introduced into the condensation of steam on a vertical flat surface, a downward boundary layer is formed as illustrated in Fig. 1(a) since the density of air is larger than that of steam. Previous works treat such cases. However, as shown in Fig. 1(b), when the molecular weight of vapor (M_v) exceeds that of noncondensable gas (M_g) an upward convective boundary layer is formed against the downward movement of the liquid film and the analyses reported so far cannot be applied. Furthermore, in an enclosed chamber, when there exists a large difference between M_g and M_v, a homogeneous main flow cannot generally be realized. Instead, noncondensable gas is separated and squeezed into a certain space in the apparatus. Hence, the heat transfer coefficient changes drastically with the shape of the chamber containing vapor and gas.

Since it is impractical to study condensation phenomena in an infinite apparatus, the present experiments were carried out in an enclosed chamber to clarify the effects of molecular weights of vapor and gas, and the convective motion induced by the vapor flow, on the heat transfer performance.

Apparatus

The general assembly of the apparatus used in the experiment is shown in Fig. 2. The condensing surface, which is cooled on the reverse side by water, is a cylindrical brass outer wall with a 22-mm OD, a thickness of 1 mm, and a height of 100 mm. Water is introduced into the condensing cylinder through a 6-mm OD copper tube and it runs out through a similar copper tube. This cylindrical condensing surface is housed vertically inside a 100-mm dia cylindrical glass vapor chamber 200-mm high and extending between 70 and 170 mm from the bottom of the chamber. Both ends of the condensing surface are insulated with bakelite cylinders.

Two vapor generators (one within the condensing chamber and the other outside), with sheathed heaters, are provided to change the condition of the main flow. By generating vapor inside the chamber, the vapor is supplied from the bottom part of the chamber . On the other hand, the vapor is supplied from the upper part of the chamber by generating vapor in a separated generator. The former and the latter conditions are hereafter called Conditions I and II, respectively. A fine stainless mesh is installed at the top of the chamber to insure a homogeneous main flow for the experiment under Condition II. To vary the relative value of M_g and M_v over a wide range, not only single component gases but also mixed gases were used as the noncondensable component.

Five 0.3-mm dia copper-constantan thermocouples are butt-welded onto the condensing surface at the heights of 10, 30, 50, 70, and 90 mm from the bottom edge of the condensing surface. The lead wires of these thermocouples are led to the surface from the reverse side so as not to interfere with the movement of the liquid film. Another five thermocouples are installed inside the chamber at the same heights to measure the temperatures of the main flow. The temperature profile near the condensing surface is measured by a 0.1-mm dia copper-constantan thermocouple fitted to the traversing device installed at the top of the chamber. The heat flux to the condensing surface was obtained by measuring the difference between the temperature of the coolant at the inlet and that at the outlet with a

Nomenclature

D = diffusivity (m^2/s)
f = buoyancy force (N/m^3)
g = acceleration of gravity (m/s^2)
ℓ = length of condensing surface (m)
L = latent heat (J/kg)
M = molecular weight (kg/kmol)
p = pressure (Pa)
Δp_i = increase of total pressure by introduction of noncondensable gas at room temperature
q = mean heat flux (W/m^2)
Sc = Schmidt number
T = temperature (K)
x = distance along condensing surface (m)
y = distance from condensing surface (m)
ρ = density (kg/m^3)

Subscript

g = noncondensable gas
i = initial state
Nu = from the Nusselt model
v = vapor
0 = liquid-gas interface
∞ = main flow

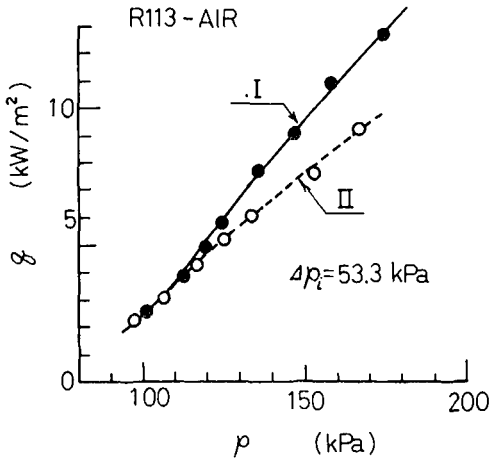

Fig. 3 Relation between q and p

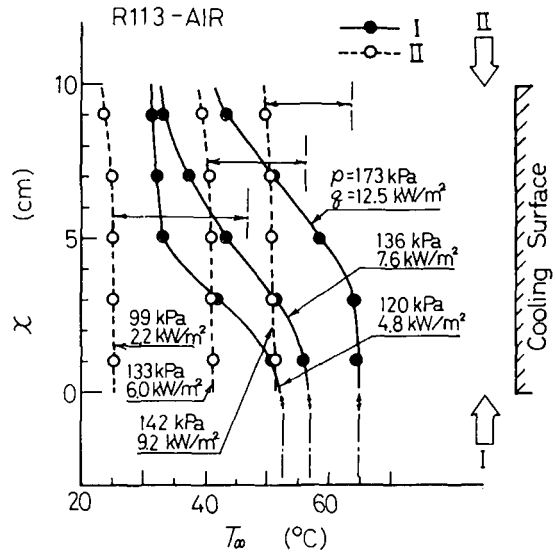

Fig. 4 Temperature distribution of main flow

thermopile, and by measuring the flow rate of the coolant. Two more thermocouples, one in the chamber and the other in the separate vapor generator, are installed to measure the surface temperature of the evaporating liquid. The total pressure of the system was measured with a mercury manometer.

Procedure

In the present work, freon 113 (M_v = 187.4) and methanol (M_v = 32) were used as condensing liquids, while air (M_g = 28.96) and mixed gases of argon (M_g = 40) and helium (M_g = 4) were used with various mixing ratios as noncondensable gas. Before the experimental run, the system was evacuated below 10^{-2} Torr, then pure condensing material was introduced in the system and condensation of pure material was carried out. After the evacuation of the whole system, a measured amount of condensing liquid was led into the separate vapor generator. When an equilibrium state at room temperature was attained in the system, a measured amount of noncondensable gas, calculated from an increase in the pressure of the system, was introduced into the chamber from the mixing tank. It took several 10 min for the system to come into a steady state, however, the measurement was made after about 2 hr to make sure of perfect film condensation. For Condition II, vapor from the separate vapor generator was supplied from the upper part of the chamber and the temperature profile and pressure were measured for various heat fluxes. To carry out experiments under Condition I, the liquid in the separate vapor generator was transferred to the condensing chamber and the vapor was then generated inside the chamber, thus supplying the vapor from the bottom part of the chamber. The existence of mist formation and the movement of the flow were also observed by making use of a laser and a camera.

Results and Discussions

To confirm the performance and accuracy of the apparatus, preliminary tests were carried out with pure vapors by realizing a complete film condensation on the vertical surface. The experimental results for Conditions I and II were found to hold a good agreement with the simple Nusselt theory for pure water and R113. In the case of pure condensing material, as there exists no vapor or gas boundary layer outside the liquid film, the velocity of vapor is thought not to give a serious effect on Nusselt number. First, an experiment with R113 and air was carried out. Air was introduced into the system until the pressure in the system increased by Δp_i = 53.3 kPa at 15°C. Measurements were taken for various heat fluxes under Conditions I and II. The temperature and flow rate of the coolant were kept constant all through the experiment. The results are shown in Fig. 3, where black circles with a solid line indicate the results obtained under Condition I (vapor is supplied from the bottom part of the condensing chamber) and white circles with a dotted line express those obtained under Condition II (vapor is supplied from the upper part of the condensing chamber). In the condensation phenomena realized in an enclosed chamber, an increase in heat flux leads to an increase in the pressure. This means that under a constant heat flux the lower the pressure the higher the heat transfer coefficient becomes. In the figure, the experimental results for both the conditions move to the right with an increase of Δp_i. The most interesting point in these results is that, for the same amount of air introduced, difference in pressure becomes more apparent with an increase in heat flux under Conditions I and II and that higher heat transfer coefficients are obtained under Condition I. This explains that higher heat flux can be obtained by supplying vapor from the bottom part of the condensing surface rather than from the upper part. To clarify this point, the temperature distributions of the main flow were measured for various heat fluxes as shown in Fig. 4. Since the increase in heat flux leads to an increase in the chamber pressure, the higher the main temperature, the higher the heat flux. As seen from Fig. 4, the temperature distributions under the respective conditions differ greatly. In Condition II, the temperature of the main flow and the deviation from the saturation temperature are almost constant with respect to height, which indicates that noncondensable gas is distributed homogeneously in the main flow. In the figure, deviation from the saturation temperature is shown by an arrow and the saturation temperature calculated from pressure is expressed by a chain-dotted line. On the contrary, in Condition I, a saturation condition is satisfied at the bottom part of the chamber. When the temperature of the main flow, thus heat flux, is high, about 20 percent of the bottom half of the condensing surface is in a saturated condition. But this saturated region is reduced with a decrease in heat flux. The temperatur of the main flow decreases drastically with height, indicating a higher concentration of noncondensable gas at the upper part of the chamber. Wall temperatures were measured to be almost constant with respect to height under Condition II but a small drop in wall temperature was observed under Condition I. Physically speaking, these factors indicate that, since the density of air concentrated in the neighborhood of the condensing surface is smaller than that of R113 vapor, air is carried upward along the surface by the upward boundary layer and is concentrated in an upper part of the chamber. This high concentrated air tends to diffuse downward to maintain the concentration in the chamber constant. But under Condition I, this downward flow of air is interrupted by an upward motion of vapor and, therefore, the air is finally squeezed into the upper part of the chamber. On the contrary, under Condition II, since the vapor is supplied from the

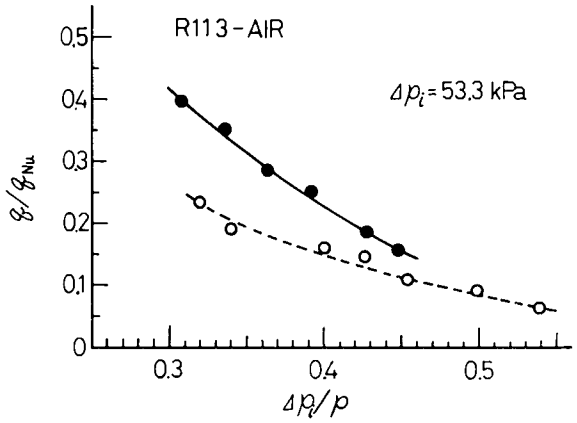

Fig. 5 Relation between q/q_{Nu} and $\Delta p_i/p$

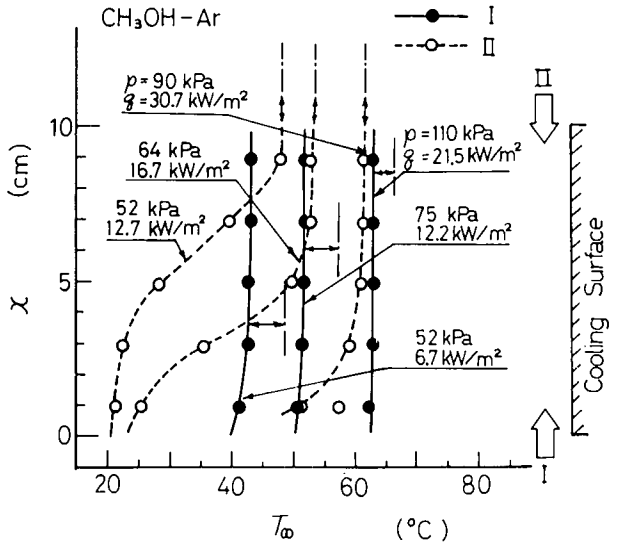

Fig. 6 Temperature distribution of main flow

same direction as the downward flow of air, air is carried to the bottom half of the chamber with vapor and, consequently, a homogeneous main flow is realized. Therefore, in the case of Condition I the degree of separation of air and vapor in the main flow depends almost entirely upon the diffusion coefficient and the velocity of vapor. This degree of separation becomes more apparent with an increase in heat flux. To clarify this point quantitatively, the ratio of the increase in the total pressure due to introduction of noncondensable gas Δp_i to the total pressure p of the chamber is plotted against the ratio of the heat flux measured, q, to the heat flux for pure vapor, q_{Nu}, in Fig. 5. Due to the temperature distribution and concentration distribution of noncondensable gas, an accurate mean mole fraction of gas cannot be obtained. However, since $\Delta p_i/p$ is considered to express the mean mole fraction of gas approximately, the results are arranged by using this nondimensional quantity ($\Delta p_i/p$). q_{Nu} was obtained from the Nusselt theory by using the temperature difference between the saturation temperature corresponding to the chamber pressure and the wall temperature at the bottom edge of the condensing surface. This figure shows that higher values of q/q_{Nu} can be obtained under Condition I and the tendency is especially marked at larger heat fluxes. Under Condition I, it is considered that the increase of p for a given Δp_i makes the noncondensable gas squeezed almost completely in the upper space of the chamber, and the gas does not give any effect on condensation performance and that the heat flux is calculated by the Nusselt's solution. However, under Condition II, as the homogeneous main flow is realized, even the inclusion of a very small amount of gas brings about a large reduction of heat flux as reported by the theories [2, 12]. The ratio of the effective length of the condensing surface calculated from the temperature distribution in Fig. 4 under Condition I to the actual length of the condensing surface agrees fairly well with q/q_{Nu} of Fig. 5. This adds a support to the aforementioned explanation. Therefore, it is considered that, by measuring the temperature distribution of the main flow, q/q_{Nu} can be predicted for other cases.

The buoyancy force, f, whose direction is against the gravity, can be written as follows in terms of temperature difference ($T_\infty - T_0$) and partial pressure difference of vapor ($p_{v\infty} - p_{v0}$):

$$f = g\rho_\infty \left(1 - \frac{\rho_0}{\rho_\infty}\right) = -g\left\{\frac{T_\infty - T_0}{T_\infty} - \left(\frac{p_{v\infty} - p_{v0}}{p}\right)\left(\frac{M_v - M_g}{M_g}\right)\right\} \quad (1)$$

where p denotes the total pressure. When f is positive, an upward boundary layer is formed and the direction of the boundary layer is reversed when f is negative. A qualitative study is made as follows, neglecting the first term in the right side of equation (1). When the molecular weight of noncondensable gas (M_g) is smaller than that of vapor, an upward boundary layer is formed and that separation of gas and vapor takes place under Condition I, whereas a downward boundary layer is formed and separation takes place under Condition II when $M_g > M_v$. A homogeneous condition is thought to be realized under both conditions when M_g and M_v are nearly equal. To confirm this phenomenon, experiments were carried out using CH_3OH as condensing liquid and mixed gases of Ar and He as noncondensable gases. The mixing ratio of the gases was varied in a wide range to study the effect of the molecular weight. Hereafter 0.6Ar:0.4He II (25.6) designates that a mixed gas consisting of 60 percent Ar and 40 percent He with average molecular weight of 25.6 was used and that the experiments were carried out under Condition II. The primary purpose of the present study is to clarify the effects of the difference in molecular weights and the way of supplying vapor on heat transfer coefficients, not to clarify the relationship between heat transfer coefficients and the concentration of noncondensable gas quantitatively. Therefore, all the experiments were carried out under the condition of Δp_i = 19.6 kPa at 15°C.

The temperature distributions of the main flow for the case of Ar-CH_3OH are shown in Fig. 6. Here, since M_g(=40) is larger than M_v(=32), argon is concentrated at the bottom of the chamber and a separation of gas and vapor is taking place in the main flow under Condition II. It must be noted that the conditions are reversed for R113-Air experiment (Fig. 4). However, as shown in Fig. 7, in the case of He the same temperature distribution of the main flow as for R113-Air is obtained and a separation of gas and vapor is seen under Condition I. To support the evidence of the separation, a gas-sampling was made at x = 0.0. No He was detected by a gas chromatograph for large heat flux in Fig. 7. The gas-sampling at other points in the chamber was not made as it was thought that the gas-sampling reduced the total amount of noncondensable gas and the experimental condition might be varied. These add further support to the aforementioned consideration.

In condensation phenomenon, since both terms, ($p_{v\infty} - p_{v0}$) and ($T_\infty - T_0$), in equation (1), are positive, when ($M_v - M_g$) takes positive value, buoyancy forces induced by temperature difference and pressure difference cancel each other. On the other hand, when ($M_v - M_g$) is negative, these two buoyancy forces combine to intensify the effect. This is why a clear state of separation of gas and vapor is seen for Condition II in Fig. 6 although the absolute value of $|M_v - M_g|/M_g = |-0.2|$, is considerably small compared with the values of Figs. 4 and 7. However, by comparing two figures it can be seen that the temperature variation of the main flow with respect to height is more conspicuous in Fig. 4 than in Fig. 7 and that a more distinguished state of separation is seen. This is because the binary diffusion coefficient of R113-Air (0.068 m²/s at 1 atm, 0°C) is small compared with that of CH_3OH-He (0.524 m²/s).

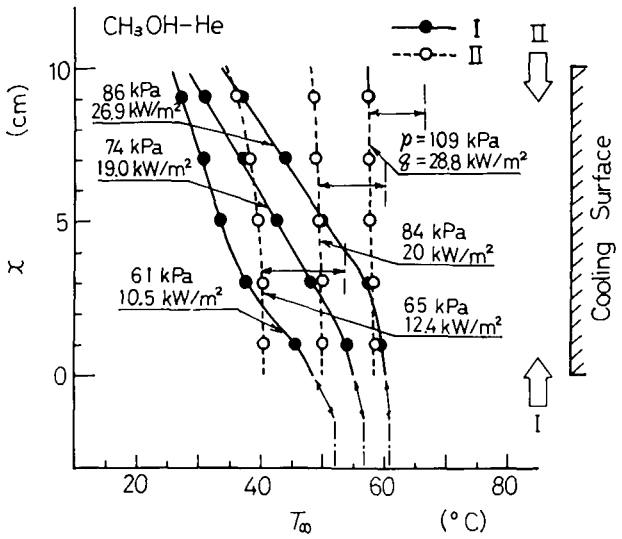

Fig. 7 Temperature distribution of main flow

In case of 0.7Ar:0.3He (29.2), as the temperature term in equation (1) is dominant, f takes negative value when the heat flux is small (low pressure). However, the pressure term comes to play a larger part with an increase in heat flux and the sign of f will be reversed. This can be clarified from the temperature distribution of the main flow shown in Fig. 8, where states of separation are seen under Condition II at low pressures and under Condition I at high pressures. Namely, the degree of separation between noncondensable gas and vapor in the boundary layer increases with f and whether they mix in the main flow or not is largely dependent on the directions and magnitudes of the diffusion and the vapor velocity. When the directions of vapor velocity and diffusion are opposite, the smaller diffusion coefficient and the larger vapor velocity bring about a larger degree of separation. The separated flow is considered to be realized more easily in a narrow flow cross section and the occurrence is examined from measurement of the nonuniform temperature distribution of the main flow.

When separation of gas and vapor occurs, the concentration distribution of gas in main flow and the local condensing rate are closely related. Therefore, it is difficult to arrange the experimental results quantitatively.

For various mixing ratios of Ar and He, q/q_{Nu} are plotted against $\Delta p_i/p$ in Fig. 9(a) and 9(b). Noncondensable gas is distributed homogeneously in the main flow in Fig. 9(a), while a separation of gas and vapor is realized in Fig. 9(b). The results obtained for 0.7Ar:0.3He are shown in both figures for comparison. In Fig. 9(a), due to its large diffusion coefficient and buoyancy force, the largest values of q/q_{Nu} are seen for He II. By following the results of 0.5Ar:0.5He II, 0.6Ar:0.4He II and 0.7Ar:0.3He II in this order, reduction in q/q_{Nu} is found with a decrease in the molar fraction of He. Almost identical values of q/q_{Nu} are found under Conditions I and II for 0.7Ar:0.3He, where q/q_{Nu} is minimum. This agrees with our prediction from the temperature distribution of the main flow. By following 0.7Ar:0.3He I, 0.8Ar:0.2He I and Ar I in this order, the heat transfer performance is seen to increase with an increase in the molar fraction of Ar. Because the diffusion coefficient of Ar in CH_3OH is approximately 0.22 times that of He and the buoyancy force expressed by equation (1) is large, comparatively smaller values of q/q_{Nu} are obtained in Ar I than in He II. The same tendency is observed in Fig. 9(b) when a state of separation is realized in the main flow. From the comparison of Fig. 9(a) to Fig. 9(b) it is clear that for the same mixing ratio higher values of q/q_{Nu} are always obtained under the conditions in which a state of separation of gas and vapor is realized in the main flow. This is also true in the case of 0.7Ar:0.3He. Especially in this case, though the buoyancy force is almost caused by the temperature term in equation (1), this free convective flow through the boundary layer prevents the separation of the components of mixed gas which might be determined by diffusions due to the concentration and temperature gradients in it.

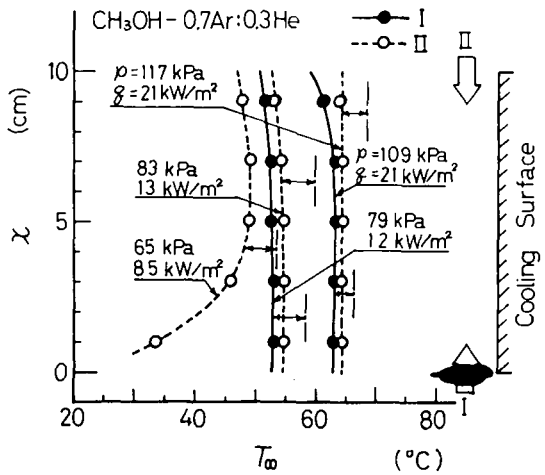

Fig. 8 Temperature distribution of main flow

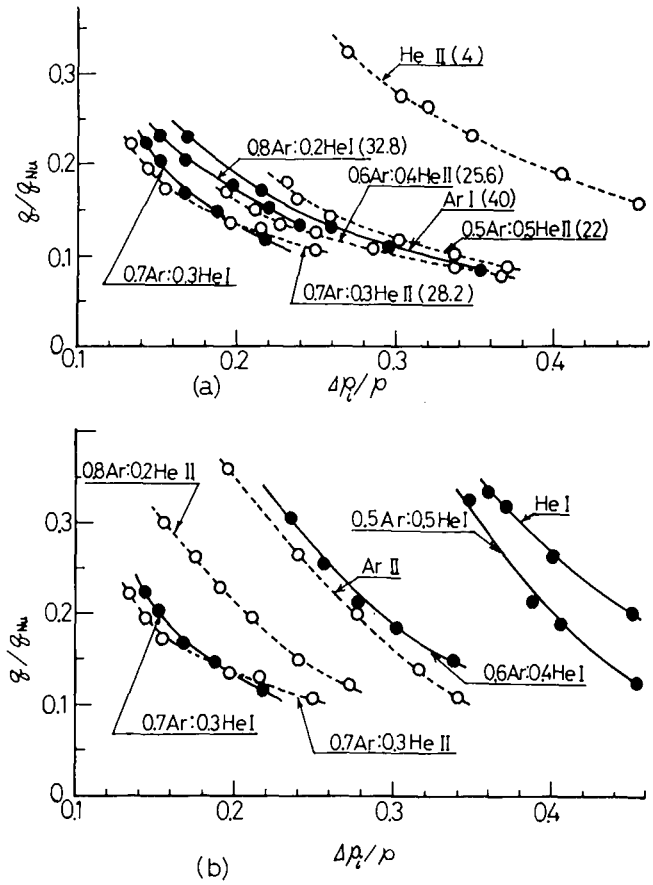

Fig. 9 Relations between q/q_{Nu} and $\Delta p_i/p$

Taking the change in density into consideration, an approximate solution of heat flux was obtained by using a boundary layer integration method where the distributions of $(\rho - \rho_0)/(\rho_\infty - \rho_0)$, $(\rho_g - \rho_{g0})/(\rho_{g\infty} - \rho_{g0})$ and $(T - T_0)/(T_\infty - T_0)$ are assumed to be expressed by quadratic equations of (y/δ), the liquid film has a negligibly small thermal resistance and the gas-liquid interface velocity has no effect

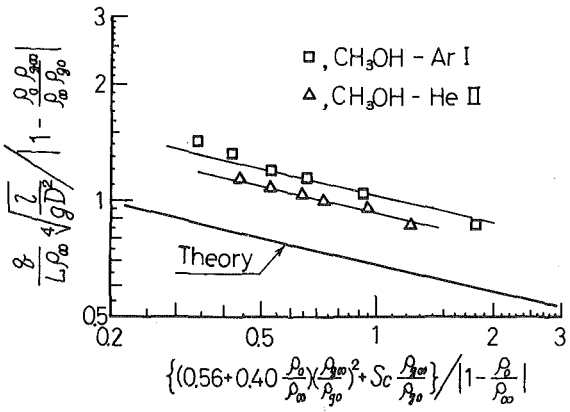

Fig. 10 Comparison between theory and experimental results

on the gas-vapor boundary layer. Then, the heat flux q under the condition of homogeneous main flow is given as follows:

$$\frac{q}{L\rho_\infty}\frac{\ell}{\sqrt[4]{gD^2}}\Big/\left|1-\frac{\rho_0\rho_{g\infty}}{\rho_\infty\rho_{g0}}\right| = 0.678\cdot\sqrt[4]{\left\{\left(0.56+0.4\frac{\rho_0}{\rho_\infty}\right)\left(\frac{\rho_{0\infty}}{\rho_{g0}}\right)^2+\mathrm{Sc}\frac{\rho_{0\infty}}{\rho_{g0}}\right\}\Big/\left|1-\frac{\rho_0}{\rho_\infty}\right|} \quad (2)$$

where the expression of absolute sign is adopted as to include the case of downward and upward boundary layers. When an upward convective boundary layer is formed against the downward movement of the liquid film, (Fig. 1(*b*)), a homogeneous main flow is realized but an assumption of constant gas-liquid interface temperature does not hold. However, as the heat resistance of liquid film is sufficiently small, the results are compared with the theory to make an estimation of the resistance in the gas layer.

Fig. 10 shows the comparison of the experiment to the theory (equation (2)) for the cases of Ar-CH_3OH I (downward boundary layer) and He-CH_3OH II (upward boundary layer). The results for the mixed gases of He and Ar are not compared due to the various problems arising in estimating the physical properties such as diffusion coefficient. In the figure, the experiment and the theory show the same tendency despite the fact that the experimental results are about 50 percent larger than the theory. As suggested by Rose, et al. [7] this is thought to be caused by significant forced convection of vapor. The average vapor velocity in the chamber calculated from the condensation rate was several cm/s and was smaller than that caused by free convection in the gas-vapor boundary layer. However, as we understood from observation of fog movement generated in the boundary layers, one of which was built up by free convection from one end of the cooling surface and the other by forced convection caused by vapor motion in the main flow from the other end. These two boundary layers encountered each other in the middle of the condensing surface and were separated off from the wall. This caused heat flux higher than that by pure free convection. It can also be considered from the figure that the resistance of the liquid film is so small that the heat transfer performance is determined mainly by the gas boundary layer and the effect of the direction of the boundary layer on the heat transfer coefficient cannot be seen so much.

Conclusion

The experiments were carried out in an enclosed chamber by changing the relative values of noncondensable gas and vapor together with the way of supplying the vapor. The following conclusions have been obtained.

1 Realization of a homogeneous main flow depends largely on the way of supplying vapor and the relative difference in molecular weights of noncondensable gas and vapor. Namely, a state of separation of vapor and noncondensable gas is realized in the main flow by supplying vapor from the bottom part of the chamber when $M_v > M_g$ and by supplying vapor from the upper part of the chamber when $M_v < M_g$.

2 For the same amount of noncondensable gas introduced, the larger the difference in molecular weights between vapor and noncondensable gas is, the larger the heat transfer coefficient becomes, and, larger heat transfer fluxes are obtained under a condition where separation of gas and vapor takes place than under a condition where a homogeneous main flow is realized.

3 When $M_v > M_g$, an upward boundary layer is formed against the downward movement of liquid film and the direction of the boundary layer is reversed when $M_v < M_g$. However, difference in heat transfer performances for both of those cases cannot be observed so much, when a homogeneous main flow is realized.

4 In the condensation phenomena with noncondensable gas, the effect of forced convection induced by vapor is remarkable.

References

1 Sparrow, E. M., and Eckert, E. R. G., "Effect of Superheated Vapor and Non-Condensable Gases on Laminar Film Condensation," *AIChE Journal*, Vol. 7, 1961, pp. 473–477.

2 Sparrow, E. M., and Lin, S. H., "Condensation Heat Transfer in the Presence of a Non-Condensable Gas," JOURNAL OF HEAT TRANSFER, TRANS. ASME, Series C, Vol. 86, 1964, pp. 430–436.

3 Minkowycz, W. J., and Sparrow, E. M., "Condensation Heat Transfer in the Presence of Noncondensables, Interfacial Resistance, Superheating, Variable Properties and Diffusion," *International Journal of Heat and Mass Transfer*, Vol. 9, 1966, pp. 1125–1143.

4 Rose, J. W., "Condensation of a Vapor in the Presence of a Non-Condensing Gas," *International Journal of Heat and Mass Transfer*, Vol. 12, 1969, pp. 233–237.

5 Othmer, D. F., "The Condensation of Steam," *Indust. Eng. Chem*, Vol. 21, 1929, pp. 576–583.

6 Henderson, C. L., and Marchello, J. M., "Film Condensation in the Presence of Noncondensable Gas," JOURNAL OF HEAT TRANSFER, TRANS. ASME, Series C, Vol. 91, 1969, pp. 447–450.

7 Al.-Diwany, H. K., and Rose, J. W., "Free Convection Film Condensation of Steam in the Presence of Non-Condensing Gases," *International Journal of Heat and Mass Transfer*, Vol. 16, 1973, pp. 1359–1369.

8 Koh, J. C. Y., "Film Condensation in a Forced-Convection Boundary Layer Flow," *International Journal of Heat and Mass Transfer*, Vol. 5, 1962, pp. 941–954.

9 Sparrow, E. M., Minkowycz, W. J., and Saddy, M., "Forced Convection Condensation in the Presence of Noncondensables and Interfacial Resistance," *International Journal of Heat and Mass Transfer*, Vol. 10, 1967, pp. 1829–1845.

10 Denny, V. E., Mills, A. F., and Jusionis, V. J., "Laminar Film Condensation From a Steam-Air Mixture Undergoing Forced Flow Down a Vertical Surface," JOURNAL OF HEAT TRANSFER, TRANS. ASME, Series C, Vol. 93, 1971, pp. 297–304.

11 Jacobs, H. R., "An Integral Treatment of Combined Body Force and Forced Convection in Laminar Film Condensation," *International Journal of Heat and Mass Transfer*, Vol. 9, 1966, pp. 637–648.

12 Mori, Y., and Hijikata, K., "Free Convective Condensation Heat Transfer With Noncondensable Gas on a Vertical Surface," *International Journal of Heat and Mass Transfer*, Vol. 16, 1973, pp. 2229–2240.

13 Johnstone, H. F., Kelley, M. D., and McKinley, D. L., "Fog Formation in Cooler-Condensers," *Indust. Eng. Chem.*, Vol. 42, 1950, pp. 2298–2302.

V. E. Schrock
Professor, Department of Nuclear Engineering.
Mem. ASME

E. S. Starkman[1]
Professor, Emeritus
Department of Mechanical Engineering,
and Vice President, Environmental Activities.
Mem. ASME

General Motors Corp.,
Warren, Mich.

R. A. Brown
Former Graduate Student,
Department of Mechanical Engineering,
University of California, Berkeley, Calif.

Flashing Flow of Initially Subcooled Water in Convergent–Divergent Nozzles

This paper presents results from a research program conducted a number of years ago on the problem of flashing flow of water in nozzles. In a previous paper [1][2] we presented results for the case of stagnation states in the low quality two-phase region. The present paper reports results for stagnation states in the subcooled region at pressures up to 9.05 $\times 10^3$ kN/m^2 and subcooling from 0 to 60°C. Pressure profiles and flow rates are reported. The results are compared with limiting cases of Bernoulli flow (meta-stable liquid flow) and homogeneous equilibrium flow. As expected neither was able to predict the experimental results. A two-step model based upon nucleation delay, "discontinuous" transition to two-phase flow followed by frozen composition gave reasonable predictions of the flowrates and pressure profiles in the convergent section.

Introduction

The work described in this paper was done 15 years ago but because it was available only in the form of a government document [2] and thesis it has not been widely known to those who have subsequently worked on two-phase critical flow. Although many papers have appeared in the intervening years on the subject of two-phase critical flow, only a few of these have involved experiments on initially subcooled liquid and there is an apparent need for more extensive data under these conditions. Two-phase flows in nozzles occur in a number of technological applications. Perhaps the first to be studied extensively was that of wet steam in turbine nozzles. The essential difference between the single and two-phase cases is the existence in the latter of slip (differences between average velocities of the two phases) and departure from thermal equilibrium within each and between phases. Slip and nonequilibrium are important in varying degrees depending upon the stagnation state. Nonequilibrium is most important when the fluid passes from a single phase stagnation state into the two-phase region, i.e., the cases of initially superheated vapor or initially subcooled liquid.

Most theoretical approaches to two-phase critical flow have considered slip but assumed thermal equilibrium [3, 4]. In the older literature, Hodkinson [5] and Burnell [6] noted the role of a metastable liquid state and attempted some quantitative explanation. Henry [7] and Edwards [8] were among the first to study the nonequilibrium effect in a more detailed way. Papers by Bouré, Malnes, Sozzi and Sutherland, Moody, Simoneau, and Rohatgi and Reshotko in a recent ASME Symposium [9] concentrated on the nonequilibrium effect. New data for the subcooled liquid case were presented there by Sozzi and Sutherland and Simoneau. A recent thesis by Reocreux [10] provides additional new data and analysis of the problem. It is not the purpose of the present paper to compare the merits of all available theoretical approaches but rather to present our previously unpublished data and show how they compare with some limiting cases and a simple model developed in our own work.

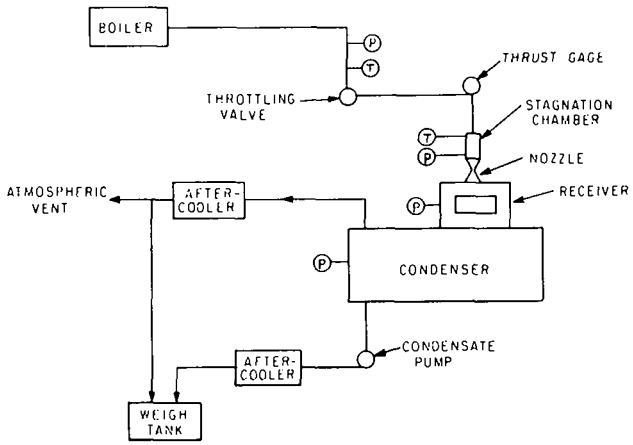

Fig. 1 Schematic of test facility

[1] Deceased.

[2] Numbers in brackets designate References at end of paper.

Contributed by The Heat Transfer Division of THE AMERICAN SOCIETY OF MECHANICAL ENGINEERS and presented at the Heat Transfer Conference, St. Louis, Mo., August 9–11, 1976. Revised manuscript received by the Heat Transfer Division February 22, 1977. Paper No. 76-HT-12

Description

The equipment used in this study was basically the same as that used for study of the initially low quality case and reported in reference [1].

A schematic of the equipment is shown in Fig. 1. Feed water was raised to high pressure by a positive displacement pump and heated to high temperature in a standard Bessler Model 3A once-through boiler, at a maximum pressure of 1.03×10^4 kN/m^2 (1500 psia) and a maximum flow rate of approximately 1.32 kg/s (2.9 lb/s). The subcooled water was passed through one of two interchangeable nozzles. The nozzle discharged into a glass walled chamber, wherein the jet could be observed, and continued into an atmospheric condenser. The nozzle throat restriction is the critical area of the system and determines a characteristic relationship between chamber pressure and temperature for a constant flow rate.

The nozzle was fed from a 6.35-cm dia stagnation chamber. The two nozzles used had throat diameters of 0.640 cm (0.252 in.) and 0.396 cm (0.156 in.) and were designated nozzles number 2 and 3, respectively, (Nozzle No. 1 had a larger throat and could be used only for tests with two-phase stagnation states). Both nozzles had conical convergent sections with 40-deg half-angle and conical divergent sections with 12-deg half-angle. At the exit plane Nozzle No. 2 had a diameter of 3.183 cm while Nozzle No. 3 had a diameter of 2.56 cm. Nozzle No. 2 was fitted with 12 and Nozzle No. 3 with 17 static pressure taps spiraled along the nozzle length. All taps were 0.0794-cm ($\frac{1}{32}$-in.) dia except the throat tap of Nozzle No. 3 which was 0.0397 cm ($\frac{1}{64}$ in.).

The pressures were read on Bourdon type gages. During operations, large fluctuations occurred as pressure and temperature readings indicated the presence of two phases, however, a relatively steady mean pressure could easily be read. Five to seven pressure gauges were used to divide the reading range and obtain an available accuracy of ±1 percent in pressure. However, the fluctuations make ±5 percent a more realistic value. A Kistler model 601 miniature pressure transducer was attached to the pressure taps and the existence of a basic mean pressure verified.

The temperature was measured in the 6.35-cm (2.5-in.) dia chamber section immediately preceding the converging section of the nozzle. An iron-constantan thermocouple connected to a Brown recording potentiometer provided a continual monitor of the chamber temperature. This allowed temperature measurements to be read to ±0.28°C (±0.5°F). A periodic variation in the temperature (and thus in the pressure and flow rates) of approximately 2-min period and 1°C amplitude was observed and was compensated for by appropriate care in synchronizing data readings.

The flow rates were read to ±0.05 kg/s accuracy. Runs were taken by first setting a flow rate and then varying the heat input from the boiler. The characteristics of the supply system made it very difficult to operate with conditions very near saturation in the chamber as the controls were not sensitive enough.

Experimental Results

Data were collected for 27 conditions using Nozzle No. 2 and 30 conditions using Nozzle No. 3 for the study of liquid stagnation conditions. However, fifteen of the runs made with Nozzle No. 2 had stagnation states very close to saturation; most of these probably were very low quality two-phase states. In the case of Nozzle No. 3, four of the 30 runs had incomplete data. Thus, reliable and complete runs were made for a total of 38 subcooled liquid stagnation states. One of the runs was made with cold water (23.3°C). Since the system characteristics produced a unique relationship between chamber

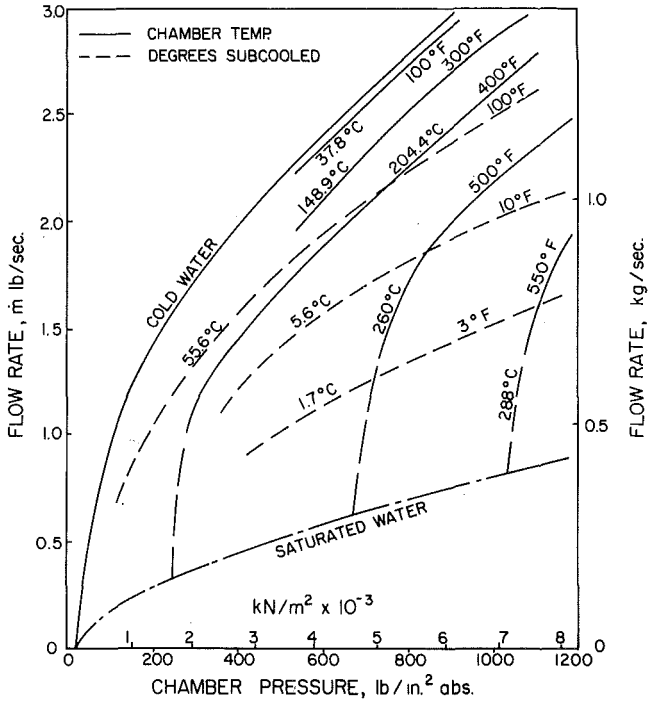

Fig. 2 Experimental flow map for Nozzle No. 3

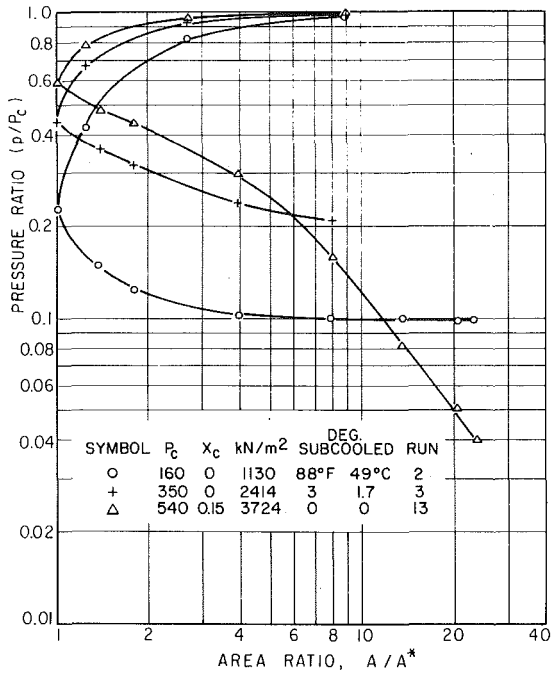

Fig. 3 Pressure profiles in Nozzle No. 2 for G = 3.5 kg/cm^2 s

Nomenclature

A = area
g_c = dimensionless units correction factor
G = mass flux
h = specific heat
$\dot{m}$ = flow rate
p = pressure
R = radius
T = temperature
u = velocity
ρ = density
σ = surface tension

Subscripts

ℓ = liquid phase
c = chamber conditions
sat = saturation conditions

pressure and subcooling, the results were mapped approximately for Nozzle No. 3 as shown in Fig. 2. Fig. 2 was constructed by fairing in constant temperature lines in the field of 26 data points. The line labeled *cold water is the calculated Bernoulli flow with atmospheric* pressure at the throat. This represents an upper bound on the flow as a function of the stagnation pressure. The lower envelop was approximated by extrapolating fitted isotherms to their corresponding saturation pressure. A similar more speculative map was prepared by Brown [2] for Nozzle No. 2.

Figs. 3–8 show the pressure profiles measured at various flow rates and chamber pressures.[3] A general feature of the results (Figs. 3, 5–8)

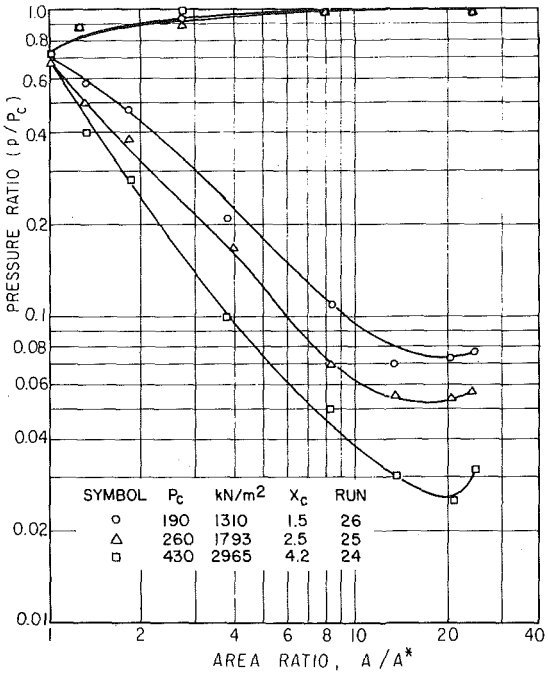

Fig. 4 Pressure profiles in Nozzle No. 2 with low quality stagnation states and $G = 1.19$ kg/cm² s

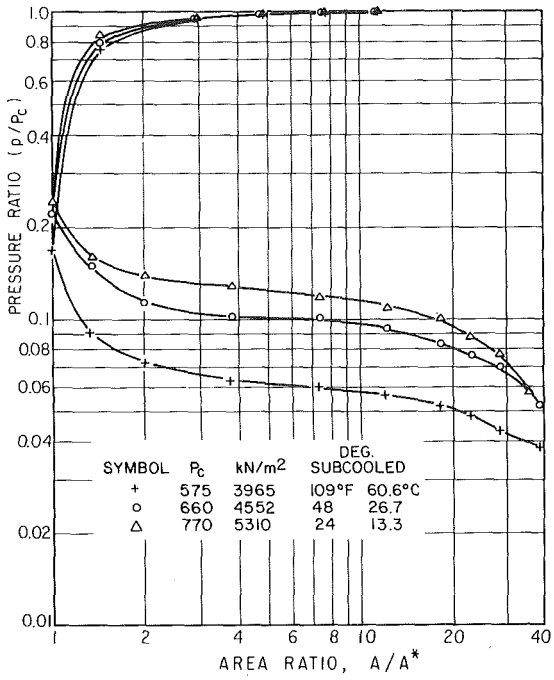

Fig. 6 Pressure profiles in Nozzle No. 3 for $G = 7.0$ kg/cm² s

is seen to be a lowering of the pressure ratio profiles when subcooling is increased while the flow is held constant. This corresponds also to a reduction in stagnation pressure according to the system characteristic. In contrast the case of initial low quality exhibits a general increase in the pressure ratio profiles throughout the nozzle, as shown in Fig. 4,[4] as the stagnation pressure is reduced. Pressure ratio profiles for other runs follow these trends. They may be found for all the data in reference [2].

It may also be seen from Figs. 3–8 that for a given flowrate the pressure ratio profile in the convergent section is not very sensitive to changes in the stagnation pressure except near the throat. Fig. 9

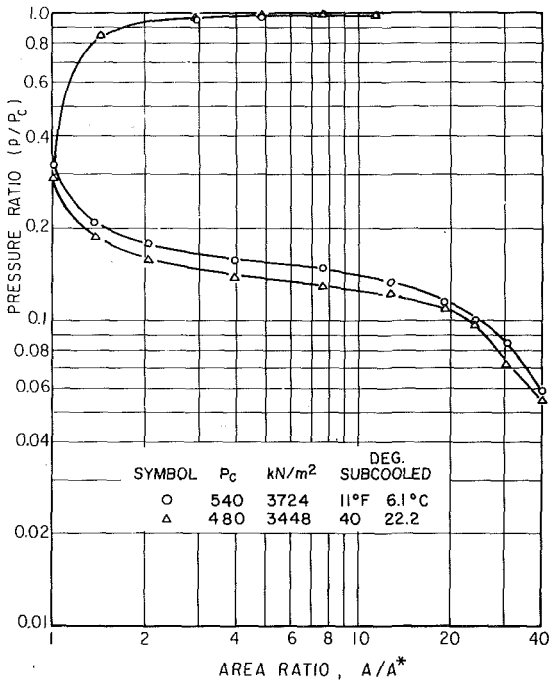

Fig. 5 Pressure profiles in Nozzle No. 3 for $G = 5.5$ kg/cm² s

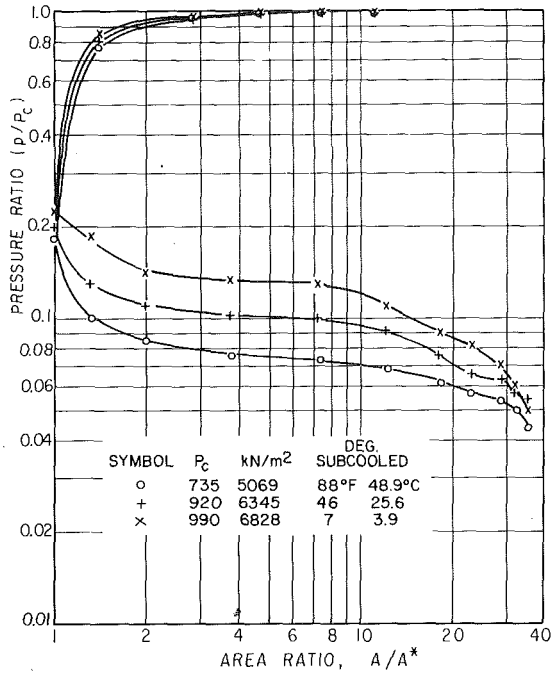

Fig. 7 Pressure profiles in Nozzle No. 3 for $G = 7.8$ kg/cm² s

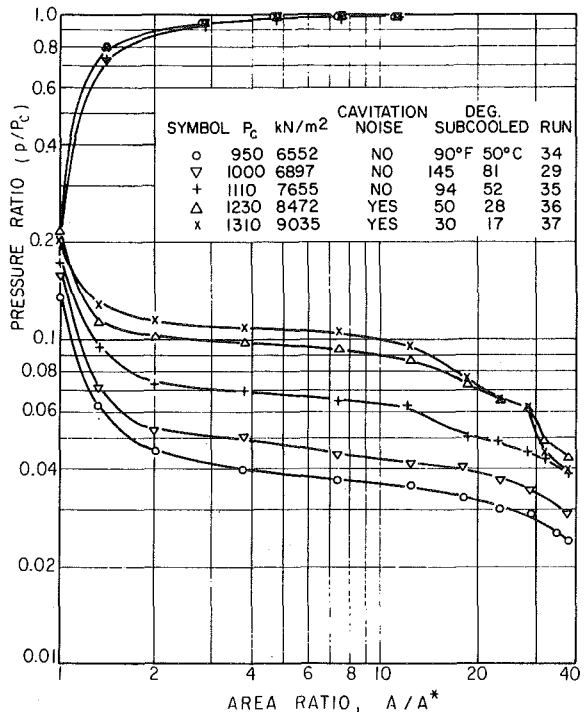

Fig. 8 Pressure profiles in Nozzle No. 3 for $G = 9.5$ kg/cm² s

shows the dependence of measured critical pressure ratio upon the subcooling. The large scatter in these data is probably due at least in part to the very strong axial pressure gradient at the throat and the considerable fluctuations that existed during tests. It is possibly due also in part to the fact that the critical pressure ratio may also depend upon stagnation pressure. However, a clear relationship could not be found from the present data for dependence upon independent variations in subcooling and stagnation pressure.

From Fig. 2 the observation can be made that as the isotherms approach the saturation values, their slope becomes increasingly steep. This results in large changes in flow rates for small fluctuations in pressure. Extreme sensitivity to small variations in chamber conditions was observed in this region, and accurate recording of data became impossible. The experimentally observed flowrates are presented in Table 1.

General Considerations

When the initially subcooled liquid enters the convergent nozzle it behaves as a single phase fluid in at least a portion of the nozzle.

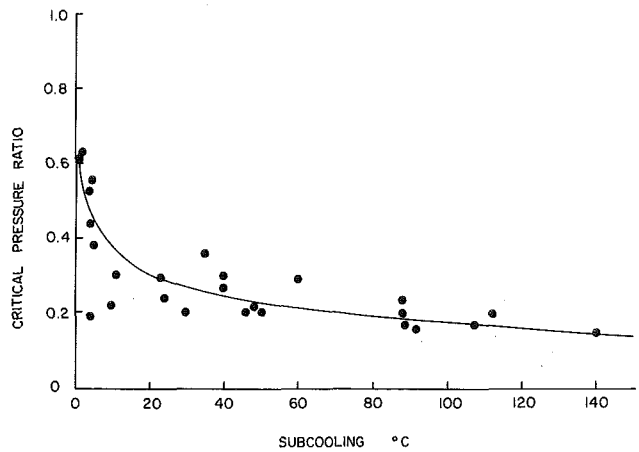

Fig. 9 Critical pressure ratio dependence on subcooling

Table 1 Experimental flow rates

Run No.	Pressure $N/m^2 \times 10^{-5}$	Temperature C	Subcooling C	Flowrate kg/sec	
1	7.94	23.3	141.1	1.14	
2	11.1	135.6	48.9	1.14	
3	24.2	166.1	1.7	1.15	
4	33.8	237.2	3.3	1.16	
5	32.8	237.2	2.2	1.16	
6	23.8	217.8	3.3	1.16	Nozzle No. 2
7	22.1	214.4	2.8	1.17	
8	22.1	213.3	1.7	1.18	
9	15.2	166.1	32.8	1.16	
10	14.8	170.0	27.8	1.17	
11	14.8	167.8	30.0	1.17	
27	50.8	215.6	48.9	0.945	
29	69.1	203.9	80.6	1.17	
30	60.1	227.5	48.3	1.02	
31	53.2	254.4	22.2	0.864	
32	56.6	265.0	6.7	0.877	
33	39.7	189.4	60.6	0.873	
34	65.6	245.0	50.0	1.17	
35	76.0	239.4	52.2	0.462	
36	84.9	270.6	27.8	1.14	Nozzle No. 3
37	90.5	286.7	16.7	1.14	
38	63.5	253.3	25.6	0.991	
39	68.4	280.0	3.9	0.959	
40	53.2	220.6	47.2	0.968	
41	32.5	176.4	61.7	0.818	
42	44.2	243.6	12.8	0.795	
46	61.5	252.8	24.4	0.955	
47	69.1	283.1	1.7	0.727	
48	60.1	275.0	0.6	0.606	
49	40.1	248.6	1.7	0.250	
50	56.6	270.3	1.7	0.845	
51	71.5	286.1	18.3	0.864	
52	45.6	231.1	26.7	0.845	
53	40.7	235.0	16.8	0.845	
54	38.0	242.8	7.2	0.695	
55	34.5	230.0	11.7	0.682	
56	37.3	240.0	6.1	0.682	
57	33.1	211.1	22.2	0.718	

Pressure drops rapidly and may reach the level of $p_{sat}(T')$ before the fluid reaches the throat. It then continues for some distance as a single phase fluid (metastable) until nucleation processes introduce the vapor phase. In the single phase region if the liquid compressibility is neglected, the steady flow is governed by the Bernoulli equation

$$\dot{m} = \rho_\ell A u = A\left[\frac{2\rho_\ell p_c g_c\left(1-\frac{p}{p_c}\right)}{1-\left(\frac{A}{A_c}\right)^2}\right]^{1/2} \tag{1}$$

For a given flowrate, this equation predicts the pressure ratio profile in the single phase region. When equation (1) is applied to convergent-divergent nozzles fed with high pressure cold water and atmospheric pressure at the nozzle exit plane, a large negative pressure is predicted at the throat. Evidently, this results in flow separation at the throat and the divergent section is not filled with liquid and does not control the flowrate. An upper limit on the flowrate is then given by applying equation (1) to the convergent section alone and assuming that the receiver pressure penetrates to the throat. Good agreement was obtained between "cold water" (23°C) test data and this method of prediction when the stagnation pressure was 700 kN/m² or higher. Under these conditions no flashing occurs in the convergent section. As mentioned above, this is the basis of the cold water curve shown in Fig. 2.

In all the hot water tests conducted in the present program (subcooling of 60°C or less) the measured flowrate was considerably less than predicted by Bernoulli flow in the convergent section. This is evidence of the fact that the limit of metastability was reached up-

stream of the throat and a two-phase region existed in the remainder of the convergent section. Two-phase choked flow then occurred at the nozzle throat with local pressure above the back pressure indicating a compressible fluid expansion in the divergent section.

Isentropic-Homogeneous-Equilibrium Model

The problem of low quality stagnation state was investigated in reference [1] using the same apparatus used for the experimental data for this paper. It was found that the isentropic-homogeneous-equilibrium model adequately described the pressure profiles and predicted the flow rates for chamber qualities above 10 percent. At lower qualities the flow rates predicted were increasingly too low. The assumptions of this equilibrium model are:

1 Thermal equilibrium exists throughout.
2 Uniform and equal velocities of both phases.
3 The pressure is uniform in a section normal to the flow.
4 The expansion is isentropic.

This model, which requires step-by-step numerical procedures, is well documented in the literature and no further details of the procedure will be given here. Applying this model to the case of subcooling involves using the Bernoulli equation to establish pressure profiles in the single phase region which terminates at the position where $p = p_{sat}(T)$.

Two-Step Model

Following earlier discussion of the existence of nucleation delay and a metastable region, Brown [2] performed some calculations for a two-step process. This model is based upon the concept of nucleation delay. Due to the short residence time (on the order 10^{-3} s), the liquid tends to enter a metastable state and becomes increasingly superheated as it moves in the convergent section of the nozzle. The limit of metastability is reached and the vapor phase appears quite suddenly as a result of copious nucleation in the bulk liquid and on the nozzle surface. The extreme limit of metastability is imposed by the molecular fluctuations within pure liquid as predicted by Volmer [11]. This theory predicts the rate of production of unstable nucleus bubbles in a pure liquid at a given liquid temperature. Nucleus bubble size is related to the pressure difference (and the associated liquid superheat) between the vapor in the bubble and the liquid by the well-known force balance equation

$$R_0 = \frac{2\sigma}{p_v - p_\ell} \tag{2}$$

The size of nucleus bubbles in pure water undergoing spontaneous nucleation is on the order 10^{-7} cm and it has been found that the corresponding liquid superheating is considerably greater than actually required to produce flashing in nozzle flow. Evidently preexisting small bubbles of gas of much larger size are present and serve to trigger the nucleation process at a much lower superheat. Cavities in the nozzle surface may also play a role in the nucleation process. Unfortunately the number and size of such bubbles is unknown in general and depends upon the past history of water pressure and temperature and other factors. There is at present no satisfactory means of predicting the number and size of microbubbles in liquids.

In the two-step model it is assumed that the limit of metastability for the impure water is known and that a two-phase equilibrium condition is instantaneously produced when the limit is reached. Some justification for this assumption is provided in Brown's thesis by comparing the bubble growth rate according to Forster and Zuber [12] with the fluid transit time in the convergent section.

The conservation of mass, momentum, and energy across the discontinuity are expressed by

$$\rho_1 u_1 = \rho_2 u_2 \tag{3}$$

$$\rho_1 u_1^2 + p_1 = \rho_2 u_2^2 + p_2 \tag{4}$$

$$h_1 + \frac{u_1^2}{2} = h_2 + \frac{u_2^2}{2} \tag{5}$$

which are the same equations as for normal shock waves in gases. These equations, together with the equation of state (steam tables), give the state on the downstream side of the discontinuity. Downstream of the discontinuity two calculation procedures were tried as follows.

Two-Step Equilibrium Model

In this model the flow downstream of the discontinuity is assumed to be governed by the isentropic homogeneous equilibrium model.

Two-Step Frozen Composition Model

Here it is assumed that the short resident time in the nozzle precludes further evaporation and the quality remains constant downstream of the discontinuity. The frozen composition model described in reference [1] applies in this region.

Discussion

Although the limitations inherent in the experimental setup made it impossible to vary stagnation chamber pressure and temperature independently and therefore hamper the process of isolating the effects of one variable the data reveal trends and support several conclusions. Observed and predicted flowrates are presented in Figs. 10 and 11. Results for the two-step frozen composition model were evaluated using $R_0 = 2.54 \times 10^{-5}$ cm (two-step I) and $R_0 = 1.27 \times 10^{-4}$ cm (two-step II). No comparison is shown for the two-step equilibrium model which gave relatively poor results. These figures show that the two-step model gives a reasonable prediction of the flowrate while the isentropic homogeneous model greatly under-predicts the flowrate. The two-step model is rather sensitive to the metastable limit (critical nucleus size) chosen, especially at high chamber pressure. The comparison indicates that a better agreement could be achieved by choosing a value for R_0 that is larger at lower chamber pressures. Such a relation between R_0 and pressure may be intuitively the correct trend, but unfortunately we have as yet no way of independently establishing the true relationship.

Fig. 12 shows comparison of a selected observed pressure profile to the various models. It is apparent that no single model adequately predicts the pressure profile. The plotted two-step profile is that of constant quality downstream of the discontinuity. This is the model that most accurately predicts the flow rates.

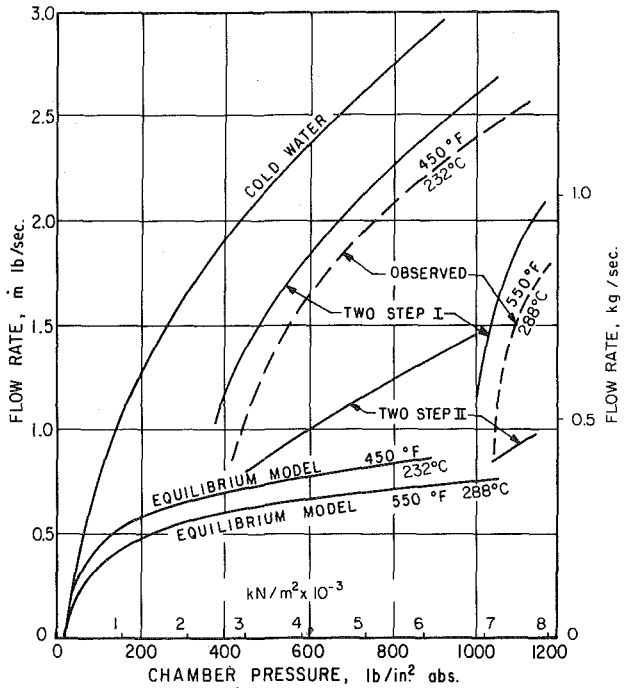

Fig. 10 Comparison of observed and theoretical flowrate for Nozzle No. 3

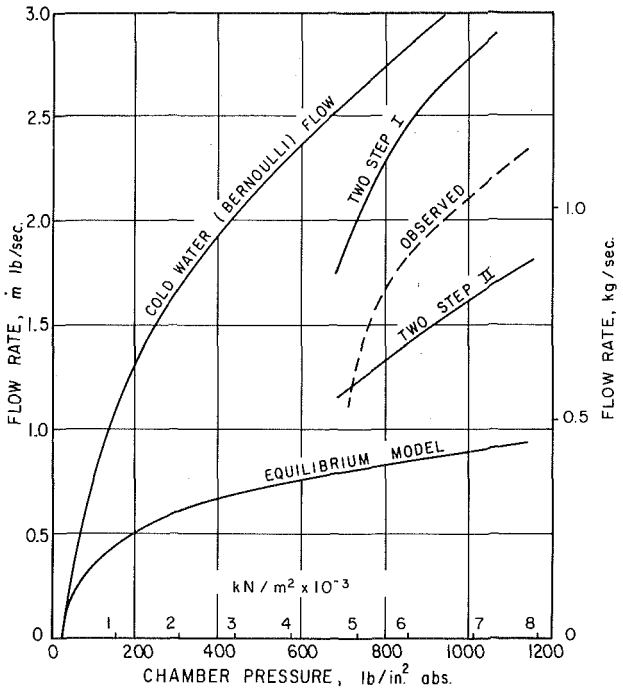

Fig. 11 Comparison of observed and theoretical flowrate for Nozzle No. 3

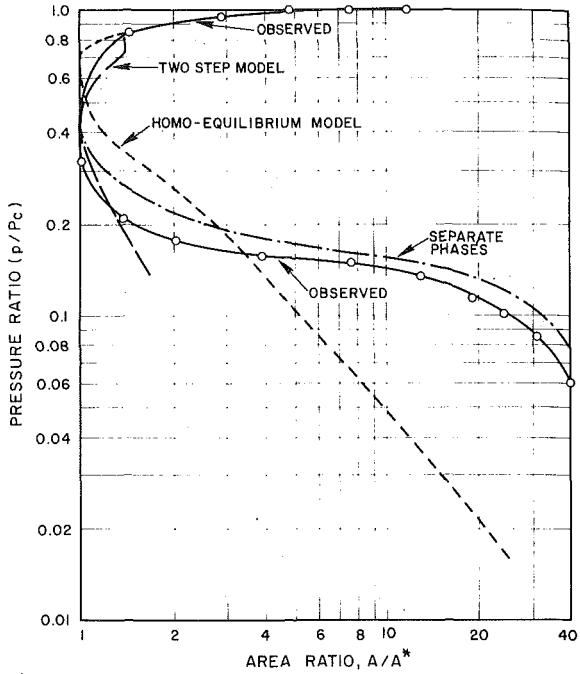

Fig. 12 Comparison of observed and theoretical pressure profiles for Run 56

Pressure drops were found to diverge from those predicted by incompressible flow in the converging portion of the nozzle, dropping more rapidly from a point shortly before the throat. Pressure measurements in this region were not numerous enough to indicate the exact point of departure to allow comparison with the predicted point of the discontinuity in the two-step theory. Pressures at the nozzle throat were reasonably predicted by the two-step model but beyond the throat measured pressures are much higher than predicted. This indicates that the frozen composition assumption is poor in the divergent section. Assuming equilibrium in the divergent section, with or without slip gave pressure profiles with trends and magnitudes similar to the observed data.

Conclusions

Data are reported for flashing expansion flowrates and pressure profiles in convergent-divergent nozzles fed with high pressure subcooled water. The following conclusions may be drawn:

1 The flowrates observed are considerably greater than predicted by the isentropic-homogeneous-equilibrium theory and below the predicted value for cold water flow.

2 When the subcooling is less than 60°C, flashing begins upstream of the throat.

3 For a given water temperature the flowrate becomes very sensitive to changes in the stagnation pressure as subcooling becomes small. Similarly at constant stagnation pressure, the observed flowrate was very sensitive to small changes in temperature when the subcooling is small.

4 A simple two-step model was proposed based on nucleation delay and discontinuous flashing. This model, based on previous observations of the metastable state in such flows, was found to reasonably explain certain aspects of the data. On the other hand, the model lacks an independent means to determine the bubble nucleus size upon which the location of the flashing front depends. For this reason, it is reported here to document an idea that has been tried rather than to present it as a useful predictive tool. Because of the sensitivity of flowrate to location of the flashing front, we may expect subcooled critical flow data to depend upon gas content and past history of the water.

Acknowledgment

This work was supported by the U.S. Atomic Energy Commission, University of California Radiation Laboratory, Livermore, California. The authors wish to acknowledge the constructive comments of Dr. R. J. Simoneau during preparation of the final manuscript.

References

1 Starkman, E. S., Schrock, V. E., Neusen, K. F., and Maneely, D. J., "Expansion of a Very Low Quality Two-Phase Fluid Through a Convergent-Divergent Nozzle," *Journal of Basic Engineering*, TRANS. ASME, Series D, Vol. 86, 1964 p. 247.

2 Brown, R. A., "Flashing Expansion of Water Through a Converging-Diverging Nozzle," MS thesis, University of California, Berkeley, USAEC Report UCRL-6665-T, 1961.

3 Fauske, H. K., "Contribution to the Theory of Two-Phase, One-Component Critical Flow," ANL-6633, 1962.

4 Moody, F. J., "Maximum Flow Rate of a Single Component, Two-Phase Mixture," JOURNAL OF HEAT TRANSFER TRANS. ASME, Series C, Vol. 87, 1965, p. 134.

5 Hodkinson, B., "The Flow of Hot Water Through a Nozzle," *Engineering*, Vol. 143, 1937, pp. 629.

6 Burnell, J. G., "Flow of Boiling Water Through Nozzles, Orifices and Pipes," *Engineering*, Vol. 154, 1947, p. 572.

7 Henry, R. E., "Two-Phase Critical Discharge of Initially Saturated or Subcooled Liquid," *Nuc. Sic. & Eng.*, Vol. 41, 1970, pp. 336–342.

8 Edwards, A. R., "Conduction Controlled Flashing of a Fluid and the Prediction of Critical Flow Rates in a One-Dimensional System," USAEA Report AHSB(S) R-147 1968.

9 "Non-Equilibrium Two-Phase Flows," *ASME Symposium Volume*, ASME, New York, 1975.

10 Reocreux, M., "Contribution a l'Etude des Debits Critiques en Ecoulement Diphasique Eau-Vapeur," PhD thesis, University of Grenoble, France, 1974.

11 Volmer, M., "Kinetik der phasen bildung," *Die Chemische Reakton*, Vol. 4, K. F. Bonhoeffer, ed., Liepzig, Steinkopf, 1939.

12 Forster, K. E. and Zuber, N., *Journal of Applied Physics*, Vol. 25, 1954, p. 493.

F. A. Morrison, Jr.

Professor,
Department of Mechanical and Industrial Engineering,
University of Illinois,
Urbana, Ill.
Mem. ASME

Transient Heat and Mass Transfer to a Drop in an Electric Field

A circulating fluid motion is generated by an electric field imposed on a dielectric drop in another dielectric liquid. The motion of the drop surface may be from the poles to the equator or from the equator to the poles. Transient heat or mass transfer results in response to a sudden change in the temperature difference or concentration difference between the drop and the surrounding fluid. The low Reynolds number, high Peclet number response is analyzed. The boundary layer equations are solved exactly using a similarity transformation. Results are obtained for both directions of circulation. While local fluxes differ greatly when the flow reverses, and despite a lack of symmetry, the overall transfer rate is independent of the direction of flow. This result applies to the transient as well as the steady state.

Introduction

When a uniform electric field is imposed on a dielectric drop suspended in another such fluid, charge accumulates at the interface. The field, acting on this surface charge, produces a force distribution generating liquid motion. Because the resultant flow will enhance heat or mass exchange between the drop and its surroundings, it is of interest for direct contact exchange between immiscible liquids.

Direct contact exchange between fluids has important applications in both heat and mass transfer. Solvent extraction is widely practiced where distillation and evaporation are not feasible. Direct contact heat exchange has also found application in oil cooling and other disparate areas. Use of electric fields to enhance direct contact exchange as shown here has the promise of yielding more compact exchangers.

The creeping motion produced by an electric field acting on a spherical drop was analyzed by Taylor [1][1] who found the stresses acting to distort the drop. He determined that a circulatory motion was induced. Two types of circulatory flow can be observed. For either case, streamlines showing such motion within and about a spherical drop are presented in Fig. 1. If the product of the dielectric constant and electrical resistivity of the drop exceeds the corresponding product for the surrounding fluid, the motion at the interface is from the poles to the equator. In the other event, circulation is from the equator to the poles.

Outside a drop of radius a, the creeping fluid flow is described by a Stokes stream function of the form

$$\psi = Ua^2[(a/r)^2 - 1] \sin^2\theta \cos\theta \tag{1}$$

while inside the drop

$$\psi = Ua^2[(r/a)^3 - (r/a)^5] \sin^2\theta \cos\theta \tag{2}$$

As shown in Fig. 1, r is the distance from the drop center and θ is the polar angle measured from the axis of symmetry.

This creeping flow solution should accurately describe the flow for Reynolds numbers at least as large as 0.1.

The velocity U is the maximum velocity generated by the electric field. This is the tangential velocity u_θ at the interface where θ is $\pi/4$. As shown by Taylor, this maximum velocity is

$$U = -\frac{9E^2 a \epsilon_2}{8\pi(2 + \sigma_2/\sigma_1)^2}\left[\frac{\sigma_2\epsilon_1/\sigma_1\epsilon_2 - 1}{5(\mu_1 + \mu_2)}\right] \tag{3}$$

The subscripts 1 and 2 refer to surrounding liquid and drop, respectively. E is the magnitude of the applied field. ϵ, σ, and μ refer, respectively, to dielectric constant, electrical conductivity and viscosity.

While creeping flow is characterized by low values of Reynolds number, Prandtl numbers and Schmidt numbers of viscous liquids are typically large, say of order 10^5. As a result, the Peclet number Pe is restricted here to large values. A thin thermal or concentration boundary layer is formed. Our attention is directed to a thin region on either side of the interface.

The transient temperature distribution is governed by the energy equation

$$\frac{\partial T}{\partial t} = \alpha\nabla^2 T - \vec{V}\cdot\nabla T \tag{4}$$

in either liquid. T is the local temperature. t is the time. α is the thermal diffusivity and $\vec{V}$ is the fluid velocity. Near the drop surface,

[1] Number in brackets designate References at end of paper.

Contributed by the Heat Transfer Division and presented at the Winter Annual Meeting, New York, N.Y., December 5–10, 1976. Revised manuscript received by the Heat Transfer Division October 19, 1976. Paper No. 76-WA/HT-43.

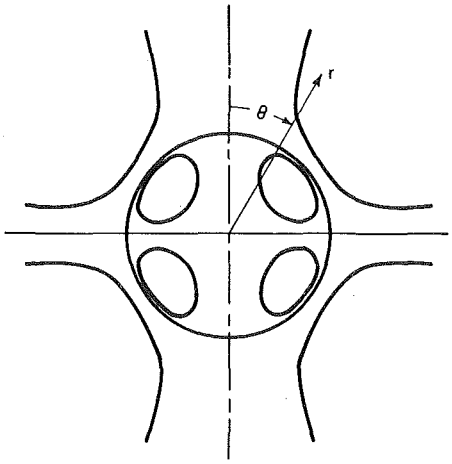

Fig. 1 Streamlines of the circulating liquid motion

within the boundary layer, the energy equation can be simplified considerably. In terms of the radial distance from the surface,

$$y \equiv r - a \tag{5}$$

the energy equation reduces to

$$\frac{\partial T}{\partial t} = \alpha \frac{\partial^2 T}{\partial y^2} - u_r \frac{\partial T}{\partial y} - u_\theta \frac{1}{a} \frac{\partial T}{\partial \theta} \tag{6}$$

The velocity distribution within the boundary layer is calculated from the stream functions, equations (1) and (2). To an order of approximation consistent with equation (6), the velocity components are

$$u_r = \frac{2Uy}{a} (\sin^2 \theta - 2 \cos^2 \theta) \tag{7}$$

and

$$u_\theta = 2U \sin \theta \cos \theta \tag{8}$$

in both liquids.

Transient heat or mass transfer from translating spheres has previously been analyzed using equivalent models. Chao [2] and Chao and Chen [3] analyzed the unsteady transfer to a translating fluid sphere. For large times, their results reduce to the known quasi-steady transfer rates [4, 5] for large Peclet number. Konopliv and Sparrow [6] determined the transient response in the fluid about a translating rigid sphere. As the quasi-steady transfer rate is approached, the first term of the Acrivos and Taylor [7] expansion is recovered.

The analysis presented here uses the technique developed by Chao [2]. When suitable, this approach yields an exact solution to the transient boundary layer relations. An exact closed form solution is obtained. Neither the transient or the quasi-steady results are previously known. While there has been no prior theoretical investigation of the effects described here, two experimental studies have demonstrated large increases in heat [8] and mass [9] transfer. An analysis of the quasi-steady transfer is presented in the Appendix.

Dimensionless Formulation

The Peclet number describing the flow induced by an electric field is defined in terms of the maximum velocity U and the thermal diffusivity of the continuous region.

$$\mathrm{Pe} \equiv \frac{2|U|a}{\alpha_1} \tag{9}$$

A suitable dimensionless time for the response is given by the Fourier modulus.

$$\tau \equiv \frac{\alpha_1 t}{a^2} \tag{10}$$

Dimensionless temperature v is defined

$$v \equiv \frac{T - T_\infty}{T_0 - T_\infty} \tag{11}$$

where T_∞ is the initial temperature in the surrounding fluid and T_0 is the initial temperature throughout the drop. A dimensionless distance from the interface, Y, is defined as

$$Y \equiv \frac{y}{a} \tag{12}$$

in the continuous region where it is everywhere positive and is defined by

$$Y \equiv \frac{y}{a} \left(\frac{\alpha_1}{\alpha_2}\right)^{1/2} \tag{13}$$

in the drop where it is everywhere negative.

Using these definitions and substituting velocity components (7) and (8) into the energy equation, we obtain

$$\frac{\partial v}{\partial \tau} = \frac{\partial^2 v}{\partial Y^2} \pm \mathrm{Pe}\, Y(2 \cos^2 \theta - \sin^2 \theta) \frac{\partial v}{\partial Y} \mp \mathrm{Pe} \sin \theta \cos \theta \frac{\partial v}{\partial \theta} \tag{14}$$

in both regions. The upper sign refers to positive U, surface motion from the poles to the equator. The lower sign applies to the opposite case.

The initial conditions on the temperature distribution are, in agreement with definition (11),

$$v_2 = 1 \quad \text{at } \tau = 0,\ Y < 0$$
$$v_1 = 0 \quad \text{at } \tau = 0,\ Y > 0 \tag{15}$$

Boundary conditions are imposed at the interface and at the outer borders of the thermal boundary layers. Temperature equality is achieved instantaneously at the interface.

$$v_1 = v_2 \quad \text{at } Y = 0 \tag{16}$$

The heat flux is also continuous across the interface. Defining a dimensionless property ratio

Nomenclature

a = sphere radius
c = coefficient in equation (25)
f = heat flux
g = function defined in equation (20)
k = thermal conductivity
Nu = Nusselt number
Pe = Peclet number
Q = overall heat transfer rate
r = spherical radial position
T = temperature
t = time
U = maximum velocity component
u = velocity component
V = velocity
v = dimensionless temperature
Y = dimensionless distance from interface
y = distance from interface
α = thermal diffusivity
β = property ratio defined in equation (17)
ϵ = dielectric constant
η = similarity variable
θ = polar angle
μ = viscosity
σ = electrical conductivity
τ = dimensionless time defined in equation (10)
χ = similarity variable
ψ = Stokes stream function

Subscripts

0 = initial, inside drop
1 = outside drop
2 = inside drop
∞ = initial, outside drop
f = final

$$\beta = \frac{k_1}{k_2}\left(\frac{\alpha_2}{\alpha_1}\right)^{1/2} \tag{17}$$

in terms of the thermal diffusivity α and thermal conductivity k, this condition becomes

$$\beta \frac{\partial v_1}{\partial Y_1} = \frac{\partial v_2}{\partial Y_2} \quad \text{at } Y = 0 \tag{18}$$

When β is small, resistance in the continuous phase dominates. Disperse phase resistance dominates at large β.

At the outsides of the presumably thin thermal boundary layers, the temperatures approach uniform temperatures equal to the initial temperatures

$$\begin{aligned} v_2 &\to 1 \quad \text{as } Y \to -\infty \\ v_1 &\to 0 \quad \text{as } Y \to \infty \end{aligned} \tag{19}$$

More strictly, the bulk drop temperature will continually approach the temperature of the surrounding fluid. The steady state obtained in this analysis is, in fact, quasi-steady. Following the initial response examined here, the transfer rate is well described using the steady-state expressions together with the instantaneous bulk temperatures. While the minimum value of Y is -1, boundary condition (19) is satisfactory because the relations are parabolic. The limit is approached at the outside of the boundary layer.

The analysis of mass transfer is analogous to that for heat transfer. For this reason, it is unnecessary to write the relations for mass transfer. At any point, the corresponding expressions for mass transfer are obtained by replacing temperature by concentration, thermal diffusivity and thermal conductivity by molecular diffusivity, and by introducing a distribution coefficient in equation (16).

Similarity Transformation

If we introduce similarity transformations of the form

$$\begin{aligned} \eta &= Yg(\theta) \\ \chi &= \chi(\theta, \tau) \end{aligned} \tag{20}$$

the energy equation (14) becomes

$$\frac{\partial v}{\partial \chi}\left(\frac{\partial \chi}{\partial \tau} \pm \mathrm{Pe} \sin\theta \cos\theta \frac{\partial \chi}{\partial \theta}\right) \pm \eta \frac{\partial v}{\partial \eta} \mathrm{Pe} \cdot \left[\sin\theta \cos\theta \frac{1}{g}\frac{dg}{d\theta} - (2\cos^2\theta - \sin^2\theta)\right] = g^2 \frac{\partial^2 v}{\partial \eta^2} \tag{21}$$

This equation reduces to the diffusion equation

$$\frac{\partial v}{\partial \chi} = \frac{\partial^2 v}{\partial \eta^2} \tag{22}$$

if two conditions can be satisfied. This great simplification is obtained if

$$\frac{\partial \chi}{\partial \tau} \pm \mathrm{Pe} \sin\theta \cos\theta \frac{\partial \chi}{\partial \theta} = g^2 \tag{23}$$

and if

$$\sin\theta \cos\theta \frac{1}{g}\frac{dg}{d\theta} = 2\cos^2\theta - \sin^2\theta \tag{24}$$

Separating and integrating this final relation, we find that we must choose g to be

$$g = c \sin^2\theta \cos\theta \tag{25}$$

in order to satisfy condition (24). c is an arbitrary constant.

Choosing c^2 to be the Peclet number, condition (23) becomes

$$\frac{\partial \chi}{\partial \tau} \pm \mathrm{Pe} \sin\theta \cos\theta \frac{\partial \chi}{\partial \theta} = \mathrm{Pe} \sin^4\theta \cos^2\theta \tag{26}$$

Using the method of characteristics and requiring that χ and τ vanish together for all θ, we integrate to find

$$\chi = \pm \frac{\sin^4\theta}{4} \mp \frac{\tan^4\theta \exp(\mp 4\,\mathrm{Pe}\,\tau)}{4[1 + \tan^2\theta \exp(\mp 2\,\mathrm{Pe}\,\tau)]^2} \tag{27}$$

The transient temperature distribution is described by the diffusion equation (22) subject to equations (15), (16), (18), and (19). These conditions are written in terms of the similarity variables if one replaces τ by χ and Y by η. Because of the symmetry about the equatorial plane, we have restricted our attention to the hemisphere, $0 \le \theta \le \pi/2$. The solution is well known [10]. Outside of the drop

$$\frac{T - T_\infty}{T_0 - T_\infty} = \frac{1}{1+\beta}\,\mathrm{erfc}\left(\frac{y \sin^2\theta \cos\theta}{2a}\sqrt{\frac{\mathrm{Pe}}{\chi}}\right) \tag{28}$$

while within the drop

$$\frac{T - T_\infty}{T_0 - T_\infty} = 1 - \frac{\beta}{1+\beta}\,\mathrm{erfc}\left(\frac{|y| \sin^2\theta \cos\theta}{2a}\sqrt{\frac{\mathrm{Pe}}{\chi}\frac{\alpha_1}{\alpha_2}}\right) \tag{29}$$

The transient temperature distributions will be examined in detail when the two directions of circulation are considered separately. One detail is worth noting here because it applies equally to the two directions of circulation. Regardless of the direction of circulation, when the time is sufficiently small, equation (27) reduces to

$$\chi \to \sin^4\theta \cos^2\theta\, \mathrm{Pe}\, \tau \tag{30}$$

With this expression and with the definitions (10), (12), and (13) of τ and Y, the small time temperature distributions are obtained.

These relations are, of course, the solution for conduction heat transfer between two semi-infinite stationary bodies. In the initial stage of the heat transfer, no angular variation is observed, the fluid velocity is irrelevant, conduction dominates. As time progresses, convective effects become increasingly important.

Heat Transfer

The heat flux at the surface of the drop will vary with the angular position and with time. Initially infinite, the flux at any location will monotonically decrease to its final steady value. Choosing equation (28) to evaluate the flux, we have at the interface

$$f = -k_1 \left.\frac{\partial T}{\partial y}\right|_{y=0} = \frac{k_1(T_0 - T_\infty)\sin^2\theta\cos\theta}{a(1+\beta)}\sqrt{\frac{\mathrm{Pe}}{\pi\chi}} \tag{31}$$

For sufficiently small time, χ is given by equation (30) and the flux is everywhere on the surface equal to

$$f = \frac{k_1(T_0 - T_\infty)}{a(1+\beta)\sqrt{\pi\tau}} = \frac{k_1(T_0 - T_\infty)}{(1+\beta)\sqrt{\alpha_1 t}} \tag{32}$$

At larger times, the convection produces angular variation in the flux.

The overall heat transfer rate for the drop can, by symmetry, be obtained by integration over a single hemisphere surface

$$Q = 4\pi a^2 \int_0^{\pi/2} f \sin\theta\, d\theta \tag{33}$$

$$Q = \frac{4\pi a k_1(T_0 - T_\infty)}{1+\beta}\sqrt{\frac{\mathrm{Pe}}{\pi}}\int_0^{\pi/2} \chi^{-1/2}\sin^3\theta\cos\theta\, d\theta \tag{34}$$

The Nusselt number of the drop is

$$\mathrm{Nu} = \frac{Q}{2\pi a k_1(T_0 - T_\infty)} \tag{35}$$

which becomes

$$\mathrm{Nu} = \frac{2}{1+\beta}\sqrt{\frac{\mathrm{Pe}}{\pi}}\int_0^{\pi/2} \chi^{-1/2}\sin^3\theta\cos\theta\, d\theta \tag{36}$$

For small time, this Nusselt number is

$$\mathrm{Nu} = \frac{2}{(1+\beta)\sqrt{\pi\tau}} \tag{37}$$

Because the small time heat transfer is conductive, this result is obtained for any flow about a sphere. Results for later times are presented in the sections dealing with the directions of circulation.

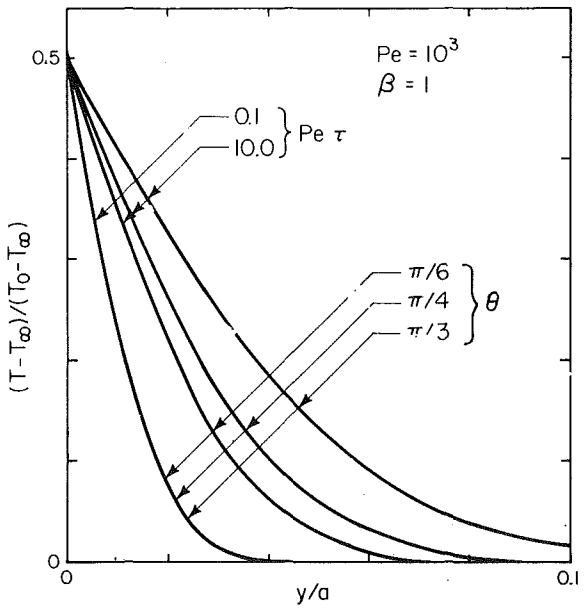

Fig. 2 Transient temperature distribution in the boundary layer outside the drop—circulation from the poles to the equator

Pole to Equator

Circulation with interface motion from pole to equator is considered first. The temperature distribution is given by equations (28) and (29) with χ from equation (27) using the upper signs.

The thermal response outside the drop is shown in Fig. 2 for one set of conditions. β is chosen to be 1 and Pe is 10^3. The temperature distribution is shown at three different values of θ and for two different times. For the short time, Pe τ equaling 0.1, no significant differences are observed at three angular positions. Conduction still dominates at this time. When Pe τ is 10.0, however, the thermal boundary layer is nearly fully established. The thickness of this layer grows as θ increases, that is, in the direction of flow.

For large time, equation (27) yields

$$\chi \to \frac{\sin^4 \theta}{4} \tag{38}$$

in this case. The steady temperature distribution is then

$$\frac{T - T_\infty}{T_0 - T_\infty} = \frac{1}{1+\beta} \operatorname{erfc}\left(\frac{y \cos\theta \sqrt{\mathrm{Pe}}}{a}\right) \tag{39}$$

outside of the drop and

$$\frac{T - T_\infty}{T_0 - T_\infty} = 1 - \frac{\beta}{1+\beta} \operatorname{erfc}\left(\frac{|y| \cos\theta}{a} \sqrt{\frac{\mathrm{Pe}\,\alpha_1}{\alpha_2}}\right) \tag{40}$$

inside of the drop.

When this steady temperature distribution is established, the flux across the interface becomes, from equation (31),

$$f = \frac{2k_1(T_0 - T_\infty)\cos\theta}{a(1+\beta)} \sqrt{\frac{\mathrm{Pe}}{\pi}} \tag{41}$$

The corresponding overall heat transfer rate is expressed as the final, quasi-steady Nusselt number. Integration of equation (36) using equation (38) yields this final Nusselt number.

$$\mathrm{Nu}_f = \frac{2}{1+\beta} \sqrt{\frac{\mathrm{Pe}}{\pi}} \tag{42}$$

The transient Nusselt number is calculated from equation (36) with the complete expression (27) for χ. Gaussian quadrature was used to evaluate the integral.

The ratio $\mathrm{Nu}/\mathrm{Nu}_f$ of instantaneous-to-final Nusselt number depends only on Pe τ, which is $2|U|t/a$ and is independent of the thermal properties of either phase. The ratio of the short time Nusselt number to final Nusselt number is, using equations (37) and (42), $(\mathrm{Pe}\ \tau)^{-1/2}$. This simple expression is accurate to within 5 percent for Pe τ less than about 0.5. When Pe τ is 1.0, the response is nearly complete since $\mathrm{Nu}/\mathrm{Nu}_f$ is only about 1.146. By Pe τ of 2.4, the Nusselt number has fallen smoothly to within 1 percent of its final value. The relaxation time of the thermal response is of order a/U.

Equator to Pole

When the surface flows from the equator to the poles, the temperature distribution differs significantly. Using the lower signs of equation (27) the temperature distribution is calculated as before. The results of these calculations are shown in Fig. 3. Again, the small time distribution is the same at all values of θ and is the same as in the opposite flow. For larger times, the boundary layer thickness grows as θ decreases. In the calculation shown, the thin boundary layer restriction is not satisfied for small θ and large time.

As the heat transfer becomes steady, we have

$$\chi \to \frac{1}{4}(1 - \sin^4\theta) \tag{43}$$

in contrast to equation (38). The steady flux distribution is

$$f = \frac{2k_1(T_0 - T_\infty)\sin^2\theta}{a(1+\beta)(1+\sin^2\theta)^{1/2}} \sqrt{\frac{\mathrm{Pe}}{\pi}} \tag{44}$$

This flux distribution may be compared with the distribution obtained with the opposite circulation. The differences resulting from reversing the flow direction are obvious.

Integration in equation (36) using the final χ for this equator to pole flow, equation (43), yields

$$\mathrm{Nu}_f = \frac{2}{1+\beta} \sqrt{\frac{\mathrm{Pe}}{\pi}} \tag{45}$$

This same result was obtained for pole to equator flow. While local fluxes differ greatly when the flow reverses and while the flux distributions display no symmetry, the overall steady transfer rate is independent of the direction of flow.

Since the interface is isothermal and at the same temperature for both directions of flow, this equality of steady transfer rates is anticipated. It has been shown [11] that the overall rate of steady forced

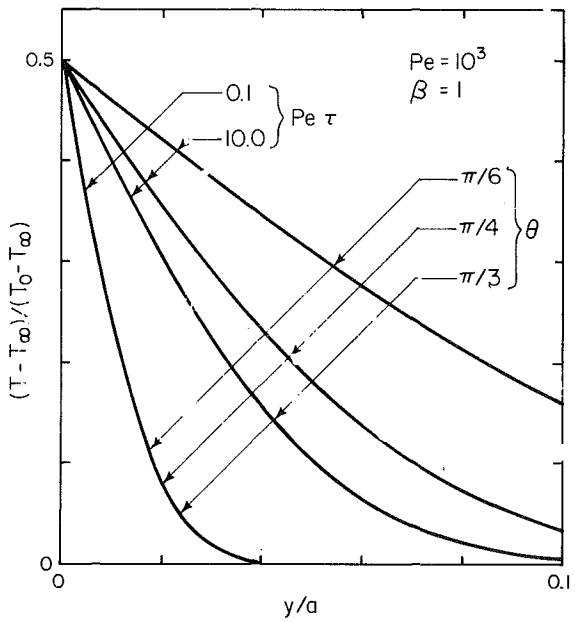

Fig. 3 Transient temperature distribution in the boundary layer outside the drop—circulation from the equator to the poles

convection heat transfer, from an isothermal body of arbitrary shape to a fluid of uniform temperature, is invariant to a flow reversal at every point.

The transient Nusselt number is obtained by integrating equation (36) using equation (27) with the lower signs. For short times, the heat transfer is conductive so that the Nusselt number must agree with pole to equator results. For long times, as the heat transfer becomes steady, the Nusselt number must again agree with pole to equator results. Remarkably, the equator to pole Nusselt number equals the pole to equator Nusselt number at all times. The transient Nusselt number is independent of the direction of flow.

References

1 Taylor, G. I., "Studies in Electrohydrodynamics I. The Circulation Produced in a Drop by an Electric Field," *Proceedings of the Royal Society*, Vol. 291A, 1966, pp. 159–166.

2 Chao, B. T., "Transient Heat and Mass Transfer to a Translating Droplet," JOURNAL OF HEAT TRANSFER, TRANS. ASME, Series C, Vol. 91, 1969, pp. 273–281.

3 Chao, B. T., and Chen, J. L. S., "Series Solution of Unsteady Heat or Mass Transfer to a Translating Fluid Sphere," *International Journal of Heat and Mass Transfer*, Vol. 13, 1970, pp. 359–367.

4 Levich, V. G., *Physicochemical Hydrodynamics*, Prentice-Hall, Englewood Cliffs, 1962.

5 Ruckenstein, E., "On Heat Transfer Between Vapor Bubbles in Motion and the Boiling Liquid From Which They are Generated," *Chemical Engineering Science*, Vol. 10, 1959, pp. 22–30.

6 Konopliv, N., and Sparrow, E. M., "Unsteady Heat Transfer and Temperature for Stokesian Flow About a Sphere," JOURNAL OF HEAT TRANSFER, TRANS. ASME, Series C, Vol. 94, 1972, pp. 266–272.

7 Acrivos, A., and Taylor, T. D., "Heat and Mass Transfer From Single Spheres in Stokes Flow," *Physics of Fluids*, Vol. 5, 1962, pp. 387–394.

8 Kozhukhar, I. A., and Bologa, M. K., "Heat Transfer in Dielectric Emulsions in the Electric Field," *Elektonnaia Obrabotka Materialov*, No. 1, 1968, pp. 51–55 (in Russian).

9 Thornton, J. D., "The Applications of Electric Energy to Chemical and Physical Rate Processes," *Reviews of Pure and Applied Chemistry*, Vol. 18, 1968, pp. 197–218.

10 Carslaw, H. S., and Jaeger, J. C., *Conduction of Heat in Solids*, Second ed., Oxford University Press, Oxford, 1959.

11 Brenner, H., "On the Invariance of the Heat Transfer Coefficients to Flow Reversal in Stokes and Potential Streaming Flows Past Particles of Arbitrary Shape," *Journal of Mathematical and Physical Sciences*, Vol. 1, 1967, pp. 173–179.

APPENDIX

Because the steady heat and mass transfer rates have not been previously obtained, this section is included to show how they may be obtained without analysis of the transients.

The development closely follows the transient analysis until the section on similarity transformation. The changes consist of dropping the storage terms on the left sides of equations (4), (6), and (14), eliminating the dimensionless time defined by equation (10), and removing the initial conditions (15).

Defining η as in equation (20) while deleting χ, the energy equation becomes

$$\pm\eta \frac{dv}{d\eta} \mathrm{Pe} \left(\sin\theta \cos\theta \frac{1}{g} \frac{dg}{d\theta} - 2\cos^2\theta + \sin^2\theta \right) = g^2 \frac{d^2v}{d\eta^2} \quad \text{(A-1)}$$

in place of equation (21). If g is chosen so that

$$\mp \mathrm{Pe} \left(\sin\theta \cos\theta \frac{1}{g} \frac{dg}{d\theta} - 2\cos^2\theta + \sin^2\theta \right) = 2g^2 \quad \text{(A-2)}$$

is satisfied, then equation (A-1) becomes

$$\frac{d^2v}{d\eta^2} + 2\eta \frac{dv}{d\eta} = 0 \quad \text{(A-3)}$$

with error function solutions.

The solution of equation (A-2) depends upon the direction of circulation. For the upper sign, motion from the poles to the equator, we find

$$g = \sqrt{\mathrm{Pe}} \cos\theta \quad \text{(A-4)}$$

while flow from the equator to the poles requires that we choose

$$g = \sqrt{\frac{\mathrm{Pe}}{1 + \sin^2\theta}} \sin^2\theta \quad \text{(A-5)}$$

The solution of equation (A-3), satisfying the boundary conditions imposed on v, is, for $0 \leq \theta \leq \pi/2$,

$$\frac{T - T_\infty}{T_0 - T_\infty} = \frac{1}{1 + \beta} \mathrm{erfc}\,(yg/a) \quad \text{(A-6)}$$

outside the drop, and

$$\frac{T - T_\infty}{T_0 - T_\infty} = 1 - \frac{\beta}{1 + \beta} \mathrm{erfc} \left(\frac{|y|g}{a} \sqrt{\frac{\alpha_1}{\alpha_2}} \right) \quad \text{(A-7)}$$

inside the drop.

The corresponding heat flux at the interface is

$$f = -k_1 \left. \frac{\partial T}{\partial y} \right|_{y=0} = \frac{2k_1(T_0 - T_\infty)g}{\sqrt{\pi} a (1 + \beta)} \quad \text{(A-8)}$$

in agreement with equations (41) and (44). The overall heat transfer rate becomes

$$\mathrm{Nu} = \frac{2}{1 + \beta} \sqrt{\frac{\mathrm{Pe}}{\pi}} \quad \text{(A-9)}$$

regardless of the direction of flow.

K. H. Chen[1]
Post Doctoral Research Engineer.

G. J. Trezek
Professor.

Department of Mechanical Engineering,
University of California,
Berkeley, Calif.

Thermal Performance Models and Drift Loss Predictions for a Spray Cooling System

The relation between the Spray Energy Release (SER) and the spray nozzle efficiency (η) is considered with the view toward increasing the utility of previous spray thermal performance information. Through the approximate analysis of an assumed counter-flow process, the relevant parameters that η depends upon have been identified as the total heat transfer factor c'/c_w, the sensible heat factor ϕ, and the SER. In general η cannot be correlated with wind speed alone. Similarities and differences between the NTU and SER methods are also considered. Values of SER are established from data obtained from a prototype spray system and a laboratory scale single column spray system. A simplified drift loss prediction model which is in good agreement with experimental data is proposed for an open atmosphere spray system.

Introduction

A number of models and correlations have been advanced for the purpose of predicting the thermal performance of single spray units as well as entire spray cooling systems. These models, ranging from being purely empirical to semiempirical in nature, are typically characterized in terms of either the spray nozzle efficiency (η), the so-called Number of Transfer Units (NTU), or more recently the Spray Energy Release (SER).

Traditionally, the spray nozzle efficiency has been defined as a simple ratio of the temperature difference between the warm water entering the nozzle (T_{c0}) and the droplets at the pond surface (T_{sp}) to the temperature difference between T_{c0} and the ambient wet bulb $T_{wb\infty}$, i.e.,

$$\eta = (T_{c0} - T_{sp})/(T_{c0} - T_{wb\infty}) \quad (1)$$

Even though attempts, such as correlating η with wind speed [1],[2] have been made at increasing the utility of the η concept, this approach still has severe limitations because it is not a fundamental description of the energy transfer process. Hence, information from one system cannot be readily extrapolated and transferred to the design of other systems.

The NTU quantity has various definitions. For example, Kelly [2] defines the spray unit NTU as the ratio of the heat rejected by a unit mass of coolant to the difference between the enthalpy of sprayed water leaving the nozzle and that of the ambient air. Hoffman [3] defines the spray unit NTU in integral form similar to the Merkel integral equation but uses an average integrand over the integration. Chen [4] and Porter and Chen [5], through the consideration of the heat and mass transfer of a completely mixed (equivalent) drop, arrived at a Merkel type integral equation on the one side, and a dimensionless parameter incorporating the complex dynamical effect on the other side. The driving potential in the integral equation is taken to be the difference between the total heat of the saturated water and that of the ambient air. The integral is defined as the NTU of the spray unit. Chen [4] has shown that for typical spray modules, the integral equation can be closely approximated by the Hoffman integral [3].

As with the NTU approach, the SER method also relies on the experimentally determined performance of a spray unit to predict that of the entire system. The details of the SER development, including the predictive procedure through the spray field once the SER dependency of the spray unit or cluster has been established with wind speed, have been given by Chen [6] and Chen and Trezek [7]. The SER yields a prediction of the droplet temperature at the pond surface as well as the local air vapor wet bulb and dry bulb temperature.

The aim here is to illustrate the similarities and differences between the previously discussed predictive approaches. In addition, further

[1] Present address: Fast Breeder Reactor Department, General Electric, Sunnyvale, Calif.

[2] Numbers in brackets designate References at end of paper.

Contributed by the Heat Transfer Division for publication in the JOURNAL OF HEAT TRANSFER. Manuscript received by the Heat Transfer Division July 26, 1976.

clarification of the efficiency concept is needed in order to interpret and use previous thermal performance data where outgoing wet bulb temperature of the air leaving the spray is not available, generally, due to lack of adequate instrumentation for this purpose [8]. Knowledge of the link between the unit approach and efficiency also finds utility in the field testing of an existing spray system where the single unit performance may not have been established in advance. A model for predicting the drift loss from a spray system is also presented.

The Relation Between SER and NTU

Consistent with the foregoing discussion, the NTU quantity can be experimentally correlated as a function of ambient wind speed. This relation enables one to determine the spray water temperature at the end of the trajectory once the weather data (wind speed, wet-bulb temperature, etc.) and the nozzle inlet water temperature are known. However, the local humidification and wind attenuation effects in a spray system render the application of the NTU method uncertain unless the local weather condition is determined. For typical spray systems investigated, where the wind attenuation in the spray field is insignificant, the wet bulb temperature variation has been incorporated to account for the local humidification [3, 5]. This consideration of the local humidification effect through the experimental investigation of a typical system restricts the further application of the NTU method when the more general systems are to be evaluated.

Chen [6], through the consideration of a group of droplets having a size distribution, obtained again a similar Merkel type of integral equation which is given as

$$\int_{T_{sp}}^{T_{c0}} \frac{c_w dT}{H_0 - H_G} = 6\left(\frac{\bar{\bar{h}}_c D_{vs}}{k}\right)\left(\frac{\rho_a}{\rho_w}\right)\left(\frac{\alpha \bar{t}}{D_{vs}^2}\right) \tag{2}$$

It has been experimentally observed that the local wet bulb temperature in the spray unit is neither ambient nor homogeneous and, in general, varies from location to location in the spray field. For the case of very low wind, approaching the condition of no wind, the local wet bulb temperature tends to be homogeneous while at high winds it tends to approach the ambient value. Thus, the local air total heat H_G in equation (2) is an undefined quantity. Also, the dimensionless groups on the right-hand side of the equation cannot be readily determined because of the absence of an experimental correlation for the average heat transfer coefficient ($\bar{h}_c$) for the spray. Through a parametric study it has been shown [6] that the integral in equation (2) can be replaced by an approximate expression termed the Spray Energy Release (SER):

$$\int_{T_{sp}}^{T_{c0}} \frac{c_w dT}{H_0 - H_G} \simeq \frac{c_w(T_{c0} - T_{sp})}{H(\bar{T}) - H(\bar{T}_{wb})} \equiv \text{SER} \tag{3}$$

Further, it follows that a minimum SER can be defined as

$$\text{SER}_{\min} \equiv \int_{T_{sp}}^{T_{c0}} \frac{c_w dT}{H_0 - H_{G\infty}} \tag{4}$$

Quantity SER is identical to NTU in that it represents the unknown dynamical parameters of the spray. However, since the experimental evaluation of this quantity depends on the air-vapor energy balance in the equation in which is is employed, the present terminology of SER is used to denote the particular approach used here. Both SER and SER_{min} are expressible as experimental functions of wind speed but are identical at large wind speed. Experimental correlations for SER and $\text{SER}_{\min}$ suffice to define performance for small wind attenuation. In the previous NTU method [4, 5], experimental correlations for NTU and a dimensionless increment in local wet bulb temperature were employed. While the wet bulb temperature varied from spray to spray, it was constant within a spray. In the present SER method a variable local wet bulb temperature is used as related to a liquid to gas ratio.

When the wind attenuation effect is significant, additional consideration of momentum exchange in the spray unit can be carried out. A discussion of the step by step computational procedure through the spray field has been previously presented [6, 7].

The Relation Between SER and η

An energy balance between the sprayed coolant rate (L) and the air (G) which participates in the energy transfer process is approximately given as

$$c_w L dT = G dH_G \tag{5}$$

If a linear approximation is assumed for H_0 such that $dH_0/dT = c' \simeq$ constant then

$$d(H_0 - H_G) = [c' - c_w(L/G)]dT \tag{6}$$

and using equation (3) with the assumption of counterflow yields

Nomenclature

c' = total heat gradient
c_w = specific heat of liquid water
C_D = drag coefficient
D = drop diameter
D_{vs} = Sauter mean diameter
f = a function
FD_x = spray drag force in the x-direction
FD_y = spray drag force in the y-direction
g = a function
$\vec{g}$ = body force per unit mass
G = participating air rate
$\bar{\bar{h}}_c$ = statistical time averaged heat transfer coefficient
H = total heat or sigma heat function
H_G = local air vapor total heat
$\overline{H}_G$ = average local air vapor total heat; $\overline{H}_G = H(\overline{T}_{wb})$
H_0 = total heat corresponding to the saturated spray water temperature
$\overline{H}_0$ = average spray total heat; $\overline{H}_0 = H(\overline{T}_0)$
j = subscript; the jth quantity
k = thermal conductivity
L = water spray rate
$\dot{M}_D$ = drift loss of a spray unit
N = number of spray units
NTU = number of transfer unit
Re = Reynolds number
R_v = cumulative volume (or mass) fraction
$\vec{s}$ = displacement
s_x = displacement in the x-direction
s_y = displacement in the y-direction
SER = Spray Energy Release
$\text{SER}_{\min}$ = minimum Spray Energy Release
S_H = height of the spray unit above pond water surface
S_L = distance of the spray unit from the downwind pond edge
t = time
$\bar{t}$ = average residence of the spray
$t^* = t/\bar{t}$
T = temperature
$T^* = (T - T_{wb\infty})/(T_{c0} - T_{wb\infty})$
T_{c0} = hot nozzle water temperature
T_d = dry bulb temperature
$\overline{T}$ = average spray temperature; $\overline{T} = (T_{c0} + T_{sp})/2$
T_{sp} = spray water temperature at the end of the trajectory
T_{wb} = wet bulb temperature
$\overline{T}_{wb}$ = average wet bulb temperature; $\overline{T}_{wb} = (T_{wb\infty} + T_{wbf})/2$
T_{wbf} = final wet bulb temperature
$T_{wb\infty}$ = ambient wet bulb temperature
u = horizontal air velocity component
u_∞ = ambient wind velocity
$\vec{U}$ = air velocity
$\vec{U}_p$ = drop velocity
v = vertical air velocity component
W_F = total drift loss fraction
α = thermal diffusivity $\theta_{wb} = (T_{wb} - T_{wb\infty})/(T_{c0} - T_{wb\infty})$
η = spray nozzle efficiency
ϕ = sensible heat factor
ρ = air vapor density
ρ_a = density of dry air
ρ_p = density of particles or drops
ρ_w = density of liquid water

$$\int_{H(T_{sp})-H(T_{wb\infty})}^{H(T_{c0})-H(T_{wbf})} \frac{c_w d(H_0 - H_G)}{\left[c' - c_w\left(\frac{L}{G}\right)\right]((H_0 - H_G)} = \text{SER} \tag{7}$$

After integrating and rearranging, equation (7) reduces to

$$\ln\left(\frac{T_{c0} - T_{wbf}}{T_{sp} - T_{wb\infty}}\right) = \ln\left[\frac{1 - \frac{T_{wbf} - T_{wb\infty}}{T_{c0} - T_{wb\infty}}}{1 - \eta}\right] = \text{SER} \cdot \left(\frac{c'}{c_w} - \frac{L}{G}\right) \tag{8}$$

Since $(T_{wbf} - T_{wb\infty}) \ll (T_{c0} - T_{wb\infty})$, equation (8) then reduces to the following relation between η and SER, i.e.,

$$\eta = 1 - \exp\left[-\text{SER} \cdot \left(\frac{c'}{c_w} - \frac{L}{G}\right)\right] \tag{9}$$

If the definition for spray nozzle efficiency is modified by using the local wet bulb temperature in the spray field, then the spray nozzle efficiency at any location in the spray field is given by equation (9), which is based on the counterflow analysis. Even though the counterflow analysis does not represent that for the actual system in which the air flow process is not defined, the analysis does give a functional relationship between the spray efficiency and other relevant spray parameters, i.e., SER, c'/c_w, and L/G.

The ratio c'/c_w, the total heat transfer factor, can be considered as the total energy transferred per unit temperature change of coolant. The quantity L/G indicates the ratio of the coolant spray rate to the amount of air participating in the energy transfer process. In considering this quantity of air, although a complex air flow process exists in a spray system, the basic mechanism that brings about the flow is the existence of the relative velocity of the spray to the air which creates the air flow process over the spray. Thus, the supply of air is achieved by the ambient air movement, the entrainment, and the thermal buoyant force. For a given spray, the participating air will depend upon the wind and the thermal effects.

Functional Relations by Dimensional Analysis

Various dimensional considerations can be used to illustrate the fact that η in general cannot be correlated with wind speed alone. Using an approach according to that of the π-theorem, it follows that a dimensional analysis for L/G yields

$$L/G = g(T_{c0}, T_{sp}, T_{d\infty}, T_{wb\infty}, \text{SER}) = f(\eta, \phi, \text{SER}) \tag{10}$$

where

$$\phi = (T_{c0} - T_{d\infty})/(T_{c0} - T_{wb\infty})$$

Consequently, the minimum number of parameters which the spray nozzle efficiency depends upon are

$$\eta = \eta\left(\frac{c'}{c_w}, \phi, \text{SER}\right) = \eta\left(\frac{\phi c_w}{c'}, \text{SER}\right) \tag{11}$$

Another illustration of the functional relationships given in equation (11) follows from the nondimensionalization of equation (2) before integration; namely,

$$\frac{dT^*}{dt^*} = 6\left(\frac{\bar{h}_c D_{vs}}{k}\right)\left(\frac{\rho_a}{\rho_w}\right)\left(\frac{\alpha\bar{t}}{{D_{vs}}^2}\right)\left(\frac{c'}{c_w}\right) \tag{12}$$

The initial condition at $t^* = 0$ is $T^* = 1$ and

$$T^* = T^*\left(t^*, \frac{h_c D_{vs}}{k}, \frac{\rho_a}{\rho_w}, \frac{\alpha\bar{t}}{{D_{vs}}^2}, \frac{c'}{c_w}\right) \tag{13}$$

At the end of the spray trajectory, $T = T_{sp}$ and

$$T_{sp}^* = T_{sp}^*\left(\text{SER}, \frac{c'}{c_w}\right) \tag{14}$$

The energy balance relation of equation (5) can be expressed nondimensionally as

$$\frac{d\theta_{wb}}{dT^*} = \frac{c_w}{c'}\frac{L}{G} \tag{15}$$

where $dH_0/dT = dH_G/dT_{wb} \simeq c'$. Thus,

$$\theta_{wb} = \theta_{wb}\left(T^*, \frac{c_w}{c'}, \frac{L}{G}\right) \tag{16}$$

At the end of the spray trajectory, $T_{wb} = T_{wbf}$; so that,

$$\theta_{wbf} = \theta_{wbf}\left(T_{sp}^*, \frac{c_w}{c'}, \frac{L}{G}\right) \tag{17}$$

or

$$\theta_{wbf} = \theta_{wbf}\left(\text{SER}, \frac{c'}{c_w}, \frac{L}{G}\right) \tag{18}$$

Since

$$\theta_{wbf} = \frac{T_{wbf} - T_{wb\infty}}{T_{c0} - T_{wb\infty}} = 1 - \frac{T_{c0} - T_{d\infty}}{T_{c0} - T_{wb\infty}} - \frac{T_{d\infty} T_{wbf}}{T_{c0} - T_{wb\infty}} = 1 - \phi - \phi_e \tag{19}$$

it follows that

$$F\left(\phi, \phi_e, \text{SER}, \frac{c'}{c_w}, \frac{L}{G}\right) = 0$$

For the open atmosphere spray systems investigated, $\phi \gg \phi_e$, equation (20) can be approximated as

$$F\left(\phi, \text{SER}, \frac{c'}{c_w}, \frac{L}{G}\right) = 0 \tag{21}$$

and

$$\frac{L}{G} = \frac{L}{G}\left(\frac{c'}{c_w}, \phi, \text{SER}\right) \tag{22}$$

However, from the approximate analysis of a counter-flow spray system as shown by equation (9),

$$\eta = \eta\left(\text{SER}, \frac{c'}{c_w}, \frac{L}{G}\right) \tag{23}$$

or

$$\eta = \eta\left(\text{SER}, \frac{c'}{c_w}, \phi\right) \tag{24}$$

The quantities c'/c_w and ϕ are not independent because the former is indicative of the total quantity of heat rejection while the latter indicates the sensible heat rejection for a unit decrease in temperature potential of the coolant. Thus, η can be further expressed per unit of total heat rejection as

$$\eta = \eta\left(\text{SER}, \frac{c_w \phi}{c'}\right)$$

The particular combination of c_w/c' and ϕ used previously was suggested by the correlation of experimental results presented here.

Experimental Considerations

Thermal performance of sprays was studied at the large laboratory spray pond located at the University of California, Berkeley's Richmond Field Station and at the nuclear service spray ponds of the Rancho Seco Nuclear Generating Station. The laboratory studies were intended to provide information of a more detailed nature such as the trajectories, heat and mass transfer, and size distribution of the spray droplets; effects of spray spacing on air circulation within and around a spray under various ambient psychrometric and wind conditions; and evaluations of a single spray unit SER. On the other hand, the field study at Rancho Seco was primarily concerned with using spray thermal data along with the ambient psychrometric and wind conditions to determine overall pond thermal performance and water losses.

The laboratory facility consists of a $30.5 \times 15.2 \times 1.5$ m rubber lined pond which is heated by means of a boiler and heat exchanger ar-

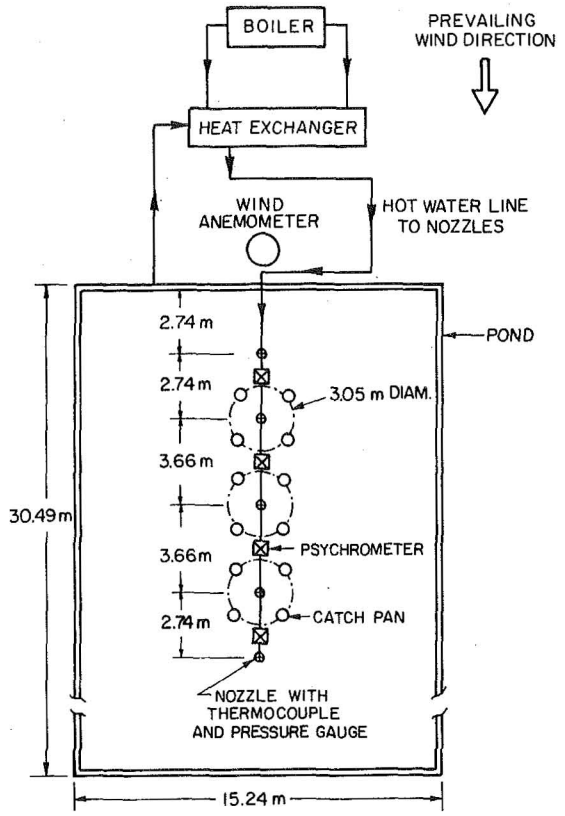

Fig. 1 Schematic drawing of experimental spray pond facility

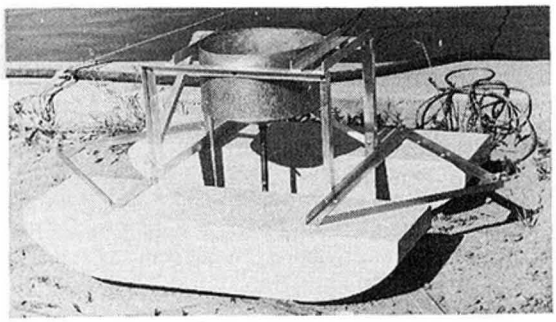

Fig. 3(*a*) Movable catch pan

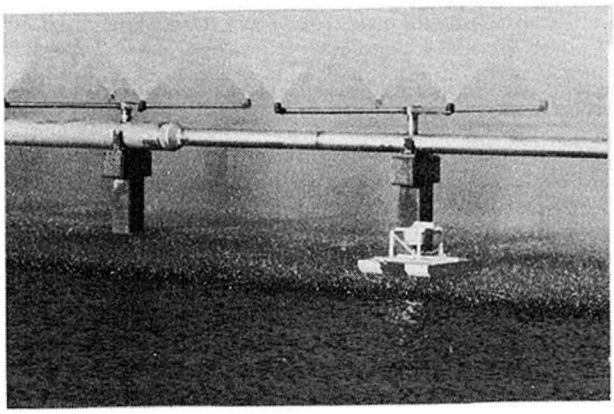

Fig. 3(*b*) Movable catch pan in spray

rangement. Spraco No. 1706 nozzles having a capacity of 10.2 l/m and 12.4 l/m with spray patterns of 3.0 m and 3.7 m at nozzle pressures of 0.34 bar and 0.48 bar, respectively, were arranged as shown in Fig. 1. By changing the pressure and operating either a five- or three-nozzle configuration, thermal performance studies of continuous, where the spray patterns slightly touch, and spaced, nontouching spray nozzle arrangements could be studied. The overall droplet trajectory was about 6.1 m. An instrumentation access platform holding the catch pans was located about 0.6 m above the water level. The spray nozzles were positioned 1.5 m above the platform. The facility was instrumented for the measurement of nozzle inlet temperatures, ambient and interspray psychrometric conditions, wind speed and direction and provided with catch pans for the measurement of droplet temperatures at the pond surface. Further details of this facility are given in reference [6].

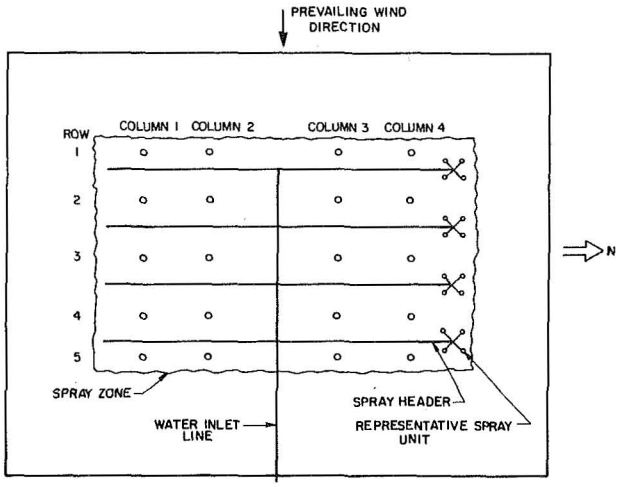

Fig. 2 Schematic diagram of spray system and location of data collection points

In addition to the basic pond performance test concluded at Rancho Seco a number of pond traverses were made of the local conditions of spray temperature and flow rate at various positions, shown in Fig. 2, within the spray pattern. The local temperature and flow rate information was obtained with a movable catch pan which could be traversed through the spray region. Essentially a catch pan was attached to a floating platform, seen in Fig. 3(*a*) which would be towed to prescribed positions in the spray pattern, shown in Fig. 3(*b*), using a guide rope and pulley arrangement.

The catch pan consisted of a 30-cm dia collection pan having a 15-cm high wall. The conical bottom funneled the collected water to a 0.6-cm dia outlet pipe located at the apex of the cone. Located just above the outlet pipe was a thermistor to measure the temperature of the collected water.

The water flow rate through the outlet pipe was controlled by the standing head in the catch pan which in turn was controlled by the local flow rate of the spray. The pipe flow produced a pressure drop in the pipe which was measured using a sensitive Statham Model PM5TC differential pressure transducer. The system was calibrated so that an oscillograph light beam deflection could be correlated with a catch pan flow rate.

The experimental data, taken from these spray pond tests has indicated the dependency of spray nozzle efficiency on the wind speed in addition to the sensible heat effect. The relation between spray nozzle efficiency and SER, Fig. 4, parametric with $c_w\phi/c'$, illustrates the dependency of η on the sensible heat transfer parameter. The more pronounced effect of this parameter is shown in Fig. 5 when L/G is considered in place of η. Consequently, it follows that if the sensible

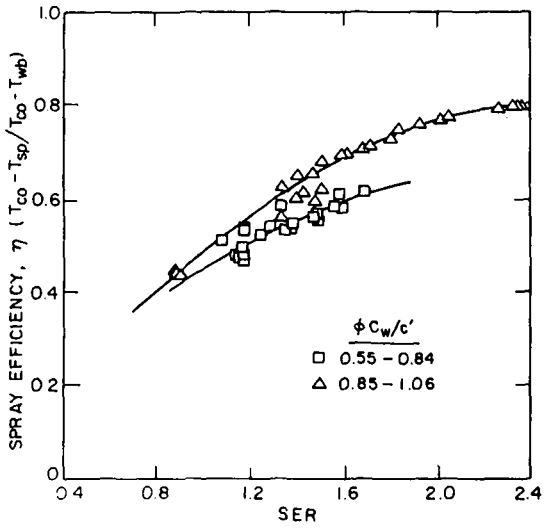

Fig. 4 Spray efficiency as a function of SER for Spraco nozzle No. 1706 at 0.34 bar (5 psig)

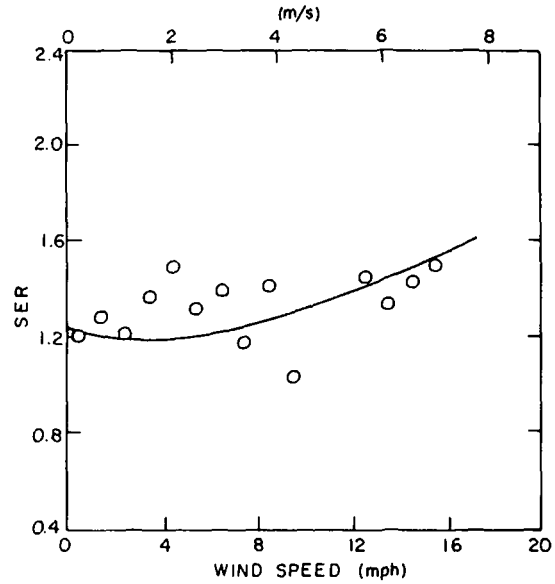

Fig. 6 SER versus wind speed for Spraco nozzle no. 1751 at 0.48 bar (7 psig)

heat transfer parameter and wind speed remain approximately unchanged, the spray nozzle efficiency based on local wet bulb temperature in the spray field will be approximately equal. Thus, if the temperatures T_{c0} and T_{sp} for two continuous spray units or cluster of spray units are known, with one of them being exposed to the ambient condition, the local ambient wet bulb temperature for the downwind unit will be given by

$$T_{wb\infty_2} = T_{c0_2} - (T_{c0_2} - T_{sp_2}) \left(\frac{T_{c0_1} - T_{wb\infty_1}}{T_{c0_1} - T_{sp_1}} \right) \tag{26}$$

where subscripts 1 and 2 designate upwind and downwind conditions.

Data of T_{sp} of the spray rows at different locations along the wind direction is available from the Rancho Seco spray pond test [1]. The upwind spray row at the leading edge and the one immediately following provide enough data to evaluate the approximate final wet bulb temperature for the spray units in the upwind row. The wind speed dependence of SER and SER_{min}, computed from the Rancho Seco data and laboratory spray pond studies [6], is given in Figs. 6 and 7, respectively. This information along with that of the spray drag [7] permits an evaluation of the spray system performance according to a previously outlined procedure [6, 7]. The spray drag-wind speed correlation has been established for the spray cluster under study as

$$FD_x = 0.3878\, u_\infty + 0.4975\, u_\infty{}^2 + 0.3542\, u_\infty{}^3 \text{ (N)}$$

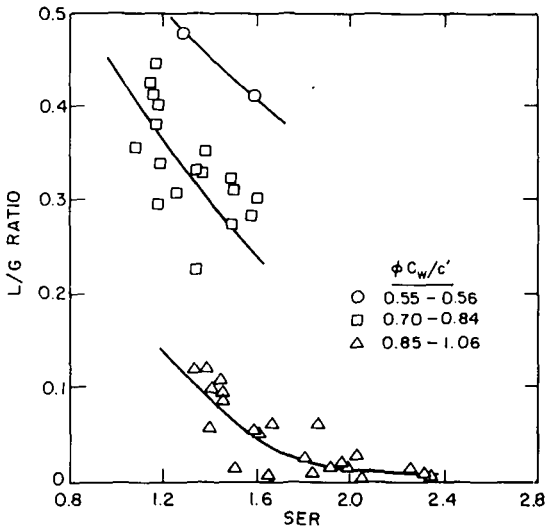

Fig. 5 Ratio of water spray rate to participating air rate, *L/G*, versus SER for Spraco nozzle No. 1706

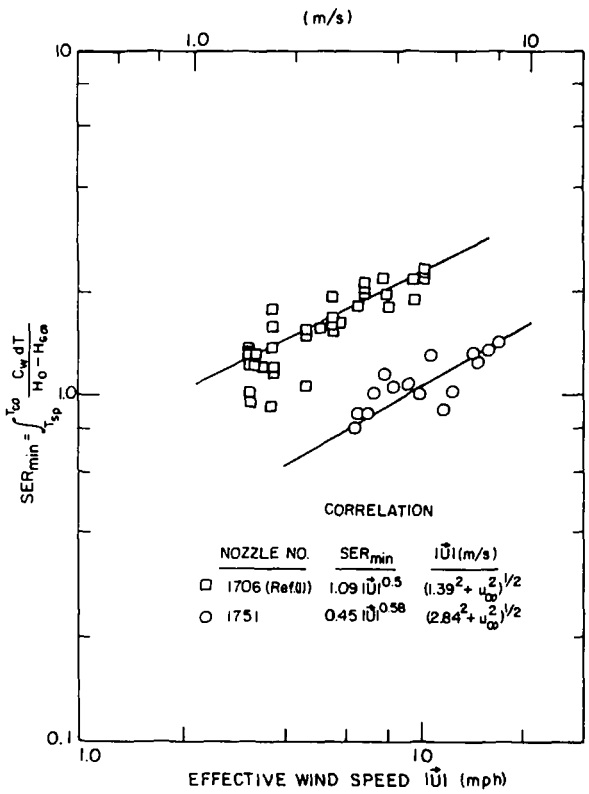

Fig. 7 SER_{min} versus effective wind speed

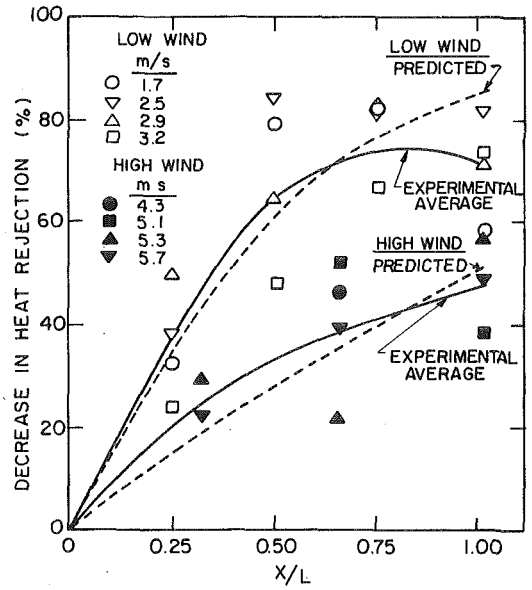

Fig. 8 Decrease in heat rejection versus distance into the spray pattern

$$FD_y = 0.7986\,[1 + (3.13/u_\infty)^2]^{1/2} FD_x;\ u_\infty(m/s) \neq 0 \qquad (27)$$

$$= 2.2237\ (\mathrm{N});\ u_\infty = 0$$

Germane to present considerations are the results of such an evaluation shown in Fig. 8 in terms of the decrease in heat rejection as a function of distance into the spray field from the leading edge. Predictions made by the SER method are within 5 percent for the low wind case and 10 percent for the high wind case of the mean of the data. The deviation at the last row, more pronounced in the low wind case, is due to the interaction of ambient air with the spray causing increased thermal performance.

Spray System Drift Loss

Spray pond drift and its effects have been studied by a few investigators. Guyer and Golay [9] studied the problem of downwind salt deposition from a salt-water spray pond system. A step-wise nonturbulent trajectory calculation approach was utilized in obtaining the droplet location. In this study, the spray pond drift is defined as droplets with size range 0–1000 μ that are transported out of the spray system. Stewart and Nelson [10] investigated the local meteorological effects of drift, icing, and fogging. The average drift size cited in the study is 50–200 μ, while a maximum drop size as seen in the figure is about 450 μ. Schrecker and Henderson [11] obtained a maximum drift particle size of 450 μ at a distance of 91.4 m (300 ft) downwind the spray system and at a height of 4.6 m (15 ft) above the water surface. The wind speed was reported as high but no specific value was given. Schrock, Trezek, and Keilman [8] reported the experimental investigation of a spray pond system and gave an empirical correlation of spray drift as a function of wind speed. At 7.2 m/s the drift loss is about 0.96 percent of the coolant water. From the cumulative distribution data of the spray generator, the drift size is found to be about 500 μ.

It is seen that the drift of a spray system is not well defined. The drift size depends on the system geometry, weather conditions, and the location at which the sample is measured. The complete description of the drift particles movement will involve the solution of the air vapor flow field on top of the spray system together with the solution of the momentum equations describing the motion of a swamp of particles having a distribution dependent upon location and time. However, the present investigation is concerned with the prediction of the amount of sprayed water lost as drift so that the detailed solution of the air vapor and particles flow fields is not necessary nor desirable. If the spray cumulative distribution function is known and if the maximum transportable particle size leaving the spray field can be determined, then the amount of drift loss is readily estimated. Since the distribution of the spray is known through actual testing or otherwise, and if the established spray distribution can be assumed valid for all the spray units in the spray field then the relevant drift loss problem is that of determining the maximum size of the particle that can be transported out of the spray field. This is determined by solving a set of simplified two-dimensional equations of motion.

In the model, the droplets are assumed to move in the relatively narrow air vapor flow field situated between the top of the spray field and the free stream. The air vapor flow field is such that the horizontal velocity component has the same magnitude as the prevailing ambient wind and is constant throughout the spray field. The vertical velocity component is equal to the upward velocity from the spray which is obtained from a momentum balance of the air-vapor flow through the spray [6, 7]. It is constant at a given location in the vertical direction but may be different at different locations in the horizontal direction. This happens because, in general, the spray units at different locations have different vertical velocities because of the differing buoyant forces produced. A further simplification is made by assuming that the air vapor vertical velocity component is the same throughout the flow field and equals that of the spray unit under consideration.

In order to determine the size of the drop that traverses a specified distance, a trial and error method is used. The drop momentum equation is solved for a number of drop sizes. This leads to the determination of the distances covered by the drops. The required drop size is determined when the computed and specified distances match. Assuming that the drift particles formed at the spray top have an initial upward velocity equal to that of the upward flow buoyant air vapor and have no horizontal velocity component, the equation of motion for the drop particle of size D is given by

$$\frac{d\vec{U}_p}{dt} = \frac{3}{4} C_D \left(\frac{\rho}{\rho_p}\right) \frac{1}{D} |\vec{U} - \vec{U}_p| (\vec{U} - \vec{U}_p) + \vec{g}\left(1 - \frac{\rho}{\rho_p}\right)$$

The initial condition is

$$\vec{U}_p = v\vec{j} \text{ at } t = 0$$

and the air vapor flow velocity is

$$\vec{U} = u_\infty \vec{i} + v\vec{j} = \text{constant for } t \geq 0$$

The air vapor density ρ is assumed to be constant. The particle drag coefficient C_D is a function of particle Reynolds number defined as $\mathrm{Re} = |\vec{U} - \vec{U}_p| D/\nu$ and has the following correlation for water drops [6]:

$$\frac{24}{\mathrm{Re}} + \frac{6}{1 + \sqrt{\mathrm{Re}}} + 0.27 \qquad 1 < \mathrm{Re} \leq 1000 \qquad (29)$$

$$C_D = 0.6649 - 0.2712 \times 10^{-3}\,\mathrm{Re} + 1.220 \times 10^{-7}\,\mathrm{Re}^2 - 10.919 \times 10^{-12}\,\mathrm{Re}^3$$

$$1000 \leq \mathrm{Re} \leq 3600 \qquad (30)$$

The displacement of the drop particle is given by

$$\vec{s} = \int_0^t \vec{U}_p dt \qquad (31)$$

where $\vec{s} = s_x\vec{i} + s_y\vec{j}$. This is an open end integration, which means that the final time is not specified. When the origin is taken at the top of the spray unit under consideration, the integration is stopped when $S_y = S_H$, where S_H is the distance between the spray top and the reservoir water surface. Equations (28) and (31) are solved for different drop sizes and a relation for S_L, which is the distance of the spray unit from the downwind pond edge, as a function of drop size $S_L = S_L(D)$ can be obtained (Fig. 9).

The experimental value of spray cumulative volume (or mass) fraction R_v as a function of drop size D, $R_v = R_v(D)$, or $D = D(R_v)$ can be combined with the foregoing to yield

$$S_L = S_L(D(R_v)) = S_L(R_v) \qquad (32)$$

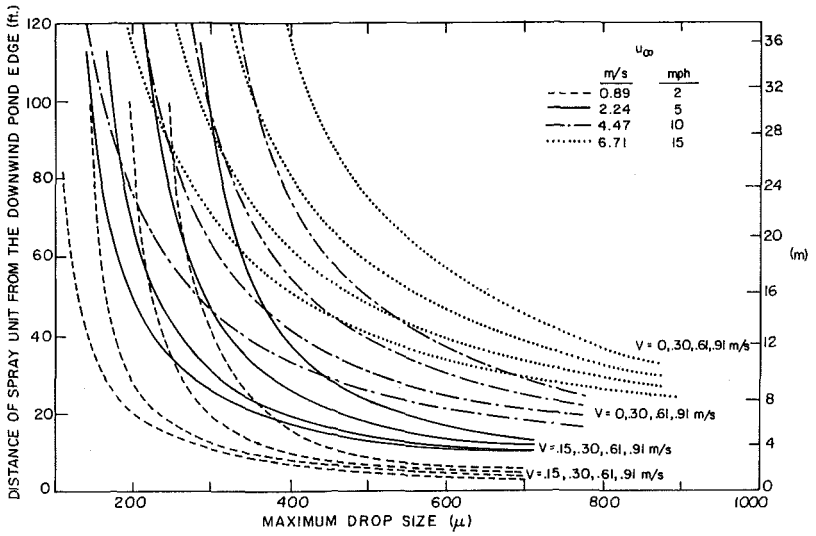

Fig. 9 Distance-drop size relationship for different wind and upward velocities

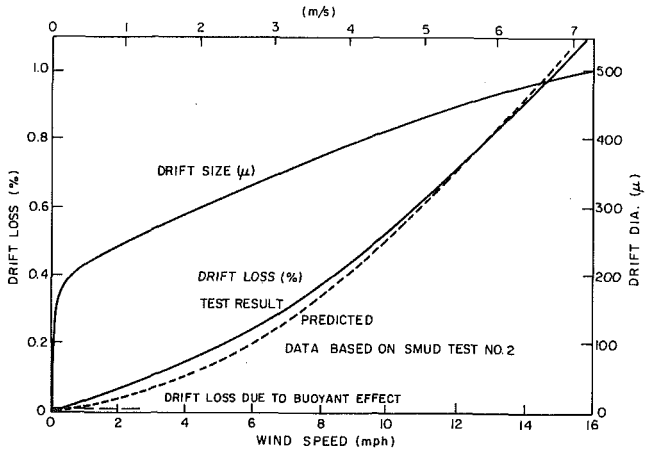

Fig. 10 Drift loss and drift particle size versus wind speed

The inversion of equation (32) gives

$$R_v = R_v(S_L) \tag{33}$$

This means that once the drop-distance relationship is known, the fraction of coolant loss can be determined. The amount of coolant water lost as drift for a single spray unit is therefore given as

$$\dot{M}_D = LR_v \tag{34}$$

The fraction of coolant lost through drift (W_F) is

$$W_F = \frac{\text{Total drift loss}}{\text{Total water sprayed}} = \frac{\sum_{j=1}^{N} L_j R_{vj}}{\sum_{j=1}^{N} L_j} \tag{35}$$

This calculational procedure, using the given relations along with Fig. 9, was used to predict the drift loss of the Rancho Seco spray test. As seen in Fig. 10, the predicted and test results are in good agreement.

It should be noted that under a no wind condition, $u_\infty = 0$, the particle will be lost as drift only when the upward air vapor velocity equals the particle terminal velocity. However, this is a limiting case because as the upward air vapor velocity is close to the terminal velocity of the particle, the settling time of the drop is very long and evaporation will reduce the drop size further. More loss would be found than that predicted.

Acknowledgment

This work was supported in part by the NSF-RANN project GI 34932, Waste Heat Management.

References

1 Schrock, V. E., and Trezek, G. J., "Evaluation of Spray Pond Performance," Waste Heat Management Report No. WHM-10, University of California, Berkeley, Oct., 1974.

2 Kelley, R. B., "Large-Scale Spray Cooling," Industrial Water Engineering, Aug.–Sept. 1971, p. 52.

3 Hoffman, D. P., "Spray Cooling for Power Plants," *Proceedings of the American Power Conference*, Vol. 35, 1973, p. 702.

4 Chen, K. H., "Thermal Analysis of Spray Design," MS thesis, Illinois Institute of Technology, Chicago, May, 1973.

5 Porter, R. W., and Chen, K. H., "Heat and Mass Transfer of Spray Canals," JOURNAL OF HEAT TRANSFER, TRANS. ASME, Series C, Vol. 96, No. 3, Aug., 1974.

6 Chen, K. H., "Heat and Mass Transfer of Multi-Spray Unit Cooling System in Open Atmosphere," PhD disseration, University of California, Berkeley, May, 1976.

7 Chen, K. H., and Trezek, G. J., "Spray Energy Release (SER) Approach to Analysing Spray System Performance," presented in the Spray Cooling Workshop, 38th American Power Conference, Chicago, Apr. 20–22, 1976.

8 Schrock, V. E., Trezek, G. J., and Keilman, L. R., "Performance of a Spray Pond for Nuclear Power Plant Ultimate Heat Sink," ASME Paper No. 75-WA/HT-41, presented at Winter Annual Meeting, Houston, Tex., Nov. 30–Dec. 4, 1975.

9 Guyer, E. C., and Golay, M. W., "A Model for Salt Drift Deposition From Spray Ponds," International Atomic Energy Agency, IAEA-SM-187/37, Vienna, 1975.

10 Stewart, R., and Nelson, R. T., "Weather Modification Due to Spray Pond Cooling," ASME Paper No. 75-HT-1, presented at the Heat Transfer Conference, San Francisco, Calif., Aug. 11–13, 1975.

11 Schrecker, G. O., and Henderson, C. D., "Salt Water Condenser Cooling: Measurements of Salt Water Drift From a Mechanical Drift Wet Cooling Tower and Spray Modules, and Operating Experience With Cooling Tower Materials," presented in the Spray Cooling Workshop, 38th American Power Conference, Chicago, Apr. 20–22, 1976.

G. E. Caledonia
J. D. Teare[1]

Physical Sciences Inc.
Woburn, Mass.

Laser Beam-Hygroscopic Aerosol Interactions

A model for the prediction of the temperature and vapor fields created about a small water droplet undergoing irradiation by a laser beam has been developed. Time-dependent and steady-state solutions of the model are discussed. Estimates of characteristic phase shifts to be expected in propagating through standard atmospheric aerosol distributions are also presented. While the model is quite general, the calculations are limited to DF *laser wavelengths.*

1 Introduction

There is considerable current interest in the effect of atmospheric aerosols on laser propagation [1–5].[2] In the case of propagation of low intensity radiation through the atmosphere the primary extinction mechanisms are absorption and scattering by both aerosols and molecules. The phenomenon of thermal blooming occurs when the absorbed laser energy heats the surrounding air. The index of refraction of this heated air will differ from ambient which in turn can cause beam defocusing and/or steering. The magnitude of this effect will depend upon both the laser pulse shape and the heating phenomenology.

The case of laser blooming resulting from molecular absorption has been treated in some detail [6]. In this instance the atmospheric heating occurs uniformly and the temperature increase at any point is directly proportional to the local laser intensity. Recently, the heating resulting from the absorption of laser energy by aerosols has received some attention [1–4]. This case is more complicated since absorption and resulting heating occur at discrete points and thus the temperature fields in the surrounding air are highly nonuniform. Blooming/scattering predictions have been presented [1–3] for the temperature fields resulting from the absorption of laser radiation by nonvaporizing aerosols.

This paper is concerned with the prediction of the temperature and vapor fields arising from the interaction of a laser beam with hygroscopic aerosols at sea level. Although the modeling presented is quite general the discussion will be limited to *DF* laser wavelengths. For convenience the aerosols will be treated as pure water droplets and effects due to scattering by aerosols will be neglected inasmuch as this scattering does not impact atmospheric heating. A crude estimate of the effect of this heating phenomenology on laser beam propagation will be provided toward the end of the text.

2 Properties of Atmospheric Aerosols

The properties of sea level aerosols vary considerably depending upon such factors as time of day, geographical location, weather, etc. [7]. The "standard" continental distribution [5, 8, 9] will be used in this section for computational purposes because of the simplicity of its mathematical form. This distribution is defined by

$$dN_A/dR,\ m^{-4} = 0.32 \times 10^{-12}/R^4; \qquad 10^{-7}m < R < 10^{-5}m \quad (1)$$

where N_A is the number of particles/m^3 of radius R. (The standard maritime distribution [5, 8, 9], although having a different shape, exhibits approximately the same aerosol mass loading as the continental distribution.) Equation (1) is only valid at low relative humidities since it has been demonstrated that hygroscopic aerosols increase in size with increasing relative humidity. A relationship widely used [5, 9] to predict the factor F by which the radius of the aerosol increases is

$$F = 1.0 - 0.9 \ln (1 - \text{R.H.}/100); \qquad \text{R.H.} < 100 \text{ percent} \quad (2)$$

where R.H. is relative humidity.

The absorption cross section for small spherical particles must be calculated by use of Mie theory which requires specification of particle size, complex index of refraction, and radiation wavelength. In specific limits this cross section may be approximated by the relationship [10]

$$Q = \tfrac{4}{3}\pi R^3(4\pi n'/\lambda) \quad (3)$$

[1] Presently at Massachusetts Institute of Technology, Energy Laboratories, Cambridge, Mass.

[2] Numbers in brackets designate References at end of paper.

Contributed by the Heat Transfer Division and presented at the Winter Annual Meeting, Houston, Texas, November 30–December 5, 1975, of THE AMERICAN SOCIETY OF MECHANICAL ENGINEERS. Revised manuscript received by the Heat Transfer Division December 21, 1976. Paper No. 75-WA/HT-42.

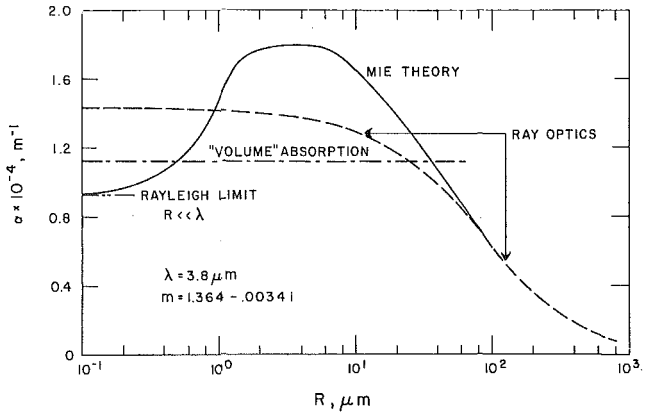

Fig. 1 The absorption cross section normalized by particle volume versus particle radius for water droplets at $\lambda = 3.8\ \mu m$

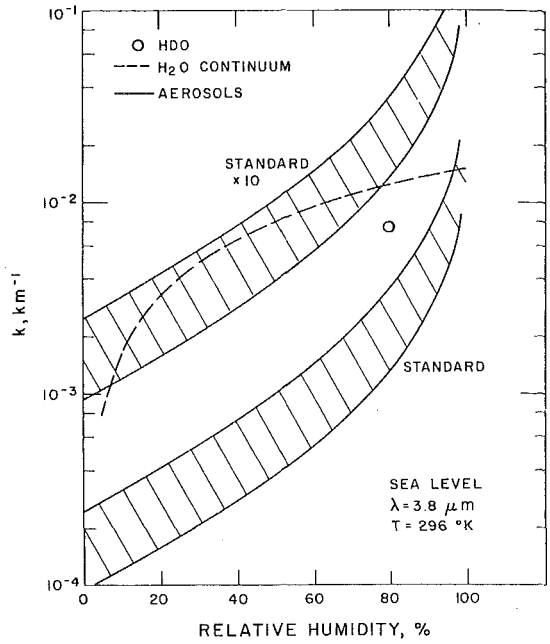

Fig. 2 Predicted absorption coefficients versus relative humidity for sea level molecular and aerosol absorption

where n' is the complex portion of the index of refraction and the quantity $4\pi n'/\lambda$ is defined as α, the volume absorption coefficient, i.e., cross section normalized by particle volume. The volume absorption coefficient as predicted from equation (3) is shown in comparison with that predicted from Mie theory in Fig. 1 for a wavelength of 3.8 μm and corresponding water index of refraction [11] of $m = 1.364 - 0.0034i$ (this wavelength corresponds to the *DF* laser line $v = 2 \rightarrow 1, J = 8$). Also shown for comparison is the absorption coefficient predicted from geometric optics which is only valid when $R \gg \lambda$. As can be seen equation (3) provides a reasonable estimate of the particle absorption coefficient for particle sizes between 10^{-1} and 10^2 μm and will be used throughout the text for providing numerical examples.

The total small signal atmospheric aerosol absorption coefficient is defined by

$$k_\lambda = \int_{R_1}^{R_2} Q(R, \lambda, m)(dNA/dR)dR \qquad (4)$$

The predicted variation of this quantity with relative humidity for $\lambda = 3.8\ \mu m$ is shown in Fig. 2 for the dry aerosol distribution defined by equation (1) and for a distribution having the same shape but ten times the mass loading. The predicted absorption coefficient for each distribution is bracketed to account for the uncertainty in the complex index of refraction of water at this wavelength [11, 12] and to compensate for the difference between Mie and volume absorption coefficients. It is to be emphasized that these predictions are specific to pure water droplets and are thus most relevant to marine aerosols on humid days. It can be seen from equations (3) and (4) that the absorption coefficient is linearly proportional to total aerosol volume or mass loading and relatively insensitive to the choice of aerosol size distribution as long as equation (3) is valid, i.e., as long as the dominant fraction of aerosols has $R \lesssim 100\ \mu m$.

The absorption coefficients for two competitive molecular absorbers at 3.8 μm are also shown in Fig. 2. The circled point is that predicted by McClatchey and Selby [13] where HDO was taken to be the dominant molecular absorber, and the dashed line is a prediction for the water vapor continuum absorption band recently observed by Burch [14]. As can be seen, molecular absorption will dominate aerosol absorption for the standard continental aerosol distribution. On the other hand much larger aerosol mass loadings are commonly observed in a variety of scenarios, and these in turn can provide the dominant absorption loss mechanism for *DF* laser radiation. This absorption can be particularly severe under conditions corresponding to mist, heavy maritime winds, etc.

3 Modeling

The phenomena to be modeled here are the time and spatial variation of the temperature and vapor fields about a water droplet

Nomenclature

A = Avagadro's number
C_p = specific heat at constant pressure
D = diffusion coefficient for H_2O vapor into air
f = fraction of absorbed energy converted to sensible heat
F = growth factor for hygroscopic aerosols
I = laser intensity
k = Boltzmann's constant
k_a = thermal conductivity of air
k_D = thermal conductivity of water
k_λ = atmospheric absorption coefficient
$m = n - in'$, complex index of refraction of water
m_D = mass of droplet
M = molecular weight
N = total gas number density
N_A = number density of aerosol particles of radius R
P = total gas pressure, taken as 1 atm
Q = droplet absorption cross section
r = radial coordinate from droplet center
R = droplet radius
R_v = specific gas constant for water vapor
t = time
T = temperature
V = gas velocity
X_v = mole fraction of water vapor
z = distance along axis of laser propagation
Z = normalized coordinate, R/r
α = droplet volume absorption coefficient
α_v = vaporization coefficient for water
ΔH_v = heat of vaporization of water
λ = laser wavelength
$\langle\varphi\rangle$ = average phase shift
ρ = density
τ_R = characteristic time for e-fold decrease in droplet radius
τ_D = characteristic time for droplet to reach quasi-steady state

Subscripts

a = air properties
D = droplet properties
v = vapor properties
∞ = ambient conditions

undergoing laser irradiation. Some aspects of this problem have been considered by Sutton [15] and Glickler [16] in their analyses of laser propagation through fogs and clouds, respectively. The steady-state solutions for an individual droplet have been discussed by Williams [17]. The fully time dependent solutions for an individual droplet have apparently not appeared in the open literature.

The phenomenology of the present problem is that the aerosol droplet absorbs energy and is heated. As the droplet temperature rises the droplet conducts heat energy to the surrounding air and undergoes surface vaporization. The vapor leaves the droplet with a directed velocity and a pressure wave is induced in the surrounding gas in response to the mass and heat addition. The present analysis is limited to the case of isobaric vaporization. (If the rate of energy absorption were sufficiently large the droplet would "explode," creating a shock wave; the laser intensity/particle size range at which this occurs has been discussed by Sutton [15].) The surrounding gas is taken to be at constant pressure. As pointed out in the foregoing, pressure gradients are induced in the gas because of the mass and heat addition from the droplet. However, for the characteristic dimension of the problem, which is ≈1 mm, the average spacing between aerosols, it can be readily shown that the acoustic transit time is short compared to irradiation times of interest.

The general relationships describing the system are conservation of mass, momentum, energy, and the water vapor diffusion equation. If the droplet is taken to be heated uniformly, the system will be spherically symmetric and the relevant equations reduce to

$$\partial T/\partial t = -V\partial T/\partial r + \frac{kk_aAT}{r^2C_{p_a}PM_a}\frac{\partial}{\partial r}(r^2\partial T/\partial r) \tag{5}$$

$$\partial X_v/\partial t = -V\partial X_v/\partial r + \frac{kT(DN)}{r^2P}\frac{\partial}{\partial r}(r^2\partial X_v/\partial r) \tag{6}$$

$$\partial V/\partial r = -2V/r + \frac{kk_aA}{r^2C_{p_a}PM_a}\frac{\partial}{\partial r}(r^2\partial T/\partial r) \tag{7}$$

for $r \geq R$.

Assuming the droplet temperature to be uniform (as will be seen later this approximation is reasonable until the droplet temperature approaches the boiling point), the energy conservation equation at the phase boundary is

$$\frac{4}{3}\pi R^3 I\alpha = \frac{4}{3}\pi R^3\rho_D C_{p_D} dT_D/dt + 4\pi R^2 k_a(-\partial T/\partial r|_R) + 4\pi R^2\Delta H_v\frac{M_v}{A}(NV)|_R \tag{8}$$

The left-hand side of equation (8) is the rate of absorption of energy and the right-hand side terms represent the energy deposition into droplet heating, conduction to the surrounding air, and vaporization, respectively. The terms involving the ordered kinetic energy of the vapor are negligible for the present considerations and have been dropped.

The vapor concentration at the surface of the droplet has been related to the droplet temperature by the Clausius-Clapeyron relationship [18], which has been used in its integral form, i.e.,

$$X_v(R) = X_{v_\infty}\exp\left[\frac{\Delta H_v(T_D - T_\infty)}{R_v T_D T_\infty}\right] \tag{9}$$

where ΔH_v is assumed constant at 2.46 MJ/kg.

The last equation connecting the droplet and gas behavior is the conservation of mass of the vapor. If one considers the infinitesimal shell of gas adjacent to the droplet surface, then it is required that the rate of mass loss of the droplet be balanced by the rate of increase of vapor within the shell plus the rate of vapor leaving the exterior of the shell. With some straightforward mathematical manipulation this leads to the relationship

$$(NV)|_R = -(1 - X_v(R))^{-1}DN\partial X_v/\partial r|_R \tag{10}$$

It was assumed in the derivation of equation (10) that the vaporization rate at the surface is controlled by diffusion. Actually vaporization at the surface is a kinetic process obeying Knudsen's equation with diffusion taking control approximately a mean free path (~0.06 μm at 1 atm) away from the droplet. Kinetic vaporization or condensation is generally modeled in terms of α_v, the "sticking" or vaporization coefficient which is a measure of the efficiency of collision processes in producing condensation or vaporization. It can readily be shown [19] that if α_v for water were unity, equation (10) would adequately represent this phenomenon for particle radii $\gtrsim 0.5$ μm. At the time that this research was in progress the value of $\alpha_v = 1$ appeared to be preferred [19]. However, very recently a measurement of $\alpha_v = 0.033$ has been reported [20] in agreement with several earlier measurements. If this latter value of 0.033 is correct then equation (10) would provide an overestimate of the vaporization rate for the droplet sizes considered.

It would appear that a correct value of α_v cannot be deduced from the existing, conflicting data base. The computer predictions to be presented in Section 4 were made using equation (10). The computer code can be readily adjusted to include the more general vaporization rate. In general, a smaller value of α_v will provide more heat conduction for a given configuration at the expense of vaporization.

So far in the analysis the effect of decreasing droplet size has not been considered. This effect can be uncoupled because the rate of change of droplet size is small compared to the rate of change of the gas parameters. It has been implicitly assumed that the time varying, rather than initial, value of R will be used in the solution of the equations. For the computer solution the governing equations have been recast in terms of the variable $Z = R(t)/r$.

Note that the quantities I and α enter only as a product in the problem, equation (8). As shown in Fig. 1 the effective value of α as determined by Mie theory can vary by close to a factor of two for particles of radius between 0.1 and 100 μm. Thus the absorption efficiency of a droplet can vary as the particle vaporizes (and thus decreases in size). Given the desire to present generalized solutions this effect was not included in the computations of Section 4.

4 Model Predictions

No analytic solution has been found for the system of equations (5)–(10). A computer program has been developed for their numerical evaluation which employs a fully implicit Crank-Nicolson finite difference scheme. In addition to the computer predictions, a quasi-steady state (QSS) solution of the equations has been developed in order to provide simplified predictions of the effects of varying fundamental parameters such as the particle radius and laser intensity.

A **Quasi-Steady State (QSS) Solutions.** In the limit where the velocity term in equations (5) and (6) can be neglected, the equations effectively uncouple, and it can be readily demonstrated that the QSS solutions for $\Delta T = T - T_\infty$ and $\Delta X_v = X_v - X_{v_\infty}$ scale inversely with r, i.e.,

$$\Delta T(r) = (R/r)\Delta T(R) \tag{11}$$

and

$$\Delta X_v(r) = (R/r)\Delta X_v(R) \tag{12}$$

Indeed, even the time dependent solutions for the case of heat conduction without vaporization [21] vary approximately as r^{-1} for $r < 2(k_a t/\rho C_{p_a})^{1/2}$. Thus, in the limit of low velocity equation (8) may be rewritten as

$$d(\Delta T_D)/dt = \frac{3}{R^2\rho_D C_{p_D}}\left\{R^2 I\alpha/A3 - k_a\Delta T_D - \frac{\Delta H_v M_v}{A}DN(1 - X_v(R))^{-1}(X_v(R) - X_{v_\infty})\right\} \tag{13}$$

One feature of interest is the maximum value of ΔT_D which is reached when the time derivative is zero. Equation (13) in this limit reduces to a transcendental equation for $\Delta T_{D\text{-max}}$ which may be evaluated as a function of the parameter $R^2 I\alpha$. The solution to this equation is shown in Fig. 3. Shown for comparison are the predicted maximum droplet temperatures for the related cases of "heat conduction only" and "vaporization only."

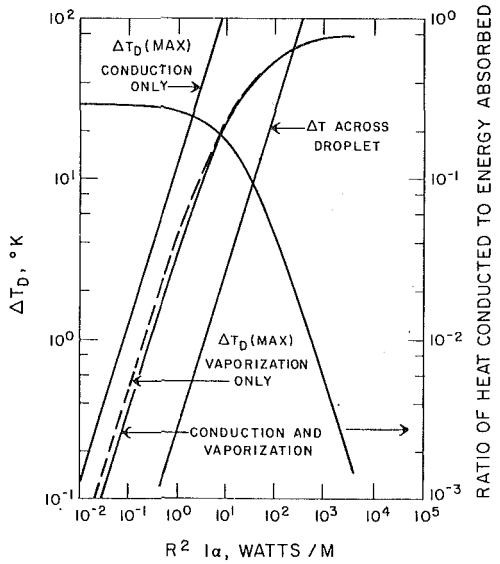

Fig. 3 Maximum increase in droplet temperature versus $R^2I\alpha$—also shown is the fraction of absorbed energy lost to heat conduction and the predicted variation in temperature across the droplet; T_∞ = 293 K, X_{v_∞} = 2.1 × 10^{-2}

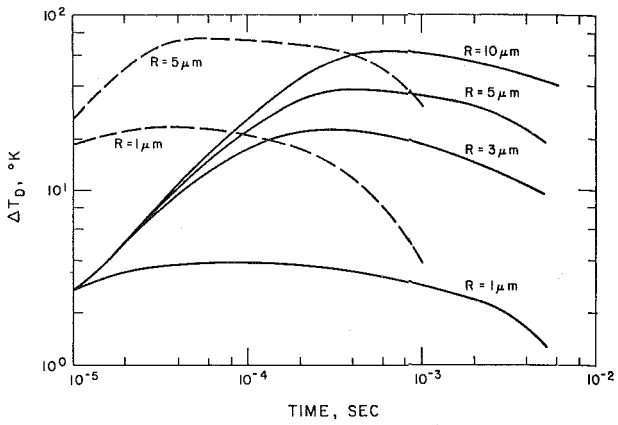

Fig. 4 Increase in droplet temperature above ambient versus time: —, $I\alpha$ = 1.13 × 10^{12} W/m³; - - -, $I\alpha$ = 1.13 × 10^{13} W/m³

Note that for the full range of $R^2I\alpha$ shown the $\Delta T_{D\text{-max}}$ predicted for the case of heat conduction alone is significantly higher than that predicted when both heat conduction and vaporization were included. On the other hand, the predictions for the case of "vaporization only" are relatively close to the full solution. The reason for this is that the major portion of the absorbed energy goes into vaporization. This is shown explicitly in Fig. 3 where the fraction of the absorbed energy which is lost to heat conduction is plotted versus $R^2I\alpha$. For low $R^2I\alpha$ this fraction asymptotes to ~0.3, and falls off rapidly with increasing $R^2I\alpha$. This rapid fall-off occurs as the droplet temperature approaches the boiling point, because the vaporization rate increases exponentially in this region, whereas the rate of heat conduction approaches a constant. The relative value of this fraction is determined by the ratio of the last two terms on the right-hand side of equation (13). For small $\Delta T_{D\text{-max}}$ this ratio reduces to

$$\frac{\text{power into heat conduction}}{\text{power into vaporization}} = \frac{k_a R_v T_\infty{}^2 A(1 - X_{v_\infty})}{X_{v_\infty} DN(\Delta H_v)^2 M_v} \approx 0.43 \quad (14)$$

in agreement with the asymptotic value shown in Fig. 3 (i.e., 0.43/1.43 ≈ 0.3).

Fig. 3 is somewhat misleading at large values of $R^2I\alpha$ because the radial gas velocity becomes large and the dominant heat transfer mechanism becomes convection rather than conduction. In this limit the gas temperature profiles no longer scale inversely with r. However, for the cases corresponding to high vaporization considered in the present work the computed radial derivatives of the temperature and water vapor distributions at $r = R$ were typically within a factor of two of those predicted from equations (11) and (12). Thus it is concluded that the present QSS analysis should adequately describe the gross phenomenology even at the higher values of $R^2I\alpha$ shown.

The fact that vaporization dominates heat conduction as an energy loss mechanism allows an approximate analytic formulation for several of the variables of interest in the problem. In particular, under QSS conditions it can be readily shown from equation (13) that the rate of mass loss from the droplet can be expressed as

$$dm_D/dt \approx -\frac{4}{3}\pi R^3 I\alpha/\Delta H_v \quad (15)$$

From equation (15) it can be seen that the characteristic e-folding time for droplet radius is

$$\tau_R = 3\Delta H_v \rho_D / I\alpha \quad (16)$$

independent of initial particle size.

Relationships (15) and (16) are valid after the droplet has reached its QSS temperature. It can be shown that prior to that time the major portion of the absorbed energy is consumed in heating the droplet. It was found through computer solutions of equation (13) that the e-folding time for the quantity $\Delta T_{D\text{-max}} - \Delta T_D$ was given by

$$\tau_D \sim 0.65\ \Delta T_{D\text{-max}} \rho_D C_{pD}/(I\alpha) \quad (17)$$

to within 20 percent for $R^2I\alpha$ between 10^{-2} and 4 × 10^3 W/m. Note that τ_D is not independent of particle size since $\Delta T_{D\text{-max}}$ is a function of $R^2I\alpha$. (Indeed, for $R^2I\alpha \lesssim 6.3$ W/m, $\Delta T_{D\text{-max}} \sim R^2I\alpha/10k_a$).

A last point before leaving the discussion on QSS solutions concerns the validity of assuming an isothermal droplet. If one considers volume absorption followed by heat conduction as the only phenomenon occurring *within* the droplet, the temperature drop from the center (T_C) to the surface is given by

$$T_C - T_S = R^2 I\alpha/(6k_D) \quad (18)$$

where k_D is the coefficient of thermal conductivity of water, taken as 0.59 W/mK. This temperature variation is also shown in Fig. 3 and can be seen to be significantly lower than $\Delta T_{D\text{-max}}$ until the droplet approaches the boiling point. Of course, equation (18) is not necessarily realistic in that region since it requires droplet superheating. In reality, vaporization could occur within the droplet and original nuclei effects, etc., could be quite important. In any event, it is clear that the approximation of a constant temperature field across the droplet is not appropriate at large values of $R^2I\alpha$.

B **Time Dependent Solutions.** Computer calculations have been performed for a matrix of values of droplet size and $I\alpha$ and representative results are shown in Figs. 4–6. Typical droplet temperature histories for values of $I\alpha$ of 1.13 × 10^{12} and 1.13 × 10^{13} W/m³ and several initial droplet sizes are shown in Fig. 4. As can be seen the time to reach peak temperature increases with increasing particle size as expected from equation (17). The decrease in droplet temperature with increasing time is a result of the decrease in radius due to vaporization. This decrease is much more noticeable at the higher value of $I\alpha$ since the characteristic e-folding time for droplet radius as given by equation (16) is ~6.5 × 10^{-4} s for this case. The predicted droplet temperature for times corresponding to the point of maximum temperature and beyond are in good agreement with the quasi-steady state predictions shown in Fig. 3.

Radial profiles of the temperature increase in the gas at several different times for cases corresponding to an initial droplet radius of 5 μm and two values of $I\alpha$ are shown in Figs. 5 and 6. For the case of $I\alpha$ = 1.13 × 10^{12} W/m³, Fig. 5, the profiles scale inversely with radius

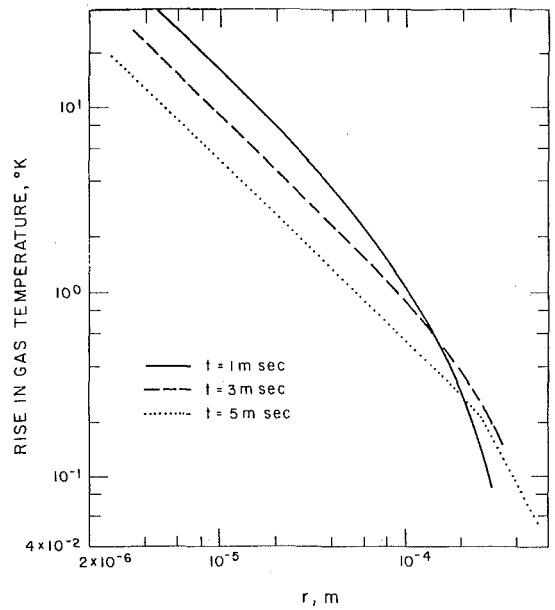

Fig. 5 Gas temperature rise versus distance: $I\alpha = 1.13 \times 10^{12}$ W/m^3; R = 5 μm

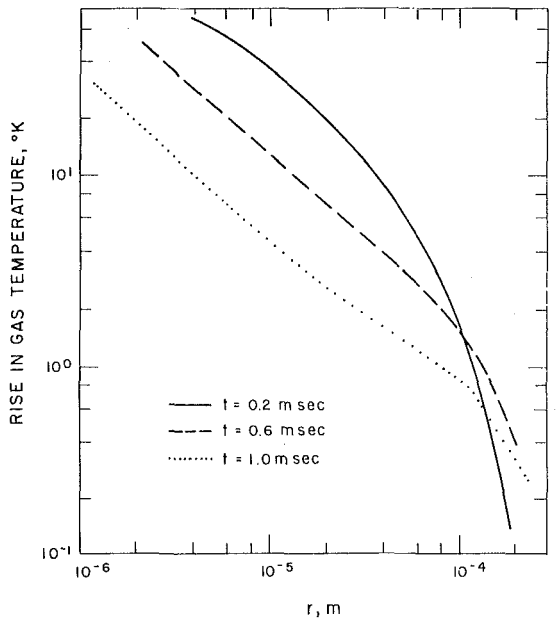

Fig. 6 Gas temperature rise versus distance: $I\alpha = 1.13 \times 10^{13}$ W/m^3; R = 5 μm

out to distances roughly given by $r \sim (4k_a t/\rho C_{p_a})^{1/2}$ in agreement with the analytic solution for the case of heat conduction with no vaporization. The overall decrease in temperature with increasing time is a result of the decreasing droplet radius. The radial profiles of water vapor mole fraction are quite similar to those for temperature and are not shown.

Similar profiles are shown in Fig. 6 for the case of $I\alpha = 1.13 \times 10^{13}$ W/m^3. In this case departures from an inverse radial dependence are obvious. This deviation occurs because of the increased importance of the convection terms in equations (5)–(7) which are coupled to the higher rate of vaporization.

5 Beam Propagation Effects

This section is concerned with the resultant effects of aerosol heating and vaporization on laser beam quality. "Blooming" of the laser beam results because the heated air around the aerosol has a different index of refraction from ambient. The variations in the index of refraction across the beam width are a complicated function of both laser intensity and the aerosol size distribution function. In general, the phase shift produced in a wave propagating through this nonuniform medium will depend upon these variables and there will be variations in beam refraction across the laser beam width. Thus the prediction of beam propagation through the temperature fields caused by heated, vaporizing aerosols is a complex problem which will not be treated in detail in this section. However, crude estimates of the resulting phase shifts will be made. More detailed analysis may be found in references [2–4].

Each irradiated droplet is surrounded by a "bubble" of heated air, of characteristic radius $r \sim (4k_a t/\rho C_{p_a})^{1/2}$. It can be readily shown [3, 4] that the *average* phase shift resulting from a heated bubble is directly proportional to the average temperature increase in the bubble. Because of this the average phase shift due to aerosol absorption will be functionally similar to that resulting from molecular absorption except that in the case of aerosols not all the energy absorbed is converted to gas heating. The average phase shift at range z may be defined by [3, 4]

$$\langle\varphi\rangle = f\frac{2\pi(n_{\infty-1})k_\lambda I z t}{\rho_\infty C_{p_\infty} T_\infty \lambda} \tag{19}$$

where $n_{\infty-1} = 3 \times 10^{-4}$, k_λ is the aerosol absorption coefficient as defined by equation (4), and f is the fraction of absorbed energy which is converted to sensible heat.

Equation (19) is only approximate since the absorption coefficient for hygroscopic aerosols decreases with increasing irradiation time because of vaporization losses. For example, from equation (16) it can be shown that k_λ would drop by a factor of two in $\sim 1.5 \times 10^{-3}$ s, if $I\alpha$ were 1.13×10^{12} W/m^3.

Furthermore the quantity f scales inversely with $R^2 I\alpha$, as can be seen from Fig. 3, and will always be ≤ 0.3. As a specific example, at an $I\alpha$ of 1.13×10^{12} W/m^3 only droplets of radius $\lesssim 4$ μm will contribute significantly to gas heating. At 98 percent R.H., approximately half of the aerosol mass loading is in particles with $R \gtrsim 4$ μm and thus for this case an approximate value of f would be 0.15. Taking α as 1.13×10^4 m^{-1} the average phase shift would then be

$$\langle\varphi\rangle/z \approx 200t, \text{ km}^{-1}$$

or a phase shift of order unity for times of ms and distances of kms.

Note that for this laser intensity the phase shift prediction is not too sensitive to the previously discussed uncertainty in the vaporization coefficient, α_v, because of compensating effects. For example if α_v were 0.033 then at the lower values of $R^2 I\alpha$ the predicted maximum droplet temperature and heat conversion efficiency would approach those corresponding to the heat conduction solution shown in Fig. 3. However the maximum temperature would also necessarily asymptote to the boiling limit at lower values of $R^2 I\alpha$ than if α_v were unity, and thus a smaller portion of the aerosol distribution would contribute to gas heating. On the other hand, with increasing laser intensity the vaporization limit is approached at smaller and smaller droplet radii and the details of the boiling phenomenon will become more important in the determination of beam quality.

The average aerosol induced phase shift of equation (20) is significantly less than that for molecular absorption for the same conditions, i.e., as deduced from equation (19) with f equal to unity and the molecular absorption coefficient of Fig. 2. However, it must be emphasized that in the case of aerosol heating the temperature fields are nonuniform and the adding and averaging of phase shifts performed in the present analysis may not be justified. In any event even the average phase shift induced by larger aerosol mass loadings, e.g., mist, etc., would exceed that due to molecular absorption.

6 Summary

A detailed model has been developed to predict the temperature and vapor fields resulting from the laser irradiation of small water droplets. The water droplets are considered to be representative of hygroscopic aerosols at high relative humidities. The model includes the effects of vaporization, heat conduction, and convection. The model was developed under the assumption of a constant pressure gas and thus is valid only up to the isobaric vaporization limit.

Both steady-state and time dependent solutions for the model have been discussed in some detail. It was shown that the predicted profiles of increase in gas temperature and water vapor scale inversely with distance from the droplet for moderate laser intensities and particle sizes where convective velocities are negligible. For larger laser intensities and/or particle sizes convection becomes dominant resulting in more bowed profiles.

A crude estimate of the phase shift resulting from heated hygroscopic aerosols has also been presented. It has been shown that the average phase shift is similar to that due to molecular absorption except that in the case of aerosols only a fraction of the absorbed energy goes into sensible gas heating. This fractional amount can be a complicated function of aerosol size distribution, laser intensity, and droplet evaporation coefficient. Furthermore, unlike molecular absorption, the aerosol absorption coefficient decreases with increasing irradiation time because of vaporization losses.

7 Acknowledgment

This research was supported by the Advanced Research Projects Agency of the Department of Defense and was monitored by ONR under Contract No. N00014-74-C-0295.

References

1 Canavan, G. H., "Thermal Blooming Due to the Heating of Aerosols," *AFWL Laser Digest*, AFWL-TR-73-273, Dec. 1973, pp. 66–68.

2 Cook, R. J., and Butts, R. P., "Aerosol Induced Thermo-Optical Degradation of a High Intensity Laser Beam," *AFWL Laser Digest*, AFWL-TR-73-272, Dec. 1973, pp. 69–90.

3 Lencioni, D. E., and Kleiman, H., "Effects of Aerosol Particle Heating on Laser Beam Propagation," LTP 27, Lincoln Laboratory, Bedford, Mass., July 1974.

4 Caledonia, G. E., and Teare, J. D., "Aerosol Propagation Effects," PSI TR-13, Physical Sciences Inc., Woburn, Mass., Sept. 1974.

5 Hodges, J. A., "Aerosol Extinction Contribution to Atmospheric Attenuation in Infrared Wavelengths," *Applied Optics*, Vol. 11, No. 10, Oct. 1973, pp. 2304–2310.

6 Wood, A. D., Camac, M., and Gerry, E. T., "Effects of 10.6μ Laser Induced Air Chemistry on the Atmospheric Refractive Index," *Applied Optics*, Vol. 10, No. 8, Aug. 1971, pp. 1877–1884.

7 Proctor, W. A., "A Short Descriptive Survey of Atmospheric Aerosols," *AFWL Laser Digest*, AFWL-TR-73-131, June 1973, pp. 69–77.

8 Barnhardt, E. A., and Streete, J. L., "A Method for Predicting Atmospheric Aerosol Scattering Coefficients in the Infrared," *Applied Optics*, Vol. 9, No. 6, June 1970, pp. 1337–1344.

9 Mason, B. J., *The Physics of Clouds*, Clarendon Press, Oxford, 1971.

10 VandeHulst, H. C., *Light Scattering by Small Particles*, Wiley, New York, 1957.

11 Hale, G. M., and Querry, M. R., "Optical Constants of Water in the 200-nm to 200-μm Wavelength Region," *Applied Optics*, Vol. 12, No. 3, Mar. 1973, pp. 555–563.

12 Ray, P. S., "Broadband Complex Refractive Indices of Ice and Water," *Applied Optics*, Vol. 11, No. 8, Aug. 1972, pp. 1836–1844.

13 McClatchey, R. A., and Shelby, J. E. A., "Atmospheric Attenuation of HF and DF Laser Radiation," AFCRL 72-0312, Air Force Cambridge Research Laboratories, Bedford, Mass., May 1972.

14 Burch, D. E., "Investigation of the Absorption of Infrared Radiation by Atmospheric Gases," U-4784, Philco Ford Corp., Newport Beach, Calif., Jan. 1970.

15 Sutton, G. W., "Fog Dispersal by High Power Lasers," *AIAA Journal*, Vol. 8, No. 10, Oct. 1970, pp. 1907–1910.

16 Glickler, S. L., "Propagation of a 10.6 μm Laser Through a Cloud Including Droplet Vaporization," *Applied Optics*, Vol. 10, No. 3, March 1971, pp. 644–650.

17 Williams, F. A., "On Vaporization of Mist by Radiation," *International Journal of Heat and Mass Transfer*, Vol. 8, 1965, pp. 575–587.

18 Glasstone, S., *Thermodynamics for Chemists*, Van Nostrand, New York, 1947.

19 Chen, C. S., "Evaluation of the Water Vapor Diffusion Coefficient in the Drop Growth Equation," *Journal of the Atmospheric Sciences*, Vol. 31, No. 3, Apr. 1974, pp. 845–847.

20 Chodes, N., Warner, J., and Gayin, A., "A Determination of the Condensation Coefficient of Water From the Growth Rate of Small Cloud Droplets," *Journal of the Atmospheric Sciences*, Vol. 31, No. 5, July 1974, pp. 1351–1357.

21 Carslaw, H. S., and Jaeger, J. C., *Conduction of Heat in Solids*, Clarendon Press, Oxford, 1959.

G. D. Raithby
K. G. T. Hollands

Thermal Engineering Group,
Department of Mechanical Engineering,
University of Waterloo,
Waterloo, Ontario, Canada.
Mem. ASME

T. E. Unny

Department of Civil Engineering,
University of Waterloo,
Waterloo, Ontario, Canada

Analysis of Heat Transfer by Natural Convection Across Vertical Fluid Layers

An analysis is presented which predicts the heat transfer across fluid layers bounded laterally by vertical isothermal surface and adiabatic surfaces on the top and bottom. The vertical temperature distribution in the core of the cavity is also predicted. Extensive comparisons of average Nusselt number and temperature distribution are made with experimental data for aspect ratios greater than 5. Good agreement between analysis and experiment is found. The heat-transfer equations for vertical layers are generalized to include layers which are tilted up to 20° from the vertical, making the results useful for the design of solar collectors.

1 Introduction

Natural convection in a narrow rectangular cavity (slot), with a temperature difference maintained between the vertical walls, has been frequently studied by physicists and engineers. The former have been motivated by the desire to understand geophysical and astrophysical motions. Engineers are more frequently interested in estimating the heat losses from buildings, and in equipment. Recent applications in solar energy have accentuated the importance of this problem, and also the related tilted-layer problem.

Several relevant experimental [1–16][1] and analytical [17–27] studies have been reported over the past 46 years. Batchelor [17] was first able to bring order to this complex problem by defining various flow regimes, and proposing equations for heat transfer across the fluid layer for each regime. Most of the subsequent analyses have been numerical solutions, mainly using finite differences (exceptions are [20, 25]). These have yielded satisfactory solutions at low Rayleigh numbers and small aspect ratios. Numerical predictions for large aspect ratios have not been shown to be in conclusive agreement with each other or with experiment. Also, the appropriate form of the solution is not obtained. At the other extreme, analyses which yield simple (closed-form) solutions have made little headway in predicting the vertical temperature stratification which occurs in the core of the slot. The heat-transfer solution of Batchelor [17] appears to contain an incorrect aspect-ratio dependence, and the integral solution of Emery and Chu [7] does not account for the thermal stratification of the fluid in the core.

The present paper reports the results of a new (simple) analysis which predicts the form of the midslot temperature distribution in the laminar boundary-layer regime, and the heat transfer across the fluid in both the laminar b.l. (b.l. = boundary layer) and turbulent b.l. regimes. The analysis is restricted to aspect ratios of about five or larger. Extensive comparisons are made with existing data; the agreement is normally very good, and reasons for disagreement among some of the earlier correlating equations are suggested. Design equations for heat transfer across vertical layers, and tilted layers for $-20 \text{ deg} \leq \phi \leq 20 \text{ deg}$, are proposed.

2 The Problem

2.1 Geometry and Boundary Conditions. Fig. 1(*a*) shows a cross section of a slot which is presumed long in the z-direction. The temperatures of the heated wall, T_h, and cooled wall, T_c, are assumed to be uniform, and the $x = 0$ and $x = H$ ends to be insulated. Densities are assumed to be sufficiently high that the fluid can be treated as a continuum. Other boundary conditions on the ends (such as a linear profile between T_h and T_c) should yield essentially the same results for large aspect ratios ($A = H/L$).

Various flow regimes have been proposed by Batchelor [17] and confirmed by Eckert and Carlson [5] and others. In all regimes, the problem is antisymmetric about the centroid of the slot ($H/2$, $L/2$) if the property values are uniform throughout. The regimes are briefly reviewed.

Conduction Regime. At low Rayleigh numbers the temperature and velocity profiles resemble those in Fig. 1(*b*). Except for the end regions where the flow turns and re-establishes itself, the heat transfer between the walls is by conduction. The velocity extremum at A divides the flow into an inner region ($0 \leq y \leq y_m$) and an outer region; the shear between these regions is zero so that, in the absence of acceleration, the buoyancy in the outer region (+'s in Fig. 1(*b*)) is balanced exactly by the shear between the counter-flowing streams.

Laminar B.L. Regime. At higher temperature differences (larger Ra), the shear between the counter-flowing streams and the heat transfer by conduction across the core diminish and, by definition,

[1] Numbers in brackets designate References at end of paper.

Contributed by the Heat Transfer Division of THE AMERICAN SOCIETY OF MECHANICAL ENGINEERS and presented at the Heat Transfer Conference, St. Louis, Mo., August 9–11, 1976. Revised manuscript received by the Heat Transfer Division January 11, 1977. Paper No. 76-HT-37.

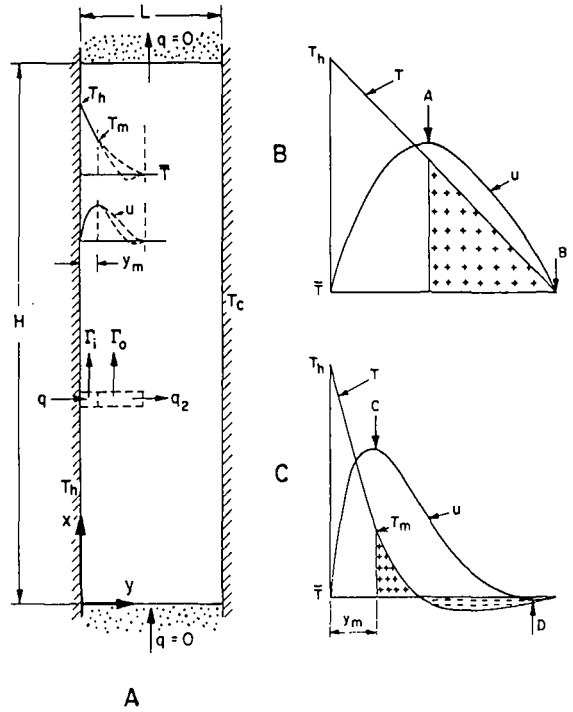

Fig. 1 (*a*) Schematic of enclosure; (*b*) velocity and temperature profiles in the conduction regime; (*c*) velocity and temperature profiles in the boundary-layer regime

vanish in the fully developed b.l. regime. Typical velocity and temperature profiles around the midheight of the slot are depicted in Fig. 1(*c*).

By the antisymmetry condition, there can be no entrainment at $x = H/2$ (for large A). Since the shear between the streams is also zero, the net positive buoyancy (+'s in Fig. 1(*c*) must then be exactly balanced by the negative buoyancy (−'s in Fig. 1(*c*)).

For $x < H/2$, Elder [8] and Gill [20] have shown that the b.l. next to the hot wall entrains fluid from the b.l. on the cold wall. This entrainment is driven by a stable thermal stratification of the core region, i.e., $\overline{T}(x)$ increases with x. Antisymmetry requires flow toward the cold wall for $x > H/2$.

Transition and Turbulent b.l. regime. At higher Rayleigh numbers, instabilities occur which lead eventually to a turbulent b.l. regime. Experiments [13] indicate that stable stratification in the core persists in this regime. For very large Rayleigh numbers, each turbulent boundary layer becomes increasingly confined to its wall, and it would seem that the influence of the other confining walls of the cavity should diminish. That is, the flow and heat transfer near each of the vertical surfaces should resemble that near a vertical plate in an unconfined environment.

Because the inner layers are isolated from events in the core of the layer by the surfaces of zero shear, it is expected that predictions from a laminar b.l. analysis should hold until "turbulence" actually penetrates the inner layers.

3 Development of Equations

3.1 Conduction Regime. Ignoring the convective heat transfer in the turning regions (large A), $\overline{\mathrm{Nu}}_L$ is

$$\overline{\mathrm{Nu}}_L = 1 \tag{1}$$

3.2 Laminar-Boundary-Layer Regime.

Inner Region. The ideas underlying the analysis of the inner region are identical to those in [29]. The heat flow across this region is assumed to be by conduction alone and the buoyancy is assumed to be in local balance with the viscous forces. The two unknowns arising from this analysis are y_m and $M = (T_h - T_m)/(T_h - \overline{T})$. The solution in the outer region, together with matching constraints at y_m will, in principle, supply other equations which permit these to be evaluated.

Outer Region. It is not possible to simplify the analysis of the outer

Nomenclature

A = aspect ratio, $A = H/L$
$A(\phi) = 0.71$ for vertical surface; for details see [29]
C_p = specific heat at constant pressure
C_1, C_2 = constants, equation (2)
C_ℓ = "universal" function of Pr for laminar flow $C_\ell = 0.50/[1 + (0.49/\mathrm{Pr})^{9/16}]^{4/9}$
C_t = "universal" function of Pr for turbulent flow $C_t = [0.14\ \mathrm{Pr}^{0.084}, 0.15]_{\min}$, where $[A, B]_{\min} = A$ if $A < B$, otherwise B
$F(x)$ = function defined by equations (A.3) in general and (4) for T_h = constant.
g = gravitational acceleration
G_ℓ = definite integral, equation (6)
G_t = definite integral, equation (10)
H = height of vertical walls, see Fig. 1(*a*)
k = thermal conductivity
L = spacing between vertical walls, Fig. 1(*a*)
m = midslot (vertical) temperature gradient at $x = H/2$; $m = (\partial\theta/\partial\zeta)_{\zeta=1/2}$
$M = (T_m - T_h)/(\overline{T} - T_h)$
$n = [(1 + \gamma)/(C_1 + C_2\gamma)] - 1 \approx 1.5$ for Pr = 0.71; $3 \lesssim n \lesssim 4$ for Pr → ∞ [2]
$\overline{\mathrm{Nu}}_L$, $\overline{\mathrm{Nu}}_H$ = average Nusselt numbers based on L and H, respectively.
$p = \frac{1}{3} - 4n/3$
Pr = Prandtl number
q = heat flow per unit time and area
Ra_L, Ra_H = Rayleigh numbers based on $(T_h - T_c)$, on the lengths L and H, respectively, and on g
T = temperature
$\overline{T}(x)$ = average temperature of fluid in any x plane
$\overline{T}_i$ = average temperature in inner region
$\overline{T}_0$ = average temperature in outer region
u = velocity component in x-direction
x = vertical coordinate, see Fig. 1(*a*).
y = coordinate normal to isothermal walls, see Fig. 1(*a*)
y_m = y distance from wall to position of first velocity extremum
z = z coordinate, orthogonal to x and y
$\alpha = \mu/\rho$
β = volumetric thermal expansion coefficient
$\gamma = \Gamma_0/\Gamma_i$
Γ = mass flow rate per unit distance in z-direction
$\kappa = k/\rho C_p$
$\theta = (\overline{T} - T_c)/(T_h - T_c)$
$\Lambda = \dfrac{k}{C_p}\left(\dfrac{\rho^2\beta}{\mu}\right)^{1/3}$, property value group
μ = dynamic viscosity
$\zeta = x/H$
ρ = fluid density
ϕ = angle of surface from vertical, positive for an upward facing heated surface

Subscripts

c = evaluated at cold-wall temperature
h = evaluated at hot-wall temperature
i = inner region, between $y \approx 0$ and $y = y_m$
m = evaluated at the position of the velocity extremum nearest wall
0 = outer region, between $y = y_m$ and $y = y_2$
2 = evaluated at the outer extreme of the boundary layer

[2] The values of n suggested above (based on estimates from profiles for heat transfer from an isothermal plate to a fluid at uniform temperature) will become inaccurate when the equations in the Appendix are applied to problems where the wall and fluid temperatures change *sharply* in the flow direction. The resulting error in the heat transfer will increase as Pr decreases. For oils, and perhaps water, adequate predictions should result; substantial errors for gases are expected if these n values are used. For the present problem, for $A \gtrsim 5$, the "ambient" (midslot) temperature variation is weak, so the stated values of n should be reasonable. In addition, the heat transfer in this case is almost independent of n, and the midslot temperature distribution depends only weakly on n.

region by dropping acceleration and convection terms so that the solution in this region remains as difficult as the solution to the original problem (before introducing the "inner" and "outer" regions). However, approximations can be introduced in the analysis of the outer region with weaker consequences on the final results than had the same approximations been made over the entire (inner plus outer) region. Indeed, if the *answers of interest* are controlled mainly by processes in the inner region, even quite crude assumptions may be admissible without severely impairing the accuracy.

An integral energy balance over the inner and outer regions contains the ratios

$$C_1 = (\overline{T}_i - \overline{T})/(T_h - \overline{T}),\ C_2 = (\overline{T}_0 - \overline{T})/(T_h - \overline{T}),\ \gamma = \Gamma_0/\Gamma_i \quad (2)$$

Prescribing some reasonable shapes for the temperature and velocity profiles in the outer regions (dotted curves in Fig. 1(*a*)) and inserting these into the integral equations would give rise to known values of these ratios. If the profile *shapes* are presumed invariant with x, then C_1, C_2 and γ would be constants. Rather than carrying out this analysis (which would yield only approximate values of these ratios in any case because the profile shapes must be guessed), the ratios are carried as constants in the analysis, to be later assigned approximate numerical values.

Combining Inner and Outer Regions. Appendix A combines the results from the differential and integral solutions, respectively, of the inner and outer regions to give a general solution for nonisothermal boundaries. Specializing this to the problem where T_h and T_c are constants gives the following equation for the mass flow rate in the inner region, Γ_i

$$\Gamma_i^{4/3} = \left\{\frac{M(1 - 5M/8)^{1/3}}{(C_1 + \gamma C_2)}\right\} \frac{4}{3}\frac{kx}{C_p}\left[\frac{\rho^2 g\beta}{3\mu}\right]^{1/3} F(x) \quad (3)$$

where

$$F(x) = (T_h - \overline{T})^{4n/3} \cdot \left[\frac{1}{x}\int_0^x (T_h - \overline{T})^p dx\right] \quad (4)$$

Here n and p are simple combinations of C_1, C_2, and γ (see Nomenclature). The average Nusselt number in the laminar b.l. regime becomes (upon integration of A.2)

$$\overline{\mathrm{Nu}}_H = \frac{\bar{q}}{(T_h - T_c)}\frac{H}{k} = G_\ell C_\ell \,\mathrm{Ra}_H^{1/4} \quad (5)$$

where C_ℓ is a function of Prandtl number (see Nomenclature) and

$$G_\ell = \int_0^1 \left\{(1-\theta)^{(p+5)/4} \Big/ \left[\int_0^\zeta (1-\theta)^p d\zeta\right]^{1/4}\right\} d\zeta \quad (6)$$

θ is the dimensionless temperature $(\overline{T} - T_c)/(T_h - T_c)$. Note that G_ℓ is just a numerical constant whose value depends on the thermal stratification in the core.

The assumption of the existence of a laminar b.l. regime has given rise to the ¼ power on Ra_H. For aspect ratios near unity (validity of the present results is not claimed for $A < 5$), this power will be incorrect. Numerical solutions of MacGregor and Emery [11] and Thomas and de Vahl Davis [22] do support the existence of a ¼-power regime for larger aspect ratios.

The distribution of θ is required before these equations can be evaluated. Attention is now turned to this.

The Core Temperature Distribution, θ. Mass conservation across any x plane demands that $[(1 + \gamma)\Gamma_i]_h = [(1 + \gamma)\Gamma_i]_c$. Since γ has been presumed constant, $[\Gamma_i]_h = [\Gamma_i]_c$ for any x. The equation for $[\Gamma_i(x)]_c$ can be obtained immediately from equation (3). Thus $[\Gamma_i]_h = [\Gamma_i]_c$ becomes

$$\Lambda_c \theta^{4n/3}\int_\zeta^1 \theta^p d\zeta = \Lambda_h (1-\theta)^{4n/3}\int_0^\zeta (1-\theta)^p d\zeta; \quad (7)$$

$$\Lambda = (k/C_p)(\rho^2\beta/\mu)^{1/3}$$

In principle, the property-value group, designated by Λ, depends on T_h, T_c *and* θ; for simplicity the properties subscripted with h and c are here simply evaluated at T_h and T_c, respectively. Rearranging equation (7)

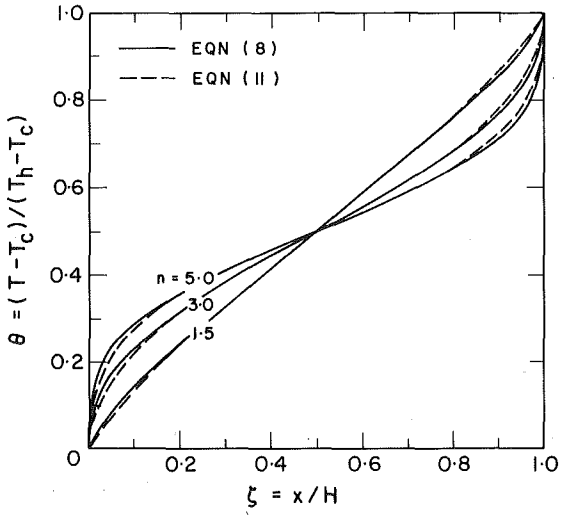

Fig. 2 Computed variation of midslot temperature distributions for n = 1.5, 3.0, and 5.0

$$\theta = \frac{g^*}{1 + g^*},$$

$$g^* = \left\{\left(\frac{\Lambda_h}{\Lambda_c}\right)^{1/3}\int_0^\zeta (1-\theta^p)d\zeta \Big/ \int_\zeta^1 \theta^p d\zeta\right\}^{3/4n} \quad (8)$$

This equation is easily solved by guessing some initial distribution of θ, calculating the resulting function g^*, from which an improved θ distribution is obtained. This is used as the next guessed θ distribution, and so on until a converged solution is found.

From equation (8), θ is symmetric about $\zeta = ½$ only when $\Lambda_c/\Lambda_h = 1$. Also $\theta(0) = 0$ is the boundary condition on θ which is consistent with $\Gamma_i = 0$. Finally, it will be noted that the prescribed shapes of the velocity and temperature profiles in the outer region affect the midslot temperature distribution through a single parameter, n (or p).

3.3 Turbulent–Boundary-Layer Regime. For fully turbulent flow, the heat transfer becomes governed by local effects. It was proposed earlier [29, 31] that the local Nusselt number for one boundary layer (e.g., on the hot face) be given by

$$qL/k(T_h - \overline{T}) = C_t A(\phi)\mathrm{Ra}_L^{1/3}[(T_h - \overline{T})/(T_h - T_c)]^{1/3} \quad (9)$$

where $A(\phi) = 0.71$ for a vertical surface, and C_t is currently taken as

$$C_t = [0.14\,\mathrm{Pr}^{0.084}, 0.15]_{\mathrm{MIN}} \quad (9(a))$$

where $[A, B]_{\mathrm{MIN}}$ is the minimum of A and B. This should be viewed as a tentative proposal, to be improved as more measurements become available for Pr far removed from unity. Integrating to obtain the average Nusselt number, $\overline{\mathrm{Nu}}_L$

$$\overline{\mathrm{Nu}}_L = C_t A(\phi)\mathrm{Ra}_L^{1/3} G_t; \quad G_t = \int_0^1 (1-\theta)^{4/3} d\zeta \quad (10)$$

Once θ is known, G_t and therefore $\overline{\mathrm{Nu}}_L$ can be evaluated.

4 Solutions for θ and Comparisons With Experiment

4.1 Laminar Boundary Layer. It is quite straightforward to carry out the solution to equation (8) to obtain $\theta(\zeta)$ once n is prescribed. The method already described for determining n would be to specify the profile shapes in the outer region, which then determines C_1, C_2, and γ. Alternatively, approximate values of these constants can be found for the profiles predicted by the similarity solution for free convection around a vertical plate [30]. Taking the latter route, n is found to be about 1.5 and 2.5, respectively, for Pr = 0.72 and 2.0.[3] Because the solution is expected to become insensitive to Pr for Pr $\gtrsim$ 5, a value of $n \approx 3.0$ to 4.0 should be appropriate for Pr $\gg$ 1.

Uniform Property Results, $\Lambda_c/\Lambda_h = 1$. For $\Lambda_c/\Lambda_h = 1$, Fig. 2 shows

[3] See footnote 2.

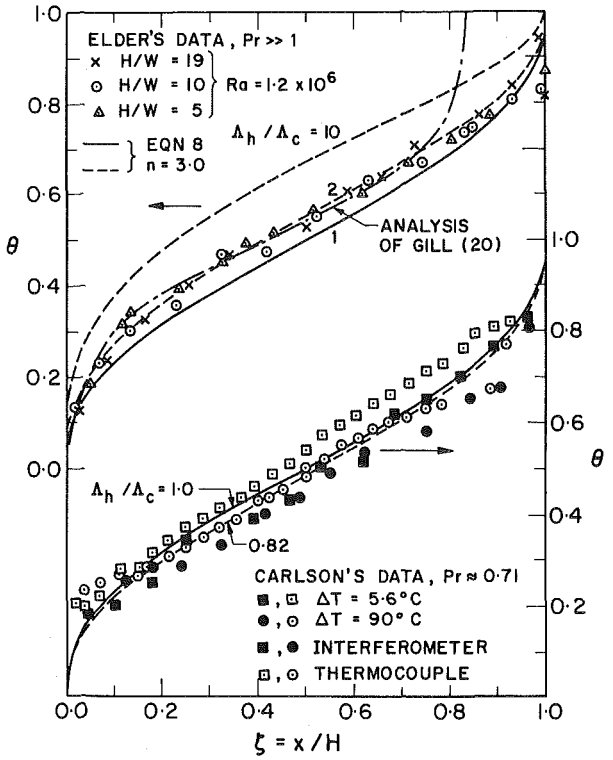

Fig. 3 Computed variation of midslot temperature distributions for $n = 3.0$ and various viscosity ratios—Predictions compared with Pr ≫ 1 data (top) and air data (below)

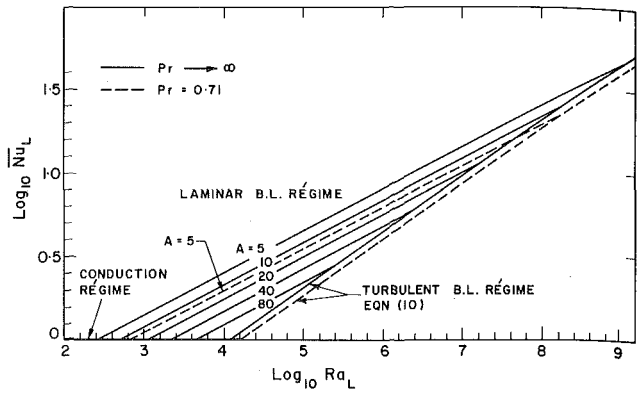

Fig. 4 Prediction of average Nusselt numbers for conduction, laminar b.l., and turbulent b.l. regimes

the distribution of θ with ζ for $n = 1.5$, 3, and 5. For $n = 1.5$, the slope $m = \partial\theta/\partial\zeta$ at the center of the slot is about 0.86. As n increases, the slope slowly decreases to $m = 0.58$ and 0.44 for $n = 3$ and 5, respectively. m becomes insensitive to n for larger values; for example at $n = 10$, $m \approx 0.40$. As already mentioned, $n = 1.5$ and $n \approx 3$ to 4 should be representative values for Pr ≈ 0.72 and large Pr.

It would be more convenient to have a closed form solution to equation (8). While this has not been found, an equation which closely fits the results is

$$\theta = \zeta^m/(\zeta^m + (1 - \zeta)^m) \tag{11}$$

This equation is plotted in Fig. 2 for comparison with the "exact" solution of the integral equation.

Comparison of m with Experiment. For high Prandtl-number fluids, Elder [8] reported $m = 0.50$ for paraffin and 0.55 for silicone 100 cS. Quon [24] finds a slope of about 0.5 for Pr = 900 and $A = 1$. The above estimate of $n = 3.0$ leads to a slope of $m \approx 0.58$, which is in good agreement. (A value of $n = 4.0$ would give $m \approx 0.50$.)

For air, Carlson [4] measured slopes ranging between 0.55 and 0.68 for an aspect ratio of 10. Mynett and Duxbury [15] report measurements which show that m has a value of about 0.8 for a well established b.l. regime. Both of these experiments show considerable scatter. Thomas and de Vahl Davis [22] confirm the magnitude of the latter measurements with their finite-difference solutions for Pr = 1. (For $A = 1$ and Pr = 1, Quon [24] finds a slope of about 0.83.) The estimate of $n = 1.5$ for Pr = 0.72, which leads to an m value of about 0.86, is therefore also in good agreement with experiment.

Predictions of θ for $\Lambda_c/\Lambda_h \neq 1$. The solid curves in Fig. 3 reproduce the curves in Fig. 2 for $n = 3$ for constant properties. The broken curve in the lower part of the figure shows the solution of equation (8) with $\Lambda_h/\Lambda_c = 0.82$, which would be typical of the ratio for gas-filled cavities with a temperature difference of order 100 K. The upper part of the figure shows results for $\Lambda_h/\Lambda_c = 2$ and 10; this latter value represents an extreme case.

Comparison of θ With Experiment. Carlson's data [4] at low temperature differences (Fig. 3) are found to fall quite consistently above their counterparts for higher differences for each of his measurement techniques; however, the scatter is large. The predicted abrupt change in θ near the ends ($\zeta = 0$ and $\zeta = 1$) are observed and the general agreement is good. It should be noted that the curves have been drawn in Fig. 3 for $n = 3$ ($m = 0.58$) which agrees well with Carlson's measured slopes, but is in disagreement with other observations for Pr = 0.71, and with the slope predicted by this analysis.[3]

The upper portion of Fig. 3 plots Elder's data for Pr ≫ 1. A value of $\Lambda_h/\Lambda_c = 2$ corresponds approximately to his experimental conditions, and the data are seen to agree well with the curve for this value. The disagreement for ζ near unity is apparently due to significant heat loss in the experiments from this (open) end.

4.2 Comparison with Gill's Analysis. Gill [20] also predicted the vertical temperature distribution in the core of the fluid layer. His comparison with Elder's data, after adjustment to match experimental and analytical values of θ and $\partial\theta/\partial\zeta$ at $\zeta = 0.5$, is also shown in Fig. 3. The agreement is less satisfactory than the present predictions based on (the appropriate) $\Lambda_h/\Lambda_c = 2.0$. Gill's analysis also contained no dependence on Prandtl number, in disagreement with both measurement and finite-difference predictions.

5 Nusselt Number Predictions Comparison with Experiment

5.1 Solutions.

Conduction Regime. The solution in this regime appears as the horizontal line, $\overline{Nu}_L = 1$, in Fig. 4.

Laminar B.L. Regime. To evaluate $\overline{Nu}_H$ (or $\overline{Nu}_L$) in this regime from equation (5), G_ℓ must be calculated. This is found from equation (6) using the solution for θ and the estimated values of n (or p) described in Section 3. The result is $G_\ell = 0.74$ for $n = 1.5$ (or Pr ≈ 0.72) and $G_\ell = 0.76$ for $n = 3$ (or Pr ≈ ∞). Because G_ℓ varies so slowly with n (or Pr), a constant value of $G_\ell = 0.75$ is used. This equation is also plotted in Fig. 4 for two values of Pr.

Turbulent b.l. Regime. $\overline{Nu}_L$ is evaluated in this regime from equation (10); G_t is found using equation (11) for θ (this agrees well with the measurements of Kutateladze, et al. [13] with $m = 0.33$ and $m = 0.50$). Upon carrying out the integration for various m it was found that G_t was very insensitive to m ($0.402 < G_t < 0.414$ for $0.3 < m < 0.6$) so that a constant G_t of 0.41 was adopted.

The resulting $\overline{Nu}_L$ values for Pr → ∞ and Pr = 0.71 are plotted in Fig. 4.

Summary of $\overline{Nu}_L$ Versus Ra_L Predictions. In plotting Fig. 4, the laminar b.l. curves for $\overline{Nu}_L$ have not been extended beyond their intersections with curves for the conduction regime and turbulent b.l. regime. It is clear that $\overline{Nu}_L < 1$ will not occur; it is assumed that the greater of $\overline{Nu}_L$ in the laminar b.l. regime and $\overline{Nu}_L$ in the turbulent b.l. regime for a given Ra_L will be appropriate.

The abrupt changes in slope between regimes depicted in Fig. 4

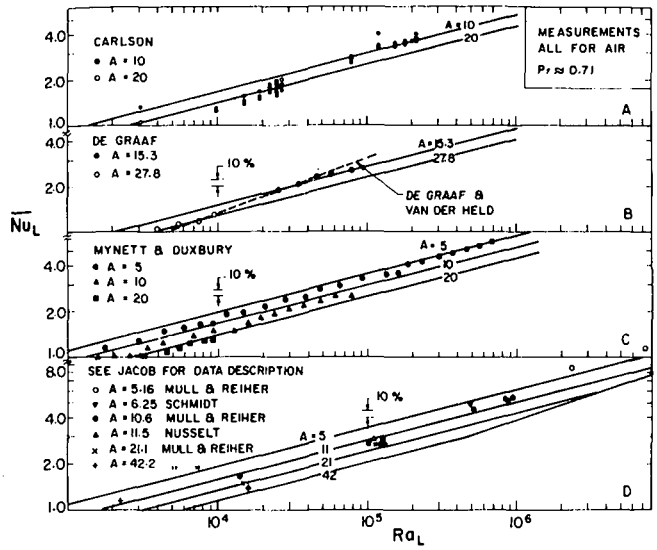

Fig. 5 Comparison of predictions with data for various aspect ratios for air

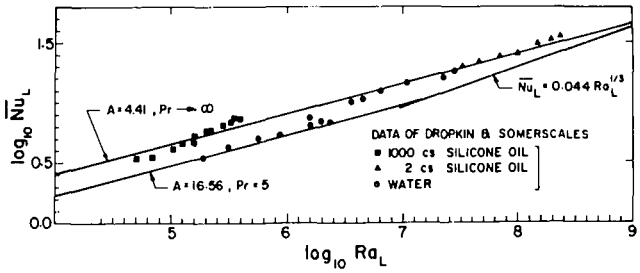

Fig. 6 Comparison of data by Dropkin and Sommerscales for water and silicone oils with present predictions

would not be expected in practice. However, it is relevant that for cylindrical and spherical layers a $\overline{Nu}_L \propto Ra_L^{1/4}$ relation is found experimentally almost down to the conduction regime [29]. Also, numerical solutions (e.g., Thomas and de Vahl Davis [22]) for the vertical slot problem display a "fairly sharp" transition. Therefore, the abrupt change in slopes is not expected to be in serious error.

The abrupt change between the laminar and turbulent b.l. regime is the simplest result to use. With the exception of MacGregor and Emery [11], who did find an abrupt change in slope in their data, there is little support for this assumption. However, neither is there evidence at present to support a more complex assumption.

Fig. 4 also graphically depicts the diminishing extent of the laminar b.l. regime with increasing A. For large enough A, heat transfer in a laminar b.l. regime would not be expected.

5.2 Validation of Laminar Predictions (Isothermal Walls). *$Pr \approx 0.71$, Air.* The data from six different studies using air are plotted in Fig. 5. Equations (1), (5), and (10) have been plotted for comparison over their appropriate Ra_L ranges.

Fig. 5(a) plots the data of Carlson [4], which has been recalculated using property values evaluated at $(T_h + T_c)/2$, for $A = 10$ and 20. The present analytical results agree to within experimental scatter with his measurements for all Rayleigh numbers. De Graaf's [2] measurements in Fig. 5(b) are in excellent agreement with the present predictions. De Graaf and Van Der Held [3] recommended a correlation equation (broken line in Fig. 5(b) which contained no aspect ratio dependence. Had data been obtained in an overlapping Ra_L range for the different values of A, the importance of retaining A would have been clear. Their recommended equation should *not* be used for design.

Fig. 5(c) shows that Mynett and Duxbury's [15] data agree with predictions at the highest Rayleigh numbers for each A, but fall 10 to 15 percent below predictions near the conduction regime. The early German measurements compiled by Jacob [1] are plotted in Figure 5(d). Here, good agreement is found at the lower Rayleigh numbers but Mull and Reiher's results at the highest Rayleigh numbers are 10 to 15 percent higher than predictions.

From these comparisons it is concluded that the foregoing equations for the conduction and laminar b.l. regimes agree with experiment to about the same degree that experiments are in accord with each other.

$Pr > 1$ and $Pr \gg 1$. The data of Dropkin and Somerscales [9] are plotted in Fig. 6. In these experiments, water and two silicone oils were used, and the aspect ratio was varied from 4.41 to 16.56. Like De Graaf and Van Der Held, a correlation equation was proposed to fit the data which did not contain a dependence on aspect ratio. Since Ra_L was increased primarily by decreasing A, it is speculated here that their use of $\frac{1}{3}$ as the power on Ra_L in their equation (rather than $\frac{1}{4}$ as here) perhaps accounts roughly for the aspect ratio effect in the measurements. Some support of this speculation is shown by plotting the outer bounds of the region in which the present analysis predicts the experimental data should have fallen. Most of the data *do* fall in this band.

The data of Arnold, et al. [16], also for water and two silicone oils, were found to be in reasonable agreement with prediction (≈ 10 percent) at high Ra_L but the data fall below predictions at low Ra_L. Other experimental data to check this disagreement, and the experimentally observed independence of $\overline{Nu}_L$ from A at low Ra_L, would be valuable.

5.3 Data With Mixed Boundary Conditions. Emery and coworkers [6, 7, 11, 12] and Landis and Yanowitz [10] have reported a large number of measurements for vertical fluid layers bounded by a hot vertical plate with a uniform heat flux boundary condition and a cold isothermal vertical plate. Fluids with Prandtl numbers from 0.02 to 30,000 were used.

$Pr \approx 0.02$. Mercury. Early measurements (Emery [6]) for $A = 4.7$ and 10 were substantially different than later measurements by MacGregor and Emery [12] for $A = 20$. The present analysis predicts that for Pr = 0.02, $\overline{Nu}_H = 0.16\ Ra_H^{1/4}$; the best curve through the MacGregor and Emery data is $\overline{Nu}_H \approx 0.17\ Ra_H^{1/4}$. There is, therefore, good agreement with their later measurements but not with the former. More work is required.

$Pr > 1$. Data by MacGregor and Emery [12] for liquids with Pr > 1 and $10 \leq A \leq 80$ can be correlated in the laminar regime by the equation $\overline{Nu}_H = 0.32\ Ra_H^{1/4}$, where the average temperature of the hot plate is used in calculating the temperature difference. There is some scatter in the data about this equation, but most lie within the band $\overline{Nu}_H = 0.40\ Ra_H^{1/4}$ to $\overline{Nu}_H \approx 0.30\ Ra_H^{1/4}$, the data for Glycerin (Pr = 20,000–30,000) lying highest. The present analysis predicts $\overline{Nu}_H = 0.38\ Ra_H^{1/4}$ for $Pr \to \infty$, and $\overline{Nu}_H = 0.34\ Ra_H^{1/4}$ for Pr = 5 (water) for the laminar b.l. regime. The agreement is within experimental scatter.

5.4 Validation of Turbulent Heat Transfer Prediction. The high Rayleigh number data of MacGregor and Emergy [11] are of great interest because they extend into the turbulent range. Because the constant heat flux boundary condition will lead to a nearly isothermal surface when the flow is turbulent, a valid comparison with the present prediction is possible. For $1 < Pr < 20$, $1 < A < 40$, their data are well represented by the equation $\overline{Nu}_L = 0.046\ Ra_L^{1/3}$. Equation (10) predicts that $\overline{Nu}_L = 0.044\ Ra_L^{1/3}$ for $Pr \gtrsim 1.0$.

The data of Jannot and Mazeas [35] for carbon dioxide and nitrogen for $3.5 \leq A \leq 100$ extend to $Ra_L \approx 10^{10}$. Nusselt and Rayleigh numbers were calculated from their measurements using property values based on $(T_h + T_c)/2$; temperature differences up to 200 K were used, making the choice of reference temperature rather important. The data showed considerable scatter, but $\overline{Nu}_L$ was generally above the predictions of the present analysis. At the large Ra_L of some of the

measurements, the heat transfer across each of the turbulent boundary layers might be expected to approach the heat transfer from a vertical plate in an unconfined environment; this was not found.

Based on the foregoing data, a conclusive statement about the validity of the present predictions in the turbulent regime cannot be made. Additional experimental work is needed.

6 Summary of Equations for Vertical and Tilted Surfaces

For laminar heat transfer from a tilted flat plate, the Nusselt number is usually found from the equation for the vertical orientation, but with g replaced by $g \cos \phi$ (where ϕ is the angle of the surface from the vertical, positive when the heated surface faces upward). Ayyaswamy and Catton [35] suggested that this scaling should hold also for a tilted fluid layer in laminar flow for $-10° < \phi < 45°$. Raithby and Hollands [29] proposed that it could also be used for turbulent flow for $\phi < 20$ deg.

Arnold, et al. [16] confirmed that the scaling correlates experimental results in the range -20 deg $< \phi < 20$ deg. The following equation, representing a generalization of the equations obtained from the foregoing analysis for a vertical layer, is therefore proposed

$$\overline{\mathrm{Nu}}_L = \left[1,\ 0.75 C_\ell \left(\frac{\cos\phi}{A}\mathrm{Ra}_L\right)^{1/4},\ 0.29 C_t\ (\cos\phi \mathrm{Ra}_L)^{1/3}\right]_{\max} \quad (12)$$

where -20 deg $< \phi < 20$ deg, $C_\ell = 0.50/(1 + (0.49/\mathrm{Pr})^{9/16})^{4/9}$, and $C_t = [0.15,\ 0.14\ \mathrm{Pr}^{0.084}]_{\min}$. This equation is in "good" agreement with data, where "good" means that the predictions agree with experiments to about the same degree that experiments are in accord with each other.

Equation (12) is applicable to the design of flat plate solar collectors, with collection surfaces within 20 deg of the vertical. For larger angles of tilt, the correlation of Hollands, et al. [33] can be used.

Acknowledgments

This work was supported by the U. S. Energy Research and Development Administration, (ERDA), Division of Solar Energy, Solar Heating and Cooling Branch, under contract number E(11–1)-2597. Mr. A. Pollard wrote the computer programs used to find θ and n, Dr. P. L. Silveston made the De Graaf thesis available to us, and Dr. M. Jannot sent several reports. Mr. D. Ruth contributed ideas in helpful discussions.

References

1 Jakob, M., *Heat Transfer,* Vol. 1, Wiley, New York, 1967, pp. 536–539.

2 De Graaf, J. G. A., "Het Verband Tussen De Warmte-Overgang En De Stromingverschijnselen In Gesloten Spouwen," PhD thesis, University of Utrecht, published by Drunkkerij Fa. Schotanus & Jens. (Utrecht), 1952.

3 De Graaf, J. G. A., and Van Der Held, E. F. M., "The Relation Between the Heat Transfer and Convection Phenomena in Enclosed Plane Air Layers," *Appl. Sci. Res.,* Vol. 3, 1953, pp. 393–409.

4 Carlson, W. O., "Interferometric Studies of Convective Flow Phenomena in Vertical, Plane Enclosed Air Layers," PhD thesis, University of Minnesota, 1956.

5 Eckert, E. R. G., and Carlson, W. O., "Natural Convection in an Air Layer Enclosed Between Two Vertical Plates With Different Temperatures," *International Journal of Heat and Mass Transfer,* Vol. 2, 1961, pp. 106–120.

6 Emery, A. F., "The Effect of a Magnetic Field Upon the Free Convection of a Conducting Fluid," JOURNAL OF HEAT TRANSFER, TRANS. ASME, Series C, Vol. 85, 1963, pp. 119–124.

7 Emery, A., and Chu, N. C., "Heat Transfer Across Vertical Layers," JOURNAL OF HEAT TRANSFER, TRANS. ASME, Series C, Vol. 87, 1965, pp. 110–116.

8 Elder, J. W., "Laminar Free Convection in a Vertical Slot," *Journal of Fluid Mechanics,* Vol. 23, 1965, pp. 77–98.

9 Dropkin, D., and Somerscales, E., "Heat Transfer by Natural Convection in Liquids Confined by Two Parallel Plates Which are Inclined at Various Angles With Respect to the Horizontal," JOURNAL OF HEAT TRANSFER, TRANS. ASME, Series C, Vol. 87, 1965, pp. 77–84.

10 Landis, F., and Yanowitz, H., "Transient Natural Convection in a Narrow Vertical Cell," Transactions, International Heat Transfer Conference, 1966, pp. 139–151.

11 MacGregor, R. K., and Emery, A. F., "Free Convection Through Vertical Plane Layers—Moderate and High Prandtl Number Fluids," JOURNAL OF HEAT TRANSFER, TRANS. ASME, Series C, Vol. 91, 1969, pp. 391–403.

12 MacGregor, R. K., and Emery, A. F., "Prandtl Number Effects on Natural Convection in an Enclosed Vertical Layer, JOURNAL OF HEAT TRANSFER, TRANS. ASME, Series C, Vol. 93, 1971, pp. 253–254.

13 Kutateladze, S. S., Kirdyashkin, A. G., and Ivakin, V. P., "Turbulent Natural Convection on a Vertical Plate and in a Vertical Layer," *International Journal of Heat and Mass Transfer,* Vol. 15, 1972, pp. 193–202.

14 Dixon, M., and Probert, S. D., "Heat-Transfer Regimes in Vertical, Plane-Walled, Air-Filled Cavities," *International Journal of Heat and Mass Transfer,* Vol. 18, 1975, pp. 709–710.

15 Mynett, J. A., and Duxbury, D., "Temperature Distributions Within Enclosed Plane Air Cells Associated With Heat Transfer by Natural Convection," *Proceedings of the 1974 International Heat Transfer Conference,* Tokyo, pp. 119–123.

16 Arnold, J. N., Catton, I., and Edwards, D. K., "Experimental Investigation of Natural Convection in Inclined Rectangular Regions of Differing Aspect Ratios, JOURNAL OF HEAT TRANSFER, TRANS. ASME, Series C, Vol. 98, 1976, pp. 67–71.

17 Batchelor, G. K., "Heat Transfer by Free Convection Across a Closed Cavity Between Vertical Boundaries at Different Temperatures," *Quart. of Applied Mathematics,* Vol. XII, 1954, pp. 209–233.

18 Poots, G., "Heat Transfer by Laminar Free Convection in Enclosed Plane Gas Layers," *Quart, J. Mech. Appl. Math.,* Vol. 11, 1958, pp. 257–267.

19 Elder, J. W. "Numerical Experiments With Free Convection in a Vertical Slot," *Journal of Fluid Mechanics,* Vol. 24, 1966, pp. 823–843.

20 Gill, A. E., "The Boundary-Layer Regime for Convection in a Rectangular Cavity," *Journal of Fluid Mechanics,* Vol. 26, 1966, pp. 515–536.

21 de Vahl Davis, G., "Laminar Natural Convection in an Enclosed Rectangular Cavity," *International Journal of Heat and Mass Transfer,* Vol. 11, 1968, pp. 1675–1693.

22 Thomas, R. W., and de Vahl Davis, G., "Natural Convection in Annular and Rectangular Cavities: A Numerical Study," *Proceedings of the 1970 International Heat Transfer Conference,* Paris, Paper NC2.4.

23 Newell, M. E., and Schmidt, F. W., "Heat Transfer by Laminar Natural Convection Within Rectangular Enclosures," JOURNAL OF HEAT TRANSFER, TRANS. ASME, Series C, Vol. 92, 1970, pp. 159–165.

24 Quon, C., "High Rayleigh Number Convection in an Enclosure—A Numerical Study," *Physics of Fluids,* Vol. 15, 1972, pp. 12–18.

25 Catton, I., Ayyaswamy, P. S., and Clever, R. M., "Natural Convection Flow in a Finite, Rectangular Slot, Arbitrarily Oriented With Respect to the Gravity Vector," *International Journal of Heat and Mass Transfer,* Vol. 17, 1974, pp. 173–184.

26 Ozoe, H., Sayama, H., and Churchill, S. W., "Natural Convection in an Inclined Square Channel," *International Journal of Heat and Mass Transfer,* Vol. 17, 1974, pp. 401–406.

27 Ozoe, H., Yamamoto, K., Sayama, H., and Churchill, S. W., "Natural Convection in an Inclined Rectangular Channel Heated on One Side and Cooled on the Opposing Side," *International Journal of Heat and Mass Transfer,* Vol. 17, 1974, pp. 1209–1217.

28 Yin, S. H., Powe, R. E. Scanlan, J. A., and Bishop, E. H., "Natural Convection Flow Patterns in Spherical Annuli," *International Journal of Heat and Mass Transfer,* Vol. 16, 1973, pp. 1785–1795.

29 Raithby, G. D., and Hollands, K. G. T., "A General Method of Obtaining Approximate Solutions to Laminar and Turbulent Free Convection Problems," *Advances in Heat Transfer,* Academic Press, Vol. 11, 1975, pp. 265–315.

30 Ostrach, S., "An Analysis of Laminar Free-Convection Flow and Heat Transfer About a Flat Plate Parallel to the Direction of the Generating Body," NACA TR 1111, 1953.

31 Raithby, G. D., and Hollands, K. G. T., "Laminar and Turbulent Free Convection From Elliptic Cylinders, With a Vertical Plate and Horizontal Circular Cylinder as Special Cases," JOURNAL OF HEAT TRANSFER, TRANS. ASME, Series C, Vol. 98, 1976, pp. 72–80.

32 Churchill, S. W., and Usagi, R., "A General Expression for the Correlation of Rates of Heat Transfer and Other Phenomena," *AIChE Journal,* Vol. 18, 1972, pp. 1121–1128.

33 Hollands, K. G. T., Unny, T. E., Raithby, G. D., and Konicek, L., "Free Convection Heat Transfer Across Inclined Air Layers," JOURNAL OF HEAT TRANSFER, TRANS. ASME, Series C, Vol. 98, 1976, pp. 189–193.

34 Jannot, M., and Mazeas, C., "Etude Experimentale de la Convection Naturelle dan des Cellules Rectangulaires, Verticales," *International Journal of Heat and Mass Transfer,* Vol. 16, 1973, pp. 81–100.

35 Ayyaswamy, P., and Catton, I., "The Boundary-Layer Regime for Natural Convection in a Differentially Heated Tilted Rectangular Cavity," JOURNAL OF HEAT TRANSFER, TRANS. ASME, Series C, Vol. 95, 1973, pp. 543–545.

APPENDIX A

Outline of Laminar B.L. Analysis

Equations (4) and (5) of [29] give the velocity and mass flow rate in the inner region. The energy equation (6) of [29] is replaced by

$$k(T_h - T_m)/y_m = (C_1 + C_{2\gamma})C_p \frac{d}{dx}((T_h - \overline{T})\Gamma_i) + (1 + \gamma)C_p \Gamma_i \frac{d\overline{T}}{dx} \quad (A.1)$$

to account for the thermal stratification of the "ambient" fluid. For a vertical surface the resulting local Nusselt number is

$$qx/k(T_h - \overline{T}) = C_\ell[g\beta(T_h - \overline{T})x^3/\alpha\kappa]^{1/4}\,(T_h - \overline{T})^{1/12}/F^{1/4} \quad \text{(A.2)}$$

where

$$F(x) = \frac{1}{x}\int_0^x (T_h - \overline{T})^{5/3}\,G dx/G(T_h - \overline{T})^{4/3};$$

$$G = \exp\left(\int \frac{4}{3}\frac{(1+\gamma)}{(C_1 + C_2\gamma)}\frac{1}{(T_h - \overline{T})}\frac{d\overline{T}}{dx}dx\right) \quad \text{(A.3)}$$

C_ℓ is the same as equation (11) of [29]; it is replaced by the equation in the Nomenclature as discussed in [31]. These equations all reduce to those in [29] for constant $\overline{T}$. Introducing T_h = constant gives the equations in the text.

R. F. Boehm
Professor.

Mem. ASME

D. Kamyab[1]
Graduate Research Assistant.

Mechanical and Industrial Engineering Department, University of Utah, Salt Lake City, Utah

Established Stripwise Laminar Natural Convection On A Horizontal Surface

A finite difference technique was used to analyze steady, laminar natural convection due to stripwise heating on an infinite, horizontal surface. The stripwise heating was accomplished by an array of alternately heated and unheated strips. Plots of the stream function and temperature field within a two-dimensional cell are given for a variety of heating and spacing configurations. From these results, the average Nusselt number was determined as a function of the Grashof number for a Prandtl number of 0.7. A plot of this dependence indicates diffusion, transition and plume modes exist, depending upon the value of the Grashof number. The present results are compared to previous experimental results for the same system, as well as results for uniformly heated surfaces. Higher heat transfer rates for the stripwise-heated surfaces compared to uniformly-heated surfaces are demonstrated for a wide range of Grashof numbers.

Introduction

Free convection is widely occurring heat transfer phenomena in both natural and engineering systems. In general, its effectiveness is decreased when the buoyant force direction is not parallel to the heating surface. An example of this is heating on an infinite horizontal surface. Here the heat is removed by a combination of conduction and instabilities whereby the heated fluid randomly tears away from the hot surface.

Heat sources on a horizontal surface have been used to form effective flows in infinite fluids. For example, during the Second World War, flames were used to line runways in an attempt to dissipate fogs. More recently groundbased heat sources have been used to effect rainfall. Other than some preliminary experimental work performed by Boehm and Alder [1],[2] investigations of the engineering aspects of this phenomena are lacking. In that work, results seemed to indicate superior performance with stripwise heating compared to uniform heating.

We have performed a numerical analysis of established, steady-state stripwise heating on a horizontal surface. A finite difference code has been used to simulate the laminar natural convection that results. This allows a detailed examination of flow field, temperature field and heat transfer performance for a wide variety of parameters. The method of analysis is given in the next section.

Method of Analysis

The physical system to be analyzed is as shown in Fig. 1, where L and H denote the low and high temperature strips, respectively. The significance of the lines denoted as "symmetry line" will be discussed later. Using the usual Boussinesq approximation on the density variation, the following governing equations result for the two-dimensional situation (see the Nomenclature section for the definition of terms)

$$UU_{\bar{x}} + VU_{\bar{y}} = -\frac{1}{\rho}P_{\bar{x}} + g\beta(T - T_\infty) + \nu\nabla^2 U \tag{1}$$

$$UV_{\bar{x}} + VV_{\bar{y}} = -\frac{1}{\rho}P_{\bar{y}} + \nu\nabla^2 V \tag{2}$$

$$U_{\bar{x}} + V_{\bar{y}} = 0 \tag{3}$$

Nondimensionalizing:

$$\text{Vorticity} \qquad \omega = \frac{L^2}{\nu}(V_{\bar{x}} - U_{\bar{y}}) \tag{5}$$

$$\text{Stream function} \qquad U = -\nu\psi_{\bar{y}},\ V = \nu\psi_{\bar{x}} \tag{6}$$

$$\text{Temperature} \qquad \theta = \frac{T - T_\infty}{T_s - T_\infty} \tag{7}$$

[1] Currently with Houston Contracting Co., Tehran, Iran.

[2] Numbers in brackets designate Reference at end of paper.

Contributed by the Heat Transfer Division of THE AMERICAN SOCIETY OF MECHANICAL ENGINEERS and presented at the Heat Transfer Conference, St. Louis, Mo., August 9-11, 1976. Revised manuscript received by the Heat Transfer Division March 4, 1977. Paper No. 76-HT-19.

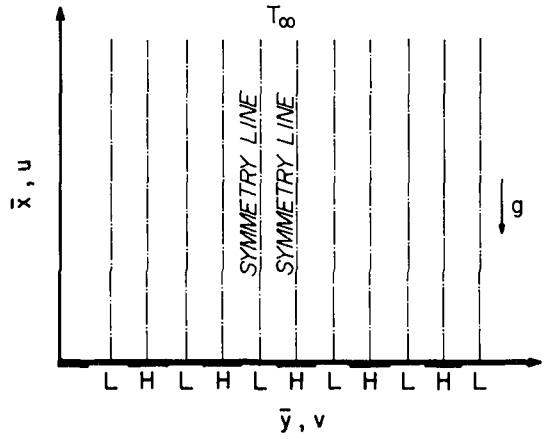

Fig. 1 Diagram of the two-dimensional system studied in the present work—*H* and *L* denote high and low temperature strips, respectively

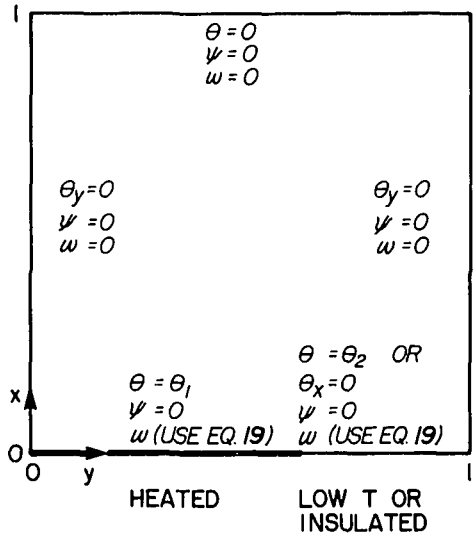

Fig. 2 Boundary conditions used in the present analysis

$$\text{Length} \qquad x = \frac{\bar{x}}{L}, y = \frac{\bar{y}}{L} \tag{8}$$

The governing equations become:

$$\omega_{xx} + \omega_{yy} = \text{Gr}\,\theta_y + (\psi_x\omega_y - \psi_y\omega_x) \tag{9}$$

$$\omega = \psi_{xx} + \psi_{yy} \tag{10}$$

$$\theta_{xx} + \theta_{yy} = \text{Pr}\,(\psi_x\theta_y - \psi_y\theta_x) \tag{11}$$

where Gr denotes the Grashof number based on the temperature difference between the hot strips and the ambient. Note that the pressure gradient has been eliminated between equations (1) and (2) in arriving at equation (9).

At this point, a transformation is used for reducing the infinite dimension (perpendicular to the surface) to a finite value to facilitate solution. Since the most important behavior is occurring next to the plate, the transformation suggested by Sills [2] is incorporated, namely:

$$X = 1 - e^{-x} \tag{12}$$

Note that this transformation is linear in the important region near the wall.

The nondimensionalized equations for the transformed space then become:

$$(1 - X)(\omega_X\psi_y - \omega_y\psi_X) + (1 - X)^2\omega_{XX} + (X - 1)\omega_X + \omega_{yy} - \text{Gr}\,\theta_y = 0 \tag{13}$$

$$(1 - X)(\theta_X\psi_y - \theta_y\psi_X) + \frac{1}{\text{Pr}}[(1 - X)^2\theta_{XX} + (X - 1)\theta_X + \theta_{yy}] = 0 \tag{14}$$

$$\omega = (1 - X)^2\psi_{XX} + (X - 1)\psi_X + \psi_{yy} \tag{15}$$

The boundary conditions are set based upon the first author's observational experience with the previously cited experimental work [1]. In that work a Mach-Zehnder interferometer was used to inspect the flow field simultaneously while making power and temperature measurements. Although interferograms of high quality did not result from that work due to optical problems (in fact no significant images were recorded photographically) two characteristics were noted. Firstly, symmetry conditions as denoted in Fig. 1 generally existed. At low heating rates (the "diffusion" and "transition" modes to be discussed later) minor instabilities did occur from time-to-time rendering the cells nonsymmetrical, but this was a transient phenomena that would ultimately return to the symmetrical situation for varying durations. Second, it was observed that the heated strip could be approximated by an isothermal surface. At high heating rates with wide strips this approximation was less accurate, but an average strip temperature was used throughout the experimental work.

With the aforementioned aspects of the physical phenomena observed, the boundary conditions for the numerical analysis were set as denoted in Fig. 2. In the present study two cases were considered.

Nomenclature

E = vorticity gradient (see equation (16))
F = vorticity gradient (see equation (16))
g = acceleration of gravity
Gr = Grashof number based on L and hot strip temperature, $\text{Gr} = g\beta L^3(T_s - T_\infty)/\nu^2$
$\overline{\text{Gr}}$ = Grashof number based on L_T and average strip temperature, $\overline{\text{Gr}} = g\beta L_T{}^3(T_a - T_\infty)/\nu^2$
$L = L_T/2$
L_H = width of heated strips
L_T = total width of two adjacent strips
Nu_{ave} = Nusselt number based on L and the average temperature of strips
Nu = Nusselt number based on L_T and the average temperature of strips
P = pressure
Pr = Prandtl number
T = temperature
$U = \bar{x}$ component of velocity
$V = \bar{y}$ component of velocity
$\bar{x}$ = distance perpendicular to surface
$x = \bar{x}/L$
$X = 1 - \exp(x)$
$\bar{y}$ = distance across strips (along surface)
$y = \bar{y}/L$
α = thermal diffusivity
β = coefficient of thermal expansion
Δ = node spacing
ν = kinematic viscosity
ω = dimensionless vorticity (see equation (5))
ψ = dimensionless stream function (see equation (6))
ρ = density
θ = dimensionless temperature (see equation (7))

Subscripts

a = average quantity
s = hot strips
w = wall value
∞ = conditions far from the surface
Coordinates used as subscripts denote partial derivatives, and numbers used as subscripts refer to location around point of interest (see definition following equation (16)).

In the first, heated strips were incorporated between insulated strips. In the second case, lower temperature strips separated the higher temperature strips, both temperatures being specified. The main complication in incorporating the boundary conditions comes into the specification of the wall vorticity, and this is described in the following.

Preparatory for numerical solution, the equations and boundary conditions were cast in finite difference form. Consideration was given to several methods for accomplishing this task including both transient and steady-state approaches. The general steady-state approach used by Greenspan and Schultz [3] to analyze the earlier problem by Torrance and Rockett [4] appeared to offer both computing economy and accuracy for problems of the present type. In this approach, the governing equations are recast using a central differencing technique, except that the convective terms were treated with a forward-backward differencing technique to preserve diagonal dominance of the resulting linear simultaneous algebraic equation system. Equation (13) then becomes

$$(1-X)\left(\frac{\psi_1-\psi_3}{2\Delta}F-\frac{\psi_2-\psi_4}{2\Delta}E\right)+(1-X)^2\frac{\omega_2-2\omega_0+\omega_4}{\Delta^2}+(X-1)\frac{\omega_2-\omega_4}{2\Delta}+\frac{\omega_1-2\omega_0+.\omega_3}{\Delta^2}-\mathrm{Gr}\frac{\theta_1-\theta_3}{2\Delta}=0 \quad (16)$$

where the points at (X, y), $(X, y+\Delta)$, $(X+\Delta, y)$, $(X, y-\Delta)$ and $(X-\Delta, y)$ are denoted by the subscripts 0, 1–4, respectively, and

$$F=\frac{\omega_2-\omega_0}{\Delta} \qquad \text{if } \psi_1-\psi_3\geq 0$$

or

$$F=\frac{\omega_0-\omega_4}{\Delta} \qquad \text{if } \psi_1-\psi_3<0$$

and

$$E=\frac{\omega_0-\omega_3}{\Delta} \qquad \text{if } \psi_2-\psi_4\geq 0$$

or

$$E=\frac{\omega_1-\omega_0}{\Delta} \qquad \text{if } \psi_2-\psi_4<0$$

Similarly, equation (14) becomes

$$(1-X)\left(\frac{\psi_1-\psi_3}{2\Delta}F-\frac{\psi_2-\psi_4}{2\Delta}E\right)+\frac{1}{\mathrm{Pr}}\left[(1-X)^2\frac{\theta_2-2\theta_0+\theta_4}{\Delta^2}+(X-1)\frac{\theta_2-\theta_4}{2\Delta}+\frac{\theta_1-2\theta_0+\theta_3}{\Delta^2}\right]=0 \quad (17)$$

and equation (15) becomes

$$\omega_0=(1-X)^2\frac{\psi_2-2\psi_0+\psi_4}{\Delta^2}+(X-1)\frac{\psi_2-\psi_4}{2\Delta}+\frac{\psi_1-2\psi_0+\psi_3}{\Delta^2} \quad (18)$$

Note that the same definitions of E, F and numbered subscripts hold as were given following equation (16). It can be shown that diagonal dominance holds as the coefficient of the diagonal term is greater than or equal to the sum of coefficients of the off-diagonal terms.

Wall vorticity values were set using

$$\omega=\frac{2\psi_\Delta}{\Delta^2} \quad (19)$$

This relation is found by using equation (10) and a Taylor's series expansion of ψ around a point on the solid surface.

For a good approximation of the values of the stream function adjacent to the wall, the set of "inner boundary" points [3, 5] were used. Hence, the stream function values adjacent to the wall (i.e., at a distance Δ) were set from the corresponding values at a distance 2Δ from the wall via the relationship

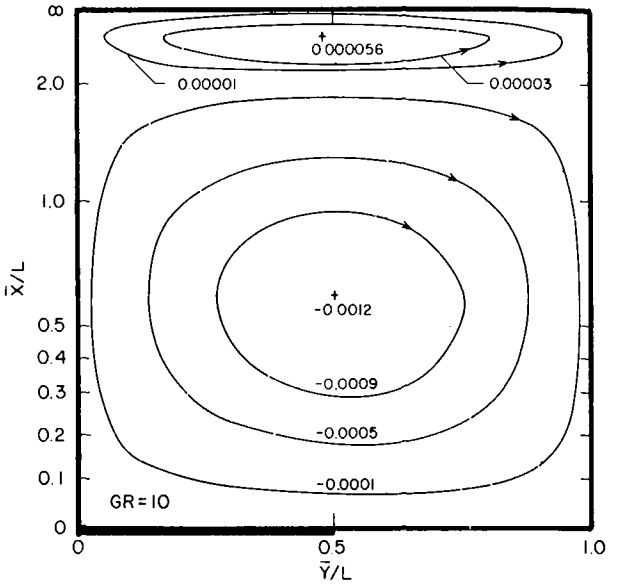

Fig. 3 Streamlines for 50 percent of surface at $\theta = 1$, 50 percent insulated at a Grashof number of 10

$$\psi_\Delta=\frac{\psi_{2\Delta}}{4} \quad (20)$$

A Gauss-Siedel point iteration method [6, 7] was used to solve the resulting simultaneous equations. This technique was chosen because it was extremely simple, required no over- or under-relaxation, and converged more quickly than the rapidly converging technique described by Greenspan and Schultz [3].

The solution was carried on the University of Utah Univac 1108 computer and associated plotter. Three grid sizes were used in selecting the optimum node spacing: 11×11, 21×21, and 41×41. The maximum variation in values for the first reduction was less than 5 percent. Comparing the results of the reduction from 21×21 to 41×41 indicated a maximum difference in values less than 1 percent. Since the computation costs increased greatly for this latter step, a 21×21 grid was used throughout.

The temperature gradient at the wall was used to estimate the heat transfer. This was chosen over the heat flux at the wall due to questions regarding the conservative qualities of the finite difference equations. As Roache [8] has correctly pointed out, "conservation properties may be lost, or at least altered in interpretation" when applying an infinite-to-finite mapping. A fifth degree polynomial was fit to the temperature values near the wall to determine the wall gradient. In retrospect this was unwarranted because the finite difference technique is at most second order accurate.

Results

In the course of the numerical study, plots of streamlines and isotherms were generated for a large variety of parameters found in the problem. Grashof numbers were considered from 10 to 10^7. Ratios of the heated strips to the total cell width were taken from 0.1 to 0.75. Also, two cases of the lower temperature surface of the cell were considered throughout: either a specified uniform temperature or insulated. For the sake of brevity, only some representative curves are presented here. In all cases, the Prandtl number is taken as 0.7.

Streamlines for two cases indicating extremes in Grashof numbers are shown in Figs. 3 and 4. Both figures are for the situation of temperature specified strips separated by insulated strips, all strips being the same width. The heavy line on part of abscissa denotes the heated portion of the surface. As the Grashof number increases, the flow pattern changes from several weak rolls (two are shown in Fig. 3, but there may be actually additional rolls that are not indicated because

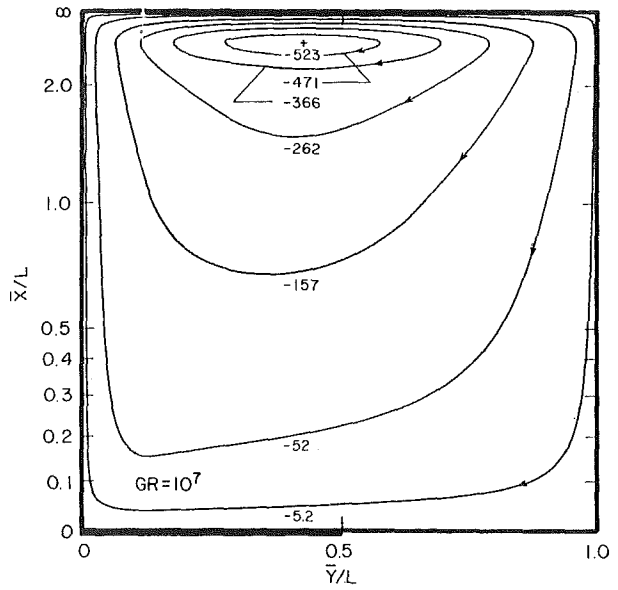

Fig. 4 Streamlines for 50 percent of surface at $\theta = 1$, 50 percent insulated at a Grashof number of 10^6

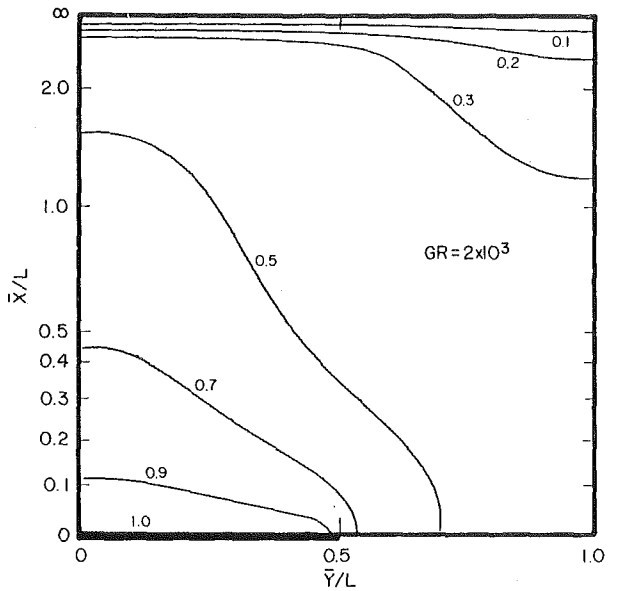

Fig. 6 Isotherms for 50 percent of surface at $\theta = 1$, 50 percent insulated at a Grashof number of 2×10^3—this is typical of the transition mode

of the $\bar{x}$ transformation that was used) to a single very strong one (see Fig. 4). At the high values of Gr there is a steep temperature gradient directly over the center of the heated strips (the left hand side of the figure). For a given Gr, the results for Case I (specified temperature strips separated by the insulated strips) always appeared qualitatively similar to the Case II results. Another item to note is that the maximum velocities varied directly with the ratio of the heated width to the total width at a given Grashof number.

Plots of the isotherms for the various situations indicated a wider variation in characteristics. θ is defined in equation (7). Samples of these results are shown in Figs. 5–8. Results for the Case II (both strips' temperatures specified) plots are not sufficiently different from the Case I plots to warrant space here.

Heat transfer results are shown in Figs. 9 and 10. Results from all cases studied are shown in Fig. 9. Note that the Nusselt number is based on the average strip temperature, but that the Grashof number is based on the hot strip temperature in the figure. The average temperature of the strips was calculated from the results of the numerical analysis. Results of the present study are compared to the earlier work [1] as well as isothermal data [9] in Fig. 10. In this figure both dimensionless parameters are based on L_T and the average strip temperature.

Discussion

One obvious item that appears from a study of the results is that the heat transfer exhibits three fairly distinct regimes. For all configurations studied here the situation is diffusion dominated below a Gr of approximately 10^3. This is demonstrated best by Fig. 5 which has approximately a conduction form. It can also be inferred from the

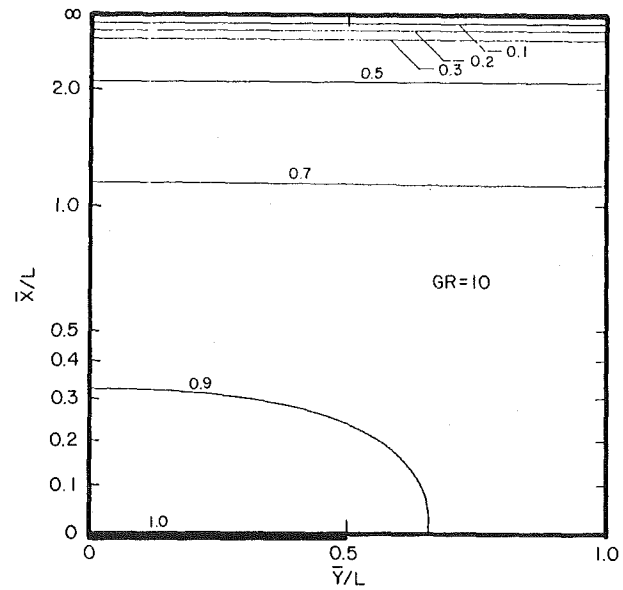

Fig. 5 Isotherms for 50 percent of surface at $\theta = 1$, 50 percent insulated at a Grashof number of 10—this is typical of the diffusion mode

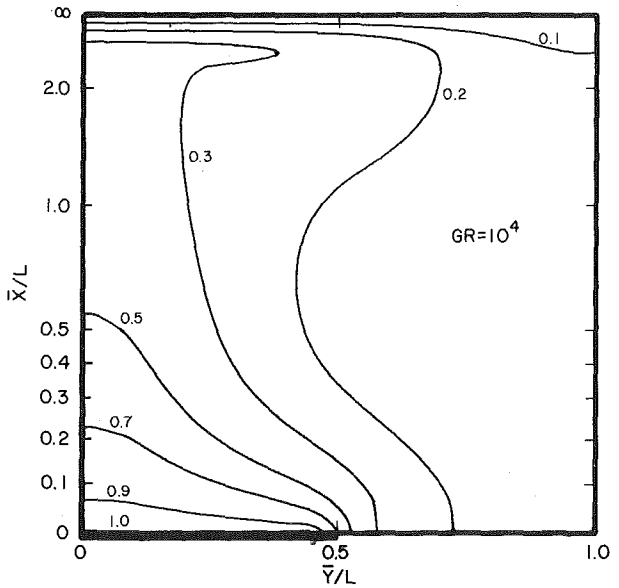

Fig. 7 Isotherms for 50 percent of the surface at $\theta = 1$, and 50 percent of the surface insulated at a Grashof number of 10^4

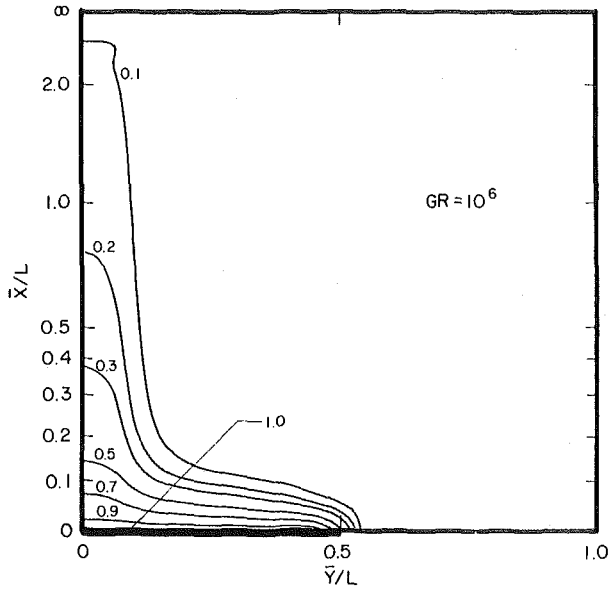

Fig. 8 Isotherms for 50 percent of the surface at $\theta = 1$, 50 percent insulated at Gr = 10^6—this indicates the plume mode

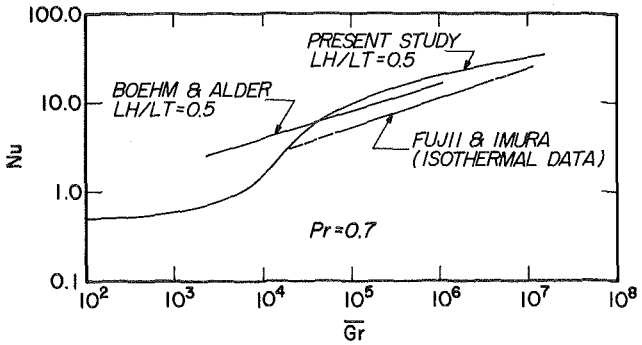

Fig. 10 Data from the present study compared to previous study data and isothermal data at Pr = 0.7—all strip data is for $L_H/L_T = 0.5$

flat portions of Figs. 9 and 10. At the larger values of Gr investigated here, the temperature field takes on a distinct plume form qualitatively very similar to the temperature field demonstrated experimentally (see related discussion in Method of Analysis section). This can be seen easily in Fig. 8. This regime appears to be clearly defined above a Grashof number of 10^4. The regime for $10^3 \lesssim Gr \lesssim 10^4$ is best termed transitional as the temperature field is seen to change from the distinctly diffusional nature to the distinctly plume nature.

Time and computer costs did not allow the investigation of the effects of all the parameters in the problem. Hence, only values judged to be of key importance were evaluated. For example, results for only a few Case II cases are given here, as they were very similar to the results from Case I.

The effect of percentage of the surface that is heated can be seen from Fig. 9 at Gr = 10^6. In general the heating appears to occur more efficiently for proportionately smaller heating strips.

Two methods of defining dimensionless variables were used in the present study. These differed in that one used a temperature difference based upon the hot strip temperature, while the other used a temperature difference based upon the average surface temperature. As noted earlier, the average temperature was determined from the results of the numerical analysis. The latter approach was used to

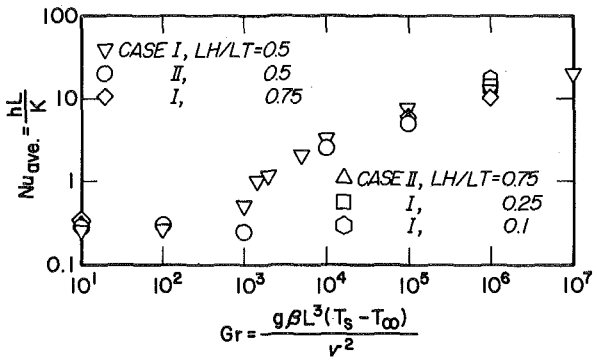

Fig. 9 Calculated data for all cases considered in the present study are shown (note that the Nusselt number is based upon the average strips temperature while the Grashof number is based on the hot strip temperature

enable comparisons to uniform surface temperature data to be made. No characteristic length appropriate for use in nondimensionalizing occurs for convection off of infinite plates with uniform heating. This makes absolute comparison very difficult. However, in the correlation of Fugii and Imura [9] for convection off of large, but finite, plates the correlation is independent of length. This allows easy comparison, and this is shown in Fig. 10. While it is difficult to compare the Gr limits as set for the Fugii and Imura correlation due to the significant length aspect, it appears that stripwise convection in the plume regime is clearly superior to the uniform heating situation. This observation holds for Gr $\lesssim$ 20,000. Also shown are the results of an experimental study of stripwise heating [1]. The differences between the experiment and computer model, particularly at low $\overline{Gr}$, is felt to be due to uncertainties in the experiment.

The numerical technique used for the solution of the governing equations worked quite well. No problems in convergence were experienced, and relatively short computation times were demonstrated. For Gr = 10^6, $L_H/L_T = 0.5$, Case I, convergence was achieved in 32 seconds on a Univac 1108. Computation time increased with decreasing Gr.

It was unfortunate, however, that an easy comparison to some other numerical solution could not be made with the present program to provide an accuracy check. There does not appear to be any solution available in the literature that can be compared to the results of our program. The fact that Greenspan and Schultz [3], using an approach very similar to ours in many ways, were able to show nearly perfect agreement with the excellent work of Torrance and Rockett [4] adds credibility to the approach. It should also be noted that the fact that the previous works involved a closed container poses a more stringent comparison.

Use of the transformation in the x-direction was very satisfactory. While it necessarily masked the phenomena far from the surface, it was felt that having the actual boundary conditions imposed on every side was desirable.

Clearly, one shortcoming of established steady-flow analysis is that the boundary conditions force the flow to be cellular. This was inferred from observations made earlier on a Mach-Zehnder interferometer [1] and is probably quite accurate at the high values of Gr, below the onset of turbulence. However, the situation was not so clear in the lower Gr range. More work of both experimental and analytical natures must be performed in the diffusional regime to define the phenomena better. The analytical work should take a different approach from that used here and should involve a stability analysis to investigate the flow threshold in the low Gr region. The definition of the initiation of turbulence would also be of value.

It appears that stripwise heating is more effective than uniform heating in natural convection in the laminar region on a horizontal surface. This may not be true both at the very low and very high values of Gr. Definitive information on these limiting conditions will only come from a different approach than that used here.

Conclusions

The results obtained from a finite difference investigation of stripwise heating on a horizontal surface with different ratios of widths of heating to unheated strips, led to the following conclusions:

1 For the present problem, the main mechanism of heat transfer is conduction for Grashof numbers less than 10^3 and convection for Grashof numbers higher than 10^4. Plots of the temperature field indicate a sharp transition occurs between the two modes of heat transfer.

2 The exponential transformation used in this study transformed the original semi-infinite direction into a finite one. The finite scale was approximately linear at the region near the plate and presented a clear view of the flow and temperature fields in this area of interest.

3 The Nusselt numbers of the stripwise heating increase sharply for decreasing values of the ratio of widths of heated to unheated strips at high Grashof numbers (predominant convective heat transfer).

4 The results of this study were compared to earlier experimental and numerical results and good agreement was observed. The major area of disagreement appeared to be in the low Grashof number range. It was concluded that additional experimental and theoretical studies should be performed for the predominately conduction ($Gr < 10^3$) regime to rationalize the differences.

5 Stripwise heating on a horizontal surface appears to transfer heat more efficiently than does uniform heating, over the bulk of the laminar range.

Acknowledgments

Many details of this work appear in the MSME Thesis by the second author, entitled "Numerical Study of Stripwise Heating on a Horizontal Surface", University of Utah, June 1975.

The authors appreciate the very helpful suggestions made by Professor H. R. Jacobs in the performance of this work. Support by the National Science Foundation through Grant GK 40797 is also appreciated.

References

1 Boehm, R. F., and Alder, R. S., "Natural Convection Arising From Stripwise Heating on a Horizontal Surface," *International Journal of Heat and Mass Transfer*, Vol. 16, 1973, pp. 853–855.

2 Sills, J. A., "Transformation for Infinite Regions and Their Application to Flow Problems," *American Institute of Aeronautics and Astronautics Journal*, Vol. 7, No. 1, Jan. 1969, pp. 117–123.

3 Greenspan, D., and Schultz, D., "Natural Convection in an Enclosure With Localized Heating From Below," *Computer Methods in Applied Mechanics and Engineering*, Vol. 3, 1974, pp. 1–10.

4 Torrance, K. E., and Rockett, J. A., "Numerical Study of Natural Convection in an Enclosure With Localized Heating From Below—Creeping Flow to the Onset of Laminar Instability," *Journal of Fluid Mechanics*, Vol. 36, Part 1, 1969, pp. 33–54.

5 Greenspan, D., *Discrete Numerical Methods in Physics and Engineering*, Academic Press, New York, 1974, p. 220.

6 Gossman, A. D., Pun, W. M., Runchal, A. K., Spalding, D. B., and Wolfshtein, M., *Heat and Mass Transfer in Recirculating Flows*, Academic Press, New York, 1969.

7 Suriano, F. J., and Yang, K. T., "Laminar Free Convection About Vertical and Horizontal Plates at Small and Moderate Grashof Numbers," *International Journal of Heat and Mass Transfer*, Vol. 11, 1968, pp. 473–490.

8 Roache, P. J., *Computational Fluid Dynamics*, Hermosa Publishers, Albuquerque, NM, 1972, p. 298–300.

9 Fujii, T., and Imura, H., "Natural Convection Heat Transfer From a Plate With Arbitrary Inclination," *International Journal of Heat and Mass Transfer*, Vol. 15, 1972, pp. 755–767.

S. W. Churchill
M. Bernstein[1]

Department of Chemical and Biochemical Engineering,
University of Pennsylvania,
Philadelphia, Pa.

A Correlating Equation for Forced Convection From Gases and Liquids to a Circular Cylinder in Crossflow

A single comprehensive equation is developed for the rate of heat and mass transfer from a circular cylinder in crossflow, covering a complete range of Pr (or Sc) and the entire range of Re for which data are available. This expression is a lower bound (except possibly for RePr < 0.2); free-stream turbulence, end effects, channel blockage, free convection, etc., may increase the rate. In the complete absence of free convection, the theoretical expression of Nakai and Okazaki may be more accurate for RePr < 0.2. The correlating equation is based on theoretical results for the effect of Pr in the laminar boundary layer, and on both theoretical and experimental results for the effect of Re. The process of correlation reveals the need for theoretical results for the effect of Pr in the region of the wake. Additional experimental data for the effect of Pr at small Pe and for the effect of Re during the transition in the point of separation are also needed.

Introduction

Convective heat transfer from a cylinder in crossflow has been the subject of repeated attempts at correlation and generalization because of its importance in a variety of applications. These attempts have not been completely successful because of: (1) the lack of a comprehensive theory for the dependence on Pr even for the boundary layer regime; (2) competitive theories for low Re; (3) the influence of natural convection at very low Re; (4) discrete transitions in the boundary layer and the wake at high Re; (5) the influence and lack of specification of free-stream turbulence; (6) the use of different and undefined thermal boundary conditions; (7) significant variation in physical properties between the surface and free stream and around the surface; (8) the incorporation of erroneous physical properties in older tabulated data; (9) end effects, particularly at low Re; (10) tunnel blockage; (11) significant scatter in most of the many sets of data; and (12) unresolved discrepancies between the various sets of data.

Douglas and Churchill [1][2] discovered that most of the experimental data for gases at large temperature differences had been misinterpreted and misplotted in McAdams [2]. They reconstructed a general graphical correlation for gases using the original measured quantities and modern physical properties. Fand and Keswani [3] recently repeated the conversion of Hilpert's [4] extensive data for air to modern physical properties.

Douglas and Churchill also proposed a semitheoretical equation for all Re and attributed the systematic deviation at low Re to free convection. (This behavior has since been shown to be due to thickening of the boundary layer, as well as to free convection.) Perkins and Leppert [5] developed graphical correlations and empirical equations for liquids based on the models of Richardson [6] and of Douglas and Churchill. Tsubouchi and Masuda [7] carried out a thorough examination of the data for both liquids and gases. They proposed a new equation for liquids and a slight modification of the equation of Perkins and Leppert for both gases and liquids. Whitaker [8] proposed a modified version of his own correlation for spheres rather than deriving a new set of coefficients and exponents for cylinders. Fand and Keswani [9] recently presented an empirical correlation for air only, based on the data of Hilpert [4], Collis and Williams [10], and King [11] only. Gnielinski [12] proposed correlation of the data for plates, cylinders, and spheres at moderate Re by taking the square root of the square of the correlations for the laminar and turbulent regimes; however, he did not have access to the very recent data which greatly extend the upward range of Re for cylinders.

The objective of this paper is to resolve, insofar as possible, the discrepancies and complications enumerated in the first paragraph, and to construct a simpler, more accurate, and more general correlation than those mentioned in the second and third paragraph of this

[1] Currently with Exxon, D104, Box 153, Florham Park, N. J.

[2] Numbers in brackets designate References at end of paper.

Contributed by the Heat Transfer Division for publication in the JOURNAL OF HEAT TRANSFER. Manuscript received by the Heat Transfer Division September 2, 1976.

Table 1 Power-dependence provided by equation (2)

Pr	0	10^{-2}	10^{-1}	0.7	1.0	10	10^{2}	10^{3}	∞
Power	0.500	0.486	0.452	0.401	0.391	0.351	0.337	0.334	0.3333

section. This is not a review. In view of the comprehensive reviews mentioned in the foregoing and the other recent ones by Zhukauskas [13] and Morgan [14], reference will be made only to those investigations directly relevant to the development of the correlations.

The recent data of Achenbach [15] and Zdanavichyus, et al. [16] have helped greatly to resolve the previously controversial behavior at high Re, and the recent papers by Morgan [14] and Katinas, et al. [17] have helped to categorize the various investigations in terms of blockage and free-stream turbulence.

The development herein of an overall correlating equation starts with consideration of the laminar boundary layer regime. The creeping-flow regime and the regime dominated by the wake are next examined. These regimes do not overlap with the laminar boundary layer regime, and interpolation is necessary. Finally, secondary effects are considered, the various sets of data are interpreted briefly in terms of the correlation, and conclusions are drawn.

Development of Correlating Equations

Laminar Boundary Layer Regime. The theoretical solutions for the laminar boundary layer regime proved to be invaluable in constructing correlating equations for forced convection to a flat plate [18] and for free convection to a cylinder [19]. Unfortunately comparable solutions are incomplete for forced convection to a cylinder.

Squire [20], Eckert [21], and Levy [22] all computed theoretical values of the Nusselt number at the forward stagnation point as a function of the Prandtl number. The values of Squire and Eckert are in reasonable agreement but those of Levy are somewhat lower. The values of Squire and of Eckert were, therefore, utilized to derive an empirical expression in the form of the general correlating equation of Churchill and Usagi [23]. This model equates the nth power of the dependent variable (here Nu) to the sum of the nth powers of the limiting solutions for large and small values of the independent variable (here Pr). The empirical exponent n is then evaluated from experimental data or theoretical points for intermediate values of the independent variable. In this application the best value of n appears to be -4.0 resulting in the expression

$$\mathrm{Nu}_s = 1.276\,\mathrm{Re}^{1/2}\mathrm{Pr}^{1/3}/[1 + (0.412/\mathrm{Pr})^{2/3}]^{1/4} \qquad (1)$$

It may be noted that the exponent of ¼ (corresponding to $n = -4$) on the term in brackets is identical to that derived by Churchill and Ozoe [24, 25] for forced convection to both uniformly heated and isothermal plates in the laminar boundary layer regime. However, the "central values" of Pr for the flat plate (the values of Pr for which the limiting solutions intersect) were much lower than 0.412. For free convection the central values as well as the exponent were found by Churchill and Churchill [26] to be essentially the same for all geometries. The difference in the central values of Pr for forced convection undoubtedly arises from the basic difference in the forced-flow pattern over the cylinder and along the flat plate. The value of 0.412 is, in any event, quite uncertain since it is the ratio of the coefficients of the limiting solutions for Pr → 0 and ∞, raised to the sixth power.

Pending the derivation of sufficient, precise values for the effect of Pr on the mean rate of heat transfer over the entire cylinder, the same dependence as in equation (1) will be postulated, yielding

$$\overline{\mathrm{Nu}} = A\,\mathrm{Re}^{1/2}\mathrm{Pr}^{1/3}/[1 + (0.4/\mathrm{Pr})^{2/3}]^{1/4} \qquad (2)$$

The approximate, theoretical calculations of Masliyah and Epstein [27] for Re = 1 and Pr from 0.7 to 40,000 indicate a value of 0.62 and the two, extrapolated, theoretical values of Jain and Goel [28] a value of 0.64 for A. An arithmetic plot (not shown) of $\overline{\mathrm{Nu}}$ versus $\phi = \mathrm{Re}^{1/2}\mathrm{Pr}^{1/3}/[1 + (0.4/\mathrm{Pr})^{2/3}]^{1/4}$ for experimental and theoretical values covering a wide range of Re and Pr indicates that equation (2) with $A = 0.62$ provides an excellent representation for $40 < \mathrm{Re} < 10{,}000$ corresponding to $5 < \phi < 80$ for Pr = 0.7. This agreement is illustrated in logarithmic form in Figs. 1 and 2. Equation (2) does not hold for Re < 5 owing to thickening of the boundary layer as discussed in the next section and does not hold for Re > 10,000 owing to the development of a significant contribution from the region of separation at the rear of the cylinder, as discussed later.

The equivalent power dependence on Pr in equation (2), defined as $d(\ln\{\overline{\mathrm{Nu}}\})/d(\ln\{\mathrm{Pr}\})$, varies from ½ to ⅓ as indicated in Table 1, thus providing a rationalization for the different powers derived in prior correlations of experimental data for different ranges of Pr.

Creeping-Flow Regime (Pe < 0.2). A number of theoretical expressions have been derived for Pe → 0, based on potential flow. The most successful appears to be that of Nakai and Okazaki [29] which can be written as

$$\overline{\mathrm{Nu}} = 1/(0.8237 - \ln\{\mathrm{Pe}^{1/2}\}), \qquad \mathrm{Pe} \le 0.2 \qquad (3)$$

Equation (3) agrees well with the computed values of Dennis, et al. [30] and with the experimental data for various fluids, as indicated by the dashed lines in Fig. 1 for Pr = 0.001, 0.7, and 1000, and discussed subsequently. The values of $\overline{\mathrm{Nu}}$ computed from equation (2) approach 0 as Pe → 0, as would be expected for pure conduction from an infinitely long cylinder to surroundings of infinite extent. The finite values observed experimentally for Re → 0 are presumably due to free convection, end effects and finite surroundings.

Nomenclature

A = dimensionless coefficient
D = cylinder diameter
D_T = tunnel diameter
$\mathcal{D}$ = diffusivity
g = gravitational acceleration
h = heat transfer coefficient
k = thermal conductivity
k_c = mass transfer coefficient
L = cylinder length
n = arbitrary exponent in Churchill-Usagi equation
Nu = Nusselt number = hD/k
$\overline{\mathrm{Nu}}$ = mean Nusselt number
$\overline{\mathrm{Nu}}_0$ = mean Nusselt number for Re → 0
Nu_r = Nusselt number in region of wake
Nu_s = Nusselt number at forward stagnation point
$\overline{\mathrm{Nu}}_\infty$ = mean Nusselt number for Re → ∞
Pe = Peclet number = RePr = DU_b/α
Pr = Prandtl number = ν/α
Ra = Rayleigh number = $g\beta\Delta TD^3/\nu\alpha$
Re = Reynolds number = DU_b/ν
Sc = Schmidt number = $\nu/\mathcal{D}$
Sh = Sherwood number = $k_cD/\mathcal{D}$
T = temperature
Tu = intensity of free-stream turbulence = $\sqrt{(U_b')^2}/U_b$
U_b = free-stream velocity
U_b' = fluctuation in free-stream velocity
α = thermal diffusivity
β = volumetric coefficient of expansion with temperature
$\Delta T = T_b - T_w$
μ = viscosity
ν = kinematic viscosity
$\phi = \mathrm{Re}^{1/2}\mathrm{Pr}^{1/3}/[1 + (0.4/\mathrm{Pr})^{2/3}]^{1/4}$

Subscripts

b = free stream
f = film, at $(T_w + T_b)/2$
w = wall

Table 2 Power-dependence provided by equation (8) for Pr = 0.7

Re	0	10^{-2}	10^{-1}	1	10	10^{2}	10^{3}	10^{4}	10^{5}	10^{6}	10^{7}	∞
Power	0	0.069	0.169	0.308	0.419	0.471	0.505	0.552	0.671	0.843	0.951	1.000

Intermediate Regime (Pe > 0.2, Re < 10,000). A considerable gap exists between the range of applicability of equations (2) and (3). This behavior can be approximated, as suggested by Tsubouchi and Masuda [7] and others, by adding a constant term, $\overline{Nu}_0$, to the right-hand side of equation (2). A value of 0.3 resulting in

$$\overline{Nu} = 0.3 + 0.62Re^{1/2}Pr^{1/3}/[1 + (0.4/Pr)^{2/3}]^{1/4} \quad (4)$$

represents the experimental data and computed values very well for Pe > 0.2 and Re < 10,000 as indicated in Figs. 1 and 2. A slightly lower value of $\overline{Nu}_0$ would give a better prediction for Pe < 0.2 but at the expense of a poorer prediction for Pe > 0.2.

The theoretical solution of King [11] for potential flow actually yielded a value of $1/\pi = 0.318$ for Nu_0 but his choice of boundary conditions has been called improper by Hill and Sleicher [31].

Collis and Williams [10] assert that an expression of the form of equation (4) is unsatisfactory because it cannot reproduce the discrete change in slope which they observe with the onset of eddy-shedding (Re = 44 for Pr = 0.7). However, such a discrete transition in $\overline{Nu}$ at Re = 44 (ϕ = 5.16 for Pr = 0.7) is not apparent in Fig. 1 and can be considered negligible for practical purposes. A possible explanation is the derivation by Virk [32] of

$$Nu_r = 2\sqrt{Pe/5\pi} \quad (5)$$

for the rear half of the cylinder in the eddy-shedding regime of 40 < Re < 2 × 10^5. The dependence on Re is thus the same as for the boundary layer, although the indicated dependence on Pr differs.

Completely Turbulent Regime. The behavior for Re > 10,000 has been uncertain for some time owing to discrepancies between the various sets of experimental data. Clark [33] predicted a linear dependence of Nu on Re in the region of the wake. Both van der Hegge Zijnen [34] and Douglas and Churchill [1] utilized such a linear dependence in their correlating equations. Richardson [6, 35] asserted that the rate of heat transfer in this region should be proportional to $Re^{2/3}$. This dependence and also $Re^{0.8}$ have been utilized in a number of correlating equations. The precise data of Hilpert [4] which extend to Re = 233,000, indicate a linear dependence but have been subject to some controversy since they generally fall below the data of other investigators. The recent precise data of Zdanavichyus, et al. [16] and of Achenbach [15] for air which extend to Re = 1.1 × 10^6 and Re = 4.2 × 10^6, respectively, now provide a sounder basis for interpretation of the behavior at high Re. (Despite their relative precision, the data of Achenbach for uniform wall temperature and $T_u \cong 0.0045$ fall above those of Zdanavichyus, et al., for uniform heat flux and $T_u \cong 0.027$, even though the opposite effect would be expected.) The evaluation of the role of blockage and free-stream turbulence by Morgan [14] and others explains most of the discrepancies between the other sets of data, at least qualitatively.

The data of both Zdanavichyus, et al., and Achenbach indicate that $\overline{Nu}$ does not increase uniformly with Re but shows an upswing at about Re = 10^5, a flattening out at about Re = 4 × 10^5 and a resumed upswing approaching linearity with Re above Re = 2 × 10^6. These transitions are associated with the downstream relocation of the point of separation and the transition from a laminar to a turbulent boundary layer. Reference to these papers is suggested for detailed discussions of the behavior of the flow field. The changes in $\overline{Nu}$ are surprisingly mild, considering the abrupt and significant changes in the flow pattern.

The following asymptotic expression for very large Re can be derived from the data of Achenbach

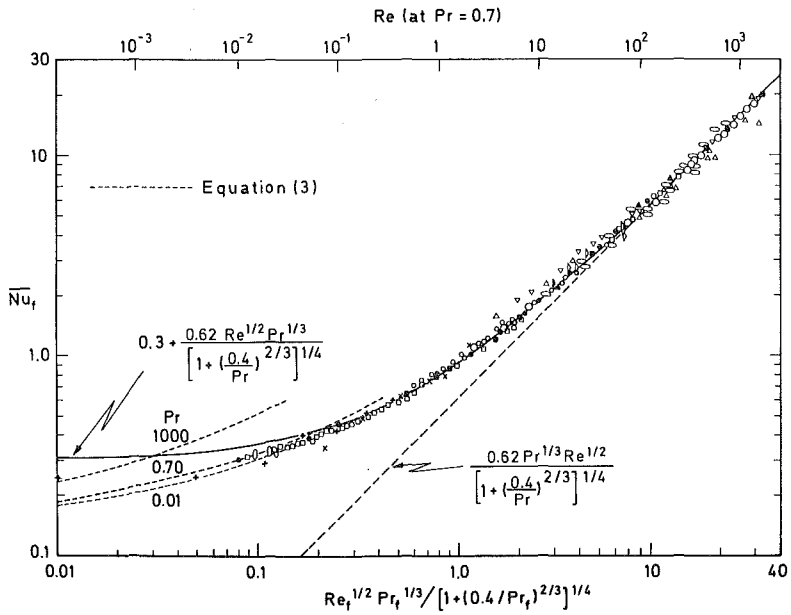

Fig. 1 Low Reynolds number regime—Legend: ● Dennis, et al. [30] (computed); ■ Masliyah and Epstein [27] (computed); ▲ Jain and Goel [28] (computed); ○ Hilpert [4] (air); ○ Tsubouchi and Masuda [7] (air); □ Collis and Williams [10] (air); ○ Gebhart and Pera [36] (air); ▽ Krall and Eckert [37] (air (uniform heat flux)); ⊂ Tsubouchi and Masuda [7], Davis [42] (water, oils (Pr = 4-600)); x Sajben [31] (mercury (Pr = 0.0225)); + Beckers, et al. [43] (paraffin oil (Pr = 1000)); ▷ Ishiguro, et al. [40] (sodium (Pr = 0.0058 and 0.0073); △ Dobry and Finn [46] (mass transfer (Sc = 1100 and 1400))

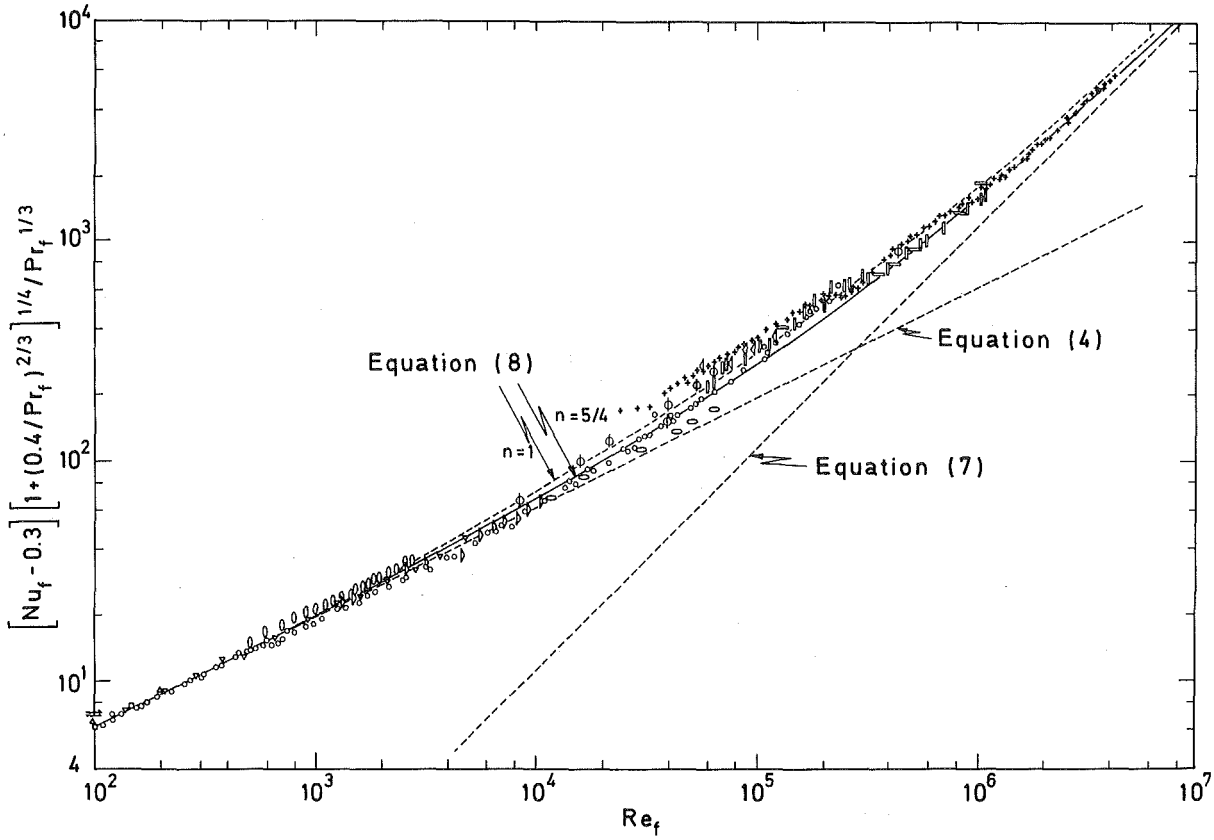

Fig. 2 High Reynolds number regime—Legend: ○ Hilpert [4] (air); □ Collis and Williams [10] (air); + Achenbach [15] (air); ▯ Zdanavichyus, et al. [16] (air); ▽ Krall and Eckert [37] (air (uniform heat flux)); ϕ Schmidt and Wenner [38] (air); ◁ Lewis [39] (air); ▷ Ishiguro, et al. [40] (sodium (Pr = 0.0058 and 0.0073)); ▭ Zdanavichyus, et al. [16] (water); ⬯ Fand and Keswani [44] (water (smoothed values)); ⬭ Fand [45] (water)

$$\overline{Nu}_\infty = 0.00091\ Re \tag{6}$$

Postulating the same dependence on Pr as in the laminar-boundary-layer regime converts equation (6) to

$$\overline{Nu}_\infty = 0.001168\ RePr^{1/3}/[1 + (0.4/Pr)^{2/3}]^{1/4} \tag{7}$$

It should be emphasized that equations (6) and (7) are the apparent asymptotes for the Achenbach data, not correlations for them.

Overall Correlation, $\phi > 0.4$. Combining equations (4) and (7) in the form suggested by Churchill and Usagi [23], as discussed in the foregoing, results in the test expression

$$(\overline{Nu} - 0.3)^n = \left(\frac{0.62Re^{1/2}Pr^{1/3}}{[1 + (0.4/Pr)^{2/3}]^{1/4}}\right)^n + \left(\frac{0.001168RePr^{1/3}}{[1 + (0.4/Pr)^{2/3}]^{1/4}}\right)^n \tag{8}$$

A value of 5/4 for the exponent, hence

$$\overline{Nu} = 0.3 + \frac{0.62Re^{1/2}Pr^{1/3}}{[1 + (0.4/Pr)^{2/3}]^{1/4}}\left[1 + \left(\frac{Re}{282000}\right)^{5/8}\right]^{4/5} \tag{9}$$

appears to provide a lower bound for $RePr > 0.4$ and a reasonable approximation for all Re and Pr, with a few exceptions to be discussed in the next section.

Equation (9) differs from prior correlating equations for forced convection to cylinders in that it provides a varying power for Re and Pr. The power of Pr was previously considered. The effective power of Re in equation (9), defined as $[\partial(\ln\{\overline{Nu}\})/\partial(\ln\{Re\})]_{Pr}$ depends on Pr. The values in Table 2, which were computed for Pr = 0.7, range from 0 to 1.0, and are in general agreement with the values determined by the correlations for narrow ranges of Re by McAdams [2], Morgan [14], and others. The values in Table 1 for the effective power of Pr hold for equations (4) and (9) as well as (2) as long as $\overline{Nu} \gg Nu_0$.

Comparison of Correlating Equations With Experimental Data

The effectiveness and limitations of the correlating equations (3), (4), and (9) are indicated in Figs. 1 and 2 by comparison with a broad range of experimental data. The properties and velocity were converted to the form of Figs. 1 and 2 insofar as possible. The sets of data which are included are those which do not scatter excessively, and which Morgan [14] and others have classified as relatively free from the effects of temperature-difference, free-stream turbulence, aspect ratio and tunnel-blockage. The many sets of early data (see, for example, Douglas and Churchill [1], Gnielinski [12], or Morgan [14] for listings) which are not included, generally fall significantly above equation (9) due to one or more of the foregoing effects. Corrections for these secondary effects are considered in the following section.

The various sets of data for air [4, 7, 10, 15, 16, 36–39] are seen to be in good agreement with equation (9) for $Pe > 0.2$, corresponding to $Re = 0.285$ and $\phi = 0.416$, with the following exceptions. The data of Krall and Eckert [37] fall somewhat above equation (9) for their lower range of Re, presumably due to uniform heating. In the range $40000 < Re < 400000$ all of the data [4, 15, 16, 38, 39] fall decisively above equation (9). This thermal behavior is associated with the downstream transition in the point of separation of the wake. A somewhat better representation for the data in this range of Re is obtained by taking $n = 1$ instead of 5/4 in equation (8) leading to

$$\overline{\mathrm{Nu}} = 0.3 + \frac{0.62\mathrm{Re}^{1/2}\mathrm{Pr}^{1/3}}{[1 + (0.4/\mathrm{Pr})^{2/3}]^{1/4}}\left[1 + \left(\frac{\mathrm{Re}}{282000}\right)^{1/2}\right] \quad (10)$$

Even so, some of the data of Achenbach [15] and of Lewis [39] fall above equation (10). In the range $1000 < \mathrm{Re} < 10{,}000$ the precise data of Hilpert [4] fall below equation (9). This latter discrepancy, which has been noted by many previous investigators, may be due to some experimental anomaly, as suggested by Morgan [14].

Reliable data to test the dependence on Pr are somewhat limited. The only reliable data for low Pr appear to be those of Sajben [34] for mercury (Pr = 0.0225) and those of Ishiguro, et al. [40] for sodium (Pr = 0.0058 and 0.0073). Representative values of Sajben read from a graph, are included in Fig. 1. They are in general agreement with equation (4) for Pe > 0.2, corresponding to $\phi = 0.50$, but fall below both equations (4) and (3) for lower values. The measurements of Ishiguro, et al., are for a nearly uniform heat flux density. The values of $\overline{\mathrm{Nu}}$ based on an integrated-mean temperature difference appear to follow equation (4) even to Re = 10000, and hence fall below equation (9) for $\mathrm{Re} > 10^3$. Based on an integrated-mean heat transfer coefficient they fall above equation (9). In any event they appear to invalidate, for this range of Re, the postulate of potential flow, upon which the theoretical solution of Grosh and Cess [41] is based.

The data of Tsubouchi and Masuda [7] and Davis [42] for various fluids with $5 < \mathrm{Pr} < 600$ scatter randomly about equation (9). The data of Beckers, et al. [43] for paraffin oil (Pr = 1000) agree with equation (4) down to Pe = 0.2($\phi = 0.14$) but fall far below the prediction of equation (3) for lower Pe. Their data for other fluids scatter widely and were omitted. The data of van der Hegge Zijnen [34] are given graphically in combined forms which preclude their inclusion in Figs. 1 and 2. The data of Gebhart and Pera [36] for oils and small wires were recognized by the investigators as anomalously high, apparently due to end effects. The data of Zdanavichyus, et al. [16] for water follow equation (9) closely and those of Fand and Keswani [44] are only slightly higher. The earlier data of Fand [45] for water fall decisively below the correlation, and almost follow the extension of equation (4), suggesting a possible delay in transition of the point of separation in these experiments.

Although the correlation is presumed to hold for mass transfer with $\overline{\mathrm{Nu}}$ replaced by $\overline{\mathrm{Sh}}$ and Pr by Sc, no data meeting the foregoing criteria were found. However, the data of Dobry and Finn [46] for Sc = 1100 and 1400, although somewhat scattered, are seen to be in general agreement with equation (9).

Secondary Effects

Physical Property Variation With Temperature. The effect of large ΔT is not well resolved and is opposite in direction for liquids and gases and for heating and cooling. Douglas and Churchill [1] were reasonably successful in handling the effect of property variation for gases and Tsubouchi and Masuda [7] for liquids simply by calculating the properties (including ρ) at the film temperature (the arithmetic average of the surface and free-stream temperatures). Collis and Williams [10] assert that for gases $\overline{\mathrm{Nu}}$ should additionally be multiplied by $(T_b/T_f)^{0.17}$. Perkins and Leppert [5] and Whitaker [8] propose the use of free-stream properties and the multiplication of $\overline{\mathrm{Nu}}$ by $(\mu_w/\mu_b)^{0.25}$ but Tsubouchi and Masuda contend an exponent of 0.14 is better than 0.25. Zhukauskas [13] proposes the use of the free-stream temperature and the multiplication of $\overline{\mathrm{Nu}}$ by $(\mathrm{Pr}_b/\mathrm{Pr}_w)^{\alpha}$ with $\alpha = 0.25$ for the turbulent regime and 0.17–0.19 for the laminar regime, but notes that $\mathrm{Pr}_b/\mathrm{Pr}_w \cong \mu_b/\mu_w$. Fand and Keswani [44] propose correlating $\mathrm{Nu}_w{}^a\mathrm{Nu}_b{}^{1-a}$ with $\mathrm{Re}_w{}^b\mathrm{Re}_b{}^{1-b}$ and $\mathrm{Pr}_w{}^c\mathrm{Pr}_b{}^{1-c}$ but do not achieve a significantly better fit than with properties at the film temperature. After reviewing the various correlations, Morgan concludes that the dependence on physical properties is still undefined and declares the need for additional experimental work. Wylie [47] and Vaitekunas, et al. [48] have recently derived theoretical solutions for laminar and turbulent boundary layers, respectively, with varying physical properties and this approach may ultimately resolve the dilemma.

In any event, equation (9) can be expected to give reasonable results for moderate temperature differences for both liquids and gases if the properties are evaluated at the film temperature. It can readily be modified in accordance with any of the foregoing schemes for large temperature differences.

Boundary Conditions. Most experiments and calculations have been carried out for essentially a uniform surface temperature. However, Boulos and Pei [49] utilized a uniform heat flux density and concluded that this boundary condition resulted in a 10–20 percent increase in $\overline{\mathrm{Nu}}$ as compared to an isothermal surface. Some of their measured values of $\overline{\mathrm{Nu}}_s$ are below the boundary layer values, casting doubt on the validity of this conclusion. Krall and Eckert [37] concluded that their measurements were 7 percent high for the same reason. These observations are consistent with theoretical calculations for the laminar boundary layer regime on a flat plate which indicate a 37 percent increase in the local values of Nu but a 37 percent increase, 3 percent increase or 3 percent decrease depending on whether $\overline{\mathrm{Nu}}$ is based on the integrated-mean heat transfer coefficient, the integrated-mean temperature-difference or the temperature difference at the midpoint [18]. These results provide the basis for a first-order estimation of a correction factor to equation (9) for a uniform heat flux or other nonisothermal boundary condition

Blockage. Morgan [14] compared a number of the expressions that have been proposed for the effect of the boundaries of the channel in which the test cylinder is located, with the limited experimental data for this effect. He concluded that the velocity in Re should be increased by the factor $1 + 0.385\ D/D_T + 1.356\ (D/D_T)^2$ developed by Vincenti and Graham [50] for small streamlined bodies in closed circular tunnels. For a jet stream from a tunnel, Morgan suggests reducing the velocity in Re by the factor $1 - 0.411\ (D/D_T)^2$ which was developed by Lock [51].

Free-Stream Turbulence. Dyban and Epik [52] proposed the expression 0.8 ReTu/(1500 + ReTu) to represent experimental data for the fractional increase in $\overline{\mathrm{Nu}}$ over the range $2000 < \mathrm{Re} < 80{,}000$ and $0.02 < \mathrm{Tu} < 0.26$. Morgan [14] reviewed the somewhat contradictory data and correlations and developed a graphical correlation for the combined effects of free-stream turbulence and tunnel blockage.

Aspect Ratio. $\overline{\mathrm{Nu}}$ depends on the length of the cylinder owing to three-dimensional disturbances in the velocity field at the ends, and perhaps to longitudinal heat losses. These effects appear to be significant only for very fine wires such as those used in anemometry. Öhman [53] has shown that $\overline{\mathrm{Nu}}_0$ should have a minimum theoretical value of $2/\ln\{2L/D\}$ for a finite cylinder. Gebhart and Pera [36] observed significant effects for large Pr, even for $L/D = 16000$. Morgan [14] proposes multiplication of $\overline{\mathrm{Nu}}$ for hot-wire anemometers by the factor $1 + 7.5(D/L)^{1/2} + 3.5 \times 10^4(D/L)^2$.

Free Convection. Since forced convection implies a temperature difference, free convection must always be present to some degree. From the general correlation of Churchill [54] for assisting, laminar convection it follows that the fractional increase or decrease in $\overline{\mathrm{Nu}}$-$\overline{\mathrm{Nu}}_0$ due to a small degree of assisting or opposing free convection is approximately $0.2\ \mathrm{Ra}^{3/4}\ [1 + (0.4/\mathrm{Pr})^{2/3}]^{3/4}/\mathrm{Re}^{3/2}\mathrm{Pr}[1 + (0.5/\mathrm{Pr})^{9/16}]^{4/3}$. For very small Re and Ra Nakai and Okazaki [29] show that the absolute increase or decrease in 1/Nu due to a small degree of opposing or assisting free convection is $0.65\ \overline{\mathrm{Nu}}\mathrm{Ra}/\mathrm{Pr}^2\mathrm{Re}^3$.

Summary and Conclusions

1 Equation (9) is proposed as a lower bound for the computed and experimental values of heat transfer by forced convection to a cylinder in cross flow for all Re and Pr such that RePr > 0.2.

2 As a lower bound, equation (9) presumably represents the behavior for low free-stream turbulence, an isothermal surface, negligible blockage, negligible end-effects, a small temperature difference and negligible free convection. A possible exception is in the range of $10^3 < \mathrm{Re} < 10^4$ where the data of Hilpert [4] for air and of Ishiguro, et al. [40] for sodium appear to follow equation (4) rather than equation (9). In the range of $7 \times 10^4 < \mathrm{Re} < 4 \times 10^5$, $\overline{\mathrm{Nu}}$ may be significantly higher than predicted by equation (9) owing to a downstream shift of the point of separation of the laminar boundary layer. Equation (10) can be used as a lower bound and predictor in this range.

3 Equation (4) can be used as an approximation for equation (9)

for $Re < 4000$ and all Pr.

4 Equation (3), which is based on the assumption of creeping flow, should provide a better representation than equations (4) or (9) for $RePr < 0.2$ if free convection and end-effects are negligible. It agrees well with such experimental data for air, but has not been tested critically for a wide range of Pr.

5 Equation (4) appears to provide reasonably good predictions even for $RePr < 0.2$ and can be modified to provide an even better representation for any single set of data by the proper, arbitrary choice of Nu_0.

6 Statistical methods were not used to evaluate the constants in equations (4) and (9) nor to characterize the scatter since the various sets of data are obviously of widely differing and unknown quality and in some cases were determined with some uncertainty from graphs.

7 Equation (9) has the advantage over prior correlating equations in that it takes into account the recent data of Achenbach [15] and Zdanavichyus, et al. [16] for an extended range of Re.

8 Equation (9) differs from prior correlating equations in that it is based, insofar as possible, on theoretical results, and provides a continuously varying dependence on both Re and Pr.

9 The success of equation (9) is quite remarkable in view of the many strong transitions in the flow field as documented by Collis and Williams [10], Achenbach [16] and others for air. Fortunately, the corresponding transitions in the heat transfer coefficient are quite weak and compensatory with the exception noted previously for $1 \times 10^5 < Re < 4 \times 10^5$.

10 An empirical equation could be constructed which follows these transitions but the behavior is not yet clearly enough defined to justify such a complex construction.

11 Expressions are suggested to estimate the increased or decreased value of $\overline{Nu}$ due to free-stream turbulence, nonisothermal boundary conditions, tunnel blockage, end-effects, large temperature-differences and free convection.

12 Additional data are still needed for the very low and the intermediate and high range of Re and for a wide range of Pr or Sc. In order to be of value these measurements must be of good precision and accuracy and free from the effects enumerated in conclusion 11.

13 Tabulations of experimental and computed values of Nu, Re, and Pr should be included in future publications for the convenience of subsequent workers.

14 Equation (9) and (4) are presumed to be applicable for mass transfer with $\overline{Sh}$ and Sc substituted for $\overline{Nu}$ and Pr, although values to test this generalization are rather limited.

Acknowledgment

The provision of the tabulated experimental values of reference [15] by Dr. Elmar Achenbach and of reference [16] by Prof. A. A. Zhukauskas is greatly appreciated. The criticisms and suggestions of the anonymous reviewers were most helpful in improving this paper.

References

1 Douglas, W. J. M., and Churchill, S. W., "Recorrelation of Data for Convective Heat Transfer Between Gases and Single Cylinders With Large Temperature Differences," *Chemical Engineering Progress Symposium Series*, No. 18, Vol. 52, 1956, pp. 23–28.

2 McAdams, W. H., *Heat Transmission*, Third ed., McGraw-Hill, New York, 1954, p. 267.

3 Fand, R. M., and Keswani, K. K., "Recalculation of Hilpert's Constants," JOURNAL OF HEAT TRANSFER, TRANS. ASME, Series C, Vol. 95, 1973, pp. 224–226.

4 Hilpert, R., "Wärmeagabe von geheizten Drähten and Rohren im Luftstrom," *Forschungsarbeiten auf dem Gebiete des Ingenieurwesens*, Vol. 4, 1933, pp. 215–224.

5 Perkins, H. C., Jr., and Leppert, G., "Forced Convection Heat Transfer From a Uniformly Heated Cylinder," JOURNAL OF HEAT TRANSFER, TRANS. ASME, Series C, Vol. 84, 1962, pp. 257–263.

6 Richardson, P. D., "Heat and Mass Transfer in Turbulent Separated Flows," *Chemical Engineering Science*, Vol. 18, 1963, pp. 149–155.

7 Tsubouchi, T., and Masuda, H., "On the Experimental Formulae of Heat Transfer From Single Cylinders by Forced Convection," *Reports of the Institute of High Speed Mechanics*, Tohoku University, Japan, Vol. 19, 1967-1968, pp. 221–239.

8 Whitaker, S., "Forced Convection Heat Transfer Correlation for Flow in Pipes, Past Flat Plates, Single Cylinders, Single Spheres, and for Flow in Packed Beds and Tube Bundles," *AIChE Journal*, Vol. 18, 1972, pp. 361–371.

9 Fand, R. M., and Keswani, K. K., "A Continuous Correlation Equation for Heat Transfer From Cylinders to Air in Crossflow for Reynolds Numbers From 10^{-2} to 2×10^5," *International Journal of Heat and Mass Transfer*, Vol. 15, 1972, pp. 559–562.

10 Collis, D. C., and Williams, M. J., "Two-dimensional Convection From Heated Wires at Low Reynolds Numbers," *Journal of Fluid Mechanics*, Vol. 6, Part 3, 1959, pp. 357–384.

11 King, L. V., "On the Convection of Heat From Small Cylinders in a Stream of Fluid," *Philosophical Transactions of the Royal Society* (London), Series A, Vol. 214, 1914, pp. 373–432.

12 Gnielinski, V., "Berechnung mittlerer Wärme- und Stoffübergangskoeffizienten an laminar und turbulent überströmten Einzelkörpern mit Hilfe einer einheitlichen Gleichung," *Forschung im Ingenieurwesen*, Vol. 41, 1975, pp. 145–153.

13 Zhukauskas, A., "Heat Transfer From Tubes in Crossflow," *Advances in Heat Transfer*, Vol. 8, Academic Press, New York, 1972, pp. 93–160.

14 Morgan, V. T., "The Overall Convective Heat Transfer From Smooth Circular Cylinders," *Advances in Heat Transfer*, Vol. 11, Academic Press, New York, 1975, pp. 199–264.

15 Achenbach, "Total and Local Heat Transfer From a Smooth Circular Cylinder in Cross-flow at High Reynolds Number," *International Journal of Heat and Mass Transfer*, Vol. 18, 1975, pp. 1387–1396.

16 Zdanavichyus, G. B., Chesna, B. A., Zhyugzhda, I. I., and Zhukauskas, A. A., "Local Heat Transfer in an Air Stream Flowing Laterally to a Circular Cylinder at High Re Numbers," *Intern'l. Chem. Engng.*, Vol. 16, 1976, pp. 121–127.

17 Katinas, V. I., Shvegzhda, S. A., Zhyugzhda, I. I., and Zhukauskas, A. A., "Streamline Flow and Heat Transfer at the Frontal Section of a Circular Cylinder in Turbulent Streams of a Viscous Liquid," *Intern'l. Chem. Engng.*, Vol. 16, 1976, pp. 469–475.

18 Churchill, S. W., "A Comprehensive Correlating Equation for Forced Convection From Flat Plates," *AIChE Journal*, Vol. 21, 1976, pp. 264–268.

19 Churchill, S. W., and Chu, H. H.-S., "Correlating Equations for Laminar and Turbulent Free Convection From a Horizontal Cylinder," *International Journal of Heat and Mass Transfer*, Vol. 18, 1975, pp. 1049–1053.

20 Squire, H. B., in "*Modern Developments in Fluid Dynamics*, S. Goldstein, ed., Clarendon Press, Oxford, England, 1938, Vol. II, p. 631.

21 Eckert, E. R. G., "Die Berechnung des Wärmeübergangs in der Laminaren Grenzschicht umströmter Körper," *VDI Forschungsheft*, No. 416, 1942.

22 Levy, S., "Heat Transfer to Constant-Property Laminar Boundary-Layer Flows With Power-Function Free-Stream Velocity and Wall-Temperature Variation," *J. of the Aero. Scis.*, Vol. 19, 1952, pp. 341–348.

23 Churchill, S. W., and Usagi, R., "A General Expression for the Correlation of Rates of Transfer and Other Phenomena," *AIChE Journal*, Vol. 18, 1972, pp. 1121–1128.

24 Churchill, S. W., and Ozoe, H., "Correlations for Laminar Forced Convection With Uniform Heating in Flow over a Plate and in Developing and Fully Developed Flow in a Tube," JOURNAL OF HEAT TRANSFER TRANS. ASME, Series C, Vol. 95, 1973, pp. 78–84.

25 Churchill, S. W., and Ozoe, H., "Correlation for Laminar Forced Convection in Flow over an Isothermal Tube," JOURNAL OF HEAT TRANS., TRANS. ASME, Series C, Vol. 95, 1973, pp. 416–419.

26 Churchill, S. W., and Churchill, R. U., "A Comprehensive Correlating Equation for Heat and Component Transfer by Free Convection," *AIChE Journal*, Vol. 21, 1975, pp. 604–607.

27 Masliyah, J. H., and Epstein, N., "Heat and Mass Transfer From Elliptical Cylinders in Steady Symmetric Flow," *Ind. and Engng. Chem. Funda.*, Vol. 12, 1973, pp. 317–323.

28 Jain, P. C., and Goel, B. S., "A Numerical Study of Unsteady Laminar Forced Convection From a Circular Cylinder," JOURNAL OF HEAT TRANSFER, TRANS. ASME, Series C, Vol. 98, 1976, pp. 303–307.

29 Nakai, S., and Okazaki, T., "Heat Transfer From a Horizontal Circular Wire at Small Reynolds and Grashof Numbers–I Pure Convection," *International Journal of Heat and Mass Transfer*, Vol. 18, 1975, pp. 387–396.

30 Dennis, S. C. R., Hudson, J. D., and Smith, N., "Steady Laminar Forced Convection From a Circular Cylinder at Low Reynolds Numbers," *Physics of Fluids*, Vol. 11, 1968, pp. 933–940.

31 Hill, J. C., and Sleicher, C. A., Jr., "Convective Heat Transfer From Small Cylinders to Mercury," *International Journal of Heat and Mass Transfer*, Vol. 12, 1969, pp. 1595–1604.

32 Virk, P. S., "Heat Transfer From the Rear of a Cylinder in Transverse Flow," JOURNAL OF HEAT TRANSFER, TRANS. ASME, Series C, Vol. 92, 1970, pp. 206–207.

33 Clark, L. G., private communication (see reference [1]).

34 van der Hegge Zijnen, "Modified Correlation Formulae for the Heat Transfers by Natural and by Forced Convection From Horizontal Cylinders, *Applied Sci. Res.*, Series A, Vol. 6, 1956, pp. 129–140.

35 Richardson, P. D., "On Hilpert's Measurements of Heat Transfer From Cylinders Transverse to an Air Stream," JOURNAL OF HEAT TRANSFER, TRANS. ASME, Series C, Vol. 85, 1963, pp. 283–284.

36 Gebhart, B., and Pera, L., "Mixed Convection From Long Horizontal Cylinders," *Journal of Fluid Mechanics*, Vol. 45, 1970, pp. 49–64.

37 Krall, K. M., and Eckert, E. R. G., "Local Heat Transfer Around a Cylinder at Low Reynolds Number," JOURNAL OF HEAT TRANS., TRANS. ASME, Series C, Vol. 95, 1973, pp. 273–275.

38 Schmidt, E., and Wenner, K., "Wärmeabgabe über den Umfang eines angeblasenen geheizten Zylinders.," *Forschung im Ingenieurwesen*, Vol. 12, 1941, pp. 65–73.

39 Lewis, J. S., "Heat Transfer for Predictions From Mass Transfer Measurements Around a Single Cylinder in Cross Flow," *International Journal of Heat and Mass Transfer*, Vol. 14, 1971, pp. 325–329.

40 Ishiguro, R., Kumada, T., Sugujama, and Ikezaki, E., "Experimental Study of Heat Transfer Around a Circular Cylinder in a Liquid-Sodium Crossflow," *Intern'l. Chem. Engng.*, Vol. 16, 1976, pp. 249–252.

41 Grosh, R. J., and Cess, R. D., "Heat Transfer to Fluids With Low Prandtl Numbers for Flow Across Plates and Cylinders of Various Cross Section," TRANS. ASME, Vol. 80, 1958, pp. 667–676.

42 Davis, A. H., "Convective Cooling of Wires in Streams of Viscous Liquids," *Philosophical Magazine*, Vol. 47, 1924, pp. 1057–1092.

43 Beckers, H. L., ter Haar, L. W., Tjoan, L. T., Merk, H. J., Prins, J. A., and Schenk, J., "Heat Transfer at Very Low Grashof and Reynolds Numbers," *Appl. Sci. Res.*, Series A, Vol. 6, 1956, pp. 82–84.

44 Fand, R. M., and Keswani, K. K., "The Influence of Property Variation on Forced Convection Heat Transfer to Liquids," *International Journal of Heat and Mass Transfer*, Vol. 15, 1972, pp. 1515–1536.

45 Fand, R. M., "Heat Transfer by Forced Convection From a Cylinder to Water in Crossflow," *International Journal of Heat and Mass Transfer*, Vol. 8, 1965, pp. 995–1010.

46 Dobry, R., and Finn, R. K., "Mass Transfer to a Cylinder at Low Reynolds Numbers," *Ind. and Engng. Chem.*, Vol. 48, 1956, pp. 1540–1543.

47 Wylie, R. G., "The Transfer Coefficients of a Laminar Boundary Layer With Variable Fluid Properties," *The Chem. Engng. J.*, Vol. 6, 1973, pp. 1–14.

48 Vaitekunas, P. P., Schlanshyyanskas, A. A., and Zhukauskas, A. A., "Influence of the Variable Physical Properties of a Gas on Drag and Heat Transfer at a Plate With Developed Turbulent Flow," *Intern'l. Chem. Engng.*, Vol. 16, 1976, pp. 403–411.

49 Boulos, M. I., and Pei, D. C. T., "Dynamics of Heat Transfer From Cylinders in a Turbulent Air Stream," *International Journal of Heat and Mass Transfer*, Vol. 17, 1974, pp. 767–783.

50 Vincenti, W. G., and Graham, D. J., "The Effect of Wall Interference Upon the Aerodynamic Characteristics of an Airfoil Spanning a Closed-Throat Circular Wind Tunnel," National Advisory Committee Aeronautics Technical Report No. 849, Washington, D. C., 1946.

51 Lock, C. N., "The Interference of a Wind Tunnel on a Symmetrical Body," Aeronautical Research Council, Report, Memo No. 1275, 1929, No. 1451, 1931.

52 Dyban, E. P., and Epik, E. Ya., "Heat Transfer in Laminar Boundary Layer With Increased Turbulence of Outer Flow," *Heat Transfer-Soviet Research*, Vol. 6, 1974, pp. 159–162.

53 Öhman, G. A., "A Note on Experimental Determination of Convective Heat Transfer From Wires at Extremely Small Reynolds and Grashof Numbers," *Acta Acad. Abo*, Series B, Vol. 30, 1970, pp. 1–7.

54 Churchill, S. W., "A Comprehensive Correlating Equation for Laminar, Assisting, Forced and Free Convection," *AIChE Journal*, Vol. 23, 1977, pp. 10–16.

J. C. Adams, Jr.

Supervisor, Project Support and Special Studies Section, Aerodynamics Projects Branch, von Kármán Gas Dynamics Facility, ARO, Inc., AEDC Division, A Sverdrup Corporation Co., Arnold Air Force Station, Tenn. Mem. ASME

Hypersonic Viscous Shock Layer Calculation of Leeward Vortex-Induced Heat Transfer on a Sharp Cone at a High Angle of Attack

An analysis technique applicable to the problem of leeward vortex-induced heat transfer on a sharp cone at high angles of incidence under hypersonic laminar flow conditions is presented. The analysis, a three-dimensional hypersonic viscous shock layer approach in conjunction with a numerical solution procedure, is shown to be both applicable and accurate based on comparisons of heat-transfer distributions, surface pressure distributions, and leeward meridian flow-field profile measurements taken in a hypersonic wind tunnel. Detailed calculations of the embedded vortex flow field on the leeward side of the cone are presented in such a manner as to clearly portray exactly how embedded vortex flow influences local heating rates.

Introduction

Lee-surface heating on aerodynamic configurations at high angles of incidence under laminar hypersonic flow conditions has often been regarded as relatively insignificant since the leeward surface is generally shielded from the mainstream flow. Recent experimental hypersonic research [1–8][1] has revealed, however, that leeward flow-field vortex phenomena are responsible for intense local heating near the leeward meridian of delta wings, cones, and Space Shuttle orbiter configurations at high incidence angles. Since such heating constitutes a potential design problem for hypersonic vehicles in sustained cruising flight, the need for improved prediction and understanding of leeward vortex-induced heat transfer is indicated. The present paper will examine this problem area from an analytical viewpoint using a three-dimensional viscous shock layer approach for hypersonic laminar flows over a sharp cone at high angles of attack. Comparison with hypersonic wind tunnel data will be presented to ascertain the basic validity and applicability of such an approach.

Analysis

The analysis technique applied in the present work is the three-dimensional hypersonic viscous shock layer (HVSL) approach as formulated by Lubard and Helliwell [9, 10] for numerical solution of the complete inviscid-viscous flow field over a sharp cone at high angles of attack, including the separated (vortex) region on the leeward side. Both the inviscid and viscous regions of the flow field are modeled in one composite set of governing equations and calculated simultaneously so that complicated inviscid-viscous interactions which occur under hypersonic flow conditions (such as the well-known displacement-induced pressure effect) are automatically included in the analysis without tedious matching of separate inviscid and viscous solutions as would be required using higher-order boundary-layer theory. The approach involves the numerical finite-difference solution of the "parabolized" Navier-Stokes equations for compressible laminar flow with the equations solved between the body surface and the bow shock wave under moderate to high Reynolds number conditions. Boundary conditions at the shock and its shape are calculated by using the Rankine-Hugoniot equations. The key point here is that the HVSL approach allows calculation of the *complete* three-dimensional flow field including both viscous and inviscid regions as well as the separated vortex flow which occurs on the leeward side for angles of attack greater than approximately the cone semivertex angle.

Following Lubard and Helliwell [9, 10], a body-oriented coordinate system is used (see Fig. 1) with x taken along a cone generator, y

[1] Numbers in brackets designate References at end of paper.

Contributed by the Heat Transfer Division and presented at the National Heat Transfer Conference, St. Louis, Mo., August 9–11, 1976 of THE AMERICAN SOCIETY OF MECHANICAL ENGINEERS. Revised manuscript received by the Heat Transfer Division, February 24, 1977. Paper No. 76-HT-43.

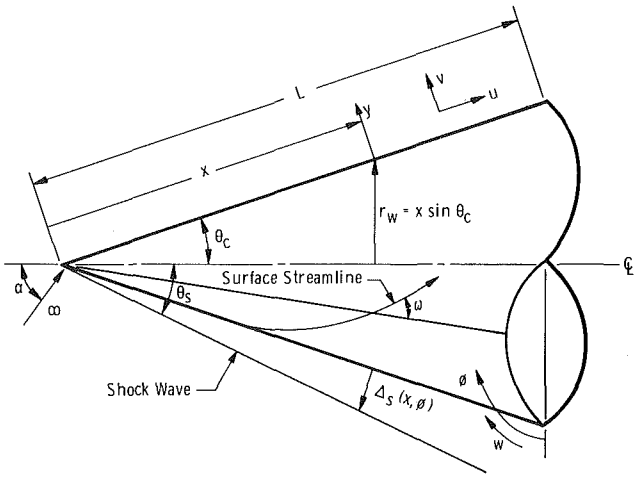

Fig. 1 Geometry and nomenclature for sharp cone at angle of attack

normal to the surface, and ϕ the circumferential coordinate where $\phi = 0$ represents the windward ray. The governing partial differential equations of laminar fluid dynamic motion are given by

$$\frac{\partial(\rho u r)}{\partial x} + \frac{\partial(\rho v r)}{\partial y} + \frac{\partial(\rho w)}{\partial \phi} = 0 \tag{1}$$

$$\frac{\partial(\rho u^2 r)}{\partial x} + \frac{\partial(\rho u v r)}{\partial y} + \frac{\partial(\rho w u)}{\partial \phi} - \rho w^2 \sin\theta_c + r\frac{\partial p}{\partial x} = \frac{r}{\mathrm{Re}}\left\{\frac{\partial}{\partial y}\left(\mu\frac{\partial u}{\partial y}\right) + \frac{1}{r^2}\frac{\partial}{\partial \phi}\left(\mu\frac{\partial u}{\partial \phi}\right)\right\} \tag{2}$$

$$\frac{\partial(\rho u v r)}{\partial x} + \frac{\partial(\rho v^2 r)}{\partial y} + \frac{\partial(\rho w v)}{\partial \phi} - \rho w^2 \cos\theta_c + r\frac{\partial p}{\partial y} = \frac{r}{\mathrm{Re}}\left\{\frac{\partial}{\partial y}([\lambda + 2\mu])\frac{\partial v}{\partial y} + \frac{1}{r^2}\frac{\partial}{\partial \phi}\left(\mu\frac{\partial v}{\partial \phi}\right) + \frac{1}{r}\frac{\partial}{\partial y}\left(\lambda\frac{\partial w}{\partial \phi}\right) + \frac{1}{r}\frac{\partial}{\partial \phi}\left(\mu\frac{\partial w}{\partial y}\right)\right\} \tag{3}$$

$$\frac{\partial(\rho u w r)}{\partial x} + \frac{\partial(\rho v w r)}{\partial y} + \frac{\partial(\rho w^2)}{\partial \phi} + \rho u w \sin\theta_c + \rho v w \cos\theta_c + \frac{\partial p}{\partial \phi} = \frac{r}{\mathrm{Re}}\left\{\frac{\partial}{\partial y}\left(\mu\frac{\partial w}{\partial y}\right) + \frac{1}{r^2}\frac{\partial}{\partial \phi}\left([\lambda + 2\mu]\frac{\partial w}{\partial \phi}\right) + \frac{1}{r}\frac{\partial}{\partial y}\left(\mu\frac{\partial v}{\partial \phi}\right) + \frac{1}{r}\frac{\partial}{\partial \phi}\left(\lambda\frac{\partial v}{\partial y}\right)\right\} \tag{4}$$

$$\frac{\partial(\rho u h r)}{\partial x} + \frac{\partial(\rho v h r)}{\partial y} + \frac{\partial(\rho w h)}{\partial \phi} - r(\gamma - 1)\mathrm{M}_\infty^2 \times \left(u\frac{\partial p}{\partial x} + v\frac{\partial p}{\partial y} + \frac{w}{r}\frac{\partial p}{\partial \phi}\right) = \frac{r}{\mathrm{RePr}}\left\{\frac{\partial}{\partial y}\left(\frac{k}{Cp}\frac{\partial h}{\partial y}\right) + \frac{1}{r^2}\frac{\partial}{\partial \phi}\left(\frac{k}{Cp}\frac{\partial h}{\partial \phi}\right)\right\} + \frac{(\gamma-1)\mathrm{M}_\infty^2 r}{\mathrm{Re}}\left\{\mu\left(\frac{\partial u}{\partial y}\right)^2 + \frac{\mu}{r^2}\left(\frac{\partial u}{\partial \phi}\right)^2 + (\lambda + 2\mu)\left(\frac{\partial v}{\partial y}\right)^2 + \frac{\mu}{r^2}\left(\frac{\partial v}{\partial \phi}\right)^2 + \mu\left(\frac{\partial w}{\partial y}\right)^2 + \frac{(\lambda + 2\mu)}{r^2} \times \left(\frac{\partial w}{\partial \phi}\right)^2 + 2\frac{\lambda}{r}\frac{\partial v}{\partial y}\frac{\partial w}{\partial \phi} + 2\frac{\mu}{r}\frac{\partial v}{\partial \phi}\frac{\partial w}{\partial y}\right\} \tag{5}$$

with all the quantities appearing in equations (1)–(5) nondimensionalized as follows: velocities with respect to the free-stream velocity, density with respect to the free-stream density, viscosity with respect to the free-stream viscosity, enthalpy with respect to the free-stream enthalpy, static pressure with respect to the product of the free-stream density and the square of the free-stream velocity, and all distances with respect to the reference length L (see Fig. 1). The foregoing equations are approximate in the sense that they are derived from the complete steady-state compressible Navier-Stokes equations by assuming that derivatives with respect to x which appear in the viscous terms are of lower order compared with the viscous derivatives with respect to both y and ϕ. In addition, $r \equiv x \sin\theta_c + y \cos\theta_c$ has been assumed to be of the same order as x which will tend to make equations (1)–(5) invalid for problems with very small cone semivertex angles or problems very close to the apex or tip of a sharp cone. Complete details concerning the derivation of these equations may be found in the report by Lubard and Helliwell [9].

In addition to the foregoing partial differential equations of motion, an equation of state relating the density to the pressure and enthalpy as well as equations relating the viscosity, thermal conductivity, and specific heat to the enthalpy are necessary to complete the system. In the present work a thermally and calorically perfect air model is used having a constant specific heat ratio $\gamma = 1.40$ in conjunction with the Sutherland viscosity law and a constant Prandtl number of 0.71.

Since the set of governing partial differential equations given by equations (1)–(5) is parabolic in the streamwise (x) direction, a marching-type numerical solution technique is used. An implicit finite-difference treatment is applied to the normal derivatives in conjunction with a Newton-Raphson method of iteration for solution of the nonlinear algebraic equations which result from differencing of the circumferential derivatives. The equations are solved between the body surface and the bow shock; boundary conditions at the shock and its resulting shape are calculated by using the Rankine-Hugoniot shock crossing relations and a one-sided differencing of the continuity equation. Complete details of the differencing technique are given in the reports by Lubard and Helliwell [9, 10]; the actual digital computer code as written for a CDC 7600 machine may be found in the report by Helliwell and Lubard [10].

As discussed in the foregoing, the system of governing shock layer

Nomenclature

C_p = specific heat at constant pressure
h = static enthalpy
k = thermal conductivity
L = reference length defined on Fig. 1
M = Mach number
M_∞ = free-stream Mach number
Pr = free-stream Prandtl number
p = static pressure
$\dot{q}$ = heat transfer to the surface
Re, $\mathrm{Re}_{\infty,L}$ = free-stream Reynolds number based on L
r = metric for the ϕ coordinate, $x \sin\theta_c + y \cos\theta_c$
St_∞ = free-stream Stanton number, $\dot{q}/\rho_\infty V_\infty (H_\infty - h_w)$
T = static temperature
T_0 = total or stagnation temperature
u = velocity in x-direction
V_∞ = free-stream velocity
v = velocity in y-direction
w = velocity in ϕ-direction
x = coordinate along the rays of the cone surface
y = coordinate normal to the cone surface
α = angle of attack
γ = ratio of specific heats
Δ_s = shock standoff distance
η = transformed normal coordinate, y/Δ_s
θ_c = sharp cone semivertex angle
λ = bulk viscosity, $-2\mu/3$
μ = viscosity
ρ = density
ϕ = circumferential coordinate
ω = surface streamline angle defined on Fig. 1

Subscripts

s = shock condition
w = wall condition
∞ = free-stream condition

equations is parabolic in the streamwise flow direction so that a downstream marching solution technique can be utilized; initial conditions must be specified at some upstream location. For the case of a sharp cone at incidence, Lubard and Helliwell [9, 10] calculate initial conditions including both the viscous and inviscid regions starting at zero angle of attack. The angle of attack is slowly increased while marching in x (0.5 deg per marching step) until the desired angle of attack is reached. The calculations are then continued at a constant angle of attack, and the solution is allowed to relax to the expected sharp cone results. Because of the method used to obtain the initial conditions, it is not possible to compare the results of the calculations directly with experimental results.

Recent work by the author has resulted in the development of a technique whereby initial or starting conditions for the case of sharp cone at incidence flows can be generated using the same Lubard-Helliwell code [10] as for the downstream marching solution. Briefly, reasonable initial profiles and circumferential shock shape are chosen for some location near the sharp cone apex but downstream of the merged-layer region near the cone tip. The initial shock shape can be taken from any available analysis for inviscid flow over sharp cones at incidence (restricted to an angle-of-attack range less than approximately the cone half-angle) or some other analysis technique, say an inviscid tangent-cone approach coupled with some adjustments for angle-of-attack effects. It is to be emphasized that these initial conditions correspond to the angle of attack of interest in contrast to the approximate method of references [9, 10]. Given these initial profiles, the solution is marched downstream using a very small constant Δx step size for a distance of approximately 10 maximum initial viscous layer thicknesses, at which time the solution appears (in all cases run to date) to reflect the parabolic nature of the governing equations and solution procedure, i.e., the effect of the initial conditions becomes less and less important as the solution marches downstream. Typically this "adjustment" region is located within the interval $0.03 < x/L < 0.06$. Complete details of this procedure are given in the Appendix of ASME Paper No. 76-HT-43 from which the present paper was taken.

With the initial conditions determined per the method discussed previously, the solution continues downstream using the Lubard-Helliwell code [10] in conjunction with the well-known Courant-Friedrichs-Lewy criterion to determine the maximum allowable streamwise (x) step size for a given (input) circumferential (ϕ) step size. Nonuniform grid node distributions are employed in both the body normal and circumferential directions (typically 50 points in the body normal grid and 26 points in the circumferential grid); a geometric progression scheme is used to cluster body normal points near the wall where viscous effects are dominant. The original circumferential iteration logic as given by Helliwell and Lubard [10] has been modified slightly to more properly reflect the elliptic character of the governing shock layer equatioss in the circumferential direction.

Digital computer CPU time for a single complete calculation (approximately 300 to 400 forward marching steps employing the normal and circumferential grid mesh discussed previously) is on the order of two to three hours on an IBM 370/165 machine using the FORTRAN H (Level 21.7) OPT = 2 compiler. Core size requirements are approximately 225K bytes in conjunction with program overlay. The sizeable execution (CPU) time is a direct reflection of the block 6 × 6 tridiagonal matrix inversion and the Newton-Raphson iterative procedure required in the numerical solution technique.

Discussion of Results

The present paper will present numerical results from the HVSL approach for the case of a 10.0-deg semivertex angle sharp cone at a 24.0-deg angle of attack under the following free-stream conditions:

$$M_\infty = 7.95$$

$$Re_{\infty,L} = 416{,}667$$

$$T_w/T_{0,\infty} = 0.40$$

$$L = 10.16 \text{ cm } (4.0 \text{ in.})$$

corresponding to the experimental investigation reported by Tracy [11] which will be used for comparison with the present analysis. The geometry and nomenclature of the sharp cone as used in the present paper are given in Fig. 1.

Presented in Fig. 2 is a comparison of the circumferential distribution of overall shock layer properties at the streamwise body location $x/L = 0.86$. The HVSL results are in excellent agreement with experiment for both the shock wave location and the viscous layer edge location (defined in terms of the total enthalpy profile behavior as the distance from the body surface to the point where H/H_∞ differs from unity by ± 0.005 when approached from the outer or inviscid part of the flow). Calculated separation location (in the crossflow sense) occurred at $\phi \approx 150$ deg with embedded vortex flow between the separation location and the leeward meridian at $\phi = 180$ deg. Here the word "embedded" means that the vortex is totally confined to the viscous layer region as opposed to a shed vortex which is convected freely downstream. Details of this embedded vortex flow will be given later.

It is to be noted that Fig. 2 shows no weak embedded shocks in the inviscid portion of the flow field on the leeward side around $\phi \approx 160$ to 170 deg. Tracy [11] experimentally observed such shocks, but the coarse circumferential grid spacing used in the present calculation (5.0-deg increments in ϕ on the leeward side) was insufficient to numerically resolve these weak shocks.

Comparisons of circumferential and streamwise heat-transfer distributions are given in Figs. 3 and 4, respectively. As can be seen from Fig. 3, the circumferential heat-transfer distribution from the HVSL analysis is in excellent agreement with experiment for the body location $x/L = 1.0$. Note that minimum heat transfer occurs at $\phi \approx 160$ deg with a rapid increase in heating as the leeward meridian (ϕ

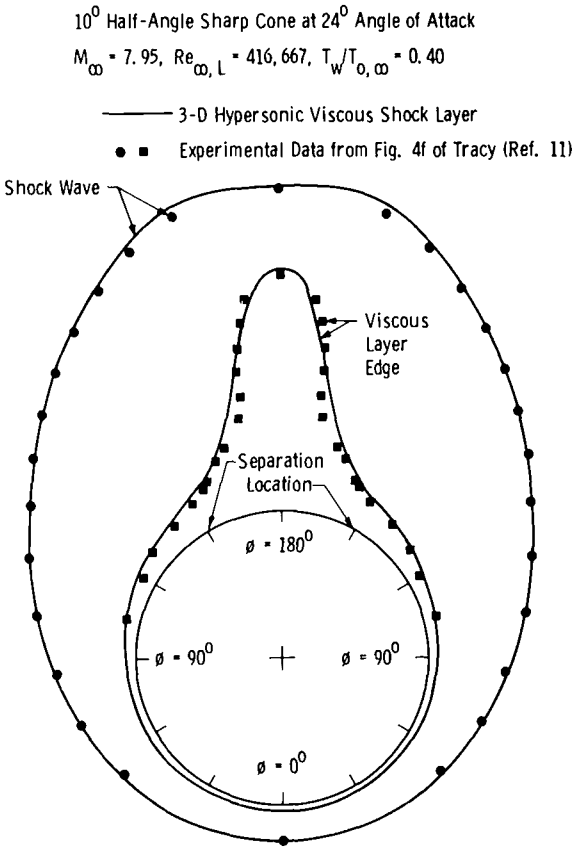

Fig. 2 *Circumferential distribution of overall shock layer properties at body location $x/L = 0.86$*

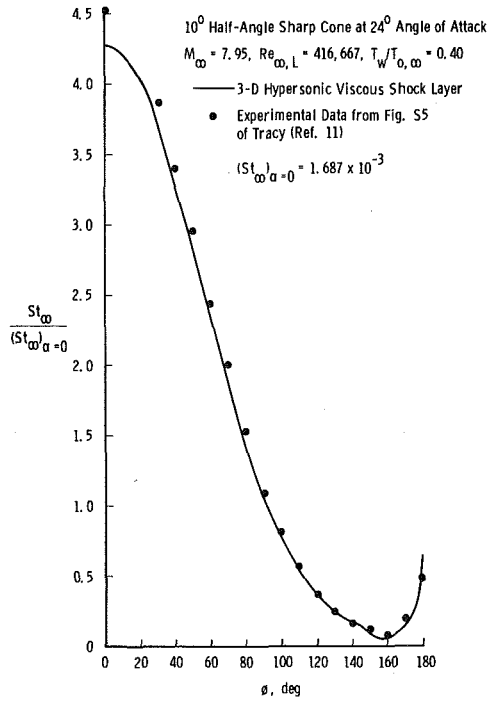

Fig. 3 Circumferential heat transfer distribution at body location x/L = 1.0

= 180 deg) is approached. This increase reflects the embedded vortex effect on heating and is more dramatically illustrated in Fig. 4. Note from Fig. 4 that the HVSL-calculated streamwise heat-transfer distribution at ϕ = 160 deg still follows the $\sqrt{x/L}$-type decay of classical sharp cone heating. Along the leeward meridian for values of x/L

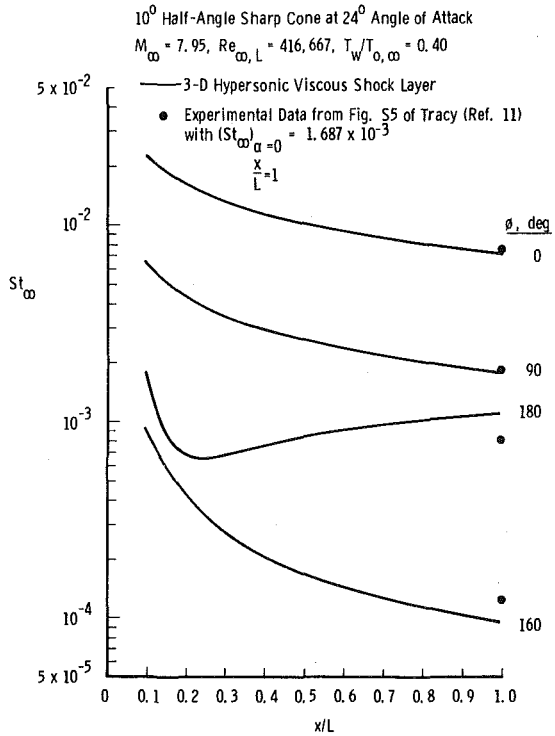

Fig. 4 Streamwise (x-direction) heat transfer distribution

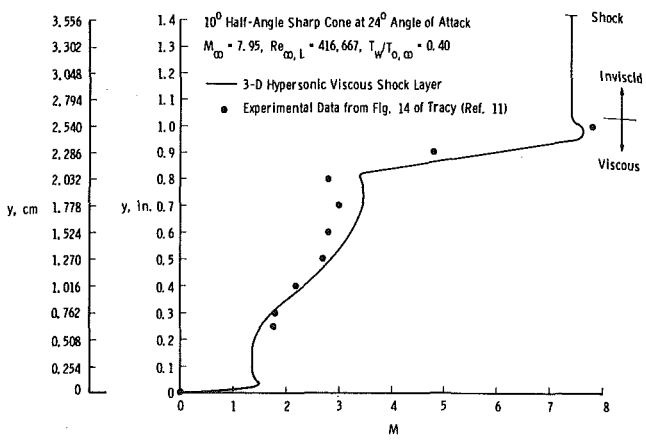

Fig. 5 Leeward ray (ϕ = 180-deg) Mach number profile at body location x/L = 0.86

greater than approximately 0.25, the HVSL analysis predicts an increase in heat-transfer rate with the magnitude at the end of the body (x/L = 1.0) in reasonable agreement with experiment. The important point to observe from Fig. 4 is that the ϕ = 180-deg leeward meridian heat transfer is approaching the ϕ = 90-deg heat transfer at the end of the body, i.e., leeward flow-field vortex phenomena are resulting in severe local heating along the leeward meridian of the cone. This is exactly the problem which the aerothermodynamicist must face in vehicle design.

In order to understand the physical mechanism whereby embedded vortex phenomena adversely affect local heat transfer, one must examine the fluid dynamic details of the leeward flow field. Such information is readily available from the HVSL analysis since the complete flow field from the body to the shock between the windward (ϕ = 0-deg) and leeward (ϕ = 180-deg) meridians is determined via the numerical solution procedure. Presented in Fig. 5 is a comparison of the leeward meridian (ϕ = 180-deg) Mach number profile at the body location x/L = 0.86. Agreement between the HVSL calculation and experiment (as deduced from pitot pressure measurements) is reasonable. Note that the calculated shock layer is approximately 75-percent viscous and 25-percent inviscid which reflects the viscous

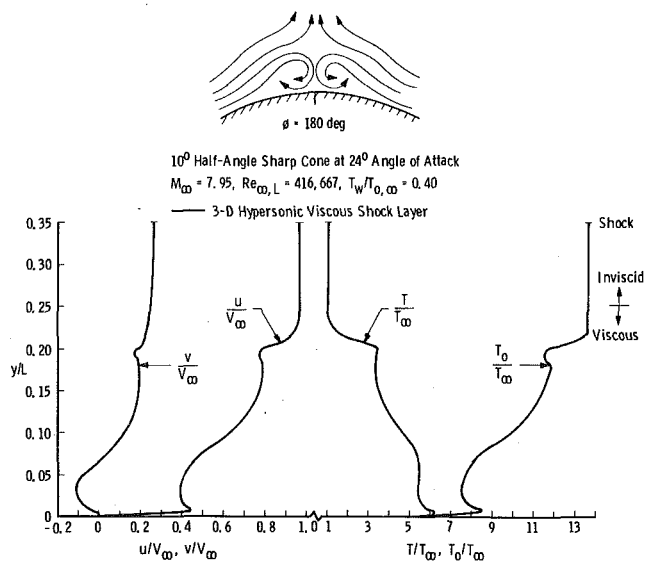

Fig. 6 Leeward ray (ϕ = 180-deg) flow field profiles at body location x/L = 0.86

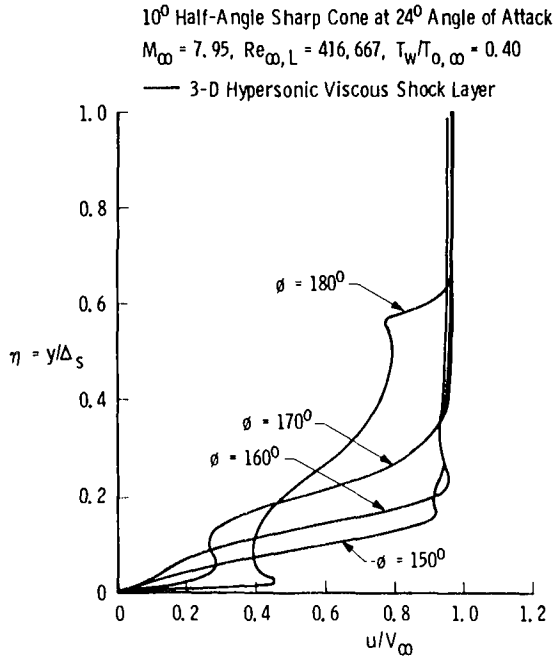

Fig. 7(*a*) Streamwise velocity

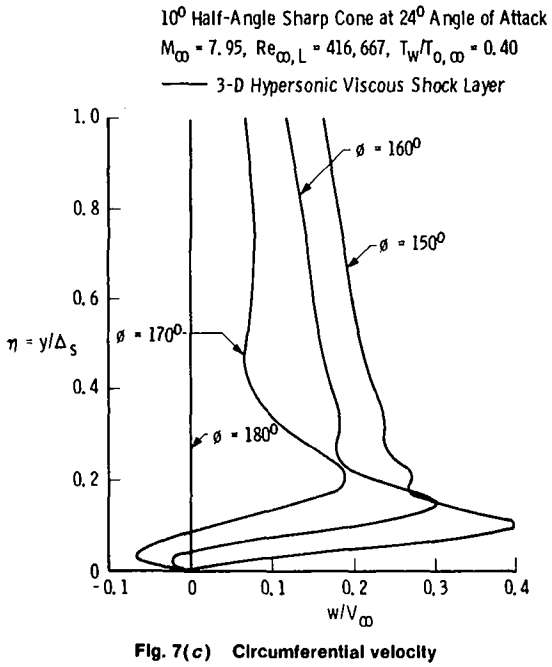

Fig. 7(*c*) Circumferential velocity

layer "hump" previously presented in Fig. 2. As is obvious from the examination of the HVSL-calculated Mach number profile in Fig. 5, the presence of the leeward embedded vortex has radically altered the character of the Mach number profile from what one is normally accustomed based on three-dimensional boundary-layer theory. The inflection point in the HVSL-calculated profile at $y \approx 2$ cm appears to be substantiated in trend by the experimental data. The more interesting feature in the HVSL-calculated profile relative to the vortex-induced heating problem is the near-wall inflection point located at $y \approx 0.1$ cm. This clearly indicates that the embedded vortex has severely altered the leeward meridian flow field in the near-wall region which it must if the local heating is to be significantly influenced.

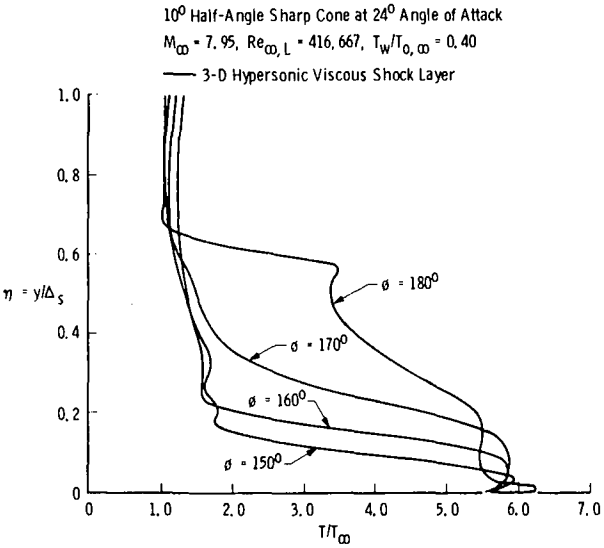

Fig. 7(*d*) Static temperature

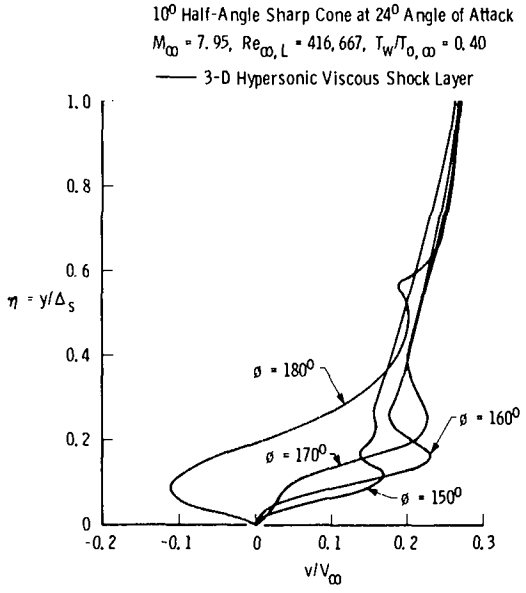

Fig. 7(*b*) Normal velocity

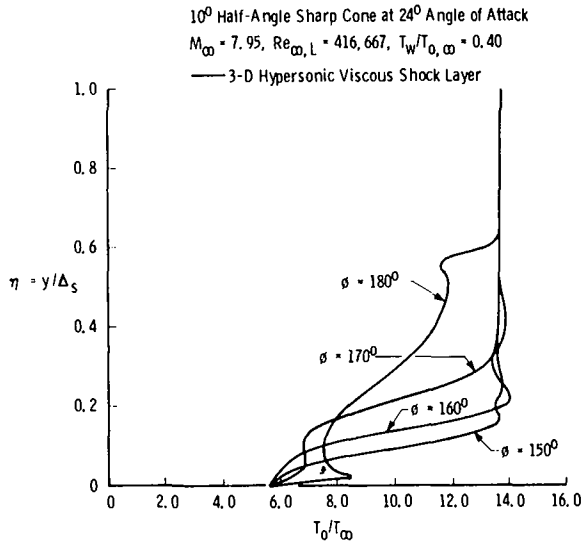

Fig. 7(*e*) Stagnation temperature

Fig. 7 Flow field profiles at body location $x/L = 0.86$

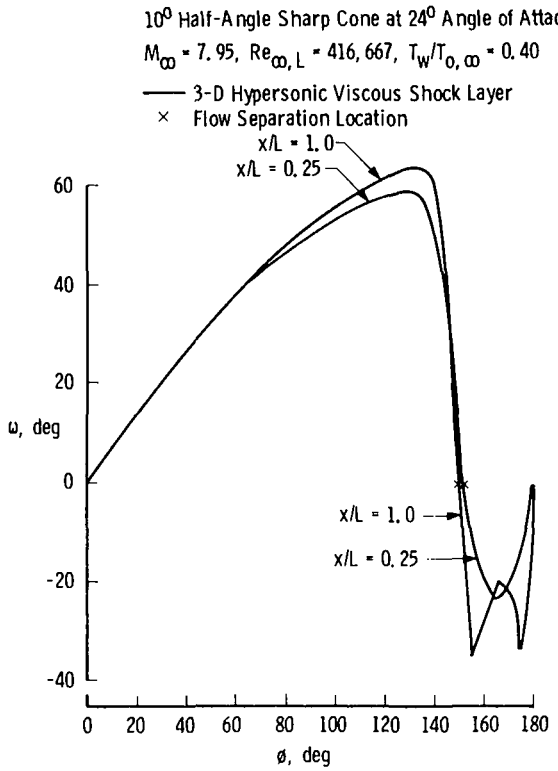

Fig. 8 Circumferential surface streamline distribution

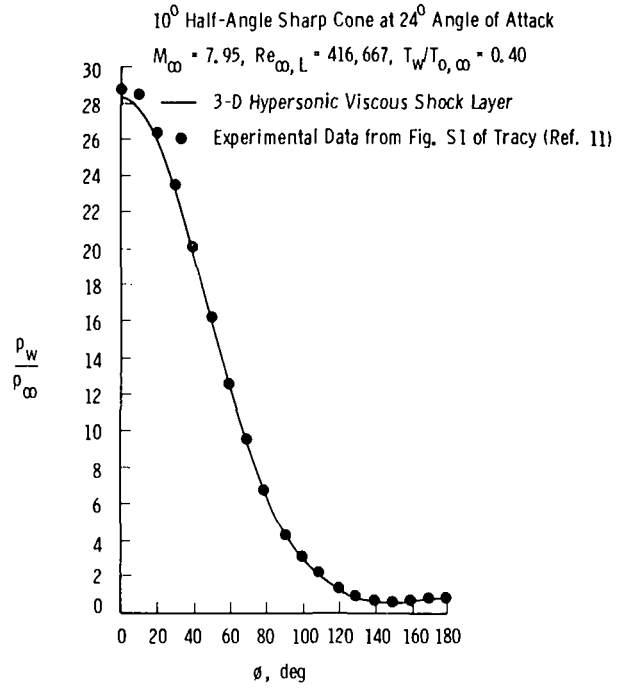

Fig. 9 Circumferential pressure distribution at body location $x/L = 1.0$

The detailed manner in which the leeward (ϕ = 180-deg) meridian flow field at the body location $x/L = 0.86$ is altered by the embedded vortex is shown in Fig. 6. Note especially the near-wall inflection points in the streamwise velocity u, static temperature T, and stagnation temperature T_0 profiles. Just as with the Mach number profile in Fig. 5, the presence of the leeward embedded vortex has radically changed the character of the flow-field profiles from what one is normally accustomed based on three-dimensional boundary-layer theory. Further note the negative normal velocity v in the near-wall region in Fig. 6. It is this velocity which directly reflects the embedded vortex effect on the near-wall leeward meridian flow as illustrated schematically on the top part of the figure.

Development of the leeward embedded vortex flow between ϕ = 150 deg and ϕ = 180 deg at the body station $x/L = 0.86$ is illustrated in Fig. 7. The relationship between the normal velocity v and the circumferential velocity w is responsible for the formation of the embedded vortex which, in turn, is responsible for the increased near-wall gradient (and hence increased heat transfer) in both the static temperature T and stagnation temperature T_0 profiles as the ϕ = 180-deg leeward meridian is approached. Similar comments apply with respect to the streamwise velocity u. The "embedded" aspect of the vortex flow becomes clear when it is noted that the vortex is contained within approximately the inner 25 percent of the shock layer nearest the wall where viscous effects are predominant; recall that the edge of the viscous layer can be determined from the total temperature profiles given in Fig. 7(e) as the distance from the body surface where $T_0/T_{0,\infty}$ differs from unity by ± 0.005 when approached from the outer or inviscid part of the flow.

Circumferential distributions of the surface streamline angle ω at two streamwise body locations, namely $x/L = 0.25$ and $x/L = 1.0$, are given in Fig. 8. Note the large positive values of ω just prior to the flow separation location at $\phi \approx 150$ deg. Flow separation is herein defined to occur in the crossflow sense at the circumferential location where the surface streamline angle is zero (denoted by "x" marks on Fig. 8). The interesting feature of Fig. 8 is the surface streamline behavior in the separated region between $\phi \approx 150$ deg and the leeward meridian (ϕ = 180 deg) for the streamwise body location $x/L = 1.0$. The HVSL calculation suggests that secondary embedded vortices, smaller in size than the primary embedded vortices, may be forming on either side of the primary embedded vortex pair. Experimental indication that such may indeed be the case is presented by Hefner [5], Hefner and Whitehead [6], and Zakkay, Economos, and Alzner [12].

It is important to examine the effect of leeward surface embedded vortex flow on surface pressure distributions, both streamwise and circumferential, since such could conceivably influence both heating distributions and vehicle aerodynamics. As shown by Fig. 9, the presence of the leeward embedded vortex flow has little obvious effect on the circumferential surface pressure distribution at the body station location $x/L = 1.0$. Similar comments apply with respect to the streamwise pressure distribution given in Fig. 10, although the well-known effects of "viscous interaction" are reflected in the HVSL results for the forward portion of the cone (values of x/L less than approximately 0.25). The leeward surface pressure distributions of Figs. 9 and 10 are in contrast to the heating behavior shown previously in Figs. 3 and 4; the increased leeward surface heat transfer is not caused by or related to an increase in leeward surface pressure, either streamwise or circumferential. The excellent agreement between the HVSL analysis and experiment shown in Figs. 9 and 10 clearly illustrates the accuracy and applicability of this approach for aerodynamic applications where streamwise and circumferential distributions of surface pressure are of importance in determination of vehicle forces and moments.

In reduction of experimentally determined flow-field pitot pressure probe data, it is commonly assumed that the static pressure is constant across the shock layer at a value equal to the measured surface pressure for a common body location. As shown by Fig. 11, this assumption is not valid on the leeward surface of a sharp cone at high angles of attack based on the present HVSL analysis. Note in Fig. 11 that the static pressure on the ϕ = 180-deg leeward meridian increases by a factor of two (2) between the body surface ($\eta = 0$) and the shock wave ($\eta = 1.0$). Recalling the development of the leeward vortex between ϕ = 150 deg and ϕ = 180 deg at the body staion $x/L = 0.86$ given previously in Fig. 7, the static pressure profiles of Fig. 11 complete the necessary flow-field information to totally portray embedded vortex

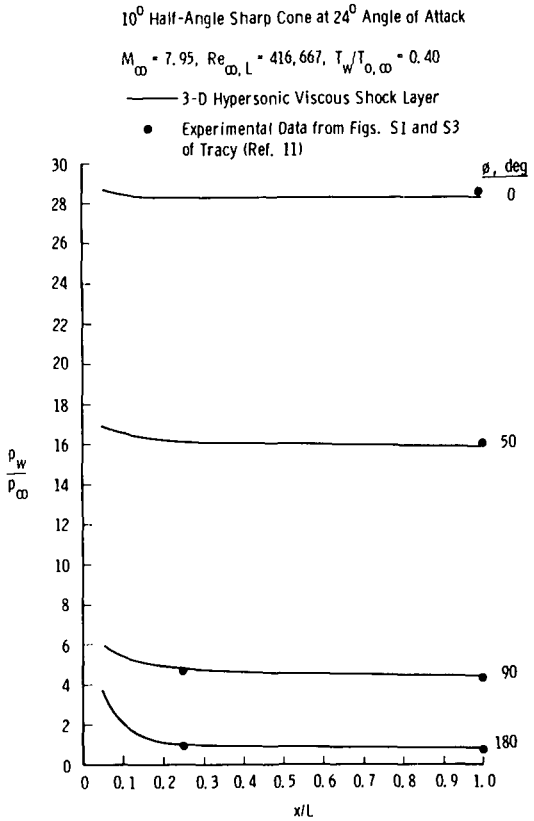

Fig. 10 Streamwise (x-direction) pressure distribution

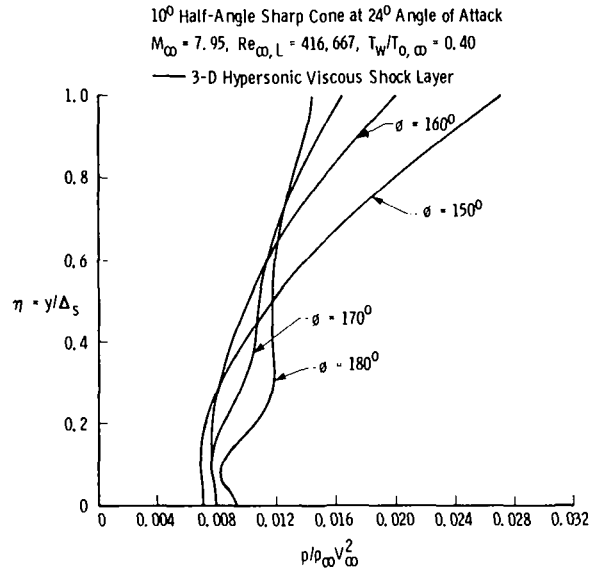

Fig. 11 Static pressure profiles at body location x/L = 0.86

flow on the leeward side of sharp cones at high angles of incidence under hypersonic laminar flow conditions. It is interesting to observe in Fig. 11 that the static pressure is essentially constant across the inner 20 percent of the shock layer nearest the wall for the ϕ = 150-deg and ϕ = 160-deg conditions. As can be seen from Fig. 7(e), this is well within the viscous region and further, from Fig. 8, $\phi \approx 150$ deg is the location of flow separation (defined in the crossflow sense). Hence it may be expected that the zero normal pressure gradient assumption of three-dimensional boundary-layer theory remains valid even near flow separation (defined in the crossflow sense). However, keep in mind that the present HVSL analysis automatically includes complicated three-dimensional inviscid-viscous interactions which occur under hypersonic flow conditions in regions of flow separation.

Concluding Summary

The present paper has presented the results of an analysis technique applicable to the problem of leeward vortex-induced heat transfer on a sharp cone at high angles of incidence under hypersonic laminar flow conditions. The analysis, a three-dimensional hypersonic viscous shock layer approach in conjunction with a numerical solution procedure, has been shown to be both applicable and accurate based on comparisons of heat-transfer distributions, surface pressure distributions, and leeward meridian flow-field profile measurements taken in a hypersonic wind tunnel. Detailed calculations of the embedded vortex flow field on the leeward side of the cone have been presented in such a manner as to clearly portray embedded vortex flow influence on local heating rates as reflected through the flow-field profiles.

Acknowledgment

Research reported in this paper was conducted by the Arnold Engineering Development Center, Air Force Systems Command. Research results were obtained by personnel of ARO, Inc., contract operator of AEDC. Further reproduction is authorized to satisfy needs of the U. S. Government.

References

1 Whitehead, A. H., Jr., "Effect of Vortices on Delta Wing Lee-Side Heating at Mach 6," *AIAA Journal*, Vol. 8, No. 3, Mar. 1970, pp. 599–600.

2 Whitehead, A. H., Jr., Hefner, J. N., and Rao, D. M., "Lee-Surface Vortex Effects Over Configurations in Hypersonic Flow," AIAA Paper No. 72-77, 1972.

3 Rao, D. M., and Whitehead, A. H., Jr., "Lee-Side Vortices on Delta Wings at Hypersonic Speeds," *AIAA Journal*, Vol. 10, No. 11, Nov. 1972, pp. 1458–1465.

4 Hefner, J. N., "Lee-Surface Heating and Flow Phenomena on Space Shuttle Orbiters at Large Angles of Attack and Hypersonic Speeds," NASA TN D-7088, Langley Research Center, Hampton, Va., Nov. 1972.

5 Hefner, J. N., "Vortex-Induced Heating to a Cone-Cylinder Body at Mach 6," *Journal of Spacecraft and Rockets*, Vol. 11, No. 2, Feb. 1974, pp. 127–128.

6 Hefner, J. N., and Whitehead, A. H., Jr., "Vortex-Induced Heating to Cone Flaps at Mach 6," *Journal of Spacecraft and Rockets*, Vol. 11, No. 3, Mar. 1974, pp. 200–201.

7 Zakkay, V., Miyazawa, M., and Wang, C. R., "Lee Surface Flow Phenomena Over Space Shuttle at Large Angles of Attack at M_∞ = 6," AIAA Paper No. 75-148, 1975.

8 Mruk, C. K., Bertin, J. J., and Lamb, J. P., "Experimental and Theoretical Study of Shuttle Lee-Side Heat Transfer Rates," NASA CR-141890, Mar. 1975.

9 Lubard, S. C., and Helliwell, W. S., "Calculation of the Flow on a Cone at High Angle of Attack," RDA-TR-150, Feb 1973, R & D Associates, Santa Monica, Calif.; see also *AIAA Journal*, Vol. 12, No. 7, July 1974, pp. 965–974.

10 Helliwell, W. S., and Lubard, S. C., "An Implicit Method for Three-Dimensional Viscous Flow With Application to Cones at Angle of Attack," Aerospace Report TR-0074(4450-64)-1, Sept. 1973, Aerospace Corporation, El Segundo, Calif.; see also *Computers and Fluids*, Vol. 3, No. 1, Mar. 1975, pp. 83–101.

11 Tracy, R. R., "Hypersonic Flow Over a Yawed Circular Cone," GALCIT Memo No. 69, California Institute of Technology, Balboa, Calif., Aug. 1963.

12 Zakkay, V., Economos, C., and Alzner, E., "Leeside Flow Field Description Over Cones at Large Incidence," AFFDL-TR-74-19, Air Force Flight Dynamics Laboratory, Wright-Patterson Air Force Base, Ohio, July 1974.

J. V. Beck
Department of Mechanical Engineering,
Division of Engineering Research,
Michigan State University,
East Lansing, Mich.

Sequential Estimation of Thermal Parameters

This paper presents a method for estimating the parameters appearing in heat transfer models. The method involves minimizing a function that is more general than that utilized in least squares. One of the unique features of the method is that it is sequential. Some of the advantages of this feature are that the basic equations are simple in that no matrix inverses are required, computer programs can be easily written to have an arbitrary number of parameters, and the sequential procedure provides information for development for better mathematical models for describing complex phenomena. Some examples are given.

Introduction

Historically, heat transfer has depended to a large degree upon experimental research. This will doubtlessly continue to be true in the future as well. In the efficient design and use of experiments, certain techniques related to statistics are not well known in the heat transfer community. The purpose of this paper is to develop a technique for sequential estimation of certain parameters that occur in heat transfer. The technique has computational advantages as well as a statistical basis. In this paper, however, the emphasis is more upon the computational than statistical aspects.

A common objective in heat transfer research is to "determine" parameters such as heat transfer coefficients, thermal properties, radiant properties, heat flux, etc. A general procedure for estimating these parameters is given herein. The word "estimate" is used rather than "find" or "determine" because any values found through experimental data for quantities (termed *parameters*) are of necessity approximations to the true ones.

The method developed herein is a *sequential* procedure in that the effects upon the parameters of adding measurements corresponding to each new time are given in the calculational process. Advantages of this procedure include the potential development of appropriate mathematical models, reduced computer memory requirements, simpler computer programs, greater physical insight, and possibility of an on-line analysis. Some of these advantages are illustrated subsequently.

The method can also be termed sequential because prior information is used. There can be the reestimation of the parameters after the results of each in a series of *experiments* become available. The concept of sequentially using new observations at each *time* to obtained updated estimates is quite similar, but not identical, to that of using prior information from one or a series of prior experiments, each containing many measurements. The mathematical treatment is different particularly when the dependent variables are nonlinear in terms of the parameters. The emphasis in this paper is upon sequential estimation when updated estimates are obtained as measurements are added one after the other.

At least three components are required in estimating parameters. First, measurements are needed. Second, a mathematical model that describes the physical phenomena must be given; this model contains the parameters of interest. The model may be an algebraic equation, a partial differential equation, or some other form. The dependent variable may be linear or nonlinear in terms of the parameters. (Even though a differential equation may be linear, the dependent variable could be nonlinear in terms of the parameters, as is illustrated in the following.) The third component is a measure of agreement between the measurements and the corresponding values given by the model. A mathematical criterion for agreement is given that is more general than in most references and can have a rigorous statistical basis.

An outline of the paper is the following. The concept of estimating parameters is introduced. A general estimation criterion is given that includes ordinary least squares, maximum likelihood, and maximum a posteriori estimation; the assumptions implicit in the criterion for each estimation procedure are given. Next a modified Gauss procedure appropriate for estimating nonlinear parameters is given for the general criterion. This procedure can be used for sequential-over-experiments analyses. For sequential analyses in which the parameter values are to be estimated each "time" a new measurement is added, an algorithm is developed from the modified procedure mentioned.

[1] Numbers in brackets designate References at end of paper.

Contributed by the Heat Transfer Division for publication in the JOURNAL OF HEAT TRANSFER. Manuscript received by the Heat Transfer Division May 27, 1976.

This estimation algorithm is the main theoretical result of the paper. The use of this algorithm is then presented for two examples, one linear and the other nonlinear. These examples illustrate the method, its claimed superior to alternative techniques, and how to utilize the technique for model evaluation.

Estimation Criteria

The basic criterion used in this paper for parameter estimation is the minimization of the function

$$S = (Y_s - \eta_s)W_{st}(Y_t - \eta_t) + (\mu_u - \beta_u)U_{uv}(\mu_v - \beta_v) \qquad (1)$$

where the repeated indices mean summations; for example, there is a double summation over s and t for the first term in equation (1) and over u and v in the second term. The ranges of s and t are 1 to n, the number of measurements of the dependent variable. The ranges of u and v are 1 to p, the number of parameters which are designated β_u. The quantity Y_s is the sth measurement of a dependent variable at the sth set of independent variables; η_s is the dependent variable value calculated from the model for the same independent variable conditions as Y_s. An example of a dependent variable is temperature which is for the position x_s and time t_s, the independent variables; Y_s would be the measured temperature and η_s the calculated temperature.

The symbol W_{st} is a weighting coefficient; W_{st} is also equal to W_{ts}. The square matrix formed from the W_{st} values must be positive definite. (This presentation is purposely given as much as possible in summation notation rather than in the usual matrix notation because heat transfer researchers appear to be generally more familiar with the former notation. Moreover, the final algorithm is more explicitly given in a summation notation.) A small measurement error in Y_s usually would result in a large value of W_{ss}.

In some analyses the terms $W_{st}, s, t = 1, \ldots, n$ are those of the inverse of the covariance matrix of the Y vector, which can be designated as having elements ψ_{st}. Sometimes estimated values of ψ_{st} may be known as when the measurement errors can be considered as being uncorrelated; in this case $\psi_{st} = W_{st} = 0$ for all s, t except $s = t$. If the elements of ψ_{st} are not known but the experiment can be repeated N times, then estimated values of ψ_{st}, designated $\hat{\psi}_{st}$, can be found from

$$\hat{\psi}_{st} = \frac{1}{N-1}\sum_{i=1}^{N}(Y_{si} - \overline{Y}_s)(Y_{ti} - \overline{Y}_t)$$

where Y_{si} is the measured value of the dependent variable at (x_s, t_s) for the ith experiment and $\overline{Y}_s$ is the average over i at (x_s, t_s). For further discussion, see references [1–7].[1]

In many applications the second term in equation (1) is not included. It can be considered as containing prior information regarding the parameters. In one meaning of this term, μ_u signifies a prior estimate (based on information independent of that in the Y_t's) of the parameter β_u. Further discussion is given later in connection with MAP estimation.

Some of the better known estimation criteria that are included in equation (1) are ordinary least squares (OLS), maximum likelihood (ML) for gaussian measurement errors, and maximum a posteriori (MAP) estimation. A brief description of these criteria is given in the following.

The most common estimation method is OLS, in which the sum of squares,

$$S_{\text{OLS}} = (Y_s - \eta_s)(Y_s - \eta_s) \qquad (2)$$

is minimized with respect to the parameters $\beta_1, \beta_2, \ldots, \beta_p$. It is the recommended procedure if very little is known regarding the measurement errors. Although no statistical information need be used in obtaining OLS parameter estimates, information is needed regarding the measurement errors if statistical statements are to be made regarding the accuracy of the estimates [3–6].

In maximum likelihood estimation, $U_{uv} = 0$ for all u and v. One set of assumptions, which results in S being equal to $(Y_s - \eta_s)W_{st}(Y_t - \eta_t)$, is that the errors in Y_s be additive, have zero mean, and be gaussian with a known covariance matrix Ψ, whose inverse has the components W_{st}. Furthermore, there are no errors in the independent variables and there is no prior information.

MAP estimation uses prior information and is sometimes called Bayesian estimation. In order to derive the criterion given by equation (1), the same set of assumptions regarding Y_s given above for ML estimation can be used. There are negligible errors in the independent variables. The second term in equation (1) describes prior information for the case of gaussian prior information regarding the parameters which have prior estimates denoted μ_u and have a covariance matrix whose inverse has components U_{uv}. In order to obtain estimates of greatest accuracy and to improve convergence of the estimation procedure, it is important to use all the available prior information [2, p. 351]. The prior information may come from various sources. It may come from the subjective information that the analyst has gained from his experience [6]. It could also come from prior experiments; in this case parameters can be reestimated after each experiment which might contain many dynamic measurements. This is one meaning of the term sequential estimation, as mentioned previously.

Even if there is little prior information, it can be useful to include the second term of equation (1). The case of little prior information can be simulated by $U_{st} = 0$ for $s \neq t$ and U_{ss} being small compared to the square of an estimate of β_s. The use of such a term can improve convergence if the initial parameter estimates happen to be chosen so that a certain matrix to be mentioned in connection with equation (7) is singular at the initial estimated values but is not singular at the converged values. The use of prior information in the design of experiments is discussed in [8].

Sequential Procedure

Before developing the main sequential procedure, the Gaussian method [1–6] is extended to cover the general sum of squares function

Nomenclature

A = heated surface area of billet
$A_j^{(k)}(\alpha)$ = summation defined by equation (20b)
$b_j^{(k)}(\alpha)$ = estimate of the jth parameter at the kth iteration and the αth time
c = specific heat
$e_\alpha^{(k)}$ = residual defined by equation (20e)
h = heat transfer coefficient
$H^{(k)}(\alpha)$ = summation defined by equation (20d)
I_p = $p \times p$ identity matrix
k = iterative superscript
$K_j^{(k)}(\alpha)$ = gain coefficient defined by equation (20c)
M_u = large value given in equation (21b)
Nu = Nusselt number
$P_{uj}^{(k)}(\alpha)$ = term of a $p \times p$ square matrix defined by equation (20g)
Re = Reynolds number
S = function to be minimized, equation (1)
t = time and subscript
T = temperature
U_{uv} = weighting coefficient for prior parameter estimates μ_u and μ_v
V = volume of billet
w_s = W_{ss}
W_{st} = weighting coefficient for correlated errors in Y_s and Y_t
x = distance from heated surface
$X_{\alpha i}^{(k)}$ = sensitivity coefficient for ith parameter and αth time evaluated using $b_j^{(k)}(n)$ for $j = 1, \ldots, p$
Y_s = sth measurement
α = time index
β_j = true value of jth parameter
$\Delta^{(k)}(\alpha)$ = term defined by equation (20a)
η = dependent variable
μ_u = prior estimate of uth parameter
ρ = density

given by (1) rather than the simpler OLS function (2). Assume that η has continuous first derivatives in β_s and bounded higher derivatives. A necessary condition at the minimum S is that the first derivative of S with respect to β_j be equal to zero for $j = 1, 2, \ldots, p$; hence

$$S_{,j} = -2[\eta_{s,j} W_{st}(Y_t - \eta_t) + U_{uv}(\mu_v - \beta_v)] = 0 \tag{3}$$

where *differentiation is with respect to the variable* β_j, which is indicated by the j after the subscripted comma. Equation (3) is true at the minimum of S even though the parameters are as yet unknown. No constraints are included on the parameters other than in the model, η.

Because the first derivative of η_s with respect to β_j has an important role in estimation, it is termed a *sensitivity coefficient* and is given the symbol X_{sj},

$$X_{sj} \equiv \partial \eta_s / \partial \beta_j = \eta_{s,j} \tag{4}$$

Let (3) be used at the $(k+1)$th iteration, yielding parameter estimates $b_u{}^{(k+1)}$, $u = 1, \ldots, p$. (For cases when the dependent variable η is linear in terms of all the parameters, iteration is not needed.) Two approximations are now used in equation (3). First, evaluate X_{sj} at $b_u{}^{(k)}$ instead of at $b_u{}^{(k+1)}$. Second, for $\eta_t{}^{(k+1)}$ use the truncated Taylor series

$$\eta_t{}^{(k+1)} \approx \eta_t{}^{(k)} + X_{t\ell}{}^{(k)}(b_\ell{}^{(k+1)} - b_\ell{}^{(k)}) \tag{5}$$

Using these approximations in equation (3) yields

$$X_{sj}{}^{(k)} W_{st}[Y_t - \eta_t{}^{(k)} - X_{t\ell}{}^{(k)}(b_\ell{}^{(k+1)} - b_\ell{}^{(k)})] + U_{jv}[\mu_v - b_v{}^{(k)} - (b_v{}^{(k+1)} - b_v{}^{(k)})] = 0 \tag{6}$$

which can be rearranged to

$$[X_{sj}{}^{(k)} W_{st} X_{tv}{}^{(k)} + U_{jv}](b_v{}^{(k+1)} - b_v{}^{(k)}) = X_{sj}{}^{(k)} W_{st}(Y_t - \eta_t{}^{(k)}) + U_{jv}(\mu_v - b_v{}^{(k)}) \tag{7}$$

which is valid for $j = 1, \ldots, p$ and thus produces a set of p linear algebraic equations that can be solved for the improved parameter values $b_v{}^{(k+1)}$ for $v = 1$ to p. Let the square matrix formed using the $j, v = 1, 2, \ldots, p$ terms in the brackets in equation (7) have an inverse whose components are $P_{uj}{}^{(k)}$. In order for the inverse to exist, it is necessary that the matrix be nonsingular (i.e., its determinant must not be zero). It is possible that the presence of nonzero U_{jj} terms can cause the matrix formed from the bracketed terms in equation (7) to be nonsingular while otherwise it would singular. The parameters are given by

$$b_j{}^{(k+1)} = b_j{}^{(k)} + P_{uj}{}^{(k)}[X_{su}{}^{(k)} W_{st}(Y_t - \eta_t{}^{(k)}) + U_{uv}(\mu_v - b_v{}^{(k)})] \tag{8}$$

which is the modified Gaussian iterative equation. The iterations on k continue until there are negligible changes in the b_j values from iteration to iteration.

The expression given by equation (8) can be used to perform sequential-over-experiments analyses. Assume that the assumptions given for MAP estimation are valid. The components of $\mathbf{U}$ would come from any prior information. After the "present" experiment is analyzed and converged values of b_j are found, data from a subsequent experiment could be analyzed to include the information from the present experiment by replacing μ_j by the converged present b_j values and the U_{sv} components by the sv component of the inverse of the present $\mathbf{P}$ matrix.

If there is only one parameter ($p = 1$), (8) simplifies to

$$b^{(k+1)} = b^{(k)} + P^{(k)}[X_s{}^{(k)} W_{st}(Y_t - \eta_t{}^{(k)}) + U(\mu - b^{(k)})] \tag{9a}$$

$$P^{(k)} = 1/[X_s{}^{(k)} W_{st} X_t{}^{(k)} + U] \tag{9b}$$

in which the subscripts for the parameters are dropped.

The main emphasis in this paper is upon development of a sequential method that provides new parameter estimates as each set of observations for a given "time" are added. In the following development it is necessary that W_{st} for $s \neq t$ either be zero or that a transformation be employed to effectively reduce the problem to one in which the weighting matrix is diagonal. Some matrix manipulations to accomplish this are given in Appendix B. For the ML method, $W_{st} = 0$ for $s \neq t$ corresponds to noncorrelated measurement errors in Y_s. For high speed sampling of dynamic phenomena, the measurements are many times correlated. In some cases the correlation can be modeled as being an autoregressive process; a transformed set of measurements involving differences of them can be given [6] that would in effect yield $W_{st} = 0$ for $s \neq t$.

Define

$$C_{uj}{}^{(k)}(i) = \sum_{\alpha=1}^{i} X_{\alpha u}{}^{(k)} w_\alpha X_{\alpha j}{}^{(k)} + U_{uj} \tag{10a}$$

$$D_u{}^{(k)}(i) = \sum_{\alpha=1}^{i} X_{\alpha u}{}^{(k)} w_\alpha (Y_\alpha - \eta_\alpha{}^{(k)}) + U_{uv}(\mu_v - b_v{}^{(k)}) \tag{10b}$$

where the summation of α is explicitly given. Recursive relations obtained from these equations are

$$C_{uj}{}^{(k)}(\alpha) = C_{uj}{}^{(k)}(\alpha - 1) + X_{\alpha u}{}^{(k)} w_\alpha X_{\alpha j}{}^{(k)}, \quad \alpha = 1, \ldots, n \tag{11a}$$

$$D_u{}^{(k)}(\alpha) = D_u{}^{(k)}(\alpha - 1) + X_{\alpha u}{}^{(k)} w_\alpha (Y_\alpha - \eta_\alpha{}^{(k)}), \quad \alpha = 1, \ldots, n \tag{11b}$$

for which *no* summation is implied by the α subscript and the starting values are

$$C_{uj}{}^{(k)}(0) = U_{uj}, \quad D_u{}^{(k)}(0) = U_{uv}(\mu_v - b_v{}^{(k)}) \tag{12}$$

Now let $P_{uj}{}^{(k)}(\alpha)$ be the uj component of the inverse of the matrix formed using the $C_{uj}{}^{(k)}(\alpha)$ values. Then a simple sequential procedure is

$$b_j{}^{(k+1)}(\alpha) = b_j{}^{(k)}(n) + P_{uj}{}^{(k)}(\alpha) D_u{}^{(k)}(\alpha), \quad j = 1, 2, \ldots, p \tag{13}$$

where equation (11) and (12) are used, where there is a summation on u, and where α starts at 1 and continues until n, at which value another iteration on k begins. The $X_{\alpha u}{}^{(k)}$ and $\eta_\alpha{}^{(k)}$ terms in $P_{uj}{}^{(k)}(\alpha)$ and $D_u{}^{(k)}(\alpha)$ are evaluated at $b_j{}^{(k)}(n)$, $j = 1, 2, \ldots, p$.

Rather than using the sequential relation given by equation (13), another one is derived that is simpler to program and that does not involve inverting a $p \times p$ matrix, as is required by the matrix $\mathbf{P}$ used in equation (13). (Many of the better least squares computer programs avoid inversion of matrices.) Let $\mathbf{C}^{(k)}(\alpha)$ be the matrix formed from the uj components given by equation (11a); then

$$\mathbf{P}^{(k)}(\alpha) = [\mathbf{C}^{(k)}(\alpha)]^{-1} = [\mathbf{C}^{(k)}(\alpha - 1) + \mathbf{X}_\alpha{}^{T(k)} \mathbf{W}_\alpha \mathbf{X}_\alpha{}^{(k)}]^{-1} \tag{14}$$

where a matrix form of equation (11a) is used. The matrix $\mathbf{X}_\alpha{}^{(k)}$ has components $X_{\alpha u}{}^{(k)}$ and $\mathbf{W}_\alpha = w_\alpha$. By using the matrix inversion lemma given by (A-3) in Appendix A, the $p \times p$ inverse in equation (14) is reduced to a scalar inverse.

A few matrix steps are now necessary. Using equations (13) and (11b) in matrix notation gives

$$\mathbf{b}^{(k+1)}(\alpha) = \mathbf{b}^{(k)}(n) + \mathbf{P}^{(k)}(\alpha)\mathbf{D}^{(k)}(\alpha) \tag{15}$$

$$= \mathbf{b}^{(k)}(n) + \mathbf{P}^{(k)}(\alpha)[\mathbf{X}_\alpha{}^{T(k)} w_\alpha e_\alpha{}^{(k)} + \mathbf{D}^{(k)}(\alpha - 1)] \tag{16}$$

where $e_\alpha{}^{(k)}$ is $Y_\alpha - \eta_\alpha{}^{(k)}$. Using both (A-3) and (A-4) in equation (16) produces

$$\mathbf{b}^{(k+1)}(\alpha) = \mathbf{b}(n) + \mathbf{P}(\alpha - 1)\mathbf{X}_\alpha{}^T e_\alpha/\Delta(\alpha) + \mathbf{P}(\alpha - 1)\mathbf{D}(\alpha - 1) - \mathbf{P}(\alpha - 1)\mathbf{X}_\alpha{}^T \mathbf{X}_\alpha \mathbf{P}(\alpha - 1)\mathbf{D}(\alpha - 1)/\Delta(\alpha) \tag{17}$$

where the superscript k on the right-hand side had been dropped for convenience. Writing equation (15) for $\alpha - 1$ gives

$$\mathbf{b}^{(k+1)}(\alpha - 1) = \mathbf{b}^{(k)}(n) + \mathbf{P}^{(k)}(\alpha - 1)\mathbf{D}^{(k)}(\alpha - 1) \tag{18}$$

which can be used to change equation (17) to the form

$$\mathbf{b}^{(k+1)}(\alpha) = \mathbf{b}^{(k+1)}(\alpha - 1) + \mathbf{P}^{(k)}(\alpha - 1)\mathbf{X}_\alpha{}^{T(k)} \times [e_\alpha{}^{(k)} - \mathbf{X}_\alpha{}^{(k)}(\mathbf{b}^{(k+1)}(\alpha - 1) - \mathbf{b}^{(k)}(n))]/\Delta^{(k)}(\alpha) \tag{19}$$

which is the desired sequential equation.

For programming purposes it is convenient to write equation (19) as the set of recursive equations in the following form:

$$\Delta^{(k)}(\alpha) = w_\alpha^{-1} + X_{\alpha u}{}^{(k)} P_{ui}{}^{(k)}(\alpha - 1) X_{\alpha i}{}^{(k)} \tag{20a}$$

$$A_j{}^{(k)}(\alpha) = X_{\alpha i}{}^{(k)} P_{ji}{}^{(k)}(\alpha - 1); \quad j = 1, \ldots, p \tag{20b}$$

$$K_j{}^{(k)}(\alpha) = A_j{}^{(k)}(\alpha)/\Delta^{(k)}; \quad j = 1, \ldots, p \tag{20c}$$

$$H^{(k)}(\alpha) = X_{\alpha i}{}^{(k)} [b_i{}^{(k+1)}(\alpha - 1) - b_i{}^{(k)}(n)] \tag{20d}$$

$$e_\alpha{}^{(k)} = Y_\alpha - \eta_\alpha{}^{(k)} \tag{20e}$$

$$b_j{}^{(k+1)}(\alpha) = b_j{}^{(k+1)}(\alpha - 1) + K_j{}^{(k)}(\alpha)(e_\alpha{}^{(k)} - H^{(k)}(\alpha)); \quad j = 1, \ldots, p \tag{20f}$$

$$P_{uj}{}^{(k)}(\alpha) = P_{uj}{}^{(k)}(\alpha - 1) - K_u{}^{(k)}(\alpha) A_j{}^{(k)}(\alpha); \quad u, j = 1, \ldots, p \tag{20g}$$

Again, a repeated subscript (except that of the Greek α) designates summation.

Note that three sets of parameters are included in equation (20): $b_j{}^{(k+1)}(\alpha)$, which is the latest estimate of the jth parameter at the $(k+1)^{st}$ iteration and the time $i = \alpha$; $b_j{}^{(k+1)}(\alpha - 1)$ is for the previous time; and $b_j{}^{(k)}(n)$ is found at the end of the kth iteration. In the $(k+1)^{st}$ iteration, the quantities $X_{\alpha u}{}^{(k)}$ and $\eta_\alpha{}^{(k)}$ are evaluated using the parameters $b_j{}^{(k)}(n)$ for $j = 1, \ldots, p$.

When programming equation (20), subscripts denoting the iteration index k are not needed. Subscripts for the measurement number α are needed *only* for Y_α and its independent variables (which do not explicitly appear in equation (20)).

A significant advantage of equation (20) is that no matrix inverses are needed. This is a rather remarkable result; if there are p parameters, one does not have to directly solve a set of p algebraic equations. This advantage results in simpler computer programming and less computer time when sequential parameter estimates are of interest.

Starting values of $b_j{}^{(1)}(0) = b_j{}^{(0)}(n)$ for $j = 1, \ldots, p$ and $P_{uj}{}^{(0)}(0)$ for $u, j = 1, \ldots, p$ are needed. The initial parameters $b_j{}^{(0)}(n)$ are the same as those that would be chosen using the Gaussian method equation (8); these are simply the best guesses of starting values. For linear estimation problems, the $b_j{}^{(0)}(n)$ values could all be chosen to be zero (or any other values) and only one iteration would be required.

The starting values $P_{uj}{}^{(0)}(0)$ must be selected in a different manner. There are two possible cases. First, if there is prior information regarding the parameters, $P_{uj}{}^{(0)}(0)$ represents the known covariance between $b_u{}^{(0)}(n)$ and $b_j{}^{(0)}(n)$; likewise $P_{uu}{}^{(0)}(0)$ is the known variance of $b_u{}^{(0)}(n)$. This is equivalent to making the matrix $\mathbf{P}^{(0)}(0)$ equal to the inverse of $\mathbf{U}$. The second case is when little is known regarding the accuracy of the initial estimates. This would also include ordinary least squares cases. In this case one can use

$$P_{uj}{}^{(0)}(0) = U_{uj} = 0 \quad \text{for } u \neq j,$$

$$P_{uu}{}^{(0)}(0) = M_u \quad \text{for } u = 1, \ldots, p \tag{21}$$

where M_u is a large number compared to the square of $b_u{}^{(0)}(n)$. This means that the variance of $b_u{}^{(0)}(n)$ is large; i.e., there is little prior information.

Three different equations (8), (13), and (20), are given previously for estimating the parameters. The same parameter estimates are obtained using each of them and each can be considered to be a modification of the Gaussian method. In certain difficult cases the Gaussian method may not yield proper parameter estimates because the problem is poorly conditioned. If there is no unique set of parameters which minimize S, no method can find a unique set. If, however, there is a unique minimum but it is indistinct, some modifications of the Gaussian method can be helpful. Many modifications have been proposed, some of which can utilize the generality of the S function given by equation (1). As mentioned in connection with equation (7), the use of $\boldsymbol{U}$ with small diagonal components can be helpful even when there is no prior information. Also if there is no prior information the Levenberg and Marquardt methods [6] can be obtained from equation (1) by replacing μ_u by $b_u{}^{(k)}$, β_u by $b_u{}^{(k+1)}$ and U_{uu} by $\lambda\Omega_{uu}$. There are various ways of choosing λ and Ω_{uu} [6].

Other methods of modifying the Gaussian method adjust the step size $\Delta_g b_u{}^{(k+1)} = b_u{}^{(k+1)} - b_u{}^{(k)}$ given by the Gaussian method by using the scalar parameter h in $b_u{}^{(k+1)} = b_u{}^{(k)} + h\Delta_g b_u{}^{(k+1)}$. If $h = 1$, the Gaussian method is obtained. In general, h can be iteration dependent. By reducing its size convergence can sometimes be improved. There are many ways of selecting h [1, 6] including halving and doubling, interpolation [1] and the Box-Kanemasu [6] methods.

Table 1 Comparison of predicted Nu values for flow normal to long cylinder (Pr = 0.72)

Re	Nu		
	Recommended values [9]	(a)	(b)
.1	.45	.451	
1	.84	.840	.89
10	1.83	1.86	1.99
10^2	5.1	4.93	5.26
10^3	15.7	15.5	15.4
10^4	56.5	58.0	51.6
10^5	245	259	253
2.5×10^5	520	493	529
No. of Par.		3	10
Largest % Difference		5.6	8.7

Example Involving Correlation for Forced Convection Over Cylinders

Since the sequential procedure given by equation (20) may seem formidable, an example which can be made linear in the parameters is given. Consider the recommended values of Nu versus Re given by McAdams [9, p. 259]; these values, reproduced in the first two columns of Table 1, are for gas flow normal to single cylinders. The Nu range of values is from 0.45 to 520 with the *relative* errors probably nearly the same for all values. This suggests that the weights w_α be chosen equal to the reciprocal of the square of the measured values of Nu. Rather than doing this, a similar-in-effect but easier procedure is to let $w_\alpha = 1$ and use the logarithm of Nu. Consider the following model, which is linear in the parameters $\beta_1, \ldots, \beta_p$,

$$\eta_\alpha = \beta_1 + \beta_2 t_\alpha + \beta_3 t_\alpha{}^2 + \ldots + \beta_p t_\alpha{}^{p-1} \tag{22}$$

where $\eta_\alpha = \log \mathrm{Nu}_\alpha$ and $t_\alpha = \log \mathrm{Re}_\alpha$.

In order to give some details of the use of equation (20), the beginning calculations are presented for the model shown by equation (22) with $p = 2$. Assume that nothing is known regarding the parameters (other than that information given by the data). Hence OLS is used. Let $\mathbf{P}^{(0)}$ have large diagonal components, say 10^5, and let $b_1{}^{(0)}(n) = b_1{}^{(1)}(0) = 0$ and $b_2{}^{(0)}(n) = b_2{}^{(1)}(0) = 0$. Notice that

$$X_{11} = \partial\eta_1/\partial\beta_1 = 1, \quad X_{21} = \partial\eta_1/\partial\beta_2 = t_1 = \log \mathrm{Re}_1 = \log(0.1) = -1$$

$$Y_1 = \log \mathrm{Nu}_1 = \log(0.45) = -0.34679.$$

A sequence of calculations for $k = 0$ and $\alpha = 1$ are given in the following with the k superscript suppressed.

$$\Delta(1) = w_1^{-1} + X_{11}{}^2 P_{11}(0) + 2X_{11} P_{12}(0) X_{12} + X_{12}{}^2 P_{22}(0)$$

$$= 1 + 1^2 \cdot 10^5 + 2 \cdot 1 \cdot 0 \cdot (-1) + (-1)^2 \cdot 10^5 = 200{,}001$$

$$A_1(1) = X_{11} P_{11}(0) + X_{12} P_{12}(0) = 1 \cdot 10^5 + (-1) \cdot 0 = 10^5$$

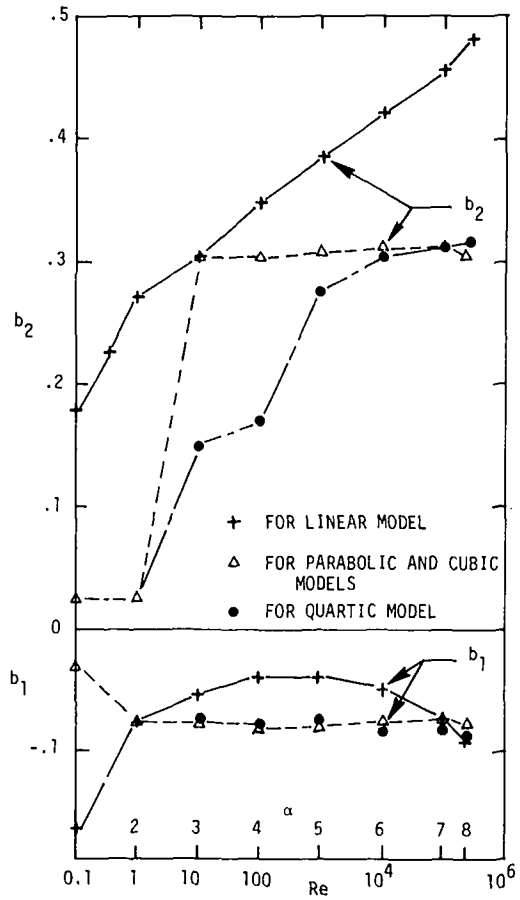

Fig. 1 Sequential estimates of parameters b_1 and b_2 for models for forced convection correlation example

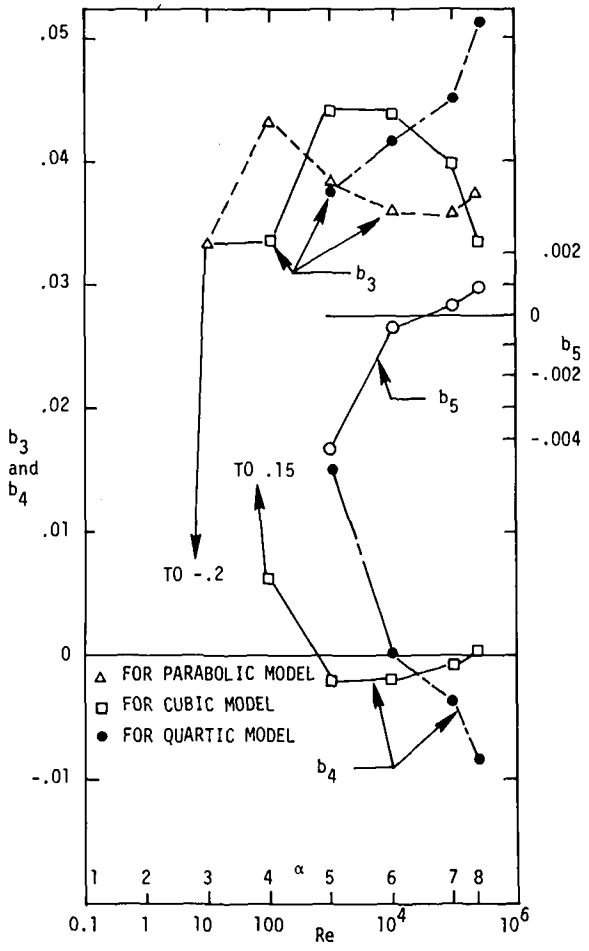

Fig. 2 Sequential estimates of parameters b_3, b_4, and b_5 for models for forced convection correlation example

$$A_2(1) = X_{11}P_{21}(0) + X_{12}P_{22}(0) = 1 \cdot 0 + (-1) \cdot 10^5 = -10^5$$

$$K_1(1) = A_1(1)/\Delta(1) = 10^5/200{,}001 = 0.4999975$$

$$K_2(1) = -0.4999975, \quad e_1 = Y_1 - \eta_1 = -0.34679$$

$$H(1) = X_{11}[b_1^{(1)}(0) - b_1^{(0)}(n)] + X_{12}[b_2^{(1)}(0) - b_2^{(0)}(n)] = 0$$

$$b_1^{(1)}(1) = b_1^{(1)}(0) + K_1(1)[e_1 - H(1)]$$
$$= 0.4999975\,(-0.34679) = -0.17339$$

$$b_2^{(1)}(1) = b_2^{(1)}(0) + K_2(1)[e_1 - H(1)] = 0.17339$$

$$P_{11}(1) = 50{,}000.25 = P_{22}(1), \quad P_{12}(1) = P_{21}(1) = 49{,}999.75$$

The calculation would proceed for $\alpha = 2, \ldots, 8$, after which, for nonlinear problems, another iteration would begin by setting $k = 1$ and starting with $\alpha = 1$ and so on. The iterations on k would continue until negligible change occurred in the parameters.

Further values of b_1 and b_2 as a function of Re or α are given in Fig. 1 for linear, parabolic, cubic, and quartic models formed from equation (22). Fig. 2 depicts values for b_3, b_4, and b_5. Conclusions drawn from these figures demonstrate some further advantages of sequential analysis. First, one can readily answer the question of the effect of the use of less data, which answer should help one to anticipate the effect on the parameters if *more* similar data should become available. By similar data is meant additional measurements at later times from the *same* experiment. (If one uses concepts of statistical design [6, 8] to select additional measurements, then this conclusion may not be valid.)

A second and very important advantage of the sequential method is for aiding in selecting the "best" model, sometimes called model-building. Statistical procedures, including the F-test, could also be used [1–6]. The method to be described does not require knowledge of the statistics of the measurement errors, however. First, observe that the parameters b_1 and b_2 for the linear model ($\eta = \beta_1 + \beta_2 t$), shown as crosses in Fig. 1, reveal definite trends with α; for example, $b_2(\alpha)$ continually increases with α. Hence, the linear model is not satisfactory. For the parabolic model ($\eta = \beta_1 + \beta_2 t + \beta_3 t^2$) the parameter estimates b_1, b_2, and b_3 are relatively constant for $\alpha = 3$ and greater; see Figs. 1 and 2. (In order to find p parameter values, at least p data points are required. Although the sequential method gives values of the parameters for $\alpha < p$, the values are dependent.) For the cubic model, the parameter estimates shown by squares in Figs. 1 and 2 are relatively stable with α for b_1, b_2, and b_3, but b_4 starts positive, goes negative, and then becomes positive again. The quartic model is even more variable in the parameters than is the cubic model.

The only satisfactory model of those investigated is the parabolic one ($p = 3$), which can be written

$$\log \mathrm{Nu} = \beta_1 + \beta_2 \log \mathrm{Re} + \beta_3 \log \mathrm{Re}\,(\log \mathrm{Re}) \quad \text{or}$$

$$\mathrm{Nu} = A\,\mathrm{Re}^{\beta_2 + \beta_3 \log \mathrm{Re}}$$

where $\beta_1 = \log A$. Using the estimates of the parameters for $\alpha = 7$ and 8 yields, respectively,

$$\mathrm{Nu} = 0.845\,\mathrm{Re}^{0.314 + 0.0358 \log \mathrm{Re}}$$

$$\mathrm{Nu} = 0.840\,\mathrm{Re}^{0.308 + 0.0379 \log \mathrm{Re}} \qquad (a)$$

A comparison of these two equations suggests that it is not appropriate

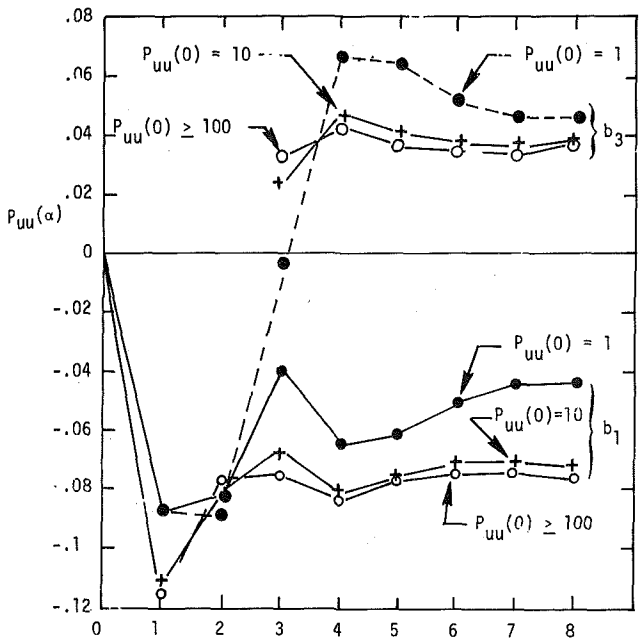

Fig. 3 Sequential values for $P_{uu}(\alpha)$ for various values of $P_{uu}(0)$ for forced convection correlation example

to give the constants to three significant figures since there are changes in the second one.

It is instructive to compare the Nu values given by (a) with the commonly used equation [9, p. 260]

$$\text{Nu} = B\,\text{Re}^n \qquad (b)$$

which is also for gases. There are five regions of Re, so there are five B's and n's or a total of ten parameters. Comparison of the values given by equations (a) and (b) with the recommended values can be made using Table 1. The equation (a) values differ less than 5.6 percent and the (b) values by less than 8.7 percent. Doubtless equation (b) values could be made to agree closer to the recommended values. If, however, the objective is to best fit (in a relative sense) the McAdams values over the entire range by using a minimum number of parameters, equation (a) with a reduced number of significant figures is recommended in preference to equation (b).

For no prior information, as in this example, the initial **P** matrix should have diagonal components $P_{uu}(0)$ such that $P_{uu}(0) \gg (b_u(n))^2$. This is true in this example since $P_{uu}(0)$ is taken to be 10^5 for $u = 1, \ldots, p$ and $(b_u(n))^2$ is less than unity for all u values. Much smaller $P_{uu}(0)$ values could be used, however. Fig. 3 shows sequential values of $P_{uu}(\alpha)$ for parameters 1 and 3 for initial $P_{uu}(0)$ values of 1, 10, and equal to and greater than 100. There are negligible changes in $P_{uu}(\alpha)$ for initial values greater than 100 in this example. This corresponds to $P_{22}(0)$ being about 1000 times greater than $(b_2(n))^2$. The final parameter estimates (those using all the data) would be almost identical to those using the usual least squares method. However, in that case the sequential information would not have been gained and up to five simultaneous algebraic equations would also have to be solved.

From other studies, such as shown by Fig. 3, it has been repeatedly found that a large range of values of M_u in equation (21) can be used. A value of $M_u = 10^4(b_u(n))^2$ is usually sufficiently large and values up to 10^8 are permissible if the computer uses at least twelve significant figures in the calculations. Larger values are not recommended because subtraction of nearly equal large numbers can occur in equation (20g).

Cooling Billet Example

A parameter estimation example that is nonlinear involves a cooled body having negligible internal thermal resistance. A solid copper cylinder 0.046 m long and .0254 m in diameter was heated to 411 K and allowed to cool in open air. The describing differential equation is

Table 2 Data for cooling billet example

Time, t (sec)	Temperature, Y K	Residuals Y - $\hat{\eta}$, K
0	410.70	
96	402.52	-.02
192	395.11	.03
288	388.32	.06
384	382.14	.14
480	376.06	-.21
576	370.85	-.16
672	366.13	-.06
768	361.84	.09
864	357.84	.16
960	354.06	.14
1056	350.60	.13
1152	347.06	-.22
1248	344.20	-.14
1344	341.59	-.03
1440	339.14	.03
1536	336.86	.07

$$\rho c V \frac{dT}{dt} = hA(T_\infty - T) \qquad (23)$$

where ρ is density, c is specific heat, V is volume, h is heat transfer coefficient, A is surface area, T is temperature, t is time, and T_∞ is the ambient temperature. Measurements of T_∞ indicate that it was relatively constant at 300.6 K.

The only parameter of interest in (23) is h, which is found to vary with time. For simplicity let $hA/\rho cV$ be modeled by

$$hA/\rho cV = \beta_1 + \beta_2 t + \beta_3 t^2 \qquad (24)$$

which when introduced in equation (23) yields the model

$$(T(t) - T_\infty)/(T_0 - T_\infty) = \exp\left[-\beta_1 t - \beta_2 t^2/2 - \beta_3 t^3/3\right] \qquad (25)$$

with T_0 being the initial temperature. Notice that although equation (23) is a linear differential equation, the dependent variable T is not linear in terms of the parameters β_1, β_2, and β_3.

In order to estimate the parameters it is necessary to choose a function to minimize. This should depend upon what is known regarding the measurements given in Table 2. These were obtained using the same thermocouple and amplification throughout the temperature range; thus, the accuracy of all the measurements can be considered equal. Lacking prior information regarding the parameters and information relative to correlation in the measurements, it is reasonable to use ordinary least squares (OLS) estimation. This means that T in equation (25) is to be η. (If the *relative* errors in T were nearly constant, then it would be appropriate to take the natural logarithm of equation (25) and reduce the problem to a linear estimation problem.)

The sensitivity coefficients are found from equation (25) to be

$$X_{uj} = \partial T_u/\partial\beta_j = -(T_0 - T_\infty)(t_u{}^j/j) \times \exp\left(-\beta_1 t_u - \beta_2 t_u{}^2/2 - \beta_3 t_u{}^3/3\right) \qquad (26)$$

where $j = 1$ for β_1, $j = 2$ for β_2, and $j = 3$ for β_3.

In order to start the iterative procedure for finding β_1 (with $\beta_2 = \beta_3 = 0$), an initial value of β_1 is needed. This can readily be found in the example by using any measurement other than at $t = 0$. Initial estimates of β_2 and β_3 can be found from observing the sequential behavior of β_1.

Sequential results are given in Figs. 4 and 5 for the converged iteration (on k) for the three models:

Model 1: $hA/\rho cV = \beta_1$

Model 2: $hA/\rho cV = \beta_1 + \beta_2 t$

Model 3: $hA/\rho cV = \beta_1 + \beta_2 t + \beta_3 t^2$

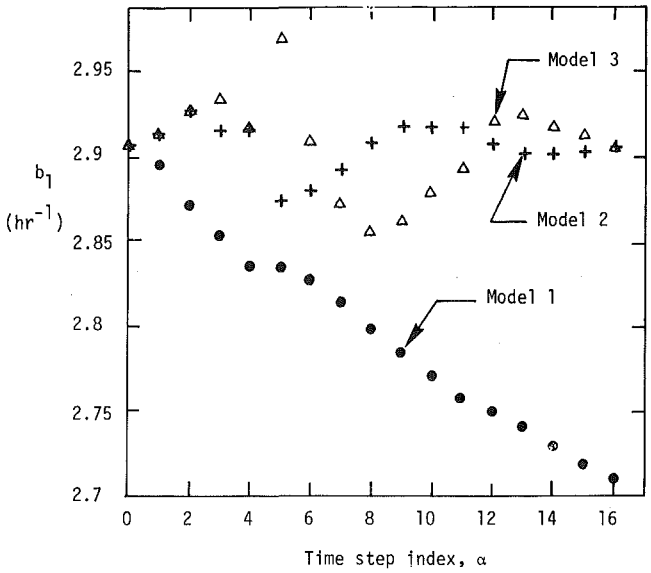

Fig. 4 Estimates of β_1 for models 1, 2, and 3 for the cooling billet data

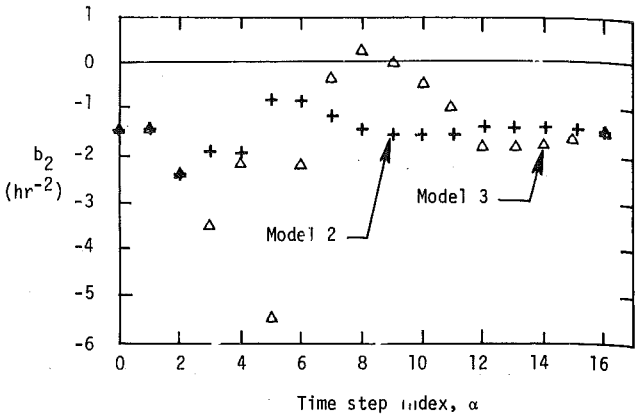

Fig. 5 Estimates of β_2 for models 2 and 3 for the cooling billet data

In each case large values of $P_{ii}^{(0)}(0)$ were chosen to start the sequential procedure. Conclusions that can be drawn from Figs. 4 and 5 are similar to those of the previous case. For example, Model 1 is not satisfactory due to the systematic decrease in $b_1(\alpha)$. Model 2 is good because $b_1(\alpha)$ and $b_2(\alpha)$, shown in Fig. 5, are quite constant for the last half of the α-values. There is some variability in Figs. 4 and 5 for Model 3, but there are large fluctuations in $b_3(\alpha)$; for example, the $b_3(\alpha)$ values for $\alpha = 5, 8, 13$, and 16 are, respectively, 37.8, −8.7, 1.6, and .07. Model 2 is clearly superior to the other two.

Another way to investigate the adequacy of a proposed model is to inspect the residuals, $Y_i - Y_i$, where Y_i is the η_i value found using the converged parameter values. A more or less random set of residuals should be obtained, with some being positive and others negative. Such a set of residuals is given for Model 2 in the third column of Table 2. Because the residuals appear to be random and small, confirmation of Model 2 is provided. The analysis of the residuals is important both for model-building and specification of confidence regions. Quantitative analyses of residuals is possible such as that given by $\hat{\psi}_{st}$ expression in the following equation (1). (This expression requires repeated measurements, however.) There are also tests for correlations in the residuals such as the run test [4, 5]; the use of automatic digital data acquisition equipment can result in many closely spaced measurements which tend to be highly correlated.

Many other models for hA/pcV could be proposed. These include temperature dependence and the use of shorter time segments [10].

From the time variation of b_1 and b_2 one can also extract some feeling of the precision of the estimated values of hA/pcV. One can do better than this by utilizing the converged components of $P_{ij}(n)$ which is related to the covariance matrix of the parameter estimates, provided certain statistical assumptions are valid. This important subject is left for later papers but some discussion is given in references [1, 3–6].

Final Comments

Due to space limitations a number of aspects of this subject had to be severely restricted or omitted. Some of these will be developed in subsequent papers. One of these in particular relates to estimation of parameters appearing in partial differential equations. Another includes examples using more statistical information regarding both measurement errors and prior information concerning the parameters. Statistical analysis of the accuracy of estimates as indicated by parameter confidence regions also had to be omitted but is an important subject.

Acknowledgment

This research was supported by the National Science Foundation under Grant No. GK-41495. The author also appreciates discussions with Professor C. R. St. Clair, Jr., on this problem.

References

1 Bard, Y., *Nonlinear Parameter Estimation,* Academic Press, New York, 1974.

2 Seinfeld, J. H., and Lapidus, L., *Mathematical Methods in Chemical Engineering, Vol. 3, Process Modeling, Estimation, and Identication,* Prentice-Hall, Inc., Englewood Cliffs, N. J., 1974.

3 Bevington, P. R., *Data Reduction and Error Analysis for the Physical Sciences,* McGraw-Hill, New York, 1969.

4 Himmelblau, D. M., *Process Analysis by Statistical Methods,* Wiley, New York, 1970.

5 Draper, N. R., and Smith, H., *Applied Regression Analysis,* Wiley, New York, 1966.

6 Beck, J. V., and Arnold, K., *Parameter Estimation in Engineering and Science,* to be published by Wiley, New York, 1977.

7 Hunter, W. G., "Estimation of Unknown Constants From Multiresponse Data," *I & EC Fundamentals,* Vol. 6, 1967, pp. 461–463.

8 Draper, N. R., and Hunter, W. G., "The Use of Prior Distributions in the Design of Experiments for Parameter Estimation in Non-Linear Situations," *Biometrika,* Vol., 54, 1967, pp. 147–153.

9 McAdams, W. H., *Heat Transmission,* Third ed., McGraw-Hill, New York, 1953, p. 259.

10 Beck, J. V., "Determination of Optimum, Transient Experiments for Thermal Contract Conductance," *International Journal of Heat and Mass Transfer,* Vol. 12, 1969, pp. 621–633.

11 Graupe, D., *Identification of Systems,* Van Nostrand Reinhold Co., New York, 1972.

12 Graybill, F. A., *Introduction to Matrices With Applications to Statistics,* Wadsworth Publishing Co., Belmont, Calif., 1969.

13 Wendroff, B., *Theoretical Numerical Analysis,* Acad. Press, New York, 1966.

APPENDIX A

Matrix Inversion Lemma

Using matrix notation and dropping the k index, equation (14) can be written as

$$\mathbf{P}(\alpha) = [(\mathbf{P}[\alpha - 1])^{-1} + \mathbf{X}_\alpha^T \mathbf{W}_\alpha \mathbf{X}_\alpha]^{-1} \quad \text{(A-1)}$$

and can be shown [6, 11] to be equal to

$$\mathbf{P}(\alpha) = \mathbf{P}(\alpha - 1) - \mathbf{P}(\alpha - 1)\,\mathbf{X}_\alpha^T \times [\mathbf{W}_\alpha^{-1} + \mathbf{X}_\alpha \mathbf{P}(\alpha - 1)\mathbf{X}_\alpha^T]^{-1}\mathbf{X}_\alpha \mathbf{P}(\alpha - 1) \quad \text{(A-2)}$$

which is valid for $\mathbf{X}_\alpha$ being an $m \times p$ matrix. For the case at hand, $m = 1$ and the inverse in the brackets of equation (A-2) is a scalar; for this case equation (A-2) becomes

$$\mathbf{P}(\alpha) = \mathbf{P}(\alpha-1) - \mathbf{P}(\alpha-1)\mathbf{X}_\alpha{}^{\mathrm{T}}\mathbf{X}_\alpha\mathbf{P}(\alpha-1)/\Delta(\alpha) \quad \text{(A-3}a\text{)}$$

$$\Delta(\alpha) = w_\alpha{}^{-1} + \mathbf{X}_\alpha\mathbf{P}(\alpha-1)\mathbf{X}_\alpha{}^{\mathrm{T}} \quad \text{(A-3}b\text{)}$$

which is called the matrix inversion lemma.

Another relation that can be derived for $m = 1$ is

$$\mathbf{P}(\alpha)\mathbf{X}_\alpha{}^{\mathrm{T}}w_\alpha = \mathbf{P}(\alpha-1)\mathbf{X}_\alpha{}^{\mathrm{T}}/\Delta_\alpha \quad \text{(A-4)}$$

APPENDIX B

Transformation to Make Weighting Matrix Diagonal

In maximum likelihood estimation for the statistical assumptions of additive, zero mean gaussian errors, the matrix $\mathbf{W}$ is the inverse of the matrix ψ which is the variance-covariance matrix of the measurement errors. ψ is symmetric and positive definite. From [12, p. 190], ψ can be given in terms of a unique lower real triangular matrix $\mathbf{L}$ with $\ell_{ii} = 1$ such that

$$\psi = \mathbf{L}\phi\mathbf{L}^T \quad \text{(B-1)}$$

where ϕ is a real diagonal matrix. The inverse of ψ (which exists since it is positive definite) is

$$\psi^{-1} = (\mathbf{L}^{-1})^{\mathrm{T}}\phi^{-1}\mathbf{L}^{-1} \quad \text{(B-2)}$$

Also from [12, p. 190], the inverse of a lower triangular matrix $\mathbf{L}$ is a lower triangular matrix.

The matrix form of equation (8) is

$$\mathbf{b}^{(k+1)} = \mathbf{b}^{(k)} + \mathbf{P}^{(k)}\left[\mathbf{X}T_{(k)}\mathbf{W}(\mathbf{Y} - \eta^{(k)}) + \mathbf{U}(\mu - \mathbf{b}^{(k)})\right] \quad \text{(B-3}a\text{)}$$

where

$$\mathbf{P}^{(k)} = [\mathbf{X}T_{(k)}\mathbf{W}\mathbf{X}^{(k)} + \mathbf{U}]^{-1} \quad \text{(B-3}b\text{)}$$

Consider now terms in equation (B-3) which involve $\mathbf{W}$. For convenience omit the iteration index k. Since $\mathbf{W} = \psi^{-1}$, (B-2) permits writing

$$\mathbf{X}^T\mathbf{W}(\mathbf{Y} - \eta) = \mathbf{X}^T(\mathbf{L}^{-1})^T\phi^{-1}\mathbf{L}^{-1}(\mathbf{Y} - \eta)$$
$$= (\mathbf{L}^{-1}\mathbf{X})^T\phi^{-1}(\mathbf{L}^{-1}\mathbf{Y} - \mathbf{L}^{-1}\eta) = \mathbf{X}^T\phi^{-1}(\mathbf{Y} - \eta) \quad \text{(B-4}a\text{)}$$

where

$$\mathbf{X} = \mathbf{L}^{-1}\mathbf{X}, \quad \mathbf{Y} = \mathbf{L}^{-1}\mu, \quad \eta = \mathbf{L}^{-1}\eta$$

Similarly the $\mathbf{X}^T\mathbf{W}\mathbf{X}$ term in equation (A-3b) can be written

$$\mathbf{X}^T\mathbf{W}\mathbf{X} = \mathbf{X}^T\phi^{-1}\mathbf{X} \quad \text{(B-4}b\text{)}$$

where in both equations (B-4a) and (B-4b), ϕ^{-1} has the former role of $\mathbf{W}$ but ϕ^{-1} is always diagonal.

Let the nonzero and off-diagonal components of $\mathbf{L}^{-1}$ be designated ℓ_{ij} so that

$$\tilde{Y} = L^{-1}Y = \begin{bmatrix} 1 & & & \\ l_{21} & 1 & & \\ \cdot & \cdot & & \\ \cdot & \cdot & & \\ \cdot & \cdot & & \\ l_{n1} & l_{n2} & \cdots & 1 \end{bmatrix} \begin{bmatrix} Y_1 \\ Y_2 \\ \cdot \\ \cdot \\ \cdot \\ Y_n \end{bmatrix} = \begin{bmatrix} Y_1 \\ l_{21}Y_1 + Y_2 \\ \cdot \\ \cdot \\ \cdot \\ \sum_{i=1}^{n} l_{ni}Y_i \end{bmatrix} \quad (B\text{-}5)$$

This equation means that modified measurements $\tilde{\mathbf{Y}}_t$ can be found such that $\tilde{\mathbf{Y}}_t$ is composed only of components of Y_i given by $Y_1, Y_2, \ldots, Y_t$. No *future* mesurements are needed.

Hence by decomposing ψ into triangular matrices as indicated by equation (B-1), it is possible to obtain sequential estimators that in effect allow $W_{st} \neq 0$ for $s \neq t$. That is, $\mathbf{W}$ is replaced by the diagonal matrix ϕ^{-1}, $\mathbf{Y}$ by $\mathbf{Y}$, η by η and $\mathbf{X}$ by $\mathbf{X}$. The lower triangular matrix $\mathbf{L}$ can be obtained using a modification of the Choleski decomposition [13, p. 126]. (A modification is needed because Wendroff [13] gives an algorithm for $\phi = \mathbf{I}$ and $\mathbf{L}$ not having unity values down the main diagonal.)

R. L. Levin[2]
NSF and Health Sciences Fund Graduate Fellow,
Research Affiliate,
Cryogenic Engineering Laboratory,
Department of Mechanical Engineering.
Assoc. Mem. ASME.

E. G. Cravalho
Professor,
Cryogenic Engineering Laboratory,
Department of Mechanical Engineering.
Associate Dean,
School of Engineering.
Mem. ASME.

Massachusetts Institute of Technology,
Cambridge, Mass.

C. E. Huggins
Chief,
Low Temperature Surgical Unit and Director,
Blood Bank and Transfusion Service,
Massachusetts General Hospital,
Boston, Mass.

Diffusion Transport in a Liquid Solution With a Moving, Semipermeable Boundary[1]

A one-dimensional model has been developed for diffusion transport in a binary liquid solution with a moving semipermeable boundary. The governing equations are basically Fick's First and Second Laws in which the solute concentrations are replaced by the logarithms of the solute volume fractions. In the limit of negligible solute volume fraction, the analysis reduces to the classical one-dimensional diffusion equation. The complete form has been employed to describe the concentration polarization of solutes within human erythrocytes during freezing. The results show that the water transport process across the cell membrane is significantly affected by both the water permeation characteristics of the membrane and the diffusion of water within the intracellular medium. These results are consistent with experimental observations of red cell survival during freezing.

Introduction

In the engineering and biological sciences, there exist a number of important applications involving the diffusion of one specie relative to another in a binary solution system bounded by a movable semipermeable membrane. These situations, which include the osmotic behavior of biological cells, the zone-refining of metals, and the separation of salt-water solutions by freezing, can all be described by a single model. The present work develops that model for the one-dimensional case in the context of the osmotic behavior of biological cells and is the second in a series of five articles dealing with the osmotic behavior of human erythrocytes during freezing [1–4].[3]

In considering the shrinking and swelling of biological cells during osmotic experiments, it has generally been assumed that the cell membrane is the main barrier to the entry or exit of water. Although this theory has its merits, we will show that the rate of water movement into and out of cells may be controlled not only by the movement of water through the cell membranes, but also by the movement of water within the intracellular and extracellular solutions. As water leaves (enters) the cell, solutes accumulate (are depleted) at the internal surface of the cell membrane, thereby reducing (increasing) the local water molar fraction at that point compared with the average water molar fraction inside the cell. The outward (inward) flow of water also decreases (increases) the amount of solute present at the external surface, thereby increasing (decreasing) the local water molar fraction at points near the external surface of the cell membrane compared with the average water molar fraction of the extracellular solution. Consequently, as shown in Fig. 1, the actual driving force for water transport will be smaller than the value obtained when the average intracellular and extracellular water molar fractions are used.

$$\frac{\Delta c_{s\,\text{actual}}}{\Delta c_{s\,\text{avg}}} < 1 \tag{1}$$

This type of physical phenomenon is termed "concentration po-

[1] This work was supported in part by the Biomaterials Science Program. Project Grant H05 P01 HL-14322 funded by the National Heart and Lung Institute under the Harvard-MIT Program in Health Sciences and Technology.

[2] Present position, Research Fellow, Biophysical Laboratory, Harvard Medical School, Boston, Mass.

[3] Numbers in brackets designate References at end of paper.

Contributed by the Heat Transfer Division for publication in the JOURNAL OF HEAT TRANSFER. Manuscript received by the Heat Transfer Division May 17, 1976.

larization" and has been considered by many investigators [5–8] studying the permeability of cell membranes to water under osmotic flow conditions. The general approach has been to model the solute concentration profile on either side of the cell membrane as an unstirred layer of constant thickness δ in series with the actual membrane. Under these circumstances, an apparent membrane water conductivity $\bar{k}_{app}$ can be defined such that [9, p. 105]

$$\frac{1}{\bar{k}_{app}} = \frac{1}{\bar{k}_m} + \frac{\delta^I}{D_{sw}{}^I} + \frac{\delta^0}{D_{sw}{}^0} \tag{2}$$

where $\bar{k}_m$ is the "true" water conductivity of the cell membrane, δ^I and δ^0 are the unstirred layer thickness at, respectively, the intracellular solution-membrane and extracellular solution-membrane interfaces, and $D_{sw}{}^I$ and $D_{sw}{}^0$ are, respectively, the solute-water mutual diffusion coefficients in the intracellular and extracellular solutions. Inspection of this equation shows that when

$$\bar{k}_m \ll \frac{D_{sw}{}^I}{\delta^I} + \frac{D_{sw}{}^0}{\delta^0} \tag{3}$$

then

$$\bar{k}_{app} \simeq \bar{k}_m \tag{4}$$

and the apparent water conductivity of the cell membrane will be close to its true value. On the other hand, when

$$\bar{k}_m \gg \frac{D_{sw}{}^I}{\delta^I} + \frac{D_{sw}{}^0}{\delta^0} \tag{5}$$

then

$$\bar{k}_{app} \simeq \frac{D_{sw}{}^I}{\delta^I} + \frac{D_{sw}{}^0}{\delta^0} \tag{6}$$

That is, when the true cell water conductivity is large, the transport of water across the cell membrane will be rate-limited by its diffusion through the unstirred layers. On the basis of such an argument, many authors have concluded that the water conductivity of a cell membrane measured under osmotic flow conditions will in general be underestimated because of the presence of unstirred layers at the inner and outer surfaces of the cell membrane.

There are two major difficulties associated with applying the "unstirred layer" hypothesis to the shrinking and swelling of biological cells. The first is that it is almost impossible to obtain reliable estimates of the thicknesses of the unstirred layers [9, pp. 104–114]. Consequently, in order to determine the amount of water retained within cells during an osmotic experiment, one must "guess" at a reasonable value for the thicknesses of the unstirred layers before applying the diffusion equations describing the nonsteady-state transport of water through the intracellular and extracellular media and the cell membrane [10]. Secondly, and even more significant, is that the concept of an unstirred layer of constant thickness is in itself only an approximation to the real physical situation, namely, the phenomenon of the concentration polarization of solutes at the internal and external surfaces of the cell membrane.

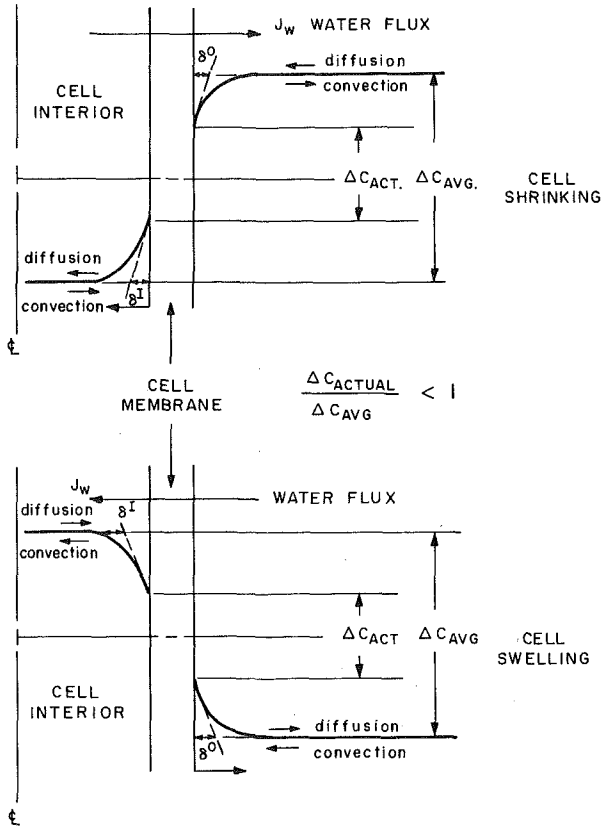

Fig. 1 Effects of concentration polarization during an osmotic experiment

Nomenclature

A_c = cell surface area
a = activity
B = cooling rate
c = molar concentration
D = diffusivity
d_c = cell diameter
F = Faraday constant (96,486.9 C/mol)
$\underline{J}$ = flux
k = cell membrane permeability
$\bar{k}$ = cell membrane conductivity
$\bar{k}_{T_g}$ = cell membrane conductivity at temperature T_g
L = characteristic length
ℓ_c = cell half-thickness
m = molality
N = number of molecules
N_A = Advogadro's number (6.023×10^{23} mol^{-1})
R = universal gas constant (8.314 J/mol k or 1.987 cal/mol K)
$\underline{r}$ = position
s = solute
T = temperature
T_g = reference temperature (293.15 K)
t = time
t^* = nondimensional time
$\underline{u}$ = velocity
V = volume
V_c = cell volume
v = characteristic velocity
$\bar{v}$ = apparent molar volume
w = water
x = mole fraction
y = position
y^* = nondimensional position
z = valence
γ = activity coefficient
δ = unstirred layer thickness
η = viscosity
ν = number of species per molecule
ξ = rational friction coefficient
σ = frictional interaction parameter
τ = time constant
ϕ = volume fraction
ψ = electrostatic potential
μ = chemical potential
$\bar{\mu}$ = electrochemical potential

Subscript

app = apparent
i = ith process or species
j = jth process or species
m = membrane
m = solute mixture
0 = initial or isotonic
s = solute or solute-fixed frame of reference
v = volume-fixed frame of reference
w = water

Superscript

I = intracellular
0 = extracellular
s = solute-fixed frame of reference
v = volume-fixed frame of reference

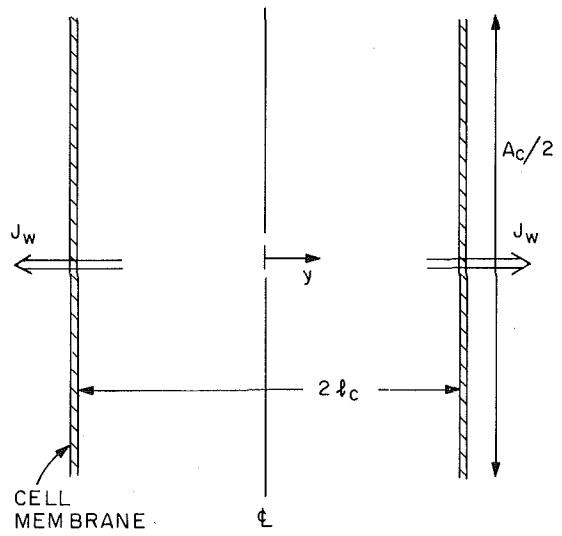

Fig. 2 One-dimensional representation of a cell

In reality, the concentration polarization of solutes depends upon the rate of the water flux through the cell membrane relative to the rates of diffusion of solutes within the intracellular and extracellular solutions. If the actual driving force for water transport is smaller than the value obtained using the average intracellular and extracellular concentrations, then,

$$\frac{J_{w)\text{act}}}{J_{w)\text{avg}}} = \frac{\Delta c_{s)\text{act}}}{\Delta c_{s)\text{avg}}} < 1 \tag{7}$$

since $J_w = \bar{k}\Delta c_s$ where $\bar{k} \equiv \bar{k}_m$ which can be assumed to be dependent upon temperature alone. Hence, the flux of water leaving (entering) the cell will be smaller for the case of solute polarization and more (less) water should remain within the cell at any given time during the shrinking (swelling) process. However, the lower the flux, the lower will be the amount of polarization. We are then confronted with a very complicated feedback mechanism in which the flux influences the amount of polarization and vice versa. All of these phenomena occur in a system in which the properties of the solution and the size of the cell are constantly changing. We will therefore model the concentration polarization phenomenon as a dynamic physical situation in which:

1 The size of the cell changes as water enters or leaves the cell.
2 The flux of water depends upon:
a the water conductivity of the cell membrane,
b the difference between the extracellular and intracellular solute concentrations at, respectively, the external and internal surfaces of the membrane.
3 The distribution of solutes within the intracellular and extracellular solutions depends upon:
a the flux of water through the cell membrane,
b the diffusion constants of the solutes in the changing intracellular and extracellular solutions.

Description of Problem

Although most solutions of biological interest are complex salt-protein-water mixtures, let us consider the case of diffusion of a single un-ionized solvent, w (water), and a single solute, s.[4] From a biological point of view, such a system may be too simplistic; however, it will be useful for the purposes of, first, developing certain useful physical concepts and, second, understanding the physics of the polarization process without being encumbered by complicated algebraic expressions. For algebraic simplicity, we will also confine ourselves to the problem of diffusion in only one dimension and the case where no solute polarization takes place in the extracellular solution.

For the case of a one-dimensional cell such as that shown in Fig. 2, the volume of the cell V_c, is related to its surface area A_c, and thickness, $2\ell_c$, by the relation

$$V_c = (A_c/2) \cdot 2\ell_c = A_c \ell_c$$

For a constant cell surface area (A_c = constant),

$$\frac{dV_c}{dt} = A_c \frac{d\ell_c}{dt}$$

where dV_c/dt is the time rate of change of the cell volume. The cell volume is also related to the volume occupied by the membrane and the intracellular components w and s:

$$V_c = V_{\text{membrane}} + N_w \bar{v}_w + N_s \bar{v}_s$$

Where N_i and $\bar{v}_i$ are, respectively, the number of moles and partial molar volumes of the ith component inside the cell ($i = w, s$). For constant partial molar volumes and a cell membrane impermeable to the solute s but permeable to the solvent w

$$\frac{dV_c}{dt} = \cancel{\frac{dV_{\text{membrane}}}{dt}}^{0} + \frac{dN_w}{dt}\bar{v}_w + \cancel{\frac{dN_s}{dt}}^{0}\bar{v}_s$$

$$\frac{dV_c}{dt} = \bar{v}_w \frac{dN_w}{dt} = \frac{dV_w}{dt} = -\bar{v}_w J_w \cdot A_c$$

where J_w is the flux of water *out of* the cell. Combining equations (9) and (11), we find

$$\frac{d\ell_c}{dt} = -\bar{v}_w \cdot J_w \tag{12}$$

That is, the thickness of the cell decreases as water leaves the cell and increases as water enters the cell. Since we are assuming that the cell membrane is impermeable to solutes, the total amount of solute within the cell is constant

$$N_s = \frac{1}{\bar{v}_s}\int_{V_c} \phi_s(\underline{r}, t)dV_c = \text{constant} \tag{13}$$

where ϕ_s is the volume fraction of solute within the cell. Hence, for our one-dimensional case

$$\phi_{s)0} \cdot \ell_{c0} = \int_0^{\ell_c(t)} \phi_s(y, t)dy \tag{14}$$

where ℓ_{c0} is the initial cell half-thickness. Consequently, to describe the polarization phenomena we must develop a set of transport equations which takes into account not only the change in cell size during an osmotic experiment, but also the constancy of the number of moles of solutes inside the cell.

Transport Equations

Mole Fractions, Molar Concentrations, Volume Fractions. In the present work we shall be concerned with aqueous solutions which are in motion with respect to an external, laboratory-fixed set of coordinate axes. The center of the cell will be considered to be fixed at the origin in the laboratory reference frame.

A volume element dV of the solution may be located by the position vector $\underline{r}$ in the external coordinate system. The composition of this volume element dV at a time t may be given in terms of either the mole fractions x_i, the molar concentrations c_i, or the volume fractions ϕ_i of each of the components. These quantities for dV at time t are related by the following expressions for a binary solution:

Mole Fractions.

$$x_w + x_s = 1 \tag{15a}$$

and

$$dx_w + dx_s = 0 \tag{15b}$$

[4] Since the diffusion of ions of an electrolyte is restricted by the condition of electric neutrality, it is permissible to treat the partial volumes, concentrations, etc., as those of the electrolyte as a whole without considering the ν_s moles of ions per molecule as separate ionic quantities.

Molar Concentrations.

$$c_i = \frac{1}{\nu_i} x_i c \qquad i = w, s \tag{16}$$

and

$$c_w + \nu_s c_s = c \tag{17}$$

Volume Fractions.

$$\phi_i = c_i \bar{v}_i \qquad i = w, s \tag{18}$$

where

$$\phi_w + \phi_s = 1 \tag{19a}$$

and

$$d\phi_w + d\phi_s = 0 \tag{19b}$$

or for constant partial molar volumes

$$\bar{v}_w dc_w + \bar{v}_s dc_s = 0 \tag{20}$$

Furthermore, it can be shown that

$$x_w = \frac{\phi_w}{\phi_w + \dfrac{\nu_s \bar{v}_w}{\bar{v}_s}\phi_s} \quad \text{or} \quad \phi_w = \frac{x_w}{x_w + \dfrac{\bar{v}_s}{\bar{v}_w \nu_s} x_s} \tag{21}$$

and

$$\frac{\partial \ln c_w}{\partial \ln x_w} = \frac{\bar{v}_s c_w}{\nu_s x_w} \quad \text{or} \quad \frac{\partial \ln c_s}{\partial \ln x_s} = \frac{\bar{v}_w \nu_s c_s}{x_s} \tag{22}$$

Flows. The material currents in a solution may be described in terms of the local mean velocity $\underline{u}_i$ for each component i. The velocity $\underline{u}_i$ does not refer to the velocity of a particular molecule of i. Rather, it refers to the average velocity with respect to the external coordinate system of the molecules of i in a microscopically large, macroscopically small region of the solution. Thus, the local mean velocity $\underline{u}_i$ is a field quantity and is a function of position and time, $\underline{u}_i(r, t)$. The velocity $\underline{u}_v$ of the local center of volume may be defined by the relation

$$\underline{u}_v = \sum_i \phi_i \underline{u}_i \tag{23}$$

The velocity $\underline{u}_v$ will, in general, vary with position $\underline{r}$ and time t. A coordinate system fixed relative to the local center of volume in one part of a fluid system will usually move with respect to a coordinate system fixed relative to the local center of volume in another part of the fluid system.

The molar current density or mole flux $\underline{J}_i$ of component i relative to the external coordinate axes is

$$\underline{J}_i = c_i \underline{u}_i \tag{24}$$

The flux $\underline{J}_i$ is the number of moles of component i crossing a plane of unit area in unit time when the plane is fixed relative to the external coordinate system and is oriented normal to the local mean velocity $\underline{u}_i$.

The diffusion current density $\underline{J}_i{}^v$ of component i relative to the local center of volume is defined as

$$\underline{J}_i{}^v = c_i(\underline{u}_i - \underline{u}_v) \tag{25}$$

The molar current density $\underline{J}_i$ is related to the diffusion current density $\underline{J}_i{}^v$ through equations (18, 23–25):

$$\underline{J}_i{}^v = \underline{J}_i - c_i \sum_i \bar{v}_i \underline{J}_i \tag{26}$$

The fluxes $\underline{J}_i{}^v$ are not all independent. Multiplication of equation (26) by $\bar{v}_i$ and summation over i yield

$$\sum_i \bar{v}_i \underline{J}_i{}^v = 0 \tag{27}$$

or for the case of a binary solution

$$\bar{v}_w \underline{J}_w{}^v + \bar{v}_s \underline{J}_s{}^v = 0 \tag{28}$$

For the case of solute polarization within a cell during shrinking and swelling, however, we are more concerned with the flow in a frame of reference fixed with respect to the volume of solute within the cell. Now the diffusion current density $\underline{J}_w{}^s$ of component w relative to component s is defined by the relation

$$\underline{J}_w{}^s = c_w(\underline{u}_w - \underline{u}_s) \tag{29}$$

where $\underline{u}_w$ and $\underline{u}_s$ are, respectively, the local mean velocities of components w and s. The flux $\underline{J}_s{}^s$ is zero:

$$\underline{J}_s{}^s = 0 \tag{30}$$

The flux $\underline{J}_w{}^s$ is related to $\underline{J}_w$ and $\underline{J}_s$ by

$$\underline{J}_w{}^s = \underline{J}_w - \frac{c_w}{c_s}\underline{J}_s \tag{31}$$

and to $\underline{J}_w{}^v$ and $\underline{J}_s{}^v$ by

$$\underline{J}_w{}^s = \underline{J}_w{}^v - \frac{c_w}{c_s}\underline{J}_s{}^v = \frac{1}{\phi_s}\underline{J}_w{}^v \tag{32}$$

Fick's First Law. For quasistationary, isothermal, isobaric diffusion processes, the partial equations of motion of Bearman and Kirkwood [11] reduce to the simple form

$$\nabla \bar{\mu}_i = -\sum_j \nu_j c_j \xi_{ij}(\underline{u}_i - \underline{u}_j) \tag{33}$$

where $\bar{\mu}_i$ is the electrochemical potential of specie i

$$\bar{\mu}_i = \mu_i^*(T, p) + RT \ln a_i + z_i F \psi \tag{34}$$

such that a_i is the activity of the ith species, z_i is the valence of species i, F is the Faraday constant and ψ is the electrostatic potential. The ξ_{ij}'s are friction coefficients defined such that

$$\xi_{ij} = \xi_{ji} \tag{35}$$

Hence, the gradients of the electrochemical potentials are linearly related through the friction coefficients to the relative velocities of the components.[5]

For a binary system consisting of a single un-ionized solvent ($z_w = 0$) and a single un-ionized solute ($z_s = 0$)

$$RT\nabla \ln a_w = -\nu_s c_s \xi_{ws}(\underline{u}_w - \underline{u}_s) \tag{36a}$$

$$RT\nabla \ln a_s = -c_w \xi_{sw}(\underline{u}_s - \underline{u}_w) \tag{36b}$$

and

$$\xi_{sw} = \xi_{ws} \tag{37}$$

For diffusion in only one dimension

$$\nabla \mu_w = RT \frac{\partial \ln a_w}{\partial y} = \frac{RT}{c_w}\left(\frac{\partial \ln a_w}{\partial \ln c_w}\right)\frac{\partial c_w}{\partial y} \tag{38}$$

Equations (29), (36a), and (38) can be combined to yield

$$J_w{}^s = -\frac{1}{\nu_s c_s}\frac{RT}{\xi_{ws}}\left(\frac{\partial \ln a_w}{\partial \ln c_w}\right)\frac{\partial c_w}{\partial y} \tag{39}$$

From the Gibbs-Duhem relation it can be shown that

$$\frac{\partial \ln a_w}{\partial \ln x_w} = \frac{\partial \ln a_s}{\partial \ln x_s} \tag{40}$$

or using equation (22).

[5] It should be noted that equation (33) is just a nonstandard formulation of Onsager's nonequilibrium thermodynamic relationships [12, 13]. For convenience and physical clarity we have chosen to express the driving forces as linear functions of the fluxes/flows ($\nabla\mu_i = \sum_j R_{ij}\underline{J}_j$) instead of the more conventional method of Onsager [12, 13] who expresses the fluxes as linear functions of the forces ($\underline{J}_i = \sum_i L_{ij}\nabla\mu_j$). As pointed out by Kathchalsky and Curran [14, Chapter 8], both of these methods are equivalent and it is always possible to pass from one system of coefficients to the other by the rules of matrix algebra.

$$\frac{1}{\bar{v}_w}\left(\frac{\partial \ln a_w}{\partial \ln c_w}\right) = \frac{\nu_s}{\bar{v}_s}\left(\frac{\partial \ln a_s}{\partial \ln c_s}\right) \tag{41}$$

Substitution of equations (37) and (40) into equation (39) yields

$$J_w{}^s = -\frac{1}{\bar{v}_s c_s}\frac{RT}{\xi_{sw}}\left(\frac{\partial \ln a_s}{\partial \ln c_s}\right)\bar{v}_w\frac{\partial c_w}{\partial y} \tag{42}$$

The friction coefficients can be written

$$\xi_{ij} = \frac{N_A \sigma_{ij}\eta}{c} \tag{43}$$

where N_A is Advogadro's number, η is the viscosity of the solution and σ_{ij} is a parameter characterizing the frictional interaction between species i and j. Hence, the foregoing expression for $J_w{}^s$ can be rewritten as

$$J_w{}^s = -\frac{1}{\phi_s}\frac{RT}{N_A\sigma_{sw}\eta}c\left(\frac{\partial \ln a_s}{\partial \ln c_s}\right)\bar{v}_w\frac{\partial c_w}{\partial y} \tag{44}$$

Since $J_w{}^s = J_w{}^v/\phi_s$ then

$$J_w{}^v = -D^v\frac{\partial c_w}{\partial y} \tag{45}$$

where D^v is the mutual diffusion coefficient for a two-component system satisfying the condition of zero volume change on mixing and is defined as

$$D^v = D_{sw}c\left(\frac{\partial \ln a_s}{\partial \ln c_s}\right)\bar{v}_w = D_{sw}\left(\frac{\partial \ln a_s}{\partial \ln x_s}\right) \tag{46}$$

where

$$D_{sw} = \frac{RT}{N_A\sigma_{sw}\eta} \tag{47}$$

D^v as defined in equation (46) is commonly known as the volume diffusivity characterizing diffusion in a frame of reference where the total volume of the solution remains constant [15]. For a binary solution, the variation of D_{sw} with composition can be expressed as [16]

$$D_{sw} = \frac{\eta_w}{\eta}\cdot\left[x_w D_{sw}{}^0 + x_s D_{ww}{}^0\right] \tag{48}$$

where $D_{sw}{}^0$ is the mutual diffusion coefficient for the solute s at infinite dilution in w and $D_{ww}{}^0$ is the self-diffusion coefficient of w in pure w. Consequently, equation (46) for the volume diffusivity can be written as

$$D^v = \frac{\partial \ln a_s}{\partial \ln x_s}\cdot\frac{\eta_w}{\eta}\cdot\left[x_w D_{sw}{}^0 + x_s D_{ww}{}^0\right] \tag{49}$$

This is Hartley and Crank's expression as modified by Robinson and Stokes [17, p. 325] for the mutual diffusion coefficient of a two-component solution at any concentration. It should be noted that in general the diffusion coefficients $D_{sw}{}^0$ and $D_{ww}{}^0$ will be dependent on temperature and that the relative viscosity of the solution η/η_w will be dependent on both the temperature and composition of the solution [2].

Fick's Second Law. For our situation of diffusion in a cell fixed with respect to the volume of solute rather than the total volume of the solution, the conventional diffusion equation is not valid. However, an equation of that form can be arranged by an appropriate coordinate transformation. Let us define a modified scale of length, y^s, such that equal increments of y^s contain equal increments of unit basic volume of solute per unit area:

$$dy^s = \phi_s dy \tag{50}$$

In this solute-fixed reference frame, the water and solute concentrations must be expressed, respectively, as the amount of w and s per unit basic volume of solute

$$c_w{}^s = \frac{c_w}{\phi_s} \qquad c_s{}^s = \frac{c_s}{\phi_s} = \frac{1}{\nu_s} = \text{constant} \tag{51}$$

For an isothermal system in which no chemical reactions are occurring, the continuity equation takes the form

$$\frac{\partial c_j{}^s}{\partial t} + \underset{\sim}{\nabla}_{ys}\cdot\left(c_j{}^s\underset{\sim}{u}_j{}^s\right) = 0 \qquad j = w, s \tag{52}$$

where $\underset{\sim}{u}_j{}^s$ is the average velocity of species $j (j = w, s)$ in the solute-fixed frame of reference.[6] Since in the solute-fixed reference frame the fluxes $\underset{\sim}{J}_j{}^s$ can be defined according to equation (24), then from equation (30), it follows that

$$\underset{\sim}{J}_s{}^s = 0 \rightarrow \underset{\sim}{u}_s{}^s = 0 \tag{57}$$

That is, for a cell fixed with respect to the volume occupied by the solute and changing in size only because of the entrance or exit of solvent, there is no net solute flow across any plane fixed relative to its initial position between the center of the cell and the cell membrane.

The continuity equation (52) therefore takes the form of

$$\frac{\partial c_w{}^s}{\partial t} + \underset{\sim}{\nabla}_{ys}\cdot\underset{\sim}{J}_w{}^s = 0 \tag{58a}$$

and

$$\frac{\partial c_s{}^s}{\partial t} = 0 \tag{58b}$$

It should be noted that equations (30), (57), and (58b) are consistent in that $c_s{}^s$ = constant. Equation (51) can be written alternatively as

$$c_w{}^s = c_w/(1 - \bar{v}_w c_w) \tag{59}$$

Therefore, for constant $\bar{v}_w$ and $\bar{v}_s$

$$\frac{\partial c_w{}^s}{\partial c_w} = \frac{1}{\phi_s{}^2} \tag{60}$$

Equation (58a) together with equations (20), (55), and (60) becomes

$$\frac{1}{\phi_s}\left(\frac{\bar{v}_s}{\bar{v}_w}\right)\frac{\partial c_s}{\partial t} = \frac{\partial}{\partial y}\left[\frac{D^v}{\phi_s}\left(\frac{\bar{v}_s}{\bar{v}_w}\right)\frac{\partial c_s}{\partial y}\right] \tag{61}$$

which can be simplified to

$$\frac{\partial \ln \phi_s}{\partial t} = \frac{\partial}{\partial y}\left(D^v\frac{\partial \ln \phi_s}{\partial y}\right) \tag{62}$$

This is the basic governing equation for nonsteady-state diffusion in a system where the total volume of the solute remains constant. An interesting result is obtained for the situation in which the solvent passes through membranes impermeable to the solute. In the steady state

$$-D^v\frac{\partial \ln \phi_s}{\partial y} = \text{constant}$$

so that if D^v could be considered to be constant, the gradient of the *logarithim of the solute concentration* would be linear and hence the concentration itself would vary exponentially with distance [15].

[6] Note: (1) Velocity transformation

$$\underset{\sim}{J}_w{}^s = c_w{}^s\,\underset{\sim}{u}_w{}^s = c_w\left(\underset{\sim}{u}_w - \underset{\sim}{u}_s\right) \tag{53}$$

Hence,

$$\underset{\sim}{u}_w{}^s = \phi_s\left(\underset{\sim}{u}_w - \underset{\sim}{u}_s\right) \tag{54}$$

(2) Diffusion coefficient transformation

$$J_w{}^s = -D^s\frac{\partial c_w{}^s}{\partial y^s}\cdot = -D^v\frac{\partial c_w}{\partial y} \tag{55}$$

Hence,

$$D^s = \phi_s{}^2 D^v \tag{56}$$

For the case in which the initial isotonic concentration of solutes within the cell suspension is uniform, equation (62) is solved subject to the following boundary conditions:

1 For $t < 0$,

$$\phi_s(y, t \leq 0) = \phi_{s)0} = \text{constant} \tag{63}$$

2 Since our one-dimensional cell is symmetric about the center line $y = 0$ (see Fig. 2), for $t > 0$

$$\left.\frac{\partial \ln \phi_s}{\partial y}\right|_{y=0} = 0 \tag{64}$$

3 At the internal surface of the cell membrane, $y = \ell_c(t)$, the net flux of water within the solution, $J_w{}^s|_{\ell c}$, must be equal to the flux of water through the cell membrane, J_w. Hence, for $t > 0$

$$J_w{}^s|_{y=\ell_c} = J_w \tag{65a}$$

or

$$-D^v \left.\frac{\partial \ln \phi_s}{\partial y}\right|_{y=\ell_c(t)} + \bar{v}_w J_w = 0 \tag{65b}$$

For the case of a cell membrane which is permeable to water only, the flux J_w, representing the net flow of water out of the cell per unit area of membrane per second, is given by an expression of the form

$$J_w = k(\mu_w{}^I - \mu_w{}^0) \tag{66}$$

where $\mu_w{}^I$ and $\mu_w{}^0$ are, respectively, the chemical potential of the water at the internal and external surfaces of the cell membrane and k is the water permeability of the cell membrane. Both $\mu_w{}^I$ and $\mu_w{}^0$ are functions of the composition of intracellular and extracellular solutions immediately adjacent to the cell membrane [1], whereas k can be considered to be a function of temperature alone [18].

Thus the complex problem of diffusion transport in a liquid solution with a moving, semipermeable boundary has been reduced here to a single partial differential equation, equation (62), together with the boundary conditions, equations (63)–(65). Equation (62), describing the transport of solutes within the intracellular solution, must be solved in conjunction with equation (11), describing the cellular volume regulation, and equation (66), describing the water volume flux across the cell membrane.

Limiting Cases. Let us now consider the relative importance of the terms in the nonsteady-state diffusion equation (equation (62)). If we define, first, a characteristic velocity v for the transport of water in our system according to equation (12) such that

$$v = -\frac{d\ell_c}{dt} = \bar{v}_w J_w|_{\ell_c} \tag{67}$$

and, secondly, a characteristic length L such that

$$L = \ell_c \tag{68}$$

then a characteristic time, τ, can be defined such that

$$\tau = \frac{L}{v} = \frac{\ell_c}{|v_w \cdot J_w|}.$$

These characteristic dimensions can then be used to nondimensionalize the coordinates t and y:

$$t^* = \frac{t}{\tau} \quad \text{and} \quad y^* = \frac{y}{L}$$

In terms of these nondimensional coordinates, equation (62) becomes

$$\frac{vL}{D^v}\frac{\partial \ln \phi_s}{\partial t^*} = \frac{\partial}{\partial y^*}\left(\frac{\partial \ln \phi_s}{\partial y^*}\right) \tag{69}$$

with boundary conditions

$$\text{(1) at } y^* = 0, \qquad \left(\frac{\partial \ln \phi_s}{\partial y^*}\right)_{y^*=0} = 0 \tag{70}$$

$$\text{(2) at } y^* = 1, \qquad \left(\frac{\partial \ln \phi_s}{\partial y^*}\right)_{y^*=1} = -\frac{vL}{D^v} \tag{71}$$

where the ratio vL/D^v is the Peclet number (Pec) and represents the ratio of the inertial forces to the diffusive forces. The Peclet number is then the scaling factor for the concentration polarization phenomenon and as such imposes two limits on equation (62).

Case 1. As Pec $\to 0$, the diffusive forces dominate the inertial forces and the right-hand side of equation (69) vanishes. That is, no concentration profiles can develop in the solution. The diffusion equation (equation (69)) becomes

$$\frac{\partial^2 \ln \phi_s}{\partial y^2} \approx 0$$

or

$$\frac{\partial \ln \phi_s}{\partial y} \approx \text{constant}$$

In order to satisfy both boundary conditions in this limit, it must be the case that

$$\frac{\partial \ln \phi_s}{\partial y^*} = 0 \quad \text{for} \quad 0 \leq y^* \leq 1$$

Thus, the volume fraction is a function of time only.

Since N_s = constant,

$$\phi_{s)0}\ell_{c)0} = \int_0^{\ell_c(t)} \phi_s(y, t)dy = \phi_s(t)\ell_c(t)$$

or

$$\phi_s(t) = \frac{(\phi_s \ell_c)_{t=0}}{\ell_c(t)} \qquad \text{for} \quad 0 \leq y \leq \ell_c(t) \tag{72}$$

where

$$\ell_c = (\ell_c)_{t=0} - vt$$

This corresponds to the lumped parameter case if Pec $\to 0$ because D^v is essentially infinite but v is finite and nonzero. However, if Pec $\to 0$ because v is vanishingly small but D^v is finite and nonzero, then

$$\ell_c \approx (\ell_c)_{t=0}$$

and

$$\phi_s \approx (\phi_s)_{t=0}$$

for all t that is, nothing happens.

Note that the magnitude of D^v depends upon the physical properties of intracellular solution species, but the magnitude of v depends upon the water permeability of the cell membrane, k, and the driving force for water transport across the cell membrane, $\Delta\mu_w$ or Δc_s.

Case 2. As Pec $\to \infty$, the inertial forces dominate the diffusive forces and the left-hand side of equation (69) vanishes. Then

$$\frac{\partial \ln \phi_s}{\partial t} \approx 0$$

or

$$\phi_s = f(y^*)$$

That is, the concentration may vary with position but not with time. The boundary condition at the membrane intracellular solution interface, equation (71), becomes

$$\left(\frac{\partial \ln \phi_s}{\partial y^*}\right)_{y^*=1} = -\text{Pec} \to \infty$$

Thus, a concentration profile develops instantaneously with infinite slope at the membrane and zero slope at the cell center line. In this limit, this profile remains unchanged for all time since the solutes are unable to diffuse with any finite velocity.

In actual fact, this limit of infinite Péclet number can never be reached or even approached since it would require the volume fraction of the solutes at the membrane to increase without bound. Before this could happen, the driving force for water transport (see Fig. 1) would

vanish, i.e., $\Delta c_{s)act} \to 0$, and the water flux would be turned off, $J_w \to 0$. When this happens, there would then be sufficient time for the solutes to diffuse down the concentration gradient. The driving force then would become nonzero and the transport of water would resume. Rather than this switching off and on of the water flux, what actually happens is that before the Peclet number becomes too large a concentration profile develops such that the solutes diffuse back into the cell interior at a rate which is just balanced by the rate at which they are deposited at the cell membrane by the water leaving the cell. This quasi-steady state is reached at a Peclet number of approximately unity when there is a balance of diffusive and inertial forces. Indeed, it is in this quasi-steady state limit that it is proper to speak of an unstirred layer of thickness δ being present at the surface of a cell membrane [9, Chapter 4].

It should also be noted that if the liquid solution of interest can be considered dilute from a volume point of view ($\phi_s/\phi_w \ll 1$), then equation (62) for nonsteady-state diffusion in a system in which the total volume of the solute remains constant reduces to the ordinary nonsteady-state diffusion equation. The right-hand side of equation (62) can be expanded such that

$$\frac{\partial \phi_s}{\partial y} = \frac{\partial}{\partial y}\left(D^v \frac{\partial \phi_s}{\partial y}\right) - \frac{D^v}{\phi_s{}^2}\left(\frac{\partial \phi_w}{\partial y}\right)^2$$

If $\phi_s \ll \phi_w$, then according to equation (19a), $\phi_w \sim$ constant = 1. Consequently, $\partial \phi_w/\partial y \sim 0$ and the foregoing expression takes the form

$$\frac{\partial c_s}{\partial t} = \frac{\partial}{\partial y}\left(D^v \frac{\partial c_s}{\partial y}\right) \tag{73}$$

which is the classical one-dimensional diffusion equation. The boundary conditions in this limit are:

1 For $t < 0$

$$c_s = c_{s)0} \tag{74}$$

2 For $t \geq 0$

(a) At $y = 0$

$$\left.\frac{\partial c_s}{\partial y}\right|_o = 0 \tag{75}$$

(b) At $y = \ell_c$

$$-D^v \left.\frac{\partial c_s}{\partial y}\right|_{\ell_c} + (\bar{v}_w J_w) c_s|_{\ell_c} = 0 \tag{76}$$

This is the set of equations used by Dick [19] in determining approximately the relative importance of the diffusion of water within the intracellular solution to its permeation across the cell membrane for biological cells placed in a hypotonic or hypertonic solution at a constant temperature.

Application of the Analysis

This study is applicable to a wide variety of physical situations, but for the purposes of illustration we have applied the analysis to determine the behavior of human red blood cells during cooling at constant rates of change of temperature ($B = dT/dt$ = constant). This situation is one of considerable clinical importance in the reversible freezing of blood for long-term storage.

Clinical experience has shown that for human red blood cells suspended in an isotonic saline solution (0.154 mol NaCl/L H_2O), ice tends to form extracellularly once the freezing point of the solution is reached. As water is removed from solution in the form of ice, the transmembrane chemical equilibrium is upset and the cell responds by expressing water across the membrane. As the water leaves the cell, the cell volume decreases and the cell membrane is displaced inwardly. Our experience [1, 16] has shown that under these conditions human red blood cells can be modeled as flat disks with half-thickness of $\ell_c = 0.741\mu$ and diameter of $d_c = 9.30\mu$. Since $4\ell_c/d_c \approx 0.32 < 1$, the cell membrane can be considered flat and infinite in the plane perpendicular to the direction of water transport and the one-dimensional analysis can be applied.

In applying the analysis we have assumed that:

1 The temperature of the cell suspension is spatially uniform but time varying.

2 The composition of the liquid phase of the extracellular medium is uniform with no polarization of solutes taking place at either the external surface of the cell membrane or at the liquid-solid interfaces.

3 The red blood cells are suspended in an initially isotonic sodium chloride aqueous solution.

4 Solid phase of pure ice forms only in the extracellular medium.

5 Chemical equilibrium prevails at all times in the extracellular medium.

6 The intracellular solution is an ideal, hydrated, nondilute, pseudobinary salt-protein-water solution initially of uniform composition.

7 The cell volume is variable although the cell membrane surface area is constant.

8 The cell membrane is permeable to water only.

For a more detailed explanation of these assumptions please refer to the other articles of this series [1–4].[7]

Our results for this application (see Figs. 3 and 4 and reference [2]) show that the water transport is significantly affected by the permeation of water through the cell membrane *and* by the diffusion of water within the intracellular medium. For cooling rates less than 100°C/min, little, if any, concentration polarization of solutes takes place within RBCs because at these cooling rates all of the solutes can diffuse within the intracellular solution faster than they are being convectively deposited at the intracellular solution-membrane interface by the water leaving the cell. However, a significant degree of solute polarization occurs within RBCs being cooled at rates in excess of 500°C/min (see Fig. 3) even though the amount of water retained by erythrocytes during cooling is not significantly affected by the concentration polarization phenomenon for cooling rates less than 5000°C/min (see Fig. 4). This cooling rate range of -5000°C/min $< B < -500$°C/min not only encompasses the peak in the experimentally measured RBC survival signature curve at $B = -3000$°C/min [20] but also encompasses the experimentally measured transition cooling rate of 850°C/min [21] for the formation of intracellular ice. In light of the many approximations made regarding the variation with temperature and composition of the numerous biophysical parameters (cell membrane water conductivity, solute diffusivities, hydration numbers, etc.) used in our analysis, this range of cooling rates may be fortuitous. We believe, however, that such is not the case, and that our model for the concentration polarization of solutes within cells during freezing and thawing provides possible physical explanations not only for cell damage at fast cooling rates due to the formation of intracellular ice, but also for cell damage at slow cooling rates due to concentrated solution effects [4]. We therefore hope that the laser interferometer technique of Lerche [8] or some sort of micro-electrode technique will soon be used to measure the time/temperature dependent spatial distribution of solutes within cells during freezing.

References

1 Levin, R. L., Cravalho, E. G., and Huggins, C. E., "The Effect of Hydration on the Water Content of Human Erythrocytes," *Biophysical Journal* Vol. 16, 1976, pp. 1411–1426.

2 Levin, R. L., Cravalho, E. G., and Huggins, C. E., "The Concentration Polarization Effect in Frozen Erythrocytes," Submitted to *Journal Biomechanical Engineering*, TRANS. ASME, in press.

3 Levin, R. L., Cravalho, E. G., and Huggins, C. E., "Effect of Solution Non-Ideality on RBC Volume Regulation," *BBA Bio-membranes*, in press.

[7] Specifically, modeling of the RBC intracellular solution as an ideal, hydrated nondilute salt-protein-water solution and the RBC extracellular solution as a dilute salt-water solution is discussed in [1]. References [1,2] also provide a detailed accounting of the numerous biophysical parameters (volumes, areas, permeabilities, diffusivities, etc.) used in the analysis. Reference [3] discusses the effect of solution nonideality on the polarization process while reference [4] considers the effect of allowing the salt and protein molecules to diffuse as relatively independent species within the RBC intracellular solution.

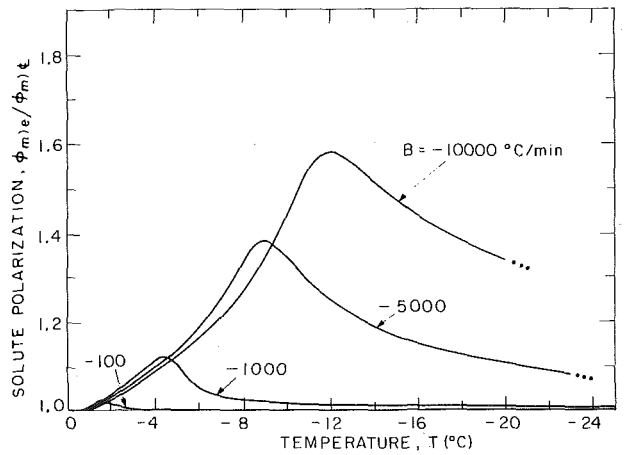

Fig. 3 Degree of solute within the ideal, hydrated pseudobinary intracellular solutions of RBCs cooled at different rates

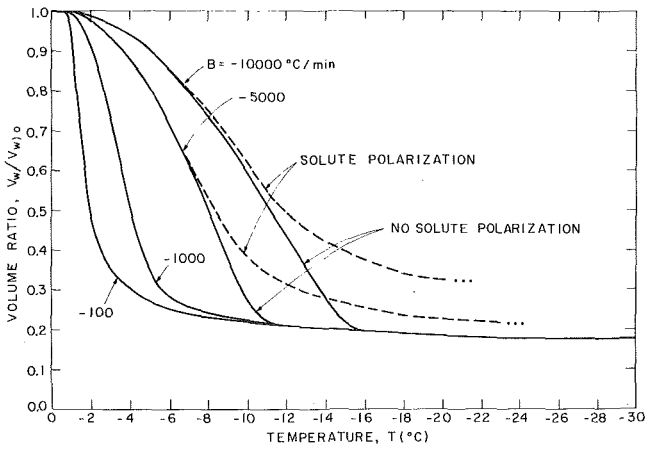

Fig. 4 Volume of intracellular water of RBCs cooled at different rates for the case of solute polarization within the ideal, hydrated pseudobinary intracellular solutions

4 Levin, R. L., Cravalho, E. G., and Huggins, C. E., "The Concentration Polarization Effect in a Multicomponent Electrolyte Solution—The Human Erythrocyte," submitted to *Journal Theoretical Biology.*

5 Kuhn, W., "Grenze der Durchlassigkeit von Filtrier-und Loslishkeitsmembranen," *Zeitschrift fur Elektrochemie,* Vol. 55, 1951, pp. 207–217.

6 Dainty, J., "Water Relations of Plant Cells," *Adv. in Bot. Res.* Vol. 1, 1963, pp. 279–326.

7 Everett, C. T., and Haydon, D. A., "Influence of Diffusion Layers During Osmotic Flow across Bi-molecular Lipid Membranes," *Journal Theoretical Biology,* Vol. 22, 1969, pp. 9–19.

8 Lerche, D., "Temporal and Local Concentration Changes in Diffusion Layers at Cellulose Membranes due to Concentration Differences between the Solution on Both Sides of the Membrane," *Journal Membrane Biology,* Vol. 27, 1976, pp. 193–205.

9 House, C. R., *Water Transport in Cells and Tissues,* Williams and Wilkens, Baltimore, 1974.

10 Schafer, J. A., Patlack, C. S., and Andreoli, T. E., "Osmosis in Cortical Collecting Tubules," *Journal Gen. Physiol.* Vol. 64, 1974, pp. 201–227.

11 Bearman, R. J., and Kirkwood, J. G., "Equations of Transport in Multicomponent Systems," *Journal Chem. Phys.,* Vol. 28, 1958, pp. 136–145.

12 Onsager, L., "Reciprocal Relations in Irreversible Thermodynamics I. *Phys. Rev.* Vol. 37, 1931, pp. 405–426.

13 Onsager, L., "Reciprocal Relations in Irreversible Thermodynamics II. *Phys. Rev.* Vol. 38, 1931, pp. 2265–2279.

14 Kathchalsky, A., and Curran, P., *Non Equilibrium Thermodynamics in Biophysics,* Harvard University Press, Cambridge, 1965.

15 Hartley, G. S., and Crank, J., "Some Fundamental Definitions and Concepts in Diffusion Processes," *Transactions of the Faraday Society,* Vol. 45, 1949, pp. 801–818.

16 Levin, R. L., "Kinetics of Water Transport in Biomaterials During Freezing," ScD thesis, Dept. of Mech. Eng., MIT, June, 1976.

17 Robinson, R. A., and Stokes, R. H., *Electrolyte Solutions,* 2nd ed., Butterworth, London, 1959.

18 Levin, R. L., Cravalho, E. G., and Huggins, C. E., "A Membrane Model Describing the Effect of Temperature on the Water Conductivity of Erythrocyte Membranes at Subzero Temperatures," *Cryobiology,* Vol. 13, 1976, pp. 415–429.

19 Dick, D. A. T., *Cell Water,* Butterworth, London, 1966.

20 Rapatz, G., and Luyet, B., "Effect of Cooling Rates on the Preservation of Erythrocytes in Frozen Blood Containing Various Protective Agents," *Biodynamica,* Vol. 9, 1965, pp. 333–350.

21 Diller, K. R., Cravalho, E. G., and Huggins, E., "An Experimental Study of Intracellular Freezing in Erythrocytes," *Medical and Biological Engineering,* Vol. 14, 1976, pp. 321–326.

journal of heat transfer

technical notes

This section consists of contributions of 1500 words or equivalent. In computing equivalence, a typical one-column figure or table is equal to 250 words. A one-line equation is equal to 30 words. The use of a built-up fraction or an integral sign or summation sign in a sentence will require additional space equal to 10 words. Technical notes will be reviewed and approved by the specific division's reviewing committee prior to publication. After approval such contributions will be published as soon as possible, normally in the next issue of the journal.

Void Fraction Measurement With a Rotating Electric Field Conductance Gauge

M. Merilo,[1] R. L. Dechene,[2] and W. M. Cichowlas[3]

Introduction

Void fraction is one of the fundamental quantities necessary to describe the flow characteristics of a two-phase mixture; yet it remains one of the most elusive to measure. The success of the numerous techniques which are available for its measurement usually depends upon the particular application [1, 2].[4] All of the methods can be categorized as either local or spatially averaged measurements.

Local methods include hot wire or hot film anemometry, optical probes, microthermocouples, isokinetic sampling, and electrical probes. Methods which average on a line or area utilize the absorption of light, γ-rays, X-rays or neutrons, and volume average techniques include quick-closing valves and impedance gauges.

While a knowledge of the detailed void distribution in a flow system is useful, the effort, cost and sheer volume of such local information can sometimes be prohibitive. This is particularly true of transient measurements and of measurements for industrial applications. In these circumstances, average values across a cross section are generally sufficient.

Electrical impedance techniques have proven attractive for many applications because of their generally fast response and relative simplicity of operation. Measurements obtained from these devices rely upon the dependence of the capacitance and resistance of the two-phase mixture on void fraction. Nonelectrolytic liquids, such as the Freons, are amenable to measurement of capacitance, whereas electrolytic liquids, such as water, require measurement of the resistance, or its inverse, the conductance.

The present work concerns the application of a newly designed conductance gauge[5] which has been developed to measure the void fraction in a pipe of circular cross section. Previous attempts to utilize conductance measurements for this purpose have generally been plagued by two problems. If the electrodes are mounted flush on the tube wall [3] to minimize the flow disturbance, the electric field is not uniform and the conductance becomes dependent on the void distribution. On the other hand, if the electrodes are designed to distribute the field [3–5] either by using parallel plates, concentric cylindrical plates, or wire grids, a considerable disturbance can be introduced to the flow. These disturbances produce accelerations in the flow field which, by changing the relative vapor and liquid velocities, affect the void fraction.

In the present design the electrodes form part of the tube wall to eliminate the disturbance to the flow. Further, the electric field, which is perpendicular to the flow, is rotated electronically to distribute it throughout the sensor volume.

Design and Principle of Operation

A simplified schematic diagram of the void fraction monitor is shown in Fig. 1. The sensor consists of six, 22.9-cm long, stainless steel electrodes separated by ceramic insulators. These electrodes and insulators form the inside perimeter of the sensor flow area. The resulting twelve-sided polygon gives a close approximation to a circle, allowing the flow coming from a tube of a diameter equal to the spacing between opposite electrodes (3.81 cm) to enter the sensor with minimal disturbance. In fact, by curving the electrodes and insulators this disturbance can be eliminated.

The six electrodes form three sets of opposing parallel plates uniformly spaced around the circumference. The three electrode pairs are excited, at a frequency of 5 kHz, by a 10 V three-phase signal such that the signal for each pair is 120 deg out of phase with the others. A rotating electric field is thus generated within the sensor volume as shown in Fig. 2.

Three identical conductance measurement circuits are also connected to the electrode pairs, and the absolute values of the signals from these circuits are summed. The resulting signal is proportional to the conductance, or average mixture conductivity, between the sensor electrodes.

A reference sensor, which produces a signal proportional to the conductivity of the single phase liquid, can be used to compensate for changes in the conductivity of the liquid due to variations in its temperature and concentration of impurities. The signal from the main sensor is divided by that from the reference sensor using an analog divider. The final output is then simply the relative conductivity of the two-phase mixture with respect to the liquid phase.

The reference sensor must be installed in a location where it "sees" only the single phase liquid. If this is not possible, the conductance gauge can be operated without it. However, the changes in the liquid conductivity must then be accounted for when interpreting the measurement.

[1] Research Engineer, Atomic Energy of Canada Limited, Chalk River, Ontario; present address: The Electric Power Research Institute, Palo Alto, Calif.

[2] President, Auburn International Inc., Danvers, Mass.

[3] Student, Mechanical Engineering Department, McGill University, Montreal, Quebec, Canada.

[4] Numbers in brackets designate References at end of technical note.

[5] Patent applied for by Auburn International Inc.

Contributed by the Heat Transfer Division of THE AMERICAN SOCIETY OF MECHANICAL ENGINEERS. Manuscript received by the Heat Transfer Division December 22, 1976.

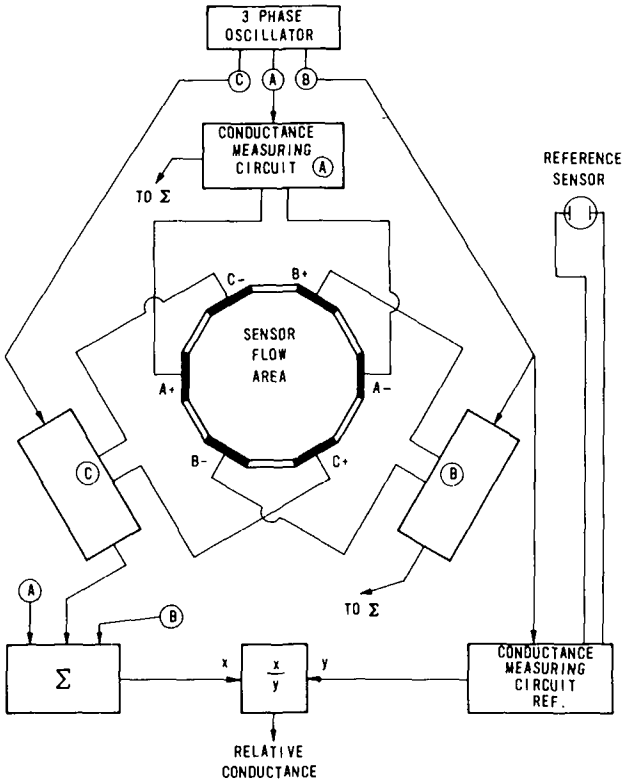

Fig. 1 Schematic diagram of the conductance monitor

Calibration

To determine the efficacy of the rotating field conductance gauge as a void fraction monitor, conductance measurements were made on flowing air-water mixtures. These results were compared with void fraction measurements obtained by using quick-closing valves.

The test section is 4-m long and consists of transparent lucite tubing with an internal diameter of 3.81 cm. The conductance sensor is located 2 m downstream of the air-water mixer, with the quick-closing guillotine type valves placed 57 cm upstream and downstream of the sensor. These valves, which are mechanically coupled to insure simultaneous closure, are driven by springs and achieve a closing time of approximately 25 ms. The volume of water which is trapped between the valves is measured by draining it into a graduated cylinder. The reference sensor is situated in the water line upstream of the air-water mixer. The water and air flow rates are individually metered and controlled.

Measurements were conducted with both vertical upflow and horizontal flow. In horizontal flow, the air-water distribution across the cross section is extremely asymmetric, thus providing a severe test of distribution effects on the void fraction measurement.

The maximum superficial velocities tested were 2.5 m/s for water and 60 m/s for air. The water temperature was not controlled and varied from approximately 15–20°C, while the test section exit pressure varied from close to atmospheric for low flow rates to about 400 kPa at high rates.

Depending on the flow pattern, fluctuations in the conductivity of the two-phase mixture can be considerable. The output from the gauge was, therefore, monitored by a strip chart recorder. To obtain an average value, the monitor output was also integrated, over a period ranging from 2 to 5 s, with an integrating digital voltmeter. As the quick-closing valves were activated after the integration period, the two-phase mixture which was trapped was not the same as that which had flowed through the sensor for the conductance measurement. This discrepancy had very little effect for relatively steady flows such as bubbly or annular, but did cause scatter in slug flow.

A Federal Scientific Ubiquitous Correlator was used for several experiments in horizontal flow to obtain probability density functions of the relative two-phase conductivity.

Results and Discussion

A comparison of the void fraction, as measured with quick-closing valves, with the relative conductivity of the two-phase mixture is shown in Fig. 3. The flow patterns indicated on this plot were determined visually and consequently suffer from all the uncertainties inherent in this technique. When examining the present data, one should, therefore, keep in mind that the transition regions are quite broad.

In bubbly flow it is clear that the orientation of the test section, and hence the distribution of bubbles in the sensor volume, has no effect on the measured conductance. It is also gratifying to note that these

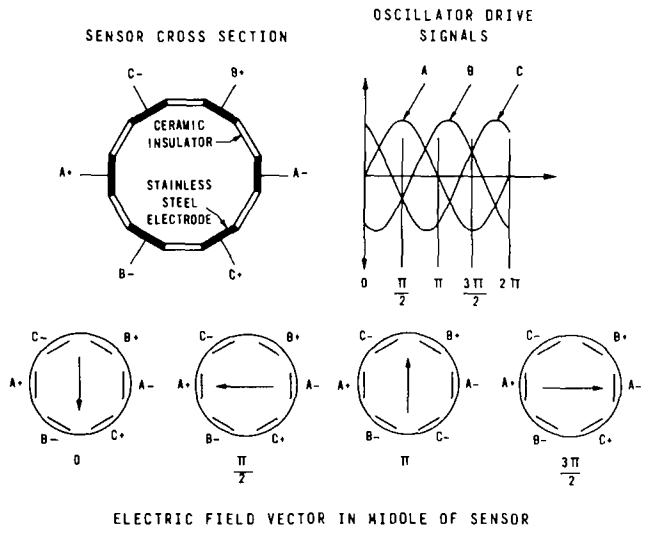

Fig. 2 Sensor excitation

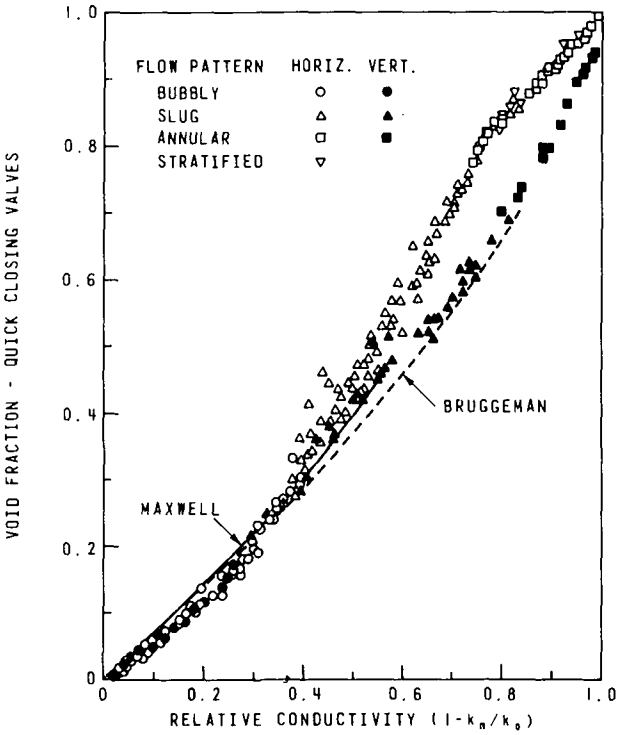

Fig. 3 Calibration curve

measurements follow the theoretical predictions of Maxwell [6] and Bruggeman [7] quite closely.

Maxwell's expression for the relationship between the mixture conductivity, k_m, and the void fraction, α, is

$$k_m/k_0 = 1 - 3\alpha/(2 + \alpha)$$

This equation was derived for noninteracting, equal size spheres of zero conductivity, distributed in a continuous medium of conductivity k_0. It should, therefore, be valid for low void fraction only, however, all the bubbly flow data are predicted remarkably well.

Bruggeman's relation,

$$k_m/k_0 = (1 - \alpha)^{3/2}$$

was derived for random size spheres of zero conductivity, randomly distributed throughout a continuous medium. The equation should, therefore, be valid for any void fraction where these bubbly flow conditions are met. For the present data these relations are valid up to a void fraction of approximately 30 percent in both vertical and horizontal flow. At higher void fraction slug flow with its associated scatter is observed.

When the flow pattern is annular, the average conductivity of the two-phase mixture clearly depends on the orientation of the test section. This is not surprising as in this regime the conductance gauge essentially measures the film thickness on the wall, and ignores completely any entrained liquid to which no conduction path exists. In horizontal flow the liquid film is highly asymmetric, resulting in a lower conductance than if the same amount of liquid were distributed uniformly. It can be seen, however, that with a constant void fraction the average conductivity of the mixture is higher for horizontal flow than for vertical. This implies that under otherwise similar conditions the amount of liquid carried as entrainment in vertical flow is higher than in horizontal, a conclusion which is in agreement with experimental observations [8].

In the slug flow regime differences between vertical and horizontal orientations do not appear until the void fraction reaches approximately 50 percent. These observations are consistent with the opinion expressed by Jones and Zuber [9]; that is, slug flow may be regarded as a periodic combination of bubbly and annular-like flow. In the low void fraction region of slug flow the sensor sees predominantly bubbly flow, for which the mixture conductivity is independent of orientation. As the void fraction increases, however, annular flow gradually becomes predominant.

Probability density functions for fluctuations in relative conductivity are shown in Fig. 4. These are obtained for horizontal flow and are similar to the results of Jones and Zuber [9] who obtained chordal measurements of void fraction in vertical flow by using X-rays. In agreement with their results, bubbly and annular flows are characterized by relatively sharp peaks at low and high void fractions respectively. Further, slug flow can be distinguished by a double peaked distribution, where the low and high void fraction peaks represent the contributions of bubbly and annular type flows respectively. The probability density functions thus provide a useful technique for flow pattern discrimination.

In summary, the rotating field conductance gauge provides a useful and versatile, yet relatively simple technique for void fraction measurement and flow pattern discrimination. Work on the optimization of the sensor design is continuing. In particular, the effects of the sensor geometry, materials, and number of electrodes on the sensor performance are being investigated.

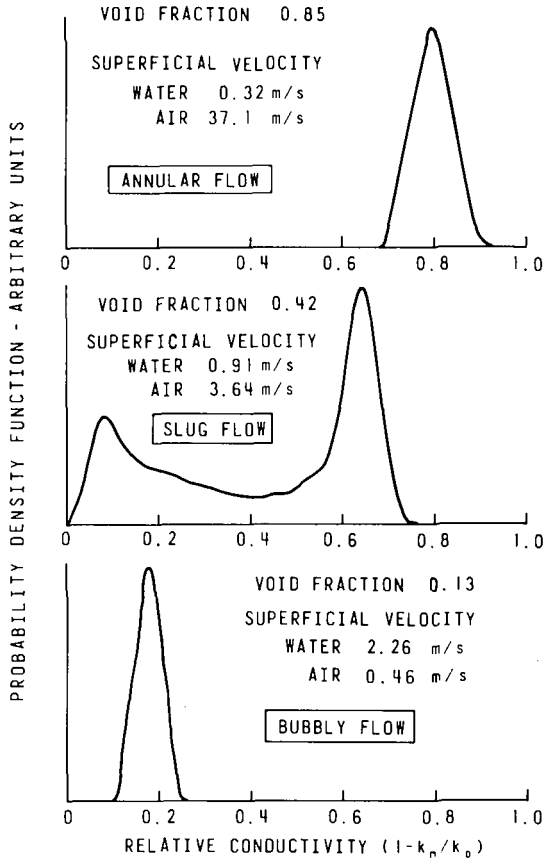

Fig. 4 Probability density functions for various horizontal flow conditions

References

1 LeTourneau, B. W., and Bergles, A. E., Co-Chairmen of a Symposium on Two-Phase Flow Instrumentation, 11th National ASME/AIChE Heat Transfer Conference, Minneapolis, Minn., 1969.

2 Hewitt, G. F., "The Role of Experiments in Two-Phase Systems With Particular Reference to Measurement Techniques," *Progress in Heat and Mass Transfer*, Vol. 6, 1972, p 295.

3 Subbotin, V. I., Pakhvalov, Yu. E., Mikhailov, L. E., Leonov, V. A., and Kronin, I. V., "Resistance and Capacitance Methods of Measuring Steam Contents," *Teploenergetika*, Vol. 21, No. 6, 1974, p 63.

4 Olsen, H. O., "Theoretical and Experimental Investigation of Impedance Void Meters," Kjeller Report KR-118, 1967.

5 Orbeck, I., "Impedance Void Meter," Kjeller Report KR-32, 1962.

6 Maxwell, J. C., *A Treatise on Electricity and Magnetism*, Clarendon Press, Oxford, 1881.

7 Bruggeman, D. A. G., "Berechnung Verschiedener Physikalischer Konstanten von Heterogenen Substanzen," *Ann. Phys., Leipzig*, Vol. 24, 1935, p. 636.

8 Hewitt, G. F., and Hall-Taylor, N. S., *Annular Two-Phase Flow*, Pergamon Press, 1970, p. 153.

9 Jones, O. C., Jr., and Zuber, N., "The Interrelation Between Void Fraction Fluctuations and Flow Patterns in Two-Phase Flow," *Int. J. Multiphase Flow*, Vol. 2, 1975, p. 273.

Application of Schwarz-Neumann Technique to Fully Developed Laminar Heat Transfer in Noncircular Ducts

J. P. Zarling[1]

Introduction

Laminar forced convection heat transfer in noncircular ducts has numerous engineering applications. Such geometries are commonly

[1] Mechanical Engineering Department, University of Alaska, Fairbanks, Alaska. Mem. ASME.

Contributed by the Heat Transfer Division of THE AMERICAN SOCIETY OF MECHANICAL ENGINEERS. Manuscript received by the Heat Transfer Division September 20, 1976.

measurements follow the theoretical predictions of Maxwell [6] and Bruggeman [7] quite closely.

Maxwell's expression for the relationship between the mixture conductivity, k_m, and the void fraction, α, is

$$k_m/k_0 = 1 - 3\alpha/(2 + \alpha)$$

This equation was derived for noninteracting, equal size spheres of zero conductivity, distributed in a continuous medium of conductivity k_0. It should, therefore, be valid for low void fraction only, however, all the bubbly flow data are predicted remarkably well.

Bruggeman's relation,

$$k_m/k_0 = (1 - \alpha)^{3/2}$$

was derived for random size spheres of zero conductivity, randomly distributed throughout a continuous medium. The equation should, therefore, be valid for any void fraction where these bubbly flow conditions are met. For the present data these relations are valid up to a void fraction of approximately 30 percent in both vertical and horizontal flow. At higher void fraction slug flow with its associated scatter is observed.

When the flow pattern is annular, the average conductivity of the two-phase mixture clearly depends on the orientation of the test section. This is not surprising as in this regime the conductance gauge essentially measures the film thickness on the wall, and ignores completely any entrained liquid to which no conduction path exists. In horizontal flow the liquid film is highly asymmetric, resulting in a lower conductance than if the same amount of liquid were distributed uniformly. It can be seen, however, that with a constant void fraction the average conductivity of the mixture is higher for horizontal flow than for vertical. This implies that under otherwise similar conditions the amount of liquid carried as entrainment in vertical flow is higher than in horizontal, a conclusion which is in agreement with experimental observations [8].

In the slug flow regime differences between vertical and horizontal orientations do not appear until the void fraction reaches approximately 50 percent. These observations are consistent with the opinion expressed by Jones and Zuber [9]; that is, slug flow may be regarded as a periodic combination of bubbly and annular-like flow. In the low void fraction region of slug flow the sensor sees predominantly bubbly flow, for which the mixture conductivity is independent of orientation. As the void fraction increases, however, annular flow gradually becomes predominant.

Probability density functions for fluctuations in relative conductivity are shown in Fig. 4. These are obtained for horizontal flow and are similar to the results of Jones and Zuber [9] who obtained chordal measurements of void fraction in vertical flow by using X-rays. In agreement with their results, bubbly and annular flows are characterized by relatively sharp peaks at low and high void fractions respectively. Further, slug flow can be distinguished by a double peaked distribution, where the low and high void fraction peaks represent the contributions of bubbly and annular type flows respectively. The probability density functions thus provide a useful technique for flow pattern discrimination.

In summary, the rotating field conductance gauge provides a useful and versatile, yet relatively simple technique for void fraction measurement and flow pattern discrimination. Work on the optimization of the sensor design is continuing. In particular, the effects of the sensor geometry, materials, and number of electrodes on the sensor performance are being investigated.

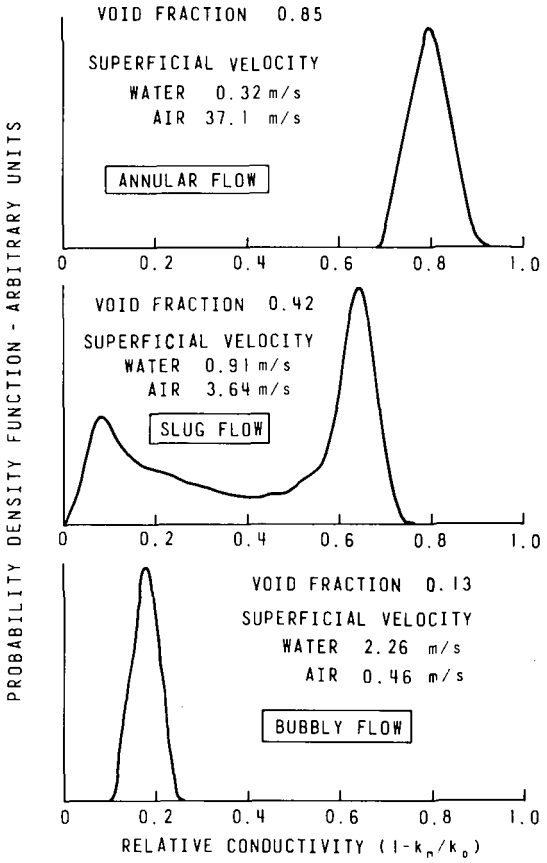

Fig. 4 Probability density functions for various horizontal flow conditions

References

1 LeTourneau, B. W., and Bergles, A. E., Co-Chairmen of a Symposium on Two-Phase Flow Instrumentation, 11th National ASME/AIChE Heat Transfer Conference, Minneapolis, Minn., 1969.

2 Hewitt, G. F., "The Role of Experiments in Two-Phase Systems With Particular Reference to Measurement Techniques," *Progress in Heat and Mass Transfer*, Vol. 6, 1972, p 295.

3 Subbotin, V. I., Pakhvalov, Yu. E., Mikhailov, L. E., Leonov, V. A., and Kronin, I. V., "Resistance and Capacitance Methods of Measuring Steam Contents," *Teploenergetika*, Vol. 21, No. 6, 1974, p 63.

4 Olsen, H. O., "Theoretical and Experimental Investigation of Impedance Void Meters," Kjeller Report KR-118, 1967.

5 Orbeck, I., "Impedance Void Meter," Kjeller Report KR-32, 1962.

6 Maxwell, J. C., *A Treatise on Electricity and Magnetism*, Clarendon Press, Oxford, 1881.

7 Bruggeman, D. A. G., "Berechnung Verschiedener Physikalischer Konstanten von Heterogenen Substanzen," *Ann. Phys., Leipzig*, Vol. 24, 1935, p. 636.

8 Hewitt, G. F., and Hall-Taylor, N. S., *Annular Two-Phase Flow*, Pergamon Press, 1970, p. 153.

9 Jones, O. C., Jr., and Zuber, N., "The Interrelation Between Void Fraction Fluctuations and Flow Patterns in Two-Phase Flow," *Int. J. Multiphase Flow*, Vol. 2, 1975, p. 273.

Application of Schwarz-Neumann Technique to Fully Developed Laminar Heat Transfer in Noncircular Ducts

J. P. Zarling[1]

Introduction

Laminar forced convection heat transfer in noncircular ducts has numerous engineering applications. Such geometries are commonly

[1] Mechanical Engineering Department, University of Alaska, Fairbanks, Alaska. Mem. ASME.

Contributed by the Heat Transfer Division of THE AMERICAN SOCIETY OF MECHANICAL ENGINEERS. Manuscript received by the Heat Transfer Division September 20, 1976.

employed in compact heat exchanger and regenerator design for industrial and vehicular uses. The advantages of these complex duct shapes are that they provide efficient, compact and economical units.

In order to solve these problems the methods used and reported in the literature range from exact to approximate solutions. Shah and London [1][2] have classified these methods into nine categories and presented results for $f \cdot \mathrm{Re}/4$ and Nu for 40 different duct geometries.

The subject of this paper is a method to solve the same class of problems which combines the Schwarz-Neumann alternating technique presented by Kantorovich and Krylov [2] with an orthonormalization least-squares point-matching procedure developed by Davis and Rabinowitz [3]. The method is applied to the duct shown in Fig. 2, a geometry commonly found in many vehicular radiators, to analyze the laminar forced convective heat transfer problem of constant axial heat transfer rate and prescribed peripheral wall temperature.

The Method

Since the Schwarz-Neumann method of solving the Dirichlet problem is discussed in detail by Kantorovich and Krylov [2], only a brief review of the method will be presented. Assume a solution is sought to a second-order elliptic linear homogeneous partial differential equation in region B, Fig. 1, which is formed by the union of overlapping regions B_1 and B_2. If this equation can be solved in regions B_1 and B_2 for any given piece-wise continuous boundary conditions, then the Schwarz-Neumann method permits one to obtain a solution, $w(x, y)$, to the foregoing equation in B from known solutions in regions B_1 and B_2.

In Fig. 1, let L_1 and L_2 be the contours of B_1 and B_2, let α be that portion of L_1 in B_2 and γ that portion of L_2 in B_1. If the solution to $w(x, y)$ in B_1 is $u(x, y)$ and in B_2, $v(x, y)$, then according to Schwarz, the determination of $u(x, y)$ and $v(x, y)$ requires the construction of a sequence of approximations $u_1(x, y), u_2(x, y), \ldots$ and $v_1(x, y), v_2(x, y), \ldots$ by solving the Dirichlet problem in each of these regions. However the boundary values of $u(x, y)$ are only known on L_1-α and unknown on α and similarily the boundary values of $v(x, y)$ are known on L_2-γ and unknown on γ. Therefore, in order to achieve solutions to either $u(x, y)$ or $v(x, y)$ boundary values must be assigned along α and γ. To initiate the solution a value $f(\alpha)$ will be assumed along α. This assumed value will then permit $u_1(x, y)$ to be determined in B_1. Next, $v_1(x, y)$ can be solved in B_2 using the values of $u_1(x, y)$ on γ as the boundary condition on γ. Stated in equation form, the sequence of functions that solve the Dirichlet problem in B are

$$\begin{aligned} u_1(x, y) &= G \text{ on } L_1 - \alpha; & v_1(x, y) &= H \text{ on } L_2 - \gamma \\ u_1(x, y) &= f \text{ on } \alpha; & v_1(x, y) &= u_1(x, y) \text{ on } \gamma \\ u_n(x, y) &= G \text{ on } L_1 - \alpha; & v_n(x, y) &= H \text{ on } L_2 - \gamma \\ u_n(x, y) &= v_{n-1}(x, y) \text{ on } \alpha; & v_n(x, y) &= u_n(x, y) \text{ on } \gamma \end{aligned} \tag{1}$$

To solve for u_n and v_n, the Dirichlet problem must be solved according to the previous boundary conditions in an alternating manner. However, the boundary values along α and λ become complex expressions due to the series form of the solution and the transformation of moving from one coordinate system location to another. Because of this complexity, the least squares method of point matching boundary conditions along α and γ is presented as a means of overcoming this difficulty.

The basic idea behind the boundary point least squares procedure is to determine the coefficients of a truncated series solution such that the boundary conditions are satisfied in the least squares sense at a set of appropriately chosen boundary points. The Gram-Schmidt orthonormalization procedure, as described by Davis and Rabinowitz [3], is a means of determining the unknown coefficients. The technique requires that a set of n particular solutions to the governing differential equation are known, from which a truncated series solution can be constructed. Applying the Gram-Schmidt method produces a set of n orthonormal vectors from a linear combination of the n particular solutions evaluated at N points ($N \geq n$) chosen along the boundary L_1 of B_1 or L_2 of B_2. Sparrow and Haji-Sheikh [4] have applied this method to flow and heat transfer problems in ducts of arbitrary shape.

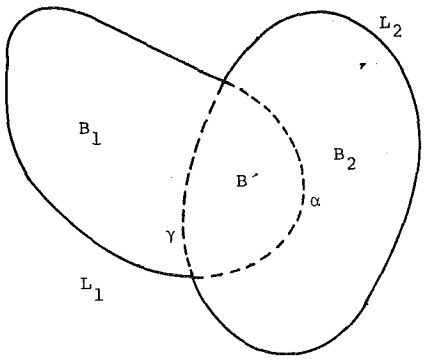

Fig. 1 Region B formed by the union of B_1 and B_2 having B' as their common part

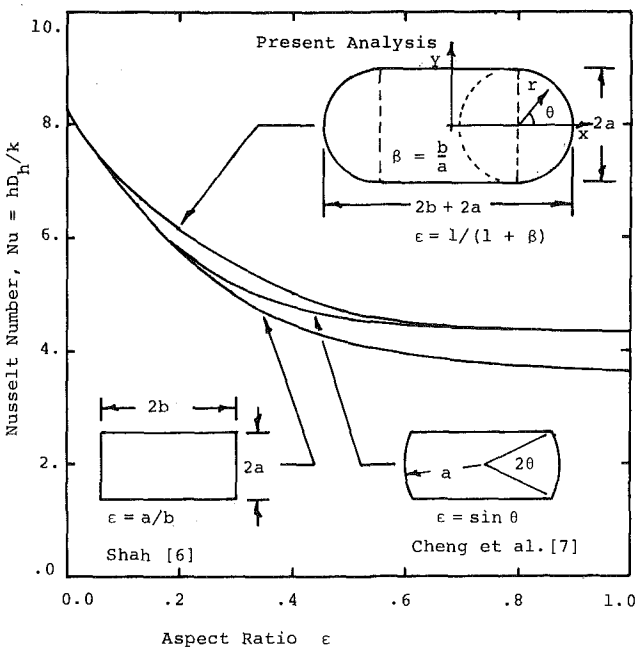

Fig. 2 Nusselt number variation for fully developed laminar flow

Velocity Problem

A steady-state, fully developed laminar flow in a duct of constant cross-sectional area is assumed. The fluid is also idealized to have the properties of ρ, μ, c_p, k constant. Then in the absence of body forces, the differential equation describing the velocity field, U, is

$$\nabla^2 U = (dP/dZ)\mu = \text{Constant} \tag{2}$$

where ∇^2 is the familiar two-dimensional Laplace operator. The solution to equation (2) satisfying the "nonslip" boundary conditions has been reported by Zarling [5] for the duct shown in Fig. 2. The nondimensional velocity distribution is given as

$$u = \frac{1 - y^2}{2} + \sum_{n=1}^{N} A_n \cos\lambda_n y \cosh\lambda_n x \tag{3}$$

[2] Numbers in brackets designate References at end of technical note.

$$\lambda_n = (2n-1)\pi/2$$

in the rectangular region, and as

$$u' = \frac{1-r^2}{4} + \sum_{n=0}^{N} B_n r^n \cos n\phi \tag{4}$$

in the circular region. In the previous equations, the variables u, u', r, x, and y have been defined as

$$u = u' = \frac{\mu^2 U}{a^2(dP/dZ)}, \qquad r = R/a, \qquad x = X/a, \qquad y = Y/a \tag{5}$$

The series coefficients in equations (3) and (4) have been determined by the Schwarz-Neumann successive approximation technique combined with orthonormalization least squares point matching. Expressions and results are also presented for average velocities, flow rates, and $f\cdot$Re for a range of values of β.

Temperature Problem

With the assumptions made in the velocity problem, the appropriate differential equation describing the thermally developed temperature field for laminar flow with no internal energy generation is

$$\nabla^2 T = (U/\alpha)(\partial T/\partial Z) \tag{6}$$

Characteristic of the fully developed thermal regime in ducts in which the heat rate, q'', is axially constant per duct length is that

$$\frac{\partial T}{\partial Z} = \frac{dT_m}{dZ} = \frac{q''S}{AU_m c_p} = \text{Constant} \tag{7}$$

This boundary condition can be realized in practical applications such as electrical resistance, radiant, or nuclear heating, and in counter flow heat exchangers when the fluid capacities are identical. Substituting this expression into equation (6) along with the velocity solutions, equations (3) and (4) yields

$$\frac{\partial^2 t}{\partial x^2} + \frac{\partial^2 t}{\partial y^2} = \frac{1-y^2}{2} + \sum_{n=1}^{N} A_n \cos\lambda_n y \cosh\lambda_n x \tag{8}$$

$$\frac{\partial^2 t'}{\partial r^2} + \frac{1}{r}\frac{\partial t'}{\partial r} + \frac{1}{r^2}\frac{\partial^2 t'}{\partial \theta^2} = \frac{1-r^2}{4} + \sum_{n=0}^{N} B_n r^n \cos n\theta \tag{9}$$

for the rectangular and circular regions. The dimensionless temperatures in the foregoing expressions are defined as

$$t = t' = \frac{T}{2f \cdot \text{Re} q'' a^4/kD_h{}^3} \tag{10}$$

The next step is to reduce equations (8) and (9) to Laplace's equation which can be accomplished by considering the temperature solution as the sum of a particular solution, t_p, and regular solution, t_c. To facilitate finding a particular solution, it is convenient to introduce complex variables z and $\bar{z}$ such that $t(x, y)$, $t'(r, \theta)$, $u(x, y)$ and $u'(r, \theta)$ are transformed to $\hat{t}(z, \bar{z})$ $\hat{t}'(z, \bar{z})$, $\hat{u}(z, \bar{z})$ and $\hat{u}'(z, \bar{z})$. Integrating these relationships with respect to z and $\bar{z}$, and taking the real part of the resulting functions, yields the required particular solutions

$$t_p = \frac{x^2+y^2}{8} - \frac{y^4}{24} + \sum_{n=1}^{N} \frac{A_n}{4\lambda_n} \times (x \sinh\lambda_n x \cos\lambda_n y + y \cosh\lambda_n x \sin\lambda_n y) \tag{11}$$

and

$$t_p' = \frac{r^2}{16} - \frac{r^4}{64} + \sum_{n=0}^{N} \frac{B_n r^{n+2} \cos n\theta}{4(n+1)} \tag{12}$$

Attention is now directed toward obtaining a solution to Laplace's equation to complete the solution. Given the surface temperature along the rectangular portion of the duct as $t(x_B, y_B)$ and along the semicircular portions $t'(r_B, \theta_B)$ and solving for t_c yields

$$t_c(x_B, y_B) = t(x_B, y_B) - t_p(x_B, y_B) \tag{13}$$

$$t_c'(r_B, \theta_B) = t'(r_B, \theta_B) - t_p'(r_B, \theta_B) \tag{14}$$

A special case of the foregoing generalized peripherally prescribed surface temperature is constant peripheral wall temperature, $T(x_B, y_B) = T'(r_B, \theta_B) = T_w = \text{const}$. For purposes of convenience, T' in equation (10) is now redefined using $(T - T_w)$ in place of T. Then $t(x_B, y_B)$ and $t'(r_B, \theta_B)$ equal zero on the duct surfaces and the first terms on the right-hand side of equations (13) and (14) are eliminated. Furthermore, it is only necessary to consider the first quadrant of the duct due to its symmetry and the constant peripheral wall temperature boundary condition. Based on the foregoing, the following boundary conditions can be written for the rectangular region

$$t_c(x, 1) = -t_p(x, 1), \qquad \frac{\partial tc}{\partial x}(0, y) = 0 \qquad \frac{\partial tc}{\partial y}(x, 0) = 0$$

$$t_c(\beta, y) = t_c'(r, \pi/2) + t_p'(r, \pi/2) - t_p(\beta, y) \tag{15}$$

and for the semicircular region

$$t_c'(1, \theta) = -t_p'(1, \theta); \qquad 0 \le \theta \le \pi/2$$

$$t_c'(1, \theta) = t_c(\beta + \cos\theta, \sin\theta) + t_p(\beta + \cos\theta, \sin\theta) - t_p'(1, \theta); \qquad \pi/2 \le \theta \le \pi$$

$$\frac{\partial tc}{\partial \theta}(r, 0) = 0 \tag{16}$$

Using the separation of variables technique and the principle of superposition in the rectangular region, the following solution to Laplace's equation is obtained

$$t_c = \sum_{n=1}^{\infty} C_n \cos\lambda_n{}^+ x \cosh\lambda_n{}^+ y + \sum_{n=1}^{\infty} D_n \cos\lambda_n{}^* y \cosh\lambda_n{}^* x \tag{17}$$

where $\lambda_n{}^+$ and $\lambda_n{}^*$ are eigenvalues defined as

$$\lambda_n{}^+ = \frac{(2n-1)\pi}{2\beta} \text{ and } \lambda_n{}^* = \frac{(2n-1)\pi}{2} \tag{18}$$

Equation (17) satisfies the middle two boundary conditions in equation (15). The first term of the right-hand side of equation (17) is zero along $x = \beta$ so that C_n must be determined to satisfy the first boundary condition of equation (15). Since this boundary condition is known, C_n can be determined by a single application of the orthonormalization least squares procedure. In a similar fashion, the second term on the right-hand side of equation (17) is zero along $y = 1$ so that D_n must be determined to satisfy the last boundary condition of equation (15). Since this boundary condition is unknown, the Schwarz-Neumann method must be used to generate this boundary condition.

The separation of variables technique is also applied to generate a solution to Laplace's equation in polar coordinates for the semicircular region. After applying the last boundary condition of equation (16) and the fact that t_c' remains finite as r goes to zero yields the regular solution.

$$t_c' = \sum_{n=0}^{\infty} B_n' r^n \cos n\theta \tag{19}$$

As in the rectangular region, the second boundary condition of equation (16) is not uniquely known and again the Schwarz-Neumann method must be used.

In order to initiate a solution in the rectangular region, the first term on the right-hand side of the last equation of equation (15) will be set equal to zero along $x = \beta$. Using this assumed boundary condition for the first approximation to $t_c(x, y)$, D_n can be determined through the least squares point matching procedure. The next step is to construct the first approximation to $t_c'(r, \theta)$ in the circular region. This is accomplished by determining B_n' in equation (19) which satisfies the first two boundary conditions of equation (16). Since the second boundary condition of equation (16) requires $t_c(x, y)$; the first approximation t_{c_1} determined for the rectangular region is used. Using these boundary conditions, B_n' are determined through the use of the least squares point matching procedure. The successive approximation procedure is continued until the series coefficients converge to a specified tolerance.

Results

Once the coefficients have been determined, the closed form temperature distribution can be constructed as the sum of equations (11) and (17) in the rectangular region and equation (12) and (19) in the circular region.

The bulk mean temperature, t_m, of the fluid can be computed by integrating the product of the velocity and temperature solutions over the cross-sectional area of the duct. Then, the average Nusselt number can be evaluated as

$$\mathrm{Nu} = \frac{hD_h}{k} = \frac{q''D_h}{k} \cdot \frac{1}{T_w - T_m} = \frac{-D_h 4}{2f \cdot \mathrm{Re} a^4 t_m} \tag{20}$$

where D_h and f are the hydraulic diameter and Darcy friction factor.

The series coefficients B_n', C_n, and D_n were determined by choosing fifty equally spaced points along the circumference of the circular arc $0 \le \theta \le \pi$, and eighty equally spaced points along $y = 1, 0 \le x \le \beta$, and along $x = \beta, 0 \le y \le 1$. In both the circular and the rectangular regions the series solutions were truncated after the first 37 terms. Although additional terms could have been included for small values of β, computational problems occurred at large values of β, due to the magnitude of the hyperbolic functions. The successive approximations to the solution were continued until the relative change in the series coefficients was less than 0.01 percent, which usually occurred after four or five iterations. An estimate of the accuracy of the solution can be made by calculating the root-mean-square error at the boundary points. In all cases, this error was less than 10^{-3} and it was concluded that the numerical results are accurate within 1 percent.

Pressure drop and heat transfer results as a function of the aspect ratio, $\epsilon(1/1 + \beta)$, are presented in Fig. 2. It is observed for the limiting cases of ϵ approaching one, circular duct, and ϵ approaching zero, infinite parallel plates, the Nusselt number approaches the limiting Nusselt numbers of 4.364 and 8.235, respectively. A comparison with the results of Shah [6] for a rectangular duct and Cheng and Jamil [7] for a circular duct with diametrical opposite flat sides is also shown.

A means of checking the accuracy of the proposed method is to compare results with a finite difference solution. Second order central difference equations were written for a 31 and 69 nodal point system for a symmetrical duct section of β equal to 1. The nodal point velocities and temperatures of the larger grid spacing agreed within 1.5 percent of the results for the smaller grid size. A comparison between velocity and temperature profiles calculated by the finite difference and series solution methods along the major and minor duct axes agreed to within 1 percent supporting the validity of the results presented in this work. An additional comparison was performed between u and u' and t and t' within, the overlapping region using the series solutions at five points along the X-axis. The maximum error was less than 0.1 percent.

Conclusions

The Schwarz-Neumann alternating technique combined with a least squares point matching method has been presented as a means to analyze fully developed laminar forced convective heat transfer in a noncircular duct with a uniform axial heat transfer rate and peripherally constant duct surface temperature. As an application of the method, Nusselt numbers were calculated for a modified rectangular duct with one set of sides semicircular in shape. The method can also be applied to the same category of heat transfer problems except with peripherally prescribed duct surface heat flux. Other fields of engineering analysis in which this method may be attractive include heat conduction, ground water hydrology, solid mechanics and electro-mechanics.

The advantage of the Schwarz-Neumann method is that it allows one to develop series solutions for complex shaped ducts from existing general series solutions in simpler geometries. Combining this technique with least squares point matching further enlarges the number of geometries which can be solved. The advantage of the S.N. method presented over a single least squares solution is that it allows one to use solutions natural to the simpler regions. The advantage of the method over the finite difference technique is that it generates a series solution, however, experience indicates the finite difference solution takes less computer run time.

Acknowledgment

A portion of the work on which this paper is based was made possible by a grant from the National Science Foundation.

References

1 Shah, R. K., and London, A. L., *Laminar Flow Forced Convection in Ducts*, Academic Press, New York, to be published.

2 Kantorovich, L. V., and Krylov, V. I., *Approximate Methods of Higher Analysis*, Interscience Publishers, Inc., New York, 1964, pp. 616–670.

3 Davis, P., and Rabinowitz, P., "A Multiple Purpose Orthonormalization Code and Its Uses," *Journal for the Association of Computing Machinery*, Vol. 1, 1954, pp. 183–191.

4 Sparrow, E. M., and Haji-Sheikh, A., "Flow and Heat Transfer in Ducts of Arbitrary Shape With Arbitrary Thermal Boundary Conditions," JOURNAL OF HEAT TRANSFER, TRANS. ASME, Series C, Vol. 88, No. 4, 1966, pp. 351–358.

5 Zarling, J. P., "An Analysis of Laminar Flow and Pressure Drop in Complex Shaped Ducts," *Journal of Fluids Engineering*, TRANS. ASME, Series I, Vol. 98, No. 4, 1976, pp. 702–706.

6 Shah, R. K., "Laminar Flow Friction and Forced Convection in Ducts of Arbitrary Geometry," *International Journal of Heat and Mass Transfer*, Vol. 18, 1975, pp. 849–862.

7 Cheng, K. C., and Jamil, M., "Laminar Flow and Heat Transfer in Circular Ducts With Diametrically Opposite Flat Sides and Ducts of Multiple Connected Cross Section," *Canadian Journal of Chemical Engineering*, Vol. 48, 1970, pp. 333–334.

Entrainment Characteristics of Buoyant Axisymmetric Plumes in Atmospheric Inversions

M. I. O. Ero[1]

Introduction

The atmosphere is the ultimate heat sink into which large thermal loads from power plants can be deposited without creating severe environmental pollution problems. The dilution and dispersal of gaseous effluents from process plants is controlled by the elevation at which gases are exhausted, the wind conditions, and the final elevation to which the gases rise under the action of initial buoyancy and fluid momentum. Ideally, it is desirable for a plume to rise to great heights before it is fully dispersed. The rate of entrainment of the ambient air determines the speed with which the mean temperature of a buoyant plume approaches the ambient atmospheric temperature, and hence the rate at which net buoyancy is depreciated.

In a study by Morton and Taylor [1],[2] it was proposed, from dimensional reasoning that the entrainment velocity is proportional to the axial flow velocity at the plume center, and that the proportionality constant is invariant with axial distance. In an extensive literature survey by Briggs [2], it was inferred that the entrainment velocity is proportional to the square root of the axial momentum flow. This result was used by Sneck and Brown [3] in an experimental program from which they derived a correlation in which the entrainment parameters varied as $\alpha_1 + \alpha_2/\mathrm{Fr}_\phi^2$, with α_1 and α_2 being constants and Fr_ϕ the local densimetric Froude number. In the study by Fox [4] it was shown that entrainment velocity varies with the buoyancy intensity of the flow, and on the expression assumed for the

[1] Asst. Professor, Purdue University, West Lafayette, Ind.

[2] Numbers in brackets designate References at end of technical note.

Contributed by the Heat Transfer Division of THE AMERICAN SOCIETY OF MECHANICAL ENGINEERS. Manuscript received by the Heat Transfer Division April 5, 1976.

Results

Once the coefficients have been determined, the closed form temperature distribution can be constructed as the sum of equations (11) and (17) in the rectangular region and equation (12) and (19) in the circular region.

The bulk mean temperature, t_m, of the fluid can be computed by integrating the product of the velocity and temperature solutions over the cross-sectional area of the duct. Then, the average Nusselt number can be evaluated as

$$\mathrm{Nu} = \frac{hD_h}{k} = \frac{q''D_h}{k} \cdot \frac{1}{T_w - T_m} = \frac{-D_h 4}{2f \cdot \mathrm{Re} a^4 t_m} \tag{20}$$

where D_h and f are the hydraulic diameter and Darcy friction factor.

The series coefficients B_n', C_n, and D_n were determined by choosing fifty equally spaced points along the circumference of the circular arc $0 \le \theta \le \pi$, and eighty equally spaced points along $y = 1, 0 \le x \le \beta$, and along $x = \beta, 0 \le y \le 1$. In both the circular and the rectangular regions the series solutions were truncated after the first 37 terms. Although additional terms could have been included for small values of β, computational problems occurred at large values of β, due to the magnitude of the hyperbolic functions. The successive approximations to the solution were continued until the relative change in the series coefficients was less than 0.01 percent, which usually occurred after four or five iterations. An estimate of the accuracy of the solution can be made by calculating the root-mean-square error at the boundary points. In all cases, this error was less than 10^{-3} and it was concluded that the numerical results are accurate within 1 percent.

Pressure drop and heat transfer results as a function of the aspect ratio, $\epsilon(1/1 + \beta)$, are presented in Fig. 2. It is observed for the limiting cases of ϵ approaching one, circular duct, and ϵ approaching zero, infinite parallel plates, the Nusselt number approaches the limiting Nusselt numbers of 4.364 and 8.235, respectively. A comparison with the results of Shah [6] for a rectangular duct and Cheng and Jamil [7] for a circular duct with diametrical opposite flat sides is also shown.

A means of checking the accuracy of the proposed method is to compare results with a finite difference solution. Second order central difference equations were written for a 31 and 69 nodal point system for a symmetrical duct section of β equal to 1. The nodal point velocities and temperatures of the larger grid spacing agreed within 1.5 percent of the results for the smaller grid size. A comparison between velocity and temperature profiles calculated by the finite difference and series solution methods along the major and minor duct axes agreed to within 1 percent supporting the validity of the results presented in this work. An additional comparison was performed between u and u' and t and t' within, the overlapping region using the series solutions at five points along the X-axis. The maximum error was less than 0.1 percent.

Conclusions

The Schwarz-Neumann alternating technique combined with a least squares point matching method has been presented as a means to analyze fully developed laminar forced convective heat transfer in a noncircular duct with a uniform axial heat transfer rate and peripherally constant duct surface temperature. As an application of the method, Nusselt numbers were calculated for a modified rectangular duct with one set of sides semicircular in shape. The method can also be applied to the same category of heat transfer problems except with peripherally prescribed duct surface heat flux. Other fields of engineering analysis in which this method may be attractive include heat conduction, ground water hydrology, solid mechanics and electro-mechanics.

The advantage of the Schwarz-Neumann method is that it allows one to develop series solutions for complex shaped ducts from existing general series solutions in simpler geometries. Combining this technique with least squares point matching further enlarges the number of geometries which can be solved. The advantage of the S.N. method presented over a single least squares solution is that it allows one to use solutions natural to the simpler regions. The advantage of the method over the finite difference technique is that it generates a series solution, however, experience indicates the finite difference solution takes less computer run time.

Acknowledgment

A portion of the work on which this paper is based was made possible by a grant from the National Science Foundation.

References

1 Shah, R. K., and London, A. L., *Laminar Flow Forced Convection in Ducts*, Academic Press, New York, to be published.

2 Kantorovich, L. V., and Krylov, V. I., *Approximate Methods of Higher Analysis*, Interscience Publishers, Inc., New York, 1964, pp. 616–670.

3 Davis, P., and Rabinowitz, P., "A Multiple Purpose Orthonormalization Code and Its Uses," *Journal for the Association of Computing Machinery*, Vol. 1, 1954, pp. 183–191.

4 Sparrow, E. M., and Haji-Sheikh, A., "Flow and Heat Transfer in Ducts of Arbitrary Shape With Arbitrary Thermal Boundary Conditions," JOURNAL OF HEAT TRANSFER, TRANS. ASME, Series C, Vol. 88, No. 4, 1966, pp. 351–358.

5 Zarling, J. P., "An Analysis of Laminar Flow and Pressure Drop in Complex Shaped Ducts," *Journal of Fluids Engineering*, TRANS. ASME, Series I, Vol. 98, No. 4, 1976, pp. 702–706.

6 Shah, R. K., "Laminar Flow Friction and Forced Convection in Ducts of Arbitrary Geometry," *International Journal of Heat and Mass Transfer*, Vol. 18, 1975, pp. 849–862.

7 Cheng, K. C., and Jamil, M., "Laminar Flow and Heat Transfer in Circular Ducts With Diametrically Opposite Flat Sides and Ducts of Multiple Connected Cross Section," *Canadian Journal of Chemical Engineering*, Vol. 48, 1970, pp. 333–334.

Entrainment Characteristics of Buoyant Axisymmetric Plumes in Atmospheric Inversions

M. I. O. Ero[1]

Introduction

The atmosphere is the ultimate heat sink into which large thermal loads from power plants can be deposited without creating severe environmental pollution problems. The dilution and dispersal of gaseous effluents from process plants is controlled by the elevation at which gases are exhausted, the wind conditions, and the final elevation to which the gases rise under the action of initial buoyancy and fluid momentum. Ideally, it is desirable for a plume to rise to great heights before it is fully dispersed. The rate of entrainment of the ambient air determines the speed with which the mean temperature of a buoyant plume approaches the ambient atmospheric temperature, and hence the rate at which net buoyancy is depreciated.

In a study by Morton and Taylor [1],[2] it was proposed, from dimensional reasoning that the entrainment velocity is proportional to the axial flow velocity at the plume center, and that the proportionality constant is invariant with axial distance. In an extensive literature survey by Briggs [2], it was inferred that the entrainment velocity is proportional to the square root of the axial momentum flow. This result was used by Sneck and Brown [3] in an experimental program from which they derived a correlation in which the entrainment parameters varied as $\alpha_1 + \alpha_2/\mathrm{Fr}_\phi^2$, with α_1 and α_2 being constants and Fr_ϕ the local densimetric Froude number. In the study by Fox [4] it was shown that entrainment velocity varies with the buoyancy intensity of the flow, and on the expression assumed for the

[1] Asst. Professor, Purdue University, West Lafayette, Ind.

[2] Numbers in brackets designate References at end of technical note.

Contributed by the Heat Transfer Division of THE AMERICAN SOCIETY OF MECHANICAL ENGINEERS. Manuscript received by the Heat Transfer Division April 5, 1976.

shear stress distribution.

In this study, the closure difficulty is resolved. It will be assumed that the flow is steady in the mean, two-dimensional, axisymmetric and turbulent. The variation of the local shear stress τ_{rz} is eliminated from the momentum equation by the usual integration. Closure was obtained by reintegrating the axial momentum equation after weighting it with the axial velocity.

Governing Equations

The continuity, momentum and energy equations for a turbulent axisymmetric jet can be integrated with respect to the radial coordinate and nondimensionalized to yield

Continuity:

$$\frac{d}{dz}(R^2UZ_1) = \rho_e R V_e \tag{1}$$

Momentum:

$$\frac{d}{dz}(R^2U^2Z_2) = I_{11}\frac{R^2\phi}{\mathrm{FR}^2} \tag{2}$$

Energy:

$$\frac{d}{dz}(P_eR^2U) = \frac{P_eRV_e}{I_{11}} \tag{3}$$

and for closure

$$\frac{d}{dz}(R^2U^3Z_3) = A_1\frac{\phi R^2U}{\mathrm{FR}^2} + A_2\rho_eR^2U^3\left(\frac{1}{U}\frac{du}{dZ}\right) \tag{4}$$

where Z is the axial distance measured from plume source, R is the local plume radius, U is the normalized axial velocity, Fr is the flow densimetric Froude number defined at the plume source, the buoyancy variable ϕ, and the density ratio β are defined by

$$\phi = (\rho_e(z) - \rho_p(0,z))/(\rho_1 - \rho_{1p}), \qquad \beta = (\rho_1 - \rho_{1p})/\rho_1$$

and

$$Z_1 = I_{11}\rho_e - I_{12}\beta\phi, \qquad Z_2 = I_{21}\rho_e - I_{22}\beta\phi, \qquad Z_3 = I_{31}\rho_e - I_{32}\beta\phi$$

$$A_1 = A_1(I_{11}, I_{21}, a), \qquad A_2 = A_2(I_{11}, I_{21}, a)$$

and I_{JK} are similarity constants defined by

$$I_{11} = \int_0^1 \eta e^{-a\eta^2}d\eta, \qquad I_{12} = \int_0^1 \eta e^{-2a\eta^2}d\eta, \qquad I_{21} = I_{12}$$

$$I_{22} = \int_0^1 \eta e^{-3a\eta^2}d\eta, \qquad I_{31} = I_{22}, \qquad I_{32} = \int_0^1 \eta e^{-4a\eta^2}d\eta \tag{5}$$

and V_e is the dimensionless entrainment velocity; the value of the variable, a, depends on the form of the similarity profile and how the edge of the plume is defined. In this study, the edge of the plume is defined as the radius at which the plume axial velocity is 0.5 percent of its value at the plume center. As in the study by Fox, the velocity profile is assumed to be in the form

$$\frac{u(r,z)}{u_1} = U(z)e^{-a\eta^2} \tag{6}$$

All the dimensionless variables appearing in equations (1) to (6) are defined in the Nomenclature.

Eliminating V_e from equations (1) and (3) yields

$$\frac{d}{dz}(R^2U\phi) = \frac{I_{11}}{I_{21}}\frac{P_e}{\beta}\frac{d}{dz}\left(\frac{\rho_e}{P_e}\right)R^2U \tag{7}$$

Thus the system of governing equations is reduced to equations (2), (4), and (7), with the corresponding initial conditions at $z = 0$ given by

$$(R^2U^2Z_2)_0 = I_{21} - I_{22}\beta, \quad (R^2U^3Z_3)_0 = I_{31} - I_{32}\beta, \quad (R^2U\phi)_0 = 1 \tag{8}$$

Entrainment Velocity

The continuity equation (1) may be used to obtain an expression for the entrainment velocity V_e. Expanding the left-hand side of equation (1), and using equations (2) and (7) to simplify the analysis, the entrainment velocity is obtained in the form

$$V_e = I_{11}\left(\alpha_1 + \frac{\alpha_2}{\mathrm{Fr}_\phi{}^2} + \alpha_3\right)RU \tag{9}$$

where

$$\alpha_1 = \left(\frac{I_{22}}{I_{21}}\frac{\beta}{\rho_e} - 1\right)\frac{1}{U}\frac{dU}{dZ}, \qquad \alpha_2 = \frac{I_{11}}{I_{21}}Sgn(\phi),$$

$$\alpha_3 = -\left(\frac{I_{22}}{I_{21}} - \frac{I_{12}}{I_{11}}\right)\frac{I_{11}}{I_{12}}\frac{\beta S}{T_e} \tag{10}$$

and Fr_ϕ is the local densimetric Froude number defined as

$$\mathrm{Fr}_\phi = \left(\frac{1}{\rho_eU^2}\frac{|\phi|}{\mathrm{Fr}_\phi{}^2}\right)^{-1/2} \tag{11}$$

Thus the entrainment parameter, α, may be defined as

$$\alpha = \alpha_1 + \frac{\alpha_2}{\mathrm{Fr}_\phi{}^2}\alpha_3 \tag{12}$$

This form, except for the appearance of the α_3 term, compares with the correlation proposed by Brown and Sneck in the form,

$$\alpha = 0.0535 + \frac{0.25}{\mathrm{Fr}_\phi{}^2}$$

The influence of the atmospheric inversion on the entrainment parameter is represented by the α_3 term. This term becomes negligible when the dimensionless density ratio, β, or the inversion parameter S, approaches zero; α_3 disappears naturally under the Bussinesque approximation according to which, [1, 3, 4], the term β/T_e is small, and is usually dropped from subsequent analysis. Retaining the α_3 term thus preserves the effect of atmospheric inversion on the entrainment rate, and consequently, its effect on the overall plume rise.

The second component of the entrainment parameter, α_2, is a constant whose sign follows the sign of the buoyancy variable ϕ. The dominant component of the entrainment parameter is α_1. In the absence of buoyancy and atmospheric inversion, α_1 represents the entrainment normally associated with a free jet in a stationary medium. Equation (10) shows that α_1 depends on the initial density ratio, β, the local dimensionless density ρ_e, and the gradient of the axial ve-

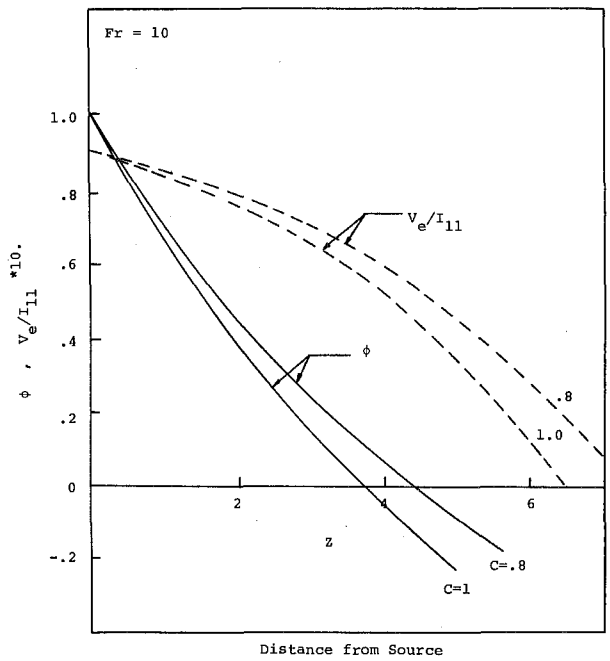

Fig. 1 General characteristics of plume buoyancy and entrainment velocity

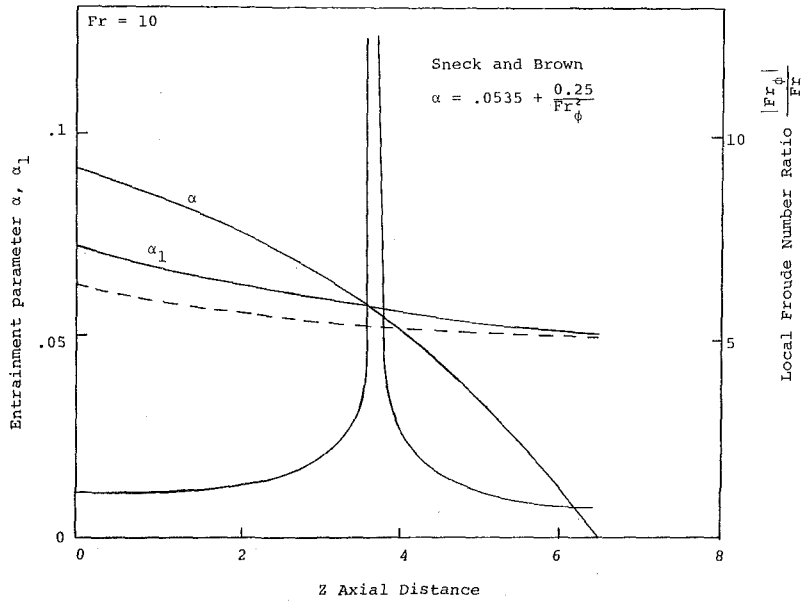

Fig. 2 Characteristics of entrainment and local Froude number

locity. Under Bussinesque approximation, the density dependence of α_1 becomes negligible, and α_1 is determined principally by the gradient of the axial velocity, and decreases as dU/dZ.

Influence of Froude Number

The magnitude of the initial densimetric Froude number, Fr, controls the forms of the governing equations, and the entrainment parameters. For large values of Fr, the right-hand side of equation (2) is approximately zero, and the momentum of the plume is approximately constant. Hinze's solution [5] for the turbulent axisymmetric jet is applicable in this limit. Since in the initial phases of the plume rise, $0 < \phi < 1$, and $Fr_\phi \simeq Fr$ for large values of Fr, the entrainment parameter given by equation (12) is reduced to the form

$$\alpha \simeq \alpha_1 = -\frac{1}{U}\frac{dU}{dZ} \tag{13}$$

Since Fr becomes large as u_1 becomes large or as $(\rho_1 - \rho_{1P})$ approaches zero, equation (13) is suitable for determining the entrainment parameter for negligibly buoyant plumes.

In the initial phase of plume rise, $0 < \phi < 1$, α_2 is positive, thus α_1 and α_2 are additive thereby increasing the effective entrainment rate. In the flow regions where $\phi < 0$ and hence $\alpha_2 < 0$, the effective entrainment rate defined by equation (12) has the potential for becoming negative. Thus the α_2 term in equation (12) determines where negative entrainment is attained. And from equation (9), with the entrainment parameter now negative, V_e is negative and the plume begins to spread out horizontally.

Results and Discussion

The results of numerical integration of the governing equations are discussed in the following.

The variation of plume buoyancy and entrainment velocity as a function of axial distance is shown in Fig. 1. Both buoyancy and entrainment velocity decrease in the flow direction; the rate of decrease depending on the inversion rate c. The variation of the local Froude number Fr_ϕ and the entrainment parameters α, α_1 are shown in Fig. 2. The cross-over between α and α_1 curves occur at $\alpha_2/Fr_\phi^2 + \alpha_3$. It can be inferred from Fig. 2 that this cross-over occurs at the point of zero buoyancy. In addition Fig. 2 shows a plot of the entrainment correlation proposed by Brown and Sneck. The variation of entrainment with initial Froude number is shown in Fig. 3, while Fig. 4 shows the influence of atmospheric inversion rate on plume entrainment. The axial distance at which zero entrainment occurs increases with the initial Froude number of the plume. For any given source condition, Fig. 4 shows that the distance to zero entrainment decreases as the inversion rate increases. The large entrainment rates obtained for plumes with $Fr < 6$ implies rapid induction of ambient air, and hence rapid reduction in plume buoyancy and plume rise.

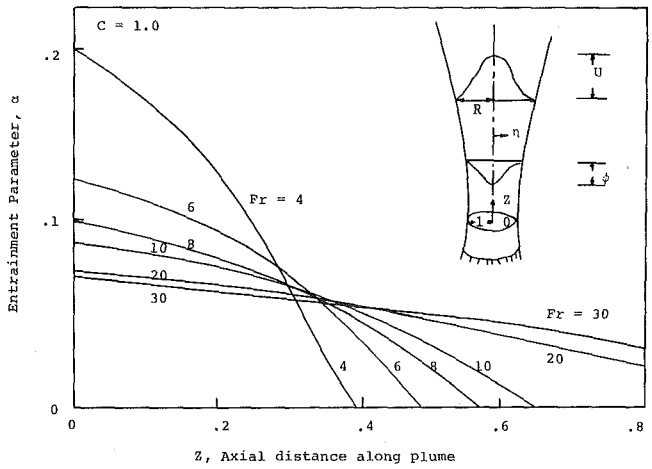

Fig. 3 Variation of entrainment parameter with initial Froude number, Fr

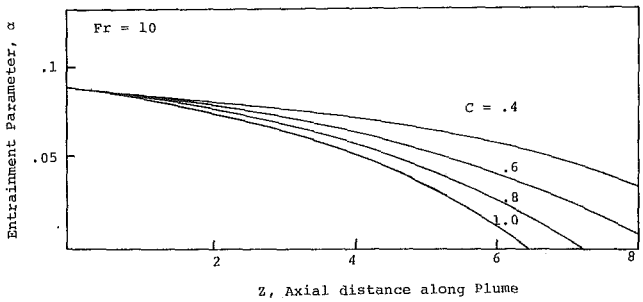

Fig. 4 Influence of inversion rate on entrainment parameter

Conclusion

The entrainment in a buoyant plume, within the similar profiles approximation assumed here, is controlled by the initial buoyancy, and the atmospheric inversion rate. The spreading of the plume, $V_e < 0$, corresponding to horizontal outflow from the plume, occurs after the plume had attained negative buoyancy. At high Froude numbers, Fr > 5, it is the initial momentum flux that characterizes the plume rise. The effect of atmospheric inversion rate on the entrainment parameter is initially small but becomes dominant in the region of negative buoyancy where α_1 and α_2 are both small and α_2 is negative.

References

1 Morton, R. R., Taylor, G., and Turner, J. S., "Turbulent Gravitational Convection From Maintained and Instantaneous Sources," *Proceedings of Royal Society*, London, Series A, Vol. 234, 1956, pp. 1–23.

2 Briggs, G. A., "Plume Rise," AEC Critical Review Series, U.S. AEC, Division of Technology Information, 1969.

3 Sneck, H. J., and Brown, D. H., "Cooling Tower Discharge Buoyant Plume Rise Through Atmospheric Inversions," GEC Report No. 71-C-311, Nov. 1971.

4 Fox, D. G., "Forced Plume in a Stratified Fluid," *Jour. Geoph. Res.*, Vol. 75, No. 33, Nov. 1970, pp. 6818–6835.

5 Hinze, J. O., *Turbulence*, McGraw-Hill, New York, 1959, pp. 411–426.

A Note on Convective Instabilities in Boussinesq Fluids and Porous Media

K. Walker[1] and G. M. Homsy[1]

Nomenclature

A = ratio of volumetric heat capacities of fluid/solid matrix to that of the fluid
g = acceleration of gravity
H = fluid depth
k = permeability
P = fluid pressure
Pr = Prandtl number, ν_f/κ
Ra = Rayleigh number, $g\alpha\Delta TH^3/\nu_f\kappa$
t = time
ΔT = temperature difference across layer
u = fluid velocity
x = spatial coordinate
α = coefficient of thermal expansion
δ_{i3} = unit vector in the vertical direction
κ = thermal diffusivity, $\lambda_{mix}/(\rho C_p)_f$
λ = thermal conductivity
μ = viscosity
ν = kinematic viscosity
ρ = density
θ = dimensionless temperature

Subscripts

f = fluid property
i, j = index for vector quantities (= 1, 2, 3).
liq = liquid property
mix = fluid/solid effective property

This note is concerned with the stability of a fluid held in an isotropic porous media between two infinite horizontal planes separated by a distance H. We express the permeability dimensionlessly as k/H^2. The problem has been solved in both the limit of $k/H^2 \to \infty$, the Bénard problem for a single viscous fluid, and $k/H^2 \to 0$, the Darcy approximation; an extensive literature exists for both problems. However for small gaps or moderately permeable materials, k/H^2 may lie between these two extremes. The problem is also of some interest in that it provides insight into the range of validity of the Darcy assumption which consists of neglecting the term $\nabla^2 u$ relative to the Darcy term $\mu u/k$.

The formulation of the problem is based upon the following assumptions:

1 Fluid and solid properties are assumed to be constant except for the density of the fluid. The Boussinesq approximation is invoked.

2 The two bounding planes are assumed to be isothermal impermeable solid surfaces.

3 The system is assumed to be governed by the following fluid field equations

$$\frac{\partial u_i}{\partial x_i} = 0 \tag{1}$$

$$\frac{1}{\mathrm{Pr}}\left(\frac{\partial u_i}{\partial t} + \frac{u_j}{\epsilon}\frac{\partial u_i}{\partial x_j}\right) = -\frac{\partial P}{\partial x_i} - \frac{H^2}{k}u_i + \frac{\partial^2 u_i}{\partial x_j \partial x_j} - \mathrm{Ra}\,\delta_{i3}\theta \tag{2}$$

$$A\frac{\partial \theta}{\partial t} + u_j\frac{\partial \theta}{\partial x_j} = \frac{\partial^2 \theta}{\partial x_j \partial x_j} \tag{3}$$

where (x_i, t, u_i, P, T) have been made dimensionless with respect to $(H, H^2/\kappa, \kappa/H, \rho_f\nu^2/H^2, T_H - T_c)$, and $\mathrm{Ra} = g\alpha\Delta TH^3/\nu\kappa$, $A = (\rho C_p)_{mix}/(\rho C_p)_f$, $\mathrm{Pr} = \nu_f/\kappa$.

In the limit of one-dimensional steady flow or creeping flow, equations (1)–(2) may be rigorously derived for a random array of rigid particles. The basic ideas of probability averaging common to this and many other two-phase problems have been reviewed by Batchelor [1].[2] The specific discussion of a porous medium was given by Howells [2], together with an explicit formula for the permeability, k, valid in the dilute region. The terms on the left-hand side of equation (2) represent generalizations of the Darcy-Brinkman-Boussinesq equations, the presence or absence of which have no consequence on the results to be reported below; see Homsy and Sherwood [3] for a discussion.

For layers heated uniformly from below, equations (1)–(3) admit a steady, stagnant conductive solution. Thus for disturbances we have:

$$\frac{\partial u_i}{\partial x_i} = 0 \tag{4}$$

$$\frac{1}{\mathrm{Pr}}\left(\frac{\partial u_i}{\partial t} + \frac{u_j}{\epsilon}\frac{\partial u_i}{\partial x_j}\right) = -\frac{\partial P}{\partial x_i} - \frac{H^2}{k}u_i + \frac{\partial^2 u_i}{\partial x_j \partial x_j} + \mathrm{Ra}\,\theta\delta_{i3} \tag{5}$$

$$A\frac{\partial \theta}{\partial t} + u_i\frac{\partial \theta}{\partial x_i} - \frac{\partial^2 \theta}{\partial x_j \partial x_j} = u_3 \tag{6}$$

Equations (4)–(6) are to be solved subject to the homogeneous conditions

$$u_i = \theta = 0 \quad z = 0, 1 \tag{7}$$

It is now common in convective instability problems of this type to develop predictions for both absolute stability (energy theory) and certain instability (linear theory). We remark that these limits are

[1] Department of Chemical Engineering, Stanford University, Stanford, Calif.

Contributed by the Heat Transfer Division of THE AMERICAN SOCIETY OF MECHANICAL ENGINEERS. Manuscript received by the Heat Transfer Division October 28, 1976.

[2] Numbers in brackets designate References at end of technical note.

Conclusion

The entrainment in a buoyant plume, within the similar profiles approximation assumed here, is controlled by the initial buoyancy, and the atmospheric inversion rate. The spreading of the plume, $V_e < 0$, corresponding to horizontal outflow from the plume, occurs after the plume had attained negative buoyancy. At high Froude numbers, Fr > 5, it is the initial momentum flux that characterizes the plume rise. The effect of atmospheric inversion rate on the entrainment parameter is initially small but becomes dominant in the region of negative buoyancy where α_1 and α_2 are both small and α_2 is negative.

References

1 Morton, R. R., Taylor, G., and Turner, J. S., "Turbulent Gravitational Convection From Maintained and Instantaneous Sources," *Proceedings of Royal Society*, London, Series A, Vol. 234, 1956, pp. 1–23.

2 Briggs, G. A., "Plume Rise," AEC Critical Review Series, U.S. AEC, Division of Technology Information, 1969.

3 Sneck, H. J., and Brown, D. H., "Cooling Tower Discharge Buoyant Plume Rise Through Atmospheric Inversions," GEC Report No. 71-C-311, Nov. 1971.

4 Fox, D. G., "Forced Plume in a Stratified Fluid," *Jour. Geoph. Res.*, Vol. 75, No. 33, Nov. 1970, pp. 6818–6835.

5 Hinze, J. O., *Turbulence*, McGraw-Hill, New York, 1959, pp. 411–426.

A Note on Convective Instabilities in Boussinesq Fluids and Porous Media

K. Walker[1] and G. M. Homsy[1]

Nomenclature

A = ratio of volumetric heat capacities of fluid/solid matrix to that of the fluid
g = acceleration of gravity
H = fluid depth
k = permeability
P = fluid pressure
Pr = Prandtl number, ν_f/κ
Ra = Rayleigh number, $g\alpha\Delta TH^3/\nu_f\kappa$
t = time
ΔT = temperature difference across layer
u = fluid velocity
x = spatial coordinate
α = coefficient of thermal expansion
δ_{i3} = unit vector in the vertical direction
κ = thermal diffusivity, $\lambda_{mix}/(\rho C_p)_f$
λ = thermal conductivity
μ = viscosity
ν = kinematic viscosity
ρ = density
θ = dimensionless temperature

Subscripts

f = fluid property
i, j = index for vector quantities (= 1, 2, 3).
liq = liquid property
mix = fluid/solid effective property

This note is concerned with the stability of a fluid held in an isotropic porous media between two infinite horizontal planes separated by a distance H. We express the permeability dimensionlessly as k/H^2. The problem has been solved in both the limit of $k/H^2 \to \infty$, the Bénard problem for a single viscous fluid, and $k/H^2 \to 0$, the Darcy approximation; an extensive literature exists for both problems. However for small gaps or moderately permeable materials, k/H^2 may lie between these two extremes. The problem is also of some interest in that it provides insight into the range of validity of the Darcy assumption which consists of neglecting the term $\nabla^2 u$ relative to the Darcy term $\mu u/k$.

The formulation of the problem is based upon the following assumptions:

1 Fluid and solid properties are assumed to be constant except for the density of the fluid. The Boussinesq approximation is invoked.

2 The two bounding planes are assumed to be isothermal impermeable solid surfaces.

3 The system is assumed to be governed by the following fluid field equations

$$\frac{\partial u_i}{\partial x_i} = 0 \tag{1}$$

$$\frac{1}{\mathrm{Pr}}\left(\frac{\partial u_i}{\partial t} + \frac{u_j}{\epsilon}\frac{\partial u_i}{\partial x_j}\right) = -\frac{\partial P}{\partial x_i} - \frac{H^2}{k}u_i + \frac{\partial^2 u_i}{\partial x_j \partial x_j} - \mathrm{Ra}\,\delta_{i3}\theta \tag{2}$$

$$A\frac{\partial \theta}{\partial t} + u_j\frac{\partial \theta}{\partial x_j} = \frac{\partial^2 \theta}{\partial x_j \partial x_j} \tag{3}$$

where (x_i, t, u_i, P, T) have been made dimensionless with respect to $(H, H^2/\kappa, \kappa/H, \rho_f\nu^2/H^2, T_H - T_c)$, and $\mathrm{Ra} = g\alpha\Delta TH^3/\nu\kappa$, $A = (\rho C_p)_{mix}/(\rho C_p)_f$, $\mathrm{Pr} = \nu_f/\kappa$.

In the limit of one-dimensional steady flow or creeping flow, equations (1)–(2) may be rigorously derived for a random array of rigid particles. The basic ideas of probability averaging common to this and many other two-phase problems have been reviewed by Batchelor [1].[2] The specific discussion of a porous medium was given by Howells [2], together with an explicit formula for the permeability, k, valid in the dilute region. The terms on the left-hand side of equation (2) represent generalizations of the Darcy-Brinkman-Boussinesq equations, the presence or absence of which have no consequence on the results to be reported below; see Homsy and Sherwood [3] for a discussion.

For layers heated uniformly from below, equations (1)–(3) admit a steady, stagnant conductive solution. Thus for disturbances we have:

$$\frac{\partial u_i}{\partial x_i} = 0 \tag{4}$$

$$\frac{1}{\mathrm{Pr}}\left(\frac{\partial u_i}{\partial t} + \frac{u_j}{\epsilon}\frac{\partial u_i}{\partial x_j}\right) = -\frac{\partial P}{\partial x_i} - \frac{H^2}{k}u_i + \frac{\partial^2 u_i}{\partial x_j \partial x_j} + \mathrm{Ra}\,\theta\delta_{i3} \tag{5}$$

$$A\frac{\partial \theta}{\partial t} + u_i\frac{\partial \theta}{\partial x_i} - \frac{\partial^2 \theta}{\partial x_j \partial x_j} = u_3 \tag{6}$$

Equations (4)–(6) are to be solved subject to the homogeneous conditions

$$u_i = \theta = 0 \quad z = 0, 1 \tag{7}$$

It is now common in convective instability problems of this type to develop predictions for both absolute stability (energy theory) and certain instability (linear theory). We remark that these limits are

[1] Department of Chemical Engineering, Stanford University, Stanford, Calif.

Contributed by the Heat Transfer Division of THE AMERICAN SOCIETY OF MECHANICAL ENGINEERS. Manuscript received by the Heat Transfer Division October 28, 1976.

[2] Numbers in brackets designate References at end of technical note.

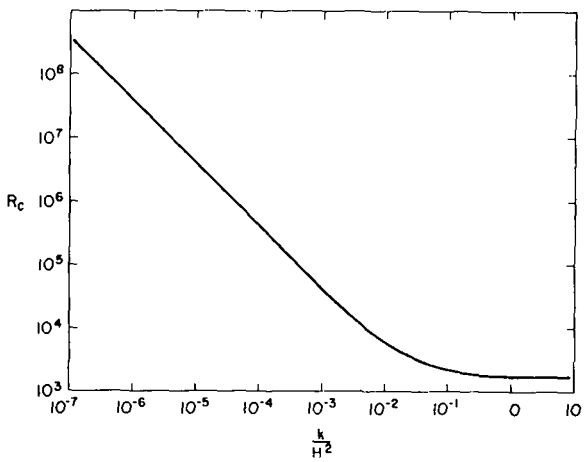

Fig. 1 The eigenvalue R_c as a function of dimensionless permeability

identical for the problem stated previously, and the necessary and sufficient conditions for instability is Ra > R_c, where R_c is the smallest eigenvalue of the system,

$$\frac{\partial u_i}{\partial x_i} = 0 \tag{8}$$

$$\frac{\partial P}{\partial x_i} + \left(\frac{H^2}{k}\right) u_i = \frac{\partial^2 u_i}{\partial x_j \partial x_j} + R_c \theta \delta_{i3} \tag{9}$$

$$\frac{\partial^2 \theta}{\partial x_i \partial x_i} + u_3 = 0 \tag{10}$$

subject to equation (7).

In the case of linear instability, we prove the remark by noting that the linearized version of equations (5)–(6) are self-adjoint, and onset is thus by the neutral mode $\partial/\partial t = 0$, Davis [4], which results in equations (7)–(10). For the energy method, it is well known that if there is no inflow across the boundaries, the base state is conductive and the linear problem self-adjoint, the energy and linear limit are identical, Davis [5]. For an alternative development showing that the Euler-Lagrange equations from the variational problem can be reduced to equations (7)–(10), see Joseph [6], Westbrook [7], and Homsy and Sherwood [3].

Standard manipulations of Fourier-decomposition and elimination of the pressure lead to

$$\left((D^2 - \alpha^2) - \frac{H^2}{k}\right)(D^2 - \alpha^2) W(z) = R_c \alpha^2 \theta(z) \tag{11}$$

$$(D^2 - \alpha^2)\theta(z) + W(z) = 0 \tag{12}$$

$$W = DW = \theta = 0 \quad f = 0, 1 \tag{13}$$

where $D = d/dz$ and α is the wave-number.

We have solved equations (11)–(13) for $R_c \equiv \min_{\alpha} \mathrm{Ra}(\alpha)$ as a function of H^2/k using the Rayleigh-Ritz method. As trial functions, we used sines for $\theta(z)$ and "beam functions" for $W(z)$; see Chandrasekhar [8]. The resulting algebraic eigenvalue problem was solved by a method due to Martin and Wilkinson [9].

The main results are shown in Fig. 1. It is seen that for low permeabilities, (large H^2/k), the Darcy limit $R_c = (4\pi^2)\, H^2/k$ is reached for $k/H^2 < 10^{-3}$. Similarly for high permeabilities, $k/H^2 > 10$, the response is close to that of a single viscous fluid, $R_c \sim 1708$. Thus there exists a range $10^{-3} \leq k/H^2 \leq 10$ for which the criteria for instability is intermediate to the two asymptotic limits.

We will briefly consider an application of these results. Recently Nir and Acrivos [10] have used the Bénard critical point as a means of measuring the effective viscosity of a suspension of spheres at low rates of strain. The effective viscosity of concentrated suspensions has been the subject of many investigations. The effective viscosity becomes very difficult to determine experimentally at concentrations of 50 percent and higher. One explanation proposed is that the difficulties encountered are due to the mixture experiencing a transition from a concentrated suspension to a porous medium [10]. The question of whether convection begins in a suspension as a single effectively homogeneous fluid or as convection in a porous medium can be examined by making an estimate of the critical Rayleigh number for each case.

The Rayleigh number for concentrated suspensions defined in terms of liquid properties is

$$\mathrm{Ra}_{\mathrm{sus}} = \mathrm{Ra}_{\mathrm{liq}} \epsilon \frac{\mu_{\mathrm{liq}}}{\mu_{\mathrm{eff}}} \frac{\lambda_{\mathrm{liq}}}{\lambda_{\mathrm{eff}}} \frac{C_{p\,\mathrm{liq}}}{C_{p\,\mathrm{eff}}}$$

For a rough estimate it is assumed that;

$$\frac{\lambda_{\mathrm{liq}}}{\lambda_{\mathrm{eff}}} \approx \frac{C_{p\,\mathrm{liq}}}{C_{p\,\mathrm{eff}}} \approx 1$$

and $\mu_{\mathrm{eff}}/\mu_{\mathrm{liq}} = 100$ from Nir's data at $\epsilon = 0.5$. These assumptions yield a critical Rayleigh number based on liquid properties of $\mathrm{Ra} = 3.4 \times 10^5 = (1708(\mu_{\mathrm{eff}}/\mu_{\mathrm{liq}})1/\epsilon)$.

The Darcy-Brinkman number, H^2/k, for the corresponding porous medium can be estimated using empirical relations for the permeability. For the particle size and cell height used by Nir and Acrivos,

$$\frac{H^2}{k} = 10^8$$

The critical Rayleigh number in terms of liquid properties for this value of H^2/k is therefore $\mathrm{Ra}_{cr} = 4\pi^2 H^2/k \approx 4* 10^9$. If the mixture behaves as a porous medium, then the critical temperature difference is several orders of magnitude larger than that which would be expected for a concentrated suspension. The reason is the extremely large resistance force exerted by particles which are held stationary. It is reasonable to expect that some of the difficulties encountered in effective viscosity measurements using shear apparatuses is also due to a transition from a concentrated suspension to a porous medium. It is important to understand what factors cause this transition.

Acknowledgment

We gratefully thank the National Science Foundation for support of this work through grant ENG-73-3955.

References

1 Batchelor, G. K., "Transport Properties of Two-Phase Materials With Random Structure," *Ann. Rev. Fluid Mechanics*, Vol. 6, 1974, p. 227.

2 Howells, I. D., "Drag Due to the Motion of a Newtonian Fluid Through a Sparse Random Array of Small Fixed Rigid Objects," *Journal of Fluid Mechanics*, Vol. 64, 1974, p. 449.

3 Homsy, G. M., and Sherwood, A. E., "Convective Instabilities in Porous Media With Through-Flow," *AIChE Journal*, Vol. 22, 1976, p. 168.

4 Davis, S. H., "On the Principle of Exchange of Stabilities," *Proceedings of the Royal Society (London)*, A310, 1969, p. 341.

5 Davis, S. H., "On the Possibility of Subcritical Instabilities," *Instability of Continuous Systems*, Leipholz, ed., Springer-Verlag, Berlin, 1971.

6 Joseph, D. D., "Nonlinear Stability of the Boussinesq Equations by the Method of Energy," *Arch. Rat. Mech. Anal.*, Vol. 27, 1966, p. 163.

7 Westbrook, D. R., "Stability of Convective Flow in a Porous Medium," *Phys. Fluids*, Vol. 12, 1969, p. 1547.

8 Chandrasekhar, S., *Hydrodynamic and Hydromagnetic Stability*, Oxford University Press, 1961.

9 Martin, R. S., and Wilkinson, J. H., "Reduction of the Symmetric Eigenvalue Problem Ax = λBx and Related Problems to Standard Form," *Numer. Math.* Vol. 11, 1968, p. 99.

10 Nir, A., and Acrivos, A., "Experiments on the Effective Viscosity of Concentrated Suspensions of Solid Spheres," *Int. J. Multiphase Flow*, Vol. 1, 1974, p. 373.

Free Convection in an Enclosure Revisited

C. Quon[1]

Nomenclature

A = Rayleigh number
C = free constant in Gill's theory
$q = q(z)$, the transformed vertical coordinate in Gill's theory
w = vertical boundary layer velocity
(x, z) = cartesian coordinate with origin at center of cavity
θ = temperature
$\xi = \pm(1/2 - x)A^{1/4}$ stretched coordinate
σ = Prandtl number
ψ_0 = stream function in the cavity
ψ_c = computed stream function at the center of the cavity

The free constant C in Gill's theory on thermal convection in a differentially heated rectangular cavity is determined from the stream function of a numerical computation. It is shown that the new value of C brings the theory closer to the experimental data at the midheight of the cavity.

Introduction

In an earlier publication [3][2] further study was promised to investigate the results of an alternative value for the free constant in a theory by Gill [2] on thermal convection in a slot. A study was made but the results were not published because they were not conclusive. It was also felt that because of the practical importance of the problem the engineering community would soon improve on Gill's solutions, and would thus make it unnecessary to publish the results.

In the intervening years we have indeed seen a number of very good publications on the subject (see [4] for a representative bibliography), but none can be considered to have improved on Gill's theory. Private conversation in the 1976 National Heat Transfer Conference in St. Louis, and the personal correspondence the author received in the last few years have convinced him that a brief communication as originally planned is warranted.

Some Background

In [3], the following assumption and results in Gill's theory were confirmed: (*a*) The horizontal boundary conditions do not appreciably affect the flow in the cavity (Gill neglected the effect of the horizontal boundaries altogether); and (*b*) The scaled velocity and temperature fields across the vertical boundary layers are invariant with respect to : (i) the Prandtl number σ, for $\sigma > 1$ (Gill assumed $\sigma \to \infty$ in the analysis); and (ii) the Rayleigh number, A, when it is sufficiently high, (say when boundary layers are scaled with $A^{-1/4}$, they should be smaller than unity, so that the boundary layers are distinctly separated).

In spite of these confirmations, comparison of the theory with other data showed that: (*a*) the theoretical stream function is 30 percent; and (*b*) the vertical velocities in the boundary layer are 25 percent too high at their respective maxima, although the comparison also shows that the calculated, experimental, and theoretical temperature distributions agree reasonably well.

In Gill's theory, the velocity and temperature fields depend strongly on the free constant C shown in equations (6.18) and (6.19) in [2]. There is no unique way to determine this constant because the solutions cannot simultaneously satisfy all the boundary conditions. The most logical way is that used by Gill himself. He determined the constant by requiring the stream function to meet the no flux condition, i.e., $\psi_0 = 0$, on the top and bottom boundaries. However, in order to compare with the temperature data, Gill had to use a different value for C.

Alternate Approaches

Alternatively one can obtain a value of C in terms of ψ from Gill's equation (6.18):

$$\psi_0 = C^3(1 + q^2)(1 - q^2)^2(1 + 3q^2)^{-11/3}$$

where $q = q(z)$ is the transformed ordinate, and $q = 0$ at $z = 0$ (midheight). Thus if one sets $C^3 = \psi_c = 0.5690$, which is the stream function obtained from the numerical computation at the center of the cavity [3], we obtain $C = 0.8275$ versus 0.9215 as calculated by Gill. The ordinate z as a function of q can be obtained by integrating equation (6.19) in [2], and z versus q plots are given in Fig. 1 for these values of C. Note that the asymptotic value for z as $q \to \infty$ is 0.34 for $C = 0.8275$. Therefore, by choosing C such that $C^3 = \psi_c$, the theory no longer provides any solution for $|z| < 0.34$. Fig. 2 compares the interior stream function $\psi_0(z)$ calculated from the theory with the numerical solution. Both the theoretical curves have infinite vertical gradients, i.e., $\psi_z = U = \pm\infty$, at the end points, and neither compares satisfactorily with the numerical result.

Fig. 3 shows the theoretical vertical velocity across the vertical boundary layer calculated from two different values of C at three levels of z as compared to the numerical solutions. By using $C^3 = \psi_c$, the theory provides a very good prediction for w at $z = 0$ as compared to both the numerical and experimental results (not shown, but see Fig. 6(*a*) in [3]). On the other hand, the new value for C has not improved the results at the other two levels, i.e., $z = \pm 0.3$. However, neither the numerical results nor the original calculations by Gill compare satisfactorily with Elder's experiments at these two levels.

Fig. 4 shows the intercomparison of the temperature distribution across the vertical boundary layer. Again, the new value for C, brings the theoretical curve closer to the numerical curve at midheight only, which compares quite well with Elder's results [3]. There is quite a spread at the other two levels between the theoretical, calculated, and experimental curves.

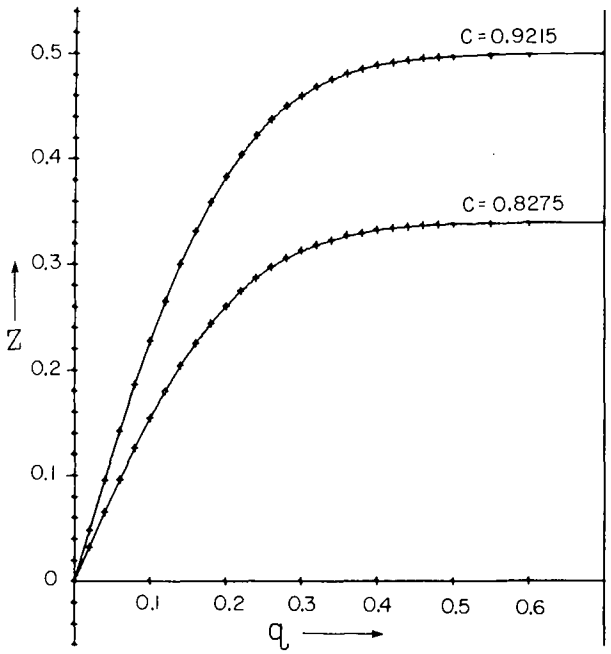

Fig. 1 Relation of transformed ordinate q and natural ordinate z for two values of C as integrated from Gill's equation (6.19)

[1] Atlantic Oceanographic Laboratory, Bedford Institute, Dartmouth, N.S., Canada.

[2] Numbers in brackets designate References at end of technical note.

Contributed by the Heat Transfer Division of THE AMERICAN SOCIETY OF MECHANICAL ENGINEERS. Manuscript received by the Heat Transfer Division October 18, 1976.

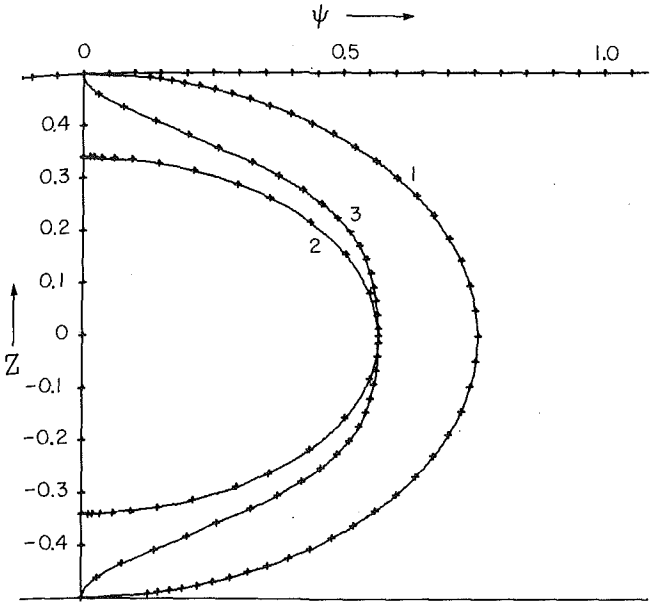

Fig. 2 Comparison of the numerical interior stream function and those calculated from theory: (1) Gill, $C = 0.9125$; (2) Gill, $C = 0.8275$; (3) numerical at $x = 0$, or along a vertical through the center of the cavity

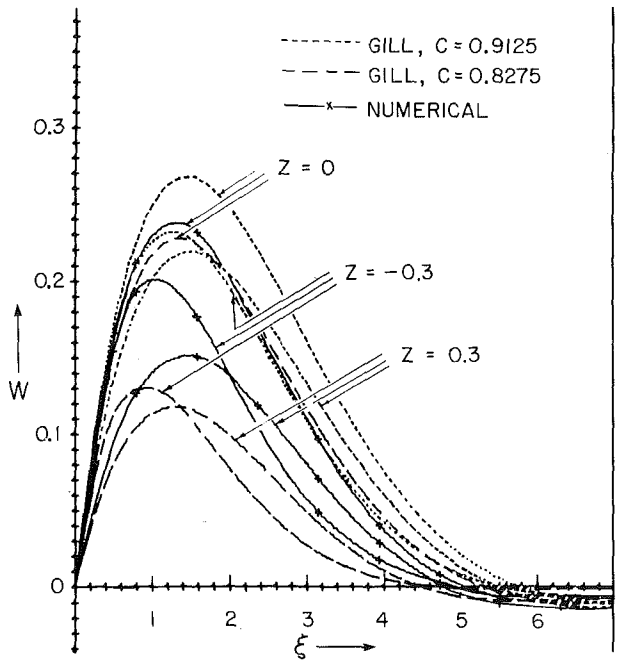

Fig. 3 Intercomparison of vertical velocity w as functions of stretched coordinate $\xi = (1/2 - x)A^{1/4}$ across the boundary layer near the hot wall at $z = 0$: A is the Rayleigh number (the wall position is at $x = \frac{1}{2}$; $z = 0$ is midheight of cavity)

A third attempt to determine C by requiring $\partial\psi_0/\partial z = 0$ at $z = \pm 0.50$ was unsuccessful because z would have become complex. A fourth attempt to use the interior vertical temperature gradient $\partial\theta/\partial z = 0.60$ at $z = 0$, the midheight of the cavity, yields $C = 1.477$. Since the theoretical values of the positions of the first zero of θ, and the first maximum of w measured from the side walls are proportional to C, and since the maximum magnitude of w is proportional to C^2, increasing C from 0.8275 to 1.477 will move the position of the first zero of θ and the first maximum of w outward by a factor of 1.8 and increase the maximum of w by a factor of 3.2. This will not improve the theory.

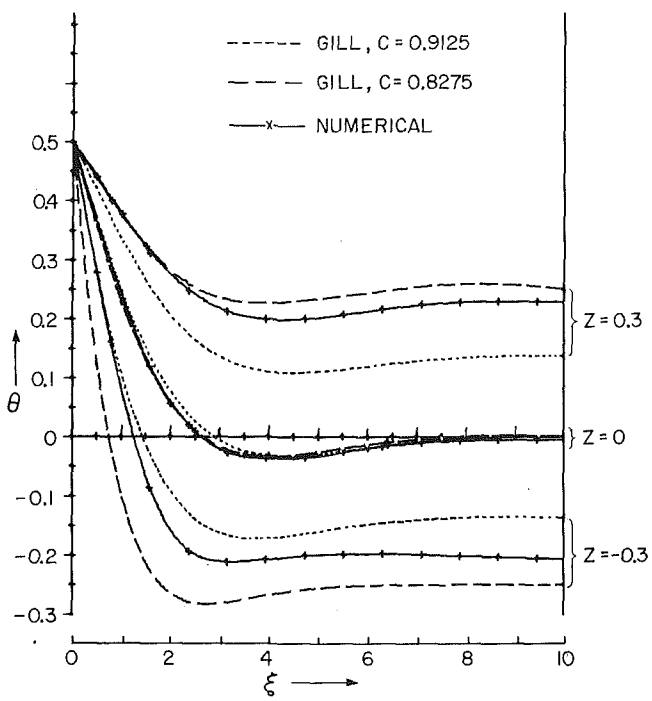

Fig. 4 Intercomparison of temperature distribution across vertical boundary layer near hot wall at $z = 0$: θ is the normalized temperature defined in $\theta = (T - \bar{T})/\Delta T$; $\bar{T}$ is the average of two sidewall temperatures and ΔT is their difference (for meaning of other symbols, see legend for Fig. 3)

Concluding Remarks

It is clear that changing the free constant in the theory has improved the theoretical prediction only locally at $z = 0$, but not the overall agreement with either the numerical or the experimental results. Although the numerical results compare satisfactorily with the experimental results for θ and w across the boundary layer at $z = 0$, the scatter of other levels at z needs to be interpreted.

There are three possible explanations for the large discrepancies between the results of the numerical and the laboratory experiments at $z = \pm 0.3$: (1) The numerical solutions are not accurate enough. The only way to show this is to repeat the computation on much finer nets, or preferably with variable grids [4]. However, the limited comparisons between two computations, on 31×31 and 40×40 grids, indicate that further refinement in the computation may only improve the results in some minor way [3]. (2) The descrepancies between the numerical and experimental results are due to differences in the aspect ratio. Elder's experiments [1] were done in containers of high aspect ratios compared to the aspect ratio unit, for the computation. The effect of aspect ratio may be small between results of high aspect ratios, but it can be appreciable when comparing results of high aspect ratios and those of aspect ratio unity, particularly in the end regions. (3) Perhaps the largest contribution to the discrepancy between experiment and computation is that the vertical velocity data used for comparison, as from Elder's Fig. 7 [1], are from a system where the two side vertical boundary layers are not distinct. Elder's experimental parameters barely meet the criterion set down by Gill, which is $[11.5\, A^{-1/4}(H/L)^{1/4}] < 1$. This criterion requires the first zero of the dynamical boundary layer to fall within half the width of the container. The interaction of two opposite flows in the boundary layers must produce effects neither the theory nor the computation is intended for.

References

1 Elder, J. W., "Laminar Free Convection in a Vertical Slot," *Journal of Fluid Mechanics*, Vol. 23, 1966, p. 77.

2 Gill, A. E., "The Boundary-Layer Regime for Convection in a Rectangular Cavity," *Journal of Fluid Mechanics*, Vol. 26, 1966, p. 515.
3 Quon, C., "High Rayleigh Number Convection in an Enclosure—A Numerical Study," *The Physics of Fluids*, Vol 15, 1972, p. 12.
4 Quon, C., "A Mixed Spectral and Finite Difference Model to Study Baroclinic Annulus Waves," *Journal of Computational Physics*, Vol. 20, 1976, p. 442.
5 Rogers, R. H., "Convection," Reports on Progress in Physics, Vol. 39, 1976, p. 1.

Local Nonsimilar Solutions for Subliming Particle-Vapor Boundary-Layer Flow

N. Nishikawa[1] and H. Oguchi[2]

Nomenclature

C_p = specific heat of vapor
d = particle diameter; d_e refers to diameter at uniform flow
h_L = latent heat of sublimation
k = thermal conductivity of vapor
L = internal diameter of pipe
$\dot{m}$ = sublimation rate
Nu_p = particle Nusselt number
P = pressure
q_w = wall heat flux
R = gas constant for vapor
T = vapor temperature; T_w and T_e refer to surface and uniform flow temperature, respectively
u = velocity parallel to wall; u_e refers to uniform flow velocity
v = velocity perpendicular to wall
x = distance parallel to wall
y = coordinate perpendicular to wall
μ = viscosity coefficient of mixture
ρ = density; $\rho = \rho_p + \rho_v$, ρ_p and ρ_v refer to density of particle cloud and vapor, respectively
ψ = stream function in (x, y) coordinate

Introduction

The purpose of this note is to present an analysis of a subliming particle-vapor boundary-layer flow by a new type of locally autonomous method. The method contains much simplifying assumptions compared with that proposed by Sparrow and Yu [1][3] but specifically provides more feasible way for analysis of thermal boundary layer together with mass and heat productions.

The problem dealt with here is the same as the one reported in [2, 3]; that is the boundary-layer analysis of a subliming particle-vapor flow inside a pipe for the case of uniform wall heat flux.

Analysis, Results, and Discussion

The same simplifying assumptions, as made by Simpson, et al. [3] in an analysis based on the integral method, are still employed with the exception that here the variation in particle size is taken into account. As for the particle of spherical shape, the particle temperature T_p and the number density n of particles are equal to respective uniform flow values over the whole region concerned. The concerned boundary layer may be identified with the one over a semi-infinite flat plate provided that the thickness is small enough compared to the pipe radius. For that case the basic equations are written as

$$(\rho u)_x + (\rho v)_y = 0 \tag{1}$$

$$\rho u u_x + \rho v u_y = (\mu u_y)_y \tag{2}$$

$$\rho_v C_p (u T_x + v T_y) = (k T_y)_y - \pi d n \mathrm{Nu}_p k_e (T - T_p) - \dot{m} C_p (T - T_p) \tag{3}$$

$$(\rho_p u)_x + (\rho_p v)_y = -\dot{m} \tag{4}$$

$$\pi d n \mathrm{Nu}_p k_e (T - T_p) - \dot{m} h_L = 0 \tag{5}$$

$$P = \rho_v R T \tag{6}$$

where the subscripts x and y denote $\partial/\partial x$ and $\partial/\partial y$, respectively, and k_e refers to thermal conductivity of vapor covering the particles with the temperature $T_p = T_e$. For the heat flux q_w, Fourier's law is introduced as the boundary condition for equation (3) for energy; i.e., $q_w = -k \partial T/\partial y$.

In introducing the dimensionless variables as follows:

$$\xi = x/[d_e \mathrm{Re} \mathrm{Pr}_e/(\mathrm{Nu}_p \pi n d_e^3)], \quad \eta = u_e \int_0^y \rho dy/(2\rho_e \mu_e u_e x)^{1/2}$$

$$f = \psi/(2\rho_e \mu_e u_e x)^{1/2}, \quad \theta = (T - T_e)/T_e, \quad Y = \rho_p/\rho$$

the boundary-layer equations and the boundary conditions reduce to

$$(Cf'')' + ff'' = 0 \tag{7}$$

$$(\rho/\rho_v)(C\theta'/\mathrm{Pr})' + f\theta' = 2\xi[f'\theta_\xi + W(\rho_e/\rho_v)(H + \theta)] \tag{8}$$

$$fY' = 2\xi[f' Y_\xi + W(\rho_e/\rho)] \tag{9}$$

$$W = \dot{m} x/\rho_e u_e \xi = \theta(\rho_p/\rho_{p,e})^{1/3}/H \tag{10}$$

$$f(0) = f'(0) = 0, \quad \theta'(0) = -(q_w d_e/k_w T_e)(\rho_e/\rho_w)(2\xi K/\mathrm{Nu}_p)^{1/2}$$

$$f'(\infty) \to 1, \quad \theta(\infty) \to 0, \quad Y(\infty) \to Y_e$$

where the prime and the subscript ξ denote $\partial/\partial\eta$ and $\partial/\partial\xi$, respectively, and $\mathrm{Re} = \rho_e u_e d_e/\mu_e$, $C(\xi, \eta) = \rho\mu/\rho_e\mu_e$, $\mathrm{Pr}(\xi, \eta) = \mu C_p/k$, $H = h_L/C_p T_e$, $K = \mathrm{Pr}_e/\pi n d_e^3$.

The solutions θ and Y can be expressed formally as

$$\theta = \theta_0 + \theta_1 \xi^{1/2} + \theta_2 \xi + \ldots \tag{11a}$$

$$Y = Y_0 + Y_1 \xi^{1/2} + Y_2 \xi + \ldots \tag{11b}$$

and then, the ξ-wise derivatives involved in equations (8) and (9) are

$$\frac{\partial\theta}{\partial\xi} = \sum_{n=0}^{\infty} \left(\frac{n}{2\xi} \theta_n \xi^{n/2} + \frac{\partial\theta}{\partial\xi} n \xi^{n/2} \right) \tag{12a}$$

$$\frac{\partial Y}{\partial\xi} = \sum_{n=0}^{\infty} \left(\frac{n}{2\xi} Y_n \xi^{n/2} + \frac{\partial Y_n}{\partial\xi} \xi^{n/2} \right) \tag{12b}$$

In order to derive a locally autonomous technique, we make an ad hoc assumption that the last terms involving $\partial\theta_n/\partial\xi$ or $\partial Y_n/\partial\xi$ in equations (12a) and (12b) are small enough to be neglected compared to the respective second terms. This assumption is justified if all the coefficients θ_n, as well as Y_n, are strongly dependent on η, while these are slightly dependent on ξ. The validity should be checked by examining the resulting solution. With this assumption, substitution of expressions (11) and (12) into equations (8) and (9) yields

$$(\rho/\rho_v)(C\theta_n'/\mathrm{Pr})' + f\theta_n' = nf'\theta_n + \epsilon W(\rho_e/\rho_v)(H + \theta) \tag{13}$$

$$fY_n' = nf' Y_n + \epsilon W(\rho_e/\rho) \tag{14}$$

where $\epsilon = 0$ for $n \neq 2$, and $\epsilon = 2$ for $n = 2$. In the foregoing derivation the variables ρ/ρ_v, C, Pr, $W(\rho_e/\rho_v)(H + \theta)$, and $W(\rho_e/\rho)$ were retained without expansion. This can be allowed if these variables are dependent on ξ much weakly compared with on η. Specifically, as can be shown from equations (9) and (10), the W involved in the terms

---

[1] Lecturer, Faculty of Engineering, Chiba University, Chiba, Japan.
[2] Professor, Institute of Space and Aeronautical Science, University of Tokyo, Tokyo, Japan.
[3] Numbers in brackets designate References at end of technical note.

Contributed by the Heat Transfer Division of THE AMERICAN SOCIETY OF MECHANICAL ENGINEERS. Manuscript received by the Heat Transfer Division September 28, 1976.

2 Gill, A. E., "The Boundary-Layer Regime for Convection in a Rectangular Cavity," *Journal of Fluid Mechanics*, Vol. 26, 1966, p. 515.
3 Quon, C., "High Rayleigh Number Convection in an Enclosure—A Numerical Study," *The Physics of Fluids*, Vol 15, 1972, p. 12.
4 Quon, C., "A Mixed Spectral and Finite Difference Model to Study Baroclinic Annulus Waves," *Journal of Computational Physics*, Vol. 20, 1976, p. 442.
5 Rogers, R. H., "Convection," Reports on Progress in Physics, Vol. 39, 1976, p. 1.

Local Nonsimilar Solutions for Subliming Particle-Vapor Boundary-Layer Flow

N. Nishikawa[1] and H. Oguchi[2]

Nomenclature

C_p = specific heat of vapor
d = particle diameter; d_e refers to diameter at uniform flow
h_L = latent heat of sublimation
k = thermal conductivity of vapor
L = internal diameter of pipe
$\dot{m}$ = sublimation rate
Nu_p = particle Nusselt number
P = pressure
q_w = wall heat flux
R = gas constant for vapor
T = vapor temperature; T_w and T_e refer to surface and uniform flow temperature, respectively
u = velocity parallel to wall; u_e refers to uniform flow velocity
v = velocity perpendicular to wall
x = distance parallel to wall
y = coordinate perpendicular to wall
μ = viscosity coefficient of mixture
ρ = density; $\rho = \rho_p + \rho_v$, ρ_p and ρ_v refer to density of particle cloud and vapor, respectively
ψ = stream function in (x, y) coordinate

Introduction

The purpose of this note is to present an analysis of a subliming particle-vapor boundary-layer flow by a new type of locally autonomous method. The method contains much simplifying assumptions compared with that proposed by Sparrow and Yu [1][3] but specifically provides more feasible way for analysis of thermal boundary layer together with mass and heat productions.

The problem dealt with here is the same as the one reported in [2, 3]; that is the boundary-layer analysis of a subliming particle-vapor flow inside a pipe for the case of uniform wall heat flux.

Analysis, Results, and Discussion

The same simplifying assumptions, as made by Simpson, et al. [3] in an analysis based on the integral method, are still employed with the exception that here the variation in particle size is taken into account. As for the particle of spherical shape, the particle temperature T_p and the number density n of particles are equal to respective uniform flow values over the whole region concerned. The concerned boundary layer may be identified with the one over a semi-infinite flat plate provided that the thickness is small enough compared to the pipe radius. For that case the basic equations are written as

$$(\rho u)_x + (\rho v)_y = 0 \tag{1}$$

$$\rho u u_x + \rho v u_y = (\mu u_y)_y \tag{2}$$

$$\rho_v C_p (u T_x + v T_y) = (k T_y)_y - \pi d n \mathrm{Nu}_p k_e (T - T_p) - \dot{m} C_p (T - T_p) \tag{3}$$

$$(\rho_p u)_x + (\rho_p v)_y = -\dot{m} \tag{4}$$

$$\pi d n \mathrm{Nu}_p k_e (T - T_p) - \dot{m} h_L = 0 \tag{5}$$

$$P = \rho_v R T \tag{6}$$

where the subscripts x and y denote $\partial/\partial x$ and $\partial/\partial y$, respectively, and k_e refers to thermal conductivity of vapor covering the particles with the temperature $T_p = T_e$. For the heat flux q_w, Fourier's law is introduced as the boundary condition for equation (3) for energy; i.e., $q_w = -k \partial T/\partial y$.

In introducing the dimensionless variables as follows:

$$\xi = x/[d_e \mathrm{Re} \mathrm{Pr}_e/(\mathrm{Nu}_p \pi n d_e^3)], \quad \eta = u_e \int_0^y \rho dy/(2\rho_e \mu_e u_e x)^{1/2}$$

$$f = \psi/(2\rho_e \mu_e u_e x)^{1/2}, \quad \theta = (T - T_e)/T_e, \quad Y = \rho_p/\rho$$

the boundary-layer equations and the boundary conditions reduce to

$$(Cf'')' + ff'' = 0 \tag{7}$$

$$(\rho/\rho_v)(C\theta'/\mathrm{Pr})' + f\theta' = 2\xi[f'\theta_\xi + W(\rho_e/\rho_v)(H + \theta)] \tag{8}$$

$$fY' = 2\xi[f' Y_\xi + W(\rho_e/\rho)] \tag{9}$$

$$W = \dot{m} x/\rho_e u_e \xi = \theta(\rho_p/\rho_{p,e})^{1/3}/H \tag{10}$$

$$f(0) = f'(0) = 0, \quad \theta'(0) = -(q_w d_e/k_w T_e)(\rho_e/\rho_w)(2\xi K/\mathrm{Nu}_p)^{1/2}$$

$$f'(\infty) \to 1, \quad \theta(\infty) \to 0, \quad Y(\infty) \to Y_e$$

where the prime and the subscript ξ denote $\partial/\partial\eta$ and $\partial/\partial\xi$, respectively, and $\mathrm{Re} = \rho_e u_e d_e/\mu_e$, $C(\xi, \eta) = \rho\mu/\rho_e\mu_e$, $\mathrm{Pr}(\xi, \eta) = \mu C_p/k$, $H = h_L/C_p T_e$, $K = \mathrm{Pr}_e/\pi n d_e^3$.

The solutions θ and Y can be expressed formally as

$$\theta = \theta_0 + \theta_1 \xi^{1/2} + \theta_2 \xi + \ldots \tag{11a}$$

$$Y = Y_0 + Y_1 \xi^{1/2} + Y_2 \xi + \ldots \tag{11b}$$

and then, the ξ-wise derivatives involved in equations (8) and (9) are

$$\frac{\partial\theta}{\partial\xi} = \sum_{n=0}^{\infty} \left(\frac{n}{2\xi} \theta_n \xi^{n/2} + \frac{\partial\theta}{\partial\xi} n \xi^{n/2} \right) \tag{12a}$$

$$\frac{\partial Y}{\partial\xi} = \sum_{n=0}^{\infty} \left(\frac{n}{2\xi} Y_n \xi^{n/2} + \frac{\partial Y_n}{\partial\xi} \xi^{n/2} \right) \tag{12b}$$

In order to derive a locally autonomous technique, we make an ad hoc assumption that the last terms involving $\partial\theta_n/\partial\xi$ or $\partial Y_n/\partial\xi$ in equations (12a) and (12b) are small enough to be neglected compared to the respective second terms. This assumption is justified if all the coefficients θ_n, as well as Y_n, are strongly dependent on η, while these are slightly dependent on ξ. The validity should be checked by examining the resulting solution. With this assumption, substitution of expressions (11) and (12) into equations (8) and (9) yields

$$(\rho/\rho_v)(C\theta_n'/\mathrm{Pr})' + f\theta_n' = nf'\theta_n + \epsilon W(\rho_e/\rho_v)(H + \theta) \tag{13}$$

$$fY_n' = nf' Y_n + \epsilon W(\rho_e/\rho) \tag{14}$$

where $\epsilon = 0$ for $n \neq 2$, and $\epsilon = 2$ for $n = 2$. In the foregoing derivation the variables ρ/ρ_v, C, Pr, $W(\rho_e/\rho_v)(H + \theta)$, and $W(\rho_e/\rho)$ were retained without expansion. This can be allowed if these variables are dependent on ξ much weakly compared with on η. Specifically, as can be shown from equations (9) and (10), the W involved in the terms

---

[1] Lecturer, Faculty of Engineering, Chiba University, Chiba, Japan.
[2] Professor, Institute of Space and Aeronautical Science, University of Tokyo, Tokyo, Japan.
[3] Numbers in brackets designate References at end of technical note.

Contributed by the Heat Transfer Division of THE AMERICAN SOCIETY OF MECHANICAL ENGINEERS. Manuscript received by the Heat Transfer Division September 28, 1976.

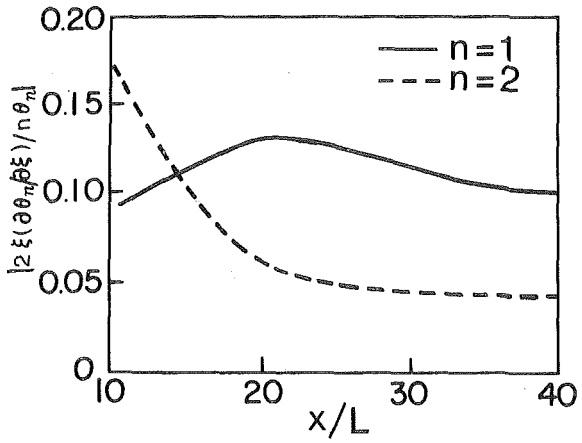

Fig. 1 Estimated variation of truncated terms, $q_w = 0.669$ W/cm^2

$W(\rho_e/\rho_v)(H + \theta)$ and $W(\rho_e/\rho)$ vanishes at the outer edge of the boundary layer as well as in the vicinity of the wall. Therefore, the terms $W(\rho_e/\rho_v)(H + \theta)$ and $W(\rho_e/\rho)$ are expected to indicate slight dependence on ξ. Consequently, the ξ is regarded as a parameter in equations (13) and (14). Then the solution for equations (13) and (14) can be solved for any fixed value of ξ locally-autonomously. In making the reasonable assumption that $\mathrm{Nu}_p = 2$, the boundary conditions for θ_n and Y_n become

$$\theta_1'(0) = -(q_w d_e/k_w T_e)(\rho_e/\rho_w)K^{1/2}, \quad \theta_n'(0) = 0 \qquad \text{for } n \neq 1$$

$$\theta_n(\infty) \to 0, \quad \text{for all } n, \quad Y_0(\infty) \to Y_e, \quad Y_n(\infty) \to 0 \quad \text{for } n \neq 0$$

It can be easily seen that all the coefficients θ_n, Y_n except the θ_1, θ_2, Y_0, and Y_2 vanish, because of the homogeneity of the equations with specified boundary conditions. Since $Y_0 = Y_e$, we have

$$\theta = \theta_1 \xi^{1/2} + \theta_2 \xi \tag{15a}$$

$$Y = Y_e + Y_2 \xi \tag{15b}$$

Consequently, the problem reduces to solve a set of equations (13) and (14) for θ_1, θ_2, and Y_2 combining with equations (7), (10), and (15) at any fixed value of ξ. Actually the solutions can be achieved as follows: for a fixed value of ξ, equation (7) for f and equations (13) and (14) for θ_1, θ_2, Y_2 are solved with an appropriate initial guess for θ and Y. Then θ and Y are re-evaluated using equation (15). With these new values of θ and Y the similar procedure is iterated until the solutions converge within a desired accuracy. In the numerical example shown in the following the so-called frozen solutions $Y = Y_e$, $\theta = \theta_1 \xi^{1/2}$ are employed as the initial guesses for Y and θ.

For comparison with experiment by Jones, et al. [2], computation has been worked out for the particle-vapor mixture of N_2 under the condition similar to one of their experiments: $d_e = 30\ \mu m$, $nd_e^3 = 0.001$, $T_e = 63.2$ K, and Re = 328.46. The constants C_p, R and the variables μ, k were taken from [4], assuming mixture viscosity to be that of vapor alone. The experiment was conducted for the flow through a pipe in the diameter $L = 1.37$ cm. However, the boundary layer is so thin that it may be identified with the one past a flat plate. The experimental data are referred to the dimensionless distance x/L, so that the present results referred to ξ or x/d_e are deduced to those referred to x/L by the relation $x/L = x/d_e(d_e/L)$ where $d_e/L = 2.19 \cdot 10^{-3}$ for the present example. The experiment covers the range $0 < x/L < 40$ or $0 < \xi < 0.48$. From the results the magnitude of the truncated terms in the present "locally autonomous method" was examined; for example, the absolute value of the ratio $(2\xi\partial\theta_n/\partial\xi)/(n\theta_n)$ at the wall is plotted against x/L in Fig. 1. The figure shows that the truncated terms are small compared to the retained terms except in the region close to the leading edge, where all production terms themselves become so small that any truncation is ineffective to the solution. This provides a support for the utility of the present method. The wall temperature variations are shown in Fig. 2 for parametric values of q_w. The results show reasonable agreement with the experiment by Jones, et al. [2]. Finally we note that the present analysis provides the particle size distribution within the boundary layer in contrast to the previous analyses [2, 3] based on the assumption of uniform particle size.

References

1 Sparrow, E. M., and Yu, H. S., "Local Non-Similarity Thermal Boundary-Layer Solutions," JOURNAL OF HEAT TRANSFER, TRANS. ASME, Series C, Vol. 93, No. 4, 1971, pp. 328–334.

2 Jones, M. C., Giarratano, P. J., and Simpson, A. U., "Heat Transfer to Solid-Vapor Mixture of Cryogens Below Their Triple Points Flowing Through Heated Tubes," *AIChE Journal*, Vol. 15, No. 6, 1969, pp. 890–897.

3 Simpson, A. U., Timmerhaus, K. D., Kreith, F., and Jones, M. C., "Heat and Mass Transfer in Dispersed Two-Phase, Single-Component Flow," *International Journal of Heat and Mass Transfer*, Vol. 12, 1969, pp. 1141–1155.

4 Hilsenrath, J., Beckett, C. W., et al., *Tables of Thermodynamic and Transport Properties of Gases*, Pergamon Press, 1960.

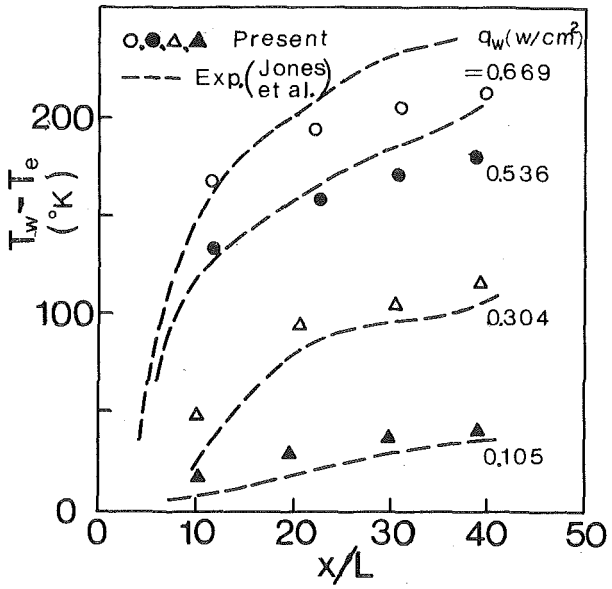

Fig. 2 Wall temperature variation: $T_e = 63.2$ K

Non-Fourier Heat Conduction in Thin Surface Layers

Tsai-tse Kao[1]

Nomenclature

C = thermal wave speed
p = Laplace transformed variable
T_w = wall temperature
T = temperature
t = time
q = heat flux

[1] Senior Thermal/Hydraulic Engineer, Nuclear Department, Foster Wheeler Energy Corp., Livingston, N. J., Assoc. Mem. ASME.

Contributed by the Heat Transfer Division of THE AMERICAN SOCIETY OF MECHANICAL ENGINEERS. Manuscript received by the Heat Transfer Division November 15, 1976.

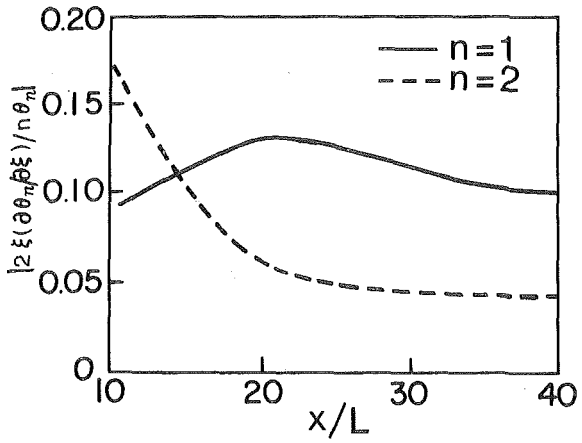

Fig. 1 Estimated variation of truncated terms, $q_w = 0.669$ W/cm^2

$W(\rho_e/\rho_v)(H + \theta)$ and $W(\rho_e/\rho)$ vanishes at the outer edge of the boundary layer as well as in the vicinity of the wall. Therefore, the terms $W(\rho_e/\rho_v)(H + \theta)$ and $W(\rho_e/\rho)$ are expected to indicate slight dependence on ξ. Consequently, the ξ is regarded as a parameter in equations (13) and (14). Then the solution for equations (13) and (14) can be solved for any fixed value of ξ locally-autonomously. In making the reasonable assumption that $\mathrm{Nu}_p = 2$, the boundary conditions for θ_n and Y_n become

$$\theta_1'(0) = -(q_w d_e/k_w T_e)(\rho_e/\rho_w)K^{1/2}, \quad \theta_n'(0) = 0 \qquad \text{for } n \neq 1$$

$$\theta_n(\infty) \to 0, \quad \text{for all } n, \quad Y_0(\infty) \to Y_e, \quad Y_n(\infty) \to 0 \quad \text{for } n \neq 0$$

It can be easily seen that all the coefficients θ_n, Y_n except the θ_1, θ_2, Y_0, and Y_2 vanish, because of the homogeneity of the equations with specified boundary conditions. Since $Y_0 = Y_e$, we have

$$\theta = \theta_1 \xi^{1/2} + \theta_2 \xi \tag{15a}$$

$$Y = Y_e + Y_2 \xi \tag{15b}$$

Consequently, the problem reduces to solve a set of equations (13) and (14) for θ_1, θ_2, and Y_2 combining with equations (7), (10), and (15) at any fixed value of ξ. Actually the solutions can be achieved as follows: for a fixed value of ξ, equation (7) for f and equations (13) and (14) for θ_1, θ_2, Y_2 are solved with an appropriate initial guess for θ and Y. Then θ and Y are re-evaluated using equation (15). With these new values of θ and Y the similar procedure is iterated until the solutions converge within a desired accuracy. In the numerical example shown in the following the so-called frozen solutions $Y = Y_e$, $\theta = \theta_1 \xi^{1/2}$ are employed as the initial guesses for Y and θ.

For comparison with experiment by Jones, et al. [2], computation has been worked out for the particle-vapor mixture of N_2 under the condition similar to one of their experiments: $d_e = 30\ \mu m$, $nd_e^3 = 0.001$, $T_e = 63.2$ K, and Re = 328.46. The constants C_p, R and the variables μ, k were taken from [4], assuming mixture viscosity to be that of vapor alone. The experiment was conducted for the flow through a pipe in the diameter $L = 1.37$ cm. However, the boundary layer is so thin that it may be identified with the one past a flat plate. The experimental data are referred to the dimensionless distance x/L, so that the present results referred to ξ or x/d_e are deduced to those referred to x/L by the relation $x/L = x/d_e(d_e/L)$ where $d_e/L = 2.19 \cdot 10^{-3}$ for the present example. The experiment covers the range $0 < x/L < 40$ or $0 < \xi < 0.48$. From the results the magnitude of the truncated terms in the present "locally autonomous method" was examined; for example, the absolute value of the ratio $(2\xi\partial\theta_n/\partial\xi)/(n\theta_n)$ at the wall is plotted against x/L in Fig. 1. The figure shows that the truncated terms are small compared to the retained terms except in the region close to the leading edge, where all production terms themselves become so small that any truncation is ineffective to the solution. This provides a support for the utility of the present method. The wall temperature variations are shown in Fig. 2 for parametric values of q_w. The results show reasonable agreement with the experiment by Jones, et al. [2]. Finally we note that the present analysis provides the particle size distribution within the boundary layer in contrast to the previous analyses [2, 3] based on the assumption of uniform particle size.

References

1 Sparrow, E. M., and Yu, H. S., "Local Non-Similarity Thermal Boundary-Layer Solutions," JOURNAL OF HEAT TRANSFER, TRANS. ASME, Series C, Vol. 93, No. 4, 1971, pp. 328–334.

2 Jones, M. C., Giarratano, P. J., and Simpson, A. U., "Heat Transfer to Solid-Vapor Mixture of Cryogens Below Their Triple Points Flowing Through Heated Tubes," *AIChE Journal*, Vol. 15, No. 6, 1969, pp. 890–897.

3 Simpson, A. U., Timmerhaus, K. D., Kreith, F., and Jones, M. C., "Heat and Mass Transfer in Dispersed Two-Phase, Single-Component Flow," *International Journal of Heat and Mass Transfer*, Vol. 12, 1969, pp. 1141–1155.

4 Hilsenrath, J., Beckett, C. W., et al., *Tables of Thermodynamic and Transport Properties of Gases*, Pergamon Press, 1960.

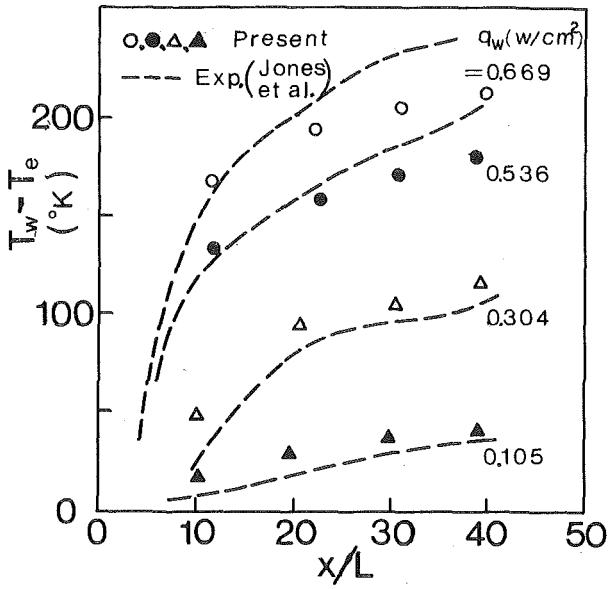

Fig. 2 Wall temperature variation: $T_e = 63.2$ K

Non-Fourier Heat Conduction in Thin Surface Layers

Tsai-tse Kao[1]

Nomenclature

C = thermal wave speed
p = Laplace transformed variable
T_w = wall temperature
T = temperature
t = time
q = heat flux

[1] Senior Thermal/Hydraulic Engineer, Nuclear Department, Foster Wheeler Energy Corp., Livingston, N. J., Assoc. Mem. ASME.

Contributed by the Heat Transfer Division of THE AMERICAN SOCIETY OF MECHANICAL ENGINEERS. Manuscript received by the Heat Transfer Division November 15, 1976.

q_w = wall flux
x, y, z = coordinators
α = thermal diffusivity
β = nondimensional time
δ = nondimensional length
θ = nondimensional temperature
Θ = nondimensional heat flux
$\bar{\theta}$ = Laplace transform of θ
$\bar{\Theta}$ = Laplace transform of Θ

Introduction

Recently, considerable interest has been generated toward the hyperbolic heat conduction equation and its importance in engineering applications. It has been shown by previous investigators [1–8][2] that this finite speed of heat propagation is important during short transient and in low temperature applications. During short time period, conduction takes place mainly in a very thin layer near the surface of the solid. The familiar one-dimensional conduction solution is often used as a first approximation. The conduction boundary layer theory that is advanced by Letcher [9, 10] can provide a rather good second approximation to the parabolic heat conduction equation, including the effect of the body's surface curvature. In this short note, the conduction boundary layer theory of Letcher will be extended to the hyperbolic conduction equation. Both the prescribed wall temperature case and the prescribed wall flux case will be treated.

Analysis

Consider a coordinate system, as shown in Fig. 1. The X-Y plane forms a tangential plane at the surface point of interest. The surface of the body can be described by an equation of the form $Z = f(X, Y)$. The hyperbolic heat conduction equation is given by:

$$\frac{1}{C^2}\frac{\partial^2 T}{\partial t^2} + \frac{1}{\alpha}\frac{\partial T}{\partial t} = \nabla^2 T \tag{1}$$

Let us define a new independent variable:

$$\zeta = Z - f(X, Y) \tag{2}$$

Next, we want to change the independent variables from (X, Y, Z, t) to (X, Y, ζ, t). The resulting equation at $X = 0$, $Y = 0$ is given by:

$$\frac{1}{C^2}\frac{\partial^2 T}{\partial t^2} + \frac{1}{\alpha}\frac{\partial T}{\partial t} = \left(\frac{\partial^2 T}{\partial X^2} + \frac{\partial^2 T}{\partial Y^2}\right)_{\substack{X=0\\Y=0}} + \gamma\frac{\partial T}{\partial \zeta} + \frac{\partial^2 T}{\partial \zeta^2} \tag{3}$$

where:

$$\gamma = \left[\frac{\partial^2 \zeta}{\partial X^2} + \frac{\partial^2 \zeta}{\partial y^2}\right]_{\substack{X=0\\Y=0}} = -\left(\frac{1}{R_1} + \frac{1}{R_2}\right) \tag{4}$$

R_1 and R_2 are the principal radii of curvature at $X = 0$, $Y = 0$.

First, we note that the heat penetration length ($\bar{\delta}$) will be of the order Ct. We are primarily interested in the time scale of the order α/C^2. By examining the order of magnitude of various terms in equation (3), it can be shown that both $\partial^2 T/\partial X^2|_{\substack{X=0\\Y=0}}$ and $\partial^2 T/\partial Y^2|_{\substack{X=0\\Y=0}}$ will be of the order $(\bar{\delta}/R)^2$, where R is the average radius of curvature at $X = 0$, $Y = 0$. The $\gamma\partial T/\partial\zeta$ term is of order $(\bar{\delta}/R)$, while the rest of the terms are of order unity. Neglecting terms of order $(\bar{\delta}/R)^2$, the equation at $X = 0$ and $Y = 0$ is given by:

$$\frac{1}{C^2}\frac{\partial^2 T}{\partial t^2} + \frac{1}{\alpha}\frac{\partial T}{\partial t} = \frac{\partial^2 T}{\partial \zeta^2} + \gamma\frac{\partial T}{\partial \zeta} \tag{5}$$

In order to proceed further, let us define by the following nondimensional variables:

$$\theta = \frac{T - T_0}{T_w - T_0} \quad \text{for prescribed wall temperature case} \tag{6}$$

$$= \frac{T - T_0}{q_w/k} \quad \text{for prescribed wall flux case}$$

[2] Numbers in brackets designate References at end of technical note.

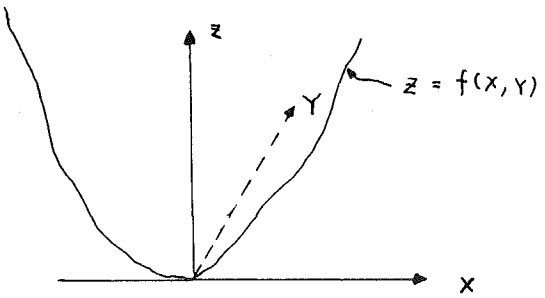

Fig. 1 Coordinate system

$$\beta = C^2 t/2\alpha \tag{7}$$

$$\delta = C\zeta/2\alpha \tag{8}$$

The resulting equation becomes:

$$\frac{\partial^2\theta}{\partial\beta^2} + 2\frac{\partial\theta}{\partial\beta} = \frac{\partial^2\theta}{\partial\delta^2} + \epsilon\frac{\partial\theta}{\partial\delta} \tag{9}$$

where

$$\epsilon = \frac{2\gamma\alpha}{C}$$

Case I—Prescribed Wall Temperature. The initial and boundary conditions for this case are given by:

$$\theta(\delta, 0) = 0, \qquad \frac{\partial\theta}{\partial\beta}(\delta, 0) = 0 \tag{10}$$

$$\theta(0, \beta) = 1 \qquad \theta(\delta \to \infty, \beta) = 0 \tag{11}$$

Let $\bar{\theta}$ be the Laplace transform function of θ with respect to β. In transformed variables, equation (9) becomes:

$$\frac{\partial^2\bar{\theta}}{\partial\delta^2} + \epsilon\frac{\partial\bar{\theta}}{\partial\delta} - (p^2 + 2p)\bar{\theta} = 0 \tag{12}$$

where p is the Laplace transform variable. The solution for $\bar{\theta}$, together with its boundary conditions, is given by:

$$\bar{\theta}(\delta, p) = \frac{1}{P}e^{-\delta/2[\epsilon + \sqrt{t\epsilon^2 + 4(p^2+2p)}]} \tag{13}$$

This can be inverted to give:

$$\theta(\delta, \beta) = e^{-\delta/2\epsilon}\left\{e^{-\delta} + \left(1 - \frac{\epsilon^2}{4}\right)^{1/2}\delta \times \int_\delta^\beta e^{-\tau}\frac{I_1\left[\left(1 - \frac{\epsilon^2}{4}\right)^{1/2}\sqrt{\tau^2 - \delta^2}\right]}{\sqrt{\tau^2 - \delta^2}}d\tau\right\}U(\beta - \delta) \tag{14}$$

where $U(\beta - \delta)$ is the heaviside step function.

First, we note that in equation (14), if $\epsilon = 0$, we will recover the solution of the hyperbolic heat conduction equation for a semi-infinite medium, as given by Baumeister and Hamill [8]. At the wave front, $\delta = \beta$. Therefore, we have:

$$\theta(\beta, \beta) = e^{-[1+\epsilon/2]\beta}$$

The curvature will increase or decrease the temperature of the wave front, depending on whether the surface is concave or convex.

In nondimensional form, the non-Fourier heat flux equation is given by:

$$\frac{\partial\Theta}{\partial\beta} + 2\Theta = -\frac{C}{\alpha}\frac{\partial\theta}{\partial\delta} \tag{15}$$

with initial conditions given by:

$$\Theta(\delta, 0) = 0 \tag{16}$$

where $\Theta = q/k(T_w - T_0)$. Application of the Laplace transform to equation (15) and initial condition at the solid surface gives:

$$\bar{\Theta}(\delta = 0, p) = -\frac{C}{\alpha}\frac{1}{(P+2)}\left.\frac{\partial\bar{\theta}}{\partial\delta}\right|_{\delta=0} \tag{17}$$

Using equation (13) in equation (17), results:

$$\bar{\Theta}(\delta = 0, p) = \frac{C}{2\alpha}\frac{1}{P(P+2)}\left[\epsilon + \sqrt{\epsilon^2 + 4(p^2+2p)}\right] \tag{18}$$

Let us investigate the effect of curvature on the non-Fourier surface heat flux. If we expand the right-hand side of equation (18) in a series of ϵ, we get:

$$\bar{\Theta}|_{\delta=0} = \frac{C}{2\alpha}\left\{\frac{\sqrt{4(p^2+2p)}}{P(P+2)} + \frac{\epsilon}{P(P+2)} + 0(\epsilon^2)\right\} \tag{19}$$

The inverse Laplace transform of equation (19) is:

$$\Theta(\delta = 0, \beta) = \frac{C}{2\alpha}\left\{2e^{-\beta}I_0(\beta) + \frac{\epsilon}{2}(1 - e^{-\beta}) + 0(\epsilon^2)\right\} \tag{20}$$

Case II—Prescribed Wall Heat Flux. The initial and boundary conditions for this case are given by:

$$\theta(\delta, 0) = \frac{\partial\theta}{\partial\beta}(\delta, 0) = \Theta(\delta, 0) = 0 \tag{21}$$

$$\Theta(0, \beta) = 1, \qquad \Theta(\delta \to \infty, \beta) = 0 \tag{22}$$

Note that for the present case,

$$\theta = (T - T_0)/(q_{w/k}) \tag{23}$$

$$\Theta = q/q_w \tag{24}$$

As shown in reference [5], upon application of the Laplace transform to the non-Fourier heat flux equation with its initial conditions, a boundary condition for the Laplace transform of the nondimensional temperature $\bar{\theta}$ at the surface $\delta = 0$ can be obtained:

$$\frac{\partial\bar{\theta}}{\partial\delta}(0, p) = -\frac{\alpha}{C}\frac{(P+2)}{P} \tag{25}$$

The Laplace transformed nondimensional temperature distribution with initial and boundary conditions given by equation (21) and equation (25) is:

$$\bar{\theta}(\delta, p) = \frac{2\alpha}{C}\frac{P+2}{P}\frac{e^{-\delta/2\left[\epsilon + \sqrt{\epsilon^2+4(p^2+2p)}\right]}}{\left[\epsilon + \sqrt{\epsilon^2 + 4(p^2+2p)}\right]} \tag{26}$$

Inversion of equation (26) yields:

$$\theta(\delta, \beta) = \frac{\alpha}{C}e^{-\epsilon/2\delta}\left\{e^{-\beta}I_0\left[\left(1 - \frac{\epsilon^2}{4}\right)^{1/2}\sqrt{\beta^2 - \tau^2}\right] + \int_\delta^\beta e^{-\tau}I_0 \times \left[\left(1 - \frac{\epsilon^2}{4}\right)^{1/2}\sqrt{\tau^2 - \delta^2}\right]d\tau\right\} U(\beta - \delta) - \frac{\alpha}{C}\epsilon\left\{e^{-\beta}\int_\delta^\infty e^{-\epsilon/2\zeta}I_0 \times \left[\left(1 - \frac{\epsilon^2}{4}\right)^{1/2}\sqrt{\beta^2 - \zeta^2}\right]U(\beta - \zeta)d\zeta + \int_\delta^\infty e^{-\epsilon/2\zeta} \times \left[\int_0^\beta e^{-\tau}I_0\left[\left(1 - \frac{\epsilon^2}{4}\right)^{1/2}\sqrt{\tau^2 - \zeta^2}\right]U(\tau - \zeta)d\tau\right]d\zeta\right\} \tag{27}$$

We note here that the solution, as given by Maurer and Thompson [5], can be recovered if ϵ is set equal to zero.

In order to observe the effect of curvature on the surface temperature, we expand equation (26) in power series of ϵ at $\delta = 0$:

$$\bar{\theta}(\delta = 0, p) = \frac{2\alpha}{C}\frac{P+2}{P}\left\{\frac{1}{\sqrt{4(p^2+2p)}} - \frac{\epsilon}{4(p^2+2p)} + 0(\epsilon^2)\right\} = \frac{\alpha}{C}\left\{\frac{1}{P}\left[\frac{\sqrt{P+2}}{\sqrt{P}} - 1\right] + \frac{1}{P} - \frac{\epsilon}{P^2} + 0(\epsilon^2)\right\} \tag{28}$$

This can be inverted to give:

$$\theta(\delta = 0, \beta) = \frac{\alpha}{C}\left\{1 + \int_0^\beta e^{-t}[I_1(t) + I_0(t)]dt - \epsilon\beta + 0(\epsilon^2)\right\} \tag{29}$$

Again, depending on whether the body is concave or convex, the curvature effect may not be negligible.

Conclusion

The influence of the surface curvature of a solid body on non-Fourier conduction has been investigated using the conduction boundary layer theory of Letcher. Both the cases of prescribed wall temperature and prescribed wall heat flux have been examined analytically. Close form solutions for both cases have been obtained in order to assess the influence of surface curvature on non-Fourier heat conduction in a thin solid layer. As shown by earlier investigators (see references [1-8]) on the subject of non-Fourier heat conduction, this non-Fourier effect is small, except under rather extreme environments and short transient. The influence of surface curvature of a solid surface with non-Fourier heat conduction are given by equations (20) and (29). These results show how the surface temperature or heat flux is modified by the surface curvature during the short period when non-Fourier effect is significant. In practice, these solutions can provide an engineer a simple means to check the significant, of both non-Fourier and curvature effect under extreme conditions.

References

1 Maurer, M. J., "Relaxation Model for Heat Conduction in Metals," *Journal of Applied Physics*, Vol. 40, 1969, p. 5123

2 Brazel, J. P., and Nolan, E. J., "Non-Fourier Effects in the Transmission of Heat," *Proceedings 6th Conference on Thermal Conductivity*, Dayton, Ohio, 1966.

3 Nettleton, R. E., "Relaxation Theory of Thermal Conduction in Liquids," *Physics of Fluids*, Vol. 3, 1960, p. 216.

4 Weymenn, H. D., "Finite Speed of Propagation in Heat Conduction, Diffusion and Viscous Shear Motion", *American Journal of Physics*, Vol. 35, 1967, p. 488.

5 Maurer, M. J., and Thompson, H. A., "Non-Fourier Effects at High Heat Flux," JOURNAL OF HEAT TRANSFER, TRANS. ASME, Series C, Vol. 15, May, 1973, pp. 284–286.

6 Kazimi, M. S., and Erdmen, C. A., "On the Interface Temperature of Two Suddenly Contacting Materials," JOURNAL OF HEAT TRANSFER, TRANS. ASME, Series C, Vol. 97, Nov. 1975, pp. 615–617.

7 T. Kao, "On Thermally Induced Non-Fourier Stress Waves in a Semi-Infinite Medium," *AIAA Journal*, Vol. 14, No. 6, June 1976, pp. 818–820.

8 Baumeister, K. J., and Hamill, T. D., "Hyperbolic Heat Conduction Equation—A Solution for the Semi-Infinite Body Problem," JOURNAL OF HEAT TRANSFER, TRANS. ASME, Series C, Vol. 91, Nov. 1969, pp. 543–548.

9 Letcher, J. S., "On Boundary Layers in the Theory of Heat Conduction in Solids," *SIAM Review*, Vol. II, No. 1, Jan. 1969, pp. 20–29.

10 Letcher, J. S., "An Improved Theory for Heat Conduction in Thin Layers," JOURNAL OF HEAT TRANSFER, TRANS. ASME, Series C, Vol. 91, Nov. 1969, pp. 585–587.

journal of heat transfer

discussion

Heat Transfer From Spheres in Naturally Turbulent, Outdoor Environment[1]

A. S. Mujumdar.[2] The authors should be complimented for an interesting experimental investigation that clearly demonstrates that near the ground the heat transfer from spherical bodies is higher than what would be estimated from wind tunnel tests using artificially induced turbulence. However, they do not offer any physical explanation for this phenomenon. The objective of this discussion is to present a possible explanation that would have to be tested by direct experimentation.

The main difference between the wind tunnel studies the authors refer to and the naturally turbulent flow is of course the presence of shear and turbulence intensity gradients and the scale (temporal and spatial). Effects of shear and turbulence intensity gradients may be ignored since the test spheres were only 7.62 cm dia. However the temporal and spatial scales are one or several orders-of-magnitude different. The scale of turbulence referred to in references [7–9] is different from the mixing length concept used by the authors. In my opinion the main difficulty in studying small objects in atmospheric turbulence resides in the definition of the appropriate scale of turbulence.

Since natural turbulence contains very small frequency fluctuations (i.e., very large wavelength disturbances which contribute significantly to the extremely large spatial scales calculated), when studying small objects one must decide what the lowest frequency is of a truly turbulent fluctuation. In other words, depending upon the low frequency "cut-off" so chosen, a corrected turbulence intensity can be computed. Thus, one must (unfortunately, empirically) define the low frequency (or low wavenumber) cut-off of the turbulence energy spectrum and then proceed to compute the turbulence scale and intensity either digitally or using analog circuitry. Both the scale and intensity thus obtained will be lower than the ones obtained by the authors which will in turn bring their results closer to the wind tunnel measurements.

In the opinion of the discusser the very low frequency fluctuations contained in natural turbulence would be seen by the small spheres as fluctuations in the magnitude and direction of the mean incident velocity (i.e., mean Reynolds number). Thus there would be some augmentation in the local and mean heat transfer rates because the body is effectively exposed to an oscillatory external flow.

Another plausible physical explanation for the phenomenon observed by the authors is that low frequency fluctuations of turbulence generally are more "energetic" and hence are better able to penetrate into the wall region and enhance the heat transfer rate. Natural turbulence has more energy contained in the low frequency region than does wind tunnel turbulence. Thus the authors' results are hardly unexpected. Some recent studies on turbulent heat transfer in pipe flow lend support to this hypothesis. It has been observed, for example, that there is a better correlation between velocity and temperature fluctuations (in the wall region) at the low frequency end of the spectrum than at the high frequency end. Indeed, at very high frequencies the two are statistically independent.

Unfortunately little work appears to have been done on assessing the influence of the turbulence spectrum on heat transfer from bluff bodies. Mujumdar and Douglas[4] made perhaps the first and only preliminary study of the effect of the free-stream turbulence spectrum on heat transfer from cylinders in cross-flow. Although these results were not sufficiently extensive they indicated that the low frequency of the spectrum is more important than the low energy, high frequency region of external turbulence in enhancing blunt body heat transfer.

Finally, if the authors have made spectral measurements of turbulence under conditions encountered in the heat transfer study, I would appreciate their comments on the hypotheses proposed here. Ideally, a more conclusive proof will require measurement of the cross-correlation between the external turbulence fluctuations and wall heat transfer fluctuation.

Authors' Closure

The authors appreciate the comments of Professor Mujumdar, and agree that the physical reasons for the large enhancement in heat transfer for spheres near the ground are not well understood. We feel that the agreement between much of the present data and the wind tunnel tests, as represented in Fig. 6 of the paper, implies that the same mechanisms are present here as in wind tunnels.

The suggestion that low frequency (large scale) fluctuations act to expose the spheres to an oscillatory flow is plausible although it should be realized that oscillations occur in flow direction as well as magnitude. However, the greatest discrepancy represented in Fig. 6 is not for the lowest oscillations which occur at the greatest height. Also, it does not seem that lowered computed values of scale and intensity will bring our results more in line with wind tunnel measurements. Rather, our results are compatible with the higher values (Fig. 6). We were mainly interested in determining heat transfer coefficients, and did not make any turbulence measurements to support these suggestions.

As discussed in the paper, turbulence scale has been found to have a negligible effect in wind tunnel studies. Our results, in the main, agree with this conclusion, even though, as the discussor points out, the conventional definition of scale differs from that used in the paper (i.e., mixing length). It is only for the largest sphere closest to the

[2] by G. J. Kowalski and J. W. Mitchell, published in the Nov. 1976 issue of the JOURNAL OF HEAT TRANSFER, TRANS. ASME, Series C, Vol. 98, No. 4, pp. 649–653.

[3] Asst. Professor, Department of Chemical Engineering, McGill University, Montreal, Canada.

[4] Mujumdar, A. S., and Douglas, W. J. M., "Some Effects of Turbulence and Wake-Induced Periodicity on Local Heat Transfer From Cylinders in Cross-Flow," 20th Canadian Society Chemical Engineering Conference, Sarnia, Ontario, Canada, Oct. 1970.

ground that a significant difference between outdoor and wind tunnel tests occurs. Here, the ratio of mixing length to sphere diameter is about 0.5, and it may be that there is some effect in this range. We agree that further experiments are needed to resolve the apparent discrepancies, and to better understand the reasons for enhanced heat transfer outdoors.

A Mathematical Model for Transient Subchannel Analysis of Rod-Bundle in Nuclear Fuel Elements[1]

S. Gołos.[2] Dr. Rowe in his paper describing the COBRA-III program assumes that "one-dimensional two-phase *slip flow* exists in each selected flow subchannel during boiling." Such assumption means that the slip ratio, following the definition of Dr. Tong[3] is as follows:

$$S = \frac{V_v}{V_\ell} = \frac{X}{1-X} \cdot \frac{1-\alpha}{\alpha} \cdot \frac{\rho_\ell}{\rho_v}, \tag{1}$$

where:
V_v = axial velocity of saturated vapor,
V_ℓ = axial velocity of saturated liquid,
X = quality,
α = void fraction,
ρ_ℓ = density of saturated liquid,
ρ_v = density of saturated vapor,
does not equal one.

Dr. Rowe has obtained his equation (3) using the relation:

$$m = \rho \cdot A \cdot u \tag{2}$$

from which he obtains his effective momentum velocity

$$u = \frac{m \cdot v'}{A} \tag{3}$$

From the foregoing relations it follows immediately that Dr. Rowe uses the identity

$$v' = \frac{1}{\rho} \tag{4}$$

The density of two-phase medium is described, using the definitions of Dr. Tong and Dr. Rowe, as well by the relation:

$$\rho = \alpha \cdot \rho_v + (1-\alpha) \cdot \rho_\ell \tag{5}$$

However the effective specific volume for momentum is defined as:

$$v' = \frac{X^2}{\alpha \cdot \rho_v} + \frac{(1-X)^2}{(1-\alpha) \cdot \rho_\ell} \tag{6}$$

Inserting relation (1) into equation (6) one obtains for v'[1] the following form of (6):

$$v' = \frac{1}{\alpha \cdot \rho_v + (1-\alpha) \cdot \rho_\ell} \cdot \left[1 + X \cdot (1-X) \cdot \left(S + \frac{1}{S} - 2\right)\right] \tag{7}$$

or

$$v' = \frac{1}{\rho} \cdot [1 + X \cdot (1-X) \cdot (S-1)^2/S] \tag{8}$$

It is obvious that identity (4) will only be true in the case when the slip ratio $S = 1$ for $0 < X < 1$. But this fact means that the *nonslip flow* model is taken into consideration, that which contradicts Dr. Rowe's assumption. It seems that Dr. Rowe should not refer to the slip flow model in his paper if just the nonslip flow model is considered.

Author's Closure

A slip flow model is included in the development of the mixture momentum equation of the referenced paper. The claimed contradiction occurs because of the definitions assumed in equations (2) and (4). The entire development of the mixture equations is done by retaining mixture mass flow rate as a total quantity. A definition for velocity as assumed by equation (2) is not used. Since the group mv'/A appears when differentiating the momentum flux terms, this group is defined as the effective momentum velocity and is denoted by u in the referenced paper and by equation (3). Therefore, equation (4) does not follow and the inconsistency does not exist.

Although not stated, the derivation implicitly assumes equal slip ratio for the axial and lateral velocities. While this is satisfactory for many applications, there are some where this could be overly restrictive. For instance, experimental data suggest that the liquid and vapor lateral velocities between subchannels are in counter flow for some situations. Since the slip ratio is not well defined through a flow reversal, an alternate formulation using a drift flux model would be preferred. This model has the added advantage of using a less confusing set of definitions which do not call for "effective" densities or velocities. The physical processes of the flow field are also more clearly displayed in the equations and the model would have wider applications. Modification to include drift flux concepts into the development of the COBRA code are currently being pursued for use in nuclear reactor safety application.

The Numerical Prediction of the Turbulent Flow and Heat Transfer in the Entrance Region of a Parallel Plate Duct[1]

A. S. Mujumdar[2] and **Y-K. Li.**[3] The objective of this communication is to present some new computational results we have obtained using the now well-known TEACH-T computer code[4] developed at Imperial College, London, England, and to compare them with the

[1] By D. S. Rowe, published in the May 1973 issue of the JOURNAL OF HEAT TRANSFER, TRANS. ASME, Series C, Vol. 95, pp. 211–217.

[2] Adjunct, Mem. PTMTS (Polskie Towarzystwo Mechaniki Teoretycznej i Stosowanej (Polish Society of Theoretical and Appl. Mechanics), Institute of Nuclear Research, Department of Reactor Engineering, Otwock—Swierk, Poland.

[3] Tong, L. S., *Boiling Heat Transfer and Two-Phase Flow*, Wiley, New York, 1965, pp. 59, 208.

[1] By A. F. Emery and F. B. Gessner, published in the Nov. 1976 issue of the JOURNAL OF HEAT TRANSFER, TRANS. ASME, Series C, Vol. 98, pp. 594–600.

[2] Asst. Professor, Department of Chemical Engineering, McGill University, Montreal, Quebec, Canada.

[3] Graduate Student, Department of Chemical Engineering, McGill University, Montreal, Quebec, Canada.

[4] Gosman, A. D., Launder, B. E., and Whitelaw, J. H., "Flow, Heat and Mass Transfer in Turbulent Recirculating Flows-Prediction and Measurements," Course Notes, Chemical Engineering Department, McGill University, Montreal, Canada, Aug. 6–8, 1976.

ground that a significant difference between outdoor and wind tunnel tests occurs. Here, the ratio of mixing length to sphere diameter is about 0.5, and it may be that there is some effect in this range. We agree that further experiments are needed to resolve the apparent discrepancies, and to better understand the reasons for enhanced heat transfer outdoors.

A Mathematical Model for Transient Subchannel Analysis of Rod-Bundle in Nuclear Fuel Elements[1]

S. Gołos.[2] Dr. Rowe in his paper describing the COBRA-III program assumes that "one-dimensional two-phase *slip flow* exists in each selected flow subchannel during boiling." Such assumption means that the slip ratio, following the definition of Dr. Tong[3] is as follows:

$$S = \frac{V_v}{V_\ell} = \frac{X}{1-X} \cdot \frac{1-\alpha}{\alpha} \cdot \frac{\rho_\ell}{\rho_v}, \tag{1}$$

where:
V_v = axial velocity of saturated vapor,
V_ℓ = axial velocity of saturated liquid,
X = quality,
α = void fraction,
ρ_ℓ = density of saturated liquid,
ρ_v = density of saturated vapor,
does not equal one.

Dr. Rowe has obtained his equation (3) using the relation:

$$m = \rho \cdot A \cdot u \tag{2}$$

from which he obtains his effective momentum velocity

$$u = \frac{m \cdot v'}{A} \tag{3}$$

From the foregoing relations it follows immediately that Dr. Rowe uses the identity

$$v' = \frac{1}{\rho} \tag{4}$$

The density of two-phase medium is described, using the definitions of Dr. Tong and Dr. Rowe, as well by the relation:

$$\rho = \alpha \cdot \rho_v + (1-\alpha) \cdot \rho_\ell \tag{5}$$

However the effective specific volume for momentum is defined as:

$$v' = \frac{X^2}{\alpha \cdot \rho_v} + \frac{(1-X)^2}{(1-\alpha) \cdot \rho_\ell} \tag{6}$$

Inserting relation (1) into equation (6) one obtains for v'[1] the following form of (6):

$$v' = \frac{1}{\alpha \cdot \rho_v + (1-\alpha) \cdot \rho_\ell} \cdot \left[1 + X \cdot (1-X) \cdot \left(S + \frac{1}{S} - 2\right)\right] \tag{7}$$

or

$$v' = \frac{1}{\rho} \cdot [1 + X \cdot (1-X) \cdot (S-1)^2/S] \tag{8}$$

It is obvious that identity (4) will only be true in the case when the slip ratio $S = 1$ for $0 < X < 1$. But this fact means that the *nonslip flow* model is taken into consideration, that which contradicts Dr. Rowe's assumption. It seems that Dr. Rowe should not refer to the slip flow model in his paper if just the nonslip flow model is considered.

Author's Closure

A slip flow model is included in the development of the mixture momentum equation of the referenced paper. The claimed contradiction occurs because of the definitions assumed in equations (2) and (4). The entire development of the mixture equations is done by retaining mixture mass flow rate as a total quantity. A definition for velocity as assumed by equation (2) is not used. Since the group mv'/A appears when differentiating the momentum flux terms, this group is defined as the effective momentum velocity and is denoted by u in the referenced paper and by equation (3). Therefore, equation (4) does not follow and the inconsistency does not exist.

Although not stated, the derivation implicitly assumes equal slip ratio for the axial and lateral velocities. While this is satisfactory for many applications, there are some where this could be overly restrictive. For instance, experimental data suggest that the liquid and vapor lateral velocities between subchannels are in counter flow for some situations. Since the slip ratio is not well defined through a flow reversal, an alternate formulation using a drift flux model would be preferred. This model has the added advantage of using a less confusing set of definitions which do not call for "effective" densities or velocities. The physical processes of the flow field are also more clearly displayed in the equations and the model would have wider applications. Modification to include drift flux concepts into the development of the COBRA code are currently being pursued for use in nuclear reactor safety application.

The Numerical Prediction of the Turbulent Flow and Heat Transfer in the Entrance Region of a Parallel Plate Duct[1]

A. S. Mujumdar[2] and **Y-K. Li.**[3] The objective of this communication is to present some new computational results we have obtained using the now well-known TEACH-T computer code[4] developed at Imperial College, London, England, and to compare them with the

[1] By D. S. Rowe, published in the May 1973 issue of the JOURNAL OF HEAT TRANSFER, TRANS. ASME, Series C, Vol. 95, pp. 211–217.

[2] Adjunct, Mem. PTMTS (Polskie Towarzystwo Mechaniki Teoretycznej i Stosowanej (Polish Society of Theoretical and Appl. Mechanics), Institute of Nuclear Research, Department of Reactor Engineering, Otwock—Swierk, Poland.

[3] Tong, L. S., *Boiling Heat Transfer and Two-Phase Flow*, Wiley, New York, 1965, pp. 59, 208.

[1] By A. F. Emery and F. B. Gessner, published in the Nov. 1976 issue of the JOURNAL OF HEAT TRANSFER, TRANS. ASME, Series C, Vol. 98, pp. 594–600.

[2] Asst. Professor, Department of Chemical Engineering, McGill University, Montreal, Quebec, Canada.

[3] Graduate Student, Department of Chemical Engineering, McGill University, Montreal, Quebec, Canada.

[4] Gosman, A. D., Launder, B. E., and Whitelaw, J. H., "Flow, Heat and Mass Transfer in Turbulent Recirculating Flows-Prediction and Measurements," Course Notes, Chemical Engineering Department, McGill University, Montreal, Canada, Aug. 6–8, 1976.